Development of Microstructure, Crystallographic Texture and Residual Stress in the interface region between substrate and a layer made by additive deposition during hybrid manufacturing of IN718

University of Strathclyde

Doctoral Thesis

Author: Matthew David Ferguson

Supervisors: Dr. Tatyana Konkova & Dr. Ioannis Violatos

A thesis submitted in fulfilment of the requirements

for the degree of Doctor of Philosophy (PhD)

2024

Declaration

This thesis is the result of the author's original research. It has been composed by the author and has not been previously submitted for examination which has led to the award of a degree.

(Author)

Date

Abstract

This research investigates how process variables in Laser Metal Deposition (LMD) of IN718 influence microstructural characteristics, residual stress distribution, and mechanical properties across the interface region in both as-deposited and post-weld heat-treated conditions for repair applications and feature additions. Specifically, the study explores the viability of LMD for IN718 components, such as hot compression disks, with a focus on the interface region. Microstructural analysis was performed using optical and scanning electron microscopy, electron backscatter diffraction, and energy-dispersive spectroscopy to characterize the metallurgical properties. Both as-deposited and post-weld heat-treated conditions were evaluated, with additional analysis of microhardness to understand the influence of laser power. Residual stresses were quantified using the multiple-axis contour method and X-ray diffraction (XRD) measurements. A thermal model was developed to predict in-situ temperature histories, correlating with microstructural features and solidification patterns. A sequential de-coupled thermo-mechanical FEA model, calibrated experimentally, was employed to analyse residual stress behaviour and the influence laser power had on residual stress fields.

The microstructure was shown to exhibit large columnar γ-grains oriented with the build direction and columnar dendrite. The laser power was shown to influence both the γ-grain size and crystallographic texture, which varied between a cube and a <001>//BD fibre. Sub-structure columnar dendrites were observed in the deposited material, extending across multiple layers in some instances. EDX analysis showed migration of alloying elements, with dendrite cores enriched in nickel, iron, and chromium, and inter-dendritic regions enriched in niobium and molybdenum. This migration led to niobium-enriched nucleation sites for Laves phase precipitation, forming networks throughout the build. Furthermore, the laser power was shown to influence the microstructural features like the volume of Laves phase produced and dissolution of precipitated phases in the interface region. Post-weld heat treatment successfully precipitated strengthening γ'' phases, enhancing phase distribution. Additive manufacturing induced complex residual stress fields, primarily from thermal gradients and rapid heating/cooling rates, with the Thermal Gradient Mechanism explaining the phenomenon comprehensively. Maximum tensile stress below the melt pool penetration depth was attributed to extreme thermal gradients and cooling rates. Residual stresses were alleviated during heat treatment, enhancing component integrity. This comprehensive investigation provides insights into optimizing LMD processes for IN718 repair applications and component enhancements.

List of Publications

Ferguson, M. and Konkova, T. and Violatos, I. (2021) '*Microstructural evolution of an interface region in a nickel-based superalloy joint produced by direct energy deposition'*. Proceedings of the International Conference on Welding and Additive Manufacturing, 15. pp. 47-54. ISSN 1307-6892.

Acknowledgements

I would like to express my deepest gratitude to my supervisors, Dr. Tatyana Konkova and Dr. Ioannis Violatos, for their invaluable guidance, support, and encouragement throughout my PhD journey. Their expertise and mentorship have been instrumental in the completion of this thesis. A special thanks to Dr. Dorothy Evans, the doctoral programme coordinator, for setting up this project and providing crucial financial support. Her efforts and dedication have been pivotal to my success.

I am profoundly grateful to the staff at the Advanced Forming Research Centre (AFRC), whose wealth of knowledge has greatly contributed to this research. I extend my thanks to the technicians, Saad Ahmed, Ryan Devine, Kornelia Kondziolka, and Ryan O'Neill, whose assistance and expertise have been essential in making this PhD possible.

I also wish to acknowledge the support of my fellow doctoral researchers, with special mention to Dr. Calum Hicks, Dr. Angus Coyne, and Dr. Michael King. Many of them have been not only excellent co-workers but also good friends. I look forward to future collaborations and wish them every success in their careers. I would like to acknowledge Dr. Laurie Da Silva, my line manager, for providing me with support and guidance throughout this process. Your assistance has been greatly appreciated.

I would like to express my deepest gratitude to my girlfriend, Laura, for her continual support, love, and guidance throughout this journey. Your unwavering belief in me and your encouragement have been my foundation, and I am eternally grateful for your presence in my life.

To my family, thank you for being there throughout the highs and lows of this PhD. Your encouragement and words of wisdom have been a source of strength and motivation, helping me to persevere through the challenges I have faced.

A special thank you to my dog, Bonnie, for keeping me sane during the difficult times of Covid. Your companionship and unconditional love have provided comfort and joy when I needed it most.

To my best friends, thank you for being my pillars of support throughout this journey. Your friendship has been invaluable, and I am grateful for the laughter, advice, and moments of respite you have given me.

Table of contents

List of figures

List of tables

Chapter 1: Introduction

1.1 General Introduction and Research Motivation

Laser Metal Deposition (LMD) is a rapidly growing additive manufacturing technology that offers significant advantages in the repair of high-performance components and the addition of complex features to critical structures. This technique is especially attractive in industries such as aerospace, power generation, and automotive, where high-value parts, like turbine blades, compressor disks, and aerospace engine components, require precise repairs or enhancements to extend their operational life. One of the materials frequently used in these applications is Inconel 718 (IN718), a nickel-based superalloy known for its excellent mechanical properties, high-temperature strength, and corrosion resistance. However, understanding the microstructural evolution, residual stress distribution, and texture formation in IN718 during and after the LMD process is crucial for ensuring the quality, reliability, and durability of the manufactured or repaired components.

IN718 is widely employed in harsh environments, where components are subjected to extreme mechanical loads and elevated temperatures. The alloy derives its strength primarily from the precipitation of γ'' and γ' phases, which provide high resistance to creep, fatigue, and oxidation. However, laser-based manufacturing and repair processes induce complex thermal cycles that can drastically affect the microstructure and residual stress state of the material. These factors have a profound impact on the mechanical performance of IN718, especially in the interface region between the deposited material and the substrate, which is critical in repair applications.

Residual stresses, which develop due to the rapid heating and cooling cycles intrinsic to LMD, can lead to cracking, distortion, and premature failure of components. Additionally, the solidification conditions during LMD influence the grain structure and texture of the material, with large columnar grains and strong crystallographic textures being common in additive manufacturing processes. These microstructural features, along with segregation of alloying elements and the formation of brittle phases such as Laves phase, can reduce the fatigue strength and fracture toughness of the material, compromising its performance in critical applications.

Despite its advantages, LMD faces significant challenges when applied to nickel-based superalloys like IN718. The high thermal gradients and rapid solidification rates can induce non-equilibrium microstructures, leading to inhomogeneous phase distribution,

micro segregation, and the formation of unwanted secondary phases. These effects can impair the mechanical properties of the material and increase the risk of residual stress-induced failures. As a result, it is crucial to investigate how process variables such as laser power, scanning speed, and layer thickness influence the microstructural characteristics, residual stress distribution, and mechanical properties of the material, both in the as-deposited and post-weld heat-treated conditions.

Moreover, post-weld heat treatment (PWHT) is often required to improve the mechanical properties of LMD-processed IN718. Heat treatment can dissolve harmful phases such as Laves and promote the precipitation of strengthening γ'' phases, enhancing the overall strength and durability of the material. However, the interplay between the as-deposited microstructure and the heat-treated condition is not fully understood, particularly regarding the evolution of residual stresses, texture, and microstructural features across the interface region.

Thus, this research aims to address these critical challenges by exploring the influence of LMD process variables on the microstructural evolution, residual stress distribution, and mechanical properties of IN718. The study focuses on both the as-deposited and post-weld heat-treated conditions to provide insights into optimizing LMD for repair applications and feature additions in high-value components. Figure 1.1 demonstrates LMD utilization for damaged aerofoils. By understanding these factors, this work contributes to the advancement of LMD as a reliable technology for the additive repair and manufacture of high-performance parts in demanding environments

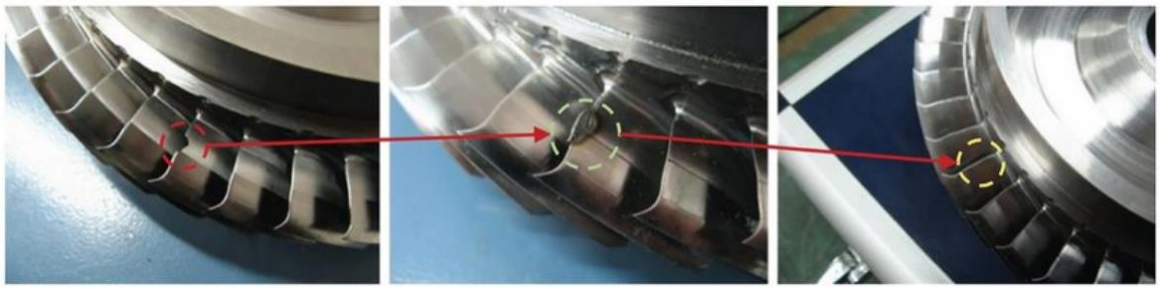

Figure 1.1 Utilization of LMD to repair damaged aerofoils, showing the stages of of repair process from damaged to machined finished. [1].

1.2 Project Aims

This research focuses on assessing the application of Laser Metal Deposition (LMD) using IN718 for repairing components in the hot section, low-pressure section of an aircraft engine, such as the aerofoils, impeller, locking lugs, blade retainers, and casing. The objectives include advancing the understanding of LMD IN718 microstructures,

texture, and associated mechanical properties. Furthermore, the study aims to establish the impact of key LMD process parameters on microstructure and residual stress evolution for optimization. The investigation will explore the microstructure evolution across an interface region for both as deposited and heat-treated conditions, along with associated mechanical properties. Additionally, a comprehensive assessment is necessary to analyse the distribution of as-deposited residual stress and any changes during the LMD repair process and subsequent heat treatment. Lastly, an examination of the effectiveness of Finite Element Analysis (FEA) thermomechanical modelling in predicting as-deposited microstructure and stress profiles will enhance design knowledge.

Primary objectives of the project include:

1. Develop transient thermal models as a tool to understand the LMD solidification conditions and evolution of microstructure across the interface region. The effectiveness and accuracy of thermal modelling for microstructure and microstructural feature prediction of LMD IN718 will be investigated.
2. Characterise the microstructure and texture across the LMD IN718 interface region from the substrate to the deposit across a range of LMD process parameters.
3. Determine the influence key process parameters have on the microstructural evolution during the LMD of IN718.
4. To characterise the deposited layer morphology, and the influence of subsequent thermal cycling during each following deposition pass, and to understand the effect of the prior substrate texture on the deposit texture.
5. Characterise the microstructure of LMD IN718 heat-treated to an industry standard schedule required by fasters and blade retainer forgings.
6. Investigate the residual stress distribution in as-deposited components and heat treated condition to understand its effect on post-machining.
7. Develop a transient thermo-mechanical model which will facilitate the understanding of *in situ* stress behaviour and post-deposition equilibrium behaviour.

1.3 Thesis Structure

This thesis investigates the microstructure and crystallographic texture evolution across the interface of a Laser Metal Deposition (LMD) joint in IN718 alloy, along with the resulting residual stress behaviour. A validated thermomechanical model for additive manufacturing was used to analyse temperature and stress responses.

- Chapter 1 introduces the project, discussing the benefits and challenges of LMD in additive manufacturing, with specific focus on IN718.
- Chapter 2 reviews the metallurgy of nickel-based superalloys, heat treatments, and relevant literature on LMD and IN718.
- Chapter 3 details the experimental setup, materials, and procedures, including residual stress analysis techniques.
- Chapter 4 focuses on melt pool formation and temperature evaluation in LMD IN718, analysing process parameter effects.
- Chapter 5 introduces a finite element analysis model, validating it with experimental results to study temperature field impacts on microstructure.
- Chapter 6 investigates microstructure and texture evolution during LMD, discussing the influence of thermal history and heat treatment.
- Chapter 7 examines how LMD parameters affect material geometry, microstructure, and hardness.
- Chapter 8 analyses residual stresses, using contour and XRD methods to understand their development.
- Chapter 9 summarizes findings, evaluates LMD for IN718 repair, and suggests future research directions.

Chapter 2: Literature review

2.1 Overview of Material

Inconel 718 (IN718), a nickel-based precipitation-hardened superalloy, is widely utilized in demanding operating conditions, particularly in low-pressure turbine blades, aero gas turbine sections, and high-pressure gas wells. It possesses exceptional strength, fatigue resistance, and corrosion resistance. The aerospace industry benefits significantly from its application in turbine blades for high-pressure operations, showcasing excellent creep strength up to 650°C [1].

In recent times, there has been substantial research interest in the laser metal deposition of Inconel 718 Alloy. This attention is primarily driven by the unique microstructural characteristics achieved, attributed to the alloy's low aluminium and titanium content. Conventional manufacturing processes for Inconel 718 sections entail drawbacks such as extended production cycles, high material wastage (resulting from post-manufacture machining), and elevated costs associated with thermo-mechanical processing, which involves high input energy.

Inconel 718, a leading superalloy, excels in intense operating conditions and finds widespread use in hydrocarbon extraction equipment, particularly in combating corrosive elements like hydrogen sulphide, carbon dioxide, and chlorides [2]. Alongside aero-foils on a aircraft engine blisk, Schlumberger has employed it in downhole applications, where aggressive volumes of hydrochloric acid are utilized to facilitate the extraction process. The alloy's superior corrosion resistance extends to hydrogen embrittlement and aggressive pitting, making it a preferred choice for aero-engine sections, with exceptional creep rupture strength up to 980°C [3]. However, a deeper understanding of its microstructures and phases is essential to meet the rising demand. Despite being highly weldable, challenges such as strain age cracking and Heat Affected Zone (HAZ) micro-fissuring necessitate careful consideration of the alloy's chemical composition during welding, especially with the introduction of Niobium as an age hardener, which introduces a further challenge of Laves phase formation in the fusion zone [4]. Table 2.1 outlines a nominal chemical composition of the alloy, detailing the volume of key alloying elements.

Table 2.1 ATSM standard Inconel 718 chemical composition [5].

Element	Ni	Cr	Fe	Nb & Ta	Mo	Ti	Co	Al	Mn	C	Other Elements
Composition (%wt.)	50 - 55	17 - 21	Balance	4.75 - 5.5	2.8 - 3.3	0.65 - 1.15	≤1	0.2 - 0.8	≤0.35	0.02-0.05	Si, Cu, N, O, P, Ca, Mg, Se

The precipitate-hardening nickel-iron-chromium superalloy exhibits excellent flow stress behaviour at elevated temperatures, which is constant from room temperature up to around 650°C [6]. To categorize a superalloy, three attributes are often defined [7]:

1. Withstand significant loads at homologous temperatures up to $0.6T_{m.}$
2. Resist mechanical degradation at elevated temperatures, i.e., thermally activated, inelastic creep.
3. Be able to withstand highly corrosive operating conditions such as hot gases, high sulphur content and the ability to withstand seawater intake which promotes oxidation.

The two precipitates that considerably enhance the mechanical properties are coherent ordered spherical face-centred cubic (FCC) γ' phase comprising of Ni_3 (Al, Ti) and articulate disc-shaped body-centred cubic tetragonal γ'' phase encompassing nickel, niobium, titanium and aluminium Ni_3 (Nb, Ti, Al) The most important strengthening mechanism arises from the γ'' precipitates [6]. Understanding the importance of strengthening precipitates, temperature and creep was demonstrated by Rahimi et al [8]. Figure 2.1. shows the IN718 tensile stress relaxation behaviours at elevated temperatures, the stress-strain curves highlight the importance of temperature and creep for IN718 applications.

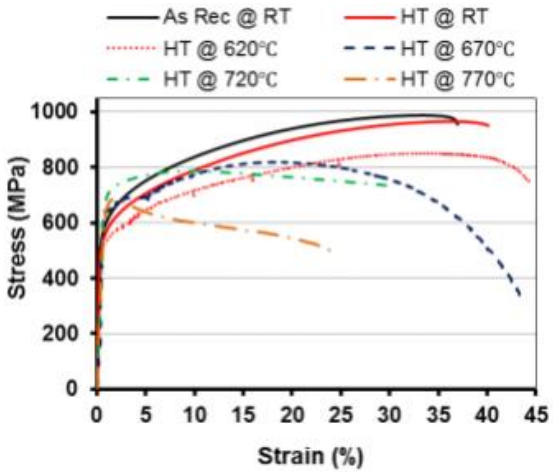

Figure 2.1 Engineering stress-strain curves for the heat-treated microstructure (HT) at various temperatures, with data from the as-received material included for comparison [8].

2.2 Microstructural phases of Inconel 718

Inconel 718 demonstrates exceptional mechanical properties across a broad spectrum of temperatures, ranging from 250°C for applications such as liquid storage containers to 650~700°C, where it serves as the primary alloy for turbine disc applications [23]. This extensive operational capability can be attributed to the microstructural characteristics and hardening mechanisms inherent in the material, primarily achieved through a solid solution/precipitation hardening process. As a precipitation-strengthened nickel-based superalloy, the principal source of strength in Inconel 718 arises from the formation of γ'' [24]. The investigation of phase stability assumes significant importance in optimizing the superalloy's mechanical properties. The main phases present in Inconel 718 are (detailed in Table 2.2): gamma prime (γ') face ordered – face centred cubic - $Ni_3(Al, Ti)$; gamma double prime (γ'') BCT – body centred tetragonal – Ni_3Nb; hexagonal ordered Ni_3Ti (η); orthorhombic ordered Ni_3Nb delta δ intermetallic compounds and other topological close-packed structures including μ and Laves phase [9].

The microstructure of superalloys is characterized by an amalgamation of various phases, (highlighted in Table 2.2), encompassing [10]:

- The gamma phase, denoted as γ, exhibits an FCC structure and in most cases forms a continuous, matrix phase to which all other phases are retained. A significant concentration of elements such as cobalt, chromium, molybdenum, ruthenium, and rhenium.
- The gamma prime precipitate, denoted as γ' and forms the precipitates which is coherent with the γ-matrix and rich in elements such as aluminium, titanium and tantalum. In the nickel-iron superalloys a related γ'' is preferred over γ'.

- Carbides and borides are often formed when Carbon, usually present at concentrations around 0.2% reacts with titanium, tantalum and hafnium to form MC carbides. During processing these often decompose residing on the γ grain boundaries which are rich in chromium, molybdenum and tungsten.
- The major hardening phase is the metastable γ'' (Ni_3Nb) phase which transforms to incoherent orthorhombic δ (Ni_3Nb) phase in equilibrium. All three major strength contributing phases are of the A_3B type: where γ'' and δ phases are based on the composition Ni_3Nb, whereas the γ' phase contains $Ni_3(AlTi)$ [11].

With a large capacity for solid solution hardening elements such as iron, chromium, molybdenum, tungsten, vanadium, titanium and aluminium. These elements have atomic diameters 1 -13% larger than that of Nickel which attributes to the hardening effect [12].

Table 2.2 IN718 phases [13].

Phase	Crystal structure	Chemical formula
γ	fcc	Ni
γ''	bct (ordered $D0_{22}$)	Ni_3Nb
γ'	fcc (ordered $L1_2$)	$Ni_3(Al,Ti)$
δ	orthorhombic (ordered $D0_a$)	Ni_3Nb
MC	cubic B_1	(Nb,Ti)C
Laves	hexagonal C_{14}	$(Ni,Fe,Cr)_2(Nb,Mo,Ti)$

2.2.1 Gamma Prime (γ') and Gamma Double Prime (γ'')

The IN718 superalloy derives its primary strength from the uniform distribution of precipitates of gamma double prime, γ', which form between 600°C and 900°C [14]. This alloy exhibits superior mechanical properties, attributed to the dispersion of precipitates possessing super lattice crystal structures within the face-centred cubic gamma (γ) matrix. These precipitates (seen in Figure 2.2) impede dislocation movement by incurring an energy penalty associated with their faulting following the passage of single dislocations [15]. Crystallographically, the intermetallic gamma prime features a face-centred cubic (L1_2) Ni3 (Ti, Al) development, containing over 2 wt.% combined Al + Ti content post-appropriate heat treatment [12]. In contrast, intermetallic Ni3Nb (γ'') coexists with γ' and has a body-centred tetragonal crystal structure with approximately 5 wt.% Nb. Gamma prime precipitation predominantly occurs via grain boundary nucleation, although the majority disperses uniformly throughout the γ matrix [29]. Nucleation is facilitated by crystallographic coherency between the gamma and gamma prime phases, hindering particle coarsening. Gamma double prime exhibits slower precipitation kinetics, being

metastable, with delta phase stability prevailing above 850°C. Rapid coarsening kinetics further diminish useful stability to about 700°C [12].

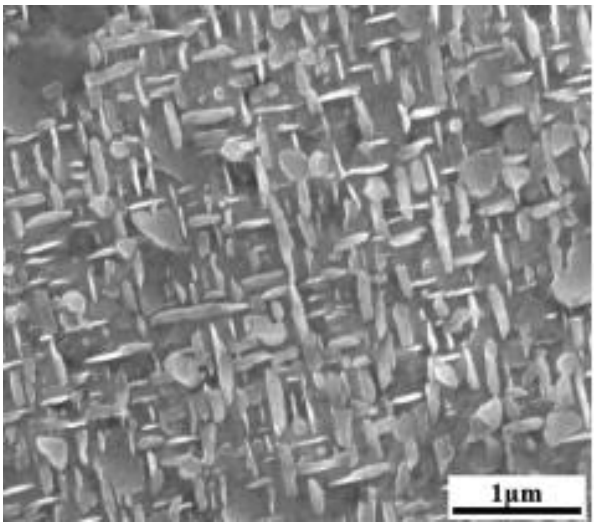

Figure 2.2 Intergranular γ'/γ'' phases in the austenitic matrix after SHT (1095 ◦C × 1 h/air cooling + 955 ◦C × 1 h/air cooling + 720 ◦C × 8h/furnace cooling at 56 ◦C/h to 620 ◦C × 8 h/air) [16].

The lattice mismatch at γ'/γ and γ''/γ interfaces serves as a strengthening mechanism by impeding dislocation movement, enhancing Inconel's strength. Additionally, the anti-phase boundary (APB) energy in ordered γ' and γ'' phases correlate with the energy required for dislocations to traverse these phases [30]. Gamma double prime (γ'') is the primary strengthener in IN718, stable between 500°C and 900°C, precipitating with a {100}γ habit and configuring the orientation relationship {100}γ'' // {100}γ ; [001]γ'' // <001>γ within the austenitic matrix [33]. A small amount of gamma prime is present in the 600°C to 900°C range, exhibiting a cube-to-cube orientation relationship with the matrix [17].

Tailoring the size distribution of embedded gamma-prime (γ') precipitates is achievable through varied heat treatments, optimizing mechanical properties for specific applications [18]. The material's performance is intricately linked to changes in precipitate size distribution (PSD) and phase chemistry, necessitating precise control and understanding of these aspects during cooling [19]. The strength of Ni-base superalloys is established through microstructural parameters like volume fraction, morphology, and size distribution of γ' precipitates [10]. Increasing the concentration of precipitate-forming elements enhances the volume fraction of precipitates, consequently strengthening the alloy [20].

The volumetric relationship between γ'' and γ' in the context of IN718 alloy has been documented to be approximately 3 according to literature [21], [22]. Li *et al.* [22] proposed that heat treatment does not significantly alter this fraction ratio. They observed that hot-rolled IN718, subjected to AMS5663 heat treatment, contained approximately 12.33 wt. % of the combined phases γ' + γ''. In peak-aged IN718, the volume fraction of γ'' is approximately 15%, whereas γ' constitutes only about 4% [23]. Consequently, it can be inferred that the γ' phase does not contribute significantly to the strength of IN718; the primary source of strengthening arises from the γ'' phase, attributed to a higher lattice mismatch and volume fraction combination [24].

2.2.2 The δ phase

In IN718, the orthorhombic crystal structure of Ni3Nb-δ forms grain boundary precipitates, typically nucleating between 700 and 1000°C [14] or within the range of 750–1020°C [25], with the fastest nucleation around 900°C [14]. Originating at γ grain boundaries, it evolves into thin plates and elongates into phase grains, exhibiting full incoherence with the γ matrix [12]. While its strengthening impact is modest, it effectively inhibits grain growth by pinning the grain boundaries (Figure 2.3). At extreme temperatures, the δ phase nucleates from the γ matrix, and at lower temperatures, over-aging of the γ'' phase transforms into needle-shaped δ [17]. Strengthening by γ'' over γ' is influenced by coherency with the matrix and tetragonal γ'' c-axis distortion. Beyond 650°C, the γ'' phase decomposes to the thermodynamically stable δ phase, leading to a concurrent strength decline [15]. This transition from γ'' to δ strengthening mechanisms accelerates above 650°C, limiting applicability to sub-conversion temperatures [26] . Delta phase precipitation occurs around 750–1050°C, with the δ phase directly precipitating from supersaturated γ matrix within 900–1000°C, exhibiting plate-shaped or globular morphologies at grain and twin boundaries [27].

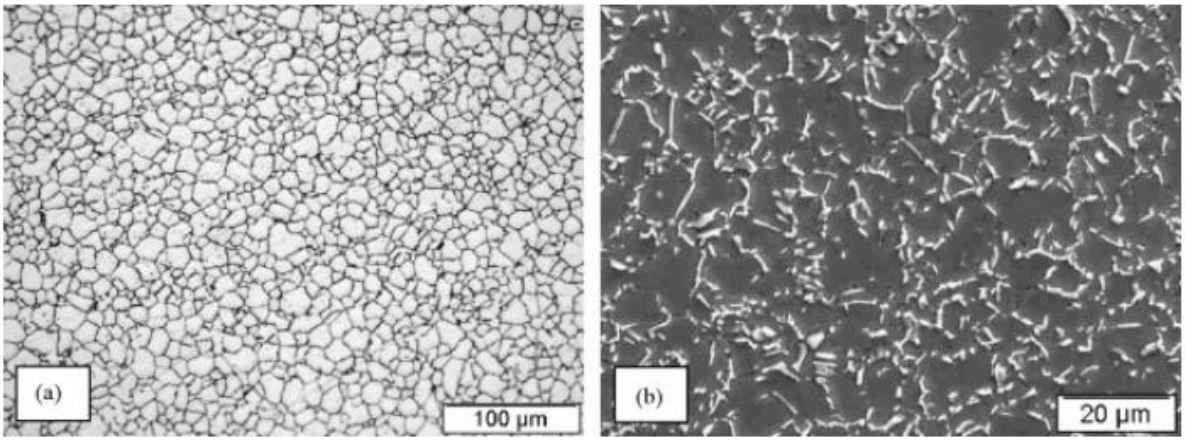

Figure 2.3 Inconel 718 Microstructure after thermomechanical treatment (a) grain size and (b) grain boundary δ-phase precipitation distribution [28].

The formation of δ precipitates in Inconel 718 is influenced by multi-element interactions and the coherent mismatch between γ'' and γ matrix [13]. Adjusting the Al/Ti ratio (beyond 1) or increasing the Al + Ti content reduces the lattice mismatch and volume fraction of γ'', inhibiting the driving force for δ phase precipitation [26][29]. Saturation of δ-phase precipitation depends on aging temperature and alloy composition [25]. Despite their morphology, δ-phase precipitates contribute minimally to IN718 strengthening. In fatigue crack propagation studies at room temperature, increased granular δ phase volumes accelerated the fatigue crack growth rate. γ'' phase transformation to δ, induced by aging time, hinders γ matrix strength [30]. The needle-like δ phase impedes dislocation movement, decreasing fatigue crack propagation [31]. During isothermal compression, plate-like δ phases spheroidize due to deformation and dissolution breakage [32]. Short-rod δ phases form on grain boundaries, significantly impacting fatigue performance alongside other strengthening phases [31].

Nucleating at grain boundaries, δ-phase precipitation follows γ'' up to around 900°C, with δ forming partially through γ'' transformation below this temperature. Between 900°C and 960°C, δ precipitates rapidly and intragranularly [12]. The crystallographic relation between γ matrix and δ-phase plate morphology is [12]:

$$\{111\}_{\gamma} \parallel (010)_{\delta;} \langle 110 \rangle_{\gamma} \parallel [100]_{\delta}$$

Phase transformations occur under specific temperature and time conditions, with γ'' transitioning to stable δ. Up to 900°C, γ'' phase precipitates before δ, beyond which further γ'' phase precipitation is not possible.

2.2.3 MC Carbide

MC carbide formation results from the interaction of carbon (up to 0.2%) with reactive elements like titanium, tantalum, and hafnium. Typically decomposing into chromium, molybdenum, and tungsten-rich M23C6 and M6C, these carbides settle on γ-grain boundaries [10]. The primary carbide, denoted as NC or (Nb, Ti)C, appears as discrete block shapes irregularly distributed within grains and along grain boundaries [13]. These boundary carbides prompt a fracture mode transition from transgranular to intergranular at room temperatures. During plastic deformation, stress concentration at the carbide/matrix interface induces micro-cracks, relieving localized stress. Depending on carbide distribution, these micro-cracks coalesce, facilitating intergranular fracture and, with sufficient size, restricting grain boundary movement to enhance rupture life [13].

2.2.4 Laves Phase

The formation of the brittle intermetallic Laves phase, represented as (Ni, Cr, Fe)2(Nb, Mo, Ti), often occurs in interdendritic regions (seen in Figure 2.4), adversely impacting morphology and composition of the Laves phase depend strongly on the thermal cycle the material undergoes [33][34]. Micron-scaled Laves, hard and brittle with irregular shapes, form due to micro-segregation of alloying elements at the end of solidification [35]. The rejection of alloying elements from dendrites during solidification, particularly high Cr and Fe content, leads to Laves phase formation in slow solidification processes, along with Nb segregation [36]. The presence of Laves phase within the structure significantly reduces mechanical properties, causing a decline in ductility, ultimate tensile strength, and fatigue behaviour [37], [38], [39]. Homogenization, an effective post-weld heat treatment, dissolves the Laves phase into the matrix to precipitate strengthening phases like γ''. However, challenges such as grain growth and recrystallization may arise, presenting practical concerns [40][41].

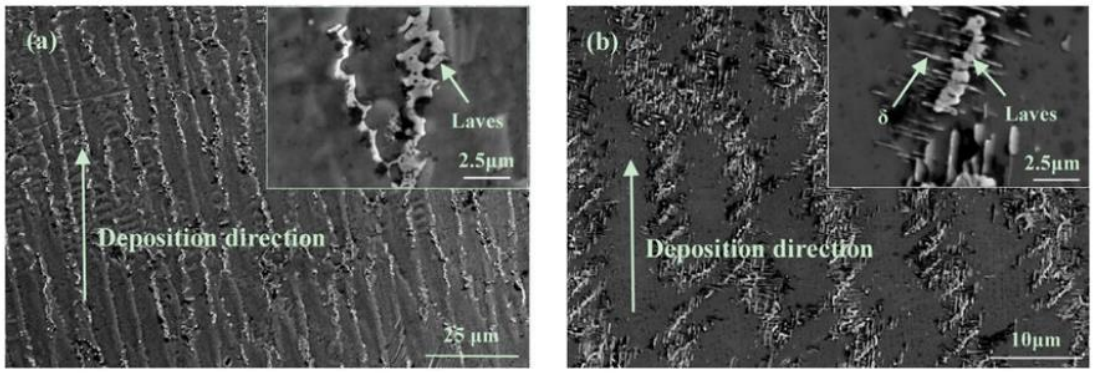

Figure 2.4 Morphology of the laves phase and δ phase in LMD Inconel 718 alloy (a) morphology in the as-deposited samples and (b) after ageing at 890°C for 12h [42].

Controlling Laves Phase through deposition techniques.

Controlling the behaviour of the Laser Metal Deposition (LMD) machine is crucial for solidification phase production. Although beyond the project's scope, current techniques for tailoring microstructural phases are discussed. Altering the pulsing technique with helium shielding gas during GTA welding significantly reduced the Laves phase volume fraction. Employing a compound current pulsing technique with helium instead of argon for shielding gas reduced the continuity and thickness of the Laves phase. Helium acted as an inert convective medium, enhancing the weld cooling rate from 43.2°C/s to 394.3°C/s, completely diminishing the Laves network [4]. This resulted in a microstructure with a mixed fusion zone of coarse equiaxed and predominant columnar dendrites [4]. The compound current pulsing pattern promoted constitutional supercooling, reducing the time at the molten pool temperature, and encouraging equiaxed dendrites. Using the higher equilibrium partition coefficient of Mo, Mo was favoured for rejection into the interdendritic liquid [43], promoting solute undercooling and microstructure refinement [4]. This modification led to a reduction in Nb micro-segregation by 25-32% [44], improving mechanical and creep properties. The accelerated fatigue crack growth and reduced low cycle fatigue life associated with the Laves phase were mitigated, as constitutional undercooling melted off secondary arms, hindering crack initiation and propagation [39].

Laves Phase Control Using Quasi-Continuous-Wave

The technique involves operating the laser in short intervals to minimize thermal effects yet maintain a near-steady state. Employing a modulated square wave with a 50% duty cycle for Inconel 718 powder melting in laser additive manufacturing, thermal analysis revealed periodic temperature oscillations. The laser on-phase peaked rapidly at 2050°C in 5 ms, stayed at 2000°C for 30 ms, and cooled below solidification temperature before the next pulse, achieving a peak cooling rate of 1.3×10^5 C/s and an average cooling rate of 2.0×10^4 °C/s [45]. Enhanced cooling rates in Quasi-Continuous Wave (QCW) modify solidification conditions, limiting Nb segregation and suppressing continual Nb concentration increase for Laves formation [46].

While rapid cooling increases thermal-cracking probability, the fine equiaxed dendritic structure with dispersed Laves phase particles reduces this risk. Mechanical properties are enhanced through microstructure refinement, but the main precipitating phase, γ'', requires further aging. Post-deposition heat treatments at 925°C and 980°C dissolve Laves phase to some extent, with needle-like delta phase precipitating around Laves particles. At 1038°C, above δ-solvus temperature, Laves phase diminishes.

Considerations for post-weld treatments are crucial, as direct aging versus solution treatment followed by aging may lead to δ-phase precipitation due to low heating rates and Laves phase dissolution during STA, especially in interdendritic regions with rich Nb content [47].

2.2.5 Solidification Processes

Understanding solidification is crucial in engineering materials, especially in research and development. In a molten state, materials are easily shaped during manufacturing, as shear stress approaches zero. However, solid materials have higher flow stress, requiring overcoming in processes like forging. Solidification involves extracting heat through conduction, convection, or radiation, and controlling the energy extraction rate is key. Heat flux, a complex system, includes cooling rate, solid formation rate, specific heat, and latent heat of fusion. This is significant in additive manufacturing, where grain structure defines solidified metals. Columnar grains near heat-sinks exhibit high aspect ratios [10]. Alloys' solidification microstructure, controlled by cooling conditions and local alloy composition, becomes challenging due to fluctuating melting and solidification temperatures. Continuous re-melting and solidifying during subsequent layer addition further complicate solidification conditions. Figure 2.5 schematically presents the complex inter-relationship with thermal gradient, G, and solidification velocity, V on the resultant microstructure.

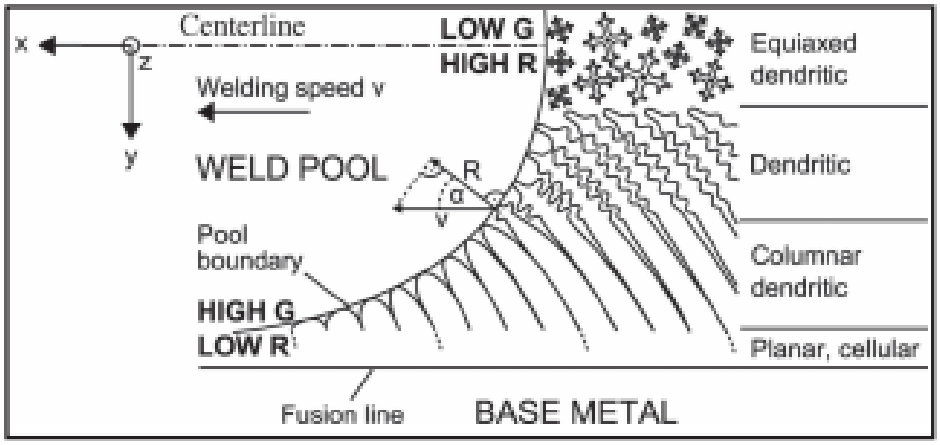

Figure 2.5 Variation in thermal gradient, G, solidification growth rate, R and corresponding grain structure [48].

Local solidification conditions dictate the formation of microstructures in both long-range and short-range order. Parameters such as temperature gradient (G), growth velocity (R), degree of undercooling, and alloy composition play pivotal roles. During solidification in the fusion zone (FZ), the temperature gradient and growth velocity vary along the

solidification front towards the rear end of the melt pool, influencing grain morphology. At the fusion line, where the melt pool contacts the 'cold' base material, temperature gradients spike. Towards the centreline, just-solidified material extracts less heat, resulting in a low temperature gradient. This variation in both G and R along the pool boundary significantly impacts nucleation and growth. A high G/R ratio favours cellular growth with little constitutional undercooling, while low G/R ratios lead to large zones of constitutional undercooling, allowing for the formation of columnar dendritic or, at extremely low G/R ratios, equiaxed dendritic structures [48].

Microstructural predictions can be obtained by understanding the relationship between Thermal gradient, G (K/cm) and solidification front velocity, R (cm/s) during the deposition process. Figure 2.5 aims to graphically display these understandings, including, G, R, arc length, undercooling and super cooling. The melt pool circumference (MPC) length attained in Figure 2.6, is the length of the circumference of the melt pool, starting from the bottom to the top of the melt pool.

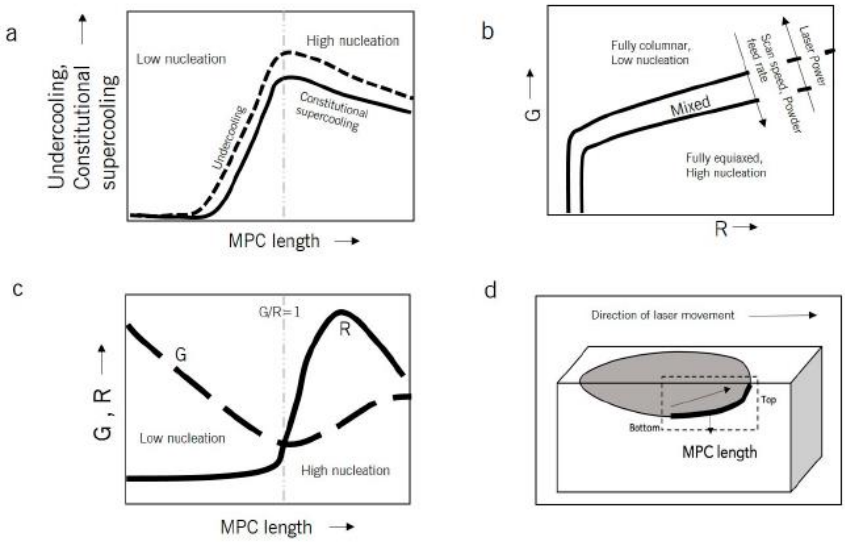

Figure 2.6 The G vs. R relationship derived from [49]***; (a) displaying undercooling/constitutional super cooling versus melt pool circumference showing the low nucleation transition to high nucleation (columnar to equiaxed transition), (b) G vs. R trend explaining columnar to equiaxed morphology, (c) variation of the G/R ratio considering the MPC length, (d) MPC length from bottom to top [50].***

Important conclusions can be derived from solidification front velocity and thermal gradient, explaining common phenomena experienced while depositing molten material [50] :

1. Heterogeneous nucleation varies with respect to scanning speed, powder feed rate and thermal energy conducted through the material. Increasing the scan speeds

and powder feed rate or reducing the heat source power decreases the thermal gradient, G, resulting in an increase in solidification front velocity, R and a higher amount of equiaxed grain structure in the part.

2. The ratio of thermal gradient to solidification velocity ratio is vital, a G/R>1 outcome a low rate of nucleation due to overpowering thermal gradient to solidification front velocity, on the contrary, G/R<1, these condition favours a high rate of nucleation due to the solidification velocity overpowering a smaller thermal gradient (Figure 2.5.c.)
3. Experimental data captured in this project (Figure 2.7) which often displays columnar dendritic morphology (smaller MPC length) near the substrate (black dashed line) and a more equiaxed microstructure away from the interface region (larger MPC length).

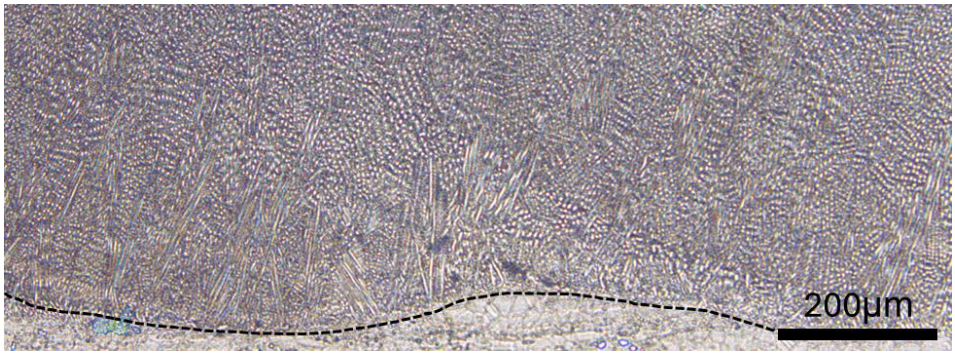

Figure 2.7 Optical cross-section micrograph of as-deposited Inconel 718 deposited using the laser power of 950W.

In reflection, as the length of the melt pool increases, an increasing trend of undercooling and constitutional super cooling results, leading to a more columnar to equiaxed transition until the G/R ratio reaches 1. Given this, by understanding the temperature history and how the different process parameters directly affect the thermal history, a microstructure evolution can be engineered according to the requirements.

2.2.6 Dendritic Growth

Numerous substances exhibit a crystallization phenomenon wherein the actual crystallization process occurs not at the melt temperature (T_M), representing the liquid-solid equilibrium, but rather at a temperature lower than T_M. This state is regarded as super cooling; the degree of super cooling corresponds to $\Delta T = T_M - T$ [51].

Nucleation theories posit that within a liquid, fluctuations give rise to small aggregates capable of initiating crystallization if their size surpasses a critical threshold at the specific temperature. The critical value is contingent upon the nature of nucleation, whether

homogeneous (involving aggregate formation within the liquid) or heterogeneous (involving solid particles on surfaces acting as nucleation trigger agents). Under heterogeneous conditions, where external particles induce nucleation, crystallization occurs at a higher temperature [51].

Solidification occurs when protrusions, formed through exothermic crystallization reactions, maintain temperatures below the local liquid temperature. If the temperature gradient exceeds the critical value, thermal rising causes the protrusion tips to melt back [52]. During phase changes, crystallization generates thermal energy, conducted away from the solid-liquid interface, influencing microstructure formation. Defects enhance solid protrusions, creating varied microstructures, with cellular and dendritic patterns depending on supercooling. Two common morphological patterns are cellular and dendritic depending on the degree of super cooling, where dendritic growth is dominant under large super cooling's[53]. Heat transfer drives solidification, removing liquid metal superheat and heat of fusion. Macroscopic and microscopic influences alter isotherms, thermal gradients, and species transport modes. Convective heat transfer affects thermal transport mechanisms and macrostructure, especially in horizontally oriented solidification under varying thermal gradients [54].

After nucleation, crystal growth occurs uniformly, driven by local heat flux. The temperature gradient ($G<0$) causes heat to flow from solid to undercooled melt, resulting in morphologically unstable interfaces evolving into dendritic grains. Unidirectional heat flux ($G>0$) leads to planar, cellular, or dendritic morphologies as heat transfers from superheated melt to cooler solid [55].

Columnar dendritic grains, prevalent in additive manufacturing give rise to anisotropic mechanical properties. The reoccurring dendrite growth comes from preferred crystallographic directions due to anisotropy in surface tension and attachment kinetics [13]. The alloy exhibits elongated grains in the build direction, forming the <001> orientation. During dendritic growth, the paraboloid-shape dendrite tip flutes laterally, developing secondary and tertiary arms. Face-centred cubic crystals mainly grow in one of the six <100> directions, aided by substrate heat sinking. Individual dendrite axes align with heat dissipation, influencing polycrystalline structures. Inconel melt pool solidification hinges on latent heat conduction, with complex interactions among temperature gradients, cooling, and growth rates determining alloy solidification dynamics [52] [54]. Figure 2.8 displays the dendritic growth into a supercooled liquid with primary, secondary, and tertiary perturbations [53].

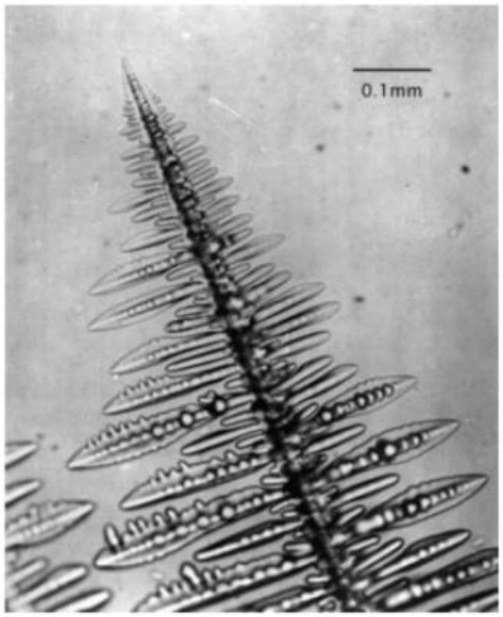

Figure 2.8 Dendrite growing into a super cooled melt of pure succinonitrile showing primary, secondary, and tertiary perturbations [53].

2.2.7 Micro-segregation during solidification

Protrusion formation forces solute to be rejected laterally and to pile at the root of the lump, this lowers the equilibrium solidification temperature, causing recesses to form, to which trigger the formation of further protrusions (Figure 2.9 depicts). In the final stages, the protrusion develops long arms or cells growing parallel to the direction of the heat flow. Solute rejection, an important phase composition in IN718 which can formulate the Laves phase solidify at the lowest temperatures in eutectic state. On the other hand, the tips grow into the hottest regions and contain the least solute concentration. As mentioned, the remaining liquid between the cells may reach eutectic composition and result in an additional phase [52].

Cellular microstructures obtain stability in a limited range of temperature gradients, as the temperature gradients are lowered, secondary arms develop, by further lowering the temperature gradients, tertiary arms develop, i.e. dendrite form.

It is noteworthy that under unidirectional solidification, there is virtually no temperature gradient perpendicular to the growth direction. The development of dendrite arm spacing significantly diminishes constitutional supercooling to minimal levels. The relationship is evident as an increase in cooling rate results in a decrease in dendrite/cell arm spacing. Consequently, longer cooling times afford less opportunity for lateral diffusion of rejected solute, necessitating smaller distances between arm spacings to mitigate constitutional supercooling [52].

Free dendritic crystal growth necessitates an undercooled liquid melt to serve as a sink for the rejected latent heat during growth [56]. The distribution coefficient, or partition coefficient (k_0), characterizes the non-uniform distribution of alloying elements within dendrite arm spacing, governed by solidification thermodynamics [57]:

$$k_0 = \frac{C_S^i}{C_L^i}$$

Where $C_S^i$and C_L^i are the concentrations of solute atoms in the solid and liquid interface, respectively.

In most cases, the distribution coefficient (k0) is less than 1, favouring the retention of elements in the liquid during solidification. Consequently, the concentration of alloying elements in the liquid increases. In alloys such as Inconel 718, under suitable conditions, the liquid composition may attain eutectic composition.

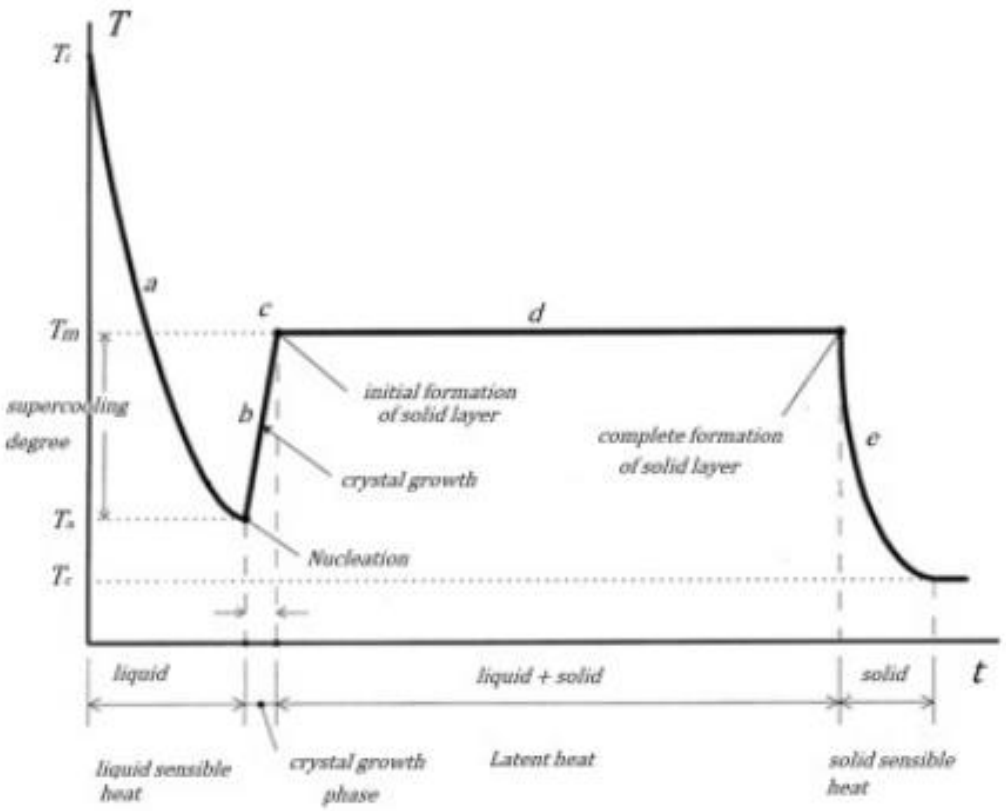

Figure 2.9 Temperature variation with respect to time during solidification process of a super cooled liquid [53].

In the past decade, substantial research has focused on comprehending and modelling mechanisms that accurately predict solidification patterns [58], [59], [60]. While significant progress has been made in predicting dendritic formation through considerations of interfacial physics and heat transport phenomena, challenges persist in

determining suitable boundary conditions at a moving interface to govern the required interfacial physics for predicting growing dendrites.

Columnar to Equiaxed Transition

Solidification processes exhibit two predominant morphologies: columnar and equiaxed. These can be categorized as constrained or unconstrained growth. Constrained growth involves isotherms limiting growth rates and inducing undercooling at perturbation tips, resulting in directional growth along the preferred <100> direction [7]. In additive layer manufacturing, achieving homogenous nucleation is challenging due to significant undercooling. Instead, heterogeneous nucleation is common, occurring on preferred sites like inclusions or substrates. Surfaces such as container walls or grain boundaries facilitate nucleation, while defect zones like vacancies or dislocations promote it [61]. Nucleation at pre-existing sites requires minimal undercooling (~1K), reducing the overall surface energy of the nucleus. The columnar to equiaxed transition is influenced by constitutional undercooling ahead of the solidification front. Under columnar growth, local temperature is regulated by heat extraction. Understanding these morphologies and nucleation conditions is crucial in optimizing additive manufacturing processes.

Local solidification conditions are influenced by isotherm location and nucleation undercooling, determining the formation of equiaxed nuclei. Research by Kurz *et al.* [55] established a critical value, indicating that below it, columnar structures persist even with equiaxed nuclei ahead of the planar front. However, increased volume fractions enable equiaxed nuclei to be incorporated into the columnar structure. Kurz *et al.'s* [55] criteria specify a fully columnar microstructure when equiaxed grain volume is below 0.66% and a fully equiaxed structure when it exceeds 49%. This critical insight, illustrated in Figure 2.10*,* contributes to understanding and controlling solidification processes for tailored material properties [55].

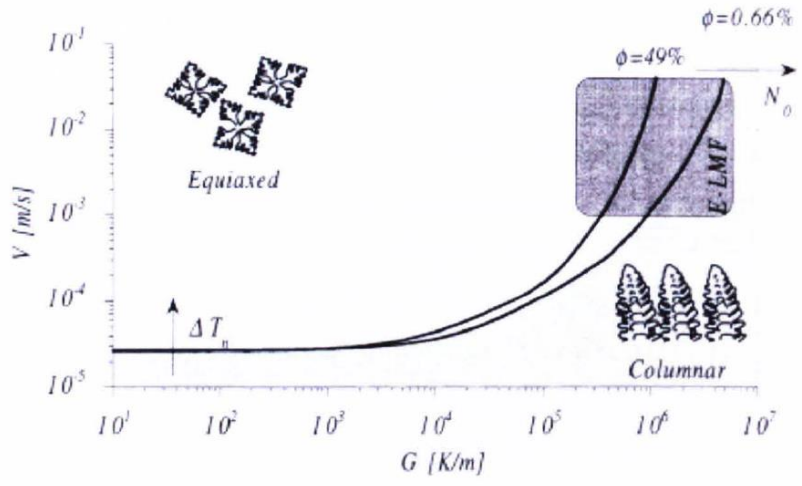

Figure 2.10 Graph of G vs. V displaying criterion for equiaxed and columnar morphology. The grey square establishes the conditions for E-LMF process. Φ is the volume fraction of equiaxed grains [71].

The combination of processing parameters can be evaluated through analytical or numerical modelling with microstructure maps to enhance the understanding of CET. Kurz *et al* [55] studied the local solidification conditions at the liquid/solid interface as a function of melt pool geometry and position along the interface region (Figure 2.11). By solving heat diffusion equations by Rosenthal, the evolution of local solidification conditions along the solidus isotherm are established for laser metal forming under specified processing conditions.

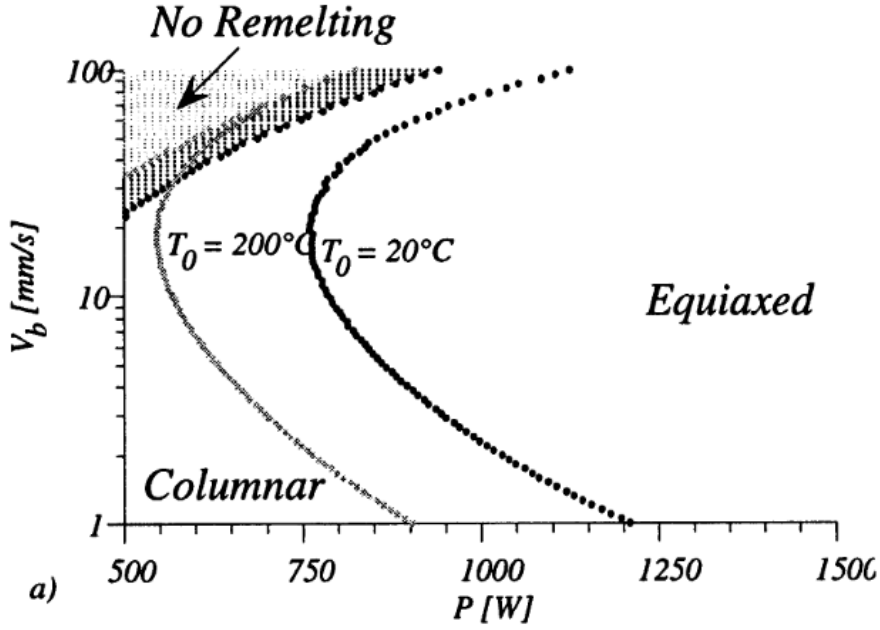

Figure 2.11 Processing map explaining dominant microstructure as a function of Laser Power vs Scanning Speed [55].

A range of empirical model's [88], [89] based on Hunt's approach to modelling the columnar to equiaxed transition for complex alloys exist, taking account for dendritic growth models, Figure 2.12. By associating local solidification conditions to conform to CET criterion, it was possible to predict the expected solidification morphology for a set of processing parameters.

According to Liu *et al.* [66], increasing the scanning speed reduces the temperature gradient and increases the solidification rate hence producing larger under cooling's with a high probability of heterogeneous nucleation contributing to the CET of grain structures.

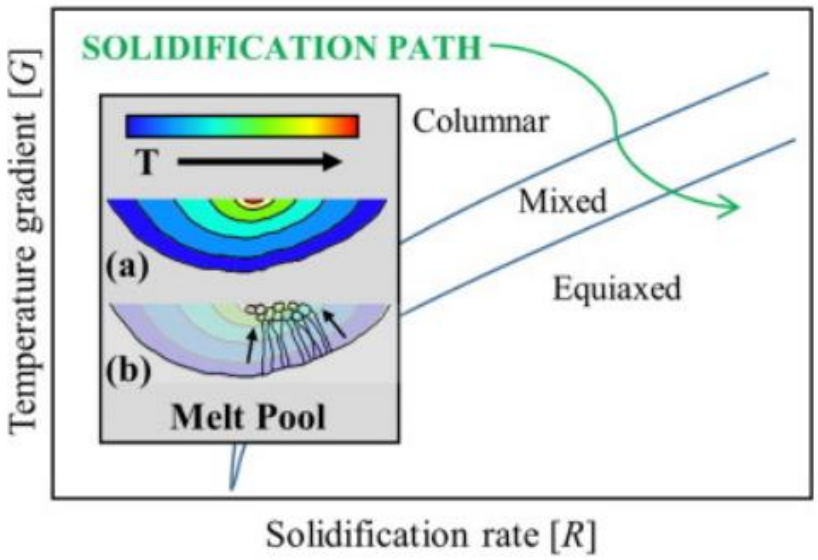

Figure 2.12 Temperature gradient G and solidification rate R on grain morphology within a solidifying melt pool [67].

Ma *et al.'s* study [68] established a significant correlation, demonstrating that subjecting Inconel 718 to higher energy levels induced a dendrite-to-cell transition (DCT) in as-fabricated sections. A morphological distribution map, examining samples at various energy per unit volume (Ev) values, revealed a monotonous increase in cell presence with higher energy. The study identified critical points determining the morphology of as-DLFed IN718 samples: dendrites, cells, or a combination, with thresholds at 220 J/mm³ and 550 J/mm³, respectively [85].

The prevalence of specific growth modes is contingent upon spatially localized solute and temperature distributions within the melt pool. As solute diffusion occurs near the solid/liquid (S/L) interface, heightened solute concentration leads to a reduction in the liquidus temperature (T_L) for the alloy. The accumulation of solute content (C_L) at the

grain front deviates from the nominal alloy composition (C_0), thereby giving rise to constitutional supercooling (ΔT_C). This constitutional supercooling is defined as the difference between the liquidus temperature (T_L) and the actual temperature (T_{actual}) within the mushy zone, normalized by the difference between liquidus and solidus temperatures [49]. Figure 2.13 graphically displays the inter-relationship co-existing at the S-L interface.

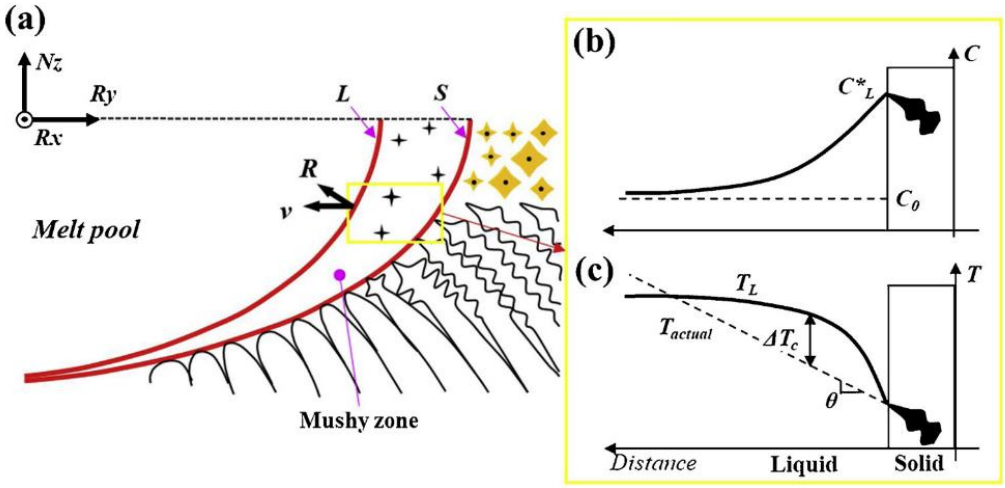

Figure 2.13 (a) Grain nucleation schematic near melt pool. L and S are liquidus and solidus, respectively, (b) and (c) hypothetical solute concentration and relevant temperature profile at the interface. Horizontal lines represent the distance from grain fronts along solidification direction. Θ is actual temperature slope, thermal gradient [49].

Heterogeneous nucleation, a rapid process during solidification, is notably influenced by undercooling, particularly constitutional supercooling. A crucial revelation in understanding growth mechanisms and local equilibrium conditions in the additive manufacturing of IN718 is that undercoolings at the melt pool's base are relatively minimal ($\Delta T<1.0K$). These small undercoolings are insufficient to initiate heterogeneous nucleation, leading to the predominance of epitaxial growth [49].

2.2.8 Rapid Manufacturing Microstructure

Inconel 718, when initially deposited, exhibits a microstructure comprised entirely of columnar dendrites growing epitaxially on the substrate material, aligned with the <100> crystallographic orientation along the build direction. Laser Metal Deposition induces the formation of a significant Laves phase during solidification due to alloying element micro-segregation, with insufficient cooling rates hindering the precipitation of strengthening phases like γ'' and γ'. Post solution treatment transforms the retained Laves phase into needle-like delta structures in the inter-dendritic region [1].

The columnar dendritic growth is influenced by epitaxial growth from partially re-melted grains in the previous layer [69], serving as pre-nuclei for crystal growth. Rapid cooling rates lead to fine dendrite arm spacing (5μm), contrasting with cast microstructures having coarser spacing (10-40 μm) [70]. Powder-Bed Fusion results in columnar dendritic or fine cellular patterns perpendicular to the build direction and a fish scale pattern parallel to it. High cooling rates foster fine dendritic morphology, micro-segregation in interdendritic regions, and the development of Nano/micro carbides and Laves phase [40].

Laser metal deposition differs from conventional methods by solidifying through epitaxial growth on the adjacent melted substrate, adopting a preferred crystallographic orientation. Solidification morphology is governed by temperature gradient and isotherm velocity, resulting in varied interfaces, from planar to cellular structures depending on growth rates [71].

2.2.8.1 Laves Formation during LMD IN718

In laser-based additive manufacturing of nickel-based superalloys, rapid solidification induces cooling rates surpassing equilibrium, causing element segregation and the formation of brittle intermetallic compounds. Notably, Nb redistribution leads to Laves phase establishment at solidification's end, with two eutectic reactions (L→γ+NbC and L→γ+Laves) resulting in the precipitation of NC carbides and Laves phase in solute-rich interdendritic liquids during different solidification stages [72].

Niobium exhibits a pronounced tendency to segregate into the liquid phase, emerging as the primary segregation element under slow-cooled conditions, fostering the formation of NC carbides and Laves phase. Ling *et al.* [73] expanded on this by investigating micro-segregation and Laves formation across cooling rates ranging from 0.1 to 14 K/s. Incomplete diffusion processes during non-equilibrium solidification lead to alloy element segregation and secondary phase formation. Cooling rates around 1K/s yield an equiaxed dendrite pattern with micro-segregation, while higher rates (up to 3K/s) increase Laves phase fraction linearly before decreasing at 14K/s. The Laves phase initiates and propagates hot cracking, contributing to high susceptibility during laser metal deposition due to intensive thermal stress in the heat-affected zone.

2.2.8.2 The Influence of the Laves Phase on Mechanical Performance

In laser deposited IN718, Laves phase, ranging from several microns to over ten microns, exhibits irregular distribution. Sui *et al.* [37] found granular Laves phases resist breakage during tensile testing, impeding crack propagation in high-cycle fatigue tests. The

heterogeneity distribution of γ'' phase and deformability difference between the austenitic matrix and Laves phase lead to stress concentration around micron-scale precipitates, influencing high-cycle fatigue behaviour. The presence and contribution of Laves phase in laser additive manufactured Inconel 718 are crucial considerations for aerospace components, necessitating a thorough investigation of their impact on high-cycle fatigue behaviour. The Laves phase acts as a detour or retarding agent for cracks during their progression, playing a crucial role in high-cycle fatigue resistance [37]. Under elevated stress levels, however, the Laves phase can break apart from the austenite matrix, forming microscopic holes or cracks that facilitate uninterrupted crack propagation.

Tabernero [74] examined the mechanical properties of laser-repaired Inconel 718 without establishing a connection to the non-uniform microstructure [96]. Investigations into the adverse impact of Laves phase on mechanical properties have been conducted [37], [75]. Despite the abundance of research on laser based manufactured IN718, there is a notable dearth in the predictability of Laves phase formation and its correlation with solidification microstructures, as well as their consequential influence on mechanical properties.

The impact of heat treatment on Laves morphology, crucial for understanding its correlation with room temperature mechanical properties, was investigated by Sui *et al.* [70]. The transformation of morphology, resulting in irregular, long striped Laves phases and granular phases, was noted. These findings on Laves phase morphology agreed with Segerstark *et al.'s*. [76] investigation analysing the crack formation during LMDed IN718. Long chains of eutectic γ/Laves phase were revealed along the cracked surfaces and due to the relatively low melting point of this secondary phase, the grain boundaries are vulnerable to liquidation during deposition. Research indicates there is a congregation of niobium segregation existing around the Laves phase, these regions contain roughly 9 wt. % of niobium. Literature suggests that the Laves phase requires more than 10 pct. niobium to precipitate, whereas γ'', the main strengthening mechanism only requires 4pct niobium [34]. As a result, almost all γ'' precipitate around the Laves phase in the interdendritic regions leading to non-uniform distribution of strengthening mechanism [77]. Concentrated zone of strain accumulated in the laser deposited zone because of the Laves phase and heterogeneous distribution of γ'' phases causing plastic deformation in the laser deposited layer as opposed to the equiaxed substrate zone. Interestingly, the Laves phase has almost no capability of plastic deformation at room temperature, rather above the critical shear stress – Laves phase slipped and broke into smaller parts [77].

Microscopic holes form where the slip occurs at the interface, eventual accumulated holes lead to ultimate failure. The introduction of post-process heat treatments found that the niobium micro-segregation regions around interdendritic Laves phases lead to γ'' phase precipitation during direct aging heat treatment. Additionally, variations in laser power influenced the size and morphology of Laves particulates, with higher power levels leading to larger particulates containing fine carbides [70]. Extended exposure to high temperatures, facilitated by high laser power and continual heat input, resulted in the formation of δ needle-like structures due to stacking faults in the γ'' phase.

Summary on as-deposited IN718 Fundamentals

This section of the literature review was developed to establish the fundamentals in Inconel 718 inclusive of the microstructure, and influential effect on mechanical performance. An overview of understandings include:

- Cooling rates significantly influence morphological features in as-deposited microstructures. In IN718, cell spacing relies heavily on cooling rates at the solid/liquid interface during solidification. Higher temperature gradients (G) and solidification rates (R) in the melt pool yield elevated cooling rates, ultimately producing a finer cellular structure [78].
- Keshavarzkermani *et al.* [79] highlighted the significance of cooling rates in determining cellular microstructural spacing. They proposed a cooling rate approximation based on the ratio of melt pool volume (Vs) to boundary area (S_b). A smaller $\frac{V_s}{S_b}$ results in faster heat dissipation to the substrate, leading to higher cooling rates during solidification, and conversely, a larger $\frac{V_s}{S_b}$ yields lower cooling rates. Figure 2.14 illustrates this with varying laser powers in an equivalent LED, where lower laser powers exhibit a smaller $\frac{V_s}{S_b}$ ratio, resulting in higher cooling rates and a finer cellular microstructure [101].
- Laves phase production in LMD is very difficult to control as the micro segregation of alloys occurs during the cooling of the deposited region. The microstructural phase is highly detrimental to mechanical properties of the as-deposited components.

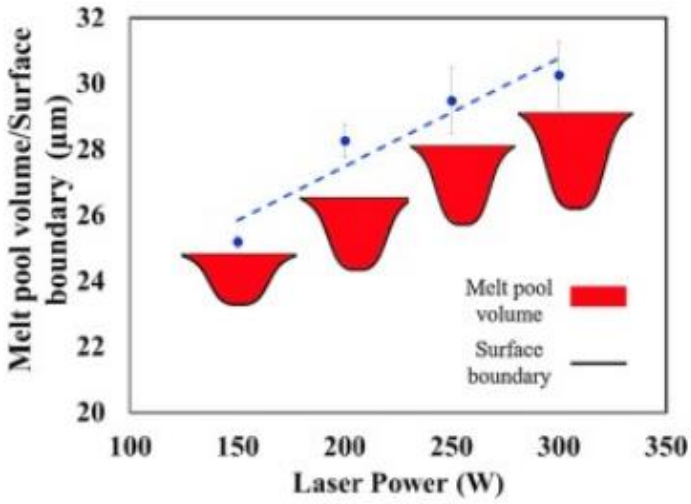

Figure 2.14 Ratio of melt pool volume to surface boundary as a function of laser power [79].

2.3 Additive Manufacturing Technologies

Additive manufacturing's near-net shape capabilities have garnered significant attention in the aerospace industry. This is attributed to potential benefits such as shortened lead times, fewer process steps, reduced machining, decreased material waste, and a more environmentally friendly approach. The industry is increasingly interested in exploring these technologies, with ongoing research aimed at better understanding their capabilities and limitations.

2.3.1 Introduction to additive technologies

The basic concept of this technology is to successfully fabricate a near-net component by the means of a focussed heat source fully or partially melting the feedstock, wire or powder, to build up parts layer by layer. Each layer is a 2D profile of a 3D geometry build part already designed on software such as Solidworks®. The term additive manufacturing compasses many sub-technologies such as Rapid Protyping, Rapid Tooling, Direct Digital Manufacturing, and additive layered manufacturing [1].

Additive layer manufacturing, (ALM) can be categorized into two main families by which the differentiation is how the feedstock material is subjected to the heat source - Powder Bed Fusion (PBF) technologies and Direct Energy Deposition (DED).

2.3.2 Powder Bed Fusion Technologies

The principle of powder bed fusion is subsequent layers of metallic powder laid on the build plate, a tool path with a selected heat source partially (Selective Laser Sintering) or fully melts (Selective Laser Melting) the powder which cools and solidifies, building the geometric shape, Figure 2.15. The substrate is fixed by means of support, sacrificial structures uphold overhangs and inert gas is pumped into the chamber. Layer-by-layer

predetermined thickness of powders are placed on the substrate and the heat source (Electron beam or laser) follows the CAD toolpath to condense build part [80].

(The original Direct Metal Laser Sintering (DMLS) process diagram has been removed by the author of this thesis due to copyright reasons. For the full illustration, see Nexa3D's "Metal 3D Printing Guide" blog post – https://nexa3d.com/blog/additive-manufacturing/.)

Figure 2.15 Laser-based powder bed fusion schematic [81].

An important consideration to achieve a high-quality built part is the homogeneity of the layer thickness. Various advancements have been developed to manage the powder control, a concise powder delivery system should maximise the powder flow ability while minimizing the formation of particle clouds [82]. PBF systems have incorporated powder layer measurement tools whereby visible-light contrasts anomalies of the entire bed, when detected, the recoating process is repeated to ensure homogenous distribution [80].

Laser based systems (Direct metal laser sintering/ selective laser sintering/ selective laser melting) (developed by Renishaw) rely on the main process parameters incorporating laser beam diameter to optimize the build quality. Whereas the electron beam power, diameter of focus, pre-heat temperature and layer thickness determine control in the electron beam systems (ARCAM) [83]. EBM's possess higher build rates but come with the penalty of inferior dimensional and surface finish qualities.

Recent advancements in powder bed fusion technologies manages the manufacturing tools and process development by in the introduction of models. Running simulations can optimize desired characteristics of the built geometries by formulating process maps which correlates parameters such as beam intensity and scan speed to grain size and melt pool geometry. A common problem for the state-of-the-art is the development of valid heat input models for build-up simulation. Based on the Rosenthal equation local temperature fields are determined for single track thermal models. From this, uncontrollable process-related thermally induced distortions are determined and adjustments to overcome these distortions implemented [84].

The build envelopes are restricted to powder bed dimensions and chamber parameters. In this thesis, especially focussing on the aero-space industry many parts are either far too large to fit within the parameters or are manufactured from high specified materials with the need of adding heterogeneous material features to components.

2.3.3 Direct Energy Deposition

Direct energy deposition is an additive manufacturing technique, whereby, powder or wire feedstock is introduced directly to a melt pool in a layer-by-layer process to consolidate into a three-dimensional shape. Initially, the work piece is placed on a surface and depending on the heat source, the atmospheric working conditions change. Laser-based sources require shielding gases to prevent the oxidization or reactivity of metallic compounds induced to thermal cycles, Figure 2.16. A major benefit of this technology is the build piece isn't limited to the build chamber dimensions. Electron beam deposition requires a vacuum environment as they accelerate electrons (rather than photons in Laser) towards the fusion zone transforming into the feedstock material into a melt pool by thermal energy. The vacuum environment ensures the electrons are propelled straight to the work area via electromagnets, and don't lose energy being attracted elsewhere. A further benefit is the vacuum creates a non-reactive working situation diminishing the oxidation of metallic compounds.

(The original Laser Metal Deposition (Direct Energy Deposition, DED) process diagram has been removed by the author of this thesis due to copyright reasons. For the full illustration, see TRUMPF's 'Laser Metal Deposition' page - https://www.trumpf.com/en_GB/solutions/applications/additive-manufacturing/laser-metal-deposition/.)

Figure 2.16 Laser deposition schematic diagram [85].

The process nozzle focusses a concentric laser or electron beam source onto the substrate surface to create a melt pool, subsequently material delivery is introduced via powder (laser-based) or wire form for electron beam technologies [86]. The nozzle follows the toolpath which has been pre-determined via a CAD file and as the source leaves a melt pool area, it solidifies and condenses into a layer of material. This process is repeated until the final geometry has been created, as this is the principle for DED technologies,

there shall now be a discussion on the following sub-categories which are defined by heat source.

The DED category encompasses of sub-categories dependent on the technology utilized for additive layer manufacturing. The component moves anywhere on a XY-plane, and the laser focuses the powder feed into the melt pool to build upon the z-axis, adding and consolidating successive layers without any tooling [87].

2.3.4 Shaped Metal Deposition

Shaped metal deposition is a relatively new concept to the additive layered manufacturing family. A novel technique to build net-shaped or near-net-shape metallic components in a layer-by-layer manner via applying metal wire and chosen heat source, electron beam, laser or electric arc (Figure 2.17). A technique patented by Rolls Royce Plc, wire and arc additive manufacturing (WAAM) [80] helps to minimize the amount of material needed during the deposition technique by depositing beads of weld material in ascending layers. The mechanical properties of deposited parts are competitive to that of cast and wrought, this is due to the improved consistent solidification conditions experienced during deposition. The WAAM technique can be further categorized into three major processes based on the type of electric torch used to melt wire; 3D GTAW (gas tungsten arc welding), 3D GMAW (gas metal arc welding) and 3D plasma. In these techniques, a wire feedstock is more favourable due to the higher deposition rate and higher efficiencies comparative to powder-based feed [88].

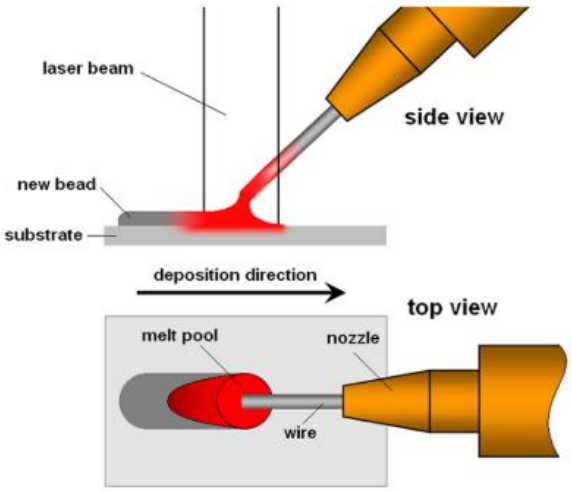

Figure 2.17 Schematic diagram of Shaped Metal Deposition [88].

The WAAM technique upholds many benefits comparative to other additive manufacturing technologies, an attractive benefit, especially for larger component fabrication, deposition can occur within or without a chamber - there is no need for a

vacuum environment. Due to the immense deposition rates and higher efficiencies, attraction has grown. On the contrary, WAAM or SMD are very limited to mass production and cannot be used to produce small intricate shapes. Furthermore, surface finish is often relatively poor and therefore requires further machining processes [88].

Due to the limitations on intricacy and the generation of small components, this technique shall only be over viewed and not implemented in the methodology section. A highly attractive, near-net-shape technology which has continued to develop is the Laser Metal Deposition.

2.3.5 Laser Metal Deposition

Compared to the conventional fusion techniques which include tungsten inert gas, many advantages favour the revolutionised technology of Laser Metal Deposition. The stability and repeatability of material deposition promotes homogenous bonding with the ability to automate the process, the repeatability of processing dynamics creates a higher production rate with similar fine microstructural characteristics [89]. The laser head, or deposition head encompasses the powder feed nozzle (either co-axial or off-axis), the laser source (concentric beam), and inert gas tubes which move on a multi-axis robot or gantry system (Figure 2.18). Continual movement between deposition head and substrate controls the melting and solidification steps. Overlapping tracks are deposited to produce a horizontal layer. The high repetition of depositing layers solidifying is the adopted approach for subsequent construction [90].

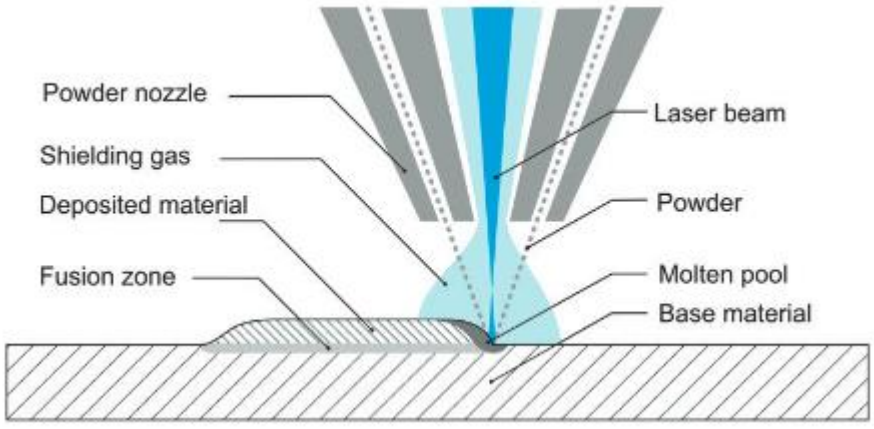

Figure 2.18 Laser Metal Deposition Schematic [91].

2.4 Summary

Given the infancy of the LMD process, developing capabilities to understand the microstructure evolution during deposition has received more attention over the decade. Understanding the thermal cycling experienced, paves way to tailor process parameters to achieve the desired microstructural evolution and therefore the mechanical properties of as-deposited materials.

Through developing simulation software and computational methods, this research aims to provide fundamental knowledge on the importance of process parameters. Correlating the adjustable configuration of deposition and simulating the thermal field experienced by the material, a microstructural analysis model with the ability to differentiate materials, processing parameters and resulting microstructure of the as-deposited layer can be verified. An understanding between manufacturing process control parameters and actual functional specification capabilities is of paramount importance [92] which urges research and development into the correlation between processing parameters and functional performance of a built part. The extensive review on how each individual variable process parameter affects the resulting outcome needs to be established during this thesis, so that, a process model for build component microstructure can be established. Firstly, the material of subject will be analysed to understand the stability behaviour.

2.5 LMD Process Parameter Fundamentals

2.5.1 Effects of Laser Power Increment

Upon review, the basic effect of laser power can be assessed qualitatively regarding single track analysis, which in turn has microstructural affect. The laser power influences the track width, cross-sectional area, productivity of the deposition (includes powder catchment and melting) and the efficiency of the laser beam (regarded as energy expenditure vs deposition energy)[93].

Thin re-manufactured sections, melt pool behaviour and processing parameters correlation becomes vital in achieving sustainable sections. A linear heat input is defined as the ratio of input power to the travel speed, an example of the influence for this parameter change was the microstructural alteration in electron beam deposited Ti-6Al-4V. By comparing 300 J mm^{-1} to 50 J mm^{-1}, a columnar microstructure containing a mixture of $\alpha + \beta$ equilibrium phases, with fine basket weave α-lath morphology comprised compared to columnar grains with acicular α' martensitic grains, respectively. The formation of the martensitic phases is the outcome for higher cooling rates [94].

A similar relation was developed showing that increasing the laser power, or decreasing the scanning time leads to the coarsening of the microstructure [87]. The length of columnar grains decreases with an increase of laser power, and a fully columnar to equiaxed grain structure transition is achieved when the laser power increases from 390 W to 516 W with a constant scanning and powder feed rate [87].

Employing direct laser fabrication for IN718, the as-built structures rectified a correlation between laser power and dendritic morphology. From 390W to 910W, although the powder feed rate needs to be reduced from 18 g/min to 7 g/min to avoid the uppermost build layers contacting the nozzle due to an increase of catchment efficiency caused by a larger melt pool dimension, the dendritic length increased from 150 μm with an aspect ratio ~3, to 2-3 mm long with an aspect ratio around 30 [70].

The melt pool geometry, cell spacing, and grain refinement of laser-based powder fused Hastelloy X (a nickel-chromium-iron-molybdenum) was analysed to build a correlation to related energy density. Interestingly, it was concluded that the laser power directly effects the melt pool depth, decreasing the laser power (with a fixed scan velocity) resulted in 60% and 30% decrease in melt pool depth and width [79]. Moreover, the primary cell spacing increased by altering laser power from 150 W to 300 W which is linked to the cooling rate. Lastly, in general, the microstructure displayed a cellular structure with epitaxial growth of grains at melt pool boundaries. But with fixed LED of 0.25 J/mm, a 90% increase of new grains is observed producing cell size increase [79].

The effect of laser power on microstructures and tensile properties of LPBF fabricated Hastelloy X superalloy was investigated by Bai *et al.* [95] The study revealed the as-built microstructure characterized by elongated grains and fibre texture along the building direction. The preferred grain orientation that the crystallographic direction {001} of most grains is parallel to the building direction. The average aspect ratio was calculated to show an increasing trend with the increase of laser power in 20 W increments. The increased laser power (energy density) contributes to larger melt pools and lowers the cooling rate, promoting the epitaxial growth of columnar crystals along the long axis. A strong crystallographic texture with maximal density poles larger than 5.7 MRD was shown in the samples. The pole distribution feature is close to the Goss texture of {110} <001> and is related to the specific heat flux direction and associated solidification. The texture intensity increases with the increase of laser power (Figure 2.19), as this trend follows the trend of increased laser power contributing to larger melt pools and lower cooling rates,

leading to larger, coarser grains aligning themselves along the favoured crystallographic direction.

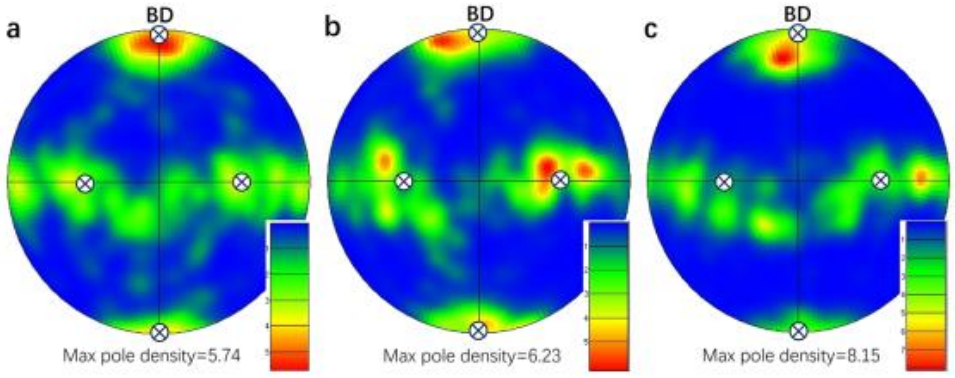

Figure 2.19 Pole figures of the crystallographic plane (001) for as-built HX with laser powers of (a) 280W, (b) 300W and (c) 320W. (Point-specific crosses denotes the {110} <001> Goss texture component) [95].

Recent work by Mueller *et al.* [96] aimed to investigate the solidification conditions for varied line energy (J/mm) whereby the laser power increased from 800 W to 2000 W with respective deposition speeds. This study concluded that the refinement of the columnar dendritic microstructure increased with increasing the deposition speed and decreasing the laser power. Moreover, Wolff *et al.* [97] reported that PDAS values decreased from 8μm to 4μm for laser powers 2000 W to 1000 W, respectively. Such refinements have a direct influence on the microhardness and can be represented as a function of cooling rate. Interestingly, it has been shown that an increased cooling rate suppresses the Laves phase and Nb micro segregation. It is well known that increasing cooling rate corresponds to a refinement in dendrite spacing [98].

Son *et al.* [99] investigated the influence of laser power on recrystallization temperature in L-PBF manufactured IN718. The as-built bottom region exhibited consistent <001> fiber texture, unaffected by laser power. Higher laser power led to an expanded melt pool volume, while width remained constant. Thermal stresses from rapid cooling acted as a significant recrystallization driving force. The 390W setting demonstrated the fastest cooling rate. Recrystallization temperature, post PWHT, was above 1095°C for 370W, approximately 1095°C for 380W, and within 1065-1095°C for 390W. This study highlights laser power's influential role in recrystallization and stresses the dual benefits of stress-relief PWHT in reducing residual stress and homogenizing the interface.

Alhuzaim *et al.* [100] investigated microstructural and mechanical properties in LMD Inconel 718 by varying laser power. This research showed increasing the laser power

from 300–500 W induced columnar grain morphology, maintaining similar grain width but increasing in length. Within the 500–700 W range, grains continued to grow longitudinally, with width starting to increase. At 700–900 W, the width stabilized, and a slight length increase persisted. Beyond 900 W up to 1900 W, width remained constant while length reached a steady state. Notably, a significant width increase occurred every 200 W until it reached a constant value. Furthermore, the Nb-segregation decreased with an increase of heat input due to the lower cooling rates experienced allow for the Nb to dissolve in the γ and γ″ phases.

Lastly, Zhu *et al.* [101] investigated the impact of laser power and beam diameter on as-deposited Inconel 718. Increasing laser power and beam diameter resulted in the enlargement of columnar grains. Ding *et al.* [102] associated dendrite core microstructure with cooling rates, revealing that high rates produced fine dendrites and nearly continuous inter-dendritic regions. Lower cooling rates led to coarse dendritic and semi-continuous interdendritic regions. Addressing structural integrity, Zhong *et al.* [103] demonstrated a reduction in porosity by elevating laser power.

2.5.2 Effects of Scanning Speed

Laser metal deposition is a novel manufacturing concept, requiring an understanding of laser/material interaction for correlating processing parameters to microstructural evolution. Wang *et al.* [104] investigated the impact of varying scanning speeds on the microstructure, mechanical properties, and texture development in Inconel 718 manufactured via Selective Laser Melting (SLM). It was initially observed that slower scanning speeds resulted in a lower width-to-depth ratio (dilution ratio), attributed to higher energy density enlarging the molten pool. At lower scan speeds, the deeper melt pool facilitated epitaxial growth, enhancing the strength of the <001> texture. Conversely, higher scanning speeds led to rapid solidification in shallower melt pools, promoting nucleation and reducing the growth rate necessary for fine grain structure. This limitation on epitaxial growth resulted in a decrease in <001> texture strength. Figure 2.20 illustrates pole figure maps for the bottom section in SLM-produced IN718 samples.

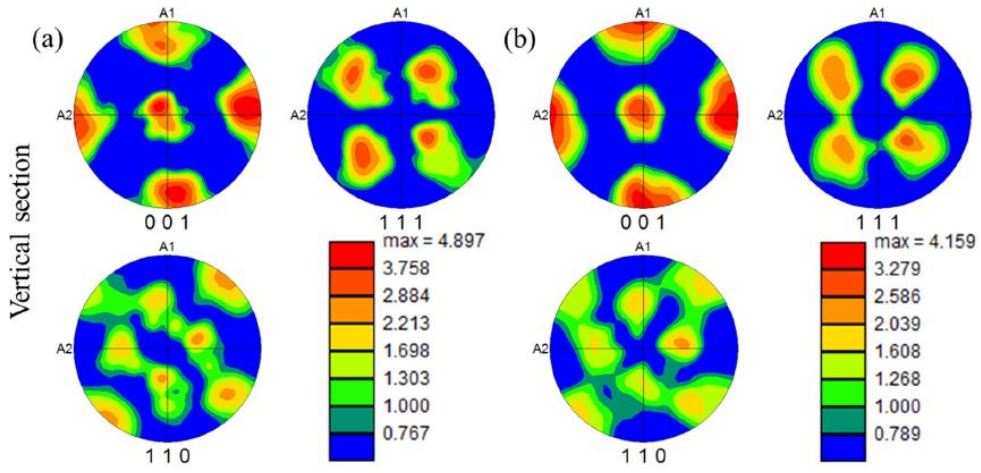

Figure 2.20 Pole figure maps of the SLM produced IN718 with different scanning speeds on the vertical plane (i.e. aligned with growth direction) for (a) 2300mm/s and (b) 2400 mm/s [104].

Direct energy deposition of Inconel 718 results in coarse dendrites aligning along the <001> direction, forming columnar dendrites parallel to the build direction [16]. Varying scanning speeds (25 to 50 mm/s) influences microstructural evolution, notably affecting dendritic spacing and equiaxed grain size in the re-melted layer (Figure 2.21). At 25 mm/s, dendritic length and spacing measure 85.6µm and 3.92µm, respectively. Higher scanning speeds, such as 50 mm/s, reduce dendritic dimensions to 36.6µm and 2.4µm for length and spacing [105]. The cooling rate exhibits direct proportionality to scanning speed (vs) and inverse proportionality to laser power.

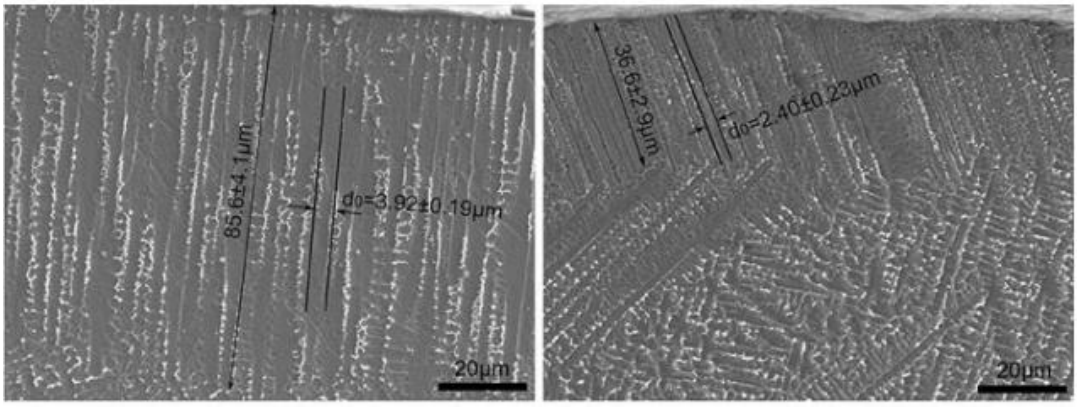

Figure 2.21 Microstructure of columnar dendrites in the top layer of re-melted Inconel 718 at scanning speeds of (a) 25 mm/s and (b) 50 mm/s [105].

By increasing the processing speed, the micro-hardness increased due to the shorter interaction time between beam and material, enhancing cooling rates providing a shorter time for grain growth. The processing speed increase resulted in a refined microstructure with better hardness properties due to the yielding of softer austenite and promotion of harder martensite [106].

The independent effects of laser power and scanning speed on IN718's precipitation and mechanical properties produced by LBPF with PWHT were analysed by Pan *et al.* [107]. The overall aim was to increase the energy density volume by marginally increasing the laser power from 200W (P1) to 300W (P2) but dramatically increasing the scanning rate from 900 mm/s (P1) to 1300 mm/s (P2). This comprehensive study demonstrated highlighted that:

- The aspect ratio of the grains produced in the deposited region along the building direction were 2.57 ± 0.50 μm and 1.99 ± 0.59 μm, for P1 and P2, respectively.
- Since the columnar grain growth of IN718 alloy is preferred to grow along the <001> direction [108], [109], the columnar grains in P1 specimens enhance the <001> texture along the building direction, while a relatively strong <011> texture is observed in the P2 specimens.
- The amount of δ phase precipitates along the grain boundaries in PWHT microstructure specimens increased in P2 comparative to P1. An average δ phase precipitate occupies a 33% and 61% area percentage in the P1 and P2 samples, respectively.
- Measuring the γ' and γ'' strengthening precipitates, it was found that the thickness of both γ' and γ'' phase precipitates in the P1 sample is about half the value compared to the P2 samples.
- The tensile and yield strength of all specimens were similar in the range of 1260-1360 MPa and 1010-1080 MPa, respectively. Comparable strength contributions were the grain size and strengthening precipitates, where texture and density were found to be minor influential factors.

2.5.3 Effect of Raster Scanning Pattern

The categorization of the scanning, raster, or hatch strategy pertains to the trajectory followed by the heat source during deposition. Various deposition strategies aim to optimize the generation of intricate geometries while minimizing waste in machining processes. Common approaches in LMD include unidirectional or bidirectional rectilinear infill. When building Additive Manufacturing (AM) components, four primary deposition patterns emerge: unidirectional, bidirectional, offset-out, and fractal (depicted in Figure 2.22). Deciding on a pattern involves considerations of part geometry, microstructural variation, and the accumulation of residual stress [110].

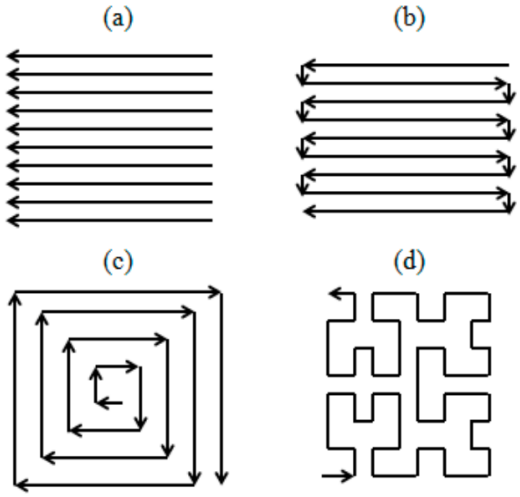

Figure 2.22 Deposition strategy: (a) unidirectional (b) bidirectional (c) offset-out (d) fractal [110].

Dinda *et al.* [111] found that the solidification morphology of as-deposited IN718 is significantly influenced by deposition scanning patterns. Unidirectional laser scanning yields ordered columnar primary dendrites at a 60° angle to the substrate, with the number of grains about an order of magnitude higher than bidirectional. Conversely, bidirectional strategy (with a 180° direction change between layers) results in primary dendrites growing at a 90° alternation between layers and a fluctuation of +45°/-45° to layer boundaries in odd or even layers, as illustrated in Figure 2.23.

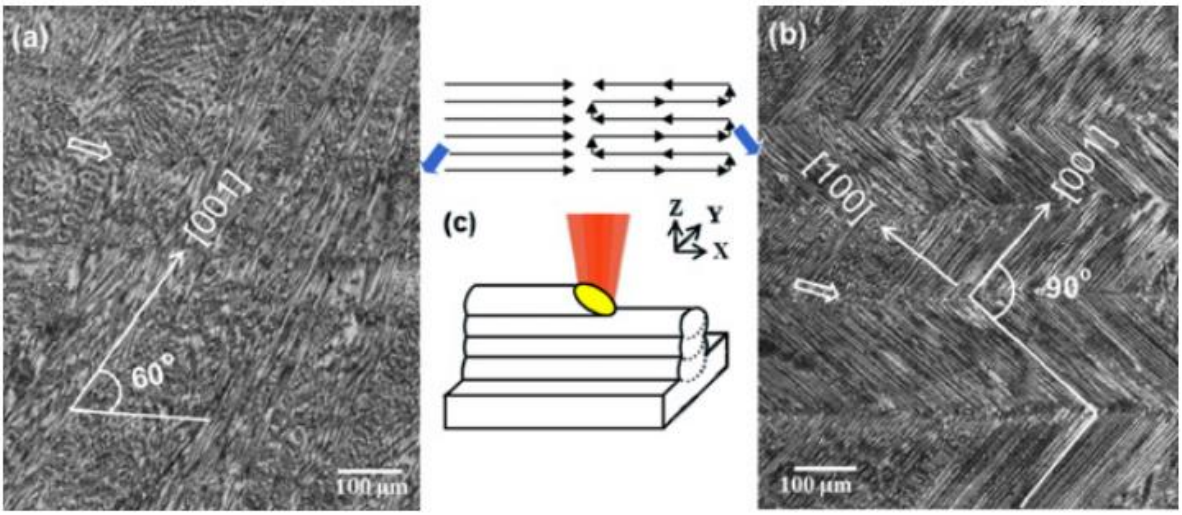

Figure 2.23 (a and b) Optical micrograph of the as-deposited IN718 samples produced by two different laser scans, shown schematically in (c)[111].

Solidification conditions dictate whether nucleation or growth rate predominates. For face-centred crystals, research highlights the <100> direction as the fastest solidification path. The growth direction of primary dendrites at 90° to the previous layer signifies the dominance of growth rate over nucleation. In solidification, secondary dendrites from the

prior layer act as a growth front for the primary dendrites in the new layer. Nucleation of new grains demands a greater driving force than the free energy needed for growth [111], [112]

Studying hatch pattern influence for Laser Solid Form (LSF) Inconel 718, Liu *et al*. [113] compared single direction raster scanning (SDRS) to cross direction raster scanning (CDRS) (Figure 2.24). Maintaining consistent parameters like laser power and scanning velocity while altering the hatch pattern revealed insights into optimal scanning strategies for mechanical properties. SDRS showed continuous directional growth of columnar grains, fostering epitaxial dendrite growth, while CDRS disrupted this pattern, promoting a more uniform grain size distribution. The study unveiled that recrystallized grain sizes reflected residual thermal stresses, with CDRS exhibiting a more uniformly distributed grain size and, consequently, a bulk uniform residual stress distribution. Despite similar tensile strength between SDRS and CDRS, the latter demonstrated enhanced ductility due to homogenous grain size. This research underscores the importance of hatch pattern variation in influencing material properties during laser solid form technology.

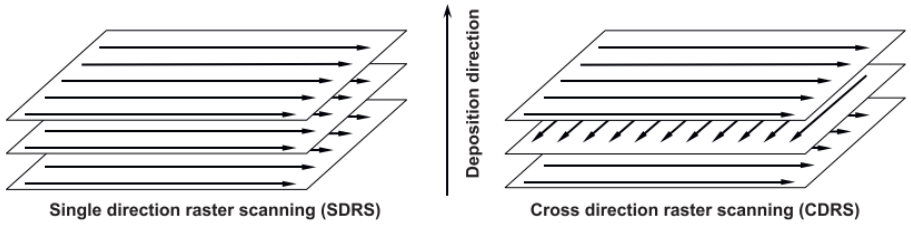

***Figure 2.24 Laser scanning paths implemented by Liu et al detailing single direction raster scanning (SDRS) and cross direction raster scanning (CDRS*) [113].**

Helmer et al. [114] studied grain structure evolution in selective electron beam melting, exploring complex thermal and hydrodynamic conditions. Different scanning strategies—cross snake (changing hatch direction every layer), cross snake ten (every tenth layer), and cross snake forty (every 40th layer)—were employed to deposit uniform Inconel718 cuboids. Figure 2.25 depicts the hatch pattern.

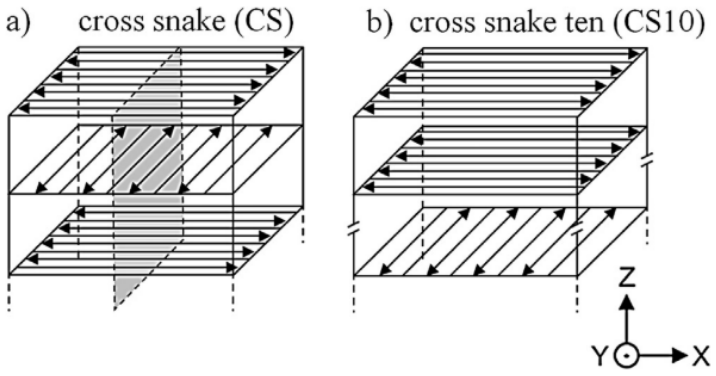

Figure 2.25 Scanning strategies: (a) Cross snake (CS) and (b) cross snake ten (CS10). During the snake pattern, the beam moves back and forth to infill each layer, upon completion of the single layer, the hatch pattern direction changes by 90° [114].

Different scanning methods in selective electron beam melting affect the microstructure. The standard approach creates a columnar texture in the build direction due to epitaxial growth and consistent temperature gradients. In contrast, multi-passing yields a finer, mostly equiaxed structure because of faster deflection speeds, reducing texture. Competitive growth is crucial, with temperature gradient changes influencing growth directions. Zigzagging columnar grain growth occurs every tenth layer, while equiaxed grains appear at intervals, indicating solidification direction's influence. Competitive growth within layers and periodic rotation affects grain alignment, shaping the final microstructure.

Dehoff *et al.* [115] showcased site-specific control of crystallographic orientation by manipulating beam scan strategies in the context of the columnar to equiaxed transition. Dynamic switching between solidification conditions and imposing predetermined three-dimensional crystallographic orientations were achieved through varied beam scanning strategies. While the bulk component was deposited using a continuous snake raster, spot melting under nominal beam parameters was employed to define the letters 'D,' 'O,' and 'E.' Rapidly altering from point to line heat source models through beam scan speed modulation enabled the manipulation of local thermal conditions. This approach led to highly mis-oriented equiaxed grain structures within the bulk part thickness, transitioning from a <001> columnar structure due to localized scan strategies influencing the columnar to equiaxed solidification growth.

2.5.4 Process Parameters Influence on Laves Phase

An appreciation for laves phase production in as-deposited microstructures is detailed. It can be shown how localised thermal boundary conditions dictate the formation of the detrimental phase.

Ma *et al.* [68] studied the impact of energy density on laser fabricated IN718, observing that higher energy density led to larger and more abundant Laves phase in interdendritic boundaries. The average volume fraction of Laves phase increased from 5.23% (at 176 J/mm3) to 19.14% (at 600 J/mm3) in the weld fusion zone. Segregation of alloying elements like Nb and Mo is a time-dependent phenomenon influenced by non-equilibrium solidification conditions. Increasing energy density and reducing scanning speed elevate heat accumulation, extending the solidification time of the molten pool. This, in turn, facilitates easier segregation of alloying elements, particularly Nb and Mo, leading to increased volume and altered morphology of interdendritic Laves phase [85].

Stevens *et al.* [84] examined mechanical properties, microstructure, and Laves phase distribution in direct laser-deposited alloy 718 cuboids, varying laser linear energy densities (125, 75, and 50 J/mm). Solidification paths differed slightly for each layer due to variations in the ratio of thermal gradient at the solid-liquid interface and interface velocity. Initial grain growth resulted in columnar and elongated grains, aligned with the most prominent thermal gradient. In the melt pool centre, decreased thermal gradient favoured nucleation overgrowth, resulting in a more equiaxed centre. Hardness varied incrementally along the hatch direction (top, middle, and bottom layers) due to the γ'' phase distribution, despite not expected in the initial rapid solidification. Top layers experienced rapid cooling, reducing segregation, while bottom layers cooled quickly upon contact with the substrate. The centre section hypothetically had the highest hardness due to lower cooling rates, promoting more segregation and available Nb for later γ'' formation. Laves/carbide phase area percent varied across regions, averaging 2.52% at the top, 3.58% at the top of the previously deposited melt pool, and 1.46% at the melt pool edge [84].

2.5.5 Conclusive remarks

Complex inter-relationships co-exist between process parameters such as laser power scanning velocity and hatch patterns. In turn, the localised thermal gradients, solidification rate and cooling rates within the melt pool are affected. The resultant microstructure which is strictly determined by these factors have influence of grain size, aspect ratio and as seen, microstructural features which then correlate to the mechanical properties across the interface region. This pins the fundamentals of process parameter influence on resultant mechanical properties, which will continue to be explored throughout this study. Mentioning a broad range of manufacturing technologies and materials has exasperated fundamental understandings to correlate the setup of

manufacturing and what implications this has on the final build microstructure. By segmenting each individual process parameter, it can be concluded that in fluctuating every parameter will attain a different temperature history experienced by the solidified part. The research has established the foundations for varying process parameters to understand the resultant microstructural evolution.

2.6 Residual Stress Characterization

Residual stress diminishes a component's capacity to withstand applied forces and arises from factors such as plastic deformation, temperature gradients, or structural alterations. During the LMD process, accumulated heat can induce localized expansion. Upon cooling, certain areas contract more than others, leading to residual stress [116]. These stresses fall into three categories based on the characteristic length over which they equilibrate.

Type I residual stresses are long-range and equilibrate over macroscopic dimensions, resulting from processes causing non-uniform strain distribution. Such stresses span multiple grains, potentially leading to macroscopic dimensional changes [155, 156]. Type II residual stresses equilibrate over several grain dimensions, while Type III stresses exist on atomic scales, balancing within a grain, such as dislocations and point defects. Low-level Type II stresses commonly persist in polycrystalline materials due to differences in the elastic and thermal properties of neighbouring grains [117], [118].

In evaluating bulk residual stress for component longevity, Type I stresses play a crucial role, whereas micro stresses (Type II and III) are often deemed insignificant. Figure 2.26 provides a summary of the various types of residual stresses.

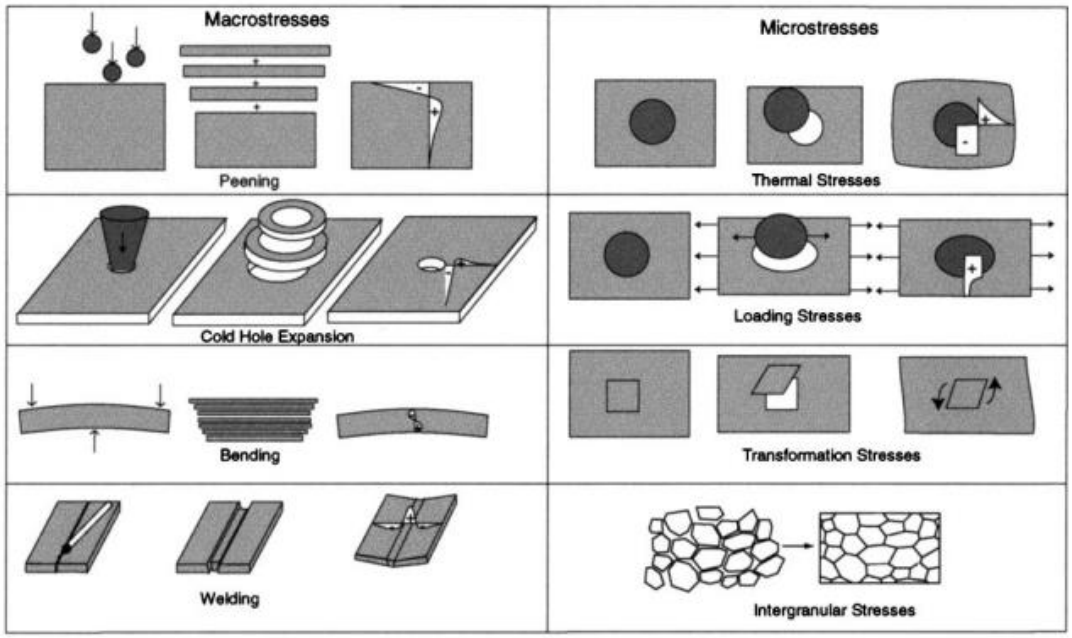

Figure 2.26 Illustration of different types of macro and micro residual stress [117].

2.6.1 Residual Stress Measurement Techniques

Table 2.3 summarises the capabilities of various techniques used for residual stress characterization including X-ray diffraction and contour method which are discussed in more detail in the materials and methodology chapter since these techniques pertain to this project. A brief outline of the hole drilling and neutron diffraction principles are described.

Hole Drilling Technique

The hole drilling technique will relax the localised residual stresses, thereby providing data for back-calculation. Using a strain gauge rosette, the principle of local relaxation will be implemented to calculate residual stress from [117]:

$$\sigma = (\sigma_{max} - \sigma_{min})\bar{A} + (\sigma_{max} - \sigma_{min})\bar{B}\cos 2\beta$$

Where $\bar{A}\ and\ \bar{B}$ are hole drilling constants, and β is the angle from the x axis to the direction of maximum principal stress, σ_{max}. It is possible to deduce the variation in stress with depth by incrementally deepening the hole (incremental hole drilling), it is often difficult to obtain reliable measurements much beyond a depth equal to the diameter. Additionally, this method is not practical for thin (~100 μm) or brittle coatings [119].

Neutron Diffraction

Neutrons possess a slight advantage over X-rays due to their wavelengths being comparable to atomic spacing, allowing penetration into engineering materials at depths

typically measured in centimetres. Figure 2.27 depicts the principle that elastic strains arise from alterations in lattice spacing within a crystalline material. Stresses are computed using the elastic properties of the material according to Hooke's law. Strains within a confined volume can be determined at different locations in the specimen and calculated using the approach outlined in [117].

$$\varepsilon_{hkl} = \frac{d_{hkl} - d^o_{hkl}}{d^o_{hkl}}$$

Where d_{hkl} is the measured d spacing for hkl reflection and d^o is the stress-free d-spacing and ε_{hkl} is the elastic strain normal to the hkl plane. Once the train is determined at the given location in three orthogonal directions, it's possible to calculate the corresponding stress from the following equation:

$$\sigma_x = E_{hkl} \frac{\left((1 - v_{hkl})\varepsilon_x + v_{hkl}(\varepsilon_y + \varepsilon_z)\right)}{(1 + v_{hkl})(1 - 2v_{hkl})}$$

Where, E_{hkl} and V_{hkl} are the elastic constraints for the direction normal to the planes for the specific hkl reflection and ε_x, $\varepsilon_x$and ε_x a are the strains measured in three orthogonal directions.

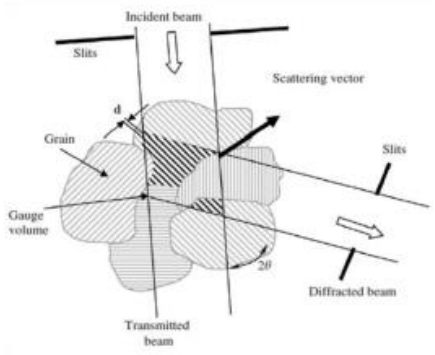

Figure 2.27 Principle of neutron diffraction technique for residual stress characterisation, showing the scatting vector for a Bragg reflection of crystal planes [120].

Table 2.3 Summary of various measurement techniques and their attributes adopted from Withers et al. [139] N.b. <II> represent volume averaged type II stresses.

Technique	Penetration	Spatial Resolution	Accuracy	Comments
Hole drilling (distortion caused by stress relaxation)	~1.2 x drill hole diameter	50μm	±50MPa, limited by reduced sensitivity with increasing depth	Measures in-plane type I stresses and is semi-destructive
X-ray diffraction (atomic strain gauge)	<50 (Al); <5 μm (Ti); <1 mm (with layer removal)	1 mm laterally; 20 μm depth	±20 MPa, limited by non-linearities in $\sin^2\psi$ or surface condition.	Non-destructive as only surface measurement; sensitive to surface preparation; peak shifts: type I and <II> peak widths: type II, III
Neutrons (Atomic strain gauge)	200 mm for Al, 25 mm for Fe and 4 mm for Ti	500 μm	±50 x 10^6 strain, limited by counting statistics and reliability of stress-free references.	Access difficulties; low data acquisition rate and costly; peak shifts: type I and <II> (widths rather broad)
Ultrasonics (stress related changes in elastic wave velocity)	>10 cm	5 mm	10%	Microstructure sensitive. All three types (I,II and III)

2.6.2 Distortion and Residual Stresses during LMD

The introduction of a highly localized heat source in laser metal deposition results in steep thermal gradients and exceptionally high cooling rates. Residual stresses produced by this process, particularly tensile stress, are often undesirable. The complexity of residual stress evolution stems from accommodating thermal expansion and contraction caused by severe thermal excursions. Understanding the stress distribution field is crucial for evaluating the as-deposited part, especially in remanufacturing, where the final component may experience distortion, warping, and delamination.

Mercelis *et al.* [121] proposed two primary mechanisms elucidating the genesis of residual stress in additive manufacturing. The first mechanism hinges on the temperature gradient during the heat source irradiation. Moving the heat source results in rapid cooling (exceeding 10^3 K/s - 10^7K/s) [156] and solidification, forming a temperature gradient up to 10^4K/mm near the melt pool [124]. The molten pool's shrinkage is constrained by surrounding material during cooling. Thermal strain transformation to plastic strain and material properties recovering during temperature decrease induce significant tensile residual stress near the melt pool [125].

These thermally induced stresses are confined by the cold material, resulting in the development of complex stress fields that evolve throughout the build and substrate. Figure 2.28 illustrates the fusion zone, temperature field, and consequently, the residual stress field.

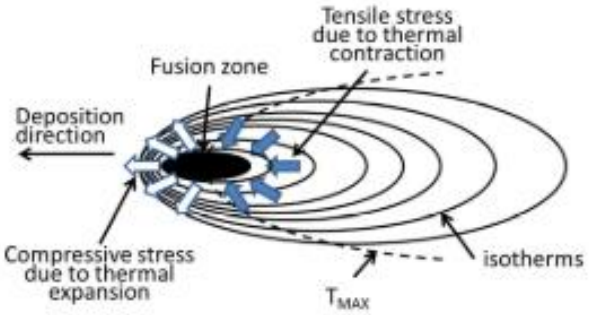

Figure 2.28 Temperature and stress field around a welding heat source [126].

The second mechanism, integral to additive manufacturing, is the cool-down mechanism, characterized by the pronounced shrinkage of each subsequently deposited layer during the cooling process. The shrinkage is constrained by the lower layer deposited previously, inducing tensile stress in the current layer, and introducing compensatory compressive stress in the underlying layer. In a layer-by-layer deposition, continuous compressive

stresses accumulate internally to counterbalance the tensile stresses concentrated near the surface [127]. Numerous researchers have substantiated this mechanism [163]-[166]. Wu *et al.* [132] employed neutron diffraction and the contour method to assess the stress distribution in an L-shaped 316L sample, revealing compressive stresses in the part's centre compensating for outer surface tensile stresses (see Figure 2.29). Levkulich *et al.* [133] confirmed this principle by demonstrating the residual stress distribution in LBF Ti-6Al-4V. This stress profile poses a threat to mechanical properties and post-manufacturing machining, necessitating a comprehensive understanding, control, and possible mitigation of residual stress behaviour.

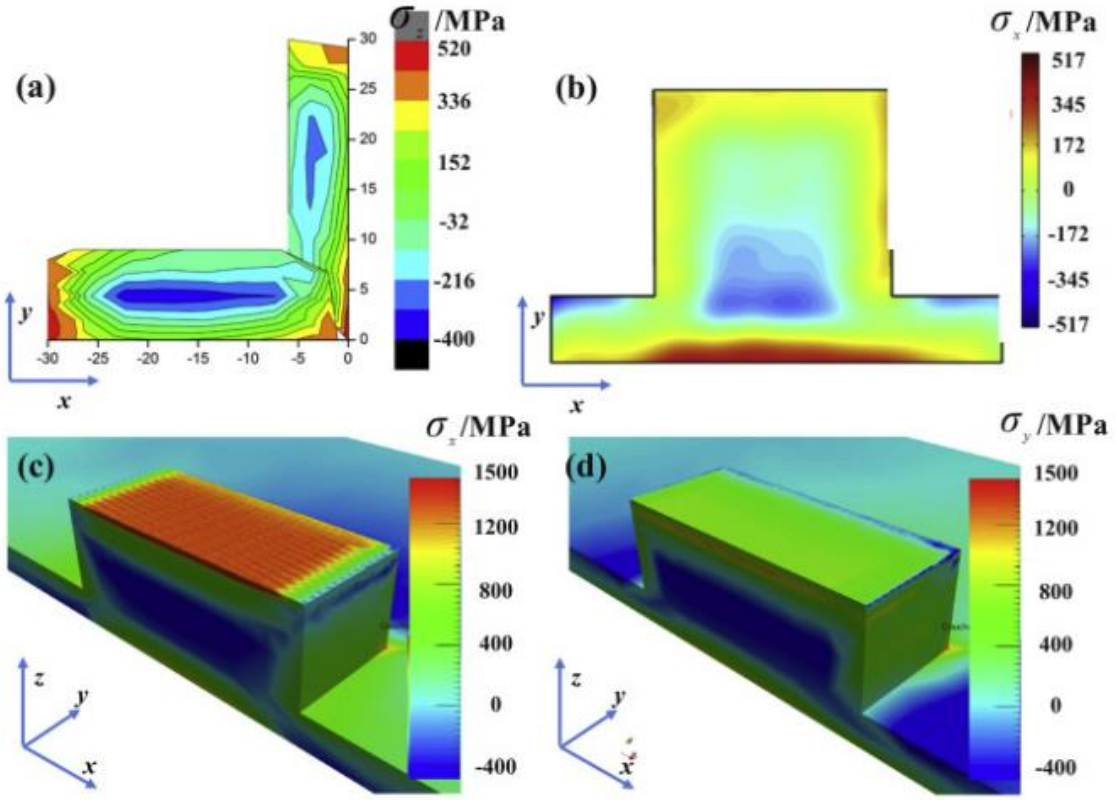

Figure 2.29 Residual stress behaviour showing compressive centre stress balancing outer surface tensile stresses in (a) L-shapred 316L specimen[132] ***and (b) a block deposited using LBP Ti-6Al-4V [134].***

Residual stress fields in direct energy deposition have gained increased attention in recent years. Limited but growing research explores the correlation between process parameters and residual stress in laser metal-deposited components through experimental [170]-[173] or modelling approaches [178]-[180]. Computational models aim to predict behaviour and resulting fields, necessitating validation through quantitative measurements, including destructive and non-destructive techniques.

2.6.3 Effect of Process Parameters on Residual Stress and Deflection

Thermal, mechanical, or a combination of treatments aim to mitigate residual stress and distortion in components. These methods include *in situ* substrate preheating, post-process heat treatment, and peening. However, in repair scenarios, the latter two methods may cause undesirable alterations to the parent material. Substrate preheating minimizes thermal gradient, cooling rate, and thermal stress in the deposited region by insulating the material. Nevertheless, caution is required, as excessive preheating can adversely impact final performance, inducing grain coarsening in the melt pool area and the heat-affected zone [149], [150].

A validated thermomechanical model developed by Cao *et al.* [144] predicted residual stresses in Ti-6Al-4V builds via electron beam additive manufacturing. Rigorous validation against neutron diffraction measurements ensured accuracy. Profiling with good precision, the finite element model explored scenarios with no preheat, single, double, and triple scans before deposition. Distortion decreased by 12% and 18% with double and triple scans, respectively. Residual stress in the first deposited layer reduced from ~320MPa (no preheat) to ~280 MPa, ~265 MPa, ~245 MPa for one, two, and three preheat passes (see Figure 2.30). Surprisingly, peak stresses in successive layers were minimally affected. Preheating decreased maximum tensile stress at the substrate-interface region by reducing thermal expansion mismatch between the substrate and newly deposited layer, thereby mitigating residual stress.

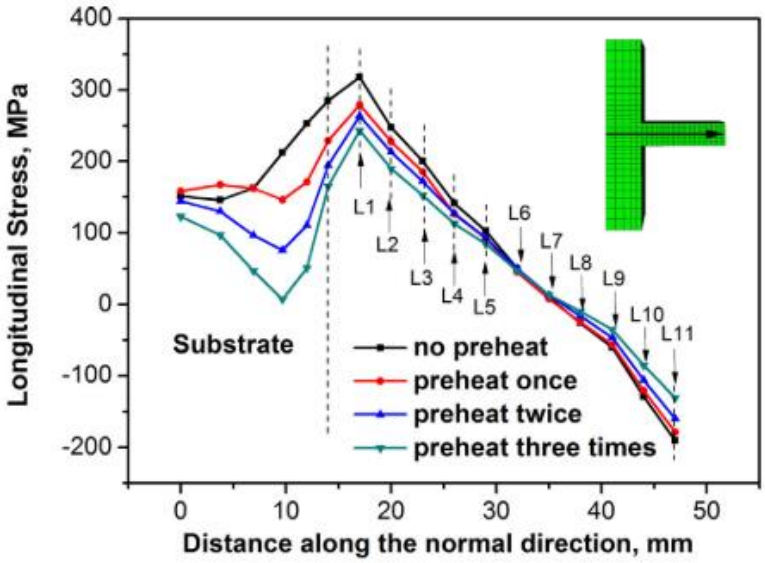

Figure 2.30 Variation in longitudinal stress along normal direction for the preheating comparison [144].

Wang *et al.* [151] investigated the residual stress and distortion phenomena during Selective Laser Melting (SLM) of AISi10Mg components utilizing X-ray methodology. The study revealed that the process parameters exert varying influences on the residual stress of the specimen. Specifically, the laser energy was identified as a critical factor affecting the energy input, with an observed escalation in residual stress values along the X-direction. The augmentation of laser power from 200 W to 300 W and 400 W resulted in an increment from 95 MPa to 115 MPa and 135 MPa, respectively. Moreover, in the Y-direction, measurements of 60 MPa, 73 MPa, and 86 MPa were recorded for laser powers of 200 W, 300 W, and 400 W, respectively, at the midpoint of the sample. Mugwagwa *et al.* [152] reported a similar correlation between laser power and scanning speed in SLM. Increasing these parameters led to heightened levels of deformation in a cantilever, as demonstrated in experiments with laser powers ranging from 80 W to 180 W, incremented in 20 W intervals. Lai *et al.* [153] contributed insights indicating that elevated laser power, coupled with reduced scanning speed, corresponds to heightened residual stress levels. Their findings underscore the intricate relationship between process parameters and the resultant material stresses in SLM. Finally, a simulation study by Ali *et al.* [154] demonstrated a direct association between increased laser power, decreased layer thickness, and an escalating trend in residual stress in SLM-produced Ti-6Al-4V. The reports collectively suggest that higher heat source power results in the generation of greater residual stress, attributable to the heightened localized maximum temperature and the corresponding increase in temperature gradient induced by increasing laser power.

Rangaswamy *et al.* [140] investigated the impact of varied raster scanning on laser-deposited IN718, characterizing residual stresses using neutron diffraction and the contour method. The study revealed that the laser rastering directions had minimal influence on residual stress magnitude parallel to the melt pool direction, remaining predominantly uniaxial in the growth direction for all sample geometries. Vrancken *et al.* [137] corroborated this dominant residual stress orientation along the build direction using the contour method. In contrast, Moat *et al.* [135] explored residual stress in laser deposited Waspaloy, employing neutron diffraction and the contour method. Varying traverse speed, laser pulse time, and cycle time consistently yielded specific energy density. Longitudinal stresses were found to be tensile near the top of the build mid-length, decreasing towards the bottom, while perpendicular stresses at the same location were negligible. At the base of the wall, perpendicular stresses were compressive towards the centre and tensile at the edges, as illustrated in Figure 2.31.

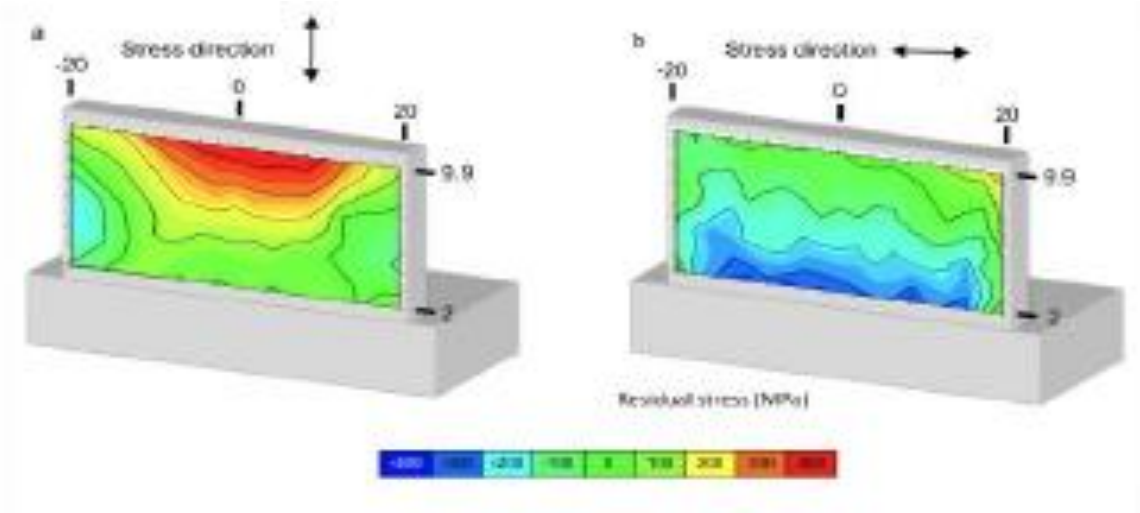

Figure 2.31 Contour residual stress maps on a 20-layered (5 mm thick) Waspaloy wall a) longitudinal, i.e., along melt-pool moving direction b) along build growth, i.e., perpendicular to substrate [170].

A comprehensive investigation into the effect of scanning strategy on residual stress development for laser powder bed fused commercially pure Ti [156] was conducted. Seven types of scanning strategies including unidirectional, bidirectional and chequerboard were chosen to determine direction of principal stress. A combination of good agreement between deflection measurements, hole drilling and contour method were utilised. It was found that residual stress in SLM components manufactured using unidirectional vectors, is primarily orientated in scanning direction with a stress roughly half the magnitude exists in the direction normal to the scan vector. The implementation of the chequerboard scan strategy had a negligible effect for reducing residual stress and making the stress less isotropic. However, work by Goel *et al.* [157]and Mugwagwa *et al.* [158] found that the chequerboard raster scanning compared to bidirectional and unidirectional contributed to least average residual stress and lowered residual stress up to 40% relative to default island scanning strategy but majorly impact build time. The lower amount of residual stress could be explained by the more homogenous heating of the powder-bed, reducing the thermal gradients.

Surface residual stress measurements were conducted using X-Ray Diffraction on multi-layered thin-walled LMD IN718 samples [159]. The local heating, rapid solidification, and self-quenching processes induced an average tensile stress of 512 MPa ± 15.46 along the X-direction (longitudinal, parallel to melt-pool direction). Post heat-treatment at 1050ºC for 1 hour (HT1050) mitigated these stresses, reducing them by over 50%. Luzin and Hoye [160] reported zero traverse and normal stress components in thin-walled Ti64 samples fabricated by Wire-Arc Additive Manufacturing (WAAM), with a longitudinal

stress component reaching 400 MPa. This aligns with findings by Szost *et al.* [161], indicating high stresses of 500 MPa for WAAM and 300 MPa for laser cladding in thin-walled Ti64 components. Notably, the study observed maximum longitudinal residual stresses in the wall-baseplate transition for both manufacturing methods, as illustrated in Figure 2.32.

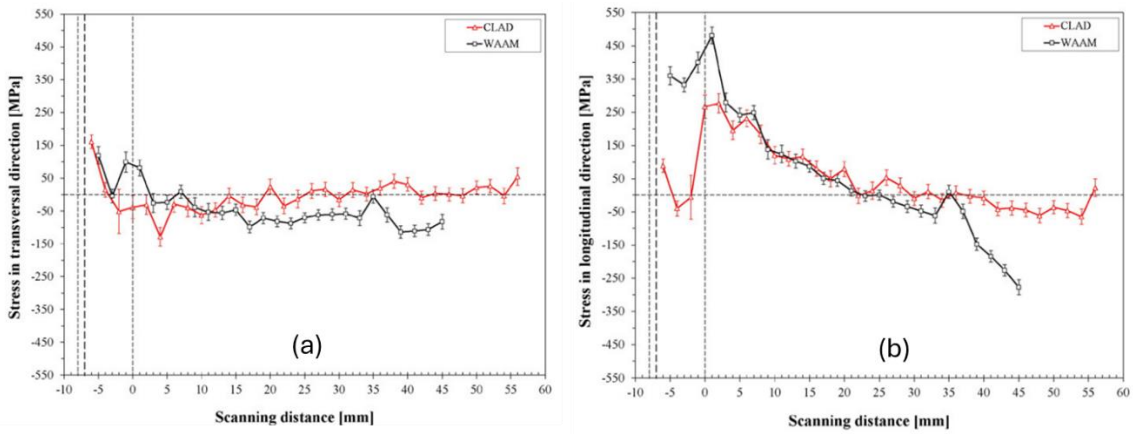

Figure 2.32 Stress measured by neutron diffraction (a) Stress σxx in transversal direction (b) Stress σxx in normal direction [161].

2.7 Research Gap with Residual Stress Behaviour

Using a combination of measuring techniques employed at various locations will aid the understanding of residual stress development from substrate to the interface region and as it progresses into the built component. A noticeable similarity for investigation results comes in the form of coupled finite element models with limited evidence of support calculating residual stress experimentally. In addition, predominately, residual stress measurements are calculated for components manufactured by selective laser melting, therefore a gap exists concerning the interface region produced via laser metal deposition and not only being simulated but experimentally calculated. The interface region requires extensive investigation as this area is subjected to large thermal gradients generating large residual stresses which could lead to undesired distortion, cracks and even premature failing of the build process or in service [73], [161]. Therefore, it becomes imperative to understand the thermo-mechanical behaviour of the material and resultant equilibrium state of the whole component to employ mitigation tactics (i.e. varied raster scanning, laser power control or even post weld heat treatment if applicable). An experimentally coupled FEA model would allow the effect of varied process parameters to be simulated in a cost-effective manner, the state-of-the-art modelling techniques will now be reviewed.

2.8 Thermal and Thermo-Mechanical Modelling of Direct Energy Deposition

2.8.1 Introduction

Simulating laser-assisted additive layer manufacturing complexity involves understanding the heating, melting, and solidification of alloy by a moving heat source in a layer-by-layer manner. A graphical representation of the simulation's complexity outlines three main model components: Thermal, Mechanical, and Microstructural [162][163]. The latter falls out with the project scope but would require an accurate experimentally validated simulation of the temperature history of the as-built component for successful prediction of microstructural evolution. The focus of this thesis is to develop thermomechanical model based on fluctuating input parameters during laser metal deposition, specifically for Inconel 718, with a primary emphasis on understanding the transient temperature history across the interface region and analyse *in situ* residual stress behaviour and the resultant stress state. Figure 2.33 acts a visual aid representing the complexity of the simulation problem and depicts how each sub-category can be further strategized to enhance the accuracy of the simulation.

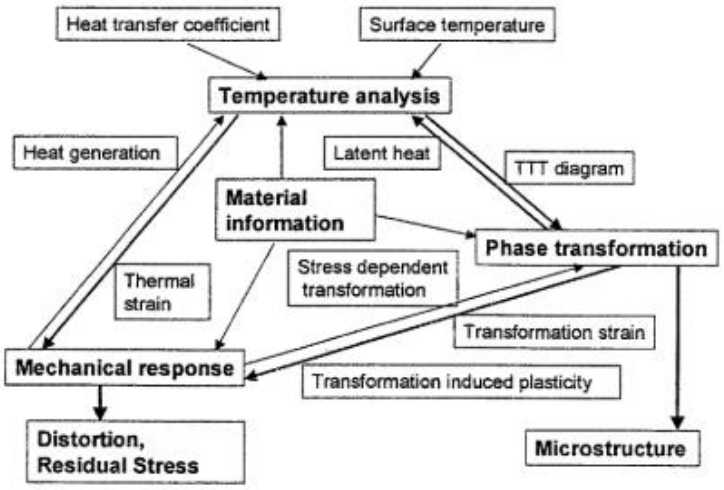

Figure 2.33 Diagram of the three sub-models and couplings to simulate thermo-mechanical processing of metals [164].

Accurate prediction of phase transformations and microstructure is crucial for developing components with desired material characteristics. Combining phase transformations and material constitutive models with thermal stress computation is essential [164]. However, the limited modelling approaches for additive manufacturing techniques pose challenges in optimizing material properties and surface qualities due to uncertainties [165]. The coupling of stress and strain is often overlooked in heat transfer equations and kinetic

models, affecting accuracy. While advancements in software allow simultaneous solutions for thermal and mechanical fields, this process is computationally demanding. The staggered approach, commonly used in Finite Element Analysis software, involves separate thermal and mechanical analyses for each time step, with the resulting temperature field as a load. Many modelling approaches follow a simplified procedure: problem identification, data collection, correlation principles determination, process model establishment using finite element analysis software, and experimental validation. As mentioned, the prediction of resultant microstructure falls out with the scope of this project but could be integrated in further work.

2.8.2 Analytical Models

Analytical models in laser additive manufacturing utilize established heat transfer principles, specifically drawing from classical heat transfer theory. These models are deliberately streamlined to minimize computational complexity, serving as an expeditious and preliminary means of simulating the manufacturing process. Their inherent limitations in precision stem from simplifications related to assumptions concerning the spatial and temporal dependencies of the laser source and the sample's geometry under irradiation.

The foundational models, inspired by Rosenthal's solution for a moving line source, facilitate the prediction of required power and laser welding speed for a single pass weld. These models integrate the temperature solution of a line source over time and motion using the equation X=$X_o + vt$ [166], where X denotes the travel distance of the laser beam, v represents the scan velocity, and t denotes time [119]. Crucial material properties, including thermal diffusion coefficient, thermal conductivity, and absorption rate, are indispensable for forecasting melt pool geometry and depth. An inherent limitation lies in the treatment of the laser as a line source, deviating from the more realistic Gaussian beam source [167]. Furthermore, these models exclusively consider conductivity as the sole heat transfer effect, assuming material properties to be independent.

Pinkerton and Li [168] developed an analytical model to predict powder flow into and out of the melt pool in the LMD process. The main advantage of this model is the incorporation of laser-powder interaction and the effect of wasted powder. Temperature averaging across the melt pool and empirical deviation of the heat conduction constant was compared with experimental results to facilitate all laser types to predict major variables in the process including melt pool length and temperature.

Constrained by limitations in experimental validation, analytical models exhibit reduced flexibility in their modelling approach [169]. Particularly, they find utility in predicting track geometry without necessitating accreditation of the process. Picasso *et al*. delved into the interactions among powder particles, the heat source, and the melt pool to anticipate track height, contributing to the comprehension of pertinent phenomena and the establishment of cladding maps [170]. However, the model's simplicity led to a significant error in evaluating the molten pool shape [170].

Building upon this, Ahsan and Pinkerton [171] formulated a more representative analytical model capable of delineating track profiles for Ti-6Al-4V under various laser powers and powder feed rates. Despite the model's successful verification process, demonstrating good alignment with thermal fields and track dimensions, its analytical nature enables the derivation of melt pool geometry directly from the temperature field, obviating the need for domain discretization [169], [171].

Kumar and Roy [172] introduced a 3D heat transfer model encompassing Marangoni convection, powder particle addition, and phase changes. By manipulating scanning speed and Marangoni number, variations in melt pool size and convection strength were observed. Marangoni-Bernard convection dominated, particularly in investigating the liquidus front of the molten pool's trailing edge, resulting in a noticeable bulge with increasing Marangoni convection values.

Peyre et al. [173], [174] proposed a 2-D analytical solution that evolved into a 3-D simplified model for Laser Metal Deposition (LMD) incorporating Arbitrary Lagrangian Eulerian (ALE) free surface motion, realistic laser irradiation, and boundary conditions, excluding fluid flow considerations. Validation of the thermal model involved a comparison with experimental data, including melt-pool analysis and thermal measurements on Ti-6Al-4V alloy for ten layers. Figure 2.34 illustrates numerical thermal cycles, showing satisfactory agreement with thermocouple measurements and simulated temperature profiles, particularly for the P=600W and V=200 mm/s condition, with a modest 50-100K difference in the first deposited layer.

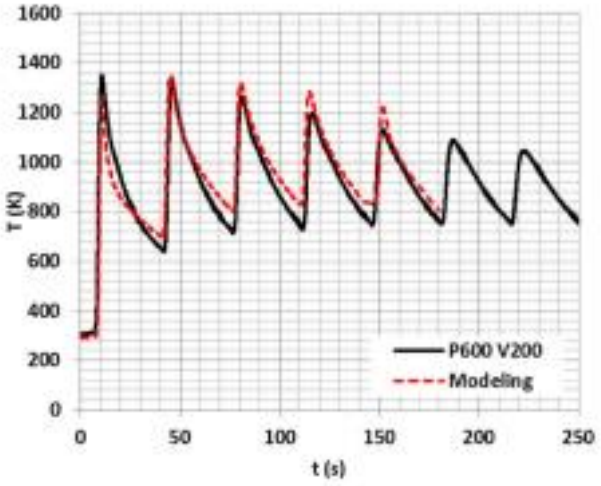

***Figure 2.34 Comparison of temperature profiles recorded by thermocouples (black) in the centre of the substrate, 3 mm from the interface and the simulated temperature profile (*red) [174].**

Analytical models enhance process understanding and parameter selection for process mapping. However, for complex substrate geometries, build complexities, and nonlinear material properties, analytical solutions become impractical. Hence, a numerical model is imperative, albeit at the cost of increased computational time.

2.8.3 Numerical Models

The imperative relationship between processing parameters and melt pool behaviour underscores the significance of comprehending it for the optimal refinement of microstructure and mechanical properties in Laser Metal Deposition (LMD) components. Computational models, commonly derived from welding principles, facilitate Finite Element Analysis (FEA) of the LMD process due to the shared interactive dynamics. However, these computational models typically omit consideration of convection or applied free convection, particularly when dealing with diminutive deposit material in relation to the substrate size. To achieve a more accurate simulation of the intricate thermal history encountered in additive manufacturing, the conceptualization of additive manufacturing as a multi-pass welding process is warranted [175], [176].

Finite Element Analysis or Method (FEA/FEM) addresses the steady-state or transient energy conservation equation under specified boundary conditions. While these analyses typically do not account for fluid flow effects, potentially leading to temperature overestimations, they proficiently capture three-dimensional steady-state or transient temperature distributions. These models, with the capacity to integrate with mechanical analyses, enable an exploration of the thermal and mechanical ramifications of LMD. The deposition of additional material is simulated through techniques such as active/inactive

or birth/death, portraying the track profile as a square profile. For optimal efficacy, these models amalgamate a microstructure with a property model, necessitating a homogenization assumption to derive macroscopic material properties [177] [169].

Hekmatijou *et al.* [178] conducted a comparative analysis between an analytical equation and Finite Element (FE) modelling in the context of laser welding aluminium alloy 5456 components. The analytical model, based on the Rosenthal equation, was observed to overestimate melt pool dimensions due to assumptions made in the analytical solution, particularly the neglect of heat losses through the substrate. The FE model, leveraging genuine material characteristics, demonstrated enhanced accuracy, and is deemed more suitable for investigating the heat transfer behaviour of welded components, particularly at higher heat inputs.

A study on modelling strategies for predicting residual stresses in single-track laser deposited IN718 employed a coupled thermo-mechanical simulation with realistic track geometry. Walker *et al.* [169] utilized a semi-analytical-numerical approach to predict track profile, temperature fields, melt pool geometry, and stress evolution. Thermocouples were encapsulated to achieve good agreement between simulated and experimentally obtained thermal histories, with a maximum error of 3.1% observed for peak temperature. Discrepancies, primarily arising after the heat source passed the thermocouple, were attributed to the non-adaptive heat source model. Despite potential heat loss through conduction between the CNC bed and substrate, incorporating this into the model would significantly increase complexity and computational burden. Overall, the process's fusion zone and associated temperature field were accurately predicted, ensuring correct representation of material expansion and contraction in the mechanical part of the Finite Element (FE) model [169].

Based on the complexity of models, FEA models can be divided as basic models which consider simple heat flux on top of the melt pool, standard models which use temperature dependent material models, accurate models which define the melt-pool shape and very accurate models which have very fine meshes and small-time steps for higher degree of accuracy [119]. The latter models are often coupled with computational fluid dynamics (CFD) [179] which are highly accurate for localised thermal gradients and melt pool formations, excellent detail for microstructural investigations but are very computationally expensive. For transient temperature profile and residual stress measurements, which are the main outcome of this study, the correct heat input could be considered rather than a detailed melt-pool shape to reduce the computational time. The

current state of the art simulation approaches will now be discussed to appreciate the market for FEA/FEM of LMD.

2.9 State-Of-The-Art Coupled Simulation analysis

A summary of recent investigations whereby thermomechanical modelling was applied in coincidence with deposition techniques are summarised in Table 2.4. This includes the details of processing route, material investigated, and validation techniques applied. Major outcomes highlight specific areas of interest for guidance in the sub-categories concerned with modelling; source of energy, element technique and validation methods collaborated for simulation accuracy.

Table 2.4 State-of-the-art Thermo/mechanical Modelling Techniques including the major outcomes of investigation.

Process	Heat Source Model	Element Technique	Type of Analysis / Software Applied	Validation Technique	Major Outcomes	Ref
Direct Energy Deposition Powder Feed	Ellipsoidal	Hybrid approach	3D Uncoupled with quasi-static incremental analysis, CUBIC	Integrated K-type thermocouples, Hole-drilling	Incorporating a measurement-based forced convection, the accuracy drastically improves temperature field results and corresponding residual stress – errors less than 11% when compared to *in situ* temperature measurements whereas free convection simulates temperatures with up to 44%	[180]
	Double Ellipsoidal	Hybrid	3D Uncoupled Thermal Model, CUBIC code by Pan Computing LLC	Not specified (Model Verification than validation)	Both methods (active and inactive element) resulted in artificial heating generation unless the temperature of the active elements are reset to initial temperature during activation to enforce discontinuity of temperature field. Inactive element method results in reduced number of degrees of freedom, requires longer computer run times than the quiet element method due to continuous equation remembering and solver initialization. New hybrid approach elements corresponding to deposition are inactive, then switched on layer-by-layer basis. Neglecting surface convection and radiation on evolving interface (region between active and inactive) leads to over predicting temperatures	[181]
	Ellipsoidal	Quiet	3D – Coupled, Not Given	K-72 Thermal couples attached top and bottom surfaces, Distortion	Thermal analysis validated through point-wise temperature history showing good agreement. Experimentally validating the mechanical simulation	[182]

				distribution with laser-scanned geometric configuration	which showed the distortion map is explained by contraction-induced bending analysis – depositing on cantilever fixture causes thermal contraction on top of the surface, thus edges bend upwards	
	Gaussian (Volumetric)	Not Given	3D – Uncoupled Temperature history with Residual stress calculations, ABAQUS	Thermocouple & Comparison of published results for stress (X-ray diffraction in study)	Under similar processing conditions IN718 is more susceptible to warping, buckling and delamination due to higher residual stress to yield strength ratio. Increasing the layer thickness, residual stresses can decreased by 30%. Doubling heat input can reduce residual stresses by 20% but increase distortion by 2.5 times – a trade-off needs organised. Residual stresses change from tensile to compressive at layer interface.	[183]

Table 2.4 Continued

Process	Heat Source Model	Element Technique	Type of Analysis / Software Applied	Validation Technique	Major Outcomes	Ref
	Goldak's Double Ellipsoidal	Hybrid quiet-inactive element activation	3D Coupled Thermomechanical, Project Pan (Autodesk Inc)	Neutron Diffraction on VULCAN	Thermomechanical model predicts two walls made under different dwell times experience similar stress versus position trends and values. Compressive stresses at transition period (interface region) while tensile at the top of the wall. Experimentally measured values agree with trends, particularly when using the not heat-treated samples, residual stress in the build mostly compressive which is in good agreement with thermomechanical model. Neutron diffraction and modelling are complementary techniques to determine residual stress and strains in AM builds	[136]
	Gaussian distribution conical shape	Inactive/Active Method & Dummy Material method	3D – Uncoupled, SYSWELD	Experimentally compared to published data (Comparative study uses ultra-high-speed digital imaging techniques)	The laser configurations were optimized to maintain a steady molten pool size. After the initial transient due to cold substrate, the dependency of laser power correlated linearly to layer number for all speeds analysed. Laser power must increase with translational velocity to maintain melt pool size. Optimizing the pool size results in a stead temperature distribution and relatively uniform microstructure of part	[184]

	Gaussian volumetric heat distribution with Conical Shape	Element-birth formulation/inactive	3D coupled thermo-mechanical structural welding simulation model, Simufact.welding7	K-type thermocouple, Digital Image Correlation (DIC)	*In situ* measurement of distortion allowed through DIC acquisition, A good agreement between final distortion – however for x-distortion results slightly deviate but for z-direction the simulation underestimates by a factor of 3	[185]
Wire Feed	Gaussian distribution	Active/Inactive Elements	3D Uncoupled, Thermomechanical model with compiled MATLAB files	Thermocouples, Distortional displacement measured	Heat convection effect of flowing fluid is 3-5 times greater than of liquid in static state, Absorptivity of laser power is approx. 15% in current laser hot-wire condition, All simulated temperature histories of thermocouples supersede experimental values, the relative error keeps within 25% - phase transformation temperatures are not considered in model which affects temperature	[186]

Table 2.4 Continued

Process	Heat Source Model	Element Technique	Type of Analysis / Software Applied	Validation Technique	Major Outcomes	Ref
Powder Bed Fusion	Gaussian Conical moving heat Source	Inactive elements	3D Coupled Thermomechanical, ABAQUS	Not Provided	The island scanning strategy obtained the highest maximum temperature. Based on the stress and deformation results, by rotating the scan patterns by 45° produced the lowest residual stress and deformation when compared to all scanning strategies. The in-out scanning approach accumulated the largest deformation in build direction.	[187]

				Room temperature neutron measurement and model prediction after cooling regarded as remarkable, in trends and in stress levels. Model correctly predicts hoop stress near the top and build plate, tensile axial stress near the edges and compressive axial in the middle. Simplified FEM model with multiple layer-wise activation provides a comprehensive residual stress prediction. Neutron diffraction is an effective reliable technique to measure residual stress non-destructively for bulk materials. Simplified FEM model with multiple layer-wise activation provides a comprehensive residual stress prediction. Neutron diffraction is an effective reliable technique to measure residual stress non-destructively for bulk materials.	
Simplified Volumetric Uniform Distribution	Layer-by-layer Activation	3D Coupled thermal-displacement, ABAQUS	Neutron Diffraction		[188]
Goldak double ellipsoidal	Quiet element approach	Thermal FE Only, CUBES – Pan Computing	Fixed surface of substrate K-type thermocouples	Captured similar peak temperatures and thermal profiles with experimental, The experimental errors between the two thermal couples (TC1, TC2) are 0.4% and 11% for Case 1 (230W and 55.03 mm/s) and 0.4% and 6.6% for Case 2 (115W and 50.80 mm/s) By excluding pre-placed powder layer from the analysis (Assuming powder layer is insulator), the maximum discrepancy at any time is a 4.4% over prediction of temperature however at distances further away from the melted and solidified region, and the maximum difference in temp prediction is 31.4%.	[189]

2.10 Contextualization of state-of-the-art modelling

From the various published literature populated in Table 2.4, the following conclusive remarks can be made:

- The Goldak double ellipsoidal heat source model with Gaussian distribution is a popular approach to model the irradiated volume.
- The incremental addition of material onto the substrate requires employing certain techniques, the 'hybrid activation model' takes advantage of both inactive and quiet modelling approach. In the hybrid activation method, non-deposited layers are eliminated, leaving only the depositing layer in the model. The non-deposited elements are scaled down using the quiet element method. The subsequent layer is incorporated, and nodes/elements are renumbered using the inactive element activation method, making its non-deposited elements quiet. This procedure yields a smaller, less ill-conditioned stiffness matrix, reducing computational effort [190].
- A 3D coupled thermo-mechanical FEA numerical model will sufficiently simulate the transient temperature field with good accuracy and the resultant simulated residual stresses agreed experimentally.
- The numerical models can be implemented prior to experimental trials for the optimization of process parameters such as rotating the scan patterns by 45° produced the lowest residual stress and deformation when compared to all scanning strategies.
- As we reduce simplified or excluded assumptions, the accuracy of simulated fields improves. By experimentally calibrating different facets of the model, such as the melt pool shape, both the transient temperature field and, if coupled, simulated stress fields show significant enhancement.

2.11 Key thermomechanical Improvements

2.11.1 Meshing

Mesh studies are often conducted to have an optimised approach to accuracy and computational time [191], [192], [193], where refinement strategies near the melt-pool are often employed which become coarser away from the melt pool to reduce computational cost. A dynamic graded mesh which becomes refined with a moving heat source is highly beneficial to eliminate the computational costs with dense meshing strategies, these are often called adaptive. The automatic meshing technique is helpful in

reducing the computational cost but requires a separate code to be implemented in the FEA solver as no commercial software employ this technique [194], [195].

The generated mesh should have a low number of elements, preferably hexahedral, with an allowable change of multiple parameters. Seeding the working domain requires intricate distancing to better improve accuracy at the penalty of computational time. The input parameters for the macro-mesh are:

- Number of elements per section
- Plate dimensions: width, breadth, height
- Number of divisions of each division of the geometry
- Ratio between first and last division

Following this, element type should accurately resemble interactions during deposition, C3D8R/DC3D8 element type allow heat storage and heat conduction. The diffusive elements have only temperature degrees of freedom and involve either first-order or second-order interpolation in three dimensions.

Structured meshes may exhibit regularity, featuring elements of uniform size in both the base plate and deposited material (Figure 2.35.a), or bias, with elements progressively varying in size along specific directions or locations (Figure 2.35.b) The application of structured meshes with uniform-sized elements necessitates the adoption of expansive meshes to ensure high-quality numerical predictions. However, this approach results in an increased number of degrees of freedom and yields substantial stiffness matrices, significantly escalating memory and CPU time requirements [196].

Structured biased meshes mitigate the previously mentioned issue by enlarging the element size in the base plate as the distance from the deposited material increases [197]. This reduction in element density helps decrease the total number of degrees of freedom while preserving the accuracy and efficiency of calculations, particularly in regions characterized by higher temperature gradients and stress concentrations.

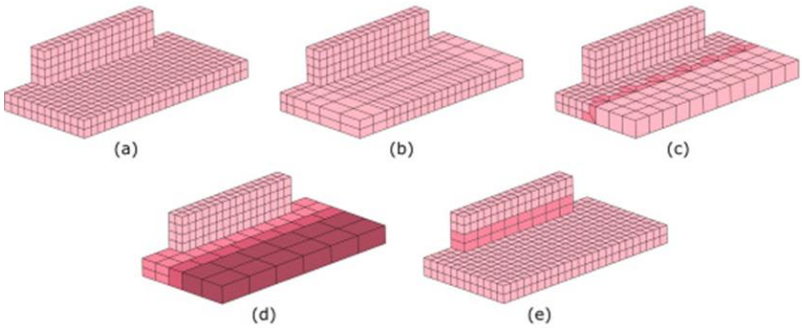

Figure 2.35 Meshing techniques utilized in FEA modelling of additive manufacturing (a) regular mesh, (b) structured biased mesh, (c) unstructured mesh with transition templates, (d) unstructured mesh with multiple deformable objects in contact, and (e) layer-by-layer mesh coarsening of the deposited material [196].

2.11.2 Boundary Conditions

The Laser Metal Deposition process involves three heat transfer mediums: radiation from the heat source, combined radiation-convection across the manufactured component's surface utilizing air convection, and conduction through the printed material and surroundings [198]. The clamping configuration in this process acts as a heat sink, influencing the heat transfer model and enhancing cooling rates at localized sections. Cooling times are determined by free convection and radiation conditions, governed by Newton's law of cooling, which relates convective heat transfer to the temperature difference between the surface and the environment. The heat flux boundary conditions involve a combination of convection and radiation to balance heat loss to the environment and conduction through the substrate. The convective heat transfer is denoted as:

Equation 2.1 Convective boundary condition

$$Q_{convection} = h\left(T_{surface} - T_{environment}\right)$$

The module surface temperature ($T_{surface}$) and surrounding ambient temperature ($T_{environment}$) are given values are usually defined experimentally. H is the convection coefficient across the printed module in $W/(m^2K)$, which is cited as 25 W/m^2 [199] [200] or 35 W/m^2K after calibration [201]. The literature displays an inconsistent implementation of convection in LMD thermomechanical modelling. Heat loss due to convection is in some cases regarded as negligible and therefore excluded in some analytical models [202] [203]. Convection is assumed to be uniformly distributed over all surfaces and equates to free convection in air (≈$10W/m^2/°C$) [204] [205].

Heigel *et al.* [180] underscore the crucial role of measurement-based forced convection in enhancing Finite Element Analysis (FEA) accuracy for Laser Metal Deposition (LMD)

processes. Comparative analysis of *in situ* temperature measurements reveals that measurement-based forced convection attains accuracy levels below 11%, whereas free convection models exhibit temperature simulations with errors exceeding 44%. Dortkasli *et al.* [206] implemented the forced convection around 35 W/m²/K to the topmost deposited elements only to simulate the forced convection attributed to the losses with the shielding delivery gas from the nozzle. Although no direct comparison was made between forced convection and not implemented, the maximum difference of the melt-pool area between *in situ* thermal measurements and simulated findings reaches 17%.

Convective boundary conditions are also applied to clamped boundaries to model the heat loss between the CNC table and substrate due to the heat sink effect. A contact heat transfer coefficient replaces the convective heat transfer coefficient. A value of 1200 W/m^{2}K was used in Walker *et al.'s* study where sink temperature for defined losses and initial substrate temperature were set to 20°C [200]. Whereas Biegler *et al.'s* simulates strong heat flow into the metallic clamping with a value of 500 W/m^{2}K [201].

The radiative boundary condition is defined according to Stefan-Boltzmann law:

Equation 2.2 Radiative boundary condition

$$Q_{radiation} = \varepsilon\sigma(T_{surface}^4 - T_\infty^4)$$

T∞ is regarded as the temperature of deposited material surface that will exchange radiative heat transfer, σ is Stefan-Boltzmann constant, and ε is deposited surface emissivity which has been cited as a temperature independent value equal to 0.54 [180], 0.6, a standard value in Simufact welding [201] to 0.8 [199]. Due to the vacuum conditions in EBM, the convective heat loss boundary condition is not considered in the analysis, only radiation losses [198].

2.11.3 Material Deposition and computational-domain growth

The quiet element approach is a commonly employed method for simulating material deposition during melting and solidification. This technique involves assigning scaling factors to the material properties of melted and solidified elements, effectively isolating their impact on the overall analysis. Upon contact with the heat source, solid properties are reinstated, fulfilling their influence on the initial conditions. Xiong *et al.* [207] utilized the element birth technique in GMAW welding, achieving strong agreement between simulated and measured results through K-type thermocouples. Denlinger *et al.* experimentally validated the modelling technique with an 11% error using the quiet element approach [208].

Additionally, the distortion field was simulated by introducing thermoelastoplastic analysis with a quiet inactive element activation strategy. A maximum error of 29% was extrapolated by simulating an electron beam deposition of a Ti-6Al-4V large part comprising over 107 layers [209]. Zhao *et al.* [146] conducted a three-dimensional analysis of single-pass multi-layered components to determine residual stress distribution, employing the quiet technique and obtaining good agreement with the hole-drilling strain-gauge method.

A further variation of the 'quiet' technique manages thermomechanical effects by incrementally adding elements in a sequential manner. Nodes entirely encircled by inactive elements are excluded from the degree of freedom. This method necessitates a code capable of automatically regenerating the finite element model or entails laborious manual efforts to ensure the proper addition of elements to the model. While this approach aligns with the underlying physical process, its implementation in commercial Finite Element (FE) codes poses challenges, particularly in the requirement for renumbering elements after each layer to reset the entire computational domain for the inclusion of additional elements.

Ding *et al.* successfully applied this technique, achieving an 80% reduction in computational time when assuming a steady-state-based model as a replacement for the transient model [210]. However, Lindgren *et al.* [211] demonstrated through simulations using both techniques that very similar temperature and stress fields were recovered. Although computational time was reduced by 5%, this improvement was attributed to the better spatial resolution of the weld rather than the specific variation in element addition.

Michaleris [181] implemented a collaborative approach, employing both techniques, wherein elements associated with metal deposition start as inactive and transition to a 'quiet' state on a layer-by-layer basis. Activation only occurs when the heat source contacts the element. This hybrid strategy resulted in a substantial reduction in computational time. Furthermore, Michaleris conducted thermoelastoplastic analysis for the deposition of a Ti-6Al-4V part consisting of 107 layers. The simulation and experimental results exhibited excellent agreement, with a maximum error of 29% [209].

2.11.4 Calibration and Validation Techniques

The calibration of thermal simulations is typically achieved through *in situ* temperature measurements using thermocouples or pyrometer equipment in experimental settings [212]. Strategic placement of thermocouples to capture readings in proximity to the

molten zone is common but introduces challenges. Segerstark *et al.* [213] identified two issues with thermocouple placement. Firstly, thermocouples are subjected to high-intensity laser radiation, leading to overheating problems and potential apparatus failure. Secondly, the emitted light raises the thermocouple temperature beyond that experienced by the material.

To address these challenges, protective shields are designed. The results indicate minimal variations in cooling times (approximately 0.1s between 850°C and 550°C) when using small and large protective shields, suggesting a negligible impact on temperature measurements [213].

To verify the effectiveness of simulation results, K or N type thermocouple placement are popular in capturing the temperature history. Investigators will often spot weld or build thermocouples into the substrate [207], [189] as close the deposition area as possible, using frequencies to capture the temperature variation during deposition.

Bock *et al.* [259] conducted additional research, investigating melt pool length during the Laser Metal Deposition (LMD) process for multiple layers using a high-speed camera. They also explored the determination of layer heights. *In situ* measurements provided a higher level of accuracy in the transient Finite Element (FE) model, as the experimentally compared melt pool geometry and validated the temporal field.

Distortion measurements, widely utilized for validating coupled thermo-mechanical simulations, have been extensively explored in prior literature. Various measurement techniques, such as as-deposited Coordinate Measuring Machine (CMM) measurements [270], [273], laser displacement sensor equipment [218] and recent advancements, including *in situ* distortion measurements directly on a LMD geometry using 3D-digital image correlation systems (DIC) [219], have been employed.

In a specific study, the *in situ* distortion behaviour of LMD manufactured Ti-6Al-4V was examined using a displacement sensor positioned beneath the bottom free edge at the free side of a cantilever plate during a 40-layer deposition. The 3D finite element model exhibited strong agreement with the thermal history indicated by in-built thermocouples (with only a 5% error). Figure 2.36 illustrates the comparison between the calculated and measured distortion. The simulated distortion profile aligns well with the experimentally measured values, although during the cooling phase, the simulation tends to overpredict and gradually diminish [220].

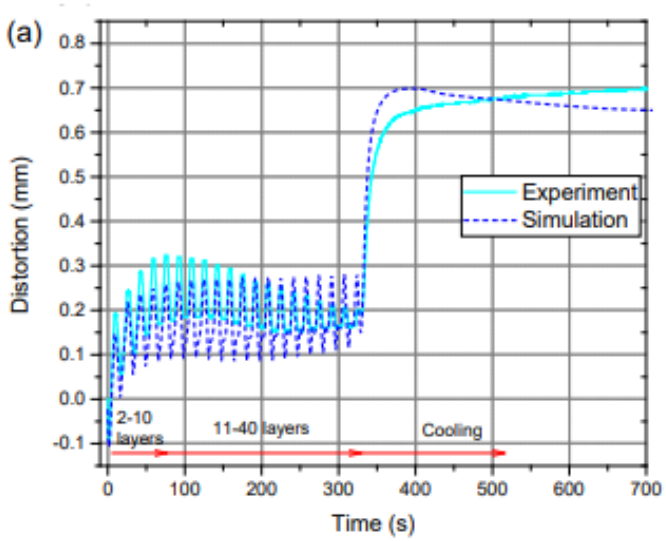

Figure 2.36 Comparison between the calculated and measured distortion using a displacement sensor during a 40-layer LSF deposition [220].

An analytical-numerical modelling strategy for predicting residual stress behaviour during LMD of IN718 was experimentally validated through neutron diffraction. Walker *et al.* [221] observed that stress profiles for single-track deposition exhibited a trend like traditional single-pass welding, with the longitudinal stress component displaying the highest magnitude. Through neutron diffraction and sample rotation (Figure 2.37), a comprehensive tri-axial stress analysis was conducted. Both finite element (FE) and experimental data demonstrated the anticipated parabolic trend for an unclamped substrate, with the maximum displacement at the centre of the plate. The maximum error was determined to be 8% for peak displacement.

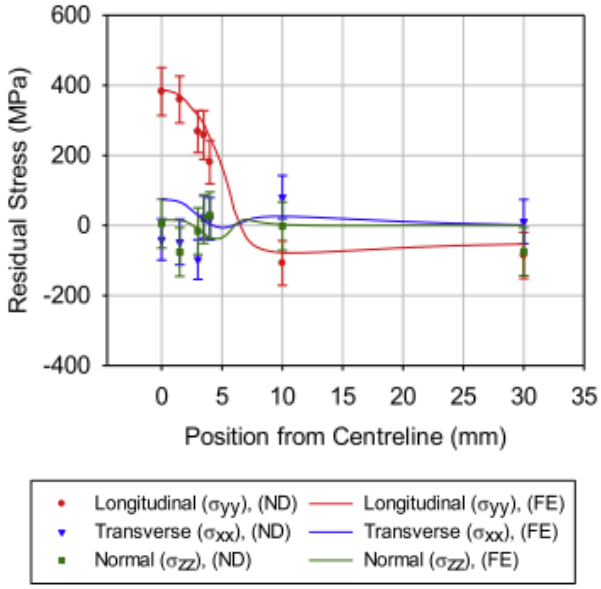

Figure 2.37 Comparison of experimentally measured and numerically predicted triaxial residual stresses using neutron diffraction [221].

In summary, researchers have historically employed residual stress measurements, utilizing techniques such as X-ray diffraction (XRD) [222], [223], neutron diffraction [128] and the contour method [224][225] to validate thermomechanical modelling. The existing literature predominantly addresses the overall behaviour of components or thin-walled structures, often overlooking the incorporation of two validation techniques specifically focused on the interface region.

2.12 Research Gaps in Modelling Techniques

Scant research exists on the coupled thermo-mechanical modelling of Additive Manufacturing parts, specifically pertaining to the Laser Metal Deposition process. The current body of literature predominantly delves into advanced thermal modelling, often concentrating on specific aspects like meshing techniques or boundary conditions. However, these studies tend to remain uncoupled from comprehensive thermomechanical analyses.

In contrast, coupled thermomechanical models strive to experimentally validate the resulting mechanical analyses, particularly focusing on metrics like distortion, which represents a bulk measurement with a millimetre-scale range. Remarkably few published works seek to establish an experimentally calibrated model based on coupled temperature and residual stress measurements. Such models that are measurement coupled are often focussed on single-track or thin-walled analysis, comparative to the simulation of multi-tracked, multi-layered builds, a methodology further validated using residual stress techniques. Notably, there is a scarcity of literature exploring these aspects, especially with a keen interest in the joint interface, as demonstrated in the methodology of the present investigation.

2.13 Summary of literature: Key findings

An exhaustive examination of the existing literature pertaining to the microstructural and residual stress evolution resulting from LMD of Inconel 718 has been conducted, encompassing the incorporation of thermal-stress modelling in the analysis of the process. The ensuing points encapsulate the present status of understanding in this field:

Inconel 718 Microstructure and Microstructural Features (Base Material):

1. The gamma phase, denoted as γ, exhibits an FCC structure and in most cases forms a continuous, matrix phase to which all other phases are retained.
2. The lattice mismatch at γ’/γ and γ’’/γ interfaces serves as a strengthening mechanism by impeding dislocation movement, enhancing Inconel's strength.

3. The volumetric relationship between γ'' and γ' in the context of IN718 alloy has been documented to be approximately 3 with peak aged IN718 obtaining around 15 wt.% γ'' strengthening phase. The primary source of strengthening arises from the γ'' phase, attributed to a higher lattice mismatch and volume fraction combination.
4. Ni3Nb-δ forms grain boundary precipitates and effectively inhibits grain growth by pinning the grain boundaries. At temperatures above 650°C, the γ'' phase decomposes to the thermodynamically stable δ phase, leading to a concurrent strength decline – an important remark to consider when understanding the temperatures experienced in and around the melt-pool.
5. Micron-scaled Laves, hard and brittle with irregular shapes, form due to micro-segregation of alloying elements at the end of solidification causing a significant reduction in mechanical properties, i.e., a decline in ductility, ultimate tensile strength, and fatigue behaviour.

Microstructure and Texture formation in as-deposited condition

1. As-manufactured deposits exhibit a heterogeneous appearance, characterized by variations in grain size and aspect ratio over short distances due to rapid and repeated thermal cycles. DLF builds of IN718 display a banded grain structure comprising columnar and equiaxed zones.
2. Heterogeneous nucleation is influenced by scanning speed, powder feed rate, and thermal energy conduction. Higher scan speeds, increased powder feed rate, or reduced heat source power led to decreased thermal gradient (G), resulting in elevated solidification front velocity (R) and a greater prevalence of equiaxed grain structure in the part.
3. Cooling rates exert a substantial impact on morphological features in as-deposited microstructures. In IN718, cell spacing is closely tied to cooling rates at the solid/liquid interface during solidification. Elevated temperature gradients (G) and solidification rates (R) in the melt pool result in higher cooling rates, ultimately yielding a finer cellular structure.
4. Columnar dendritic grains, prevalent in additive manufacturing give rise to anisotropic mechanical properties. The alloy exhibits elongated grains in the build direction, forming the <001> orientation. Grain orientation in the build significantly relies on the direction of the moving heat source. Literature on LMD technique indicates that dendrites typically align along the ⟨100⟩ crystallographic

orientation, growing epitaxially from the substrate. While some studies attribute the presence of a ⟨100⟩ fibre texture in LMD samples to grain alignment towards the moving heat source.

5. LMD induces the formation of a significant Laves phase during solidification due to alloying element micro-segregation, with insufficient cooling rates hindering the precipitation of strengthening phases like γ'' and γ'.

Influence of Process Parameters on Microstructure

1. The laser power influences the track width, cross-sectional area, productivity of the deposition (includes powder catchment and melting) and the efficiency of the laser beam (regarded as energy expenditure vs deposition energy).
2. The increased laser power (energy density) contributes to larger melt pools and lowers the cooling rate, promoting the epitaxial growth of columnar crystals along the long axis.
3. Increasing the laser power incrementally started to enlarge the length of the columnar grains followed by an increase in width as the laser power surpassed a threshold. At about 700-900W, the width stabilized and a slight increase in grain length was found.
4. The refinement of the columnar dendritic microstructure increased with increasing the deposition speed and decreasing the laser power.
5. It had been shown that an increased cooling rate suppresses the Laves phase and Nb micro segregation. It is well known that increasing cooling rate corresponds to a refinement in dendrite spacing.
6. At lower scan speeds, the deeper melt pool facilitated epitaxial growth, enhancing the strength of the <001> texture. Conversely, higher scanning speeds led to rapid solidification in shallower melt pools, promoting nucleation and reducing the growth rate necessary for fine grain structure.
7. To underpin the control of texture via hatch pattern, site-specific control of crystallographic orientation by manipulating beam scan strategies in the context of the columnar to equiaxed transition. Dynamic switching between solidification conditions and imposing predetermined three-dimensional crystallographic orientations were achieved through varied beam scanning strategies.
8. The overlap fraction can facilitate the precipitation of detrimental microstructural features such as Laves phase. Increasing the energy density and reducing scanning speed elevate heat accumulation, extending the solidification time of the molten

pool. A higher overlap fraction and therefore, a higher energy density led to larger and more abundant Laves phase in interdendritic boundaries.

Residual Stresses:

1. Parts produced by LMD and the substrate often face intricate residual stress fields due to localized heating and cooling, leading to as-deposited stress-induced distortions and tensile stress fields near yield strength.
2. The choice of process parameters in LMD significantly influences residual stress behaviour, demonstrated through experimental trials and modelling.
3. Laser energy emerges as a critical factor affecting energy input, showing a direct correlation with increased residual stress values. Higher laser power is linked to elevated final distortion, predominantly characterized by maximum longitudinal stresses.
4. Despite studying the impact of process variables on residual stress, particularly at the interface region, there is limited experimental validation.
5. Residual stress mitigation techniques, such as varied raster scanning, process parameter optimization, or post-weld heat treatments, have been modelled with minimal experimental confirmation.
6. An experimentally coupled Finite Element Analysis (FEA) model provides a cost-effective means to simulate the effects of varied process parameters.

Thermo-mechanical modelling:

1. Numerous analytical and numerical models have been developed to comprehend the transient temperature field and residual stress behaviour during Laser Metal Deposition (LMD), but there is a paucity of experimental validation for these findings.
2. While extensive modelling efforts have been dedicated to single-track welds or small build geometries, there is a notable lack of modelling for LMD components in real-time applications, such as repairing industrial components or incorporating complex features.
3. State-of-the-art modelling endeavours have utilized computational fluid dynamics (CFD) to understand melt pool morphology and behaviour, a facet beyond the scope of this work but worthy of inclusion in future studies.
4. In-depth exploration is needed to understand the transient thermal behaviour and residual stress effects on resultant microstructure through modelling techniques.

5. Limited literature addresses the experimental calibration of models based on coupled temperature and residual stress measurements, especially for multi-tracked, multi-layered builds. The present investigation highlights the scarcity of literature exploring these aspects, particularly at the joint interface.

Potential for further investigation

Limited data exists on microstructure evolution, texture, and residual stress development during LMD. Existing research programs often focus on a single process variable, such as geometrical accuracy, microstructure, or residual stress. LMD is sensitive to various process parameters, and those optimal for geometrical accuracy may not be suitable for optimizing microstructure and residual stresses. Thus, a comprehensive understanding of the build process is essential to identify conditions that minimize stresses while optimizing microstructure.

The following areas require further investigation:

- Influence of the LMD process parameter selection, and its effect on the microstructure and texture components of IN718 components.
- The evolution of texture and grain morphology during LMD of IN718-on-IN718 base material.
- Understanding process parameters effect on grain morphology and microstructural features along the interface region of a component repaired via LMD.
- The relationship between the microstructure, texture and key deposit parameters at the interface region and initial layers deposited.
- Modelling and experimental analysis of residual stress in both the build and substrate generated through the manipulation of process parameters.
- Modelling of residual stress behaviour and its validation though experimental routes.

Hence, in the present study, the project aims to address the crucial aspects outlined.

Chapter 3: Methodology

3.1 Introduction

Detailed in this chapter is the experimental route used to produce the DEDed IN718 samples and the characterisation techniques used to assess their microstructural development and residual stress evolution. A description of the LMD setup located at the Advanced Forming Research Centre (AFRC), the University of Strathclyde, is presented, alongside the machine configurations. In addition, this chapter includes a description of the microscopy techniques used to characterise the samples, as well as the methods to characterise residual stress.

3.2 Workpiece and Powder Material

A series of powder-fed IN718 single track, thin-walled and solid blocks were fabricated on forged Aerospace grade IN718 substrate (28 mm width (X) x 24 mm length (Y) x 23.7 mm height (Z)) for analysis of a laser-based AM repair application. The substrate was received in a full heat-treated condition, conforming to Aerospace Grade AMS-5662, as shown in Figure 3.2. Table 3.1 details the composition of chemical composition of the substrate used in this study.

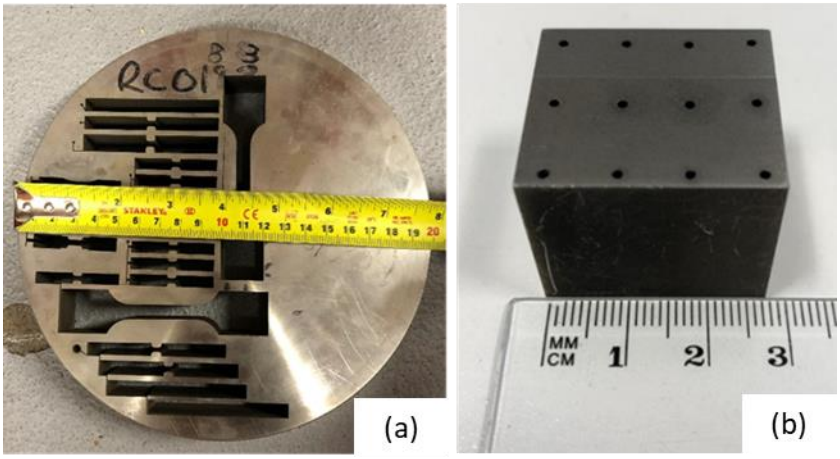

Figure 3.1 (a) Parent IN718 billet to which (b) cuboidal substrates were sectioned with thermocouple holes drilled.

Table 3.1 Inconel 718 Ingot parent disk chemical composition (taken from suppliers Certificate of Conformity)

	Fe	Ni	Cr	Nb + Ta	Mo	Ti	Al	C	Co	B
Alloy 718	18.33	Bal.	17.96	5.38	3.02	0.96	0.51	0.026	0.08	0.003
	Mn	**Co**	**Si**	**Cu**	**P**					
Alloy 718	0.02	0.08	<0.03	<0.10	0.0011					

The standard doubled-ageing heat treatment (shown in Figure 3.2) is followed to obtain the dissolution of any unwanted phases that might have occurred during manufacturing, as well as to obtain a more uniform grain size and to allow the precipitation of the strengthening phases (γ' and γ''). The homogenization stage is employed to eliminate or decrease elementally segregated phases by carefully dissolving Laves phase and promote sufficient diffusion of Nb into dendritic regions. The detrimental Laves phase dissolves into the γ matrix at 1180ºC [226] and keep the carbides, which begins to dissolve at approx. 1270ºC [227]. Solution annealing, Step 2 is carried out to dissolve phases formed during previous process which is normally carried out between 900-1050ºC to enhance precipitation elements for strengthening phases. The δ phase precipitates of about 871ºC and has a solvus temperature of 1010ºC. Solution temperatures just below this solvus temperature are often executed to retain a small fraction of the precipitate phase to inhibit grain growth [12]. Lastly, stage 3, a doubled-aging heat treatment allows the precipitation of strengthening phases γ' and γ'', which tend to precipitate as fine particles uniformly throughout the microstructure between 600 and 850ºC.

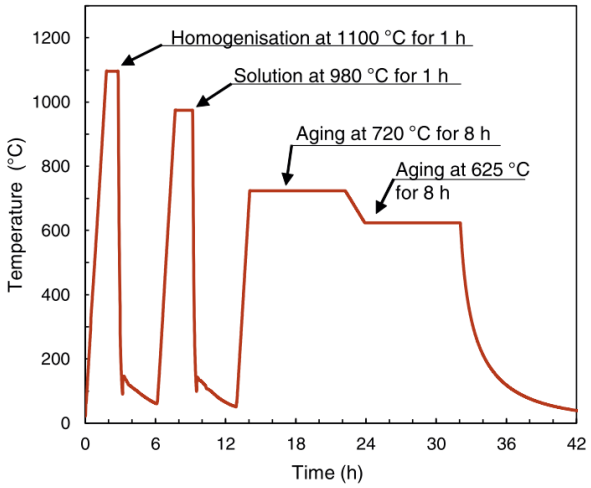

Figure 3.2 Heat Treatment methods employed for IN718 according to Aerospace Material Specifications [34].

Although mechanical properties of this parent material were not provided, Table 3.2 outlines the mechanical performance as set by ASTM International '*Standard Specification for Precipitation-Hardening Nickel Alloy Bars, Forgings, and Forging Stock for High-Temperature Service'* to give baseline values and to what effect the LMD repaired component has on mechanical performance upon testing. These values are set to conform with aerospace grade IN718 for turbine applications and are believed to have been met following the appropriate heat treatment in as-received condition.

Table 3.2 Mechanical Properties as per ASTM International **[228].**

Material Property	Value	Ref
UTS	1275 MPa	[229]
0.2% UTS	1034 MPa	[229]
Hardness	350 HV	[229]
Elongation	12 %	[229]

3.3 Gas Atomised Inconel 718 Particles

All samples fabricated in the present work were made using Gas Atomised Inconel Alloy 718 powder supplied by Carpenter® Technology. The chemical composition of the powder is reported in Table 3.3. The powder particles size of approximately 45 to 106 µm was aligned with ASTM B214 sieve specification boundary limits. IN718 powder was produced through gas atomisation by Carpenter Additive®. The supplied powder was delivered with a Certificate of Conformity stating that powder particles were 45-106 µm based on sieve analysis. Mean particle size measured through SEM image acquisition and analysis, verified that the particle size varies between ~7 to ~146µm with 90% of powder between 40 to 100 µm (Figure 3.3).

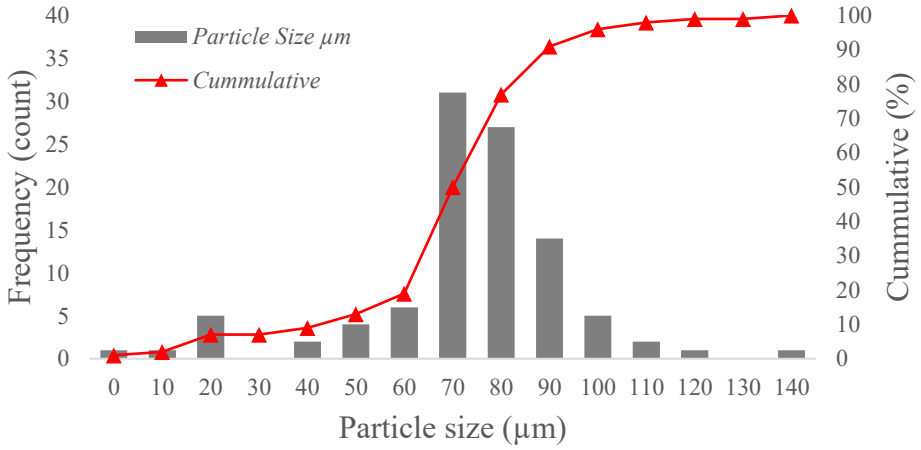

Figure 3.3 Powder size distribution of gas atomised IN718 powder.

Using Scanning Electron microscopy, a sample of the powder (Figure 3.4 & Figure 3.5) was analysed. Due to the small sample size of the powder utilised for microscopic examination in relation to its entire population, the characteristics of the powder processed through the hopper may depend on the place of the collection, i.e., top layer might be exposed to ambient conditions prior to deposition. To reduce ambiguity of powder analysis, multiple samples analysis was carried out.

Table 3.3 Chemical composition of the IN718 powder batch (provided by supplier) showing the % of alloying element

	Fe	Ni	Cr	Nb + Ta	Mo	Ti	Al	C	Ca	Mg
Alloy 718	Bal.	52.86	18.53	5.2	3.1	0.95	0.54	0.03	<0.01 (ppm)	<0.01 (ppm)
	O	**Co**	**Si**	**Cu**	**P**	**S**	**Se**	**N**	**B**	**Mn**
Alloy 718	0.01	<1	0.06	0.1	<0.005 (ppm)	<0.001 (ppm)	<0.005 (ppm)	0.01	<0.001 (ppm)	0.07

From the inspection it can be deduced that the powder was characterized by a spherical or spheroidal shape. Randomly dispersed powder particles had sintered satellites adhering to the main bodies, causing inhomogeneous shape distribution which can affect the flow properties and flowability of the powder. All the powder samples collected contained <20% of non-spherical particles with highly developed surface. These are most often the result of single particles or a group of particles connected by solidified material which could arise as defects during gas atomization process, due to already formed particles with non-solidified or partially solidified material [230].

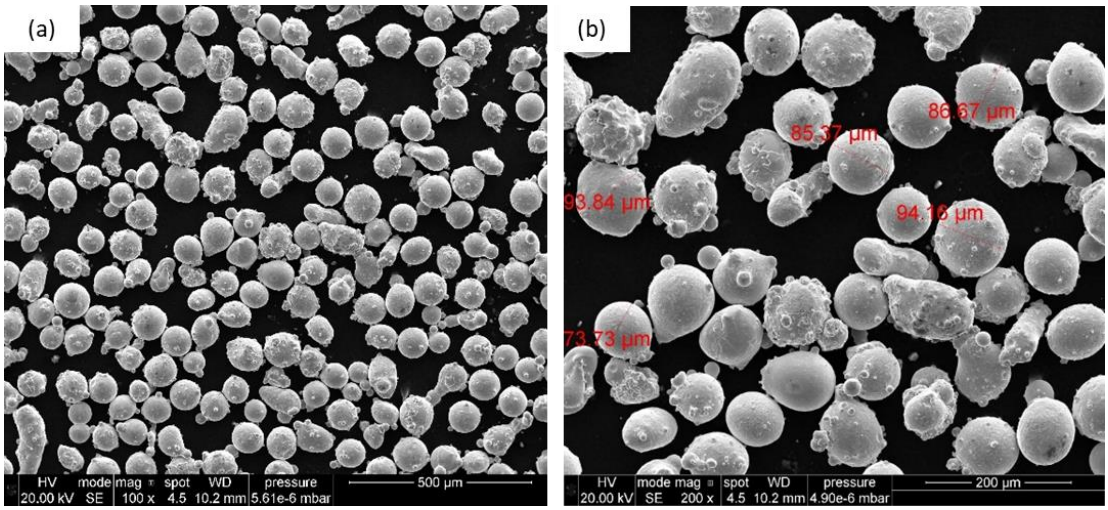

Figure 3.4 (a) GA IN718 Powder at 100x revealing satellites and showing morphology and (b) 200x showing measured diameters with irregular morphologies.

The surface morphology of the non-etched GA particle and micro dendritic structure of a mounted, sectioned, and polished IN718 powder specimen are shown in Figure 3.5a. These networks are a result of the rapid solidification associated during the gas atomization process reaching cooling rates of about 100°C/s [231]. Cross sectioned samples revealed small internal porosity measuring < 2 µm in pore size, (arrows in Figure 3.5.b) located randomly throughout the powder sample. Given the size and volume, the internal porosity would be deemed almost negligible on build performance.

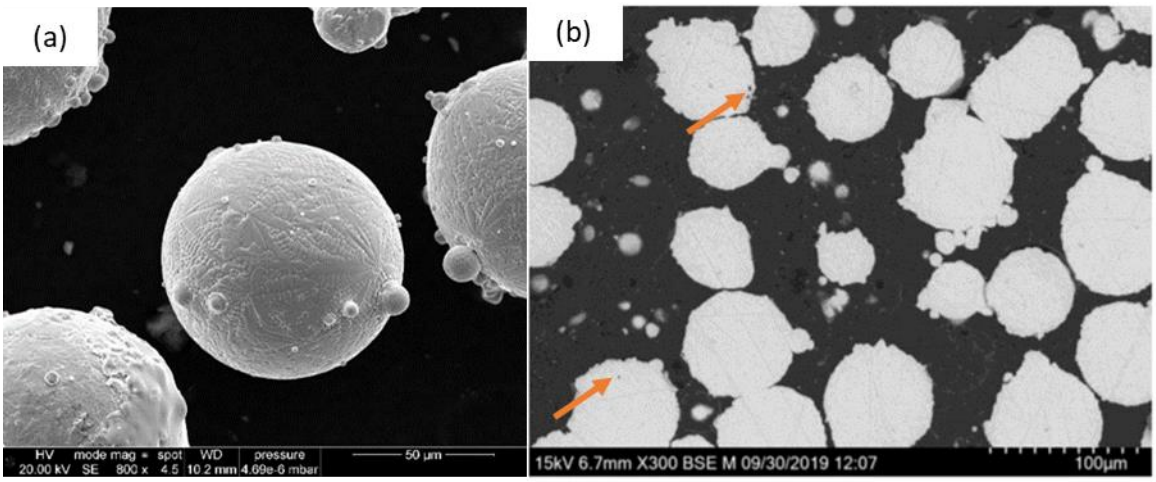

Figure 3.5 (a) Fine dendritic structure on GA in718 powder particle and (b) cross-section of powder at 300x BSE image revealing very small internal porosities.

3.4 Laser Metal Deposition (LMD) Experimental setup

3.4.1 Deposition Configuration

LMD IN718 samples were fabricated using a *n*Light alta^{TM} Fiber Laser with a fibre optical system transferring the laser beam to laser optic operating with a wavelength near 1080 µm. The laser delivery system consists of a water-cooled Nd:YAG fiber laser with maximum output power between 1.5-2.5 kW with near gaussian distribution beam. The HYBRID^{TM} AMBIT^{TM} series deposition head operates under quasi-continuous waveform (QCW). The standoff distance between substrate surface and deposition head is nominally 10 mm, obtaining a 2 mm working laser diameter. Laser power calibration checks were completed prior to deposition which measures losses in the system such as imperfections in mirror and lenses, this is measured using a calorimeter cube. Hardened high alloy steel clamping fixtures secure the substrate in-place and two supportive metallic plates ensure the substrate surface is levelled. Before deposition occurs, a probe attached to the coaxial head measures the level. The configuration of the system is a 3-axis CNC table with a fitted 2-axis Nikken rotary/tilt unit which allows 5-axial movement in X, Y, Z, rotary, and tilt coordination. Thermocouple extension cables were fitted out-with the movement box of the deposition head and were connected to the chassis outside the build envelope. Argon is used as a carrier gas for the powder to ensure create an inert localised atmosphere, as well as being a shielding gas to protect the lens from particles that rebound from the deposit. Figure 3.6 details the configuration inside the build area and demonstrates how supportive slits assisted build quality.

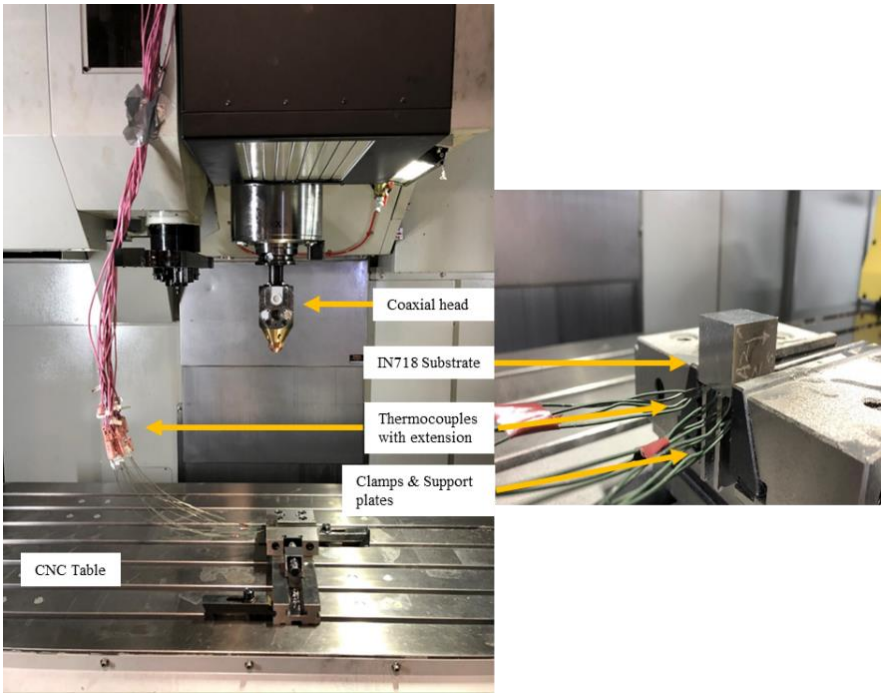

Figure 3.6 Laser metal deposition machine configuration detailing the thermocouple fixture and extension apparatus.

3.4.2 Powder Feeder

An Oerlikon volumetric powder feeder supplies the powder to the powder nozzle using a rotating disc and wiper system to distribute the powder to the outlet. Powder feed rate is determined by disc rotation speed and had been calibrated prior to deposition. The calibration process involves setting disk %rpm to 20 and enabling powder flow for 90-120 s, saving the collected weight then zero scales and repeat for 40% and 60% disk rpm. Figure 3.7 details the powder calibration program graph which constructs linear section for each run and the gradient of the lines are recorded. A linear best fit forced through (0,0) is constructed using 3 gradients as points and the gradient of this line of best fit is used for setting disk %rpm. It can be concluded that hopper delivery was consistent with desired powder flow rate with sufficient working settings.

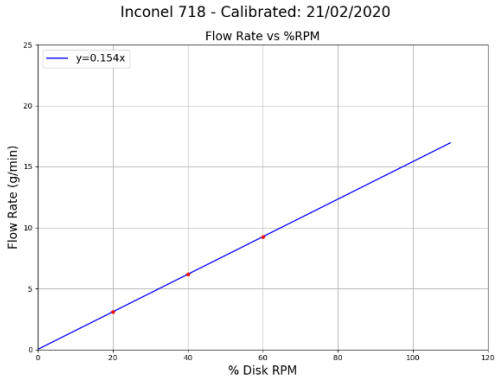

Figure 3.7 Powder Calibration for %disk rpm for IN718.

3.4.3 IN718 Builds

The investigation aimed to analyse the effect of varying laser power on the localised temperature history profile to deduce microstructural evolution for a remanufactured component. Firstly, a single track was deposited to establish key melt pool configurations and aid heat source calibration. Single track, thin-walls and solid blocks were deposited using the machine configurations set in Table 3.4. The thin-wall deposits consisted of 1-, 5- and 10-layer height of a single-track thickness. For notation, X-direction is transverse direction (TD), Y-direction is normal direction (ND) and Z direction is build direction (BD).

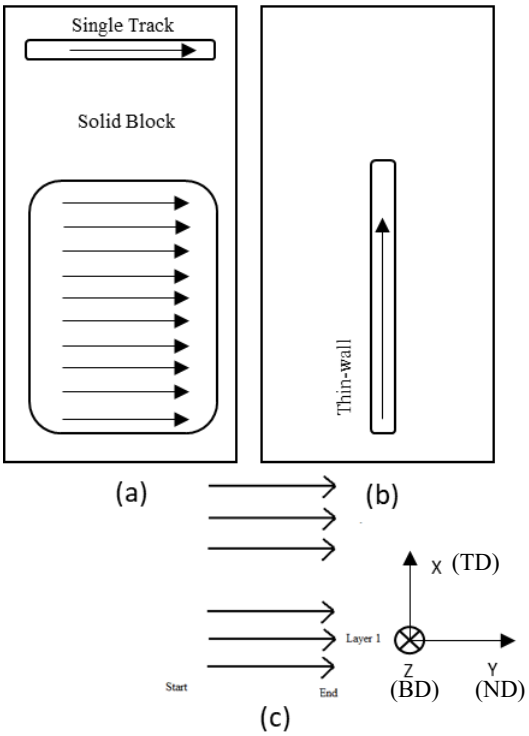

Figure 3.8 Top view detailing the hatch pattern employed for (a) Single and Solid block deposits, (b) thin-walled components and (c) with reference to local coordinate system used for machine and thermomechanical model.

Solid blocks consisted of ten-adjacent clad tracks deposited unidirectionally for a ten-layer build height, this would replicate an in-service repairment and provide key microstructural information. By depositing both single track thin-walls and solid blocks components, the development of microstructure and texture evolution across the interface can be compared, drawing conclusions on temperature histories experienced. Builds were analysed in three stages whereby Stage 1 was the single clad, Stage 2 comprised of thin-walled Samples and Stage 3, the multi-layered solid blocks. To assess the effect of laser power, the 10-layered component blocks were manufactured by fluctuating the laser power while keeping all other process parameters constant. A unidirectional hatch strategy (Figure 3.8) was used for simplification of thermal behaviour and interaction. The deposition path vectors remained constant throughout all tracks and subsequent layers added. An approximate 48 s delay was introduced between the end deposition time of the single track and start of the block; this was a sufficient time for the block to return to near uniform temperature around 20-35°C, prior to depositing the block which was determined by the single-track analysis thermocouple.

Table 3.4 Experimental configuration for process parameters.

Case Number (Specimen)	1 T1	2 T12	3 A1	4 A3	5 Thin Wall
Nominal Laser power (W)	950	950	750	550	750
Travel speed (mm/s)	10	10	10	10	10
Powder Flow rate (g/min)	6	6	6	6	6
Pass length (mm)	21	21	21	21	14.36
Number of passes per layer	10	10	10	10	1
Number of Layers	10	10	10	10	10
Overlap fraction (%)	20	20	20	20	100
Inter-pass dwell time (s)	1	1	1	1	n/a
Intra-layer dwell time (s)	3	3	3	3	3
Deposition time (s)	2.1	2.1	2.1	2.1	1.5
Beam Diameter (mm)	2	2	2	2	2
Argon Shielding Gas (l/min)	8	8	8	8	8
Nozzle Gas (l/min)	5	5	5	5	5

3.4.4 Thermocouple Configuration and Measurement

During LMD, temperature measurements were recorded to experimentally calibrate the thermal model and record the temperature history experienced. Nicotherm D^{TM} sheath with 1 mm diameter thermocouples were placed inside the substrate blocks by drilling twelve 1.1mm holes to a depth of 23 mm. The depth of 0.7-1 mm from surface was selected to capture an accurate thermal history meanwhile not damaging the thermocouple during deposition (1250 °C maximum operating temperature). Figure 3.9 details the locations of the twelve 1.1 mm diameter holes used for *in situ* temperature measurement. The positioning of the thermocouples was to capture as much temperature history for comparisons, i.e., start of the laser process, mid-track build, middle of the solid blocks and the edges given the complex thermal behaviours associated with positioning. Figure 3.10 shows the combination of single track, thin-walled and solid blocks deposited under various process parameters.

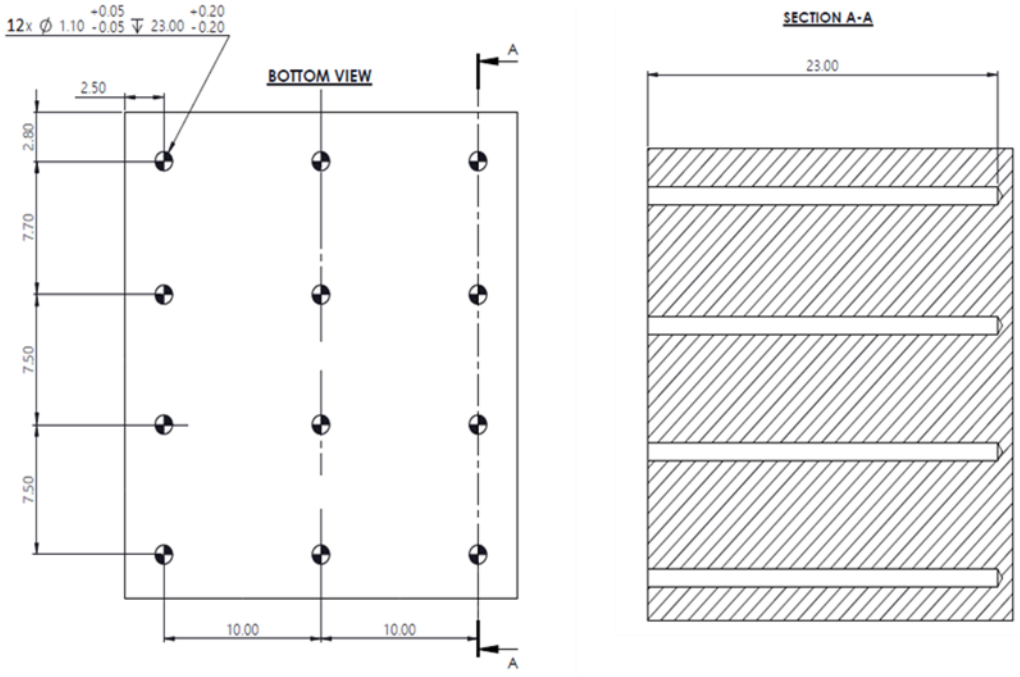

Figure 3.9 Internally positioned drilled holes into the substrate for temperature history capture.

The in-house calibrated Nicrotherm D^{TM} N-type thermocouples have a measuring uncertainty of ± 2.4°C (error for Martel electronics Temperature Recorder (0.6°C) and 1.8°C (for reference thermocouple) and a maximum operating temperature of 1250°C, details of this calibration process including the calibration graphs can be found in appendices.

Thermocouple analogue output voltage signals were acquired through 3 m extension cables (ensuring clearance of moving parts) using a National Instrument multi-component CompactDAQ Chassis connected via USB to a PC. The signals were recorded in Labview®

environment at a rate of 50 Hz. A high resolution, high-speed setting equates to roughly 0.02 s response time.

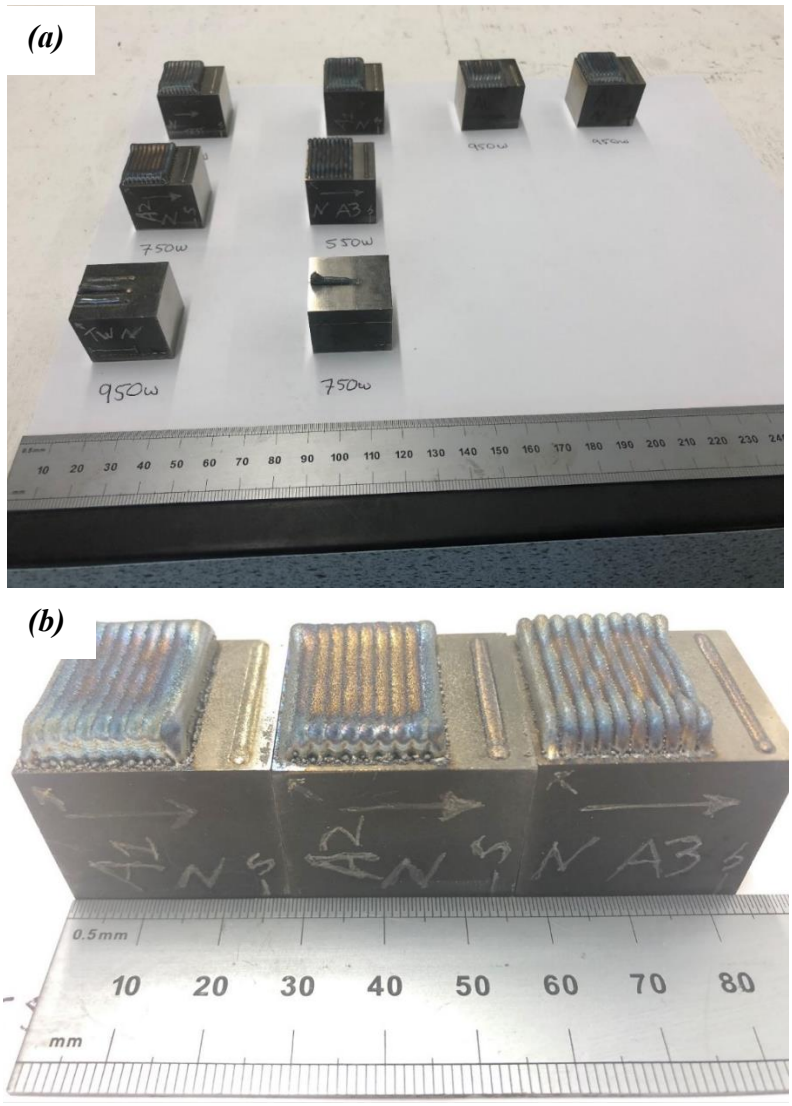

Figure 3.10 (a) Combination of Single Weld tracks, Thin-walled and Solid blocks deposited under various process parameters and (b) Displays the solid blocks deposited under 950W, 750W and 550W from left to right, respectively.

3.5 Microstructural Characterisation

The microstructure of the as-manufactured component is important to indicate the final material properties. The microstructure was evaluated in different sections depending on the local thermal history to draw conclusive remarks.

3.5.1 Sample Preparation

Samples were sectioned using a precision cutter with a SiC cutting wheel or by wire Electric Discharge Machining (EDM). The interface regions of the samples were investigated in the cross section either in parallel (X-Z) plane, or transverse (X-Y) to the build direction. The

sectioned samples were mounted in conductive copper resin. To understand what effect subsequent layer addition had on the interface region, the planes mentioned were investigated for single, thin-walled, and solid block deposition.

Mounted samples followed a metallographic preparation for IN718. A coarse grit paper (P240) was used to produce a flat surface and remove contamination from the cutting process. Further grinding included a p400, p600, p1200, p2500 step followed by a final grinding at p4000. The polishing stage was crucial for EBSD and included sometimes doubling the process time at particle size of 9 µm, 3 µm, 1 µm followed by a 0.5 µm diamond suspension. The final automet polishing stage included a micro cloth with a 0.02 µm colloidal silica suspension. As the region of interest acted like heavily deformed IN718, the samples were subjected to a 24 h, low amplitude Vibropolish in a bath mixture of 0.06 µm, 0.04 µm and 0.02 µm colloidal silica suspension.

The substrate and as-deposited material reacted differently to the etchant process so careful considerations were taken to reveal the solidification microstructure. The deposited region was attacked rapidly so required only a few seconds of etchant, whereas the substrate required an additional 10 s. Prior to etching, the samples were subjected to 2 min on the micro cloth with 0.02 µm colloidal silica suspension. This created a more uniform etched surface. A mixture of submersion and swab for 3-5 s using Kallings No.2 Reagent (5 g CuCl2 + 100 ml HCl + 100 ml ethanol + 190 ml H2O) was implemented for precipitate analysis.

To analyse grain boundaries, a combination technique of immersion and swabbing was carried out for 40-60 s using Glyceragia Reagent (10 ml HNO3 + 20-50 ml HCl + 30 ml glycerol).

3.5.2 Image analysis

Image analysis was performed using ImageJ® software to measure grain size, Primary Dendrite Arm Spacing (PDAS) and the size of Heat Affected Zones.

Grain size measurement was executed by highlighting the outline of the grain by paint and then a threshold of this outline will pick the grains as particles. The ‘Particle measurement’ function in ImageJ allows various measurements from particles to calculate area fraction and particle/grain size. For aspect ratio, an equivalent ellipse which is fitted into the grains and the ferret maximum is considered as grain size. The ratio of ferret maximum to ferret minimum is taken as the aspect ratio of the grains. Calculating the PDAS involved using the straight-line distance tool and fitting it across approximately ten primary dendrites, then dividing the line distance value to give an average width for the primary arm dendrites. This method is especially

useful for deciphering partly etched/hardly visible dendrites and regards each dendrite at its widest section i.e., mid-length and not tip. Lastly, to measure the heat affected zone for both the X-Y and X-Z plane, the image was thresholded to produce a binary image isolating the primary features.

3.6 Optical Microscopy

Etched and un-etched specimens were investigated under the Leica™ DM12000 Optical Microscope.

The following investigations were carried out using Optical Microscopy:

Porosity: The deposits were quantified using images taken from sectioned planes of an etched sample, from the HAZ to the interface and throughout the entire build. For porosity measurements, both the X-Y and X-Z planes were investigated to understand intralayer and interlayer development and if the interface region was affected along several layers and between tracks. Un-etched areas, specifically near the top of the build were analysed for porosity.

Solidification microstructure: In each scenario, i.e., a single-track, thin-walled, or solid block the dendritic shape, orientation, and other formed characteristics were examined. This analysis was conducted through a combination of micro and macro images under etched conditions, employing the map-stitch functions in the Leica Application Suite (LAS) software. The focus of this investigation was to enhance understanding of the activities in the interface region. As a result, the substrate-to-initial layers analysis was carried out to gain a comprehensive understanding of the process.

3.7 Scanning Electron Microscopy

A comprehensive study was carried out using SEM to examine the microstructure development in the grains and to study secondary phases. Secondary electrons and back-scattered electrons (BSE) imaging modes were used to understand topographic and compositional information about the specimen respectively. SEM was used for the following investigations:

i) Powder characterisation: to assess the powder size distribution, morphology and microstructure and any defects present in the powder. A FEI Quanta™ 250 FEG microscope (operated at 15-20 kV) was used in this study. Powder particles were mounted on conductive tape prior to deposition and imaging was carried out to exhibit the external morphology. Five images were captured at 100x magnification

to measure several hundred particles for size distribution using the image analysis tool. The powder was further analysed for the presence of internal porosity under BSE configurations (operated at 15 kV).

ii) Grain size: Grain size analysis was carried out by stitching several images together to obtain a mm area. The images were captured using a FEI Quanta^{TM} 250 FEG-SEM in the BSE mode, operated at 15 kV.

iii) Secondary phases: A FEI Quanta^{TM} 650 FEG equipped with Oxford Instruments Energy Dispersive X-ray spectroscopy (EDS) detector was used to investigate the chemical composition and microstructure of intermetallic secondary phases for single clad tracks, thin walls and solid blocks. The SEM operated at 20 kV with a 3.5 mm spot size for EDX analysis.

3.8 Electron Backscattered Diffraction (EBSD)

The interface for the deposited region was investigated by EBSD to analyse the macro and micro texture development for single clad track, subsequent layer addition and finally, solid blocks. Grain size distribution was also quantified at the interface region by using Channel 5 software. A FEI Quanta 250 SEM fitted with an Oxford Instrument EBSD detector was used to generate EBSD maps, detailing crystallographic orientation of individual grains. A large area was mapped by taking several EBSD maps, at 250x – (approximately 400x magnification through Oxford instruments) and stitching them together to form an area of approximately 3.5 mm x 1.5 mm, covering the interface of nearly 2 full tracks. For these large area maps, a 1µm step size was used to evaluate the macro-texture. Further mapping was performed to obtain the micro-texture, over small areas of dimensions (input next EBSD scans) with a step size of 0.5µm, especially at the substrate/deposit interface where fine grains were present. EBSD mapping with a high indexing of >95% was performed in this project. The maps were collected in both the TD-BD and ND-BD cross-sectional planes at the interface region. The data was analysed using HKL Channel 5 Mambo to construct pole figures and MTEX, the Matlab toolbox. The {100} γ pole figures were constructed with the growth direction in the centre (parallel to vertical Z direction) to understand the orientation of grains and texture. Pole figures were plotted for the substrate, heat affected zone (HAZ), fusion zone (FZ) and initial layers.

3.9 Microhardness

A Struers Durascan G5 microhardness testing machine was used to measure the microhardness evolution across the interface region on the sample TD-BD cross section. The measurements would be used to analyse the mechanical performance of the joint and deduce key

microstructural features. The acquired measurements conformed to ASTM E-384-16 standard using a diamond shaped Vickers indenter by applying 0.2N for a 10s dwell time with close attention to avoid sites of adjacent porosity thus providing a zero measurement. All measurements surpassed the 20µm minimum diagonal value with intermittent spacing of around 150µm. Indentations were made across the region of interest which ranged from substrate to build, making sure to incorporate HAZ, PMZ and FZ vertically in the build direction (Z-direction). Diamond indentations were analysed with a 20x objective lens, zoom 2, to produce a microhardness map.

To increase repeatability and validation, 2 vertical lines of measurements for 3 different tracks were carried out across the region of interest as seen in Figure 3.11. Measurements ranged from -2.85 mm to +2.25 mm, comparative to the interface (0 mm) to include all affected zones.

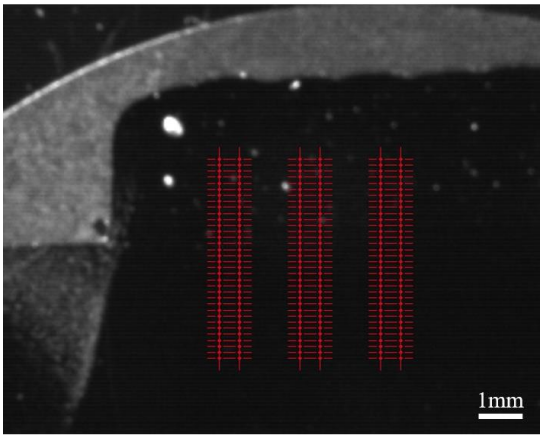

Figure 3.11 Hardness Indentations map plot

3.10 Residual Stress Measurement

Residual stress was characterised using a combination of the contour method for through-thickness measurements and X-ray Diffraction for near-surface measurements to provide experimental data to validate the thermomechanical model and to understand stress distribution across the interface region. As stated in the literature, the complexity of residual stress distribution in an as-deposited component is the product of fluctuating thermal-induced stresses in the form of steep thermal gradients and fast cooling rates. By employing both methods, it was possible to investigate the residual stress distribution induced from LMD in both build (BD) and Transverse (TD) direction using XRD, and with the contour method, normal (Y) direction. The contour method was executed first to deduce the bulk stress profile, followed by the XRD measurements on the cross-sectioned plane. It is important to note that XRD measurements were performed on the cross-section face after being machined. A superposition of the measurements was further calculated to understand the bulk residual stresses in the as-deposited initial state i.e. prior to sectioning.

3.10.1 Surface contour measurements

The contour method is a destructive process that involves removing material or sectioning a part to release residual stress and induce deformations from which the stresses can be back calculated. The technique is explained schematically in Figure 3.12. The sample is sectioned in half to relieve the stresses on the face of the cut and the stress perpendicular to the middle plane is completely relaxed. This relaxation cut causes the surface to deviate from planarity where tensile stresses will pull the surface back and compressive stresses will push the surface outward, as in situation B. Hence, by returning the cut surface back to the original cut place and a new equilibrium, the stresses accountable for the deformation can be calculated.

The contour method is carried out by measuring both halves of the cut cross-sectional surface to provide a full 2D map of residual stress distribution across the as built and substrate samples. The contour method was conducted in four main steps: cutting, contour measurement, data analysis and finite element analysis. Each of the stages will be explained hereafter.

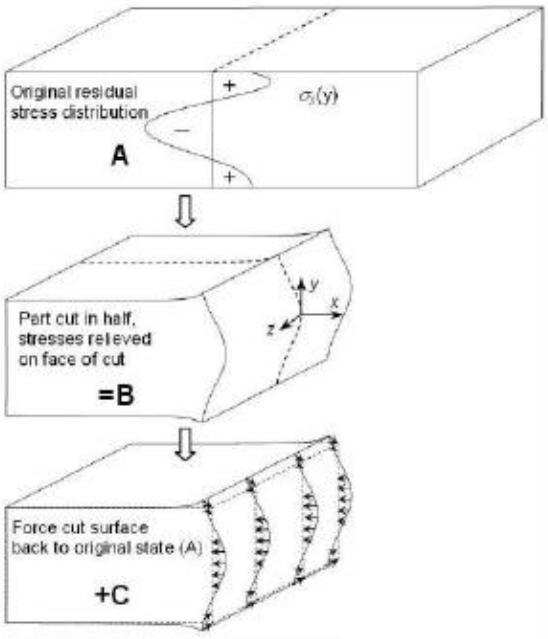

Figure 3.12 Principle of the contour method. Residual stresses in the x-direction act across the middle plane which are released during the sectioning along the middle-plane, deforming accordingly in situation B. By forcing the cut surface to reach equilibrium to the original plane in situation C, the stresses acting in the x-direction across the entire plane can be measured [232].

3.10.1.1 Part Cutting

As the contour cut relaxes the stresses normal to the cut plane, this is the first step in the experimental route. Sectioning the part in two requires the use of Wire Electro-Discharge Machining (WEDM). Part cutting requires the material to be electrically conductive with close to '*skim-cut'* configurations giving better precision and finer surface finish as it will minimise any recast layer and cutting induced stresses [233]. Wire tension and diameter, pulse time and pulse current are specific to IN718 to achieve a high precision-controlled cut to remove μm sized material and to diminish the bulge error. An Agie Charmilles Wire EDM FL440 operating the settings specified in Table 3.5 was utilised for sectioning the part for residual stress analysis.

Table 3.5 Wire-EDM configurations.

EDM Configuration settings	
Wire Diameter	0.25mm
Pulse-on time (A)	0.1µs
Pulse-off time (b)	6µs
Short PULSE TIME (TAC)	0.1µs
WIRE TENSION	2.0daN
Pulse CURRENT (IAL)	0.4amps
Voltage (V)	120V

Mechanical methods (abrasive cutting) cause localised plastic deformation from large contact forces and result in a build-up of stresses in the material, these will interfere with the residual stress profiles needing measured. Wire-EDM is required for the contour method due to the precision and accuracy of the cut to achieve very tight tolerances and does not induce plastic deformation as cutting is non-contact. In addition to the wire settings, the part remains constrained using clamping fixtures on both sides during the cutting to relieve the stresses and minimize cut deviation from original cut plane (Figure 3.13). Prior to surface contour measurements, the components receive a careful chemical clean to remove any debris from the surface. The part is submerged in temperature-controlled deionized water during cutting to minimalize thermal effects.

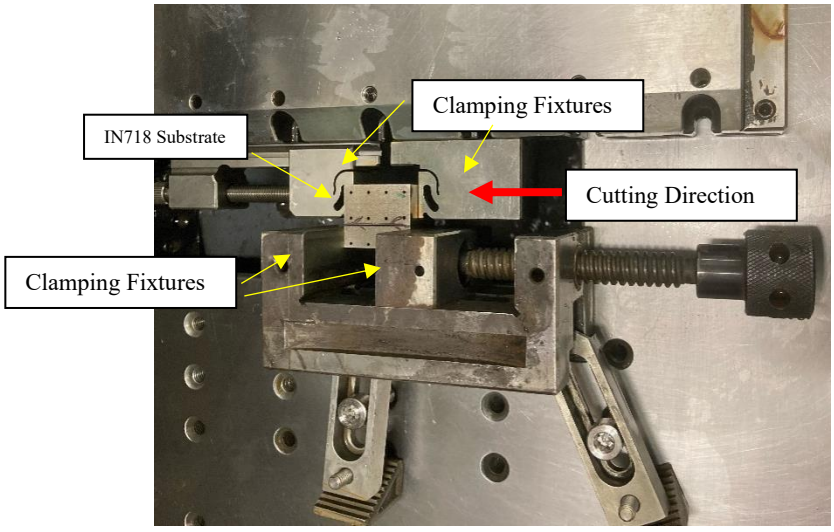

Figure 3.13 Wire-EDM clamping configuration.

Figure 3.14 details the components post contour method. The polished surface preparation was only done after contour method was completed as these would destroy surface measurements, although it is a necessary step for X-ray diffraction.

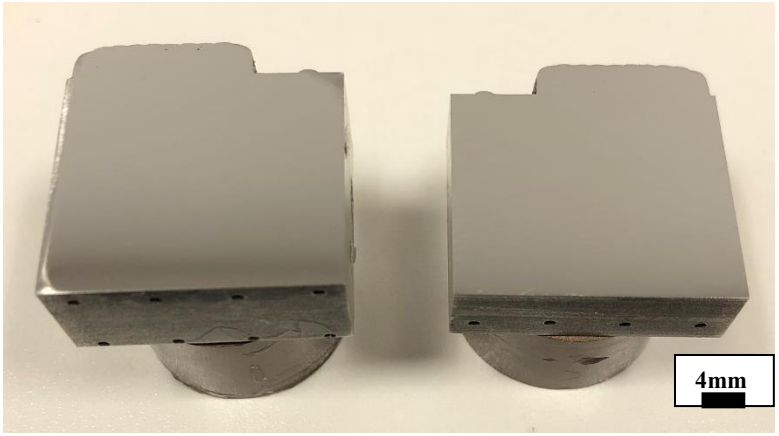

Figure 3.14 Cross-sectional view of the built component prepared via electro-polishing for XRD analysis.

3.10.1.2 Contour Measurements

Following the unclamping of the sectioned deposited components, a swift chemical cleaning procedure utilizing methanol was employed to eliminate any surface debris that might obscure results. Subsequently, surface contouring activities were executed using the Alicona Infinite Focus, as elucidated in Figure 3.15. Meticulous attention was exercised to ensure non-impingement or disruption of the surface conditions of the measured face.

The varying surface displacement was non-destructively gauged with spatial resolution, and a profile was meticulously constructed for each cut face. The Focus-Variation technology amalgamates the limited depth of focus inherent in an optical system with vertical scanning techniques, thereby furnishing topographical and colour information derived from the variation in focus. A comprehensive depth of field is achieved through the precise movement of optics along the vertical axis, continuously capturing surface data. Proprietary algorithms adeptly convert the sensory data into comprehensive 3D information and a true-colour image, thereby ensuring a full depth of field.

The Focus-Variation technique, known for capturing high-resolution 3D surface measurements, delivers measurements with a repeatability for surfaces characterized by a local Ra of 0.009 µm at a lc of 2 µm. The high-density measurement system guarantees adherence to detailed tolerances within the micrometer range, maintaining consistently high lateral and vertical resolutions across extensive measurement volumes.

A meticulously configured motion control script within the Alicona software facilitated the generation of approximately 200,000 points on the surface. Once the initialization process was established, the system seamlessly executed its operations automatically until the task was completed. Raw data concerning vertical profile measurements and encoding steps for X-Y motion underwent conversion to coordinate data in millimetres, and this data was systematically and automatically stored in a text file concurrent with its acquisition. Both halves of the sectioned component were meticulously scanned and their respective data files were organized accordingly.

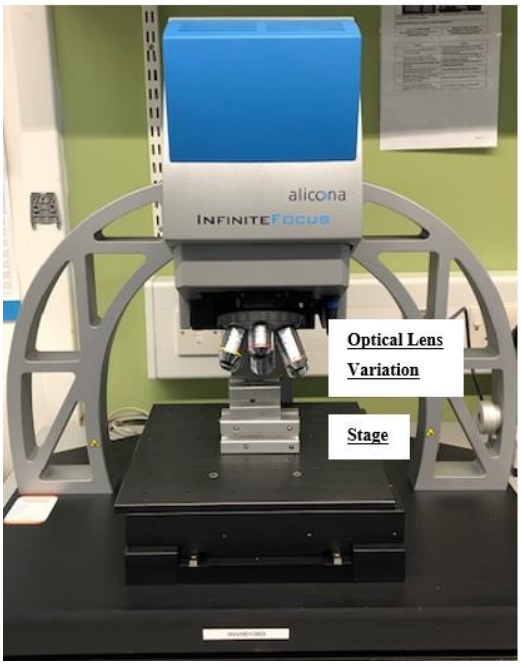

Figure 3.15 Alicona Infinite Focus – surface contouring measurement device.

The contour method for measuring stress focuses on the normal Y stresses of a component, which has been cross-sectionally sectioned through Electrical Discharge Machining (EDM), leading to stress relaxation at the designated plane of interest. In this method, both the left and right sides of the cross-section must be scanned, and the contour of each opposing surface created by the cut is precisely measured. Surface contour deviations from planarity result from the elastic relaxation of residual stresses, enabling the calculation of the original residual stresses. The primary strength of the contour method lies in its ability to furnish a comprehensive cross-sectional map of residual stress components perpendicular to the cross-section, thereby offering a detailed distribution of behaviour.

An effective implementation of the contour method involves utilizing a Coordinate Measuring Machine (CMM), wherein a touch probe establishes surface locations by contacting the

component surface. Subsequently, surface contours are logged, capturing X, Y, and Z values. Following the retrieval of surface roughness data, displacement values are employed to measure the distribution of residual stress across the face. This is achieved by inputting the surface data into a sophisticated computer program that details local residual stress values. Prior to the part being loaded onto the stage, a meticulous chemical cleaning process is undertaken to eliminate any debris from the component.

3.10.1.3 Data Analysis

The raw data is collected in a .txt format giving all the cloud points in the form of x,y and z data but needs to be processed through a sophisticated Matlab script to convert these into a form suitable for calculating stresses with an FE model. The post processing of data includes a series of cleaning, aligning, and fitting of the data to calculate the residual stress experienced:

1) Cleaning of the point cloud data converts the .txt file to Matlab readable format and plotting the collated data points in graphical format. Rogue point clouds, deemed by the user, are points in the cloud-based file that obscure the results, this could be from contamination on the part surface and therefore needs to be removed from the data source file. Both sides of the scanned sectioned are cleaned. The obvious outliers are deleted from the data set which could significantly affect the results as the stress depends on the curvature of displacement field and high frequency content has high curvature.
2) An outline of the data is collected which traces the perimeter of the collated points and all surface data measurements.
3) Due to the local coordinate system used to measure both sectioned surfaces are different, the point cloud from one surface, right/left side was reoriented. In this case, flipping one cloud of data in y-direction plots the two clouds on the same coordinate system to coincide with each other. These point clouds are now aligned.
4) The clouds are interpolated onto a common grid and pointwise averaged. Taking the cloud data from both aligned surfaces and computing average value.
5) Eliminating roughness and noise is then accomplished by fitting the data to a smooth surface e.g. bivariate spline. Uniform spline smoothening to minimize uncertainty requires the data to fit to a continuously defined surface without gridding the data. Spline fitting step size is controlled whereby occurring every 1 mm of depth between 0.5 mm to 10 mm spline.

3.10.1.4 Calculation of residual stress using finite element simulation

Final displacements after the process of averaging and filtering are inverted about the surface normal and interpolated/extrapolated to node locations on the finite element surface displacement boundary conditions. Each surface was elastically deformed into the opposite shape of its measured contour using the commercial code, Abaqus FE model. The displacement in the direction normal to the surface of the cut is specified on all nodes on the cut surface. Additionally, point boundary conditions are applied to the model to restrain rigid-body motion. Figure 3.16 shows an example of the following rigid-body motions being constrained: translation in x and y. The minimalistic constraints ensure that the calculated residual stress map satisfies equilibrium. The resulting stresses on the plane of the cut in normal direction are the results of contour measurement, representing internal residual stress prior to part sectioning.

A 3D finite element model assuming isotropic elasticity was used to evaluate the residual stress contour data. For this purpose, two material behaviours were assigned to sections of the part namely, the substrate and deposit. A Youngs modulus of 200-208 GPA [40], [234] for the substrate and 180 GPA (160GPa ±18) [40], [235] for the deposition section and Poisson ratio of 0.3 and 0.33 accordingly [236]. The 2D perimeter of the cross-section attained by the Alicona was aligned and transposed into the finite model software. By extruding the 2D cross-sectional face by the corresponding thickness of the part sectioned, a 3D model was produced for calculations of residual stress development. Mesh seeds were attributed to each of the nodes on the outline and along the extrusion edge. The seeds were biased by allocating a finer pitch near the cross section of the model which represents the cut surface, and a coarser pitch towards the other end of the model, this reduces the computational time and is less important for stress analysis. Parts were modelled in Abaqus CAE and meshed with element spacing of 0.3 mm on the cut surface and 0.1-0.8 mm with single bias away from the surface, Figure 3.16 details the meshing technique. The element type was C3D20R; a 20 node brick quadratic element as used by Rae *et al.* [237].

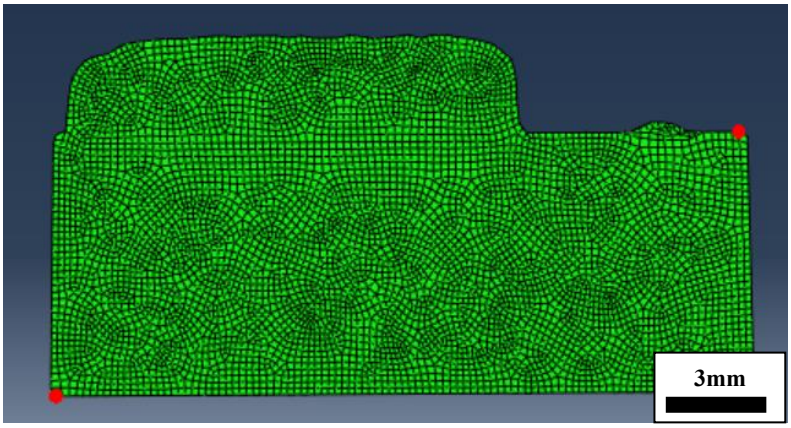

Figure 3.16 Finite element mesh of half-block after displacement boundary conditions are applied.

Stress was calculated by forcing the cut surface into the opposite shape of the averaged contour data [237], [238]. Applying the opposite of the measured surface contour as a z-direction displacement boundary condition on the surface corresponding to the WEDM cut. The traverse deformations are not calculated (x and y) and left unconstrained in the FE model enforcing τ_{xz} and τ_{yz} to be zero on the surface during FE analysis, therefore σ_z can be returned. To prevent rigid body motions along the x-y plane and accompanying numerical resultants, fixed-node constraints were applied inducing no reaction forces.

3.10.2 Residual stress characterisation using X-Ray Diffraction (XRD)

Prior to near-surface residual stress measurement using X-ray diffraction method, the samples which had already undertaken the metallographic preparation stage were subjected to a final stage known as electro-polishing.

3.10.2.1 Electro Polishing

Upon completion of mechanical polishing, NPL's Determination of residual stresses by X-ray Diffraction [239] states the surface profile for metallic material in polished state only achievable via electro-polishing. The process involved the work piece serving as a positively charged anode and connected to the positive terminal of a DC power rectifier. The negatively charged cathode, in the form of stainless steel is connected to the negative terminal. Both anode and cathode are immersed in a temperature-controlled bath of electrolyte solution containing a mixture of high-viscosity sulphuric and phosphonic acid. The electric current is conducted from the anode to the cathode through the electrolyte causing metallic ions on the work-piece surface to oxidise and dissolve in the electrolyte resulting in micron-level thickness of surface removal. Fortunately, this process gives the surface a slight etching effect and therefore features become visible under microscope.

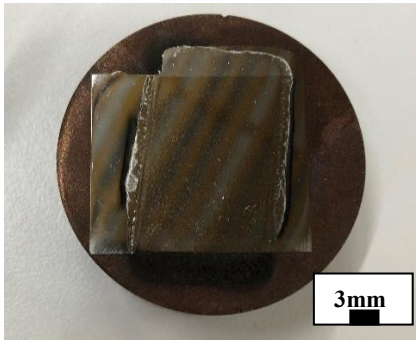

Figure 3.17 Electropolishing of 950W block (clearly shows the area exposed during electropolishing as left blemish marks)

3.10.2.2 Xray Diffraction

X-Ray Diffraction (XRD) characterizes residual stress non-destructively by utilizing crystalline structure as a strain gauge. Crystals, composed of atoms in a three-dimensional periodic pattern, create interference patterns through diffraction. The nature of these patterns depends on inter-planar spacing (d) and incident radiation wavelength (λ). Unlike other methods, XRD measures lattice strains specific to individual lattice planes and phases. Residual stress alters the inter-planar spacing (d), detectable through diffraction adhering to Bragg's condition. Synchrotron and neutron diffraction measure lattice strain precisely by analyzing inter-planar spacing (dhkl). Bragg's Law forms the theoretical foundation of XRD:

$$n\,\lambda = 2d\sin\theta,$$

where λ is wavelength of the incident x-ray beam, θ is the Bragg's angle, d is crystal d-spacing and n is an integer.

Therefore, strain within the lattice can be calculated by converting 2θ peak positions into d-spacings using Bragg's Law.

The NPL good practice guide no.52 explains the determination of residual stresses by X-ray Diffraction [240]. Performing the strain measurements requires the sample to be placed in the X-ray diffractometer and exposed to an X-ray beam which interacts with the crystal lattice to cause diffraction patterns. By scanning through an arc of radius, the diffraction peaks can be located. A clear relationship exists between diffraction pattern observed when X-rays diffract through crystal lattices and the atomic distance planar spacing within the material. Inter-planar spacing of a strain-free material will produce a characterised diffraction pattern. However, when the material is strain, elongations and contractions are produced within the crystal lattice,

which change with inter-planar spacing of the {hkl} planes. Measurement of this shift, the change in inter-planar spacing can be evaluated and thus strain within material is deduced.

Several XRD measurements are made at different psi tilts and the inter-planar spacing, or 2-theta peak position is measured and plotted. The stress can therefore be calculated from the plotted curve by calculating the gradient of the line and incorporating elastic properties of the material. Assuming a zero stress at $d=d_n$, where d intercepts on y-axis when $\sin^2\psi=o$, stress is given by:

$$\sigma_\phi = \left(\frac{E}{1+v}\right)m$$

Where m is the gradient of the d vs $\sin^2\psi$ curve.

If we consider the strains in terms of inter-planar spacing, implementing strains to evaluate the stresses then:

$$\sigma_\phi = \frac{E}{(1+v)sin^2\psi}\left(\frac{d_\psi - d_n}{d_n}\right)$$

Thus, stress can be calculated in any chosen direction from the inter-planar spacings determined from two measurements, made in a plane normal to the surface and direction of stress to be measured.

The changes in d-spacings due to the strain are very small, in the region of $1x10^{-3}$, therefore selecting an X-ray wavelength which will give a reflection, from our sample, at the highest possible 2-theta angle is crucial. Ideally, the radiation source should give a reflection at a Bragg angle greater than $120°2\theta$.

X-rays do penetrate some distance into the material: penetration depth is dependent on the anode, material and angle of incidence hence an averaging over a few microns depth under the surface of the specimen. Monochromatic (X-rays) provide very intense beams of high energy X-rays which have higher penetration depth than conventional X-rays. Increased depth means the diffraction can provide high spatial resolution, three-dimensional maps of the strain distribution to millimetre depths in the engineering component. An advantage of this is that the intense narrow beams of 1 μm -10 μm in size are possible which leads to spatial resolutions that are limited due to crystalline size within the sample, not by the instrument [241].

X-ray Diffraction experiments were performed to characterise the residual stress development in the substrate, interface and build component. Measurements were performed using the PROTO LXRD®2000 (ISO17025 Certified) to calculate the surface residual stress measurements after sectioning.

Specific points were located across the specimens surface to understand the evolution of residual stress from the substrate to the initial few layers deposited (outlined in Section 8.2.1.1). To show development, at least eighteen measurements, ranging from -15 mm to +3 mm were performed on the identified surface profile for each sample. Development of residual stress in the interface region incorporated the measurements form -1 mm to +1 mm. For each point, both directions were measured i.e. longitudinal and transverse with a 1s exposure time for each measurement. These were sufficient to obtain an adequate number of counts to construct strong peaks used in stress analysis. A round collimator with a 1mm radius and ten ψ-offset angles in the range of maximum ± 30° were employed.

The X-ray elastic Constants (XEC) $½S_2$ and -S1 were defined as $6.33409x10^{-6}$ MPa and $1.424015x10^{-6}$MPa, respectively. And material property defined in the Proto database considers inverse (E_{eff}/ν) as 702239.79.

The experimental set up is shown in Figure 3.18. The system uses 2 detectors ‘L1’ ‘R1’ as provided by Proto Manufacturing with beam of synchrotron X-rays with tube elements of Mn radiations operating at 25 kV, 20 mA and 2.10314 Å wavelength. A 1 mm round aperture was used with tilt geometries ranging from -30°>0>30° with a Bragg Angle of 151.88°. For the direction normal to the planes for the specific {311} reflection and ε_x, ε_y, and ε_z are the strains measured in the three orthogonal directions. A combination of the system XRD Win2.0 and The Measurement Good Practice Guide of National Physics Laboratory No.52 standard uncertainties were followed.

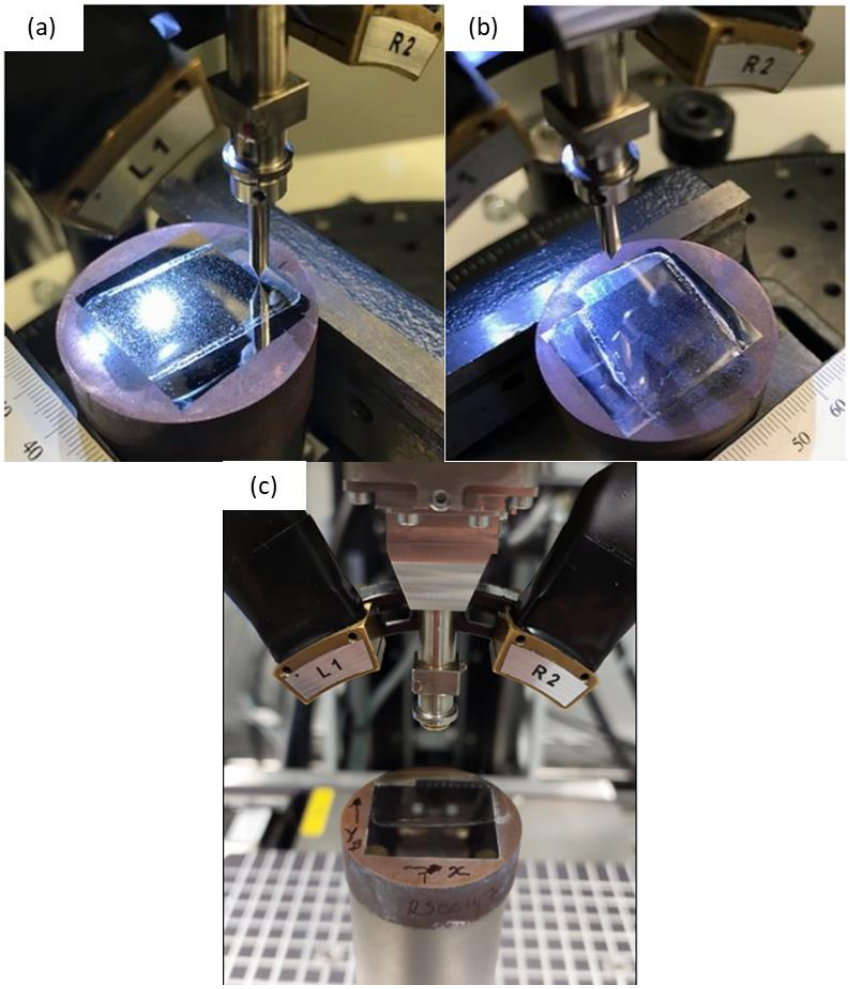

Figure 3.18 XRD machine configuration for (a) build direction, (b) transverse direction and (c) overview without alignment aperture.

3.11 Inverse Heat Transfer Coefficient

It is evident that the deposition process causes development of large quantities of thermal energy within a relatively small, localised area. The inverse heat method allows for the closest possible experimental and analytical approximation of thermal state during the deposition process. Nonlinear processes that involve intensive heat conduction, can successfully be solved using inverse problems of heat transfer. In the present project, the inverse heat conduction problem is used to determine the thermal boundary conditions in the case of Alloy 718 being deposited onto a substrate.

The iterative regularization method or optimization was chosen as it can be calculated for nonlinear inverse problems and was calculated algorithmically using DEFORM-3D finite element software package. By inputting site-specific temperature history data, an accurate definition of local heat transfer coefficients, as a form of temperature, was obtained to properly model transient thermal process. DEFORM then provides an optimization-based Inverse Heat

Transfer Coefficient (HTC) that extracts heat transfer coefficients from experimental thermocouple data.

A Carbolite® furnace (Figure 3.19) was used to heat Alloy718 substrates with internally fixed n-type thermocouples. The cooling curves were retrieved from 1200°C, 1100°C, 1000°C, 800°C, 600°C and 400°C. Using LabVIEW Signal express® the components were held at each specified temperature for 45 min to stabilize, then taken out and allowed to cool under NTP (Standard temperature and pressure) conditions. The data logger, chassis and software mentioned in the laser metal deposition trials were used to measure the cooling curves from each thermocouple for experimental validation.

Figure 3.19 Inverse heat transfer experimental set-up.

Chapter 4: Experimental Trials of Inconel 718 fabricated using LMD

4.1 Introduction

The repeatability and reproducibility of LMD manufacturing remains a crucial aspect to investigate to concrete the future of this processing technology. A series of experimental trials aim to characterise the laser / material interaction. Using a Taguchi Orthogonal array in the Design of Experiments remains popular amongst understanding parameter influence and optimizing build developments [91], [242], [243], [244], [245]. Although this very methodical approach establishes experimentally verified process parameter, it involves considerable processing and analysis time, energy, and material costs, and can become exponentially expensive when considering full factorial analysis. To overcome these penalties, this research will aim to base parameter selection on a combination of published literature, operating expertise, and analytical modelling.

After reviewing substantial published literature on additive manufacturing of Inconel 718 and gaining melt pool information through analytical modelling, this chapter will detail the LMD process optimization route for IN718 single clad tracks (Stage I), thin-walled builds (stage II) and solid blocks (stage III). Additionally, the quality of the as-received powder, and defect detection is presented. The main objective of the experimental trial route was to use optimised LMD configurations to produce defect-free, high-quality joins along the substrate-component interface and to investigate the evolution of microstructure and residual stress behaviour experienced by Inconel 718 deposited under various process parameters. The experimental trials would establish presence of strong metallurgical bond between deposited component and substrate without defects such as delamination or debonding, ensuring the powder deposited is sufficiently melted in the melt pool.

4.2 Process Window for Parameter Selection

The Laser Energy Density (LED) is calculated by considering the laser power (P) (in Watts), the scanning velocity (v) (mm/s) and the laser beam diameter (d) (mm). A generic formula is used as a guidance towards numerically correlating the process parameters to the resultant microstructure and microstructural phases [246].

Equation 4.1 Laser Energy Density Relation

$$Laser\ Energy\ Density\ (LED) = \frac{P}{vd}$$

The LED serves as a comprehensive guide, correlating values to optimized manufacturing despite the fluctuating process parameters in the resultant microstructure. By presenting previous data on microstructures, process parameters, and outcomes, the researcher established a baseline for conforming manufacturing settings. Optimization can be achieved by leveraging insights from similar manufacturing routes in previous research.

A simplistic overview of LMD processes was constructed by Dass *et al.* [50] giving optimal processing ranges for common aerospace alloy systems such as Inconel, Ti-6Al-4V and H13 Tool steel (Figure 4.1). The graph reveals three distinct regions of porosity formation influenced by the process parameters. Keyholing occurs when the laser power exceeds the optimal level, resulting in porosity due to oversaturation of the melt pool. Lack of fusion arises from inadequate linear heat input coupled with a high powder feed rate, leading to insufficient metallurgical bonding. Mid-porosity is observed when there is a significantly high linear heat input accompanied by a high powder feed rate, resulting in a combination of both types of porosity formation.

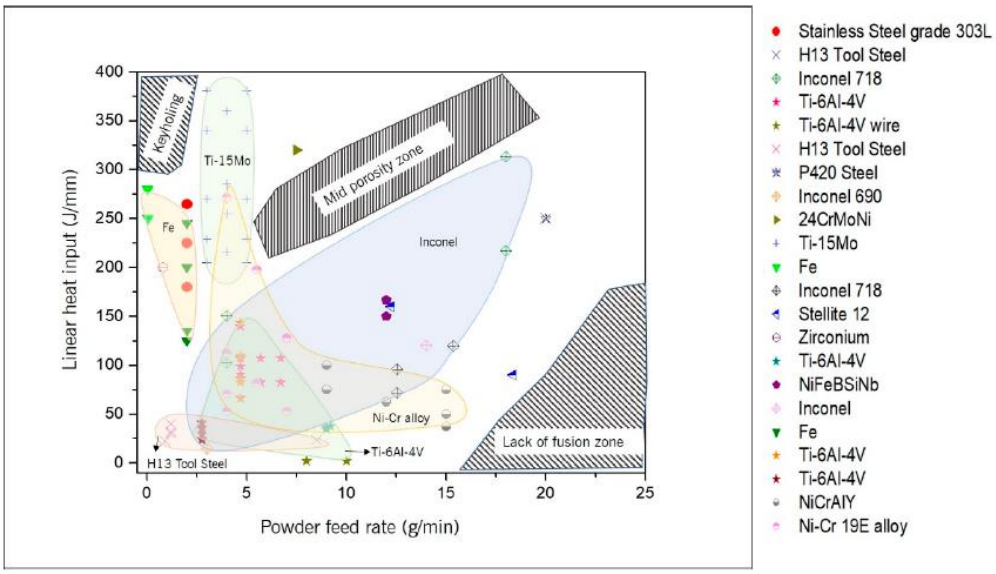

***Figure 4.1** Optimised processing parameters for a variety of alloys collaborated with areas of unsuitable processing zones [50].*

Previous work demonstrates successful part repair in various applications, focusing on high-value parts. Yu *et al*. [247] compared repair methods for grey cast iron, finding that LMD resulted in a significantly smaller heat-affected zone compared to gas metal arc welding. Praniewicz *et al.* [248] employed an additive/subtractive strategy for turbine blade repair, reducing machining time by 18%. Liu *et al.* [249] utilized DMD for repairing Inconel 718 parts with machined holes and grooves, achieving a defect-free transition from cast to welded sections. The mechanical properties crucial for IN718 component

repair via laser metal deposition include ultimate tensile strength, yield strength, hardness, and, for fusion welding purposes, porosity. A comprehensive review of the literature, summarized in Table 4.1, details process parameter selections for various Inconel 718 applications manufactured by direct energy deposition, providing key insights from each investigation.

Furthermore, Table 4.2 collates current studies investigating Inconel 718 builds which have been post heat treated to address some of the manufacturing issues with laser-based repairment including anisotropy which refers to the directional dependence of material behaviour under mechanical loads and detrimental phase production.

Table 4.1 Investigation on mechanical properties of additively manufactured IN718 components

Property Investigated	Value / Range	Laser Type	Laser Input Power (Watts)	Laser Scanning Speed (mm/min)	Powder Feed Rate (g/min)	Laser Energy Density	Ref	Key Highlights
Ultimate Tensile Strength (MPa)	1182	CO_2	1500 - 2000	480-720	5	93.75	[77]	All samples (DA, 720 °C×8 h/furnace cooling to 620 °C×8 h/air cooling) no solution heat treatment as deteriorate substrate. Yield strength around 970 MPa. Average tensile properties of 50%LAMed Inconel 718 superalloy were slightly lower than wrought criterion (AMS 5662M) around 88.9% UTS and 89.4% YS.
Ultimate Tensile Strength (MPa)	520 - 800	Diode	1100	700	5.2	N/A	[74]	Comparing precipitation-hardened HT, UTS was 20% higher in all cases with ductility 100% higher. Maximum UTS was slightly over 1000 MPa, while the values of the base material were between 1200–1300 MPa. The properties of these specimens do not match those of wrought Inconel 718.
Ultimate Tensile Strength (MPa)	845	CO_2	2350	480	6	97.91	[250]	Poor mechanical properties due to porosities caused by hollow particles in GA powders hence promote micro-porous coalescence failure. Post HT (Solution + Double Aging) the UTS was 1.5 times larger with 1240 MPa (Wrought IN718 1340 MPa). Consisted of columnar dendrites growing along <100> crystallographic orientation with 5µm primary arm spacing. Further improving mechanical performance, the gas atomised powder was replaced by PREP IN718 powder and heat treated to obtain 1360MPa UTS.
Ultimate Tensile Strength (MPa)	700-760	Diode	1800	1000	18	50	[251]	Samples solution annealed to 1065°C (AMS5664) for one hour to reduce warping.

Property Investigated	Value / Range	Laser Type	Laser Input Power (Watts)	Laser Scanning Speed (mm/min)	Powder Feed Rate (g/min)	Laser Energy Density	Ref	Key Highlights
								~~insufficient strength due to~~ Laves & lack of precipitates.
Ultimate Tensile Strength (MPa)	854 936 919 820	Fibre	600 1000 1500 2000	1000	N/a	35.99 29.94 29.99 29.94	[252]	The as-deposited microstructure altered from a fine columnar dendritic in the low laser power with smaller beam diameter to coarse columnar dendritic formation in the high laser power with largest 4 mm beam. Sample produced via 1000W laser power and beam diameter of 2 mm, resulted in the highest yield strength and UTS, 729MPa and 936MPa, respectively.
Ultimate Tensile Strength (MPa)	937 745	Fibre	350 1350	760	6.5 19.5	30.6 30.4	[253]	No reported tensile values were comparable or suitable for weld repairs without any additional heat treatments. However, evaluating the microstructure, a smaller and more refined grain structure of the low-energy process yielded greater tensile strength and elongation in comparison to high-deposition rate.
Ultimate Tensile Strength (MPa)	932	Fibre	1000	333	4.1	57.6	[254]	The mechanical performance of L-DMD was compared against As-cast and half-cast/half-DMD. The DMD built for reference purposes exhibited the highest yield strength and UTS with slight effect on specimen orientation i.e. vertical build tensile samples and horizontally built tensile samples. (UTS_{HOR}=909MPa and UTS_{VER}=932MPa) Analysing the interfaces, a smooth transition from cast section to DMD material without lack of fusion. Tensile specimens extracted from transition zone had UTS_{max}=782MPa with plastic deformation occurring in the cast section. Fracture locations happened in the cast section.
0.2% Yield Strength (MPa)	525	Diode	2950	1500	0.583	29.5	[229]	Solution heat treatment of as-deposited dissolves the detrimental Laves phase into grain boundary δ phase. After heat treatment + HIP mechanical properties enhance. Hardness increased by 53%, from 300HV to 467HV – *industry requirement 350VHN.* UTS increased by 54% from 847 MPa to 1301 MPa and 0.2% yield strength more than doubles from 525 MPa to 1120 MPa In comparison to casting IN718 (AMS5383) and wrought IN718 (AMS5662) which have UTS of 862MPa and 1276MPa and YS of

Property Investigated	Value / Range	Laser Type	Laser Input Power (Watts)	Laser Scanning Speed (mm/min)	Powder Feed Rate (g/min)	Laser Energy Density	Ref	Key Highlights
								respectively once HIP + Heat treated LMD IN718 held 1301MPa UTS and 1120MPa YS.
0.2% Yield Strength (MPa)	590	CO_2	2350	480	6	97.91	[250]	Post HT (Solution + Double Aging) yield strength doubled to 1133 MPa
Hardness (VHN)	325-450	NA	550	408	NA	NA	[255]	Fewer mis-orientated grains with higher hardness found near the interface region which was attributed to enhanced precipitation in bottom builds due to Nb segregation concentrated along inter-dendritic regions as well as within grains near eutectic products. Hardness heterogeneity was attributed to enhanced precipitation in the bottom region of builds due to Nb segregation and multiple thermal gyrations.
Hardness (VHN)	358	Fibre	2350	700	10	67.14	[256]	Higher intensity of intermetallic Ni_3Al element leads to increased hardness.
Hardness (VHN)	Around 300	NA	650	400	6.45	97.49	[257]	Heat treatment AMS5596 increased hardness to approx. 500 VHN. Prior to heat treatment, columnar dendritic crystals form along the <111> and <200> direction epitaxial from the substrate with precipitated phases retained. Post AMS5596 heat treatment, a compositional homogenous matrix with dispersive Nb-C and Mo-rich precipitate phases forms.
Hardness (VHN)	251 255 281	Fibre	250	120 200 300		125 75 50	[258]	Decrease in hardness was found with increasing the linear energy.
Hardness (VHN)	264	Fibre	2900	1500	33.33	29	[259]	Significantly high porosity – speculates that as-deposited IN718 cannot directly be used, post heat treatments are necessary to improve strength.
Hardness (VHN)	260-300	Fibre	250	300 150	28.52 28.52	250	[260]	Change in microhardness didn't follow any trend i.e., scanning speed difference/distance from interface. Strong microstructural changes were seen along the height of the DLMD part.
Hardness (VHN)	234		1400	600	7.02	56	[261]	A defect free build conforming to the requisite dimension of a thin wall at constant laser beam diameter without pores or irregularities was achieved.
Porosity	Less than 1%	Diode	1100	700	5.2	N/A	[74]	Pores didn't exceed 5µm.
Porosity	0.41%	Diode	2950	1500	0.583	29.5	[229]	Hot Isostatic Pressing reduced porosity in the as-built deposits

Table 4.2 Process parameter investigation on mechanical properties of heat treated additively manufactured IN718 components (*s – denotes solution heat treatment followed by air cooling, *HSA – denotes homogenization treatment- solution heat treatment - double aging heat treatment)

Laser Power (W)	Laser Energy Density LED	UTS (MPa)	UTS (MPa)	Yield Strength (0.2%) (MPa)	Yield Strength (0.2%) (MPa)	VHN	VHN	Key Highlights	Ref
1250 1300 1350 1400	37.5 39 40.5 42	687 (s) 726 (s) 756 (s) 718 (s)	1278 (hsa) 1307 (hsa) 1342 (hsa) 1298 (hsa)	313 (s) 328 (s) 340 (s) 325 (s)	1061 (hsa) 1093 (hsa) 1129 (hsa) 1077 (hsa)	220 (s) 232 (s) 239 (s) 228 (s)	485 (hsa) 491 (hsa) 496 (hsa) 488 (hsa)	Microstructure most uniform small grain size at 1350W after first solution treatment Under 1350W, the UTS and Yield Strength of HSA treated IN718 are highest due to precipitated γ' and γ'' in the grains and δ in grain boundary causing dislocation pinning and impede movement	[262]
450 850	60.24 75	970 (AF) 980 (AF)	1380 (DSA) 1300 (DSA)	720(AF) 680 (AF)	1250 (DSA) 1200 (DSA)	285.3 (AF) 366.1 (AF)	367 (HSA) 358 (HSA)	Faster cooling rates yielded coarse Laves phase, short aging treatment can successfully form enough γ'', improving strength by 96% (Low power) and 76% (high power). Direct heat treatments did not change columnar structure or dissolve Laves phase. *AF – as fabricated *DSA – direct short aging (732° for 4h, oven cool)	[263]
2200 4000 4000	73.33 66.66 53.33	Values in Figure 4 – Displays results from uniaxial compression test under strain rate 0.001/s whereby sample 1, 2 and 3.				**N/a**	**N/a**	In this paper, input density is regarded as power/beam diameter resulting in dendrite spacing's of: Sample 1 (P=2200W) – 7.16μm Sample 2 (P=4000W, laser spot diam =4mm) – 18.82 μm Sample 3 (P=4000W, laser spot diam =5mm) – 11.18μm Finely close dendrite wall spacing resulted from low input energy that impede dislocation movement, hindering plastic deformation and cause increased strength.	[1]

Laser Power (W)	Laser Energy Density LED	UTS (MPa)	UTS (MPa)	Yield Strength (0.2%) (MPa)	Yield Strength (0.2%) (MPa)	VHN	VHN	Key Highlights	Ref
								Narrowest primary spacing exhibited higher flow stress Columnar grains along the build height caused higher strength in scanning directions than deposition direction which vanished after full heat treatment.	

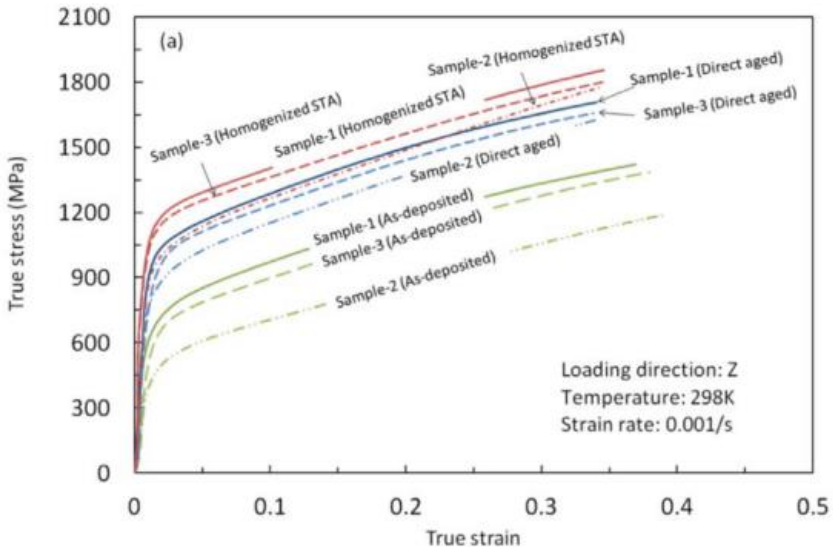

Figure 4.2 True stress-strain relationship for samples 1-3 (LMD IN718 samples deposited using different process parameters) denoted in* Table 4.2 *[1].

To adhere to industry standards, mechanical properties are dictated by AMS 5596 (for sheets ≤ 4.7 mm thickness) and AMS 5597 (for sheets ≥4.7 mm), specifying 'Nickel Alloy, Corrosion and Heat Resistant, Sheet, Strip, And Plate' [264]. However, in practical terms, the workpiece should ideally exhibit in-service condition properties to align with the mechanical standards outlined in Table 4.3, ASTM B670, titled 'Standard Specification for Precipitation-Hardening and Cold Worked Nickel Alloy Bars, Forgings, and Forging Stock for Moderate or High Temperature Service' [265].

Therefore, employing Laser Metal Deposition (LMD) for the repair of superalloy IN718 ideally yields as-deposited properties closely matching B670 standards, meeting the requirements of AMS 5596. This approach aims to surpass the properties of as-cast

material, thereby diminishing the necessity for total replacement, which would result in substantial expenses, energy consumption, and waste generation.

Table 4.3 displays the room temperature mechanical properties of superalloy IN718 in different forms and heat-treated conditions. The heat treatment consists of solutioned condition (940°C to 1010°C, held 0.5 h min, then cooled at rate equivalent to air or faster) followed by the precipitation heat treatment consisting of 718°C ± 14°C held for 8 h, furnace cooled to 621°C ± 14 °C hold until total precipitation heat treatment time has reached 18 h, and then air cooled [265].

Table 4.3 Inconel 718 Superalloy mechanical properties in Aerospace Grade

Alloy Conformity	Heat Treatment	Tensile Strength, min (MPa)	Yield strength (0.2% offset) min, (MPa)	Elongation in 2 in. [50 mm] or 4D, min, %	Reduction of Area, min, %	Hardness (HRV)
N07718 *ASTM B637* [228]	Solutioned & Precipitation hardened.	1241	1034	12	15	346
AMS5596 – Sheet (≤ 4.7 mm thick)	Solutioned	965	551	30	n/a	270
	Solutioned + Aged	1240	1035	12		350
AMS5597 – Sheet (≥ 4.7 mm thick)	Solutioned	965	517	30	n/a	260
	Solutioned + Aged	1240	1035	15		365

The optimal process parameters for meeting technical requirements in repair applications are delineated in

Figure 4.3 through a comprehensive review of published literature. The investigation into as-deposited mechanical performance reveals that achieving substantial mechanical properties necessitates post-process heat treatments, indicated within the orange window. Machine configurations that offer comparable mechanical performance but entail larger volumes of powder and energy are identified in the blue window. Lastly, the green window denotes optimized process parameters that surpass the properties of casted IN718 while aligning with the ultimate tensile strength (UTS) specifications of AMS 5596.

It can be concluded that to reach the mechanical performance of in-service grade IN718, post-process heat treatments would be required, however this could be detrimental to the substrate properties. Therefore, to understand the evolution of microstructure and

mechanical performance, this investigation shall explore both as deposited and post-process heat treatment that has been developed to preserve substrate performance.

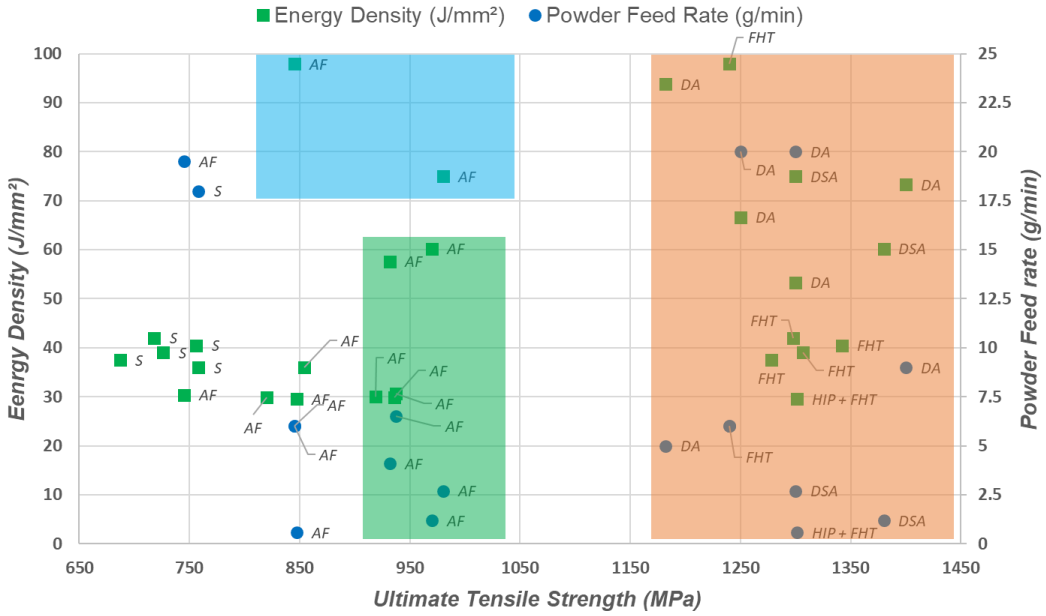

ABBREVIATION	HEAT TREATMENT PROCESS
AF	As fabricated
S	Solution annealed (AMS5664) 1065°C/1100°C for one hour, air cooled)
DA	Double-aged (720 °C, 8 h/furnace cooling at 50 °C/h, to 620 + 620 °C, 8 h/air cooling)
DSA	Direct short aging (732°C for 4h, oven cool)
HIP + FHT	Hot isostatic pressed followed by AMS5583D homogenization (1093±14 °C; 2 h/air cooled); solution annealed (954 °C–982 °C, 1 h/ air cooled); double aging (718±8 °C, 8 h, and then cool it down to 621±8 °C for 10h) and then cool it down in air to room temperature.
FHT	Full heat treatment: homogenization treatment (1093 °C, 1 h/air cooling) – solution treatment (980 °C, 1 h/air cooling) – double aging (720 °C, 8 h/furnace cooling at 55 °C/h to 620 °C, 8 h/air cooling.

Figure 4.3 Process Window for Optimised Direct Energy Deposition Configuration (Green box denotes majority of suitable energy density and powder federate conditions; Blue box denotes similar mechanical performance but requiring substantially more energy density; Orange window represents highest UTS with post processing heat treatments.

4.3 Process Parameter Selection

Drawing on conclusions from Table 4.2, Table 4.3 and Figure 4.3, a distinct correlation exists between the mechanical performance of as deposited IN718, which is heavily influenced by process parameters and can be tailored as per key product. Therefore, the energy density is recommended to remain between 25-60 J/mm^2 with a powder flow rate between 2.5-7.5 g/min. The spot diameter of the laser was focussed at a 2 mm diameter spot. Thus, the aim of this study is to examine the relationship between process parameters and microstructural evolution for repair applications, by varying the laser power only, which is the key parameter. Additional observations can be made leading to the correlation between laser power and local thermal history which directly influences

the evolution of microstructure, mechanical properties, and residual stresses. Repair applications require adequate mechanical performance, sufficient bonding strength and good control of the microstructure which can be achieved by optimizing the energy and power consumption as per the following sets of parameters:

i. Upper limit of process window, i.e. the laser power was set to 950 W (corresponding to 47.5 J/mm^2)

ii. Intermediate condition, i.e. the laser power was reduced to 750 W (ED = 37.5 J/mm^2)

iii. Bottom limit of process window, i.e. the laser power was reduced further to 550 W (ED = 27.5 J/mm^2)

4.3.1 Comparing Selected Process Parameters to other optimized windows

Mechanical property studies on as-fabricated (AF) specimens indicate that employing correct process parameters can yield a substantial ultimate tensile strength within the range of 760 MPa up to 980 MPa. Due to the anisotropic nature of crystal growth during solidification and the complexity and non-linearity of the fabrication method, peak strength can be achieved when the direction of applied load in a tensile test is parallel to the growth direction of the dendrites. Liu *et al.'s* [266] investigation explored the impact of energy density on the forming accuracy and physical properties of Inconel 718 fabricated through the LENS technique. Figure 4.4 suggests an energy density process window of 83.33 J/mm² to 137 J/mm², with values beyond this range leading to high surface roughness or low relative density. While relative density provides a quick indication of part quality, further examination of porosity size, volume, and distribution is crucial for correlating energy density with defect-free builds, mitigating stress concentration regions.

Ma *et al.* [68] study focused on the influence of energy input on the microstructural evolution of LMD IN718 alloy. Energy density (E_v) was defined as the laser energy per volume and was calculated by considering the overlap rate between two neighbour tacks, the measured width of the tracks and the layer thickness. Examining a range from 175 J/mm³ to 600 J/mm³, Figure 4.5 illustrates the influence of energy densities on relative density, calculated using image processing software.

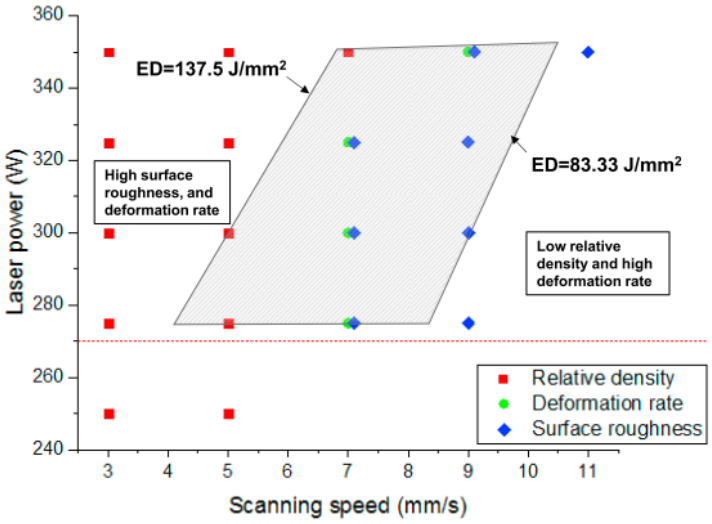

Figure 4.4 Energy density window for LENS process Inconel 718 [266].

Results from Ma *et al.* [68] indicate that a process window from 220 J/mm^3 to 550 J/mm^3 (Figure 4.5) resulted in satisfactory relative density, although it must be noted that all experiments were carried out in a glovebox, sealed with oxygen content less than 50 ppm. Interestingly, the lower E_v led to a more refined microstructure with less amount of detrimental Laves phase and more precipitated phases of γ'' and γ' in the matrix using a small overlap fraction. Moreover, it was concluded that if the volumetric energy dropped below 220 J/mm^3, it could lead to lack of fusion and a relative density of 99.2-99.4%.

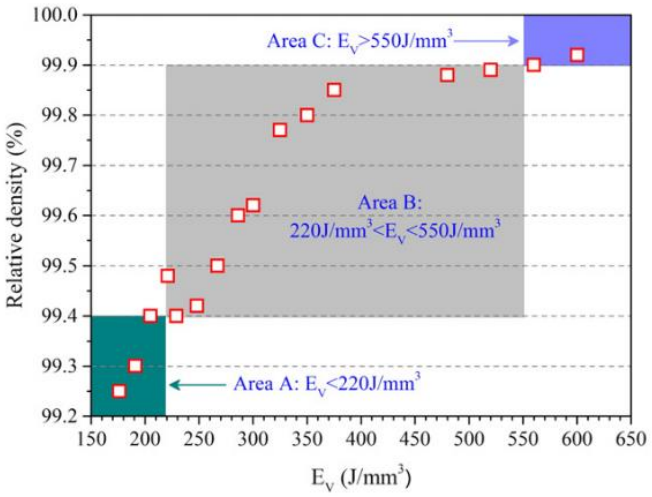

Figure 4.5 Relative density of the as-fabricated IN718 samples deposited using different E_v [68].

4.4 Overlap Configuration

During multi-track deposition, a small overlap distance exists between two adjacent tracks to ensure good bonding and continuity of the build. The overlap can be defined as a percentage by Roverlap = (1-L/D) x 100, where L is the offset distance between adjacent

laser spot centres and D is the laser diameter. The selection of the overlap value is essential for any additive manufacturing technology as it directly correlates to surface finish, residual stress distribution and the final microstructure based on the thermal gradient (G) and solidification rate (R). Cao *et al.* [267] concluded that the residual stresses in the overlap area were significantly higher and fluctuated more intensely than in the inner-pass area. Furthermore, as shown in Figure 4.6, the average and peak values of residual stresses increased with increasing the overlap ratio, while the variation of residual stresses was more gradual.

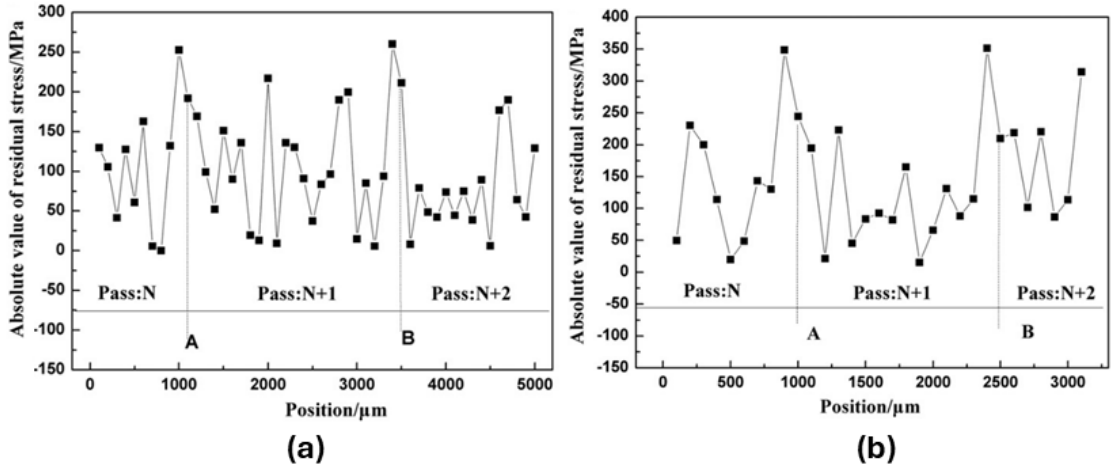

Figure 4.6 Residual stress measurement of LSFed Inconel 718 samples with overlaps rates (a) 20% and (b) 50% [267].

Ma *et al.* [68] investigated the microstructural evolution of LMD IN718 superalloy to determine an optimised volume energy density based on various process parameters which included the overlap percentage which was ranging from 20% to 50%. The increase of overlap percentage resulted in the increase of the size and volume fraction of Laves phase in the inter-dendritic boundaries, which coincidently, depleted the regions of Nb content for strengthening phases due to micro-segregation of the alloying elements Nb and Mo, thus forming Laves phase more easily. The accumulated density of the γ'/γ'' phases was depleting, and the particle size was increasing with increasing the energy volume density, as Figure 4.7 shows. As the volume energy density is increased, the melt pool dimensions will increase and solidify at a lower rate, and thus precipitated γ'' and γ' could be partially dissolved due to surrounding higher temperatures. The volume fraction of precipitated strengthening phases at the lowest Ev of 176 J/mm^3 without any post-process heat treatment was 7.12%, whereas the higher energy density volume of 600 J/mm^2 resulted in only 2.66% volume fraction of precipitated strength phase.

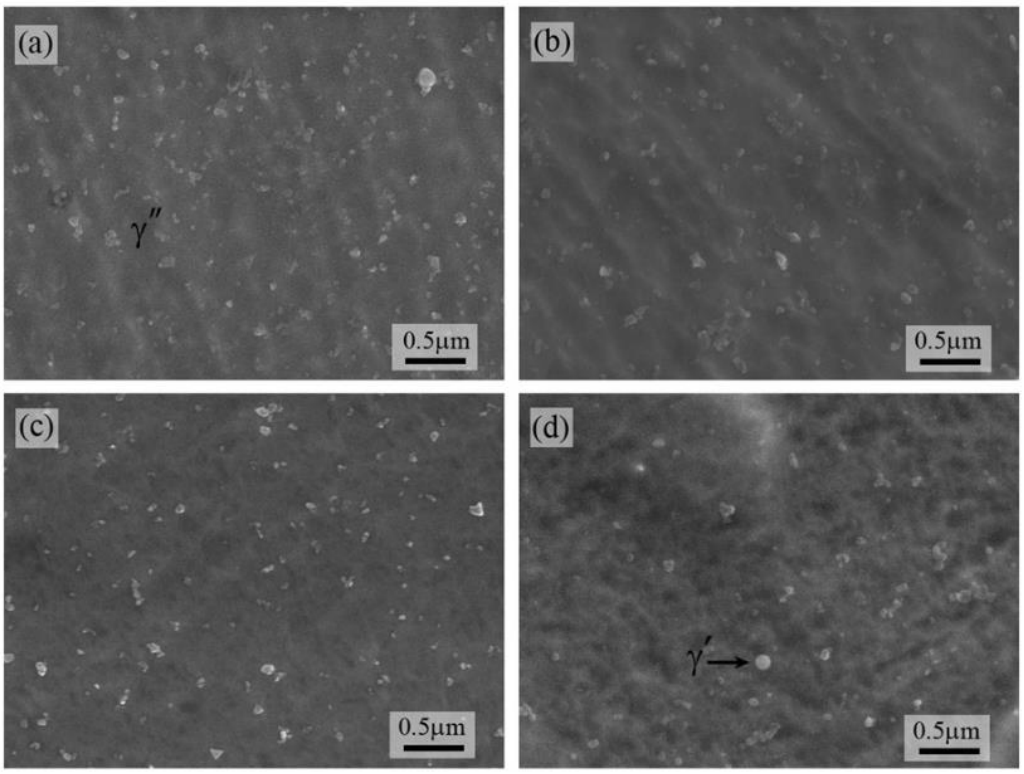

Figure 4.7 SEM micrographs of the as-DLFed samples detailing the precipitated phases γ'/γ'' in the matrix for E_v of (a) 176 J/mm^3, (b) 248 J/mm^3, (c) 350 J/mm^3 and (d) 600 J/mm^3 [68].

4.5 Concluding Remarks on Optimised Process Parameters

From published work, some key observations can be made with respect to LMD IN718 process parameters and the corresponding mechanical properties:

1. The primary focus of published literature is as-built components, build quality and mechanical performance, with little attention directly focussing on the interface section between base workpiece and as-built component.
2. The evolution of microstructure varies throughout the deposited component which is highly dependent on the local thermal history experienced. Consequently, the mechanical properties can fluctuate depending on the location, i.e., higher hardness nearer the interface region due to a faster cooling rate as compared to the mid-section of a component.
3. Anisotropic material behaviour is expected in as-built components; therefore, the properties of the repair should be considered prior to selecting a deposition direction and/or path. The tensile strength when the build direction runs parallel to loading direction outperformed other directions.
4. Post-LMD heat treatments are essential to enhance the UTS and YS, because the rapid cooling rates during LMD produce transient thermal cycles which

inhibit the precipitation of strengthening phases and promote the formation of detrimental phases.

5. Appropriate heat treatments will depend on the evolution of microstructure and mechanical properties of the component i.e., may only need a direct aging heat treatment.
6. Since mechanical properties are essential for repair applications, presence of defects and inclusions must be documented, with measures taken to mitigate these, i.e., post-process HIP.
7. UTS, YS and Hardness are the key properties reported in Table 4.1 and Table 4.2, however for repair investigations the process parameters could be optimised for toughness, high creep strength, high temperature fatigue strength or high temperature corrosion resistance.
8. In some studies, direct conclusions cannot be made due to lack of published details, i.e., Zhu *et al.'s* investigation into laser power effect on mechanical performance has no mention of the powder feed rate that was used [262].
9. An overlap percentage selection below 20% for all three laser powers will be beneficial for the resultant as-deposited IN718 microstructure to inhibit the growth, volume, and morphology of the detrimental Laves phase which coincidently increases the probability of strengthening precipitated phases to form without subsequent heat treatment.
10. A higher overlap percentage could lead to an increase of residual stress in the overlap area and intensely fluctuate more in the overlap area than that of the inner-pass area. The average value and peak value of residual stress could increase with further increase of the overlap percentage.

From an industrial manufacturing stance, the beneficial aim to decrease the overlap fraction from high 40-50% [1], [37], [268], [269], [270] to ≤20%, was to create an overall reduction in energy and material consumption. From literature [267], high overlap fractions generate high residual stresses, precipitation and growth of unwanted detrimental phases and larger overall production costs. By reducing the overlap percentage between adjacent tracks, the volume of powder deposited to the area and incurred wastage will significantly reduce to reach a net-shape manufactured component. Furthermore, the energy consumption and overall cost to manufacture an as-deposited component significantly reduces as the repetition of tracks to reach a near net shape width

will subsequently be fewer. Thus, the proposed deposition strategy will further enhance the sustainability aspect of AM and LMD.

Based on the selected process parameters, an analytical model was developed to provide melt pool dimension information. This information was analysed and compared later against single track deposits to make any adjustments necessary to the LMD configuration.

4.6 Analytical Model for Process Development

The overall simplicity and applicability of the model is to make an appropriate starting model to predict temperature history as a function of time, temperature gradient, cooling rate and solidification rate, which could be further developed. However, with its simplicity follows these assumptions:

- Thermophysical properties such as thermal conductivity, density, and specific heat capacity are temperature independent and latent heat due to phase change is negligible.
- Velocity and power input are constant, leading to quasi-stationary condition of the temperature distribution around the melt pool.
- There is no heat losses from the workpiece; surface convection, melt pool convection and radiation are ignored, therefore heat transfer is purely conduction through the substrate.
- Heat source is a point source not gaussian, volumetric or conical.
- The deposition of powder has insignificant influence on melt pool size and the laser interaction with powder is ignored.
- The substrate is modelled as a semi-infinite body meaning that one surface is bounded and extends to infinity in other directions acting as a massive heat sink.

The resulting analytical solution can be described as Rosenthal's equation [271] giving a three-dimensional, steady state temperature field for a point heat source moving in x-direction:

Equation 4.2 Steady state point heat source

$$T = T_0 + \frac{\lambda P}{2\pi k R} exp\left[-\frac{(V(R+\xi)}{2\alpha}\right]$$

$$P = \eta \text{ x p}$$

Where T_0 is the temperature of the base material, λ is laser absorptivity, P is the laser power provided (including efficiency), k is the thermal conductivity, V is the scanning velocity and α is thermal diffusivity. The weld scanning direction was performed in the y-axis; so, to perform welding velocity and time in the equation, y-Vt is substituted by ξ and the distance from the beam location to the point of interest is:

$$R = \sqrt{x^2 + y^2 + z^2}, \text{ which when substituting for y, } R = \sqrt{x^2 + \xi^2 + z^2}$$

Where the coordinates are relative to the position of the energy source such that $x=x_b - x_p$, $y=y_b - y_p$, $z=z_b - z_p$, in which b subscripts are the beam coordinates and p subscripts are the coordinates of the point of interest.

Since the Rosenthal equation does not account for any temperature-dependent material properties, the properties at room temperature, shown in Table 4.4. The effectiveness of the laser to successfully melt the Inconel 718 powder particles in this project is currently unknown, i.e., the laser fibre efficiency. An experimental study from Sainte-Catherine *et al.* [272] indicated that the absorptivity of Inconel 718 tends to increase with higher temperature. Considering the prevailing literature, which reports efficiency values spanning from 0.3 to 0.55 [145], [273], [274], a laser fibre efficiency of 0.4 is chosen for the initial melting of Inconel 718. This selected value serves as an initial benchmark, subject to further scrutiny through both experimental and finite element analysis (FEA) models. MATLAB was employed for calculations, focusing on discerning melt-pool characteristics such as width, depth, and molten area.

Laser absorptivity, denoting the ratio of absorbed laser energy to melt enthalpy (i.e., the energy needed to melt a unit volume of material) [275] was considered. This is usually a dimensionless value which latest research derived absorptivity is related to the morphology and temperature of the melt pool [276]. To simplify the calculation, many mathematical models approximated absorptivity as a constant [277]. Literature suggests this value to be between 0.3 and 0.87 for the absorptivity of IN718 [277]. Gruber *et al.* [230] analysed four states of IN718 powders (virgin, used, overflow and spatter) for LPBF process found that average laser absorption of IN718 powder in all states ranged from 66.6-76.1% with the virgin powder averaging 68.8% for the wavelength spectrum 900-1100nm fibre laser. Based on this wavelength and feedstock powder being very similar to that of the configurations used in this project, an absorptivity of 78% was selected which agrees closely with Huynh [278].

Table 4.4 Room temperature thermal properties of Inconel 718 used in Rosenthal equation.

Parameter	Symbol	Unit	Value
Laser Power	P	W	950, 750, 550
Laser Fibre Efficiency	η	---	0.4
Laser Absorptivity	λ	---	0.78
Ambient Temperature	T_0	K	293
Solidus Temperature	T_S	K	1533 [145]
Liquidus Temperature	T_L	K	1609 [145]
Specific Heat Capacity	Cp	J/KgK	536 [145]
Density	ρ	kg/m^3	7993 [145]
Thermal Conductivity	k	W/m^2K	21 [145]

The analytical solution will provide a baseline on how the melt pool dimensions evolve with varying laser power and provide a prediction for the transient temperature field. It offers a cost-effective means for quick analysis of melt pool formation, guiding LMD configurations. Predicting melt pool dimensions aids in validating process parameters for depositing IN718, reducing computational burden and cost in exploring parameter space.

4.7 Simulated Melt Pool Dimensions

According to the Rosenthal equation, the temperature maximises when $R \to 0$, due to the infinitely concentrated heat source, therefore this solution is useful when examining cases where the heat application is much smaller than the dimensions of features of interest [279]. The computation of fusion width and depth and total molten area were determined for the welding velocity 10 mm/s when the laser power is 950 W, 750 W and 550 W. A time selection of 1 s will ensure the laser beam will have moved 1 mm in the y-axis encapsulating close to the mid-point of the experimentally analysed single deposited track. Solution of equations were obtained by means of MATLAB software.

Figure 4.8 displays the predicted melt pool dimensions and HAZ for the three sets of process parameters, i.e. the varying laser power; the liquid-solid transition temperature (1336-1260°C) was used to define the melt-pool dimensions. In all three process conditions, the calculated analytical model simulates the melt pool dimensions for width, depth and molten area which can help to select the machine configurations. The size of the melt pool determines the overlap between tracks, the focusing height and the offset between layers, among other set-up parameters, to achieve a continuum solid with good bonding between tracks and/or layers.

If the laser configurations are set improperly, defects such as lack of fusion or pores from keyhole conduction (excessive penetration) will appear in the final formed component

[280]. Keyholing in LMD refers to a phenomenon where the laser beam melts the material to such an extent that a hole or "keyhole" is formed in the melt pool. This keyhole is essentially a void or cavity created by the intense energy of the laser beam, allowing the molten material to flow around it. Keyholing can occur when the laser power density is sufficiently high, causing vaporization and displacement of material. It is often desirable in processes like welding as it can promote deep penetration and fusion between the materials being joined. However, in LMD, excessive keyholing can lead to defects such as porosity or irregular bead shapes if not controlled properly [281], [282].

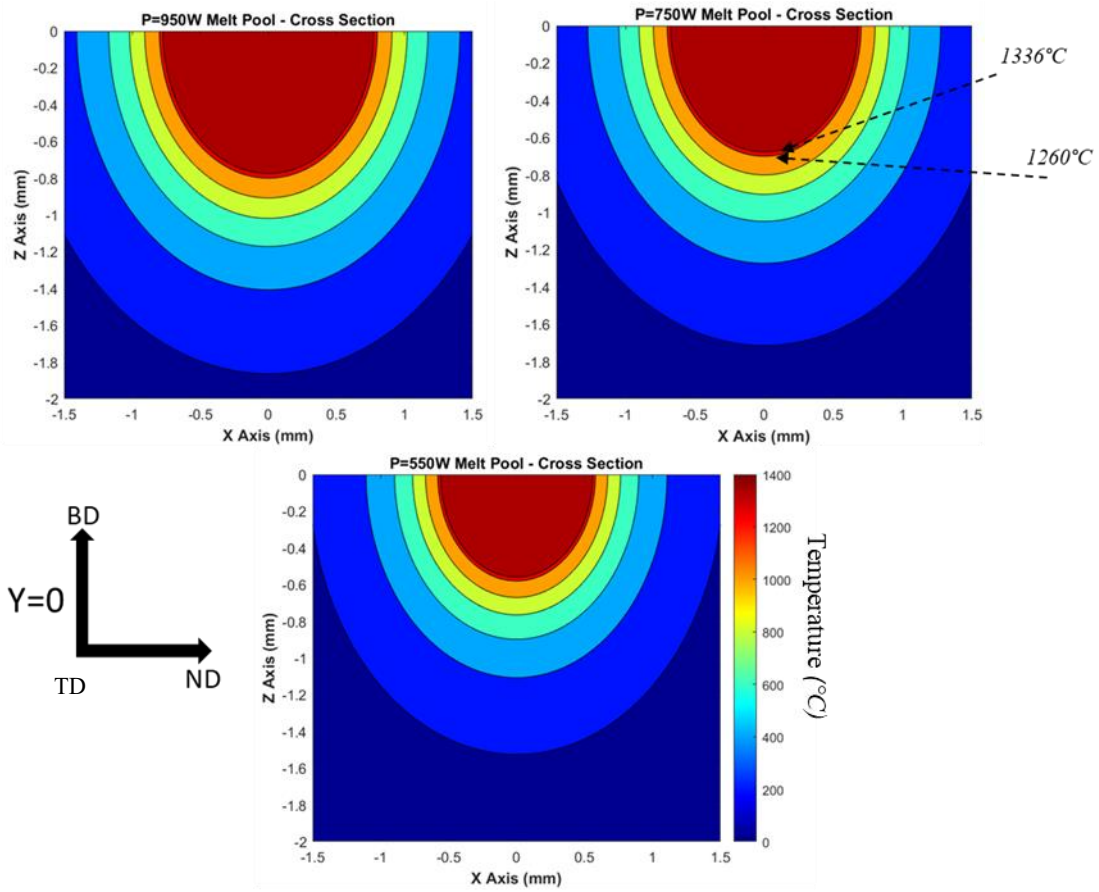

Figure 4.8 Predicted cross-sectional melt pool dimensions for (a) 950W, (b) 750W and (c) 550W.

Fluctuating the laser power has a direct influence on melt pool geometry as depicted in Figure 4.8, an increased laser power intrinsically provides more energy to a localised spot on the substrate surface. The increase of laser energy provided establishes wider molten pools with deeper penetrative distance. Higher LED leads to increased energy input, resulting in a larger melt pool, as confirmed analytically. Experimental studies by Aversa *et al.* [283] and Keshavarzkerman *et al.* [79] revealed substantial variations in melt pool dimensions with changes in laser power. Both studies demonstrated a notable reduction

in melt pool depth and width by decreasing the LED while maintaining constant scanning velocity. This trend was further validated by an analytical solution based on the Rosenthal equation [277].

The analytical temporal temperature behaviour for the substrate surface is shown in Figure 4.9 which details a top view of the moving heat source. When t=1, which corresponds to the heat source travelling during mid track deposition, it can be deduced that the higher laser power results in a larger molten pool and heat affected zone in the surrounding substrate as would be expected based on Rosenthal equation. As there is sufficiently more energy provided to the substrate during deposition with higher laser powers, the energy absorption is projected to increase as well.

The longitudinal cross-section shape of the melt pool plays an important role in the determination of the final quality for LMD repaired parts due to the interface properties and HAZ of the substrate, which are heavily influenced by time under temperature. Figure 4.10 details the temporal temperature field for the transverse laser scanning direction using laser power variation. Experimentally capturing the melt pool geometry is difficult due to the small temporal and spatial scale and continuation of the laser path melting the previously solidified material. However, the longitudinal section contributed to the understanding of physical mechanisms in the LMD and justify the assumptions presented in the analytical model in terms of melt pool depth.

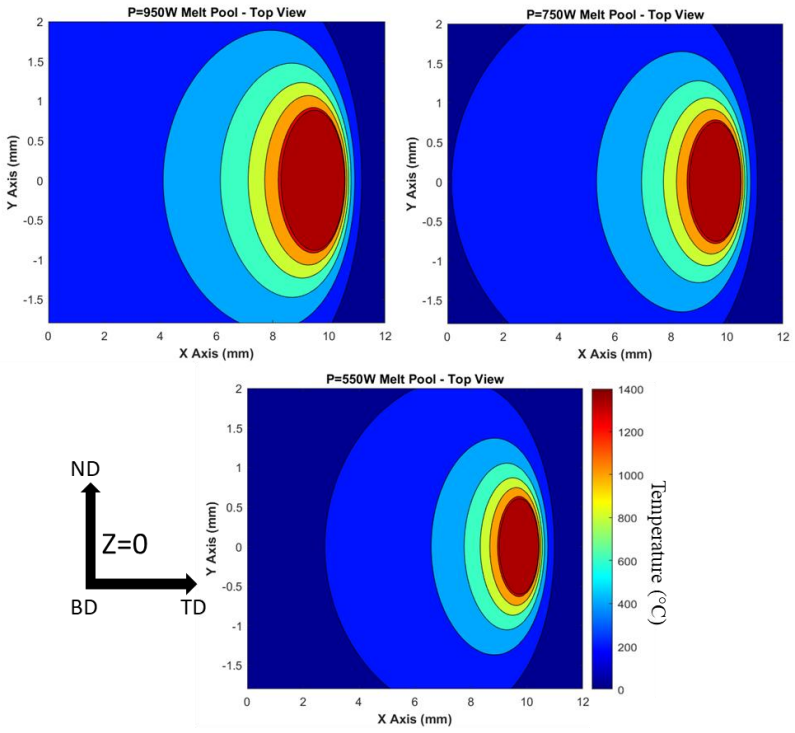

Figure 4.9 Top view of the molten pool on the substrate surface.

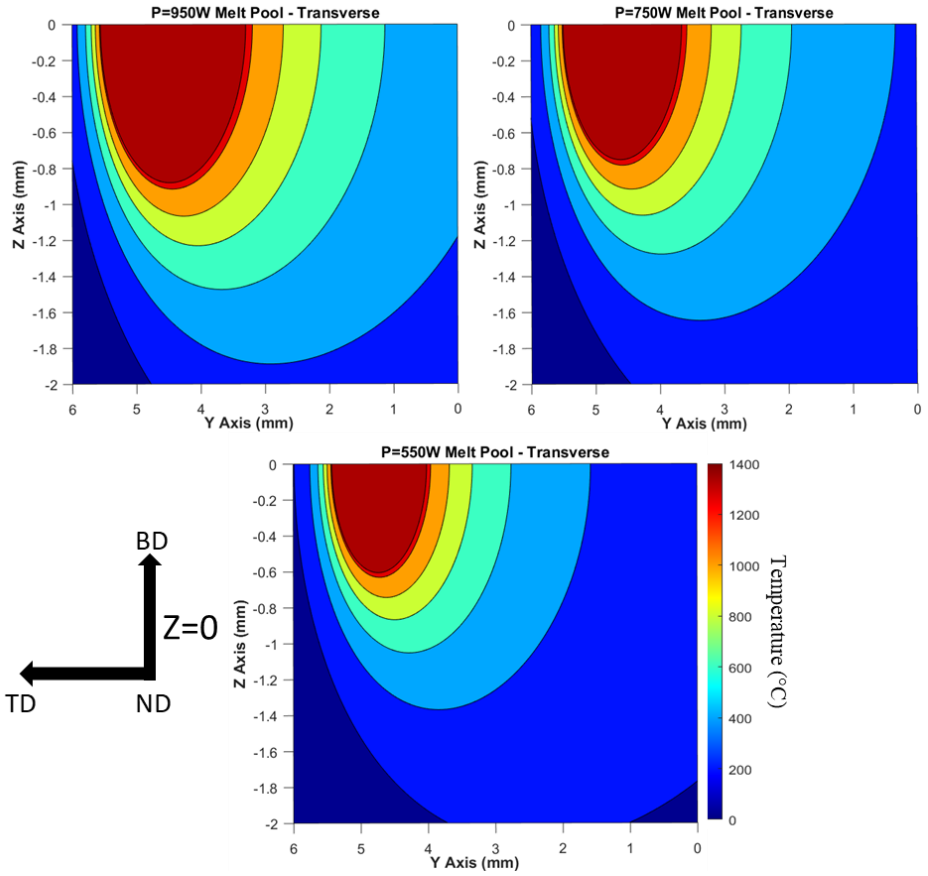

Figure 4.10 Cross-section of Melt Pool in YZ plane i.e., transverse (laser moving from right to left)

A transverse cross section of the single deposited track using 950W is detailed in Figure 4.11, care was taken to try capture the single-track mid-width. Furthermore, by analytically and experimentally capturing the transverse cross-section, the laser behaviour phenomena can be analysed. As shown in Figure 4.11, the interface's depression profile exhibits minimal non-uniformity, presenting a wavy appearance. This variation in height and depth of the single track, could be linked to a combination of inconsistent powder feed, energy input, and their interaction which can alter the fluid dynamics of the molten pool. As the laser movement itself is controlled via a high precision CNC, irregularities in the depth profile must be down to factors which are intrinsically harder to control such as localised powder delivery due to non-uniformities in powder size, morphology and carrier gas interaction that could expel power from molten area causing the localised energy to be absorbed deeper into the substrate. The fluctuation in melt pool dimensions arises from the interplay of two opposing forces: energy absorption and dissipation. Assuming a constant LED supplied from the heat source, the amount of energy absorbed by the melt pool would change depending on the volume of powder delivered as the heat source moves along the deposition path [284].

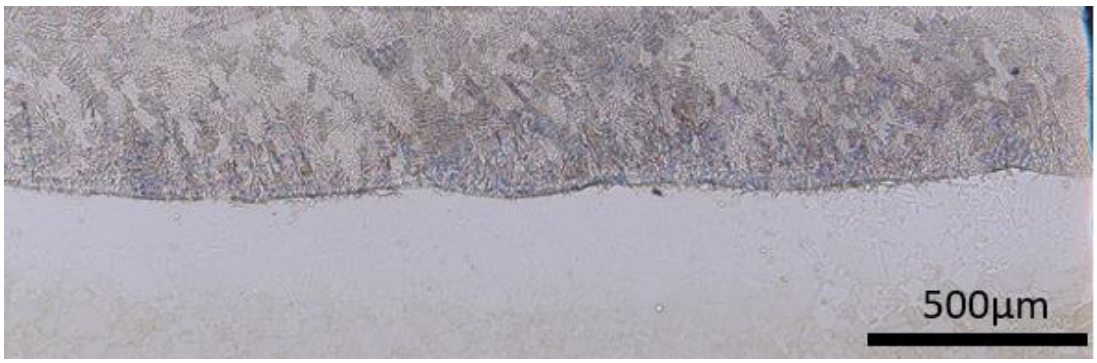

Figure 4.11 Transverse YZ cross-section of melt pool deposited under P=950W

Solving the melt pool dimensions in both the XZ (cross-section), XY (top view) and YZ (transverse travel direction) for the three independent laser powers allows the LMD configurations to be optimised accordingly, aiming to enhance the efficiency of the overall process in terms of energy consumption, volume of material deposited and wastage. The results of the calculated molten pool are shown in Figure 4.12. To validate the accuracy of the solution, experimental cross-sections of the single tracks deposited using varied laser power is carried out. Due to the simplifications of the analytical model, the predicted melt pool dimensions should be used as a guide, rather than taken precisely. To validate the accuracy of the solution, the cross-sections of the single-track deposition trials for each laser power were characterised. Comparisons between the simulated analytical model and the experimentally measured dimensions will now be discussed and explained in more detail.

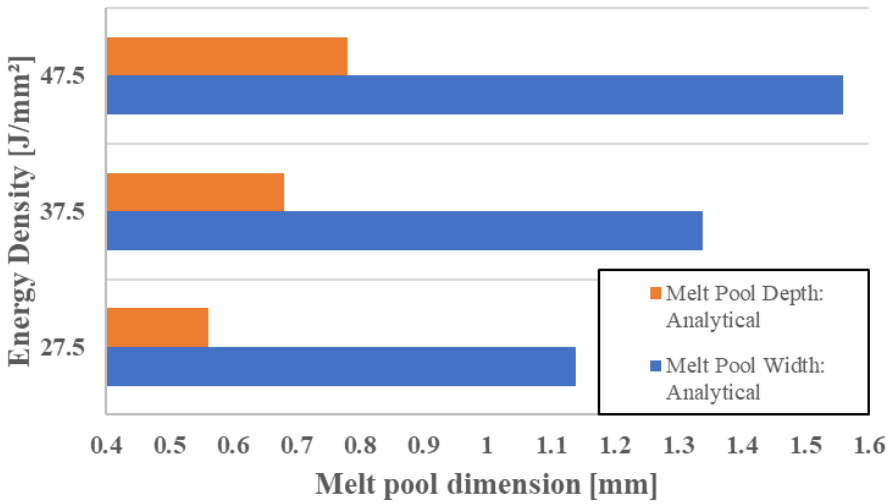

Figure 4.12 Analytically derived melt pool dimensions.

4.7.1 Determining experimental melt pool dimensions

To experimentally verify the accuracy of this simplistic analytical model and to understand the influence of energy density on the melt pool, the cross-sections of the

single clad tracks were characterised. Due to surface tension and the added volume of deposited powder material, clad area above the surface of the substrate will form. Therefore, the molten area from the deposition trials will be defined by the width (w), depth (d), height (h), while the molten area will be defined as S1+S2, see Figure 4.13.

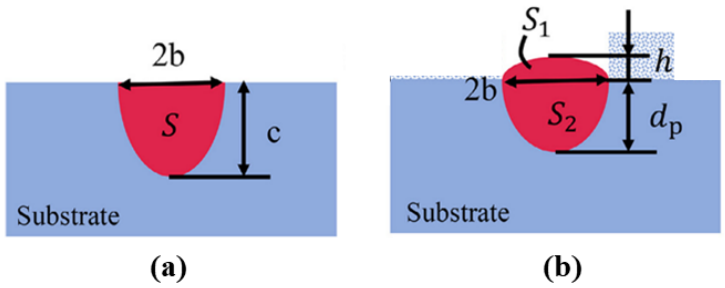

Figure 4.13 Melt-pool schematic cross-section with considerations as followed: (a) bare substrate with no powder (b) the first layer with powder inclusion [285].

Dezfoli *et al*. [286] developed 3D finite element (FE) model of the DED process which was integrated with cellular automaton (CA) to predict molten pool characteristics of deposited Ti-6Al-4V and was experimentally validated. To evaluate the thermal simulation, the depth and width of the molten pool were compared against experimental data captured for a single clad deposition [79]. The predicted molten pool width and depth were close to the experimental results for all examined cases.

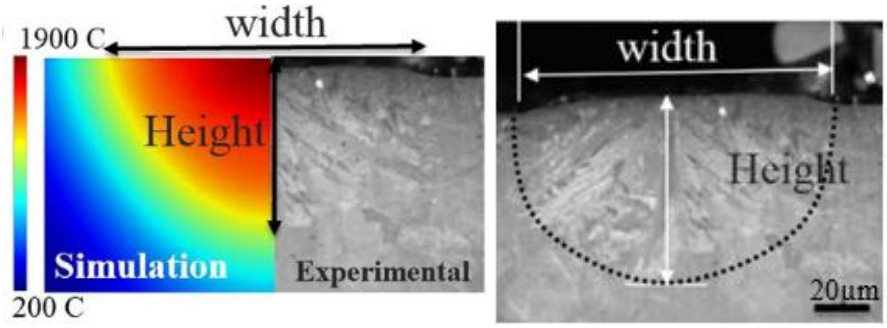

***Figure 4.14 Shape and dimension of the molten pool at the cross section after laser deposition (a) simulated molten pool dimensions, (b) molten pool for scanning velocity 1250 mm/s* [286].**

The mean values of depth, width and molten area measured on the macrographs of the sample's cross-section: the values in the table represent an average of three measurements performed on the same track section. The results of the comparison are tabulated summarised in Table 4.5, showing the calculated average measurement. Using ImageJ processing software, all measurements were taken from the according relevant macrograph. Figure 4.17 (a)-(c) displays the macrographs for the single clad track cross section deposited using 950 W, 750 W and 550 W, respectively. To define melt pool

dimensions experimentally, a definitive microstructural change was found between as-solidified material and substrate, therefore, to compare against the analytical model, liquidus-solidus (1336-1260°) transition was used as discussed.

Table 4.5 Melt pool dimensions of experimentally measured and analytically simulated.

Melt Pool Dimensions			
950W	*Experimental*	*Analytical*	*Error*
Width (mm)	2.016	1.61	20.14
Depth (mm)	0.695	0.78	10.90
Area (mm²)	1.03	1	2.91
750W	*Experimental*	*Analytical*	*Error*
Width (mm)	1.829	1.39	24.00
Depth (mm)	0.66	0.68	2.94
Area (mm²)	0.761	0.769	1.05
550W	*Experimental*	*Analytical*	*Error*
Width (mm)	1.4	1.14	18.57
Depth (mm)	0.78	0.58	25.64
Area (mm²)	0.6499	0.53	18.45

It can be found from Table 4.5 that the analytical method utilised for the design of experiments and the set-up of LMD in this section is aligned with the experimental results, though the absolute values differ significantly. A cummalative error deviation of 28%, 34%, and 63% was measured when compared to the experimental measurements of melt pool dimensions at 750W, 950W, and 550W laser powers, respectively. The agreement between the analytical model and experimental outcomes is satisfactory for mid and high laser powers. The melt pool depth and area had a cummalative error devation of ~4% and ~14% for the 750W and 950W, respectively.

4.7.2 Melt Pool Geometry: Experiment and Analytical Solution

By evaluating the experimentally captured melt pool dimensions from Figure 4.15 using a laser power of 550 W, 750W and 950 W, the width of the melt pool increased from 140 0µm, to 1800 µm and 2012 µm, respectively. This trend of wider melt pool dimensions for higher laser power was aligned with the analytical model, but the model underpredicted the experimental values by 18.5%, 24% and 20.14%, respectively. This was expected due to the clad width dependence on the melt pool size. The expected maximum depth was overpredicted when calculated by the analytical solution by 10.9%, 2.94% and 39.3% for laser powers 950 W, 750 W and 550 W, respectively.

Both model and the experiement results were in a good agreement for the mid and high laser powers. At the same time, it can be found that in case of the increased laser power, the width of the melt pool obtained through the Rosenthal equation is much smaller than the experimental but the depth profiles agree, seen in Figure 4.15. Since the heat source

is simulated as a point source as opposed to a Gaussian distribution (a well-established shape of the heat source for laser additive manufacturing) the highly localised, uniform energy input means that the heat is inherently focussed towards the centre of the melt pool, disregarding laser intensity behaviour and producing a deeper, narrower melt pool [287]. Furthermore , temperature dependent material properties, mass accretion from the powder material, heat convection and radiation, and contact convection from the carrier gas are all ignored in the Rosenthal equation. Thus, the depth of the melt pool is overestimated while the width is underestimated.

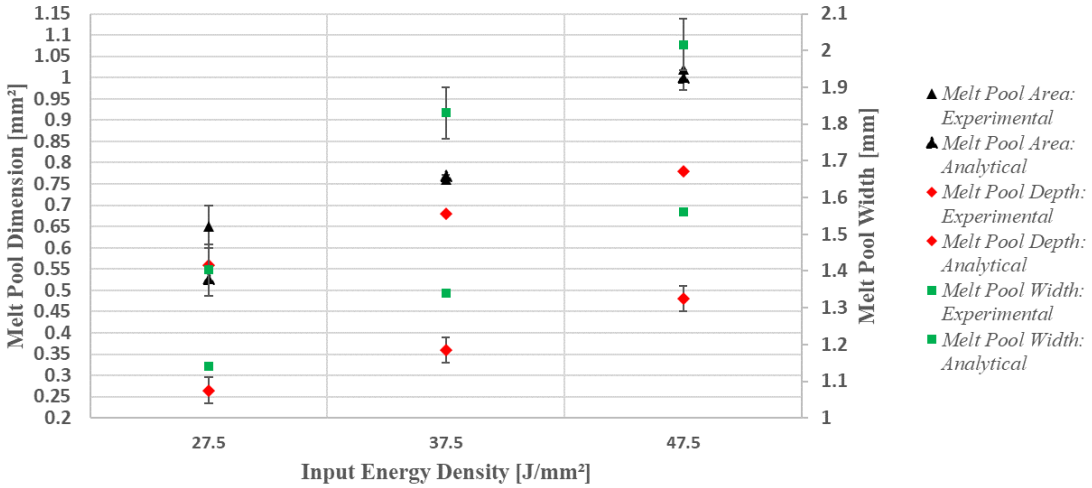

Figure 4.15 Melt pool dimensions comparing analytically derived versus experimentally captured.

Remarkably, the lowest laser power resulted in a melt pool with the deepest penetration and the narrowest width, meaning more energy was spent towards the centre of the laser. This observation will be discussed extensively in the following section, which investigates the melting regime. The analytical model, as predicted and experimentally demonstrated, shows that the highest laser power produces the largest molten area, which decreased with lower laser powers. The microstructural response will be explored in detail in Chapter 6, but it is expected that with smaller molten pool area, the rapid cooling rates could lead to a finer sub-structure, i.e. variation in width of the elongated similar length dendrites. As the absorbed heat in the melt pool dissipates from the boundary of the melt pool to the surrounding substrate, an approximation of the cooling rate can be based on the ratio of melt pool volume (m_a) to boundary area (S_b) [288]. A small $\frac{m_a}{S_b}$ would result in faster heat dissipation to the substrate and hence, higher cooling rate during solidification. Opposingly, a larger $\frac{m_a}{S_b}$ would have a lower cooling rate. A comparison of the simulated and experimentally captured cross section of the melt pool formed using a

750 W laser power is detailed in Figure 4.16. By extracting temperature history information from coordinates in the analytical solution, the evolution of microstructure can be deduced. However, by decreasing the laser energy, the $\frac{m_a}{s_b}$ ratio begins to reduce, therefore higher cooling rates would be expected. The analytical solution serves as a valuable tool to capture the molten pool geometry and temperature history profile which would otherwise be experimentally difficult to attain.

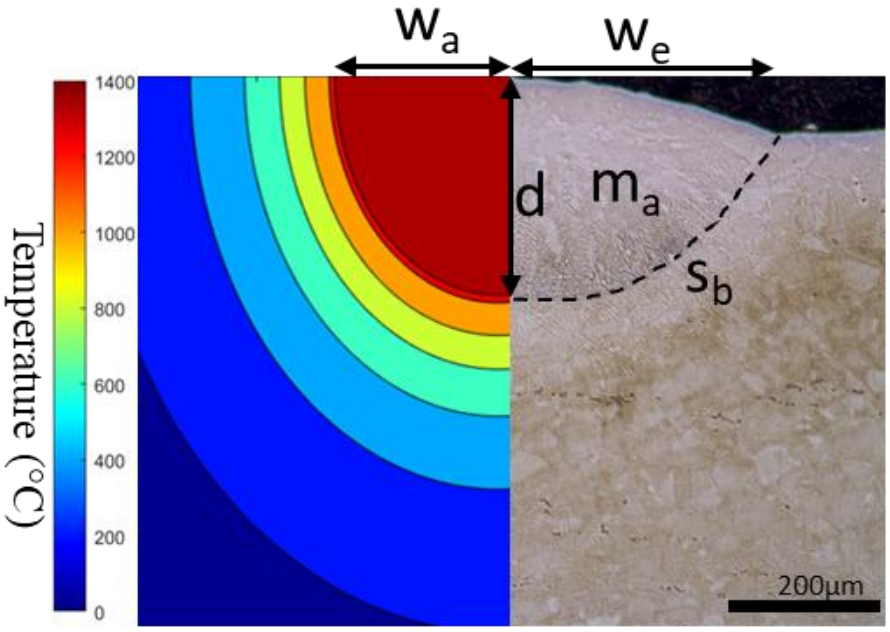

Figure 4.16 Comparative molten pool dimensions (a) analytical solution and (b) experimentally captured using 750W (W_a - analytical width, w_e = experimental width, d= depth, m_a = molten area and s_b = surface boundary)

Upon reviewing Table 4.5 and as indicated in Figure 4.15, the maximum penetration depth predicted by the analytical solution satisfies the experimental measurements for high (~11%) and mid laser powers (~3%) but signifcantly underpredicts the lower laser power (~25%). Finally, upon examining the volume of molten material above the substrate interface in Figure 4.17, it is apparent that the 950 W laser power configuration exhibits a significantly greater amount of molten material above the interface, resulting in a thicker layer deposition and a higher energy expenditure above the interface. Considering the dilution ratio, as discussed earlier, the 550 W laser power is characterized as over-diluted, potentially leading to inferior mechanical properties along the interface but does have a textbook melt pool shape. Moreover, from an economical, productivity and sustainability point of view, the 550 W laser power would produce layers with smaller

thickness and therefore the process would require more material and layers to reach the desired component geometry.

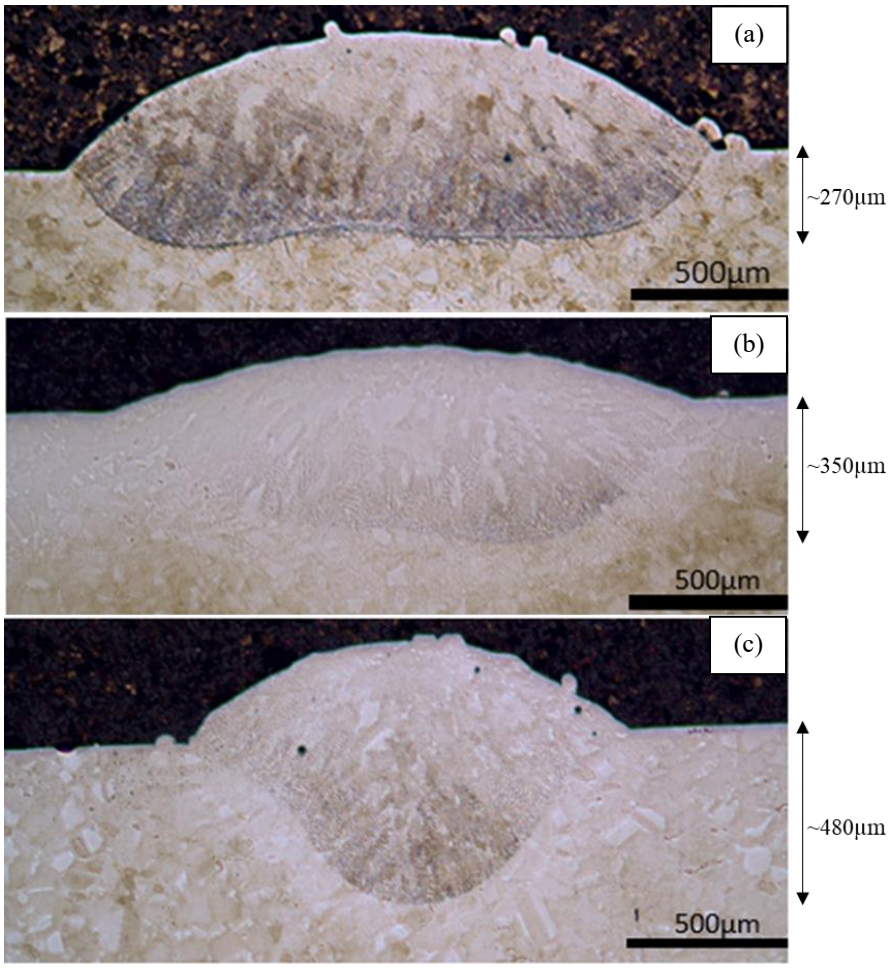

Figure 4.17 Cross-section macrograph of Single Clad Tracks deposited using (a) P=950W, (b) P=750W and (c) P=550W. Scan speed = 10mm/s.

Unlike observed trends in several studies [79, 81– 83], where higher laser power resulted in increased penetration depth and dilution, this investigation found that, during the deposition of IN718 single clad tracks, the maximum penetrative depth decreased with higher laser power. Contrary to the expected outcome based on previous publications, an increase in laser power did not lead to prolonged energy transfer to the substrate, causing the formation of deep melt pools. This contradiction will be addressed in the following section.

Overall, the molten area which considers both depth and width strongly agree with experimental results and the trend is well captured, therefore justifying the use of analytical solutions as a quick implementation of melt pool geometries and temperature profiles. To improve the accuracy of the analytical model, an exploration into laser efficiency and absorptivity of material can be carried out. Additionally, the Rosenthal

equation overlooks factors such as temperature dependence of the material, surface convection, radiation, and forced convection from the carrier gas. Consequently, the depth is overestimated, and the width is underestimated. However, the finite element (FE) model developed in this project aims to address these limitations.

4.7.3 Melting regime under varied LED levels

Figure 4.18 schematically illustrates the anticipated depth profile in comparison to the observed melt pool profile for the 750 W specimen. The black dashed line delineates the observed periphery, while the blue dashed line delineates the expected melt pool depth profile. Although the fluid dynamics of the melt pool is beyond the scope of this project, a general appreciation is crucial to further investigate the dynamics of melt pool formation.

The higher energy intensity at the center of the laser beam leads to an increase in surface temperature of the melting metal, causing larger recoil pressure on the melt pool, which can result in a greater surface depression in the area. This depression, coupled with higher temperatures at the central zone of the melt pool, serves as a driving force for melt pool penetration, resulting in an increase in melt pool depth [79]. It would be expected with that the increase in laser power would result in a greater depression depth based on the volume of localised energy, instead it was observed experimentally that the depths (mm) decrease with increasing laser power but form wider melt pools.

To understand this phenomenon the driving forces in the melt pool and their effect must be analysed, as depicted in Figure 4.19.

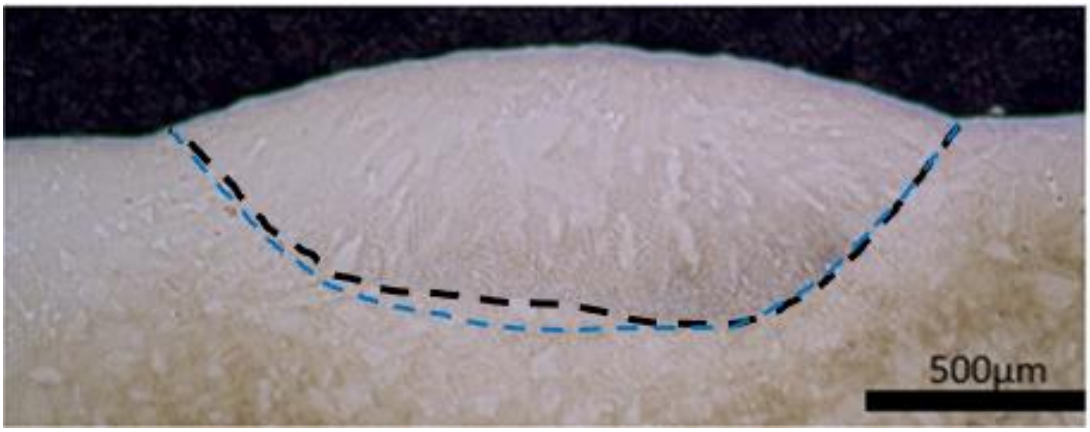

Figure 4.18 Cross-section of single track deposited using P=750W (N.B. Black dashed line displays the experimentally measured depth profile, blue dashed line displays expected depth profile)

In the liquid melt pool generated during laser additive manufacturing, four primary forces govern fluid flow: buoyancy forces (originating from spatial variations in liquid-metal

density), Marangoni forces (originating from surface tension gradients), shear forces (originating from laser-generated vapor or plasma), and gravity [289]. These driving forces, along with their interactions, collectively give rise to intricate flow patterns within the melt pool. The buoyancy forces are generated from the spatial variation of liquid-metal density, primarily attributed to temperature fluctuations and, to a lesser extent, local compositional variations affecting density as a function of material temperature. The material's density decreases with increasing temperature due to phase transformations, adhering to fundamental principles.

The temperature gradient within the melt pool, with higher temperatures at the upper region compared to the bottom, induces upward movement due to buoyancy-driven convection (whereby the higher temperatures in the upper region led to a lower density in that portion of the liquid metal). However, the buoyancy effect is deemed negligible in comparison to the dominant Marangoni forces in laser melting [290]. Marangoni force, also known as thermocapillary, plays a pivotal role in laser additive manufacturing, generating shear force at the free surface and driving convective flow within the melt pool. The temperature gradient is identified as the primary driver of fluid flow in alloyed materials. As the highest temperature, located at the centre of the melt pool, decreases rapidly, it results in a surface tension difference, inducing an outward melt flow. It's important to note that while buoyancy contributes to the upward movement, other forces, such as the Marangoni force, play a more significant role in laser melting.

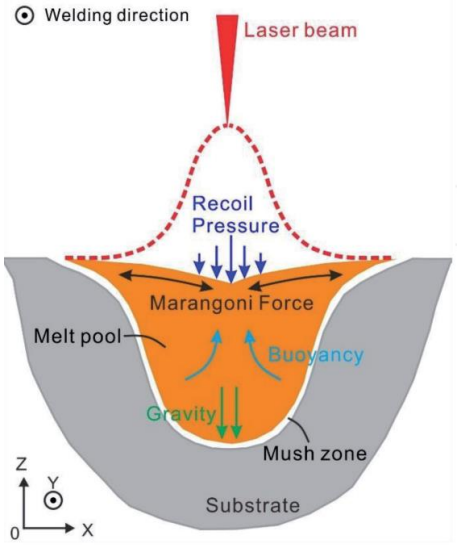

Figure 4.19 Driving fluid forces acting on the weld pool [289].

Exploring fluid dynamics and driving forces influencing melt pool behaviour lies beyond the scope of this project; however, it is important to understand the factors impacting melt pool convection can be briefly categorized [289]:

i. Laser related parameters: The energy density significantly influences the temperature field and material evaporation. Higher laser power results in larger temperature gradients, leading to higher surface tension and more intense radial convection. Increased laser power enhances recoil pressure, pushing the centre of the top surface of the melt pool downwards. At the highest laser powers, the significance of recoil pressure vs Marangoni forces diminishes results in shallower penetration depth as the molten material is pushed along the thickness direction.
ii. Scan parameters: Depending on the laser velocity, the temperature gradient in the front side of the melt pool is much steeper than the trailing edge. Thereby reducing the scanning velocity will increase the interaction time and thus, peak temperature, leading to stronger Marangoni fluid convection and larger melt pool.
iii. Increased surface tension: The higher laser powers lead to an increase of temperature gradient within the melt pool arising to a higher surface tension. This tension will resist the penetration of the molten material into the substrate.
iv. Gas/powder-related parameters: The blown powder particles with low temperature impacting the melt pool will change melt pool temperature field and in addition, the impact force may affect the flowability and penetration of the melt pool – this is where fused particles were seen in the melt pools of higher laser powders meaning expended energy fusing the blown powder.
v. Evaporation effects: At higher laser power, the intense energy can lead to increased ablation and vaporization of the material. This can result in more pronounced ejection of material from the surface, affecting the depth of the melt pool due to the material undergoing melting and penetration to substrate.
vi. Laser beam profile behaviour: Although the laser beam profile was calibrated prior to the deposition using a beam profiler, the *in situ* stability behaviour of the laser is difficult to monitor and adjust. The shallow penetration behaviour seen in middle of the melt pool for the trial under 950 W, (Figure 4.20), compared to the edges could be linked to the changing melting regimes from the preferred conduction to keyhole mode causing extensive energy conduction and absorption towards the edges and loss of powder to the middle of the melt pool. A proposed feedback system would be to incorporate high-speed thermal IR/pyrometer

camera to show transient melt pool shape [291]. Current laser powder bed fusion (L-PBF) machines have a suite of *in situ* process monitoring capabilities such as QM coating module for Concept Laser GmbH, Laser Power Monitoring (LPM) for SLM Solutions Gmbh or InfiniAM for Renishaw PLC machines. These aim to provide operational behaviour of the laser to aid in early potential fault detection [292].

vii. Excess blown powder: By increasing the molten pool area due to the increasing energy density, excess blown powder could absorb the energy needed to produce a more uniform depth profile and caused partially melted powder to fuse sporadically across the perimeter of the melt pool above the substrate interface, demonstrated by Figure 4.20.

Figure 4.20 Fused partially melted powder with P=950W.

4.7.4 Conclusions of Analytical Model

While the Rosenthal solution offers insights into melt pool characteristics, its applicability to model repetitive thermal cycling is constrained by the necessity for an initial steady temperature condition, which is not characteristic of LMD processes [293]. Nevertheless, the analytical model in general effectively captures the impact of increased energy density, illustrating the formation of a larger melt pool in both width and depth and the consequent experience of diverse thermal histories. Subsequently, the results pertaining to melt pool configuration will be directly incorporated into the LMD setup to construct thin-wall and solid block components, simulating laser repair on small-scale demonstrators.

The three-dimensional (3D) Rosenthal solution provides a fundamental but very basic understanding of the relationship between process variables and associated thermal conditions at solidification. However, only analytical, or semi-analytical models are considered applicable due to their efficiency when compared to more advance Finite Element of Fluid Dynamic models. Utilizing analytical models for temperature

distribution prediction and melt pool width allows for efficient optimization of process parameters, such as laser power and travel speed, with minimal cost and time investment [294]. Analytical models serve as indicative tools for comprehending thermal conditions associated with various process variables. Nevertheless, their limitations, including non-temperature-dependent properties, semi-infinite substrate characteristics, and neglect of boundary conditions with an infinitely small heat source, highlight the advantages of experimentally validated numerical models, such as the Finite Element Model proposed in Chapter 5.

After the single-track analytical models, an examination will be conducted across the interface to ascertain the establishment of a robust metallurgical bond under the selected process parameters. Additionally, the stability and structural integrity of thin-walled components, constructed from multiple successive layers, and solid blocks will be analysed.

4.8 Interface Assessment and Fabrication Imperfections using Single track deposition.

The process parameters were selected by reviewing published literature and analytical models aiming to obtain defect-free builds interface joints and strong bonding. Based on the literature and expertise within the area, it was decided that the process parameters would vary in laser power in 200 W increments from 550 W, acting as a low power scenario, to 750 W, being a moderate laser power, up to 950 W, being a high laser power scenario for depositing material. Other process parameters were kept constant as this was deemed most influential to the interface joint layer cohesion. To optimise the process, the overlap was kept at 10% for all three laser powers as this would inherently use much less material, energy, and time, which would result in a more economically viable and sustainable application for repairing and remanufacturing of IN718 aerospace components. By limiting the process parameters, the study was focused on the direct correlation between laser power and bond integrity through the close examination of interface thermal history, and hence the evolution of microstructure, mechanical properties, and residual stresses in this critical region.

4.8.1 Single track dilution ratio

One of the primary objectives was to determine suitable values for these process parameters through an investigation of the metallurgical bond between delivered powder and substrate. Conventional metallography techniques on laser track cross sections facilitated measurement of track dimensions (height and width) and dilution values. Melt

pool dimensions are highly sensitive to process parameter variations, necessitating a thorough understanding of their correlation. In repair applications, dilution ratio is crucial, representing the extent of mixing between track and substrate materials. Achieving an optimal dilution is essential for preserving the chemical composition and homogeneous properties of the coating material. Geometric dilution is influenced by deposit height and depth, while chemical dilution corresponds to the enrichment of elements diffusing from substrate to deposit layer [85]. Accepted dilution ranges between 2% and 10% is generally desirable, which can be controlled through the laser power, shape of the laser beam, focal beam diameter and powder jet [295].

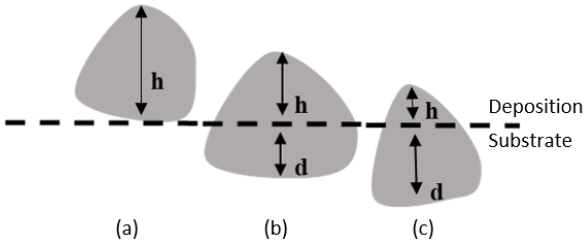

Figure 4.21 Dilution zones (a) zero penetration occurred (d=0) meaning lack of fusion and very weak/ no metallurgical bond (b) optimal level of dilution (region of 2-10%) (c) high level of d, leading to key holing effect [295].

A minimum dilution zone is often a prerequisite to optimising process parameters whereby an investigation into the dimensionless value of metallurgical bonding takes place. Dilution can be defined as:

Equation 4.3 Dilution relationship

$$D = \frac{d}{h + d}$$

Where d is the depth of penetration below the substrate/bond interface and h is the height of the material deposited (Figure 4.21). The energy required to establish the right size of melt pool bond will fluctuate dependent on laser power, scanning speed, powder feed rate and size of focal beam diameter. A low energy density or high powder feed rate may result in lack of fusion between the layers, on the contrary, a high energy density or low powder feed rate contributes to a high dilution, initiating the key holing phenomena.

Optimum dilution is important as mentioned, but physical defects such as porosity and hot cracking must also be considered because their appearance can lead to significant decrease in mechanical properties across the interface region. Figure 4.22 shows the influence of laser power on dilution ratio for the cross-sections of single deposited tracks.

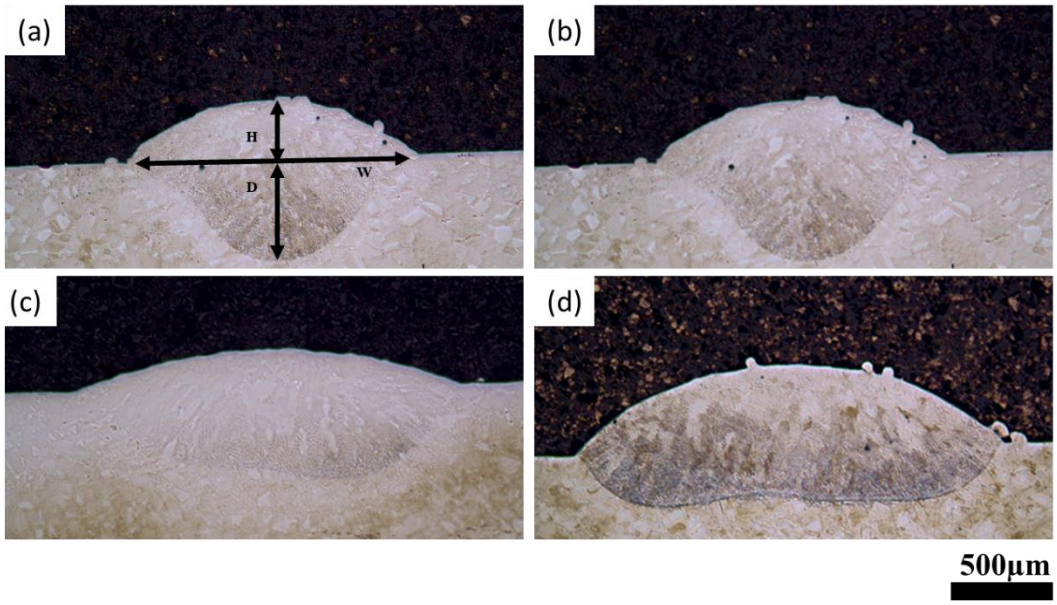

Figure 4.22 Cross-sectional view of single clad tacks deposited using (a) 550W with schematic measurement technique, (b) 550W, (c) 750W and (c) 950W.

4.8.2 Deposition Quality Acceptance Criteria

The quality of the depositions produced in the experimental trials was assessed against a set of welding acceptance criteria from several international standards on welding as illustrated in Appendix A. A key international standard is, '*The American Welding Society Standard, AWS D17.1:2001*' [296] the laser metal depositions were subjected to a rigorous check. Other standards, include the European standard, BS EN ISO 13919-1:2019 [297] it was developed for generic electron and laser-beam welded joints for steel, nickel, titanium, and their alloys; BS EN 12932, which was developed for laser-arc hybrid welding of steels, nickel, and nickel alloys [298].

Different welding imperfections are characterised in the standard ISO 6520-1:2007 [299], that classifies geometric imperfections in fusion welding metallic materials as described:

- Crack – Imperfection produced by local rupture in the solid state which may arise from the effect of cooling or stresses. These can be further categorized into:
  - Longitudinal crack = crack parallel to axis of the weld
  - Transverse crack = perpendicular to axis of the weld
  - Radiating = cracks radiating from common point
  - Crater crack = fracture at the end of a weld
  - Connecting = cracks that branch from common region
  - Microcrack = only visible under microscope
- Incomplete fusion and penetration: Lack of unity between weld metal and parent material

- Porosity: Gas cavity formed by entrapped gas essentially in spherical form
- Inclusions: Solid foreign object substance entrapped in weld metal
- Undercut: Irregular groove at a toe of a clad track in parent material or weld material
- Shrinkage groove: Undercuts visible on each side of the clad track
- Underfill: A channel in the surface of a weld due to insufficient deposition
- Root concavity: A shallow groove due to shrinkage of a butt weld at root
- Excess weld or penetration: Excess weld metal protruding through the root of a weld
- Burn through: collapse of the weld pool resulting in hole in the weld.

Porosities and undercuts, being stress concentrations, demand standardization limits. Undesirable features like shrinkage grooves, underfill, undercut, and root concavity pose risks for components under dynamic loading, acting as stress concentrators and initiating fatigue cracks. Tailoring process parameters for each deposition is crucial to avoid excessive penetration and undercut which is especially challenging in repairing thin workpieces like turbine blades [300].

Table 4.6 Weld quality assessment criteria from Table I applied to IN718 single track deposited under range of process parameters as defined by AWS D.17.1, BS EN ISO 13919-1 and ISO 6520-1:2007 [296], [297], [299].

Laser Power (W)	Width of track (µm)	Track Height (µm)	Track Depth (µm)	Dilution ratio	Qualities	Imperfections
550W	1401	284	477	62.7%	No cracks present including micro-cracks. Complete fusion Complete penetration No burn through No presence of inclusions	Over-dilution Porosity (≤160 mm, measured approx. ½ max) Porosity spacing – *Class B* AWS Standards Excess penetration (≤ 0.2 mm+0.15 t)
750W	1810	210	361	64.9%	No cracks present including micro-cracks. Complete fusion Complete penetration No burn through No presence of inclusions No porosities present.	Over-dilution Excess penetration (≤ 0.2 mm+0.15 t)
950W	2016	430	265	38.1%	No cracks present including micro-cracks. Complete fusion Complete penetration No burn through No presence of inclusions	Slight Over-diluted Porosity (≤125 mm, measured approx. ½ max) Porosity spacing – *Class A* AWS Standards Excess penetration (≤ 0.2mm+0.15t)

Quantitatively, dilution is computed as the ratio of molten substrate to molten material during the cladding process. Table 4.6 reveals that the reduction in laser power increases dilution ratio. In all power cases, observations note partially melted powder fused to the single clad and pores in the 10-20 µm region, induced by the shielding delivery gas. Despite excessive dilution in both 550 W and 750 W, this study prioritizes microstructural evolution, crystallographic texture, and residual stresses, warranting further investigation due to the observed good metallurgical bond. High dilution is reported to induce keyhole porosity [50], but the 950 W case, exceeding 30% dilution, maintains strong metallurgical bonding without keyhole-induced porosity. Contrarily, the optical microscopy reveals robust metallurgical bonding (Figure 4.23), with no lack of fusion or keyhole-induced porosity and substantial intermixing of substrate and deposited powder. Thus, despite dilution ratios of higher than 30% no keyhole porosity or internal pores were detected.

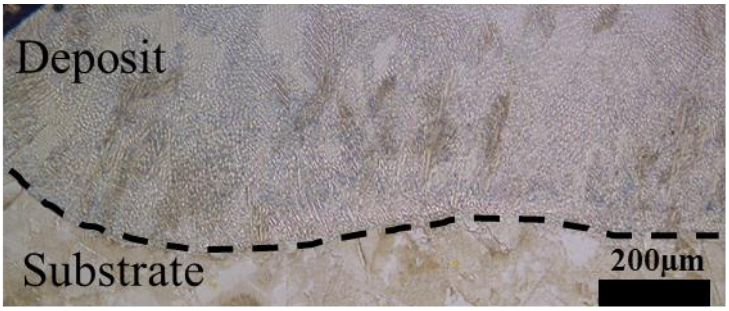

Figure 4.23 High power, P=950W single-clad cross-sectional interface detailing no keyhole induced porosity

In these trials, though keyhole porosity was absent, excessive dilution compromises the preservation of the original chemical composition and homogenous substrate/coating properties. SEM examination of the interface region for single deposited tracks reveals microstructural details captured directly at the deposit-workpiece interface (Figure 4.24). The dark and grey areas signify the austenitic FCC γ-phase, while the bright white phase represents the interdendritic Laves phase growing perpendicular to the deposition direction and parallel to the build direction. An enhanced microstructural study is completed in Chapter 6.

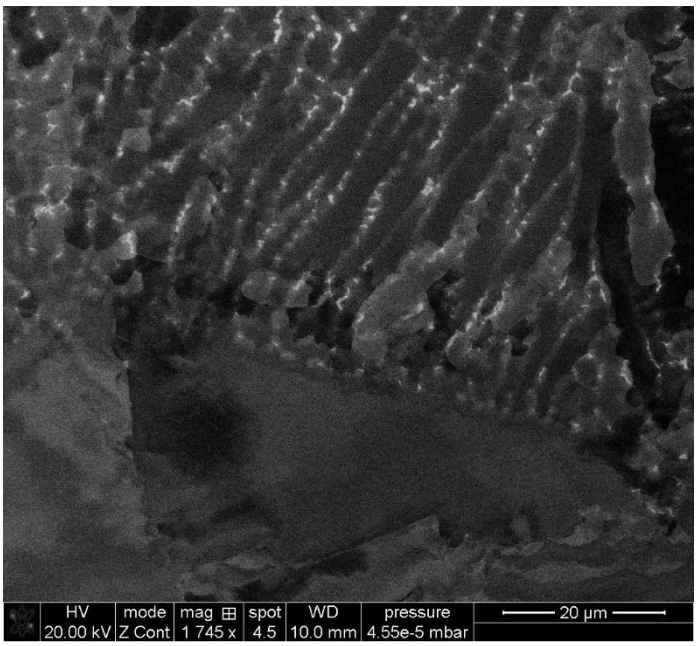

Figure 4.24 Interface region of single-clad track deposited using 550W.

During the deposition process, the sequential between extreme heating and rapid cooling rates experienced at the interface region can introduce expansion and contraction of the surface material. As a result, cracks, warp, and delamination can occur across the interface region when the thermal-induced transient and residual stresses lead to excessive plastic deformation. Under closer examination, the interface between single clad track and the substrate did not present any evidence of warping, cracks, microcracks, swelling or delamination which could have been generated from thermal-induced stress.

The substrate displayed high volumes of primary carbides which form during solidification. At 1280°C, as the temperature drops, the carbon concentration in the remaining liquid increases, surpassing the solubility product of NbC and initiating the precipitation of NbC [301]. The fusion zone obtained very minimal to no presence of these precipitates. The appearance of carbides (depicted as yellow square-like formations, as shown in Figure 4.25) within the melt pool area of the initial layer suggests significant metallurgical blending between the substrate and the deposited material. This occurs when carbides from the substrate migrate into the melt pool, facilitated by the turbulent convective fluid dynamics generated during the formation of the melt pool. These flows enable the movement of carbide precipitates within the cross-sectional area of the melt pool.

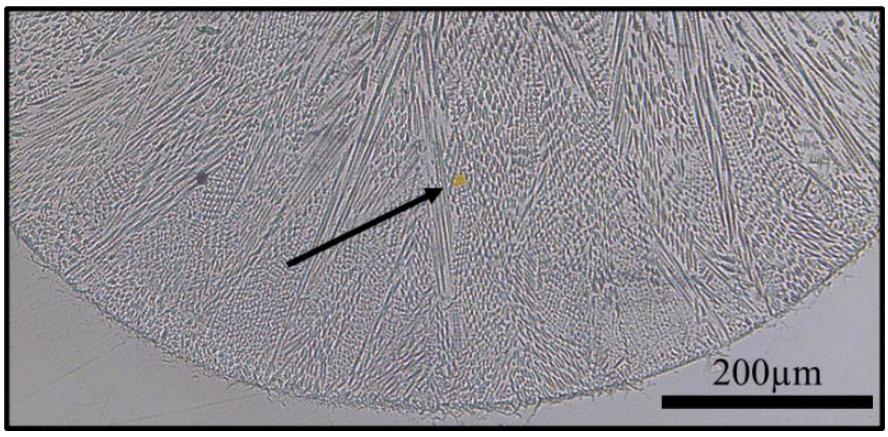

Figure 4.25 (a) Single track cross sections for 750W laser power showing the presence of primary carbide phases present at the liquid-solid interface.

In conclusion, the chosen process parameters meet the fusion welding standards outlined by both the American Welding Society and ISO BS EN for IN718 deposition. Single welds exhibited complete fusion with laser powers adequately penetrating to form a melt pool. Optical and SEM inspections revealed no defects along the interface. The 950W sample, with the lowest dilution, proved most suitable in this case, minimizing excessive mixing of substrate and deposited material. Conversely, the 750 W sample exhibited no porosity in three examined locations. Nevertheless, in both specimens, the melt pool profile exhibited an anomaly where the middle portion displayed atypical penetration behaviour. The 550 W sample exhibited excellent melt pool profile with a conduction melting regime but excessive dilution. Nevertheless, all single clad tracks meet the welding quality criteria and now, the focus is shifted to the fabricated thin-walled samples and solid blocks to gain a comprehensive understanding of the thermal history.

4.8.3 Interface Assessment and Fabrication Imperfections using Thin-walled depositions (Stage II).

The objective of these 5 and 10-layer deposits is to comprehend short dwell times and continuous cyclic thermal exposure with layer addition on the interface microstructure and crystallographic texture. The continuous heat input from successive layers initially expanded the melt pool, successfully fusing blown powder to it (Figure 4.26). Short intervals between layers facilitate comparisons of shortened cooling time and evolution of crystallographic features. Furthermore, as the surface deviated from the nominal planar geometry and displayed a wavy rough surface finish, there were evidence of inconsistent powder delivery and warp induced by thermal gradients [302].

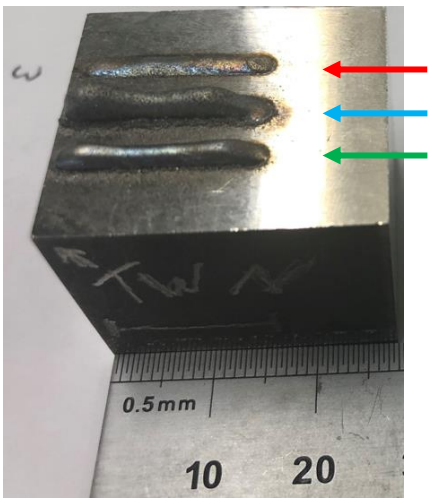

Figure 4.26 Thin-walled samples fabricated using P=750W (N.b the red arrow represents a single track, the green arrow represents 5-layers, and the blue arrow represents 10-layers.

The growth of the multiple piled track deposition was uncontrollable, showing strong deterioration due to the presence of powder particles stuck along both melt clad surface and track borders. This instability resulted from high powder feed in a minimized melt pool region and continued subsequent laser power. Such track deterioration becomes critical in successive depositions, impeding constant laser/substrate interaction and leading to issues like porosity, lack of fusion, and unstable melt pool formation. Given the implications for build quality, the interface metallurgical bond will be assessed for potential adjustments to machine configurations. Figure 4.27 details the interface region for the successive 5- and 10-layer deposition with Figure 4.28 revealing a higher magnification inspection of the metallurgical bond across the interface which remained defect-free with no prevalent sign of lack of fusion or pores across this region.

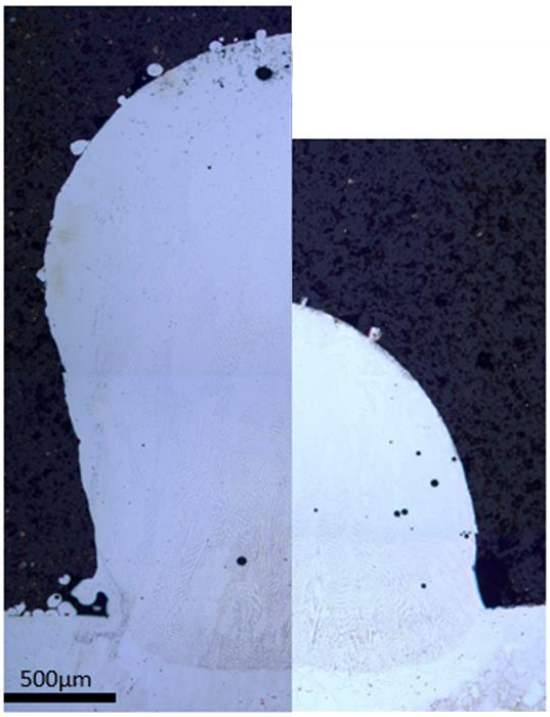

Figure 4.27 Optical microscopy for the thin-walled deposits using 750W power for 10 layers (left) and 5 layers (right).

Although the subsequent builds deteriorated, the concept of developing a strong metallurgical bond at the interface remained. Figure 4.27 and Figure 4.28 act as evidence for the development of thin-walled builds, showing that the region of interest remains stable with strong laser/substrate interaction and formation of joint layer. An optimization study for thin-walled samples would be essential to produce homogenous layers.

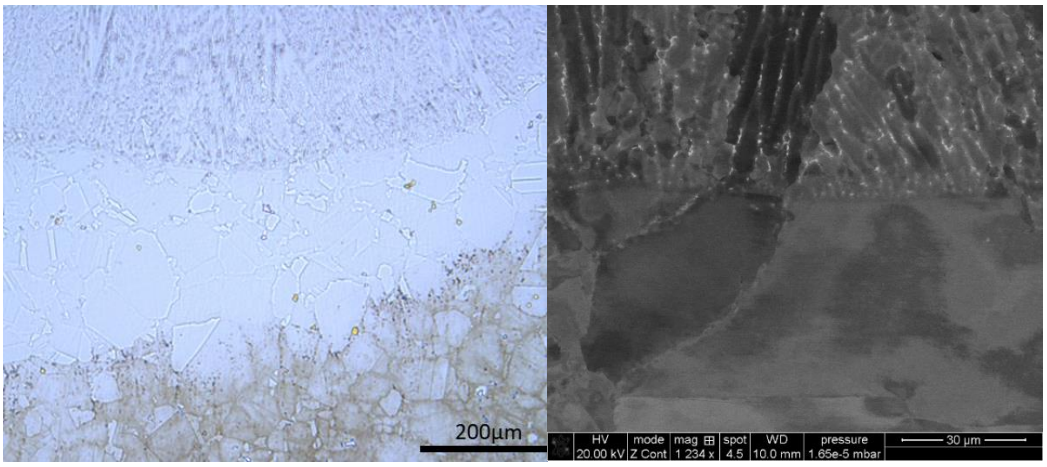

Figure 4.28 Closer inspection of the metallurgical bond for thin-walled samples using 750 W: (left) Optical micrograph of 5-layer and (right) SEM image details the bond between substrate and interface for 10-layer.

A recommendation is to implement *in situ* monitoring, utilizing an IR-camera and/or pyrometer [303], [304] to observe the melt pool size and morphology. Subsequent adjustments to the powder delivery rate or laser power, such as reducing laser power or

powder delivery as layers progress, can prevent warping. Future work for this investigation involves refining the already established initial joint and tailoring the Laser Metal Deposition (LMD) process configurations to enhance build quality.

4.8.4 Interface Assessment and Fabrication Imperfections using Solid-Block Depositions (Stage III)

The selection of process parameters prioritized the overall mechanical performance of the full build; therefore, defect-free solid blocks would be advantageous. However, the primary focus of this investigation is to ascertain the influence of process parameters on the joint layer region. Consequently, the assessment of build quality above the interface region lies beyond the scope of this project. The investigation will delve into the thermal response concerning microstructure, texture formation, and residual stress across the interface region as laser power varies from low to high. Recommendations will be provided as conclusive remarks. Figure 4.29 depicts an optical micrograph of the full build (*10 layers of 10 adjacent tracks*) cross-section fabricated using a higher laser power (P= 950 W), highlighting the presence of defects, primarily in the form of pores.

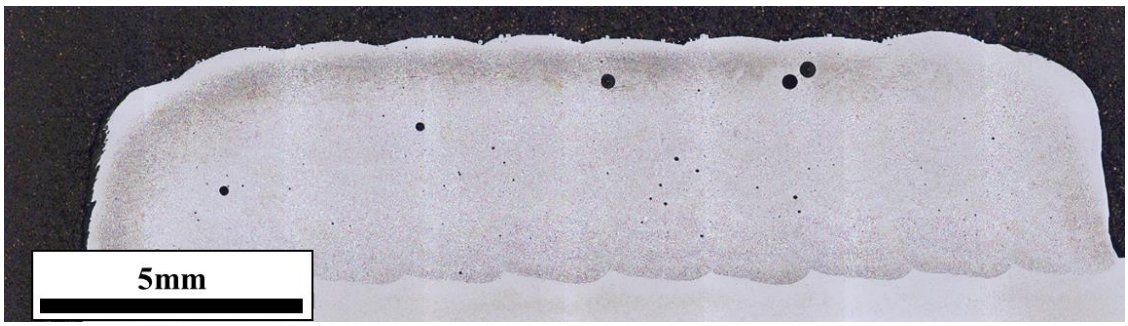

Figure 4.29 Cross section of high laser power (P=950W) full solid block made by stitching multiple optical micrographs together.

Tracks 1 to 10 were deposited from left to right which include some large defects within the build. Pores of 160-280 µm in size with spherical shape are located at the starting point of the deposition process, at the edges of the melt pool and towards the top of the build. These large pores were detected at one location/cross-section, but smaller pores were observed throughout the cross-section indicating that larger pores may be present at the interface, middle, or right end of the blocks at a different location. Porosities existed as both interlayer and intralayer porosity. Pores located at the melt pool edge between adjacent tracks occur in case of inadequate fusion or incomplete deposition of the material during the LMD process. This defect can be the result of insufficient heat input related to poor process parameter selection. Intralayer porosity is linked with the use of inert shielding gas deposited during LMD which promotes gas entrapment. These pores are

usually spherical in shape, occurring at random locations throughout the build within regions of lower solidification rates, i.e., top of the build owing to vaporization which leads to gas trapped porosities, though smaller pores distributed throughout the build, and a large pore was even present at mid-height of the second track in Figure 4.29.

Although high amounts of pores were found within the built component, when analysing the interface by optical microscopy there were no other obvious defects, i.e., lack-of-fusion, or thermal cracking caused by the extreme thermal gradient difference. Repair applications designed for high stress applications should be fully dense and defect-free to optimise mechanical performance and minimise part failure during service. Although the main scope of this work was to investigate the interface region, it is worthwhile to note that the presence of such pores is undesirable and requires further investigation and process control systems to optimize parameters for reducing porosity or additional manufacturing steps such as hot isostatic pressing which has been a successful way to improve mechanical properties by pore closure [305], [306] Moreover, the entrapment of smaller porosities (<10 μm) could be introduced by internal porosity included in the raw material powder being deposited. Non-uniform size distribution of the powder will give rise to more porosity in the final build, which to a certain extend is the case for the used powder.

Nevertheless, the successful deposition trial achieving the target build geometry and metallurgical bonding under high laser power (950 W) acted as incentive to further optimization of the process by keeping a low overlap fraction. A 10% overlap fraction in all three process parameters significantly reduced the volume of powder and energy consumption during fabrication, resulting in minimized excess powder waste compared to higher overlap fractions ranging from 30-50% [75], [307], [308] or even up to 70% [309]. This reduction in laser power and maintaining the overlap fraction as low as practically possible was aiming to greatly reduce environmental impact and improve sustainability by increasing powder utilisation, reducing energy consumption, and hence reducing cost of production and lead times. Furthermore, Mingming *et al.'s* [68] investigation demonstrated that higher overlap fractions led to the formation of an increased size and volume of the detrimental Laves phase in interdendritic boundaries, resulting in brittle, Nb-rich areas that exacerbate the opportunity for the formation of precipitated phases of γ''/γ'. Unfortunately, inadequate overlap of adjacent tracks, as depicted in Figure 4.30, resulted in lack of fusion in both mid and low laser power scenarios.

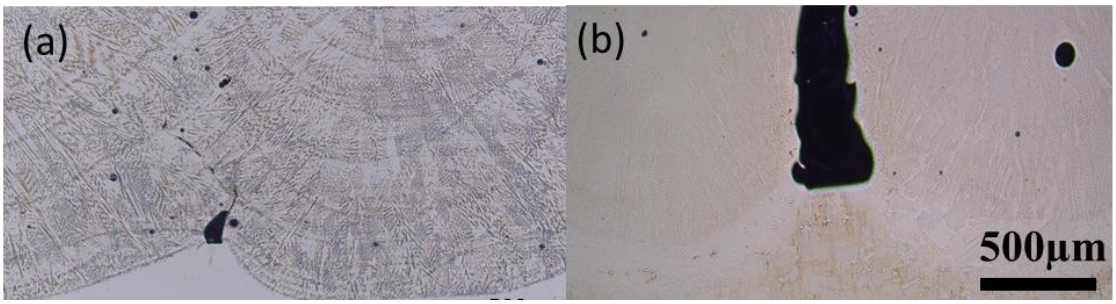

Figure 4.30 Lack of fusion between adjacent tracks for (a) 750W and (b) 550W.

Upon further investigation, the lack of fusion between adjacent tracks measured <100 µm and ≅ 200 µm, for the 750 W and 550 W, respectively. In the 750 W specimen (Figure 4.30(a)), the lack of overlap was obliterated in the following successive layers and were only present in the initial first 3 layers. This could be a result of the melt pool flow behaviour of material and could be classed as forming consolidated builds with minor process alteration. In the 550 W specimen (Figure 4.30(b)), the lack of fusion was progressively worse from the interface towards the top of the build due to wrong overlap calculation/setting in the machine. Nevertheless, the microstructural evolution and temperature evaluation will be focused on the interface from the substrate zone to the fusion zone with emphasis on the centre of the melt pool where complete fusion occurs.

This lack of fusion defects occurred in the multi-track, multi-layer clad samples due to the process parameters, i.e. overlap were not sufficient to produce a solid component. With respect to remanufacturing and repair treatments, these build defects would be detrimental to mechanical properties and would inevitably lead to rejection of the work, indication that manufacturing parameters were not optimized successfully as opposed to the actual cladding parameters. However, as the interface region remains the focal interest for the project, no microcracks, pores or delamination occurred. Characterising the evolution of microstructure and residual stresses across the interface region will provide valuable information on the influence of laser power in interface properties and characteristics.

4.9 Chapter Summary

LMD IN718 demonstrates commendable processability, exhibiting a notable absence of detrimental failures in the interface regions. This investigation is centred on analysing the temperature history experienced by the interface region throughout the deposition process, utilizing a diverse set of process parameters. Employing material and machine parameters derived from existing literature, various interfaces were successfully

deposited for both single, thin-walled, and solid block components using low, medium, and high laser parameters. The main findings from this chapter are:

1. The analytical model demonstrated the effect of varying laser power on melt pool formation. The dimensions of the melt pool with respect to melt pool area was in good agreement with experimentally measured values and the depth of the 950W and 750 W was predicted within 11% of the experimental results. However, due to limitations of the Rosenthal solution, there were extensive under predictions of the width of the melt pool in each laser power. Although, the trend of decreasing laser power resulting in a narrower melt pool with less penetration was captured well. The analytical solution can be implemented as a quick, inexpensive guide to understand melt pool formation with respect to laser power.
2. In each specified condition, the melt pool consistently met the required standards for metallurgical bonding and welding, avoiding the generation of solidification defects along the joint layer. However, it is noteworthy that the resultant solidification defects in subsequent builds demand further optimization and additional manufacturing steps, which fall beyond the purview of this project.
3. Given the successful intermixing of substrate and deposited material without the occurrence of macro and micro defects in the interface region across all three process conditions, a comprehensive investigation into microstructural evolution based on thermal response is imperative.
4. Cross-sections of the entire builds presented defects observed throughout the build in the form of interlayer and intralayer defects. However, the interface region remains the focal interest for the project, no microcracks, pores or delamination were observed.
5. While instances of lack of fusion were observed between adjacent tracks in the medium laser power setting, the overlap in subsequent layers proved adequate for successful fabrication. Conversely, the lower laser power setting consistently exhibited lack of fusion between adjacent tracks. To address this, a recommended increase in overlap by 5-10% would suffice to achieve metallurgical bonding.

Chapter 5: Thermal Modelling of the LMD repaired application: Modelling and Validation Techniques

5.1 Introduction

An experimentally validated simulation is a powerful tool for understanding temperature history in additive manufacturing. Additively manufactured parts often exhibit complex microstructural evolutions due to cyclic thermal behaviours, a critical understanding for predicting the evolution of microstructure is essential. Experimental characterization of such thermal profiles is costly and challenging due to equipment limitations. In this study, 3D thermal models for laser-based deposition were developed. The thermal model was validated experimentally using thermocouples and metallography. The validated model aids in correlating process parameters with temperature development, is cost efficient when compared to experimental trials. Models were created using MSC software Simufact Welding 8.0 with slight variations for laser powers to accurately predict complex temperature profiles.

5.2 Modelling Approach

The deposition process was modelled using the "quiet-element technique", to simulate the molten powder addition by activating elements transiently based on moving heat source location. In this method, the first steps include the thermal and mechanical properties of the a-priori deposit geometry being significantly scaled down by a factor making all material properties negligible (quiet state). As the propagating heat source aligns with the elements constituting the deposition process, they are activated in a step-by-step approach via element-birth formulation. This technique, as described in the literature review, involves two steps: the virtual bounding box surrounding the heat source geometry activates the quiet elements and nodes thermally once inside activation box. As the nodal temperature reaches the melt point, the mechanical properties are scaled up to full stiffness.

The basic principle in this technique requires the filler elements to have an extremely low thermal conductivity and as these elements experience a significant increase in temperature from a direct external power source, their material properties are restored. Implementing this technique involves the following computation [310]:

Equation 5.1

$$P(T) = \gamma(T_{max})P_{act}(T) + (1 - \gamma(T))P_{quiet}$$

Where P_{act} and P_{quie} represent generic material property in active and quiet state respectively, γ is the activation function depending on T_{max} that is the maximum temperature experienced by the element from the start to the current simulation time. An activation function transition is dependent on a temperature range, rather than a specific temperature value to avoid simulation convergence issue. The activation starts and end temperatures are set to the material liquidus and solidus temperature, respectively.

The Direct Energy Deposition modelling approach is slightly different to the conventional approach as previously explained, all elements except the first element set are deactivated at the beginning of the simulation (deactivated elements are no longer part of the matrix solution). As the second layer begins to deposit, the next element set is switched from deactivated to quiet state and then calculated, using a hybrid approach.

5.3 Thermal Modelling Equations

Conservation of energy is key in thermal analysis for deposition. In this context, stress, strain, and displacement are disregarded, focusing solely on energy. Heat transfer in DED involves convection, conduction, and radiation, depicted in Figure 5.1. Energy from the laser is absorbed, lost through melting and various forms of heat transfer, with a minor heat gain from solidification's latent heat. The simplified energy transfer process is outlined below:

Equation 5.2

$$Q_{stored} = Q_{supplied} - Q_{conduction} - Q_{\ convection} - Q_{\ radiation} \pm Q_{latent}$$

Where the Q_{stored} is stored energy in the material expressed as:

Equation 5.3

$$Q_{stored} = \rho C_p v_s \frac{\delta T}{\delta t}$$

Where ρ is the density of material (kg/m^3), C_p is specific heat capacity (J/g°C), v_s is volume of deposit sample (m^3), T is the current temperature (K) and t is time (s).

The energy directed into the melt pool varies based on factors like the additive process, work envelope, substrate, and feedstock. $Q_{supplied}$ represents energy supplied to the deposition surface, calculated as the product of laser power (P), laser efficiency (e), absorption rate (γ), and melt catchment efficiency (β). Accounting for incident energy losses during deposition, the actual energy reaching the melt pool is computed as:

Equation 5.4

$$Q_{supplied} = \eta . P, \text{ where } \eta = e.\gamma.\beta$$

The energy lost via conduction can be written as:

Equation 5.5

$$Q_{conduction} = \lambda v_s \nabla^2 T, \qquad where\ \nabla^2 = \left(\frac{\partial^2}{\partial x^2}\right) + \lambda_y \left(\frac{\partial^2}{\partial y^2}\right) + \lambda_z \left(\frac{\partial^2}{\partial z^2}\right)$$

Where λ (W m^{-1} K^{-1}) is thermal conductivity of the material.

During the welding process, boundary conditions are defined as heat exchange between substrate, molten pool and surrounding environments which includes heat contact conduction between supporting fixed clamp fixtures and substrate, convection between air and build envelope and liquid in the melt pool, as well as radiation from build envelope and melt pool to surrounding ambient atmosphere. Heat losses are imperative to the accuracy of the model and will be applied during the welding process, therefore heat loss due to convection of the weld plate and air in Eq5.6. The convection and radiation formulas can be written as [311], [312]:

Equation 5.6

$$Q_{convection} = -h_c A_0 (T_s - T_\infty)$$

and

Equation 5.7

$$Q_{Radiation} = \varepsilon \sigma A_0 (T^4 - T_\infty^4)$$

where h_c is the convection coefficient, A_0 is the heat transfer area, T_s is the current temperature of molten pool, T∞ is ambient temperature, ε is emissivity of the material, σ is Stephen-Boltzmann constant ($5.67\ x10^{-8}\ \frac{W}{m^2.K^4}$) and therefore the above equations can be written as:

Equation 5.8

$$\rho c v_s \left(\frac{\partial T}{\partial t}\right) = \eta . \gamma . P - \lambda v_s \nabla^2 - hA_0 (T - T_\infty) - \varepsilon \sigma A_0 (T^4 - T_\infty^4) \pm Q_{latent}$$

Defining the interaction between laser energy supplied and surface area of the material, (denoted as laser spot diameter, Γ), the heat flux is calculated. Hence, the total energy supplied per element can be distinguished as:

Equation 5.9

$$Q_{flux} = \eta \; x \; P/\Gamma$$

Therefore, the boundary condition for the top surface elements where the deposition is carried out can be given as:

Equation 5.10

$$Q_{flux} = \lambda v_s \nabla^2 T + hA_0(T - T_\infty) + \varepsilon\sigma A_0(T^4 - T_\infty^4) \pm Q_{latent}$$

And for the other surface elements where the only heat loss conditions are via conduction, convection, and radiation:

Equation 5.11

$$\lambda v_s \nabla^2 T + hA_0(T - T_\infty) + \varepsilon\sigma A_0(T^4 - T_\infty^4) = 0$$

For the initial condition, the temperature is selected as ambient temperature T_0, i.e.

Equation 5.12

$$T(x, y, z, 0) = T_0$$

Therefore, equation 5.8 can be solved using the above boundary conditions (Equations 5.9 to 5.12) to predict temperature profile.

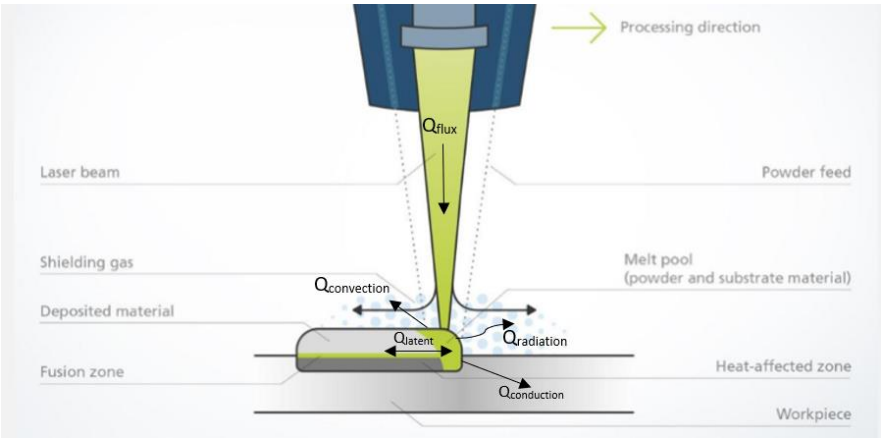

Figure 5.1 Schematic illustration of DED process to show configurations, heat input and heat losses [313].

5.4 Mesh Sensitivity Analysis

A mesh sensitivity analysis ensured thermal results' independence from mesh size, while a convergence study optimized mesh refinement for accuracy. Increased refinement raises degrees of freedom (DOF) but extends computational time. A convergence study

confirms FEA model solution convergence, justifying mesh independence and avoiding excessive refinement.

Mesh convergence utilized the single clad track experimental approach with coupled thermal history data. The model covered 50% of the substrate, measuring 14 mm (X) x 24 mm (Y) x 23.7 mm (Z), enhancing computational efficiency, disregarding unaffected elements. The substrate mesh was partitioned into zones for refinement. Zones 1, 2, and 3 represented the deposited, affected, and outer regions. Biased meshes were applied to the base plate in the Z direction (Figure 5.2)

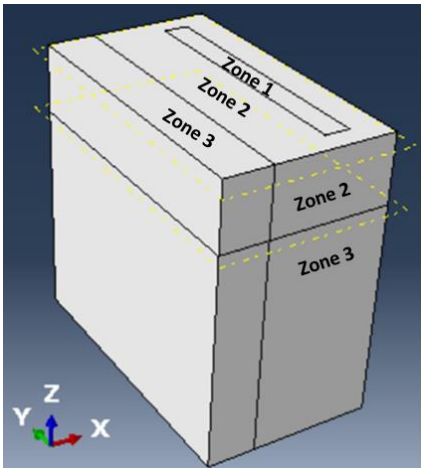

Figure 5.2 Partitioning strategy of substrate for single deposited analysis.

The elements number and therefore DOF were increased from Cases 1 to 4, with case 4 obtaining the highest number of elements at greater refinement and case 1 meeting the minimal requirements as per Simufact welding software protocol for the double ellipsoidal heat source, as seen in Figure 5.3[314]:

- 2-4 elements over the width (b)
- 3-4 elements over the length ($a_f + a_r$)
- 2-3 elements over the depth (d)

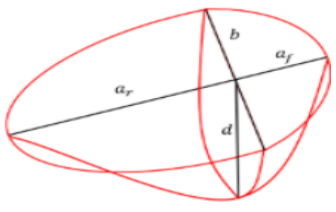

Figure 5.3 Goldak Double Ellipsoidal Heat Source [315].

The dimensions of the heat source model (width (b) and depth (d)) were extrapolated from the single track deposition in Table 4.5 and the front length (a_f) and rear length (a_r) were taken as 0.6 x (b), and 2 x (b), respectively, according to the information provided

in Simufact [314]. This ensured the laser power influence on melt pool dimensions was accurately captured and experimentally defined.

A high-quality mesh must be considered in zone 1 because the material in the fusion zone and heat affected zone will experience high temperature gradients, a denser mesh will capture the profile and a coarse mesh could lead to an inaccurate representation of the heat source shape and thermal distribution. To analyse the convergence for accuracy, the captured temperature profile variation, and the number of elements in all three coordinate directions was increased to verify mesh sensitivity study.

Linear brick elements with 8 nodes (DC3D8) were chosen for the structured mesh, while quadratic elements with 20 nodes (DC3D20) were not considered due to marginal accuracy gains and significant computational time increase [316], [317]. Mesh details are summarised in Appendix B, indicating refined zones. Computational time for a single weld pass grew with refinement; case 4 was 32 times more time-consuming than case 1. Given the complexities of multi-track, multi-layered solid block deposition, such high refinement requires substantial justification. The finest mesh (model mesh 1) was selected as the reference for its accuracy and node/DOF count.

The temperature histories were extracted from the thermal model at five different positions in the mid-section of single-track deposition. Temperature positions were selected to evaluate temperature change across X, Y and Z directions with P3 being an exact representation of Thermocouple T10 used for comparison basis. Particle placement (*data extraction point*) for extracted thermal data were P1 (24.4, 12,73, 23.7), P2 (24.4, 12.73, 21.7), P3(T10) (25.73, 12.73, 19.75), P4 (22.4, 12.73, 23.7) and P5 (20.4, 12.73, 23.7). Figure 5.4 details the schematic of particle placement with respect to the substrate top surface (Figure 5.4(a)) and cross sectional (Figure 5.4(b)). The model with the finest DC3D8 elements towards the interface region were expected to provide the most accurate reading due to containing the highest number of nodes and degrees of freedom, therefore the simulation with Mesh 4 will be used as a reference model.

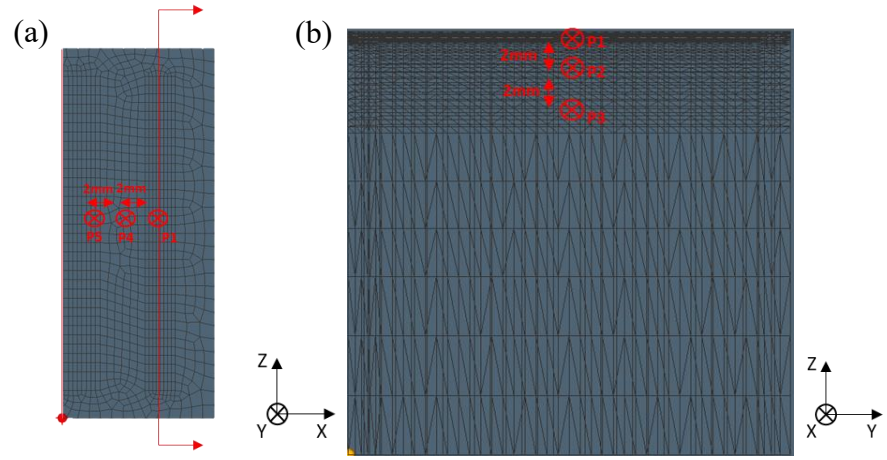

Figure 5.4 Temperature history data collection points P1-5 for (a) Top view and (b) cross-sectional view for single deposition.

Temperature histories were extracted from thermal models at P1-P5, enabling a direct correlation between accuracy and computational cost assessment. Mesh variations yielded similar peak temperatures and thermal trends, with only minor discrepancies. Figure 5.5 compares simulated temperature profiles for P3 and experimental data from T10. Accurate simulation capturing thermal history is crucial, especially in regions with extreme thermal gradients affecting microstructural response tied to peak temperature, thermal gradient, and cooling rates.

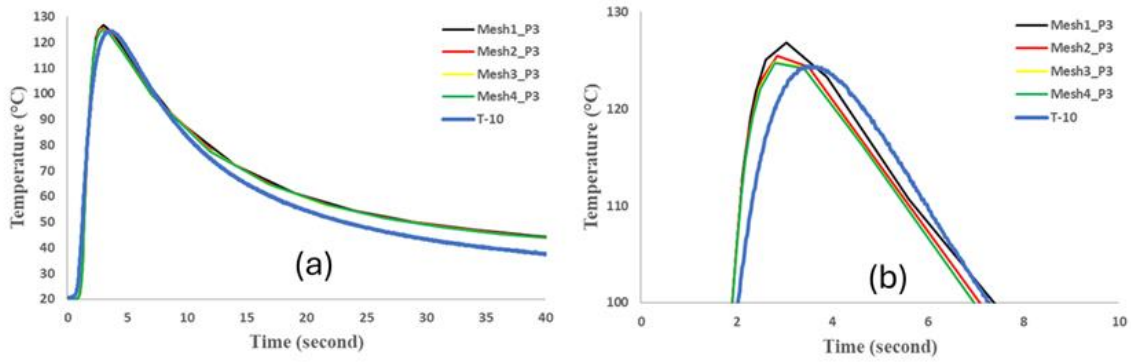

Figure 5.5 Temperature histories for case study mesh 1 to 4 for single weld analysis in for (a) Position 3 showing a direct comparison with the thermocouple (T10) and defined peak temperatures with each mesh strategy in (b).

Table 5.1 presents a comparison of peak temperatures predicted for P1-P5, including the percentage difference relative to the reference model (*mesh 4 – comprised of the highest DOF, therefore most accurate).* Additionally, P3's predicted peak temperature is compared against the experimental value (denoted as %Exp) recorded by thermocouple T10. Generally, the model with coarse 8-noded elements showed the most deviation from the reference. Nevertheless, differences were negligible compared to the reference in all cases, except for P1 where model case 1 predicted about 8% higher than the reference.

Given the significant temperature disparity in P1, where the peak temperature surpasses the melt temperature and induces plastic flow, the thermal data profoundly influences stress prediction.

Table 5.1 Comparison of predicted peak temperatures (° C)

Mesh Case	1	2	3	4	T10 (Exp)
Position 1	1705.89 *(+7.07%)*	1626.65 *(+2.10%)*	1600.78 *(+0.47%)*	1593.24 (Ref.)	
Position 2	317.15 *(+1.08%)*	314.22 *(+0.15%)*	313.5 *(-0.07%)*	313.76 (Ref.)	
Position 3	126.85 (+1.70%) *(+2.01% Exp)*	125.49 (+0.60%) *(+0.90% Exp)*	124.81 (+0.06%) *(+0.37% Exp)*	124.73 (Ref.) *(+0.31% Exp)*	124.34 *(-0.3%)*
Position 4	360.91 *(+1.78%)*	355.63 *(+0.29%)*	355.24 *(+0.18%)*	354.61 (Ref.)	
Position 5	122.48 *(+1.05%)*	121.74 *(+0.44%)*	121.20 *(0.00%)*	121.20 (Ref.)	

Table 5.2 shows the comparison of CPU time used for calculations in each model. To expedite mesh convergence study, the models considered only 50% of the substrate and a single deposited track. Comparing data in Table 5.1 and Table 5.2, the substantial computational effort for enhanced accuracy yielded only marginal improvements. For instance, the dense mesh refinement scheme in Mesh 4 had over 10 times the DOF and 15 times more elements than the coarsest linear brick elements in Mesh 1. Consequently, the former needed over 30 times the computational time for temperature history calculations. Given practicality and explicit thermal solution requirements, achieving such density (Mesh Case 4) isn't feasible despite the accuracy boost.

Table 5.2 Computational time taken for the varied mesh sensitivity study.

Mesh Type	Mesh 1 DC3D8	Mesh 2 DC3D8	Mesh 3 DC3D8	Mesh 4 DC3D8
CPU time (seconds)	313	958	4157	10200
Time factor	--	3.06	13.28	32.59

In conclusion, a practical approach for meshing large-scale thermal simulations in experimental deposition trials involves a refinement technique. Proper partitioning,

emphasizing areas with extreme thermal gradients, achieves a balanced strategy for accuracy and computational time. Considering comparisons to the reference model and experimental data, a meshing technique like Mesh Case 2 would offer a reasonable balance of accuracy and computational efficiency.

5.5 Material Properties

To improve the accuracy of the thermomechanical model, previously published literature of temperature-dependent thermal and mechanical properties of IN718 were used in this model. The thermo-physical properties were taken from literature and are tabulated in Table 5.3 and Table 5.4.

The temperature-dependent mechanical properties were also required to analyse the stress during the deposition. The yield stress is a vital mechanical property and has significant effect on the residual stress. Thus, accurate temperature-dependent yield stress data must be used (Figure 5.6). The thermal expansion coefficient of the material with temperature and yield stress were taken from the experimental and modelling results from a heat-treated IN718 quench trial by Dye *et al.* [318] and Denlinger *et al.* [319].

Table 5.3 Thermal model material and process properties aiding model calibration.

Thermal Property	Units	Value	Reference
Latent Heat of fusion	(kJ/Kg)	227	[310]
Latent Heat of vaporization	(kJ/Kg)	6400	[320]
Solidus Temperature	(°C)	1260	[321]
Liquidus Temperature	(°C)	1336.11	[321]
Laser efficiency	%	0.35-0.45	[316]

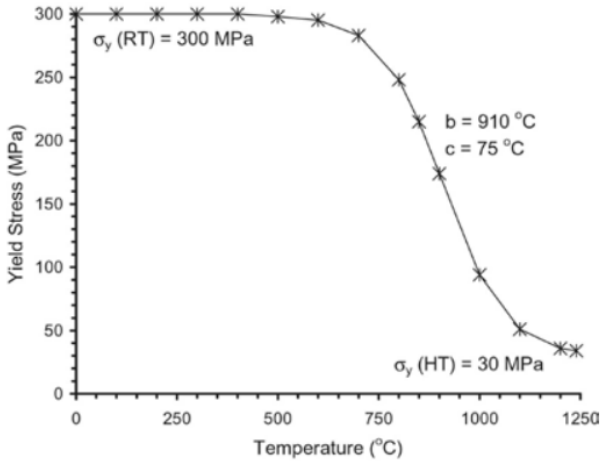

Figure 5.6 Variation in yield stress used for heat treated IN718 from Dye [318].

Table 5.4 Temperature dependent density, heat capacity and thermal conductivity of IN718 (*denoting the melting temperature)

Temperature (°C)	Density (kgm^{-3})	Specific Heat Capacity ($Cp:JK^{-1}Kg^{-1}$)	Thermal Conductivity ($\lambda:Wm^{-1}K^{-1}$)	Mean Thermal Expansion Coefficient α (10^{-6})	Young's Modulus E (GPa)
0	8226	424	11.02	12.8	197
100	8190	434	12.75	13.1	197
200	8160	448	14.36	13.4	197
300	8130	463	15.96	13.8	197
400	8090	480	17.6	14.2	197
500	8050	500	19.18	14.5	196
600	8010	525	20.77	15.1	194
700	7960	560	22.36	15.7	187
800	7910	605	23.95	16.4	165
850	7890	625	24.53	16.8	145
900	7860	636	25.1	17.1	130
1000	7810	645	26.83	17.5	115
1100	7810	650	28.56	17.8	105
1200	7810	650	30.5	18.1	95
1250	7727	720	31	18.3	90
1500	7250	720	31	15	90

5.6 Geometry, mesh, boundary conditions and key assumptions.

5.6.1 Thermal model

The thermal model was developed and validated using experimental thermal measurements from internally placed thermocouples, as detailed in the methodology. A single clad track, measuring 2 mm, 1.8 mm, and 1.4 mm in width (x direction) for high, medium, and low laser powers respectively, was created. This track spanned a total length of 21 mm (Y direction). A dwell time of 48 s was applied to ensure the substrate cooled to near-ambient temperature. Following this, a ten-layered, ten-track solid block, each layer approximately 0.3 mm thick, was deposited on a substrate measuring 25 mm x 28 mm x 23.7 mm (XYZ dimensions). The transient 3D model utilized DC3D8 elements and

was seeded and meshed in ABAQUS before being converted from .inp to .bdf format using a Matlab script for import into Simufact.

A mesh refinement strategy was based on the mesh sensitivity analysis and Mesh 2 approach was selected. The elements in the substrate were refined towards the interface region in the Z direction due to contact area between the elements activated during the deposition process, the heat source interaction and localised change in temperature. These were refined to 0.05 mm up to 1 mm below the top surface of the substrate, increasing to 0.38 mm for the next 5 mm below the surface and finally coarsened towards the clamping end to 2.5 mm to reduce computational time.

During the experimental process, there was an overlap of 10% between the adjacent passes, these were calculated in the trajectory files and implemented during the thermal model meaning elements in between neighbouring passes were firstly activated then partially reheated during the neighbouring pass. This type of consideration is usually ignored in other simulations [119] but more accurately simulates the deposit thermal history. The width, length and height of each element were calculated by using the minimum requirement as per stated in Simufact meshing info sheet to accurately represent the heat source. The deposition of the solid block was divided into 72 elements in the X direction (TD), 30 elements in Y (ND) direction and 20 elements in the Z direction (BD). A total of 43200 elements were used for the solid block deposition and 720 for the single clad track. The substrate involved more intricate partitioning and meshing due to the contact interaction between the moving heat source across the substrate surface. The substrate contained 134879 hex elements. The meshing technique employed is highlighted in Figure 5.7.

The substrate was fixed into position by steel clamps measuring the full width of the substrate and height measured during the experimental stage, the supportive plates in the experiments were eliminated from the simulation as negligible effect results. At the clamped boundaries and at the lower surface, the substrate was held by steel clamps. For these contacts, a higher heat loss is modelled through an expression like Equation 5.6. A convective boundary condition is required to model the heat loss between the CNC table and the substrate due to the heat sink effect. This value is often higher than natural convection and radiation, based on trial and error to model the higher rate of energy exchange between the substrate and the clamp fixtures. The convective heat transfer coefficient is replaced by a contact heat transfer coefficient α with a value of between

500-1200 W m^{-1} K^{-1} to simulate strong heat flow into the metallic clamping fixtures [221], [322].

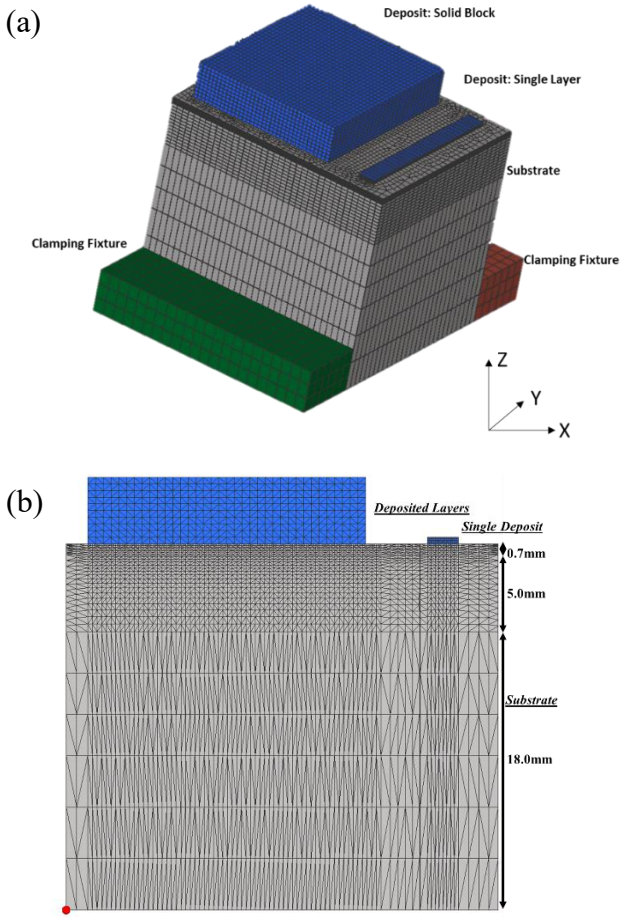

Figure 5.7 Meshing of the thermal model for the single layer and solid block deposition showing the deposit, substrate and clamping fixtures (a) with an accompanied cross sectional view to detail the mesh refinement strategy (b).

The energy (Q) simulated as the double ellipsoidal heat source was calculated using:

Equation 5.13

$$Q_{flux} = \frac{\eta x P}{A * S_F}$$

Where, Q_{flux} is the heat flux, A is the top surface area of the element, where it is obtained by multiplying the element size in X and Y directions. The number of elements to be activated in each direction are defined by the minimum number of nodes per element inside the heat source distance. A scaling factor (S_F) or search distance factor allows the actual dimension of the heat source to be scaled up or down during the search process where '1' means exactly the heat source dimension utilised. Increase in the value, increases the search range in the radial and depth direction. P is the laser power used in

the deposition process (varied from 550 W-950 W), and η is the efficiency of the laser process.

The totalling modelling process can be divided into the following stages:

Stage 1: The temperature of all the elements in the substrate and deposit are 25°C and all elements which are created as sets are initially deactivated using the scaling factor.

Stage 2: Start of the deposition, activating elements sequentially along the path. Heat from the moving source triggers depth-wise activation of elements meeting conditions (exceeding solidus temperature of 1260°C, at least 8 nodes) for time dt as per scan speed. Elements lose heat via conduction, with outermost substrate elements experiencing convection and radiation losses. Contact with clamping fixtures leads to added heat loss through convection.

Stage 3: Element activation continues until all elements in the deposited geometry are activated based on each trajectory path.

Stage 4: The part begins to cool via conduction, contact conduction, convection, and radiation to room temperature.

The convection coefficients values were experimentally calculated by the Inverse heat transfer method. These determine coefficient values increasing from a fixed value during the cooling process from high temperatures. The values were temperature dependent and applied during both deposition and cooling. Forced convection coefficients associate with the Ar gas blown into the melt pool while carrying the powder and providing localised shielding were not considered in the model.

Another challenging value to capture experimentally and subsequently model is the laser process efficiency. Various factors complicate the assessment of total attenuation efficiency due to the laser beam's interaction with the powder. These factors include localized reflections from both powder and substrate, along with energy absorbed by excess powder that doesn't contribute to the build. In the experimental approach, laser beam efficiency was measured and calibrated using a solid-state laser power measuring tool called a "primes cube." Figure 5.8 illustrates the stability of laser power, ensuring an

efficiency exceeding 80% before considering other counterproductive interactions. Further details on laser power calibration are available in the appendices.

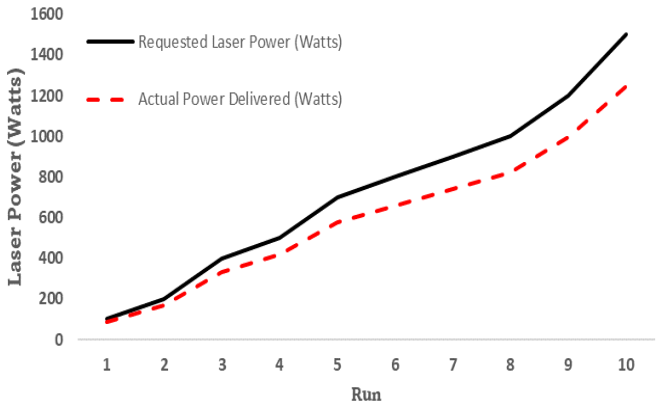

Figure 5.8 Laser power efficiency experimentally captured by power cube prior to experimental trials.

5.6.2 Radiation Emissivity (ε)

For radiation losses, the emissivity of IN718 was taken from the ranged published values between 0.4-0.8 [119] [323], [324], therefore 0.5 was selected. The emissivity of most materials is a function of surface condition, temperature, and wavelength of measurement.

The impact of radiation is more pronounced at elevated temperatures (near the weld), while it becomes negligible at lower temperatures (further from the weld). However, for a more precise estimation of heat loss due to radiation at the critical interface, where radiation losses play a crucial role but are challenging to measure directly, the temperature history was interpolated at T10 (the midpoint of a single weld track). The outcomes of various radiation coefficients are presented in Figure 5.9. These coefficients were maintained within the previously established range in existing literature.

Despite minor disparities in temperature measurements at this specific position (approximately 4.1 mm from the interface), the temperature profiles exhibit a remarkable alignment. Optimal agreement is achieved when a radiation emissivity (ε) of 0.6 is chosen.

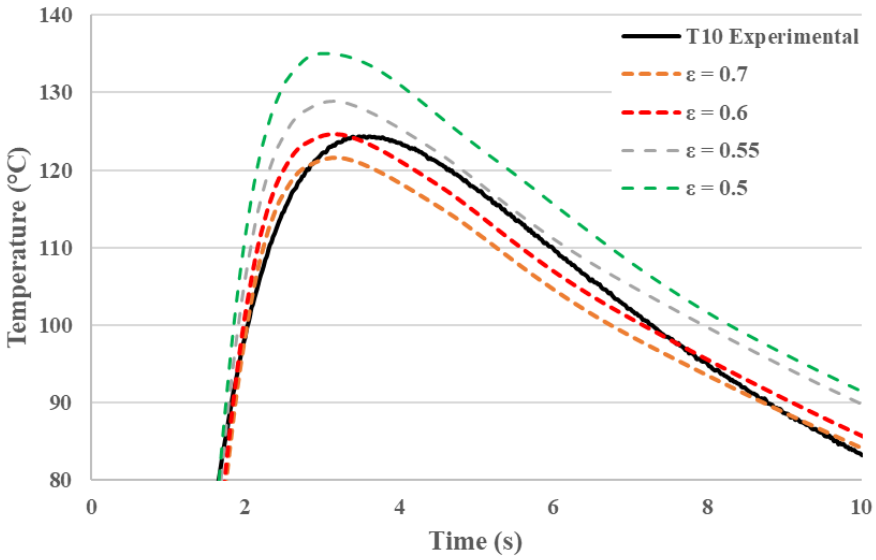

Figure 5.9 Radiation coefficient calculated from single track analysis.

5.6.3 Process efficiency calibration (η)

Laser efficiency significantly impacts melt pool dimensions, causing varied temporal patterns and deeper penetration as it increases. The numerical model is calibrated via inverse simulation to deduce unknown efficiency and emissivity values that yield the least percentage error when compared to *in situ* thermal history, as detailed by Denlinger *et al.* [130], [325], [326]. Efficiency calculation involved incremental 2% raises (20-45%). Comparative analysis against TC-10 (*located under single track deposition mid-length*) revealed optimal match at 29.5% efficiency (Figure 5.10). Factors for low efficiency include energy interplay, reflectivity, and laser attenuation by the powder stream, influencing localized behaviour.

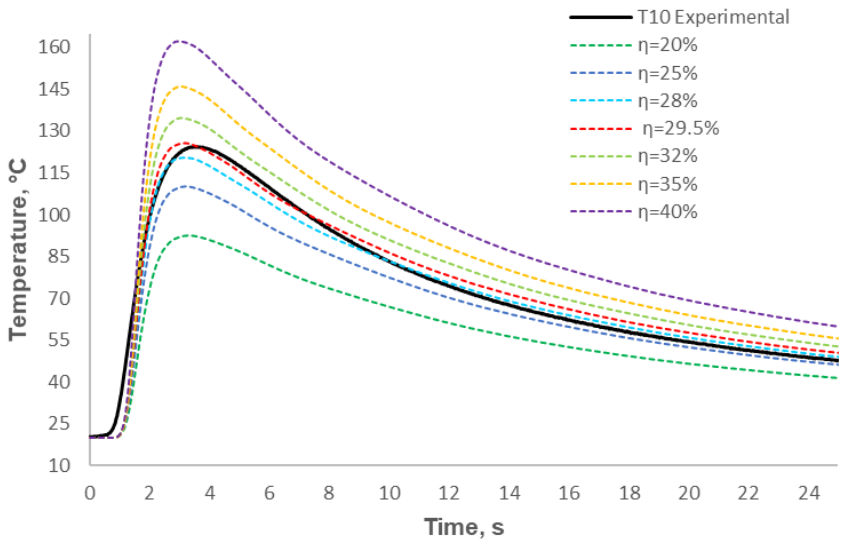

Figure 5.10 T-10 Temperature profile during the single laser track deposition, located mid-way along the track. A selection of various efficiencies effect on the temperature profile.

Laser metal deposition involves three key dimensionless system efficiencies: energy transfer, melting, and deposition efficiency, determining overall process effectiveness. Energy transfer efficiency reflects absorbed energy by the workpiece to incident laser energy ratio. Melting efficiency quantifies energy used for forming a molten weld pool from delivered and absorbed energy. Deposition efficiency measures actual deposition rate to total powder mass flow rate. Factors like laser power, scanning speed, and powder feed rate significantly influence these efficiencies. Understanding absorption, melt, and deposition efficiencies is crucial for assessing laser metal deposition effectiveness, with faster scanning speeds and increased laser power enhancing melt efficiency.

A summative review of lasers in additive manufacturing by Lee *et al.* [327] stated that Yb-doped fibre laser obtains high quantum efficiency (around 94%) which agrees well with the calibration carried out prior the deposition in this project. However, in addition to a few limitations encountered when unexpected polarization change caused by fibre bending, vibration and temperature variation, alongside deposition and melting efficiency, the process efficiency is deemed to be 10-30%, agreeing well with efficiencies in this project [327]. Furthermore, Pinkerton and Li [168] proposed an energy distribution model for 316L stainless steel deposition using an 800W Nd:YAG laser. Findings showed that about 54% of laser power was reflected by the substrate, 30% absorbed by the substrate, 11% reflected by the powder, 4% lost due to dispersed powder, and only 1% attributed to deposited powder. While this project doesn't cover interactions between direct diode lasers and powder streams in direct energy deposition, the study underscores the significance of powder trajectories and retention time within the beam in relation to absorption phenomena.

5.6.4 Key Assumptions

Several key assumptions are made to manage the complexity of the process and enhance computational efficiency. These assumptions apply to the numerical model i.e. both thermal and thermomechanical model:

- The part created is situated in a 3D space and its shape is cuboidal and continuous
- Each track is deposited as continuous cuboidal hex-elements
- Radiation, convection and contact convection boundary conditions are all considered. Forced convection from the shielding gas is not considered (discussed in section 5.6.5).

- The density, specific heat capacity, thermal conductivity, mean thermal expansion coefficient, young's modulus and yield strength material properties are temperature dependant. All other material properties used are constant and not temperature dependant.
- Material vaporization is not considered, as it's negligible in the process.
- Latent heat of fusion is considered
- An element-by-element activation was used assume material addition, ignoring finer details like melt pool dynamics
- A Gaussian distribution model with overall process efficiency is used, ignoring complexities like beam-material interaction, reflection etc.
- The de-coupled thermal/thermomechanical model does not account for microstructural evolution of material (grain growth etc). Instead, the focus is on macroscopic thermal and mechanical properties.
- The models assume weak coupling between thermal and mechanical simulations, where the thermal model runs independently and feeds temperature data into the mechanical model, rather than a fully coupled simulation.
- The material is assumed to behave elastically below the yield point and plastically above it. The flow curves were recalculated to consider creep as discussed in section 8.9 to account for thermal softening effects.
- Anisotropic material behaviour is not considered in the deposited material.
- The material model is non-linear elastic-plastic with isotropic strain hardening law.

5.6.5 Inverse Analysis for solving heat transfer coefficient.

Some studies uniformly integrate free convection in air on all surfaces (≈ 10 W m^{-1} K^{-1}) [328], [329], [330] while others adopt higher uniform convection [331], [332] to account for gas jet-induced convection. Incorporating measured forced convection for gas jet-induced effects improved accuracy by 44% [333]. Neglecting or uniformly applying convection suits simple single-track models but causes errors in multi-layer DED models due to prolonged processing and higher temperatures. Substantial errors can arise from inaccurate convection models in such scenarios. The purpose was to determine the heat transfer as a function of surface temperature from the deposition surface of the IN718 substrate from the experimentally captured internal thermocouples. DEFORM-2D inverse analysis was selected as described to solve the heat transfer coefficient.

A method is outlined to estimate the convective heat transfer coefficient for an Inconel 718 substrate. It involves solving heat transfer characteristics for the substrate's top surface (where deposition occurs), deriving the coefficient under ambient conditions based on time and temperature. Assumptions include steady-state heat transfer at room temperature and standard air pressure. Accurate representation of convection and radiation between the solid surface and surroundings is essential. The convective heat flux is determined as the coefficient multiplied by the temperature difference. Notably, the coefficient (hc) varies and depends on flow properties, parameters, and geometry. The method employs temperature measurements taken from thermocouple tips within the material through inverse heat conduction. DEFORM software was utilized to run cooling simulations from various initial temperatures to encompass a range of heat transfer coefficients relevant to deposition conditions.

Figure 5.11(a) shows the temperature-dependent heat transfer coefficient for the IN718 substrate material using DEFORM-2D optimized solver using temperature domain. The coefficient was calculated based on each of the separate temperature cooling profiles, then optimised to run from 1200°C.

As temperature rises, the convective heat transfer coefficient tends to change non-linearly. As the laser travels, the recently solidified material will undergo a high surface heat transfer coefficient with strong heat exchange with ambient atmosphere. At lower temperatures (<500°C), a convective heat transfer coefficient of ~ 100W/m^{-1} K^{-1} was calculated. Above 500°C, saw a non-linear ramp in convection rate. This 'high' convection rate is relative to uniform ambient air convection, although it is drastically smaller compared to quenched surfaces. This temperature dependence convection coefficient could be attributed to several factors:

- Increased thermal conductivity: As the solid material increases, the thermal conductivity increases, thus indicating a more efficient heat transfer between the solid surface and the surrounding air.
- Increased temperature gradient: At higher temperatures, the temperature difference between the solid surface and surrounding air is greater. Since the heat transfer coefficient is directly proportional to temperature difference, therefore greater temperature gradient, greater heat transfer coefficient.
- Enhanced molecular energy: As the solid material is heated, the surrounding air molecules gain energy and velocity, causing an increased molecular motion and promoting better fluid flow.

- Reduced air viscosity: At the higher temperatures with the air molecules obtaining greater kinetic air energy, this causes a reduction in air viscosity. As a result, there is less resistance to fluid flow around the solid surface leading to higher heat transfer coefficient.

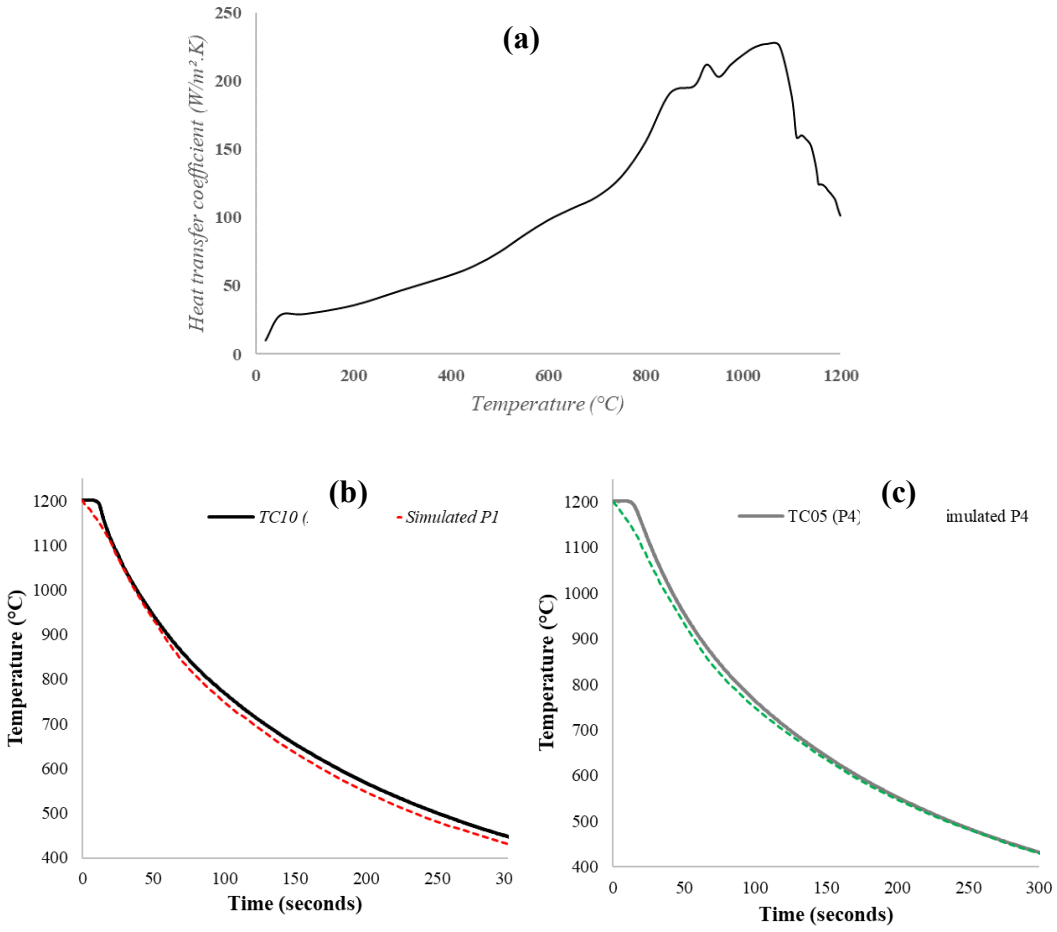

Figure 5.11 (a) Convective heat transfer coefficient results calculated for IN718 substrate block with (b) simulated temperature history cooling from 1200°C for P1 and (c) P4

Interestingly, the heat transfer coefficient does tend to increase with increasing temperature (up to around 1000-1050°C) followed by a fall with continual increasing temperature (up to 1200°C) as simulated by DEFORM. Beyond a certain point, heat transfer coefficient can be limited by other factors which come into play to reduce the HTC, i.e:

- Material properties: At higher temperatures, the material properties of the surface will begin to change as a result of degradation, oxidization, corrosion which reduces their heat transfer capabilities. High temperature oxidization and corrosion was observed experimentally by colour change and material degradation as the substrate began to cool with flakes of material ejecting during

ambient cooling. Thermal stresses generated from the high temperatures most likely lead to surface flaking and degradation.

- Radiative heat transfer: At very high temperatures, radiative heat transfer can become more significant. Although radiative heat transfer is typically less efficient than convective, at extremely high temperatures the effect could contribute to a lower HTC.

Other factors become influential when calculating heat transfer coefficient such as surface roughness, air flow conditions and the properties of the material, all of which should be considered when analysing the temperature dependence of the heat transfer coefficients but fall out with the scope of this project.

The inverse problem of heat conduction is relatively important problem. It is important in guiding significancy to improve the accuracy of the simulation model. As seen from the temperature history results from the experimentally captured data and simulated temperature history for P1 (Figure 5.11(b)) and P4 (Figure 5.11(c)) with optimised convection coefficients, the simulation temperature curve gradually fits with the experimental values and the final curve being almost exactly the same. The inverse analysis was used to simulate the heat treatment process, and the obtained simulation temperature curve had a high coincidence degree with the experimental temperature curve. In the air-cooling process, the ambient temperature remains unchanged and the DEFORM wizard can more accurately predict the HTC. As can be seen from the figure, the relative error control of experimental temperature and simulation temperature history is within 2%, indicating that the heat transfer values obtained by inverse analysis method are accurate and reliable.

Defining convective heat transfer as temperature increases is crucial due to its significant impact on heat exchange between a solid surface and its surrounding environment Understanding this variation is important for several reasons, i.e.:

- Accuracy of Thermal Models: Thermal models aim to predict temperature distribution accurately. Accurate knowledge of the convective heat transfer coefficient ensures the model's reliability, especially at elevated temperatures where convective effects become more prominent.
- Process Optimization: In various applications, such as additive manufacturing or material processing, accurate temperature control is vital for achieving desired

material properties and avoiding defects. Understanding changes in the convective heat transfer changes with temperature aids in optimizing these processes.

- Process Scaling: Processes that involve heating materials on a larger scale can experience different convective effects. Accurate knowledge of how convective heat transfer changes with temperature enables smooth scaling of processes.

In essence, understanding evolution of the convective heat transfer with temperature enhances process control and prediction of thermal modelling across a range of applications involving heat exchange between materials and their surroundings. Future work would include calculating the heat transfer convection coefficient for a moving heat source using a more advanced inverse HTC analysis for 3D problems. As calculating coefficients for a 3D moving heat source involves more complex calculations including conjugate gradient methods which fall out-with the scope of this project.

5.7 Thermal model Validation

5.7.1 Temperature Measurements

Figure 5.12 displays temperature profiles across the substrate at six locations during LMD. These spots include TC-10 (midpoint during single deposition), TC-03 (beginning of tracks 1-2), TC-11 and TC-06 (beginning and midpoint of tracks 5-6), and TC-14 and TC-02 (beginning and end of tracks 9-10 per layer). Post-deposition, thermocouple depths were remeasured to ensure traceability and alignment with simulations. Depth variations were noted due to thermocouple sheath damage, oxidation, and kinks. The single deposition's temperature reached was lower due to the substrate's initial cold state. However, as the first layer of the solid block was deposited, the substrate temperature slightly rose from the heat input. With ongoing deposits and solid block building, the substrate retained thermal energy, raising the start temperature for each layer. Moving away from the substrate and thermocouple locations, each built layer exhibited a temperature decrease. Comparing TC-14 (green) and TC-11 (yellow), slight depth variations existed, and sharper thermal gradients appeared in TC-14 due to its proximity to the laser. TC-11 collected temperature data at a lower substrate depth. By the tenth layer, the substrate experienced peak temperatures around 500°C, located 5 mm below the deposit (3 mm build height + 2 mm beneath the substrate's top surface) when the laser head was directly above the thermocouple.

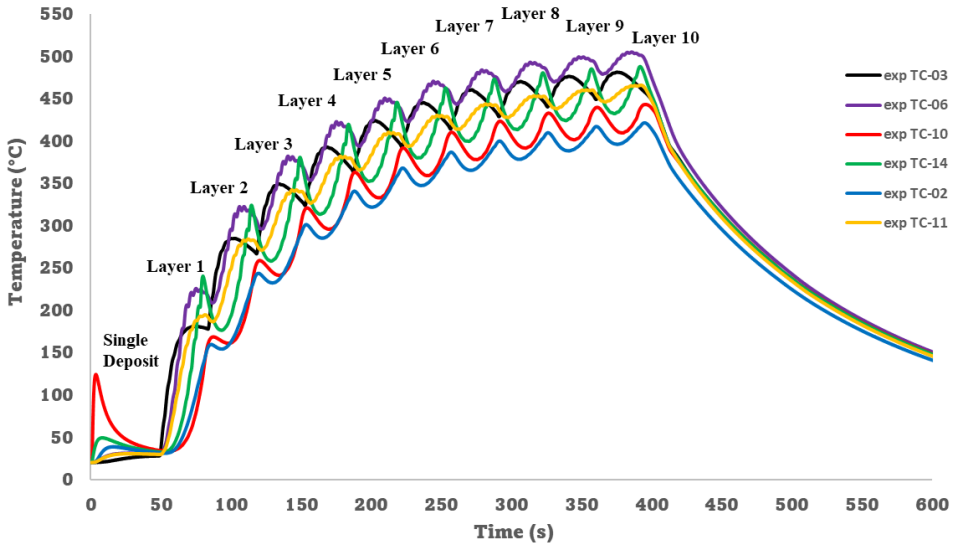

Figure 5.12 Temperature history captured at six different locations during the LMD for the single deposit and 10 layered solid block (Laser power: 950 W, scan speed: 600 mm/min, unidirectional hatch pattern)

5.7.2 Single Tracks Calibration

The temperature field calibration involved aligning the simulated weld pool shape with the experimental cross-sections obtained from polished and chemically etched weld samples. Within the finite element (FE) model, the fusion zone was defined as the region above the solidus temperature (1260°C). Figure 5.13 illustrates examples of this approach. To assess the heat-affected zone (HAZ) width, it was compared it to the white crescent band formed beneath the melt pool, which is visible in Figure 5.13 (b) and Figure 5.13(c). In the finite element analysis (FEA) model, this critical temperature was approximately 800°C, a temperature level sufficient to induce microstructural changes, such as the dissolution of strengthening phases.

While there is some apprehension surrounding the accuracy of the Finite Element Analysis (FEA) in replicating the curved geometry of deposited material, it is noteworthy that both the FEA model and the actual specimen exhibit comparable fusion zone (FZ) and heat-affected zone (HAZ) penetration depths across various laser power settings. This alignment suggests that the laser source geometry was justifiably simulated.

Figure 5.14 depict the simulation of a moving heat source in the cross-sectional y-z plane, a task that is more challenging to perform experimentally. These results show that increasing the laser power led to a larger melt pool volume, creating a larger trailing edge. At higher laser powers, it would be expected that the solidification angle, θ, would be greater across the solid-liquid interface. Such results would imply a reduction in R value

across the solid-liquid interface leading to a less elongated melt pools at higher laser powers [334].

It would be expected that an increase in laser power resulted in higher penetrative depths in the substrate, however the 550 W sample verges from this hypothesis. A potential reason for this result was that the 550W specimen was deposited after many trials on the 950 W and 750 W laser power with an increased overall process efficiency. The increase in efficiency of the Yb (ytterbium) fibre laser beam used in the LMD process may be due the beam quality improving with part counts and the mode and optics of the laser output becoming more thermally stable as the systems deposits in equilibrium. Other additional influencing factors could be that the cooling system used to control the temperature of the laser wasn't stabilized thus giving inconsistent optical properties. A spike or fluctuation in power supply could negatively influence the melt pool geometry formation. Lastly, the stand-off distance, which dictates the distance between the focal point of the laser and the substrate surface would need to be calibrated for each laser power. The overall stability of the system directly correlates to the quality of the deposited material and final product with many influential factors including the systematic factors, thermal stabilization, material properties and process parameter optimization which can introduce anomalies during the deposition and such, explain the non-nominal trend of increasing laser power with increased penetrative depth as suggested by the FEA model and literature. Figure 5.15a shows thermal history simulated at the start, middle and end of the single-track deposition for the 750W specimen and compared it against the thermocouple data. By comparing the simulated vs experimental temperature field, the process efficiency was back calculated based on an optimised fit for each laser condition. Figure 5.15 shows strong agreement for the single-track deposition temperature field and a 32.5% efficiency and Gaussian parameter of 2.8 aligned the simulated heat source well with experimental outcomes. The Gaussian parameter controls the curve steepness, influencing energy per area [315]. Lowering the Gaussian parameter hindered achieving the depth profile, while increasing it to 3 rectified depth measurement by narrowing the bell curve. For the 950 W and 550 W specimens, the process efficiencies were experimentally calibrated as 30% and 38%, respectively.

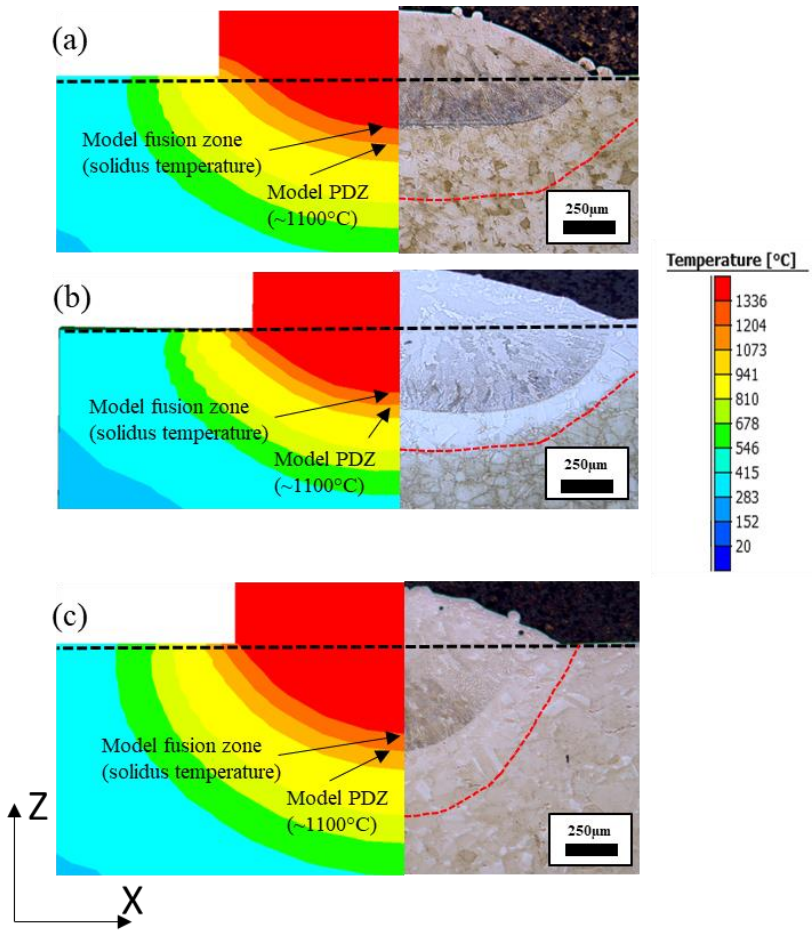

Figure 5.13 Cross sections of the simulated melt pools comparative to experimentally captured for (a) 950W, (b) 750W and (c) 550W.

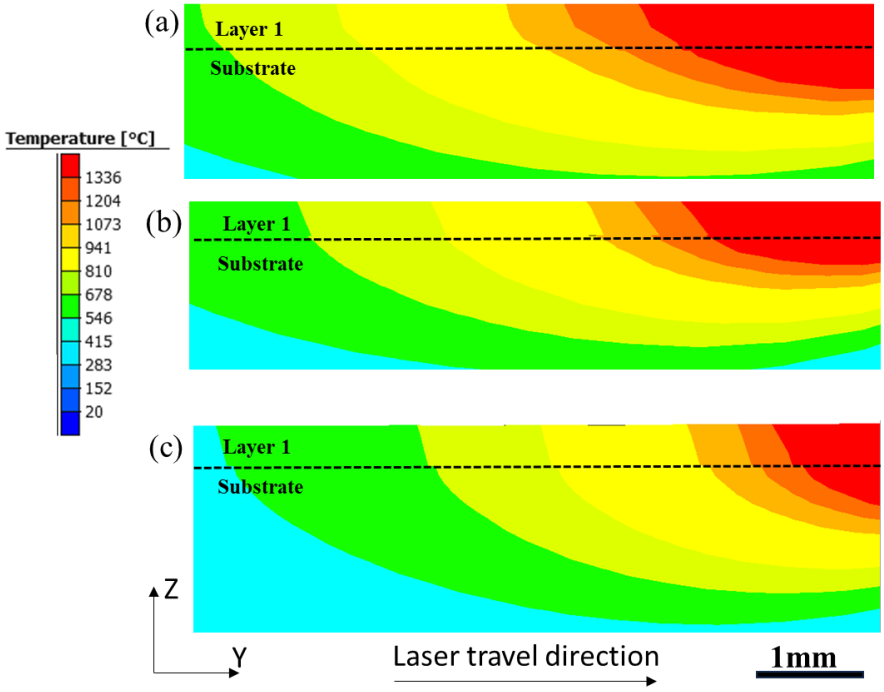

Figure 5.14 Temperature contours obtained from the thermal analysis for the Y-Z cross-sectional (a-c) melt pool showing the FEA model and experimental macrograph juxtaposed under three process conditions (a) 950W, (b) 750W and (c) 550W.

The temperature profiles for the initial 6 s of deposition at the midpoint of the melt pool, precisely at the substrate/deposit interface (as marked in Figure 5.14.a), are illustrated in Figure 5.15.b. These results align somewhat with the expectations, demonstrating that an increase in laser power leads to a higher peak temperature. Notably, the peak temperature at 550 W surpasses that at 750 W, which can be attributed to the improved efficiency of the laser source, as demonstrated in the preceding section.

Interestingly, all test specimens exhibit a similar temperature trend, characterized by a slight temperature increase (approximately 500°C) around the 1-second mark, followed by a maximum peak around the 4-second mark. In accordance with the experimental setup, the laser is theoretically positioned directly over the measurement point at around 2 s. The slight initial temperature rise at 1 s is hypothesized to be a result of a delay in the laser's activation before it begins to move. This delay was experimentally observed as wider melt pools at the starting points of single laser tracks.

The occurrence of a temperature peak after the laser source has moved beyond the measurement point could be attributed to several factors. First, thermal inertia plays a role; there is a delay in heat transfer and thermal response due to the material's properties, causing the material to continue rising in temperature as it absorbs more heat. Additionally, the material's behaviour in terms of reflection and absorption of thermal energy from the laser source may introduce a delay. Initially, there may be a high level of reflection, which gradually decreases as more thermal energy is absorbed by the material, resulting in a delayed peak temperature. Finally, the accumulation of residual heat within the material after the laser source has passed can lead to a significant delay in reaching the peak temperature.

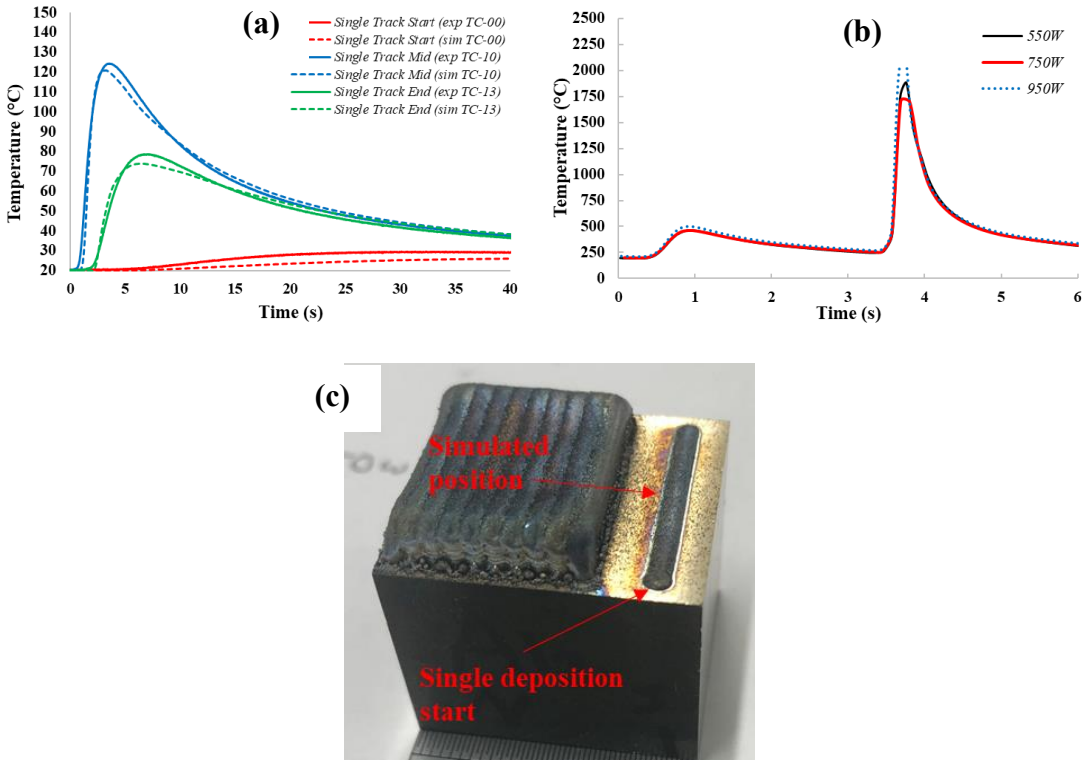

Figure 5.15 Simulated FEA thermal history vs experimentally captured for the single tracks (a) P= 750 W, comparing the start, middle and end of the single-track deposition and (b) Simulating the temperature history at the mid-point for all laser conditions (c) experimental mid-point of single-track and wider melt pool at start

5.7.3 10 Layered Block Calibration

Full simulations of the deposited blocks for all laser conditions were executed. Figure 5.16a illustrates the arrangement of thermocouples in each specimen, indicating the specific locations where temperature histories were interpolated in relation to both the construction and single deposition phases. Moving to Figure 5.16b, a comparison is presented between the thermal histories generated through numerical simulations and those obtained experimentally. This comparison is focused on the high laser power scenario at TC14 measuring position, strategically placed directly under the start of tracks 9-10 within the substrate as depicted in Figure 5.16a.

The temperature values projected by the simulation were interpolated from nodal points, akin to particle placements within the Finite Element Analysis (FEA) model. This interpolation closely mirrors the actual thermocouple placements in the experimental setup. Analysing the implications of Figure 5.16b, it becomes evident that the transient thermal model provides highly accurate forecasts of the temperature history across the entirety of the build, specifically noted in TC12. Moreover, not only are the peak

temperatures effectively replicated, but the projected heating and cooling rates also exhibit a robust correlation with the measured values.

Three distinct thermal Finite Element Analysis (FEA) models were both simulated and experimentally validated. This was necessitated by variations in laser power, which induced changes in melt pool geometries—details of which are elaborated upon in the ensuing section—and prompted the need for transient thermal calculations. The experimental arrangement of thermocouples remained constant across all scenarios, encompassing meshing, thermal boundary conditions, and underlying assumptions. It is important to acknowledge that, in each laser power instance, the depths of the thermocouples had to be individually calibrated to ensure precise measurements.

The simulated temperature distributions exhibited a remarkable alignment with the experimental data gathered for each condition, as visually depicted in Figure 5.16c. Both the numerical and experimental temperature profiles harmonized well with the simulated model. This congruence encompassed the replication of temperature peaks, thermal fluctuations, and the cooling process following the final layer deposition. As previously highlighted, the accuracy of the simulated temperature distribution improved progressively with the establishment of incrementally heightened process efficiencies.

An intriguing observation emerged in the comparison of different laser power cases. The process efficiency for the specimen processed at 550 W manifested an almost 10% advantage over the efficiencies observed in the cases of 950 W and 750 W. While factors delineated in the process efficiency section contribute to this trend, it is worth noting that the 550 W deposition followed the sequences of the 950W and 750 W specimens. This leads to a hypothesis: the elevation in process efficiency could potentially be linked to laser components, such as gain mediums and optical elements, attaining a state of optimal warm-up and stabilization. Prolonged operation would ensure that these components reach thermal equilibrium, promoting a consistent and more efficient performance.

Furthermore, an important detail pertains to TC03 in the 550 W scenario, which was situated approximately 0.5 mm closer to the interface region compared to TC12 in the 750 W case. This spatial difference contributes to an overall higher thermocouple measurement in the 550 W scenario, underscoring the intricacies of the experimental setup and measurement of thermocouple depth placement.

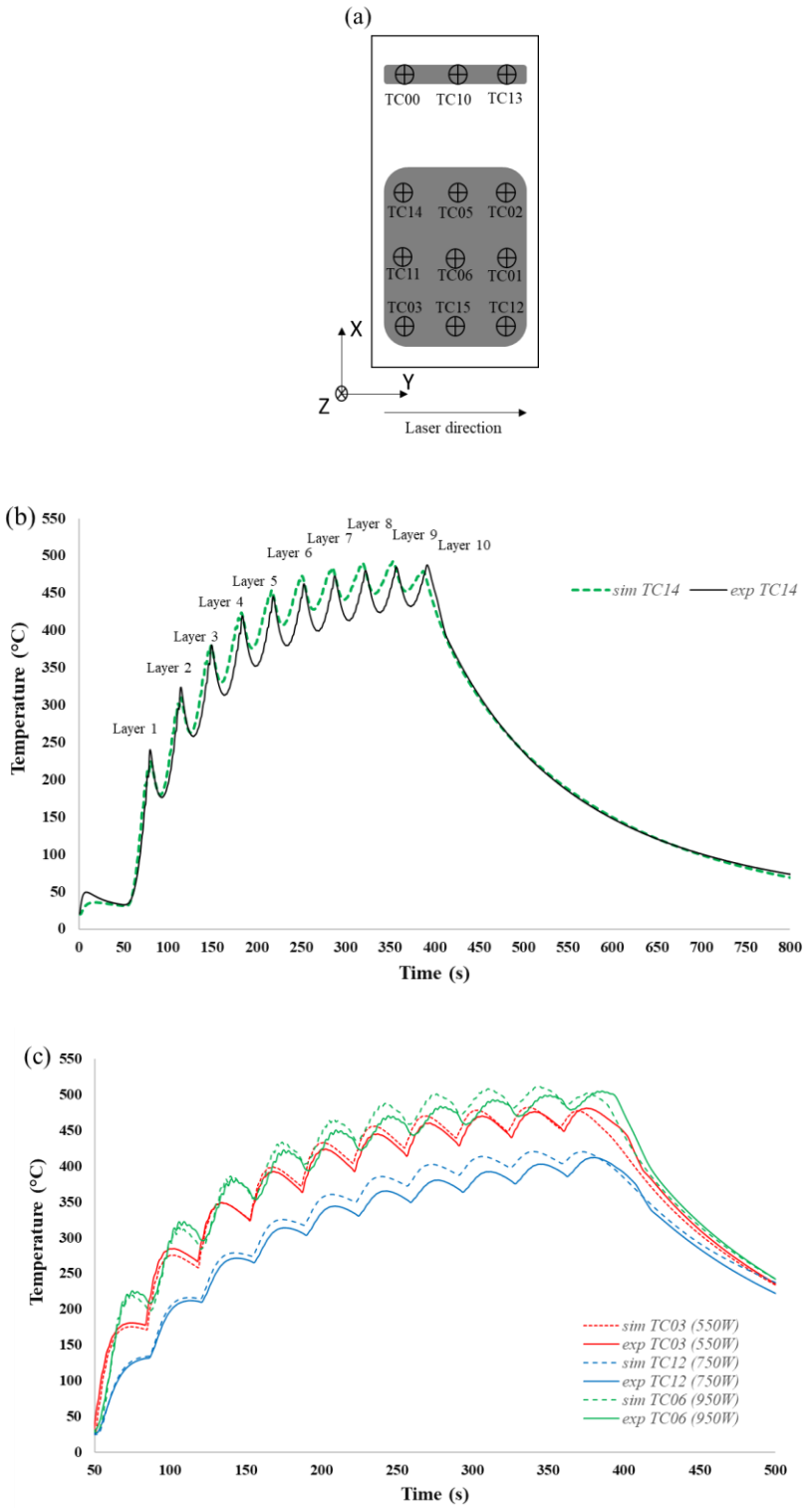

Figure 5.16 (a)Thermocouple configuration for all specimens with (b) comparison of thermocouple and predicted data for TC 14 in the 950W detailing the full deposition cycle and (c) comparison of three separate thermocouples (TC03, TC06, TC12) and predicted data in each specimen condition.

In summary, the simulated temperature distributions exhibit a robust alignment with the experimental outcomes across various thermocouples and under different laser processing conditions. This close concurrence observed between the simulated and experimental data serves as a compelling validation, warranting the progression and refinement of the

thermal model. This progression is substantiated by the model's ability to compute crucial non-measured experimental data, encompassing intricate parameters such as thermal boundary values, heat source geometry, process efficiencies and location specific (melt-pool interface) temperature profile —elements that are typically challenging to directly capture through experimentation.

5.7.4 Efficiency Alterations

It was noted by simulating the temperature history, a constant process efficiency was inadequate for accurately representing the experimentally captured profile. Using a constant efficiency of 29.5% for the single deposit underestimated thermocouple temperature in the full block simulations. Experimentally derived single-source parameters were applied to additional laser sources in later model stages. Efficiency incrementally rose from 29.5% for layer 1 tracks to 36.5% for track ten. The gradual efficiency increase could be linked to rising workpiece temperature, potentially affecting powder melt efficiency through surface tension changes. In the simulation, the deposited layer height was determined by multiplying the single-track height by the number of layers. For instance, the total build height for 950 W was 4.3 mm, given a single deposited height of 0.43 mm. The numerical model doesn't consider remelting and solidification of vertical tracks. To address this, process energy was linearly increased with layer heights to match the temperature history. This hypothesis warrants further research beyond this project's scope.

5.8 LMD Temperature Profile

A comprehensive simulated temperature history profile is available for the 10-layer blocks fabricated using laser powers of 950 W, 750 W, and 550 W. An illustration of the thermal history outcome at the interface region, approximately 250 µm below the substrate surface of the 550 W configuration can be observed in Figure 5.17. The cyclic thermal history portrays the step-by-step deposition process of each layer. In the initial deposition phase, the first layer encounters a prominent peak temperature. This temperature rapidly decreases below the solidus threshold, yet it does not have sufficient time to reach the ambient room temperature before the consecutive tracks and layers are deposited. This leads to a swift temperature surge once again.

Upon introducing the second layer during deposition, the middle region of the primary layer undergoes remelting to ensure effective fusion between these two layers. Subsequent to each additional layer's introduction, the peak temperature diminishes.

Concurrently, there is a gradual escalation in localized temperature, indicating the accumulation of residual heat within both the deposition material and the substrate.

Throughout the progression of the build, the oscillation in temperature between layers gradually diminishes. Upon the accomplishment of the entire fabrication process, the localized region takes approximately 8 minutes to cool down and attain the ambient room temperature.

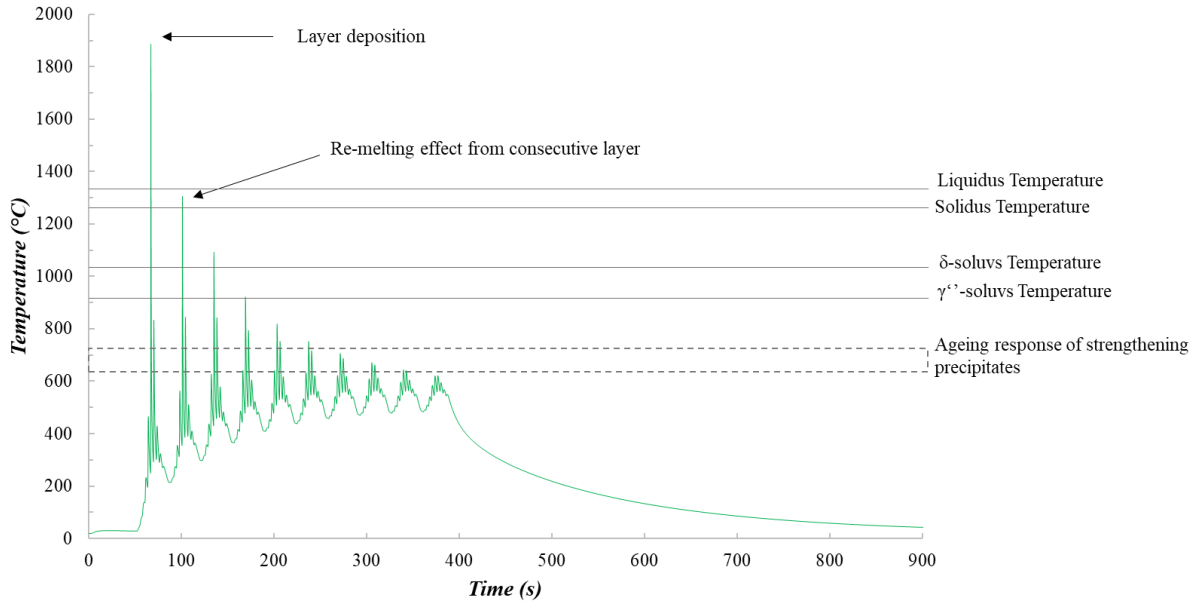

Figure 5.17 Thermal history simulated from the interface region located mid-deposit of track 5, 250µm below substrate/deposit interface of the 10-layer specimen deposited with 550W.

The forecasted evolution of the microstructure stems from the simulated temperature history observed during the deposition at the fusion line. As the material undergoes the cooling process from the liquidus temperature, the emergence of γ grains and potential dendritic growth takes place. The rate at which the cooling transpires between the liquidus and solidus temperatures wields a significant impact on the formation and spacing of dendrites. Further, the cooling rates below the solidus temperature substantially influence both the size and morphology of the γ grains. This cooling rate also serves to restrict the kinetics of precipitation by impeding the diffusion rate of alloying components within the regions encompassing dendrites and the spaces between them.

The temperature history simulated in this context offers substantiation that any δ-phase formation occurring in the intermixed region will indeed dissolve during the initial three layers, and any solidifying precipitates will encounter hindrance in dissolution after the initial four layers. Subsequently, the material within this region becomes exposed to temperatures akin to those encountered in a typical aging treatment. The combination of

the temperature and duration of aging significantly governs the size, distribution, and mechanical attributes of the precipitates.

Furthermore, considering the inevitable occurrence of Laves phase formation in the interdendritic regions, it can be predicted that, if any reinforcing phases were to precipitate out of the γ-matrix, these occurrences would likely manifest near areas enriched with niobium.

5.9 Chapter Summary

In summary, a comprehensive experimentally validated thermal model has been developed using Simufact welding software. Key outcomes from this chapter are as follows:

1. A mesh convergence study was successfully developed to optimise computational time and accuracy. Using a biased seeding approach in ABAQUS, the interface region was densely meshed to accurately describe thermal variation between the elements and portray melt pool dimensions.
2. The modelling environment facilities for both convective and radiation losses (which can be experimentally determined and temperature-dependently associated), heat conduction through the substrate and clamping fixtures and the energy associated with liquid to solid phase transformation. However, limitations are involved in the LMD modelling, such as melt-pool shape, deposited material shape, melt-pool thermal gradients and associated forced convection losses due to gas flow.
3. According to the thermal model, the process efficiency becomes increasing proficient with layer addition.
4. The complex thermal histories were well captured by the FEA based model in Simufact welding. The Simufact FEA based model was significantly advantageous to the project due to their inherently ease of modelling capabilities of complex geometries consisting of multiple tracks and layers.
5. Through experimental calibration of good agreement with melt pool dimensions and thermocouple validation, the thermal history data can be extrapolated from location specific data points.
6. To improve the accuracy of LMD computational modelling many require multi-physics packages, experimentally captured thermo-mechanical material property data and *in situ* calibration experiments such as thermal camera. Nevertheless, simulating localised temperature profiles associated with the interface region,

whereby experimental methods would prove difficult, a correlation between temperature history and microstructural response can be established and requires microstructural characterization across the interface region.

Chapter 6: Microstructure and texture evolution across the interface region of an LMD joint layer

6.1 Introduction

LMD is a complex additive manufacturing process involving interactions between the laser source, powder feed, and substrate material. These interactions, combined with the deposition of multiple tracks and layers, result in a complex thermal history characterized by thermal gyrations, sharp temperature gradients, and rapid cooling rates [335], [336], [337]. This chapter seeks to examine the interface region of as-deposited microstructures in LMD Alloy IN718, with the goal of advancing the comprehension of the microstructural evolution occurring within this zone. Figure 6.1 provides a cross-sectional view of the build. The interface region includes the Fusion Zone (FZ), Partial Melted Zone (PMZ), Heat Affected Zone (HAZ), and Substrate Zone (SZ), each exhibiting distinct microstructural differences. Key aspects to be explored include grain morphology, crystallographic texture, solidification, precipitation phase behaviour, and dendritic morphologies. Understanding these microstructural changes is crucial for optimizing the mechanical properties across the interface region, particularly in repair applications where post-weld heat treatments will be limited to ensure substrate material properties remain. Detailed analyses of process parameters will be further investigated in Chapter 6.

Analysis of the microstructure and crystallographic texture evolution across the interface from the substrate zone, to the as-deposited region, involves categorising the HAZ region into two separate regions; partially melted zone, often referred to as the *'mushy zone'* [338], [339], [340], [341] and the heat affected zone.

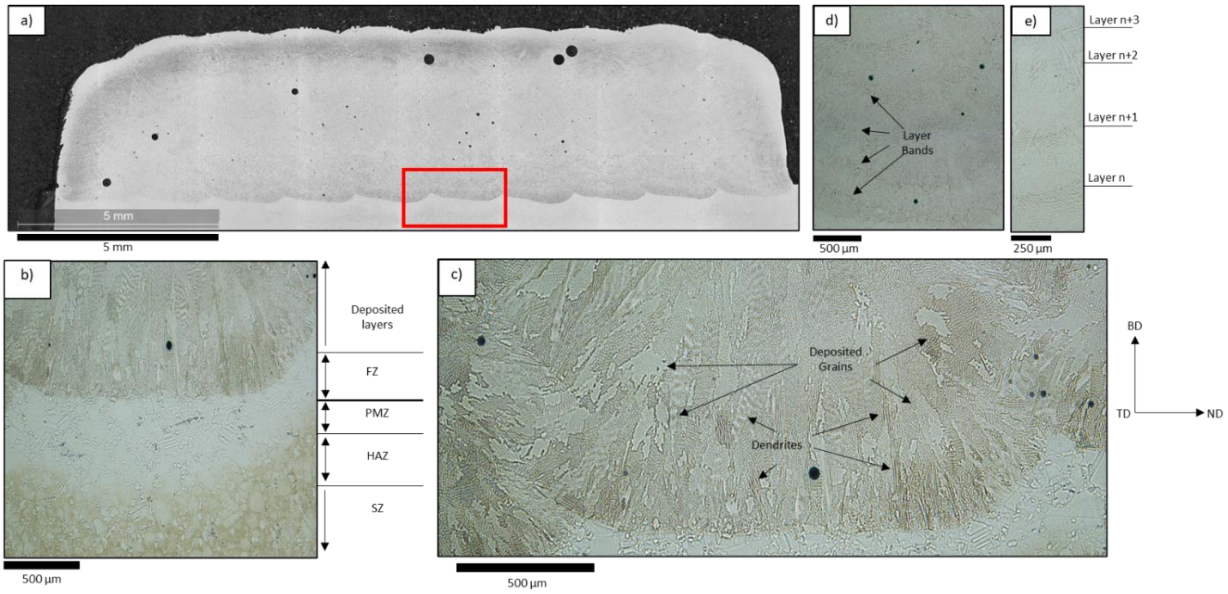

Figure 6.1 Microstructure of specimen under High HI conditions: (a) overview, and (b) magnification of area outlined in (a), (c) detail of the deposited layer at the interface with (d) outlining the subsequent deposited layers and (e) magnification of the layer bands showing the dendrite microstructure.

6.2 Macrostructure

All the specimens analysed in this study exhibited elongated columnar austenite (γ) grains of several millimetres in length and were aligned along the build direction (BD). The micrograph of the interface region (Figure 6.2) shows the transition from the deposited layers to the substrate. The parent material (PM) displayed a combination of larger equiaxed grains interspersed with smaller grains. A bright etched band delineates the partially melted zone (PMZ)/heat-affected zone (HAZ) and substrate, while a distinct change in microstructure marks the transition between the substrate and the deposit. This transition is characterized by a shift from equiaxed morphology to columnar grains with intergranular dendrites aligned along the BD. In this work, the PMZ and HAZ are categorized and investigated separately, distinguishing them from previous literature that grouped them together as the HAZ [342], [343], [344]. The PMZ/HAZ region reacted more strongly to the chemical etchant, resulting in a bright white band, which made it challenging to study the γ-austenite grain morphology using optical microscopy (OM). Therefore, electron backscatter diffraction (EBSD) will be utilized as the primary technique to investigate the grain morphology in the PMZ/HAZ.

The presence of layer bands was observed in every layer of the LMD deposit, indicating a distinct microstructural change (Figure 6.1.d). This sudden change is characterized by an increase in Primary Dendrite Arm Spacing (PDAS), which will be further discussed in this chapter. An explanation for the formation of these band-like structures in LMD

deposits is that during deposition of each subsequent layer, the surface of the pre-deposited layer is re-melted and re-solidified [345]. The newly solidified grains continue to grow in the same direction, resulting in elongated columnar dendrites. This continuation occurs because the heat flow from the bottom is uniformly transferred parallel to the negative Z-axis (BD direction), which is perpendicular to the substrate. The height of each band can vary based on processing parameters and localized conditions such as thermal gradient and heat sink effects during layer formation.

The LMD process involves building the sample layer by layer, with each layer deposited right on top of the previously deposited layer. Figure 6.2 illustrates the substructure dendrite evolution during the LMD process. In the first layer, the high temperature gradient and rapid cooling rate at the bottom of the melt pool led to the formation of columnar grains. As solidification progresses, the cooling rate and temperature gradient decrease towards the top, resulting in the formation of equiaxed grains. It was observed at the bottom of the sample (Figure 6.2**.**d) where long primary dendrites grow aligned with the build direction. Towards the centre of the builds (Figure 6.2.c) due to the change in localised thermal conditions with a reduction of thermal gradient and cooling rate, an equiaxed structure is observed also forming equi-dendritic regions, which is present until the top layer (Figure 6.2.b), where the equiaxed structure ceases and the elongated dendrites grow opposite to the build direction.

When multiple tracks are deposited in a unidirectional manner, the equiaxed grains in the overlapped region partially remelt and serve as nuclei for promoting the regrowth of columnar grains. This process continues with each subsequent layer, where the grain morphology of layer n+1 becomes similar to layer n. Additionally, the columnar grains in the overlapped region continue to grow epitaxially towards the region with the maximum thermal gradient. This cyclic process persists across many consecutive layers, leading to the growth and dominance of columnar grains in the overlapped region.

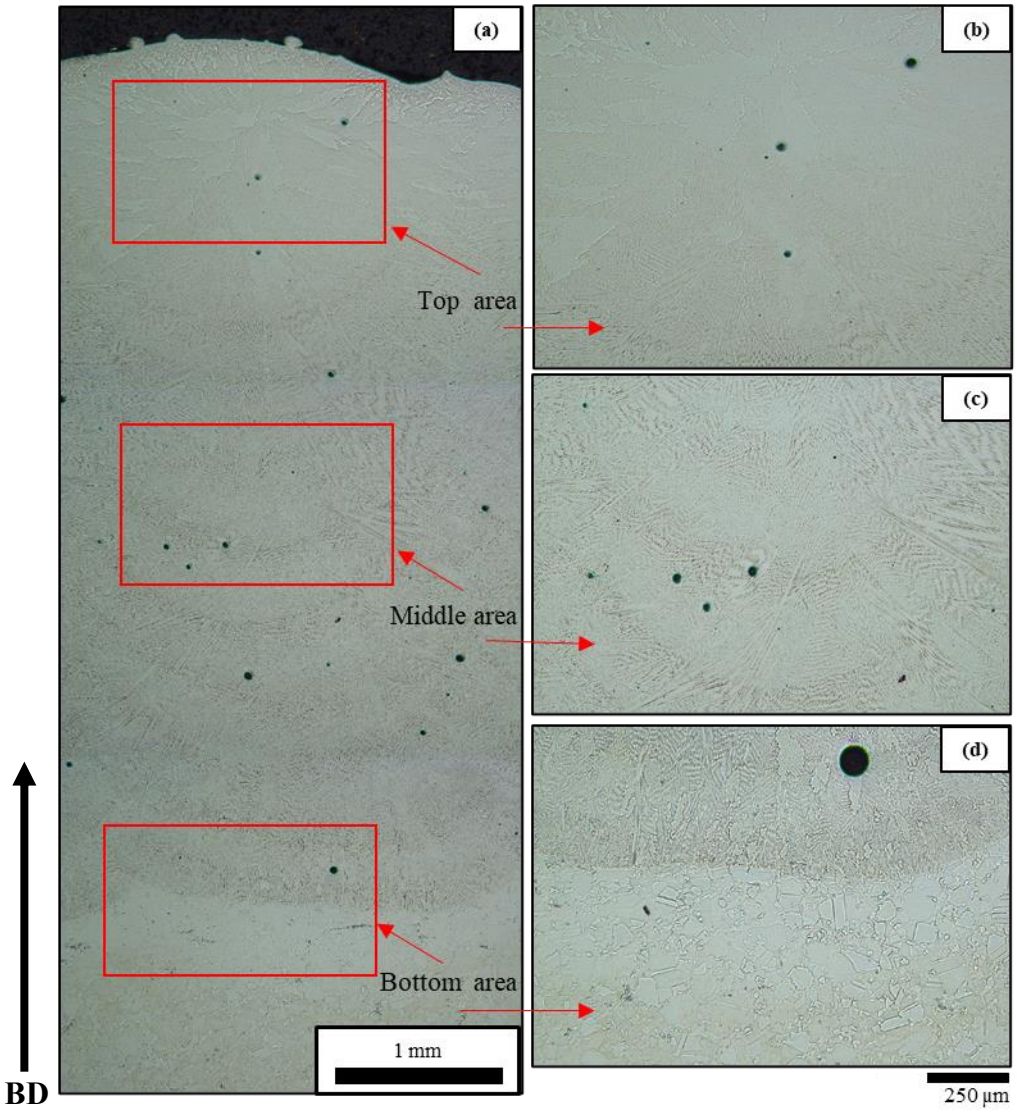

Figure 6.2 Dendrite evolution of the (a) whole LMD IN718 deposit and each region; (b) the top region; showing the transition from the equiaxed structure to the elongated dendrites growing opposite to the build direction, (c) the middle region; demonstrating the gradual change in solidification conditions resulting in more equiaxed grains/sub-grains and (d) the bottom region; showing elongated grains growing aligned with the build direction.

6.3 FCC γ-phase Grain Morphology

Figure 6.3 illustrates the typical γ grain morphology observed at the fusion line between the substrate and the as-deposited material for all three process conditions.

The substrate consists of randomly oriented equiaxed grains with no preferential crystallographic relationship, i.e. no clear relationship between specific planes and directions of two crystals on either side of boundary which can often form because of thermomechanical processes. Moving into the PMZ/HAZ, the grains appear to be approx. 1.6x larger than the substrate average grain size. This potentially indicates grain growth due to the thermal energy of the laser but could also be region specific measurements, i.e. the substrate grain size at that location was at the lower end of the overall average grain

size. The austenite columnar grains tend to grow perpendicular to the fusion line and towards the centre of the melt pool, forming a dominant grain orientation of <001>//BD fibre texture, indicated by mostly red-coloured grains. Epitaxial growth of grains can be observed across the fusion line, with the growth direction changing to the transverse direction. At the fusion line, there is a competition between nucleation and grain growth. This preference for growth along the direction containing fewer atoms results in faster growth [346]. Smaller equiaxed grains and thin columnar grains can be seen along the fusion line, measuring <20 µm in width and 50 µm in length. These grains exhibit a different texture compared to the dominant, red-coloured columnar grains. These nucleated grains tend to occur where the substrate grain deviates from the preferential <100>//BD direction, represented by blue and green coloured grains (Figure 6.3).

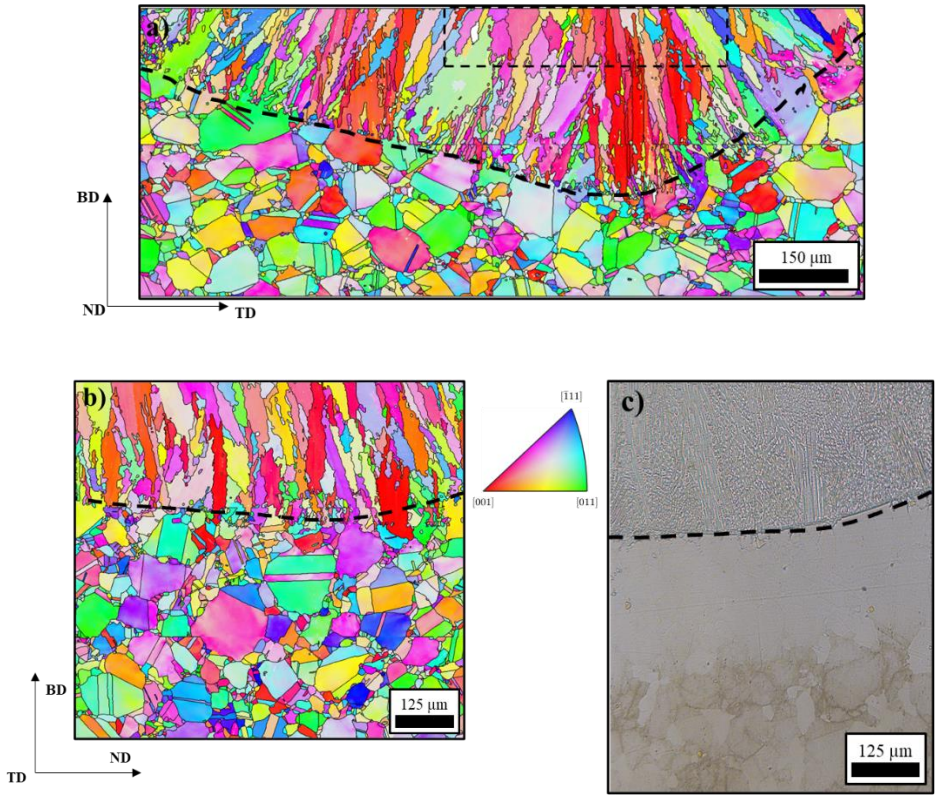

Figure 6.3 EBSD OIM IPF maps of specimen low HI cross section with directions plotted || BD, in the (a) BD-TD plane, and (b) BD-ND plane. (Black dashed line represents the fusion line transition between as deposited material and substrate, the black dashed box represents the overlap between layer n and layer n+1).

6.4 FCC Gamma Phase (γ) and Texture Evolution During LMD

Figure 6.4a depicts the grain orientation information within an individual ~50 µm powder particle separated from the interface region (top left region). Figure 6.4a & b details the grain orientation of partially melted powder particles fused at the edge of a multi-layered track close to the substrate/deposit interface. The grain morphology within the partially

fused region consisted of a mixture of very fine equiaxed/irregular γ grains. The grain size diameter distribution of these highlighted in Figure 6.4a grains, can be seen in Figure 6.5. The partially melted powder fused to the track cross-section exhibited a grain size diameter ranging from 2.5 µm to 10.5 µm, with over 65% cumulative percentage falling within this range.

In Figure 6.4c, a micrograph of a cross-section of a single deposited track is shown. Fused to the top of the track, circular features (highlighted by green arrows and red outline) observed in the micrograph are presumed to be partially melted powder particles, present at the edge of deposited tracks without overlap in the low heat input condition and on the top surface of several specimens. The morphology and size of these particles align with the powder size range. From literature, melting conditions are known to affect the metallurgical bonding or fusion between the fully melted powder particles and substrate, partially fused particles are often referred to as spattering. Spattering occurs when material vaporizes under high laser power density, causing ejection or expulsion of liquid metal from the melt pool surface [341]. Similar observations of partially melted powder particles adhering to as-deposited structures as heterogeneous nucleation sites have been reported by other researchers [231], [288].

Progressing along the fusion line from edge towards the melt pool centre, the columnar grains transform into an equiaxed morphology. In this central region, the columnar grains are wider (approximately 70.5 µm) but shorter (approximately 81.1 µm), resulting in a reduced aspect ratio of 1.15 compared to the grains near the melt pool edges. These edge grains exhibit an aspect ratio of 5.3, measuring around 160.7µm in length and 30.25µm in width. This difference is attributed to the rapid cooling experienced at the edges, caused by the heat sink effect from the substrate. The centre of the melt pool concludes solidification later due to the thermal energy and volume of surrounding molten material. This central region is characterized by fine equiaxed grains with an average size of 42 µm with <1.5 aspect ratio. Analysing towards the fusion line in the middle of the melt pool, a band of columnar γ grains have grown parallel to the build direction (BD). During solidification, a competition of nucleation and/or growth of these grains exists due to localised thermal conditions. With a high thermal gradient, G vs solidification rate, R, these columnar grains cease to grow further into the melt pool due to the equiaxed grains formed during solidification. Transitioning into the substrate/HAZ, Figure 6.5.b depicts the grain size information, which can be characterized by grains with an equiaxed

morphology containing many twin boundaries. Majority of these grains (>45%) measured between 2.5-7.5 µm with a low aspect ratio (~2.1).

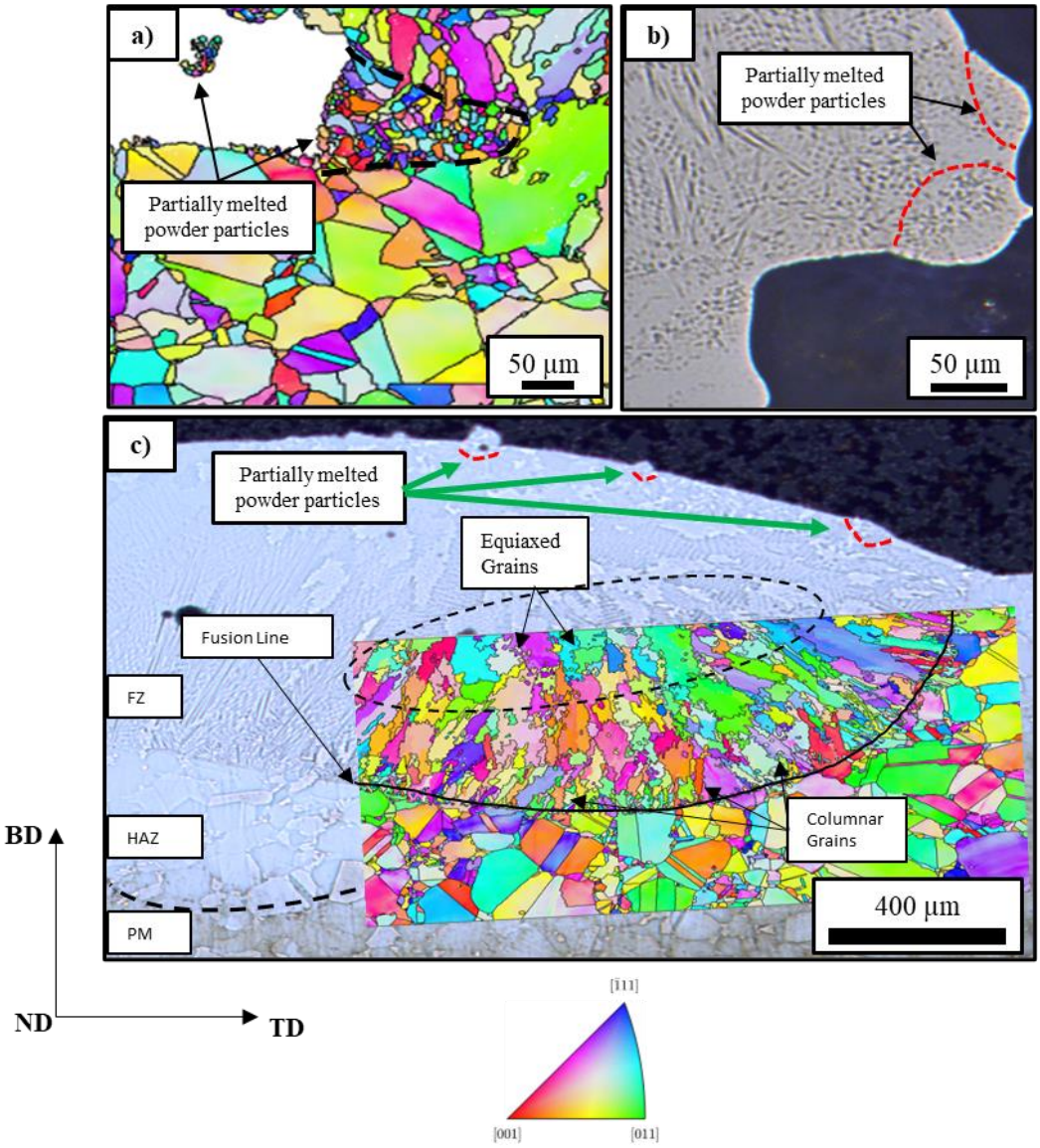

Figure 6.4 (a) OIM IPF map of partially melted powder fused to the side of (b) the edges of outer tracks and top of single track deposited as noted in (c) which details micrograph of etched specimen consisting of a single deposited track with an IPF map overlaid showing the morphology of the grain structure as it transitions through the PM, HAZ and deposited material.

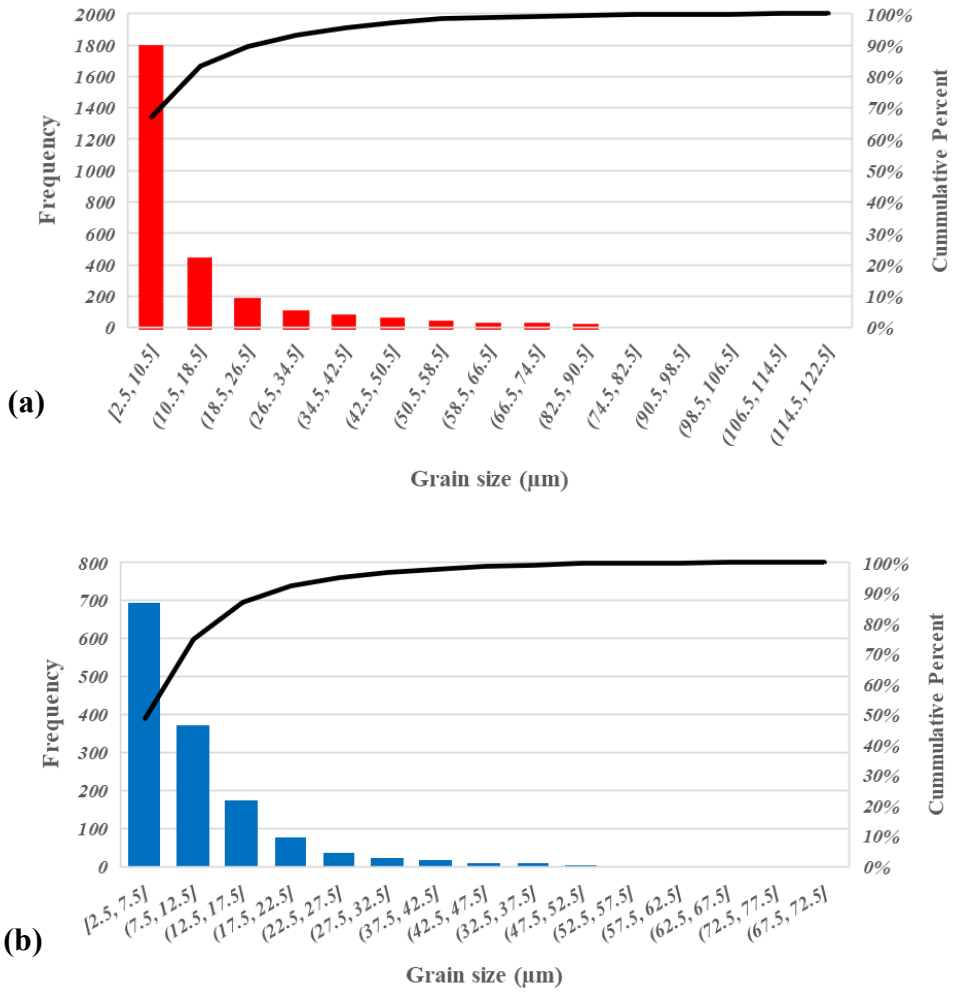

Figure 6.5 Grain size distribution of (a) transverse cross section of partially melted powder particles of the LMD IN718 specimen highlighted in Figure 6.4a and (b) the substrate.

6.5 Discussion

Investigating the epitaxial columnar grains which have grown from the substrate into the melt pool as highlighted by the 'columnar grains' notation in Figure 6.4c, display IPF colours matching closer to the (111) direction, rather than the ideal (001) direction. As described in Figure 6.6, during the solidification process at the interface region, the melt pool generated by the laser beam, and liquid metal undergoes solidification starting from the trailing edge. The growth direction and rate of solidifying columnar grains are influenced by the characteristics of the melt pool, including its size, shape, and movement speed. The dynamic and curved shape of the melt pool at the fusion line between the melt pool and substrate causes fluctuations in the values of thermal gradient (G) and solidification rate (R), thereby influencing the direction of columnar grain growth from the fusion line towards the centre of the melt pool. Laser power also plays a role in determining the growth direction and rate, which will be further investigated in a subsequent section. The curved top surface of the melt pool, resulting from the melting

and accumulation of powder particles, exhibits compressed and expanded isotherms along the scanning direction. The largest thermal gradient direction is perpendicular to the curved surface of the melt pool and determines the preferential growth direction of {001} γ grains.

In the interface region of all three process conditions, it is interesting to observe that most grains grow along the thermal gradient of the solidifying liquid and perpendicular to the fusion line, aligned with the BD direction. Additionally, grains in the fusion zone tend to tilt towards the centre of the melt pool, contrary to the heat flow direction. The growth of grains along the semicircle fusion line leads to a dispersed orientation. In the overlapped region, a strong texture is observed due to the directional temperature gradient and heat flow. These grains are affected by subsequent layer addition, resulting in a grain orientation of <001>//BD. However, grains at the fusion line that grew epitaxially along the <100>//BD direction but may not be coloured red, and still have a grain orientation related to the laser scan direction (ND) as depicted in Figure 6.4.c. In the centre of the melt pool and overlap region, most grains closely align with the <001> direction. Towards the edge of the melt pool cross-section, grain orientation deviates from the strong red colour and angles towards the centre of the melt pool. This deviation from alignment with the BD direction is attributed to a deviation of the maximum temperature gradient from the build direction, influenced by the laser scan direction and resulting in grain growth towards the centre of the melt pool.

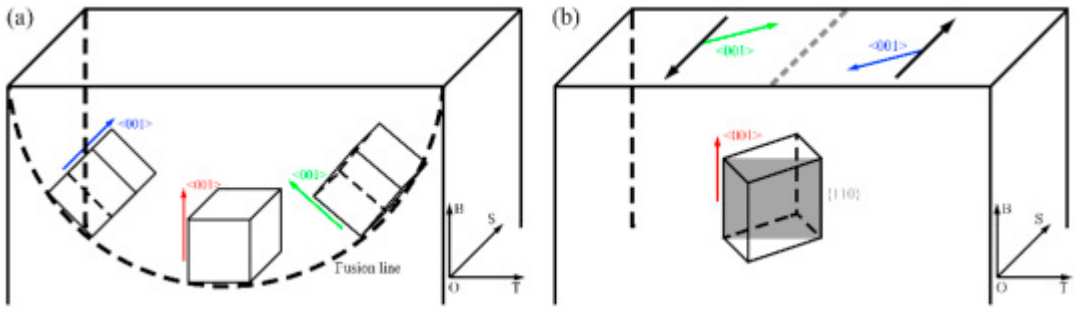

***Figure 6.6 Schematic diagram of the grains growing in the (a) melt pool fusion line and (b) overlapped area** [347].*

In the microstructure observed at the fusion zone in this study, a consistent pattern emerged across all specimens. The initial layer exhibited large columnar grains, which were then impeded by the growth of smaller equiaxed grains at the top region, indicating different solidification mechanisms at play. Epitaxial growth, a common phenomenon in LMD-produced Inconel 718 microstructures[70], [348], [349], [350] led to the formation of columnar grains that extended through multiple layers, often reaching several

millimetres in length. During the laser metal deposition process, as the laser beam moved in the scan direction, the melt pool underwent solidification from the base material towards the interior. Columnar grains grew epitaxially in the direction of maximum temperature gradient or heat flow. This is consistent with solidification principles, as crystals tend to grow faster along the heat flow direction due to the larger thermodynamic driving force in that direction, which is shown by the tilted grains towards the centre of the melt pool in Figure 6.4c.

As solidification progressed, the thermal gradient reduced, causing a larger number of equiaxed grains to nucleate ahead of the solidification front. These equiaxed grains impeded the growth of columnar grains and became the dominant structure in the solidification process. The final temperature of the melt pool fell below the solidus temperature, marking the termination of the solidification process.

In addition to these solidification mechanisms, incomplete melted powder particles acted as heterogeneous nuclei, leading to the formation of smaller equiaxed grains in the upper region of the melt pool. The presence of a constitutionally supercooled region ahead of the solid/liquid interface, along with the nucleation possibilities provided by incomplete powder particles, played crucial roles in the columnar-to-equiaxed transition observed during LMD. The supercooled region was introduced in the literature review section 2.2.7 but can be considered using Figure 6.7.

During the solidification process of an alloy with a partition coefficient less than 1 ($K<1$), solute atoms are rejected at the solid/liquid interface, leading to an increase in the localized concentration of the solute. This concentration continues to rise until a steady state is reached. In this state, the solidification temperature ahead of the liquid/solid interface is dictated by the localized composition of the liquid [351][352].

If the temperature at the solid/liquid interface equals or exceeds the liquidus temperature, there is an absence of a constitutional supercooled region, preventing dendrite formation but facilitating planar growth. The critical temperature for planar growth initiation is denoted as Gc, and if the temperature surpasses Gc, planar growth remains stable. However, if the actual temperature gradient falls below Gc, protrusions develop in the melt pool in cellular or dendritic form.

The temperature gradient in the melt pool decreases from the bottom to the top of the deposited layer, resulting in varying degrees of constitutional supercooling throughout the thickness of the deposited track. Both temperature gradients and solidification rates

exhibit variations with distance in the melt pool, causing the solidification conditions to differ from the bottom to the top of the deposited layer [353], [354].

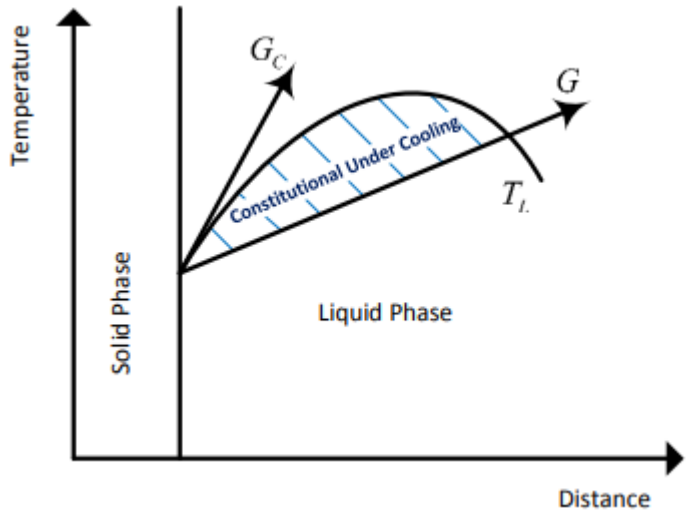

***Figure 6.7 Constitutional super cooling at the solid/liquid interface** [351].*

The density of heterogenous nucleation sites from additional powder particles within the melt pool was influenced by process parameter factors such as powder feed rate and efficiency of the machine. If the powder feed rate exceeds the optimal value needed for that specific heat source, the excess powder may only partially fuse to the deposited track, such as those seen in Figure 6.4. The machine's efficiency hinges on the actual energy absorbed by the heat source to reach the melt temperature effectively. The Gaussian distribution behaviour of the laser source implies that powder particles aligned near the beam centre are more likely to attain melt temperature compared to those situated at the periphery. Factors such as the supercooled region, density of heterogeneous nucleation sites, and their combination are crucial when considering the first deposited layer and melt pool interactions.

An active density of nucleation sites emerges within the supercooled region, with an increased likelihood of nucleation enhancing the formation of equiaxed grains. Adjusting these parameters can diminish local thermal gradients, promote a larger constitutionally supercooled region, and improve nucleation conditions for equiaxed grain formation. Adjusting these parameters can reduce the local thermal gradients, promote a larger constitutionally supercooled region, and enhance nucleation conditions for equiaxed grain formation. This phenomenon was demonstrated by Okugawa *et al.* [355]whom demonstrated that equiaxed grains can be formed near the fusion line in a L-PBF-built

Al-Si alloy formed during intrinsic heterogenous nucleation mechanism. The multi-phase-field simulation predicted that Si crystalline particles remain near the fusion line after the rapid remelting process, serving as heterogenous nucleation sites during the solidification process. Moreover, research conducted by Zhu *et al.* [356] has demonstrated that the transition from a columnar to equiaxed morphology in the LMD of Ti-Alloys necessitates both a significantly supercooled region preceding the solid/liquid interface and nucleation possibilities within this supercooled region arising from incompletely melted powder particles. The resemblance between the grain morphology of the individual particle and the region of equiaxed grains in the single deposited layer supports the theory of incomplete melted powder particles acting as heterogeneous nuclei within the constitutionally supercooled region [357].

Overall, the complex interplay of solidification mechanisms, thermal gradients, and nucleation possibilities from incomplete melted powder particles contributes to the development of the microstructure observed at the interface region during LMD. Understanding these processes is essential for optimizing the microstructural and mechanical properties of LMD-produced components.

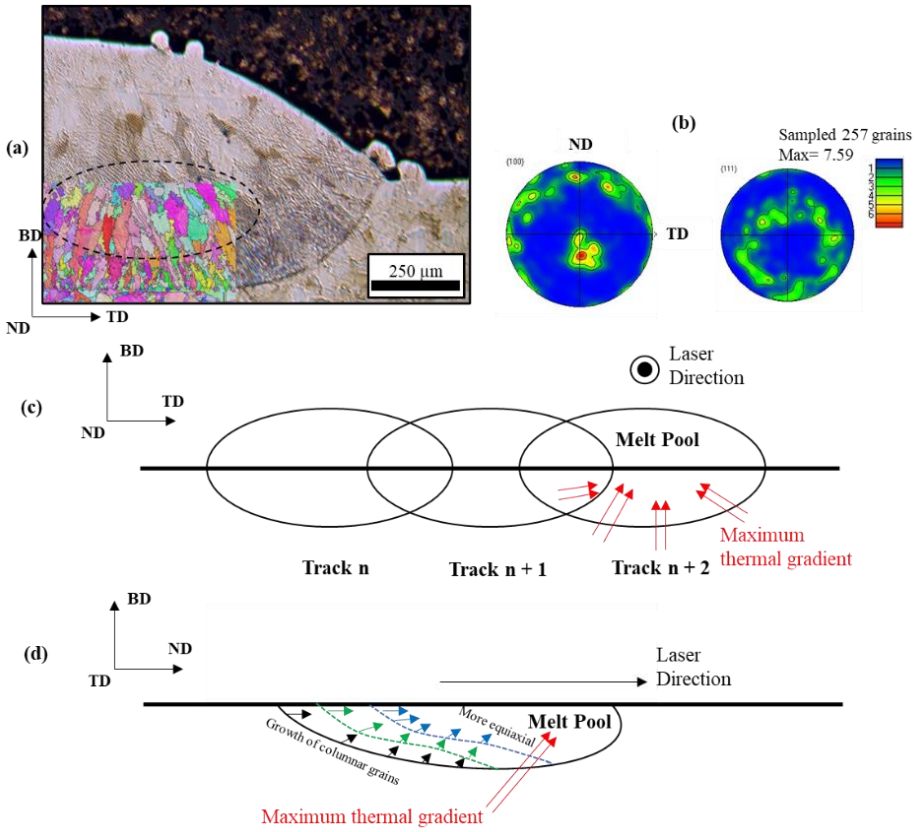

Figure 6.8 Growth of columnar to equiaxed grains during the deposition of a single track with (b) the associated pole figure of the equiaxed grains depicted by the dashed circle in (a), while (c-d) Schematically illustrate the maximum thermal gradient and progress of columnar grain growth with respect to moving melt pool geometry.

The pole figure delineated in Figure 6.8b is the grains enclosed by the dashed outline is presented in Figure 6.8a. The observed texture of these grains closely aligns with the ideal fibre distribution of poles, suggesting that, with a minimal angular deviation, the predominant texture of these centrally located grains within the melt pool conforms to a fibre texture. This is evident in Figure 6.8b, particularly in the (100) and (011) pole figures, which exhibit a texture maximum in the <001>//BD fibre texture with a peak intensity of approximately 7.6.

The (100) pole figure indicates that the predominant texture of grains slightly deviates in the negative ND direction, as evidenced by the clustering of peak data on the pole figure. Given that this is a cross-section, it can be inferred that the track was deposited as denoted by laser scan direction, negative to ND direction. The (111) plane displays a common fibre texture, suggesting that the grains deposited are solidified with free rotation clockwise or anticlockwise to the ND direction.

In directional solidification, the heat flow is opposite to the growth direction, towards the maximum thermal gradient and the rate of advance of the isotherms constrains the solid-liquid interface to grow in a steady state at this velocity [358]. In cubic structures, such as the face centred cubic (FCC) γ phase, it is easier for the atoms within the liquid to adhere to the least closely packed plane, corresponding to the {001} planes [359]. The FCC grains with their {001} plane closely orientated to the direction of maximum thermal gradient will solidify faster and grow to supersede less preferentially orientated grains. Although the <100> direction tended to grow along the build direction during LMD, the growth of highly orientated uniform grains is difficult due to the columnar to equiaxed transition condition, whereby the nucleation and growth of equiaxed grains in the liquid ahead of the columnar front exists. The complex morphology observed during solidification in LMD is influenced by the interplay between thermal gradient (G), solidification rate (R), and cooling rates. In the bottom region of the melt pool, where heat dissipation is rapid due to contact with the substrate, a high G/R ratio results in the preferential formation of columnar growth. As the G value decreases towards the centre of the melt pool, columnar grains widen and gradually transition to a more equiaxed grain morphology. Cooling rates play a vital role in determining the microstructural scales, with slower cooling rates leading to larger columnar structures away from the substrate. The columnar-to-equiaxed transition (CET) phenomenon occurs when the G/R ratio falls below the critical value [360], leading to the nucleation of equiaxed grains near the columnar dendritic front. The CET is driven by the release of more heat into the mushy

zone than can be conducted to solid, where the liquidus and solidus temperature isotherms bound a two-phase region of the melt pool.

6.6 Evolution of γ-grain texture in the as-deposited condition

In order to trace grain selection along the build height and understand texture formation, pole figures were plotted at different locations across the interface region. Figure 6.9 shows the microtexture {001}{111} pole figures constructed from separate locations of EBSD data as marked in Figure 6.9a and by keeping the plotted projection plane constant, the texture represents grains growth in the build direction. The polycrystalline substrate displays a relatively weak cubic random texture, and the reason for a slightly enhanced MUD value of 4.78 is in the relatively large (>150 μm) grains encompassing substrate analyzed region. In the dissolution zone, the texture becomes weaker and more randomised (MUD value = 3.25), this phenomenon could be explained by comparing the substrate to dissolution zone where it appears from Figure 6.9a, the formation of small (2-10 μm) equiaxed grains in the dissolution zone is an order of magnitude higher and the number of larger grains presented in the substrate is higher, this would enhance the randomisation of pole figure generated.

In the case of the first layer, there is a tilt in the fibre direction into the direction of maximum thermal gradient, much like that of the single layer as previously discussed. The second layer shows the columnar grains continuing to grow in the build direction with an increased width by 47% comaprative to the first layer. This is an indication that the cooling rate has reduced significantly, comparative to the first layer due to the heat sink effect deminishing. The pole figure shows a <100> fibre texture which is 8x random. In solidification of LMD alloys, fibre textures are more common [70], [349], [361], whereby the grains tend to be orientated along the moving heat source and, simultaneously, have their <100> direction well-alligned with the build direction. The scattering intensity along the rim of the pole figure imply that the grains are randomly rotated about the build direction. As the build progresses, in layers 3 and 4, slight marginal tilt in the BD axis and into the direction of the maximum thermal gradient of the previously deposited layer was observed. The texture intensifies as the influence of the substrate texture slowly diminishes and the localised conditions favour the grains in the centre of the melt pool to grow along the heat flux direction. Such a phenomenon is explained by the majority of grains being kinetically favoured as there is no nucleation energy required because of heterogenous nucleation rather than homogenous nucleation,

therefore require a lower activiation energy. The minority of new grains within the layer will grow with a tilted fibre texture along the heat flow direction in the new layer [362].

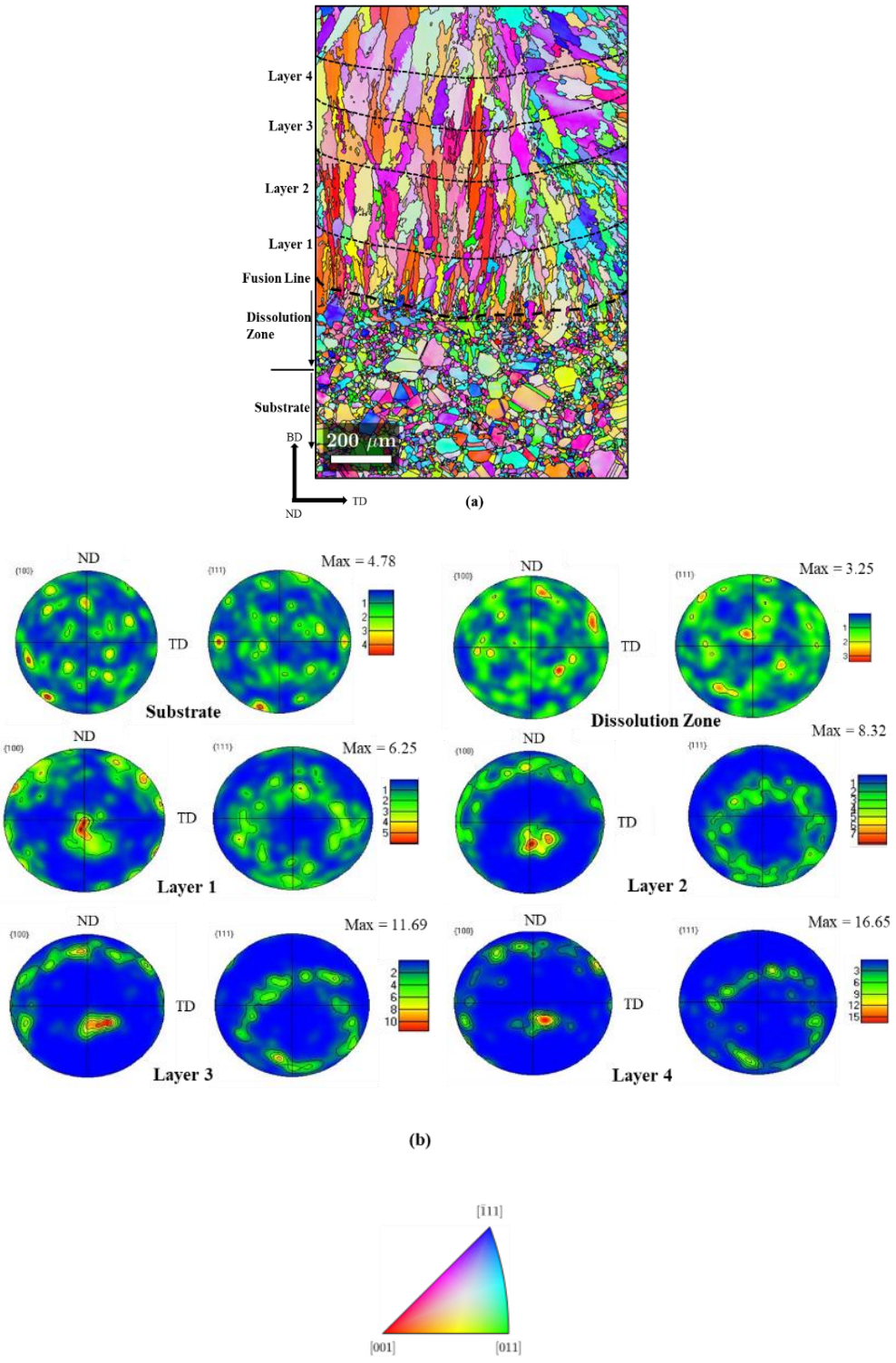

Figure 6.9 IPF map of the first 5 layers deposited using 950W with the accompainied plotted pole figures for each zone and layer.

For all specimens analysed in this work, the global texture as it evolves across the interface region from the substrate which has a generally random texture into the HAZ, comprising of a texture similar to that of the substrate into a <001>//BD fibre texture with

the remaining poles alligning with the laser travel directions (ND and TD axes). The intensity of the MUD values increases from layer to layer due to the influence of the substrate dissipating and the unidirectional hatch pattern. As a result, the heat source direction remains constant between layer n and layer n+1 forming a strong macro-texture. The observed <001>//BD fibre texture has been noted by others for AM of Ni-based superalloy including Waspaloy [363], IN718 [70], IN625 [364] and using alternative AM techniques such as WAAM [349].

During the build process, the subsequent layers will re-melt a signnificant portion of each initial layer especially where the differentiation between two layers as seen described in Figure 6.10. The top layer from each track and the overlapped region by two adjacent tracks will be remelted and resolidified rapidly, however evidence of the original layer grain structure is still present. Based on this understanding, the grain structure development from the initial layer to multiple tracks has been presented in Figure 6.10, and was similar results were reported by Lui *et al.* and Hicks *et al*. [357], [365] studying solidifcation in near β Ti-alloys.

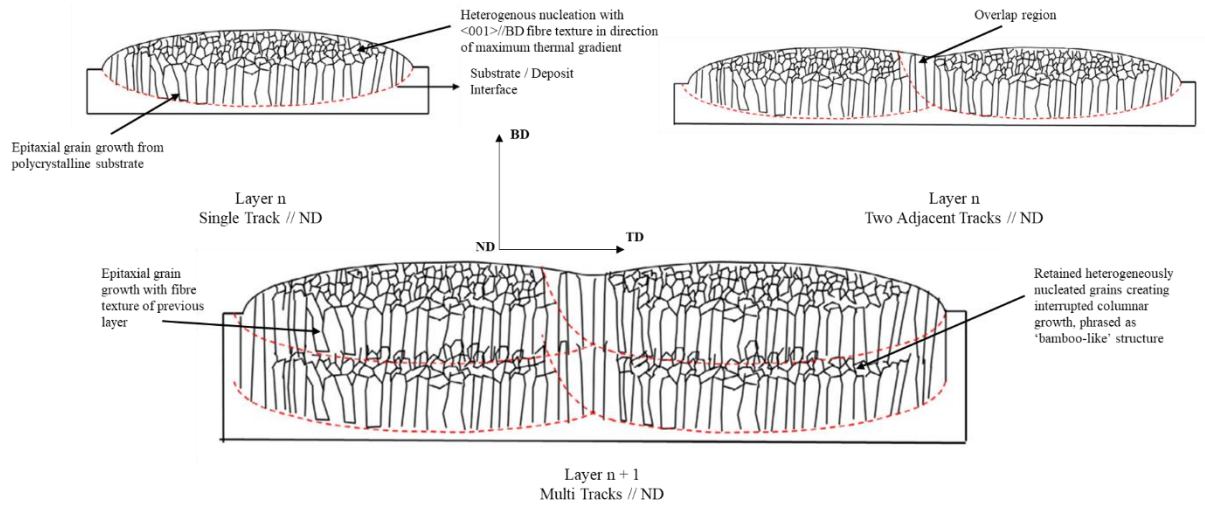

Figure 6.10 Schematic explanation of grain structure development from the first single track layer to detail small equiaxed grains retained throughout the microstructure after the deposition of multiple layers and tracks [367].

At the interface whereby the solidification conditions are favourable for epitaxial growth of the polycrystalline substrate, i.e. high G vs R ratio and of which have a favourable <001> direction tend to grow the fastest, epitaxial grains grow from the bottom of the melt pool and are impeded by heterogenous nucleation forming in the centre and top region of the melt pool. These heterogeneously nucleated grains will display a slight shift tilt in their fibre texture away from the BD and into the direction of maximum thermal gradient. With subsequent layer addition, most of these grains will be remelted. The

retention of these fine grains in the final microstructure is dependent on the localised thermal history (i.e. remelting depth of the subsequent layer) and the size of the heterogenous nucleated grains region [357]. The morphology of columnar grains with inter-layer sections of equiaxed grains has got limited citing to the best of the authors knowledge in AM of Ni-alloys [366], [367]. The retention of these nucleated grains hinders the columnar γ grain size by impeding the columnar grains that would continue to grow epitaxially through many layers.

6.7 Evolution of γ-grain texture at the FZ

An investigation of the γ-grain morphology adjacent to the specimen edge of the fusion zone is shown inFigure 6.11. The γ grain morphology and dendritic growth morphology revealed a pronounced tilt by approx 44° in their columnar growth direction away from BD and towards the specimen free surface, TD. The grains located in region (a) have grown epitaxially from the substate and appear to have grown along the <011> direction, however as schematically shown in Figure 6.11c, due to the curvature of the melt pool it would be expected that these grains are growing preferentially along the <001> crystal direction. The fibre texture direction of these grains is similiarly tilted away from BD and towards the specimen's free edge by approx. 43° (Figure 6.11ai). The grains towards the centre of the melt pool appear to have a semi-strong cubic texture with the nucleation of new grains being the favoured competitive growth front. The grains solidifying adjacent to the free edge of the melt pool will have significantly different morphology to the grains located within the centre of the fusion zone. The grains in region will experience a higher cooling rate due to the surrounding thermal mass, resulting in comparably different thermal gradients and solidifcation conditions to those in region (b).

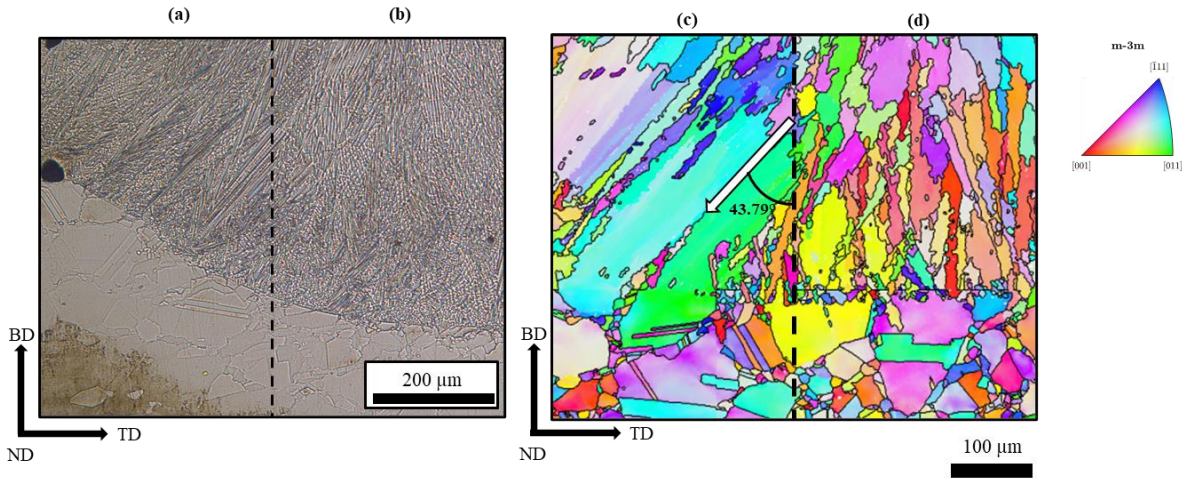

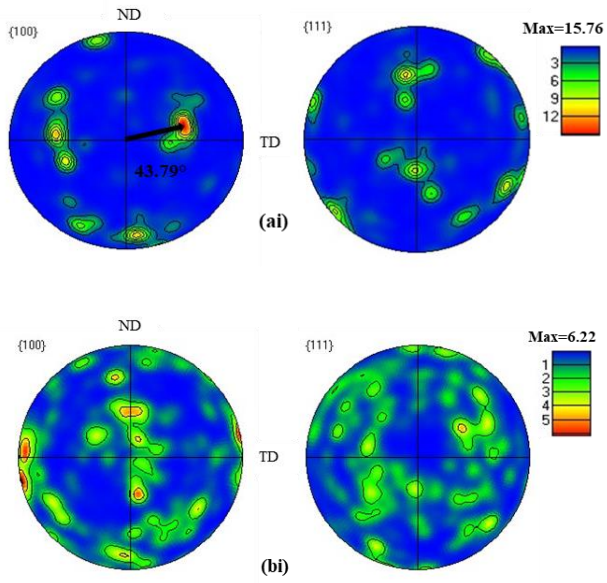

Figure 6.11 (a-b) Optical micrograph of cross-sectional melt pool for 750W adjacent to specimen edge (c-d) associated IPF map detailing the degree of tilted grains with (ai-bi) associating pole figures for the grain areas of (a) and (b), respectively.

The behaviour as seen in Figure 6.11 with the dendrite trunks growing preferentially with the <100> crystal orientation and a presence of <001> fibre texture was observed by Moat *et al.* [363] and Dinda *et al.* [111] with their work of LMD of Waspoloy and IN718, respectively. In Moat *et al.* study [363], the <001> fibre axis was found to be tilted away from growth direction (BD) i.e. perpendicular to beam travel direction (ND), by an amount which varied with process conditions. This effect was attributed to the unidirectional scanning pattern used and curvature of the rear of the melt pool, which changed with different process conditions. Due to the lack of overlap that existed at the FZ between the two adjacent tracks deposited using 750 W, the curvature at the edge of the melt pool was more prominent and at a higher degree of tilt than if sufficient overlap existed between two adjacent tracks whereby grains located towards the edges of the FZ have a more complex tilt due to the remelting and re-solidifcation effect towards the next adjacent maximum thermal gradient. Even with sufficient overlap such as in the case of 950 W, it would be expected that the grains located at the edges of the entire build profile i.e. outer edges of track 1 and track 10, would have morphology that close to those in region, Figure 6.11a.

6.8 Dendritic Growth Behaviour

The backscattered electron images of the as-LMD IN718 samples show an intragranular, dendritic structure with the darker grey austentic phase and the bright interdendritic material forming long-chain networks of Laves phase (Figure 6.12). The results of the associated SEM EDS elemental line composition and point ID maps for dendrite analysis

are shown in Table 6.1. As expected, the γ' and γ'' phases cannot be resolved at the low magnification SEM due to the very high cooling rates experienced during the deposition, resulting in very fine precipitates [368]. The samples investigated in Figure 6.12 are from the interface region at the cross section deposited using the 950 W laser power. The coloured boxes defined the regions of interest with associated higher magnifications and the BSE vs SE micrographs as depicted in red, highlight the contrast of local variation in composition.

Figure 6.13 shows the composition analysis of the dendritic and interdendritic regions of Figure 6.12. Line scans reveal a clear migration of solute elements, with dendrite cores enriched in nickel, chromium, and iron, while interdendritic boundaries and eutectic products exhibit enrichment of niobium, molybdenum, and titanium. These micro-segregations are consistent with the solidification sequence observed in previous studies. Elements with partition coefficients (k) less than 1, such as Nb, (0.525 [369]) tend to segregate to the dendritic boundaries, promoting the formation of Laves phase. Experimental findings indicate that the Nb content in the interdendritic region should exceed 20 wt.% [370] for Laves phase formation, which aligns with the measured Nb content from the EDS analysis. The presence of molybdenum enhances the formation of Laves phase, as reported in the literature. Similar segregation patterns have been observed in LMD of IN625 [364].

During γ dendrite formation, there is an enrichment of the remaining liquid with Nb, and the presence of carbon can lead to the formation of NbC in the interdendritic region through an eutectic reaction [370]. The interdendritic liquid becomes enriched with carbide-forming elements, resulting in the formation of MC carbides. The eutectic reactions occur at temperatures ranging from 1280-1265°C for NbC precipitation and 1160-1075°C for Laves phase formation. The interface region of LMD IN718 exhibits a significant number of γ/Laves eutectics, which is considered a predominant minor microstructure feature. Formation of NbC precipitates is limited in the first layer of deposition. The Laves phase forms in the interdendritic region due to solute rejection during solidification, exhibiting island-like morphology at the bottom region and network-like morphology propagating in the build direction. The composition of the Laves phase typically consists of (Ni, Fe, Cr)2(Mo, Nb, Ti) which locally depletes the Nb needed for the strengthening γ'' (Ni_3Nb) phase [371]. Many researchers have studied the formation of Laves phase and its effects on the mechanical properties of the superalloy by experimental or calculational methods. Sui *et al.* [372], [373] found that there were

many hard and brittle Laves phase existed in the deposited region, which were the main causes for microscopic cracks which can result in ductile failure. Liu *et al.* [374] demonstrated that the large amount of brittle Laves phase precipitated in the interdendritic due to the Nb segregation, resulting in a decrease of mechanical performance. Tabernero *et al.* [375] concluded that cracks formed easily in the deposition area due to the Laves phase and the mechanical properties could only reach 75% of the forged material. The existence of Laves phase is deemed harmful to LMD IN718 superalloy.

The results show a significant increase in the Nb content, from less than 5% in the γ-dendrite bulk core to nearly 20% at the interdendritic boundaries. This indicates that Nb is prone to segregation during LMD of IN718. The depletion of Nb in the dendritic core and its enrichment in the interdendritic regions, particularly the liquid surrounding the Laves phase, is of critical importance. Nb is a crucial component in the γ'' strengthening phase, which plays a key role in enhancing the mechanical properties of IN718 through coherency strain hardening. Therefore, the distribution and behaviour of Nb control the formation of γ'' and its volume. The segregation of Nb towards the interdendritic region promotes the formation of the brittle intermetallic Laves phase. The interface between the Laves phase and the γ matrix is known to be a preferential site for crack initiation and propagation, leading to significant degradation in mechanical properties [37], [376]. Achieving the appropriate post-manufacturing heat treatment becomes challenging when dealing with an optimized parent material and treatable deposited material, as any additional heat treatment would impact both regions.

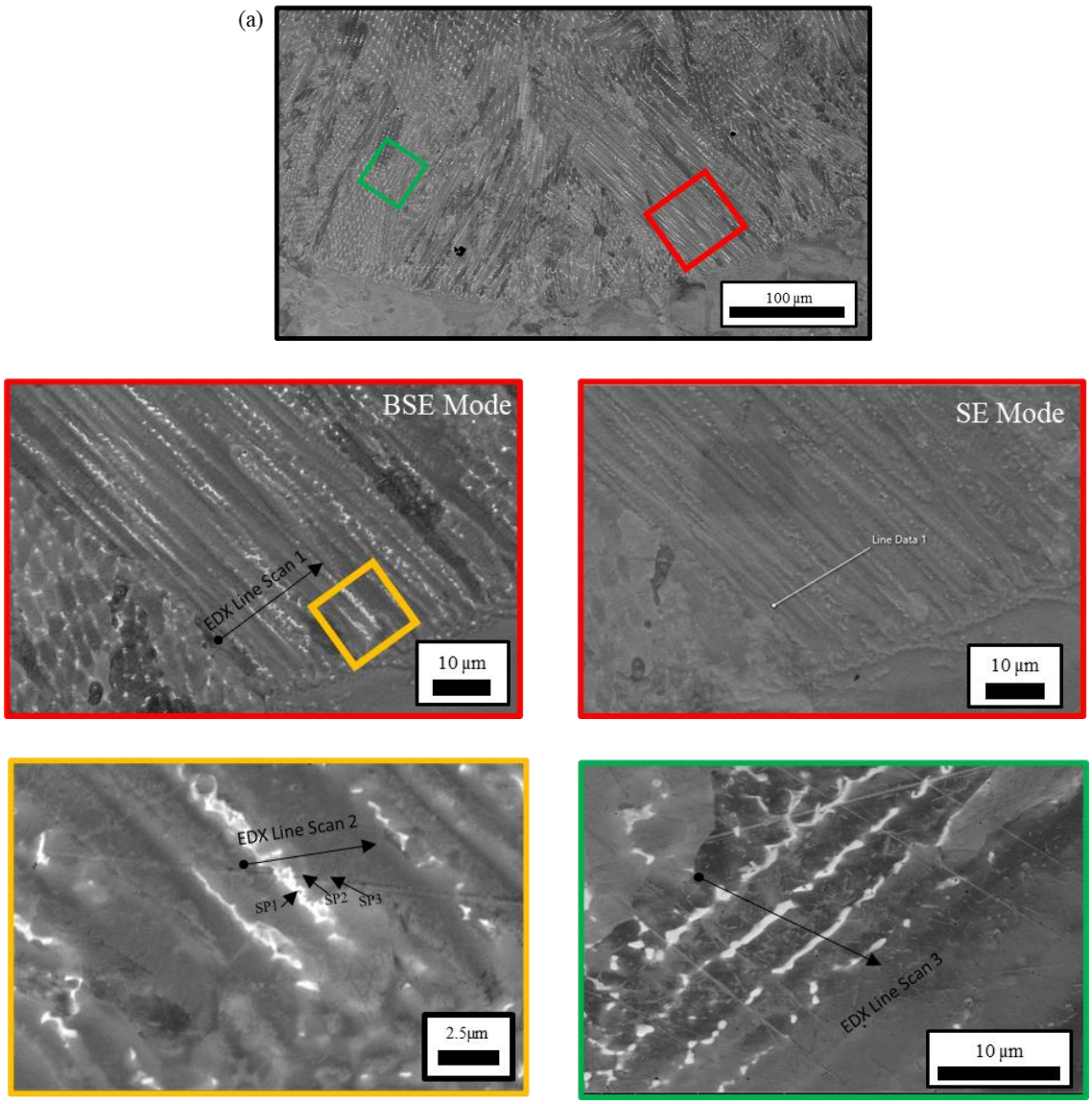

Figure 6.12 (a) Dendritic morphology located at the substrate-deposit interface for the high laser power with higher magnification location dependent compositional analysis as depicted by the coloured boxes.

Table 6.1 EDS Point scan chemical composition of various regions in Figure 6.12.

Spectrum	Phase	Al	Cr	Fe	Mo	Nb	Ni	Ti
SP1	*Laves Phase*	0.7	15.2	14.2	4.1	19.6	44.4	1.5
SP2	*Nb-enriched surrounding liquid*	0.8	16.2	15.2	4.0	13.8	48.4	1.6
SP3	*γ - matrix*	0.5	19.7	20.2	2.9	2.8	53.3	0.7

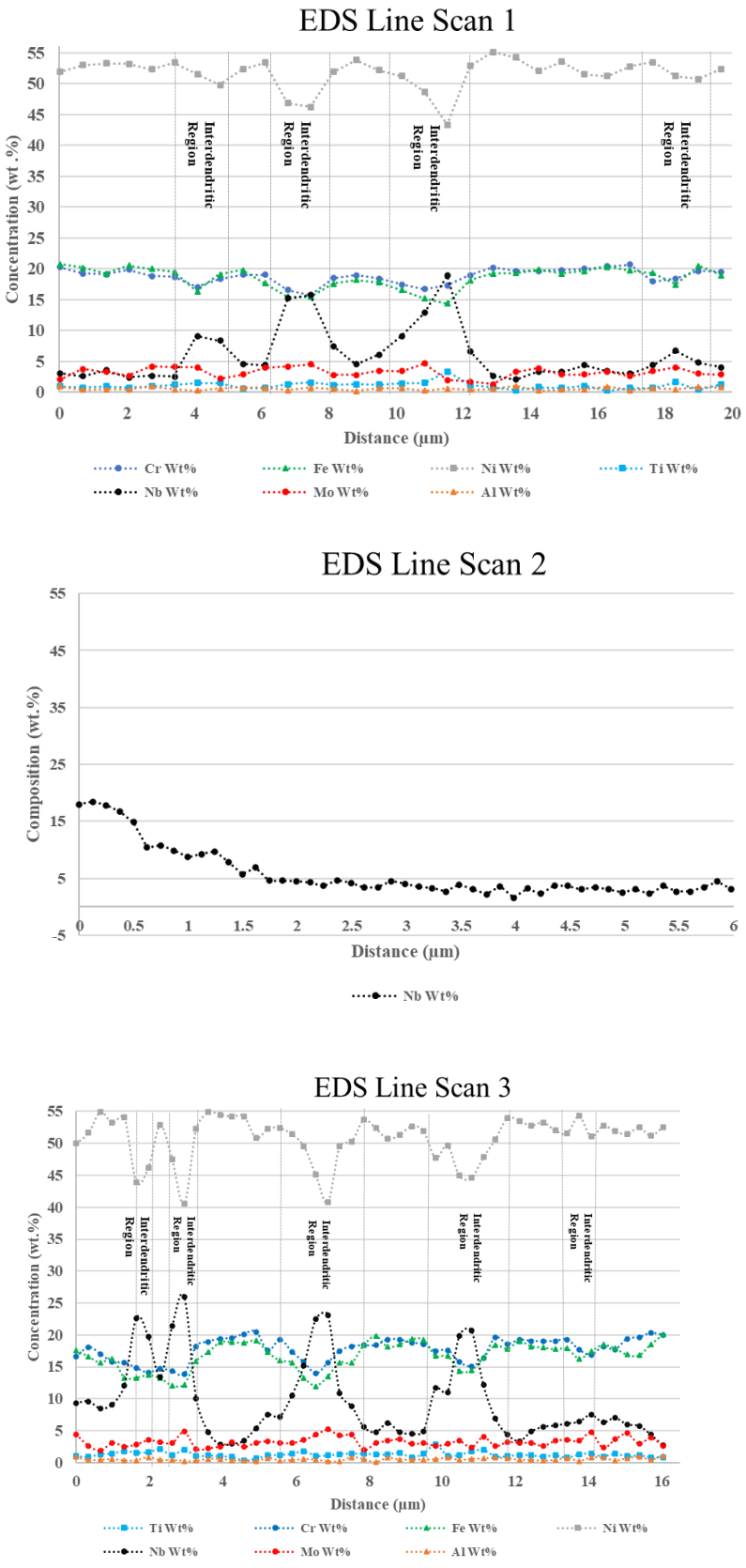

Figure 6.13 EDS line scan results retrieved from EDS Line Scan 1,2 and 3 in Figure 6.12.

The high cooling rates associated with LMD (10^3-10^5 °C/s) [155] processing make the spacings of columnar sub-structures shorter with enhanced cooling rates. The dendritic

spacing of around 5µm was associated with the high cooling rates [377] during LMD but more detailed cooling rates can be calculated from the Primary Dendrite Arm Spacing (PDAS). As expected, temperature measurements from the interface region show that low HI condition have a higher cooling rate at higher temperatures comparative to higher laser powers used in the study. The cooling rates were compared to the temperature history plots for the interface region in each process condition whereby the cooling rate was taken as the average moving cooling rate, time taken for the localised region to cool from melting (1335°) to final solidification at ~1170°C [378]. The PDAS was measured at the fusion line for the three conditions. Measurements taken from the melt pool fusion line were used to obtain the cooling rate:

Equation 6.1

$$\lambda = \frac{80}{\varepsilon^{0.33}}$$

Where the PDAS is denoted as λ in µm, and the cooling rate, ε, is in °C/s. This equation developed by Katayama and Mastsunawa [379]. The equation was developed for high cooling rates and assumed relevant for the case in this alloy. Figure 6.14 depicts a SEM analysis of the precipitation structure of the LMD specimen detailing several measuring points on the cross-sections at the interface region between the substrate/deposit boundary. Quantification of the PDAS was determined by averaging the spacing between the interdendritic channels as detailed by the red arrows in Figure 6.14. The PDAS were measured from 3 separate tracks in all three process conditions with 10 measurements taken from each to get an average and standard deviation as represented in Table 6.2.

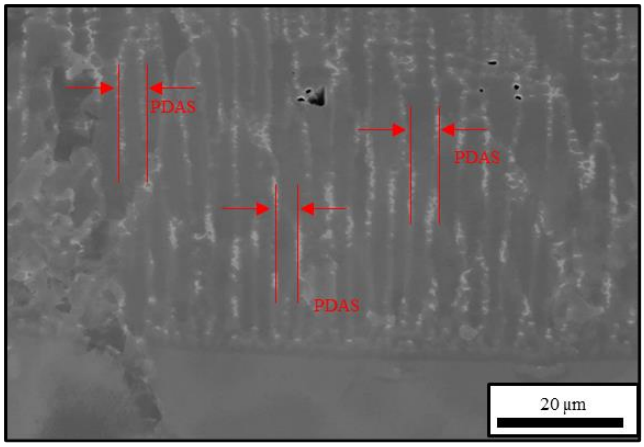

Figure 6.14 Microstructure morphologies and depiction of measured primary dendrite arm spacing (PDAS) of the cross-sectional as-deposited microstructure at the interface region.

Table 6.2 Measured cooling rates from the PDAS calculation from all three process conditions in simulated model.

	Low HI	Medium HI	High HI
PDAS (µm)	5.39	5.52	6.44
Standard deviation (µm)	0.75	1.16	1.06
Calculated cooling rate (°C/s)	2389.7→5590	1850→6770	1305→3576.2
Thermomechanical Calculated cooling rate (°C/s)	4300	2600	1200

The cooling rates estimated from PDAS measurements align well with the thermomechanical model. The cooling rate predicted by the thermomechanical model falls within the range of the cooling rate calculated using PDAS. The cooling rate for the low HI sample was the highest, as expected. With increasing the laser power, the volume of the melt pool increased and therefore during LMD, the high HI sample is expected to take the longest time to reach final solidification temperature due to the volume of thermal energy associated with the localised point (substrate/deposit boundary) of the melt pool and surrounding liquid. The cooling rates measured from Equation 6.1 generally agree with the moving average cooling rates associated with the thermal model. Discrepancies between the thermal model cooling rate and calculated cooling rate from PDAS could be due to the refinement of mesh used at the substrate/deposit interface meaning a larger average area was associated in the thermal model. Moreover, discrepancy between the results is due to the limitations of all thermomechanical models whereby assumptions are made to simplify computational time. The extent of micro segregation which causes localised supercooled regions which were used to measure PDAS were not considered in the model.

6.9 Precipitation behaviour at the interface for LMD of IN718

6.9.1 As-deposited LMD of IN718

Figure 6.15 depicts the cross-sectional interface boundary of the 950 W specimen in an etched state. Notably, Nb-rich carbides with irregular morphologies are commonly observed, dispersed randomly throughout the substrate. This suggests that these carbides formed during the solidification process. These solid solution carbides, characterized by a high melting point of 3600°C [380], were found near the substrate/deposit interface, even within the fusion zone deposited at low laser power. Consequently, the interface region experienced temperatures ranging from 1336°C to 3600°C during LMD. The presence of these carbides, originating from solid-solution formation and considering the rapid cooling rates associated with LMD, indicates significant metallurgical intermixing

between the deposit and substrate within the melt pool. Given that temperatures did not surpass the carbide melt temperature and considering the complex flow dynamics inherent in LMD, it can be inferred that the entrapment of NbC from the substrate in the fusion zone underscores a robust metallurgical intermixing process, with turbulent buoyancy forces pushing the carbides further into the fusion zone during solidification. These Nb-rich carbides were consistently observed across all specimens investigated in this study.

Furthermore, small cubic TiN precipitates are visible in Figure 6.15.b. TiN precipitates typically form at temperatures exceeding the liquidus temperature of IN718. In addition to these, both irregular and regular (small) (Nb, Ti) C carbides, as well as a mixture of carbides, were observed in the interface region. It is posited that the irregular carbides and the carbide mixture formed during solidification, whereas the regular carbide precipitates originated from the matrix in the solid state.

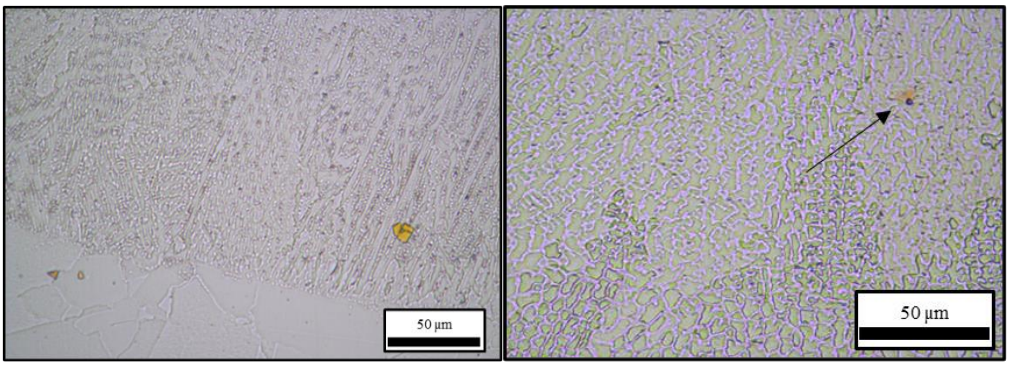

Figure 6.15 Optical micrograph of the substrate/deposit interface region for the low laser power showing the NbC carbides (yellow block-like morphology) and (b) TiN precipitates with grey appearance.

Figure 6.16a shows the typical primary and secondary phases in double aged IN718 material phases needed for aerospace applications. It can be seen at relatively low magnification (~10,000x) in BSE mode, the presence of solid-solution carbides, grain-pinning δ-phase and homogenously distributed γ’’/γ’ strengthening precipitates. The bright white interdendritic channels with irregular structure in the backscatter electron image in Figure 6.16(a-d) indicate the presence of a heavier element (Nb) compared to the rest of the matrix that is richer in a lighter element (Ni). Microstructural studies were performed for the interface region of the 950 W laser power to assess the microstructural heterogeneity in the precipitate structure, especially with respect to γ’/γ’’, Laves, and carbide phases. Figure 6.16b shows the Laves phase morphology in abundance at the interface which details an irregular island morphology which has precipitated below the channel network morphology of the interdendritic regions. In the as-deposited state, the

areas surrounding the Laves phase exhibit an enrichment in Nb compared to the matrix, albeit lower than the precipitate content, as evidenced by the EDX investigation. These regions, depicted in Figure 6.16c, may be conducive to the formation of aging precipitates. It is anticipated that these regions are in an under-aged condition with poor dispersion. Nevertheless, Figure 6.16d reveals a higher magnification of the channel-like network of interdendritic Laves, displaying faint small precipitates gathered at the interdendritic regions measuring below 500 nm. The disparity in chemical composition provides a clearer insight into potential strengthening phases; however, a more in-depth examination using TEM would be necessary for clarification.

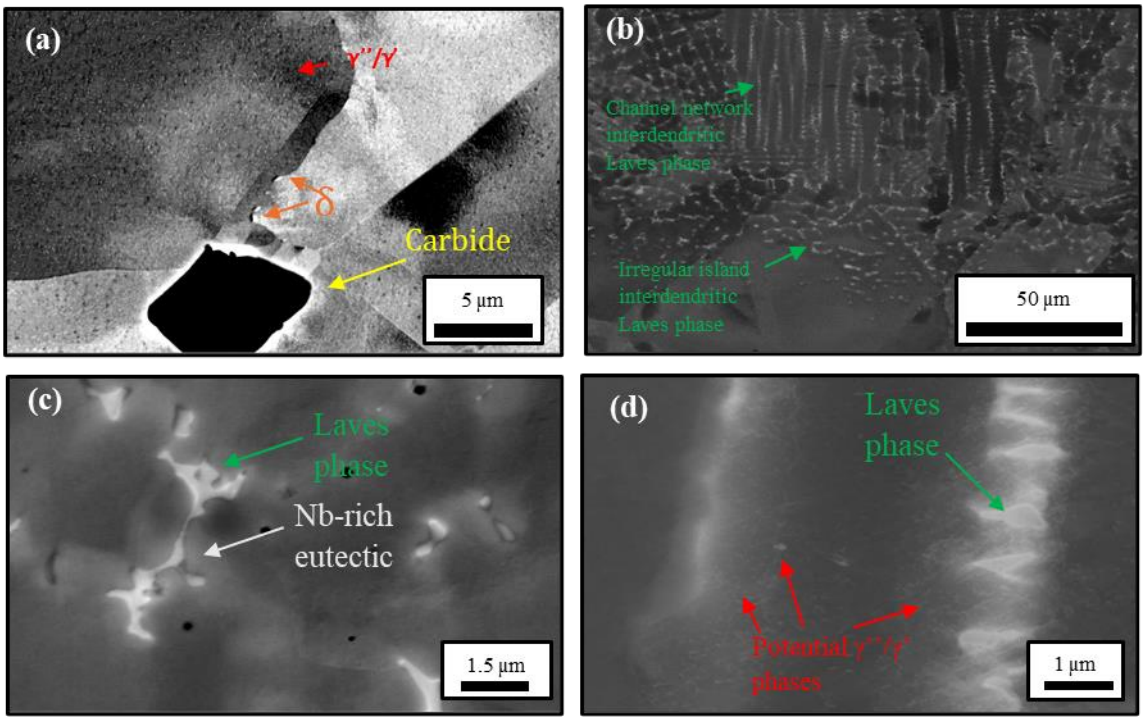

Figure 6.16 BSE micrographs of the intermetallic phases in (a) the substrate, (b) the interface region of the high laser power, and (c) the irregular island Laves phase at a higher magnification, (d) the channel Laves phase at a higher magnification

Furthermore, Figure 6.17 illustrates FEG-SEM micrographs showcasing a different track to Figure 6.16, in the as-deposited cross-section of the fusion zone for the 950 W block specimen. Lamellar and irregularly shaped precipitates, identified as Laves phase, were observed in the micrographs. Upon closer examination at higher magnification, γ'' and γ' precipitates were noted around the Laves phase. While TEM analysis would be necessary to confirm these precipitates, it falls beyond the scope of this project. Nevertheless, based on morphology, size, and EDS results in Figure 6.12, which indicate a high concentration of Nb (>6 wt.%) up to 1.5 µm from the Laves phase, it can be inferred

that these precipitates are indeed present. Additionally, needle-like phases observed growing within the Laves phase (Figure 6.17c) may plausibly be identified as the δ-phase.

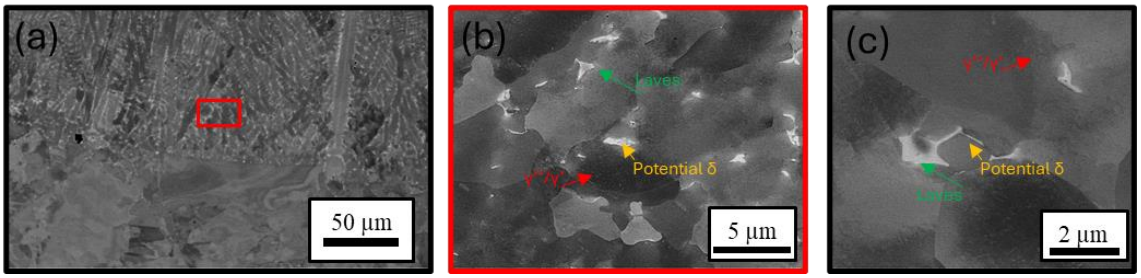

Figure 6.17 FEG-SEM micrographs of the as-deposited IN718 at the fusion zone with (a) detailing an overview location and (b, c) increased magnification to show the secondary phase formation.

Through analysis of thermal history and microstructure, the holding time within the precipitation band for the δ phase was correlated with image analysis of the fusion zone. It is established that δ phase precipitation occurs within the temperature range of 780°C-980°C when aging time is less than 100 h, with the fastest precipitation rate observed at 900°C [381]. Figure 6.18 presents localized thermal cycles for the interface region, as measured using the thermomechanical model, indicating a holding time of approximately 14 s for the δ-phase precipitation band. Idell *et al.* [382] detected platelet-like precipitates at interdendritic regions using TEM and concluded that the δ phase can form and grow where Nb concentration exceeds 6.8% molar fraction [382]. Nonetheless, due to the deposited cooling rates experienced at the fusion zone interface and the limited time under the precipitation band, further analysis via high-resolution FE-SEM/nano-SEM or TEM is necessary to conclusively ascertain the presence of these precipitates.

Furthermore, thermal history and microstructure analysis, one could interpret this cycle to be close to typical aging heat treatment of deposit. The temperature readings indicate that the time within the 600°C - 800°C range, where γ''/γ' precipitation is favourable, was only about 90 s in total. This duration is significantly shorter than the usual aging heat treatment time. From these thermal measurements depicted in Figure 6.18, during the deposition of successive layers, the 1st layer goes through the γ'/ γ'' precipitation window for the entirety of ten thermal cycles. It would therefore be expected that the hardness in the 1st layer to be progressively higher than following deposited layers given the time to precipitate strengthening phases. However, this behaviour was not evident from the measured hardness values in Figure 7.22. Contrastingly, it is plausible that, even though the 1st deposited layer passes through the γ'/ γ'' precipitation window multiple times, the cumulative time that it spends within the precipitation window is inadequate to

have significant impact on the growth of γ''/γ' and therefore, the hardness values. It should also be noted that at the interface region, temperatures well above γ'' solvus were endured with the repetitive thermal cycles. A normal TTP-diagram for γ'' precipitation is empirically gathered from heat treatments for homogenous material with nominal composition and does not consider compositional changes due to segregation. A TTP diagram for the γ' and γ'' phases in LMD 718 were plotted by Segerstark *et al.* [383] using complementary elemental data from JMatPro. It was concluded that the precipitation kinetics of the strengthening phases were significantly increased closest to the Laves phase and estimated a precipitation time of 30 s for 0.5wt% of γ'' to form.

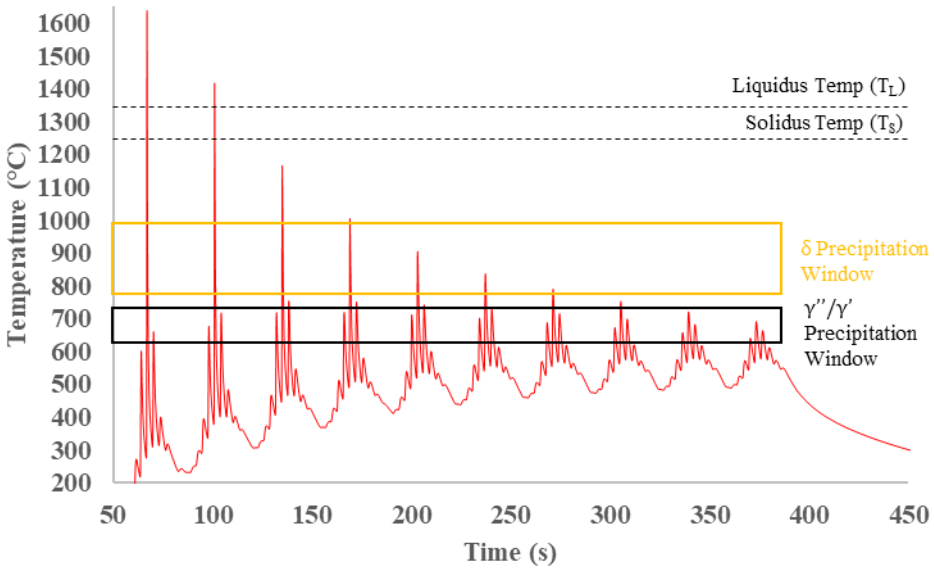

Figure 6.18 Temperature history from the bottom region at the interface for the 950W laser power.

It can be speculated that the γ'', γ' and δ phases precipitated owing to the heat accumulation of the successive deposition and continuous heat input from the surrounding material. Thus, this phenomenon has been experimentally understood to occur in deposits manufactured by WAAM process. The relatively high heat input of WAAM induced heat accumulation causes a longer precipitation band and slower cooling rates comparative to the LMD process [384]. To understand the δ-phase grown from the interdendritic Laves phase, Kuo *et al.* [385] subjected LMD produced Alloy IN718 to a solution treatment (ST) of 980°C for 1h. TEM images of the as-built specimen revealed discontinuous δ phases measuring 47-70 nm distributed in the grains and arrayed along the grain boundaries. The δ phases of the ST subjected material began to aggregate and coarsen in the interdendritic region growing an order of magnitude larger (approx. 400-

705 nm). As mentioned, the utilization of TEM would be needed to detect δ-phase in the interdendritic regions of the LMD deposited specimen.

Parimi [155] noted very small globular precipitates (around 200-300 nm) with a disk-shaped morphology in the Nb-enriched liquid located in the bottom, interdendritic region of as-deposited IN718. A line scan showed that the phase was rich in Ti, Nb and Al, the principal elements of the γ'. However, these were too small to accurately measure the composition to confirm them to be γ' with the need of TEM. Additionally, Tian *et al.* [255] built blocks of 12.7 mm using a similar laser power, 550 W, to that used in this project. Under ultra-high magnification, mottled white contrast was observed in the matrix near the eutectic products were characterized using TEM. It was concluded that most of the precipitates measuring 15 nm average are predominantly γ'' in the as-deposited builds. A higher precipitate density was found closer to the interdendritic boundary which is attributed to the partial dissolution of the Nb-rich eutectic products during subsequent layer addition, surpassing the solidus temperature (T_s). This finding was backed by Segerstark *et al.* [383], where results from a FEI Nova NanoSEM 450 with high-resolution field emission gun (FEG) showed nano-sized γ' and γ'' at very close proximity to the Nb rich constituents in the interdendritic regions with no strengthening phases in the dendritic core. This localised enrichment of Nb near along the interdendritic eutectic products is expected to increase the driving force of nucleation with the precipitate size and number density decreasing drastically with increased distance from the eutectic region to dendritic core.

6.9.2 Heat-treated LMD of IN718

To enhance the mechanical performance of the interface region, the specimens were subjected to a heat treatment described by Barron [386] and used in commercial practice (AMS5596C) [12] to enhance the mechanical performance of the interface region. The heat treatment consists of 1 h solution treatment (954°C) and air cooled, which will dissolve all the γ' and γ'' while at the same time precipitating a limited amount of δ-phase to control grain growth by pinning grain boundaries. Followed by ageing of 760°C/5h – furnace cooled + 650°C/1h – air cooled. This heat treatment is common practice, originally developed for repaired jet engine components to prevent coarsening of γ'' precipitates in the parent component. Figure 6.19 depicts an SEM micrograph illustrating the grain structure at the interface following the heat treatment.

All heat-treated specimens evaluated in this study exhibited similar phase compositions regardless of deposition power. The interdendritic regions in the deposited region formed

needle-like plates with a Widmanstatten structure, measuring around 1-3 μm and the irregularly shaped Laves phase with columnar channelled morphology were dissolved as seen in Figure 6.19 (a-c). Areas of the dendrite cores were darker in appearance comparative to the γ-matrix due to the difference in atomic number contrast as compared to the γ-matrix surrounding the interdendritic regions.

Since the temperatures during the heat treatment did not exceed the homogenization treatment temperature (approximately 1100°C) and remained below the solution temperatures (around 980°C), the grain structure within both the substrate and deposit areas largely retained their original morphology. The grain structure initially present in the deposition process remained consistent, maintaining epitaxial growth across multiple layers, particularly within the predominantly equiaxed substrate.

The substrate's grain structure remained unaltered as the heat treatment applied remained below the δ-solvus threshold [387]. Furthermore, the original grain structure of the deposition process remained unaffected, as the heat treatment temperature remained below both the solution temperature range (980-1030°C) and the reported static recrystallization temperature of 1020°C [388], thereby preserving any δ-phase nucleation occurring during subsequent heat treatments in LMD.

Research indicates [389] that even after subjecting the material to a 1 h homogenization treatment at 1080°C, Laves phase formation and elemental segregation, which occurred during additive manufacturing, persisted without complete dissolution, leaving the original texture and grain structure unaffected. However, a complete recrystallization and stress relief, resulting in equiaxed grain morphology within the deposited region, were achieved following a 4 h homogenization treatment at 1080°C [390]. Furthermore, a post-weld standard solution treatment and ageing treatment (STA) (980 °C, 1 h/air cooling) (720 °C, 8h/furnace cooling to 620 °C, 8 h/air cooling) of LMD IN718 was reported to have improved mechanical strengths of STA heat comparable to the wrought material, while the ductility dramatically decreased due to the precipitation of fine γ′ and γ″ phases in the austenitic matrix and needle-like δ phases in the grain interior and boundaries due to the micro segregation behaviour of alloying elements [391].

Upon higher magnification the precipitates seem to be more developed closer to the δ-phase, precipitating from the as-deposited Laves phase. Given their needle characteristic morphology and the results from EDS, these precipitates are confirmed as (Ni_3Nb) δ-phase. Although referred to as needle shaped, these precipitates are likely to be more

plate-like when viewed in 3D with only the thin 0.2 µm in width edge and one long side visible. Interestingly, subjecting the specimens to 954°C for 1h has had the ability to dissolve the channel-like morphology of networked Laves phase to particulate microstructure with majority of the content dissolved. To completely dissolve the Laves phase and promote a homogenization distribution of alloying elements would require temperatures exceeding 1150°C [392]. However, similar to Liu *et al.* [393] the Laves phase had "broken" from continuous and long strip shape Laves formed in the interdendritic channels to large granular shape with the networked channels being serrated by the δ-phase into pieces and these Laves phases are dissolved more easily and rapidly to smaller granular shape. This "cutting" effect is demonstrated in Figure 6.19c, where the lateral direction of the δ phases are seen precipitating close to the Laves phase and in the interdendritic region of the as-built microstructure. A possible reason for this result could be the change in local driving force for precipitation of the δ phase in the regions due to local segregated composition [394]. During the solution heat treatment, Nb is released due to the dissolution of Laves phase with a tendency to diffuse to the localised surrounding interdendritic areas, promoting the nucleation and growth of δ-phase. This is in good agreement with Kumara *et al.* [394] study who modelled the transformation kinetics showing that the δ-phase was predicted to precipitate due to elemental segregation during a solution heat treatment of 954°C for 1h.

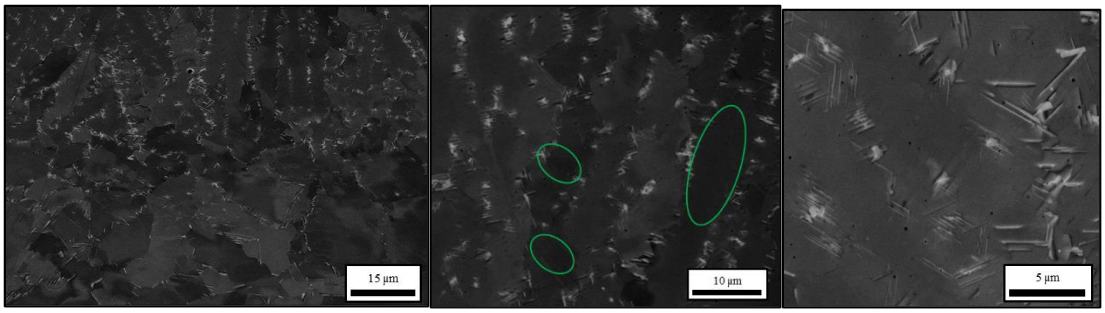

Figure 6.19 SEM Image of the laves phase regions post-heat treatment in LMD IN718 (a) the extent of morphology transition across the interface region with (b) detailing the dissolution of channel-like Laves in the interdendritic regions and (c) Widmanstatten needles precipitating from the Laves phase in the deposit LMD structure.

Figure 6.20a illustrates the niobium content (Nb wt. %) obtained from a compositional line scan spanning approximately 15 µm across dendritic and interdendritic regions in all three laser conditions. Consistent with the as-deposited specimens, the line scan demonstrates that the Nb content is lower in the centre (2-5.5 wt.%) of the dendritic core compared to the interdendritic regions, as anticipated due to micro segregation. Figure 6.20b & c depict the Nb content (wt. %) spanning from the dendrite core to the

interdendritic region in the heat-treated 550 W specimen. The significant rise in Nb content towards the end of the line scan indicates localized enrichment persisting in the interdendritic region, which facilitated the precipitation of the δ-phase. It has been documented that the formation of the δ-phase necessitates a Nb content ranging between 6-8 wt.% [395].

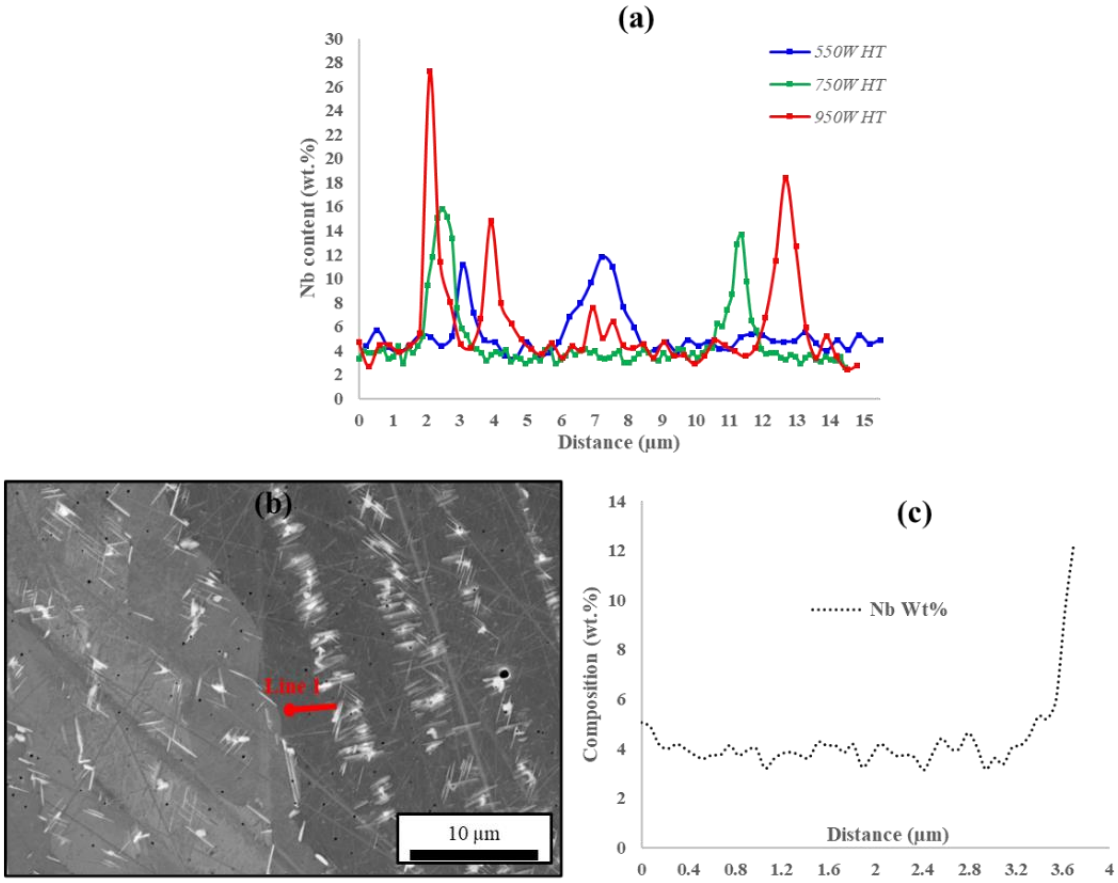

Figure 6.20 EDS Nb content line scan across the dendrite core and interdendritic regions for heat treated samples in (a) all three laser conditions and (b, c) detailing the EDS line scan from the dendritic core towards the interdendritic channel in the 550W specimen.

The EDS line scan results (Figure 6.20a) demonstrate the influence of laser power on localized alloy segregation across interdendritic regions and dendrite cores. Analysis of niobium behaviour reveals persistent segregation in the as-deposited samples even after heat treatment, with the 950 W specimen exhibiting the most significant enrichment in interdendritic regions compared to the 750 W and 550 W specimens. It could be argued that a reason for this could be due to the combination of increased dendrite arm spacing (which is denoted by physical spacing between the spikes in Nb content for each laser power) due to slower cooling rates encountered by the increased laser power resulting in a slightly higher fraction of Nb-rich constituents in the HI interdendritic regions. The higher segregation of Nb and increased diffusion distance are the result of more time for

the Nb to diffuse through the matrix evenly. If unevenly distributed, Nb could contribute to an uneven precipitation behaviour of strengthening precipitates given the dependency of Nb to precipitate. An uneven distribution of strengthening phases could incur problems during service since the higher Nb-content in the interdendritic regions would accelerate the coarsening of γ''. In the meantime, the γ'' would coarsen at a slower rate in the dendritic core. Such discrepancies in strengthening precipitate content could lead to uneven distribution of strain and strain concentrated areas in the material [383], eventually leading to detrimental failure if the strain surpasses the materials maximum strain. Further investigation is required to draw conclusions on the effect of uneven distribution of strengthening precipitates has on the mechanical properties of the material.

Figure 6.21 shows a high magnification of the interdendritic region in the fusion zone for heat-treated 750 W deposit. The larger bright phases with acicular morphology, measured around 100nm in width and are the precipitated δ-phase from prior Laves. Upon closer examination, the smaller indistinctive morphology phases are believed to be the γ'' phase given their brighter appearance due to the presence of heavier atomic element of Niobium. The post-weld heat treatment aging duration was shorter than standard aging time for IN718, meaning the elements would have less time to diffuse and congregate to form γ'', therefore only measuring approx. 10-50 nm in width. Moreover, their volume density area acts as evidence of their presence with none to very few precipitating close to the δ-phase and more densely populating as the distance from the δ-phase increases, as depicted by the white arrow in Figure 6.21. Due to the heat treatment, the γ'' coarsening was prevented in the base material and a more homogenous distribution of γ'' phases were present across the interface region from the deposition region (Figure 6.2a) into the base material (Figure 6.2b). Given their size, TEM analysis would be beneficial to concrete this abundant phase in both the substrate and deposit.

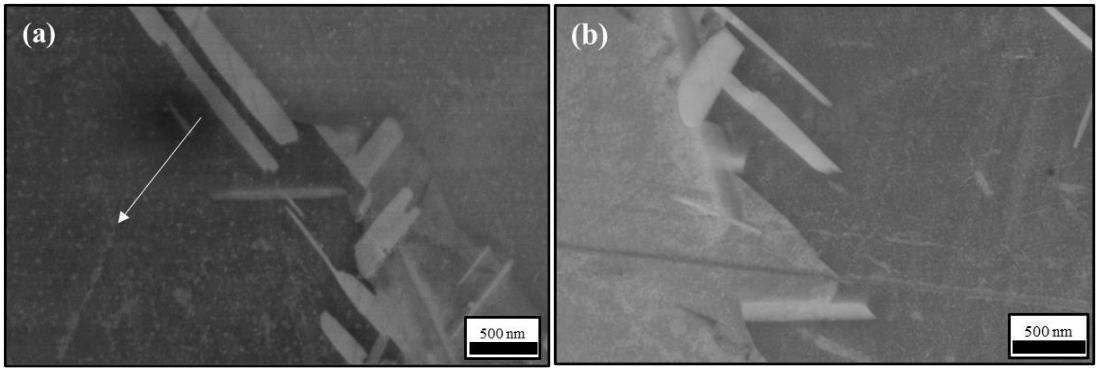

Figure 6.21 BSE-SEM of the precipitate formation in the (a) deposited sample using 750W and (b) the base substrate.

Li *et al.'s* [396] investigation into the effect of varied heat treatments on microstructural evolution of SLM Inconel 718 agreed with some key microstructural findings in this study. The microstructure of the directly aged treatment showed a similar response to as-built condition consisting of columnar dendrites and regularly distributed needle-like δ phase in the Nb-rich interdendritic regions. Nanoscale γ' and γ'' phases precipitated from γ matrix during the DA treatment. The maintained large-scale micro segregation and high fraction of δ phases degrade mechanical properties such as creep.

The metastable γ''-phase is replaced by the incoherent δ-phase with the same Ni_3Nb composition at temperatures above 750°C. Increasing temperatures above 750°C causes the coherency of γ and γ'' to be reduced as the conversion reaction of γ/γ''→ δ accelerates [397]. Particle-shaped δ-phase grows into acicular shape due to the solution treatment at the δ-subsolvus temperature of 980°C. Performing a solution treatment of 954°C/1h was selected for the LMD IN718 specimens in this study to prevent the coarsening of γ''/γ' phases in the substrate and enhance a homogenous distribution of γ'' preferential sites during subsequent direct aging in the deposit region, however a two-fold penalty of γ'' replacement by δ-phase and the acceleration of δ-phase precipitates to δ acicular needle, which occurs between 815 to 980°C [398] was obtained in the specimens.

This change in morphology leads to poorer creep resistance because the particle shaped δ-phase has lower energy than the needle δ-phase, meaning the incoherent particles would easily open up and form cleavage cracks rather than voids [398]. A small amount of δ phase would inhibit grain growth in the repaired section by pinning the grain boundaries which could uphold the increased strength and hardness through grain refinement [399]. However, given the extent of plate-like δ-phases, the strength of the alloy would be decreased since the formation of δ phases consume the Nb inhibiting the precipitation of strengthening γ'' phases [400].

Achieving an appropriate post-deposition heat treatment becomes more challenging when the base material already possesses the desired microstructural condition for service. However, the post-deposition heat treatment selected in this study successfully prevented the coarsening of γ'' precipitates found in the base material and inhibited grain growth by preserving the grain boundary pinning effect controlled by the δ-phase.

As per Thompson [401], subjecting specimens to a homogenization temperature (approximately 1065°C) surpassing the δ-solvus (1010°C) aids in Nb diffusion into the γ matrix and partially dissolves the Laves phase still bound at the grain boundary. However,

this process also dissolves the δ-phase responsible for controlling grain size in the substrate, leading to undesirable grain growth, and compromising base mechanical properties.

6.10 Chapter Summary

The as-deposited grain morphology, crystallographic texture, dendritic morphology and phase morphology have been investigated to develop our understanding of the microstructure evolution that occurs across the interface region during LMD of Inconel 718 for repair applications. These results provide an overview of the as deposited and post-deposited heat treatment microstructural features of as it evolves from the substrate across the interface region to the deposited area. Based on these findings, an optimised as-deposited microstructure through varied LMD process parameters will be described in the following chapter of this work as conclusive correlations will be drawn from process parameters to *in situ* temporal evolution and to what effect this has on the interface region. Integral points of this chapter include:

1. During LMD of IN718, a bright white band delineates the PMZ/HAZ, often noted as the mushy zone which is a result of the chemical etchant making the investigation of γ-austenite grain morphology difficult with OM imaging, therefore requiring EBSD data. Due to the temporal temperature evolution, the extent of microstructural features affect will be investigated in each LMD in the following chapter.
2. Multi-layered as-deposited LMD IN718 microstructure is characterized by long columnar epitaxial γ grains growing several millimetres in length aligned in the build direction. The dominant orientation of these grains is a <001>//BD fibre or cube texture depending on laser power.
3. During the deposition of each track, the large thermal gradients aligned perpendicular to the curved melt-pool facilitating epitaxial growth phenomenon. As the thermal gradient reduces through the build direction of the melt-pool, a shift in morphology is noted from epitaxial growth to heterogenous grain nucleation. These grains are much finer in scale (≈42μm) compared to the columnar epitaxial grains and are equiaxed in morphology. The presence of these grains in both single track layers and multi-layered deposits are consistent with the interdependence model, with their formation requiring nucleation potential from partially melted powder particles in a region of supercooled liquid ahead of the solid-liquid interface. The crystallographic pole figures of the heterogeneously

nucleated grains reveal a <001>//BD fibre texture tilted in the laser travel and track succession direction. This behaviour correlates with the direction of maximum thermal gradient associated with each deposited track.

4. Isolated clusters of the heterogeneously nucleated grains are typically observed in the overlap region between subsequent layer deposition. During each new layer, the top section of the previously deposited track is re-melted, eliminating the region of equiaxed heterogenous nucleated grains. Therefore, the typical as-deposited microstructure of LMD multi-layered builds of IN718 is dominated by epitaxial columnar grains from the first layer.
5. The γ grain morphology adjacent to the free surfaces, at each side of the melt-pool along the interface region of LMD IN718 display a tilt (of ≈44°) in their morphology and crystallographic texture away from the build direction and towards the specimen edge. The local thermal gradient direction and solidification conditions are believed to be the driving force for this outcome in each deposited track adjacent to the specimen free edge.
6. Sub-structure columnar dendrites have been observed in the as-deposited material along the interface region in the deposited region which have extended across many layers in some instances. EDX analysis of the dendrites revealed a migration of refractory alloying elements with the dendrite cores enriched with nickel, iron and chromium; whilst the inter dendritic regions are enriched with niobium and less obviously, molybdenum. Such migrations produce regions locally enriched with niobium and are therefore preferable nucleation locations for detrimental Laves phase precipitation. Such precipitation had formed channel-like networks of Laves throughout the build. At the interface region, the multi-layered build has believed to have an aging affect, precipitating strengthening phases and δ-phase. However, such presence was inconclusive in this study and further TEM analysis would be required for conclusion.
7. A post weld heat treatment selected for this repairing application of IN718 superalloy was successful in precipitating strengthening γ'' phases in both the parent and deposited structure giving a more homogeneous distribution of phase constitutes. Although the grain morphology remained largely unaltered, the dissolution of detrimental Laves phase was initiated, therefore precipitating δ-phase due to the enrichment of niobium. The effect of this heat treatment will now be analysed on both a mechanical property and residual stress level as it has potential to have a beneficial two-fold effect.

Chapter 7: Process Parameters Influence on Microstructure and Crystallographic texture Evolution across the Interface Region of Laser Deposited IN718

7.1 Introduction

The process parameters of LMD used for repairing IN718 components have significant effects on the interface region, microstructural features, crystallographic texture, and mechanical properties. This chapter aims to investigate the influence of these parameters on the interface region, including the HAZ, partially dissolved zone, fusion zone, and entire build geometry. It will also explore their impact on grain morphology, phase volume and morphology, crystallographic texture, and microhardness distribution.

Influence on Melt Pool Geometry

Figure 7.1 illustrates different zones across the interface region, and the temporal temperature evolution will be analysed to draw conclusions about microstructural features.

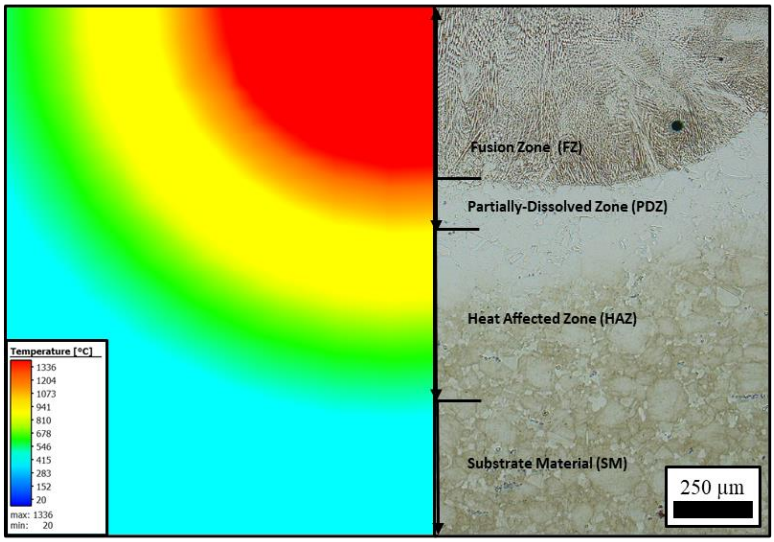

Figure 7.1 Cross section of the high laser power detailing the temperature regions for each simulated zone (left) and the accompanying microstructural evolution across the interface (right).

Figure 7.2 outlines the variability of HAZ penetration (which was inclusive of PDZ), FZ penetration and deposited track height for single track analysis with LMD, varying laser power from 550W to 950W. The HAZ was measured from the optical microscopy images where the bright white band etchant affect had occurred, in each case an average from 5 measurements were taken as the HAZ penetration reached a maximum penetration at the centre of the melt pool comparative to the edges due to the gaussian distribution behaviour of the laser during LMD. Greater laser powers increased both the HAZ and FZ penetration

almost linearly. However, the deposited track height, taken as the distance from the substrate interface to the top of the track, shows almost no distinguishable relationship between variability of height with the range of laser power.

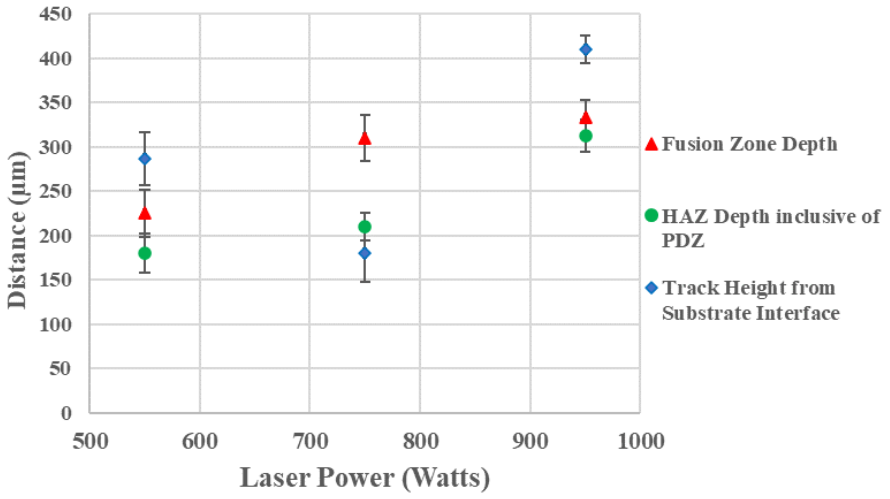

Figure 7.2 Melt pool dimensions associated to laser power

These results are indicative to the localised maximum temperatures reached for each laser power, which can be cross-checked with the simulated temperature history. From this, some conclusive hypotheses can be drawn:

- An increase of laser power will increase the penetrative depth of maximum temperature experience incrementally from the substrate/deposit interface down, opposite of the build direction.
- The maximum temperatures subjected to each zone will intrinsically have an effect on the dissolution of precipitated phases as the δ-solvus is approx. 1010°C [14] and the metastability of the γ'' phase makes it transform into a stable δ-Ni_3Nb during long-term exposure at temperatures above 650°C.
- With continual sharp thermal gradients and rapid cooling rates, the introduction of thermal-induced residual stress near the interface is entirely plausible [223] and will be investigated in the following chapter.

7.2 Single Track Investigation

Figure 7.3 illustrates the substructure at the interface during the 550W power deposition. At the bottom, where the temperature gradient "G" is exceptionally high and the ratio of G to the growth rate "R" is very low, dendrites tend to form a cellular structure. Prior to the dendritic structure, a "honeycomb" pattern is observed, representing the cross-section of cellular dendrites aligned along the build direction, following the maximum heat flow of the traveling laser (ND) [402]. With increasing dendritic growth rate "R," columnar

dendrites align with the build direction towards the maximum heat flow. As "R" further increases and the thermal gradient decreases, fine equiaxed dendrite structures form due to rapid cooling. Since the melt pool is semi-circular in all three conduction cases, "R" increases from the interface to the top of the melt pool. Consequently, the G/R ratio decreases from bottom to top, resulting in a transition from cellular to columnar dendrites to equiaxed dendrites.

Microstructures at the bottom of the melt pool exhibit distinct characteristics. For the 950W condition, a honeycomb structure appears before the dendritic structure, representing the cross-section of cellular dendrites oriented along the build direction, in line with the traveling laser's maximum heat flow (ND) [402]. The transition from cellular to dendritic structures is attributed to the increased solidification velocity and slower cooling rates compared to the 550W condition. Eventually, equiaxed dendrites hinder further dendritic growth, forming a relatively coarse equiaxed dendritic structure. During LMD, dendritic growth tends to favour crystallographic orientation <001> aligned with the build direction, with dendrites aligned along the direction of the highest temperature gradient outgrowing others. However, their growth is impeded with the formation of equiaxed dendrites ahead of the solid/liquid interface in the supercooled region.

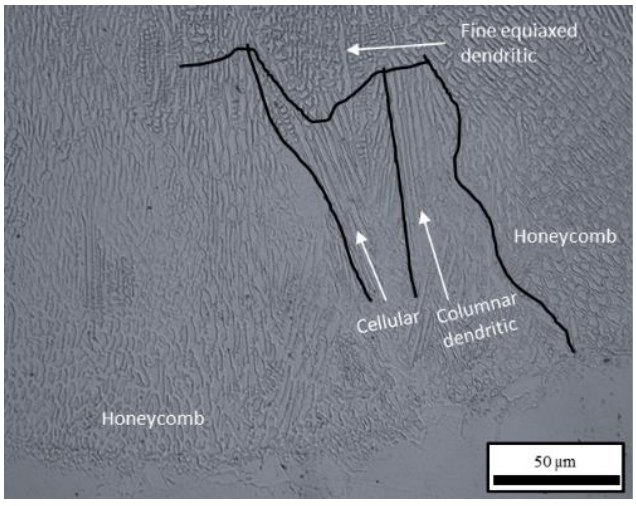

Figure 7.3 Complex structure interplay exhibited at the 550W substrate/deposit interface.

7.2.1 Discussion

Figure 7.4a-c shows the cross-section of specimens deposited using various laser powers, with details of the microstructure demonstrated in Figure 7.4 d-f. The morphology of each single-track presents a near uniform U-shape, however there are some differences because of varied laser power. The high laser power (Figure 7.4a) appears to have a slight rise abnormality in the centre of the melt pool where the profile looks non-uniform. As the power decreases to 750W (Figure 7.4b), the melt pool profile changes with a

discontinuous uniform penetration at the bottom of the substrate/deposit interface giving rise to deeper penetration towards the right side of the melt pool. The melt pool geometry uniformity improves at the lowest laser power, Figure 7.4c. These abnormalities associated with melt pool geometry are due to the complex forces such as Marangoni effect, recoil pressure and buoyancy which are exasperated at higher laser powers [66]. Moreover, these flaws could be associated with machine behaviour during the deposition with focal distance shift or inconsistent laser power being supplied to the coaxial head.

At 950W, the microstructure consists of a mix of columnar and equiaxed γ grains which will be investigated further with EBSD. Unmelted powders were visible around the periphery as indicated by the arrows. Details of the microstructure towards the top of the single deposited track in Figure 7.4g reveals the evidence of partially melted powder fused to the top of the track with a complex dendritic growth interface with slight equiaxed dendrites from the fully melted track superseded by the growth of columnar primary dendrites from the rapidly cooled partially melted powder. The microstructure of the dendrites at the interface shows the evolution of secondary and tertiary arms, which develop through a slower cooling rate comparative to the 550W sample which showed little to no secondary dendrite arm formation. The significant dendritic sub-structure growth makes recognizing γ grain boundaries difficult, this will be investigated further through EBSD analysis. All specimens investigated showed signs of converging and diverging dendritic growth from the <001>//BD direction dendrites, this behaviour is particularly highlighted in Figure 7.4e. These stray grains develop from random nucleation at the melt-back interface around the perimeters of the aligned dendrites. The presence of secondary and tertiary arm formation in the higher laser power sample show that during constitutional supercooling, protrusions will form at the solidification front because any perturbation will grow out faster into the undercooled region and develop into long arms, growing parallel to the heat flow, resulting in a cellular microstructure, as for the case in 550W. However, with lower thermal gradients, greater constitutional supercooling (increased solute rejection) and greater growth velocities a wider ‘mush zone’ is produced, where secondary and tertiary arms can develop leading to dendritic growth. Additionally, in the 950W sample there are equiaxed dendrites growing between the volume of two primary dendrite channels. It could be suggested that during the solidification, the remaining molten material is agitated to a point where dendrite arms have become detached from the solidification front. If these detached dendrites are above a critical size, they will continue to grow leading to a near equiaxed structure rather than remelting back into the molten material. At 750 W, there is significantly less melted

powder particles observed around the periphery and within the deposited structure. Additionally, the tertiary arm formation ceases to exist as the thermal gradient increases with a higher cooling rate. If favourable orientated grains (FOG) (denoted by green arrow in Figure 7.4e) are the ones which have the <001> direction aligned with the build direction due to heat flow direction compared, then unfavourable oriented grains (UOG) (denoted by red arrows in Figure 7.4e) have random orientation. In the case for converging grains, the dendritic tops of UOG impinge upon sides of FOG and cannot grow any further. Whereas in the diverging grains case, secondary and tertiary arms develop from FOG. In both cases, the converging and diverging grains ceases to grow as the FOG overgrow UOG [403]. At 550W, the deposited structure consists of very low values of partially melted powder particles at the periphery of the melt pool. Moreover, the substructure is limited to the growth of primary arms with no secondary or tertiary arms growing. This is due to an increased thermal gradient existing at the interface region in partnership with super high cooling rates due to the volume of liquid to cool being a good degree less.

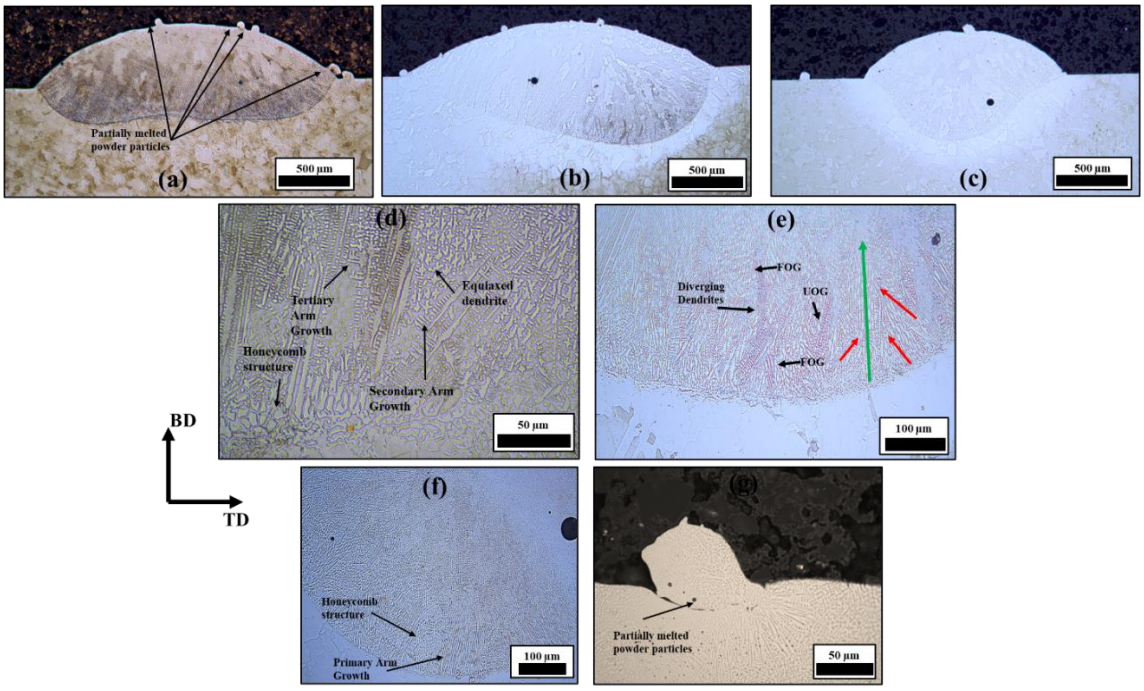

Figure 7.4 Single tracks deposited at different laser powers: (a) 950W, (b)750W, and (c) 550W. Detail of micrographs at the interface region: (d) 950W, (e) 750W and (f &g) 550W.

Results from EBSD analysis of the single deposited tracks were overlayed on the optical micrographs are shown in Figure 7.5. Figure 7.5a shows the OIM of the specimen deposited with 950 W with columnar γ grains at the bottom of the melt pool and a more equiaxed structure towards the middle of the deposit. A dashed line has been annotated to denote a transition from columnar to equiaxed/widened columnar grains, and a solid

line denotes the substrate/deposit interface as characterized by a shift from equiaxed substrate structure to the columnar grains of the deposit growing towards the maximum thermal gradient (centre of the melt pool). Figure 7.5b shows the OIM of the specimen deposited with the low laser power, 550W, with the overlayed IPF map. A greater presence of columnar γ grains and fewer fine equiaxed grains were observed in comparison to the 950W specimen. Also, a region of grain nucleation from incomplete melted powder particles was present at the periphery of the melt pool.

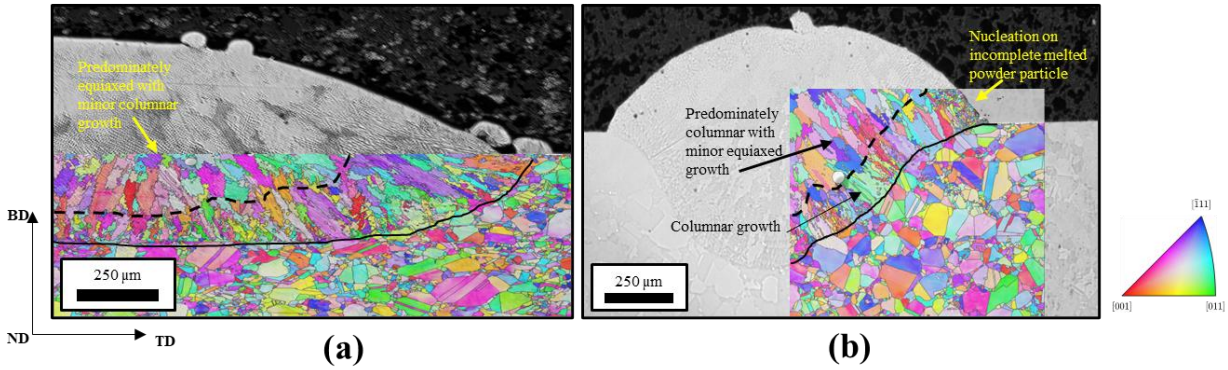

Figure 7.5 OIMs of single deposited tracks with overlayed grain structure from EBSD analysis for (a) High laser power and (b) Low laser power.

Melt pool IPF maps show the grain growth due to epitaxial growth of the grains at the melt pool boundary for all process parameters in the build direction. Additionally, several nucleated grains are observed at the centre of the melt pool and at the edges of the melt pool with misorientation of more than 15° with neighbouring grains. As previously mentioned, grain nucleation mechanism is important to identify. Different nucleation mechanisms for the formation of new grains at the solid/liquid interface—namely dendrite fragmentation, homogeneous and heterogeneous nucleation, thermal gradients and undercooling, and grain detachment—are identified during rapid solidification [404].

7.3 Laser Power Influence on Stray/Random Nucleated Grain (S/RG) Behaviour

Stray/Random nucleated grains (S/RG) formation are often referred to as grains which grow randomly throughout a deposit and are grains that do not confirm to single-crystal structure (SX) or directionally solidified grains (DS) [405], [406]. Work by Anderson *et al.* [407] looked at predictive modelling to understand the influence of processing conditions on SG formation to avoid/minimize their occurrence [408], [409], [410]. The presence of stray grains act as stress concentrators and can initiate crack propagation during solidification, as the material undergoes thermal contraction during solidification, stresses concentrate at the boundaries between the single crystal matrix and stray grains.

Although this work is not concerned with the epitaxy behaviour and stray grains formation during the repair of DS Ni-based superalloys using LMD, there was a high amount of stray grain formation along the fusion line within and out with epitaxially grown grains from a polycrystalline IN718 substrate.

Figure 7.6 details the randomly orientated near equiaxed γ-grains concentrated at the substrate/deposit interface, representative of all specimens. Regardless of laser power, these randomly nucleated grains were found within epitaxial columnar γ-grains (grey arrows in Figure 7.6) and nucleated all along the fusion line (black dashed line) in the 'mushy zone'. Given the block-like morphology, size (≈5 μm) and location at grain boundary, the black arrow indicates an NBC carbide which has been indexed by the EBSD as both the γ grain (FCC) and NBC carbide (FCC_B1) have very similar crystal structures.

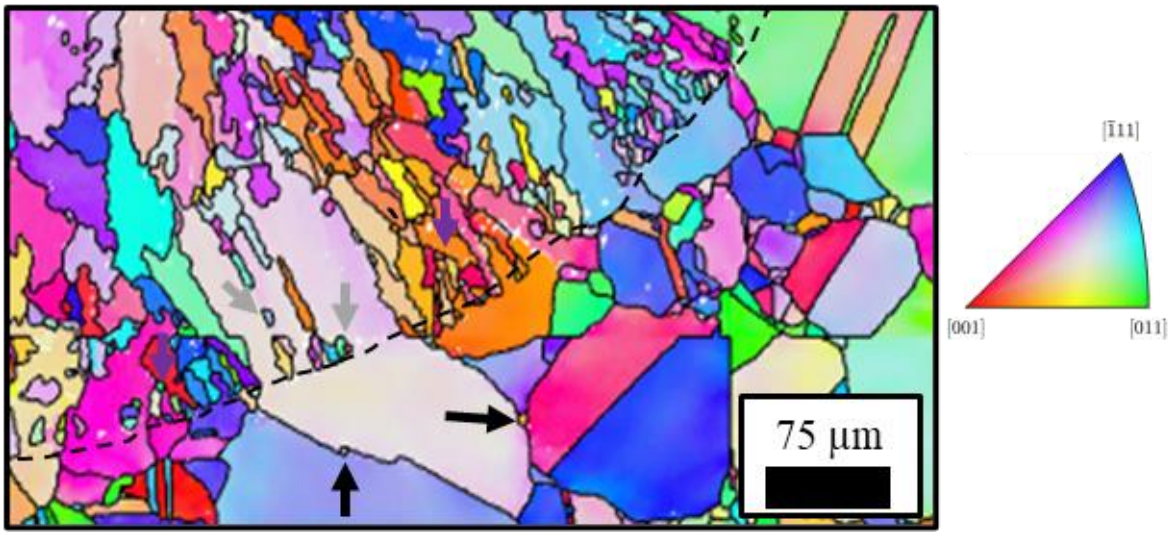

Figure 7.6 IPF Randomly nucleated very small <10 μm equiaxed to semi columnar grains found along the fusion line in the 'mushy region' in each specimen. (black arrows indicate NbC, grey arrows indicate nucleated inside other grains, purple arrows indicate nucleation outwith favourable grain). This example is taken from P=750 W single track.

To quantitatively assess the number of SG formation at the melt pool boundary, a region measuring approx. 1200 μm^2 was selected from melt pool centre encompassing the FZ only. Examining individual deposited tracks reveals that recrystallization of previously deposited grains, typically induced by subsequent layer deposition, is prevented. The grain structure within the deposited layer remains unaltered and undisturbed since there is no additional heat input to initiate melting of the grains. Consequently, the microstructural integrity of the single track is preserved.

Figure 7.7 displays the count and area fraction of stray and regular grains in the extracted region of the single laser tracks for each laser power. In Figure 7.7b, the average grain size of the grains in the melt pool centre region is outlined. Figure 7.7c illustrates the stray and regular grains formed in the region, highlighted in cyan, adhering to the specified differentiation limits. To differentiate between stray grains and epitaxial grains, grains with an equivalent radius of less than 5 µm were considered (where the average grain size in this region for 750 W is approximately 12.5 µm), along with an aspect ratio equal to or less than 1.5.

Demonstrated by the concentration and volume of purple coloured grains in Figure 7.7c, it can be seen that the grains at the fusion line have a diameter <10 µm but a large proportion of these grains have an aspect ratio >1.5. By comparing the laser powers (Figure 7.7a), a distinctive decrease in stray grains between the high laser power comparative to the medium and low laser power was observed for the fusion zone in multi-layered blocks. It is also worth mentioning, that the number of grains in the medium laser power and low laser power was similar but their grain area fraction was distinctively less in the lower laser power. This could be attributed to the cooling rate, which in the case of 550 W, would be the highest hindering the growth rate of equiaxed grains.

Several theories exist for melt-pool border nucleation where Drezet *et al.* [411] show how constitutional fragmentation of dendrite arms can implicate new grain formation at the border. Guiterrez *et al*. [412] have shown that precipitates at the melt pool border act as heterogenous nucleation sites and prevail during welding as a stagnant liquid layer close to melt pool border where the temperatures were lowest in the melt pool. In the bulk of the material, the comparatively small equiaxed grains (<10 µm) remelt and re-solidify due to the penetration of high temperatures from the subsequent laser pass. Rausch *et al.* [413] found that nucleation of stray grain was triggered when the solidification conditions at the melt pool border were different from those present when the base material solidified. Due to inhomogeneous concentration distribution from segregation occurring in the deposited and concentration gradients forming along this border, constitutional undercooling forms at the start of solidification.

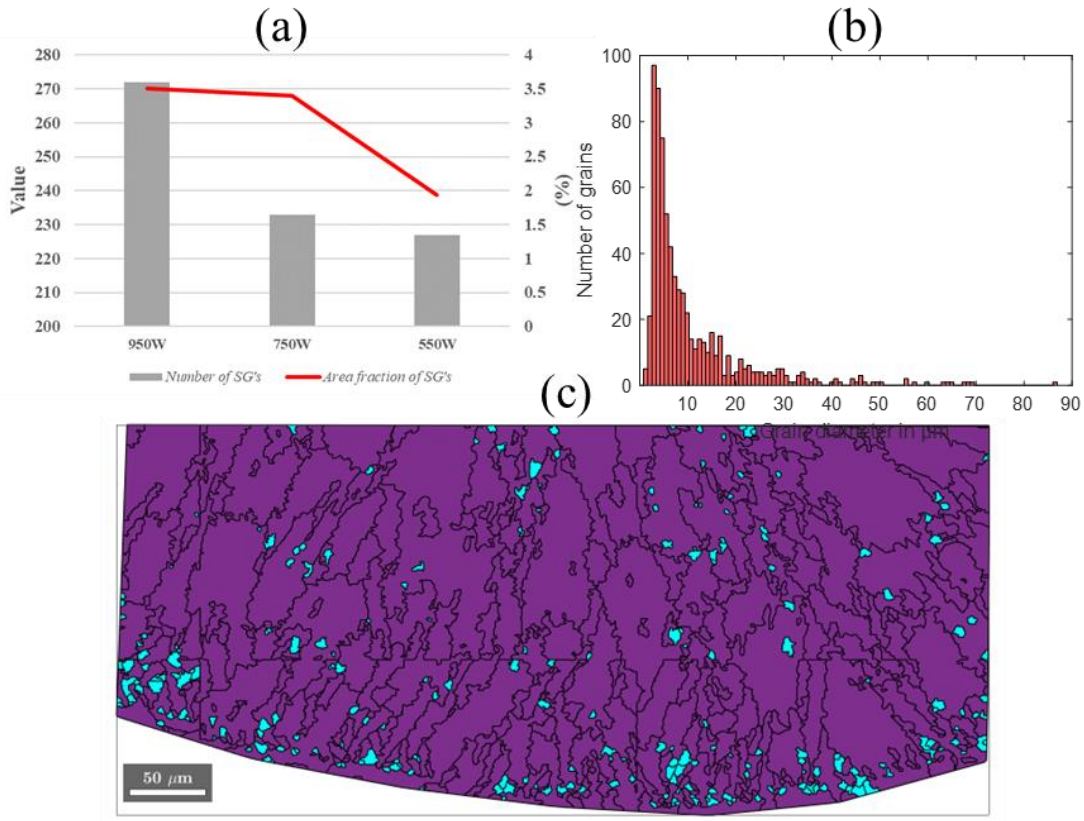

Figure 7.7 Stray grain content per regional area with (a)comparing laser power and (b) grain size for the 750W condition with (c) detailing an epitaxy (purple) vs stray grain (cyan).

The discontinuity of columnar grain morphology at the interface region by these so-called stray grains occur where the epitaxial growth is frequently interrupted by nucleation of new γ grains at the solidification front. As suggest by literature, these stray structures are usually formed in the case of high thermal gradients, high cooling rates and a fast-moving heat source [414]. These stray structures are formed during constitutional supercooling at the solidification front, combined with dendritic fragmentation when dendritic growth is present [358]. It has also been reported that high superficial and endogenous heterogeneous nucleation site act as nucleation sites of new grain formation ahead of the solidification front which promotes stray formation. A higher amount of stray grain formation such as that found in the 950W specimen could be particularly important as the higher amount of stray grains along the interface, inherently equate to more grain boundaries. Since the grain boundaries are more chemically active due to their higher energy states, they can be more prone to corrosion and oxidation. Furthermore, higher amount of grain boundaries can lead to higher concentration of defects, impurities and segregated alloy elements. Such imperfections can reduce the strength of the material and make the boundaries more susceptible to deformation and failure. Lastly, these grain boundaries can provide paths for the faster diffusion of atoms, which can lead to issues

such as grain boundary sliding at high temperatures, promoting creep deformation. While grain boundaries can impede dislocation movement, thereby increasing the strength of the material through mechanisms like grain boundary strengthening (Hall-Petch relationship), they are also the locations where failure is more likely to initiate under stress, particularly at high temperatures or in corrosive environments. Therefore, in a general sense, grain boundaries are considered weaker than the grains themselves.

The columnar to equiaxed transition (CET) model is suitable for the formation of stray grains which are equiaxed due to localized solidification conditions. However, further investigation is required to justify the S/RG's formed within the predominately <001>//BD columnar grains, highlighted by the black circles in Figure 7.8 which displays an IPF map of the fusion zone deposited using 950W. These S/RG's that form at the substrate interface will be reserved in the deposit as the S/RGs cannot be entirely remelted by the subsequent layer due to their close proximity to the substrate/deposit interface. The formation of these S/RGs is closely related to the columnar to equiaxed transition (CET) resulted from nucleation and growth of equiaxed grains in constitutional supercooling region ahead of the solid-liquid interface. Many researchers have focused on the fundamental mechanisms of CET to control epitaxial growth and inhibit SG formation in directionally solidified or single crystal superalloys [415], [416] but ultimately become extremely difficult to control in polycrystalline substrates.

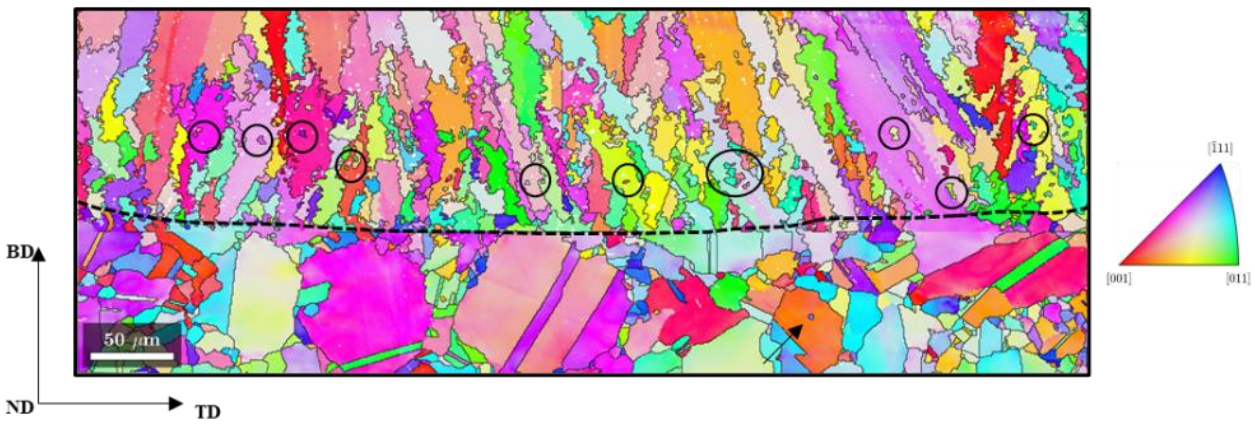

Figure 7.8 IPF Map for the interface region of the specimen deposited with high laser power.

7.3.1 Discussion

Stray grain formation during solidifying can be well understood if the degree of constitutional supercooling presented ahead of the dendritic tip is considered. Clarified by Hunt, columnar to equiaxed transition is caused by excessive constitutional supercooling [417]. If the degree of constitutional supercooling in the liquid surpasses the critical undercooling limit for nucleation, the equiaxed grains become possible to nucleate

ahead of the columnar dendrites. A decrease of G or increase of V, such as the case for the high laser power compared to the lower laser powers, will increase the degree of constitutional supercooling and have a larger constitutional supercooled region ahead of the dendrites forming, promoting stray grain formation [418]. At the interface region, the G/V is high due to the high localised cooling rate as result of the heat sink effect and the growth rate (V) = cooling rate (K/s) / thermal gradient (K/m) and has the units (K/m) meaning favoured conditions for cellular epitaxial growth.

The effect of substrate crystallographic orientation on stray grain formation during LMD of IN718 was noticed. Figure 7.9 shows the grains at the substrate/deposit boundary for the 750 W laser power. Here, grains A and B are equi-distance located on either side of the middle of the melt pool, therefore localised G/R ratio should be consistent, if not, very similar. With substrate grain A with a <011> direction, the density of stray grain formation along the melt pool boundary radically increases as compared to grain B, with the <001> crystallographic direction. It is well known that when the preferential <001> direction of the deposited grain is aligned with the maximum thermal gradient parallel to the build direction, grow is the fastest. Dendrites grow from the bottom of the melt pool in the <001> direction, coincident with the heat-source direction which causes the maximum growth velocity to equal that of the heat-source velocity in this location. This is the result of the <100> direction being the least close packed direction, therefore being thermodynamically favourable to grow epitaxially. Considering solidification, a <001> fibre solidification growth direction has been reported to be parallel to the maximum thermal gradient for most cubic systems. DuPont *et al.* [414], [419] explain stray grain content for single crystal growth along different crystal directions, allowing the effect of substrate orientation to be analysed. Their results show that although G and V normal to the solidification interface do not change with substrate orientation, the distribution of the critical values G_{hkl} and $V_{hkl,}$ which is the G and V along the growth direction are strongly affected with substrate orientation. In the regions where the dendrite growth axis do not run parallel to the direction of greatest heat flow, SG concentration was the greatest. Mokadem *et al.* [420] describe this phenomenon as “off-axis” heat flow. The off-axis heat flow will greatly reduce the G_{hkl} and will induce a faster V_{hkl} than if the dendrites grow parallel to maximum heat flow. The resulting low G/V ratio at this location will cause substantial SG formation.

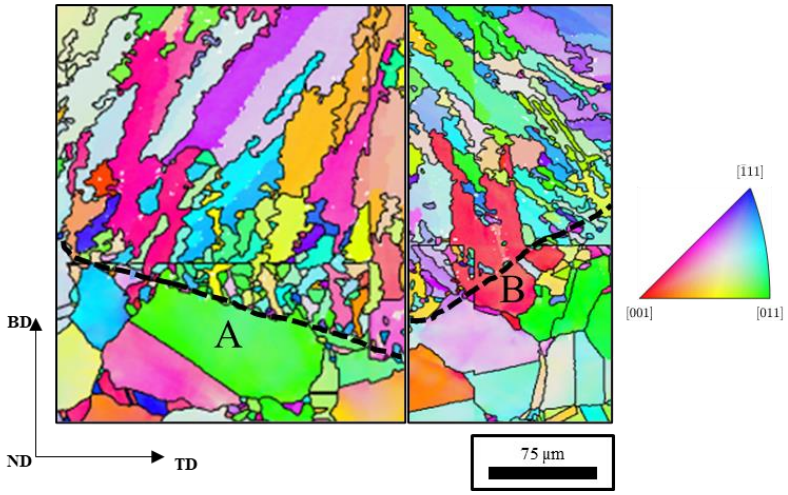

Figure 7.9 Epitaxy and new stray grain formation with influence of substrate grain orientation in ten-layered block deposited using 750W.

Grain A populates a higher density of stray/randomly nucleated grains comparative to grain B. Looking at the crystallographic orientation, the grains which have their <001>//BD aligned achieve epitaxial growth with very few randomly nucleated SG. For grain A, there is more time for nucleation of new grains to occur as the solid is not consuming the liquid, i.e. the solidification rate is lower. Figure 7.10 schematically represents the time lapsed during solidification.

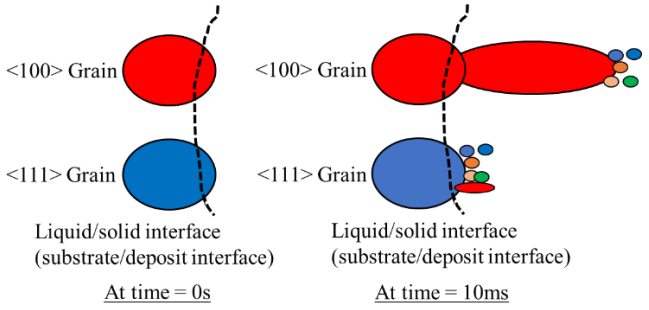

Figure 7.10 Schematic representation of crystallographic orientation effect on SG formation.

After a very short period of time (≈10 ms) during solidification, the epitaxial columnar/cellular grains of <100> grains are hindered in growing further due to the growth of equiaxed grains and this is because G/R ratio begins to increase ahead of the already solidifying grain. For the <111>/<011> grain, the R can be lower because there is more time for the nucleation to occur as the solid is not consuming the liquid (diffusing into the liquid). This is because the grains that would have grown the fastest <001>//BD due to the least close packed direction are not present, thus the equiaxed grains that impeded the epitaxial grain growth after 10 ms are now energetically favoured to nucleate due to the competitive growth that occurs at the solid/liquid interface.

Stray grain formation is closely related to the columnar-to-equiaxed transition (CET) resulted from nucleation and growth of these equiaxed grains in constitutionally supercooled region ahead of the solid-liquid interface. To determine whether CET occurs, a developed model proposed by Guamann *et al.* is given [55], [358], [421]:

Equation 7.1

$$\frac{G^n}{V} = a\left\{\sqrt[3]{\frac{-4\pi N_0}{3ln[1-\Phi]}}.\frac{1}{n+1}\right\}^n$$

Where G is the thermal gradient, V is the growth velocity normal to solidification front, N_0 is the number of nucleation sites, Φ is the volume fraction of equiaxed grains, a and n are material properties. CET is controlled by solidification conditions (G and V) which is governed by process parameters and is suitable for SGs which are equiaxed grains.

In Figure 7.8, the SG formation can be explained by separating the region to which they form. Figure 7.11 shows the relative temperature gradients and constitutional supercooling which is consistent with the structure seen in A. At the beginning of solidification, the substrate is remelted and a melt pool form using laser irradiation. The temperature gradient was high, and the crystal growth velocity was as low as zero at the bottom of the melt pool and under these solidification conditions, the solid-liquid interface was stable, a cellular/planar growth occurred. Highlighted by the black circles in Figure 7.8 (near the solid-liquid interface), these S/RGs could form because during the solidification of alloys, the solute would pile up ahead of the solid-liquid interface because the distribution coefficient is less than one. A mass of solute accumulated near the substrate/deposit interface because of the limited solute diffusion in the solid. The accumulation of localised solute content influenced the local equilibrium solidification temperature. When the localised temperature gradient controlled by the heat dissipation of solid was lower than the equilibrium liquidus temperature, a constitutionally undercooled zone was formed in a micro area ahead of the interface. This constitutional supercooling increased, eventually changing the crystal growth mechanism from planar to cells and dendrites. As previously discussed, segregating solute develops a constitutionally supercooled zone that restricts further growth of the primary solid γ grains and enables neighbouring nucleate particles to activate and seed new grains. Lei *et al.* [422] demonstrates this SG formation occurring right at the fusion interface region between the deposit and the substrate when using LMD on DZ125 (directionally solidified) Ni-based superalloy.

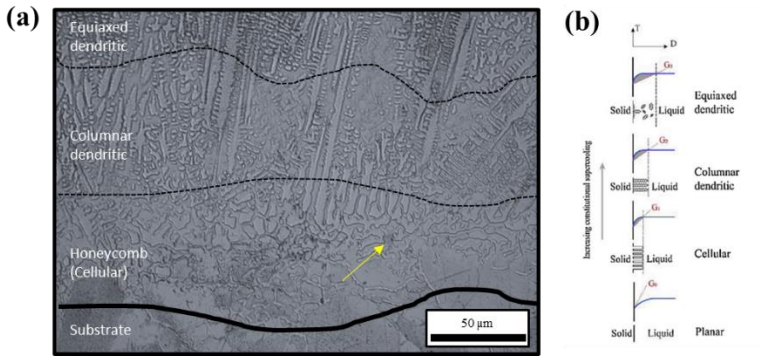

***Figure 7.11 Solidification structure of a single melt pool cross-section deposited using 950W with dashed lines representing a transition in structure, solid line representing the substrate/deposit interface and the yellow arrow detailing a NbC carbide present in the fusion zone with (b) detailing the solidification modes with respect to temperature gradients (G) and constitutional undercooling** *[422]*.

Dendrite fragmentation may also act as grain nucleation sites, and this can occur if current solidification conditions and underlying or remelted dendritic concentration profiles do not coincide. Demonstrated by fluid flow calculations, dendrite fragmentation is unlikely to occur during non-forced-convective conditions [423], however because of the protective gas used in LMD, these create localized forced convection which is non-uniform. The value of this forced convection induced by the shielding gas was suggested to be in the range of 18-30W/m^2/°C [180], [424], with reports of 80W/m^2/°C in WAAM [425], several times higher the value of natural convection. Solute enhancement has also been a potent mechanism for initiation of fragmentation [426], [427]. Work by Ruvalcaba *et al.* [428] showed that dendritic fragmentation can be initiated by transient growth conditions which occur naturally in solidification where solute is transported into the mush region by gravity-induced liquid flow. The initial fragmentation was found to grow in a dendritic manner, consuming intercolumnar undercooling as it was transported to the columnar front by buoyancy in the melt pool, leaving behind solute-rich liquid that settles further into the mush region. Therefore, the imbalance causes a cascade of new fragments in the wake of the first one, becoming a mechanism for initiating CET during solidification.

Figure 7.9 shows the deposit grain selection from the polycrystalline substrate detailing the mixture of grain morphology with average diameters between 2.2-80 µm at the bottom of the melt pool, which was observed in all three laser conditions. As the build develops, these randomly oriented, near equiaxed grains with aspect ratios close to 1 are re-melted back by subsequent layers. In the first layer, the build is much closer to the substrate and the melt pool rapidly solidifies producing and trapping non-uniform grains. After a few

layers of deposition, the density of these stray grains is greatly reduced due to the remelting and solidification of the preferentially orientated grains combined with a reduction of cooling rate. In welding, grains begin to nucleate from the fusion line to the weld line, i.e., from the tail of the melt pool and grow towards the centre of the melt pool due to the maximum thermal gradient in this direction. Towards the centre of the melt pool, the grain size is dependent on thermal solidification conditions whereby an increase of laser power results in a larger and wider central region where stray grain nucleation probability is enhanced.

7.3.2 Summary of Laser Power on SG Formation

To summarise the influence of laser power on stray grain formation:

1. Stray grain formation in the fusion zone is associated with localised solidification conditions, a higher temperature gradient is beneficial to promote epitaxial grain growth i.e., reducing the formation of stray grains.
2. G has a larger effect on stray grain formation than V. A negative influence of increasing laser power on stray grain formation can be correlated by considering its effect on temperature gradient. An increase to power will produce a decrease in temperature gradient, thus promoting more stray grains to form in the melt pool.
3. A higher laser power will reduce the thermal gradient and as the G/V ratio is reduced, more SG form due to increased constitutional supercooling, with reducing the laser power, leads to a slight increase in G with a corresponding increase in the G/V ratio, leading to a reduction in SG content.
4. Stray grains may nucleate and grow if there are other heterogeneous nuclei such as unmelted γ' phases such as NBC carbides presented in the fusion zone and fragmentized dendrites resulting in a N_0 increase.
5. A larger melt pool in terms of volume produced with the high laser power leads to greater intermixing of powder and substrate, therefore increase the probability of localised undercooling caused by solute content inhomogeneity therefore promoting SG formation.
6. A lower thermal gradient induces a wider supercooled zone where nucleation can occur, which is conductive for grain nucleation combined with a high cooling rate which further induces large undercooling of supercooled liquid.

7.4 Multi-layered Thin-Walled Investigation

To understand the microstructural evolution during the repetitive thermal cycles, Figure 7.12 shows the cross-sectional grain structure of single deposit thin walls 1-, 5, and 10

layers high. For simplicity, the single, five- and ten-layer deposition of thin-walled structures are named 750W-1, 750W-5 and 750W-10, respectively. The layers were deposited directly after one another with <2s inter-layer dwell time in a unidirectional pattern.

7.4.1 Grain Structure

In Figure 7.12, the samples are shown with the EBSD inverse pole orientation map put as an overlay on the OM. The respective pole figure in each mapping is shown aligned with the build direction. The single deposit, as discussed earlier has a polycrystalline structure with elongated coarse columnar grains growing in the build direction with frequent equiaxed grains hindering further growth were observed. In both the 750W-5 and 750W-10, the presence of equiaxed grains was limited with a few random equiaxed grains remaining predominately at the layer boundary (depicted by black dashed line). At the fusion boundary region, competitive growth between epitaxial and nucleation was evident with the epitaxial growth of large grains forming towards the edges and nucleation of new grains presented towards the centre. The grains towards the centre in the n+1 layer were generally coarser than those at the edges and grains found in layer n, a common trend observed amongst all three conditions. A clear shift in grain orientation was found in the multiple layered samples with long columnar grains growing vertically caused by the heat flux direction magnitude remaining greater vertically towards the substrate than horizontally towards any free edges.

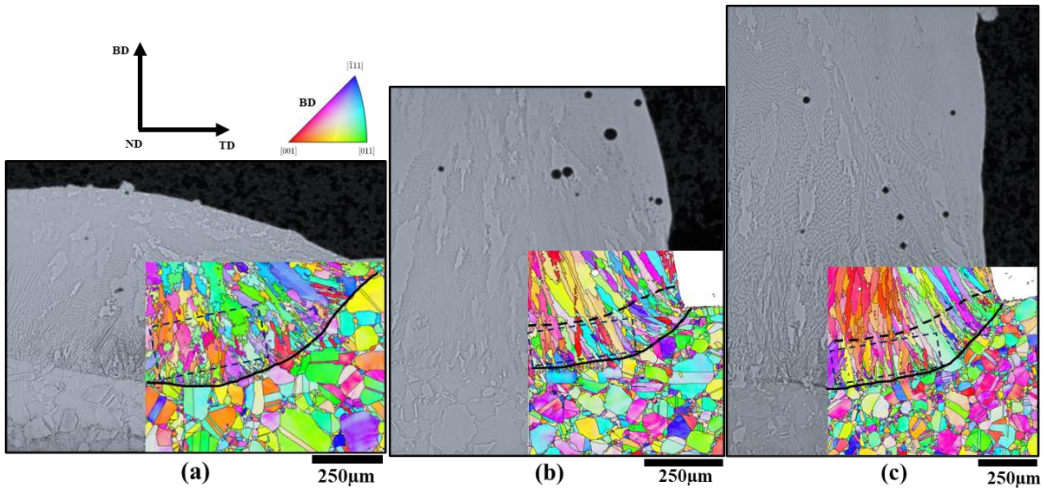

Figure 7.12 Cross-sectional interface region of the 750W sample deposits with respective inverse pole figure maps superimposed over the OM-image (a) Single layer deposit, (b) Five-layer deposit and (c) ten-layer deposit with black dashed line depicting new layer and the black-dashed box highlighting the region used for statistical analysis in Figure 7.13.

To quantify the microstructural inhomogeneity in terms of grain size, the grain size distribution was measured in the fusion zone over an area of 850 µm x 450 µm for all three process conditions in the X-Z plane, the results are shown in Figure 7.13. Columnar grains of different sizes and aspect ratios were observed. For the single deposited layer, the average grain size was ~11.2 µm with a maximum grain size of 102µm. In the five-layer FZ, the average grain size was 15.3 µm with a maximum of 119 µm. In 750W-10, the average grain size was 14.4 µm with a maximum grain size of 165 µm. Overall, the average grain size in the FZ did not change dramatically but the maximum size of the grains found increased substantially from the single to the ten-layered (approx. 161% increase). More importantly, the aspect ratio for the grains inside the FZ varied considerably by taking the c-axis as the length of each grain. Comparing the 5-layer and 10-layer deposition effect on the fusion zone, it can be deduced that the grain size, aspect ratio and grain morphology remain unchanged and by analysing the temperature history plotted for this region, conclusive remarks can be made.

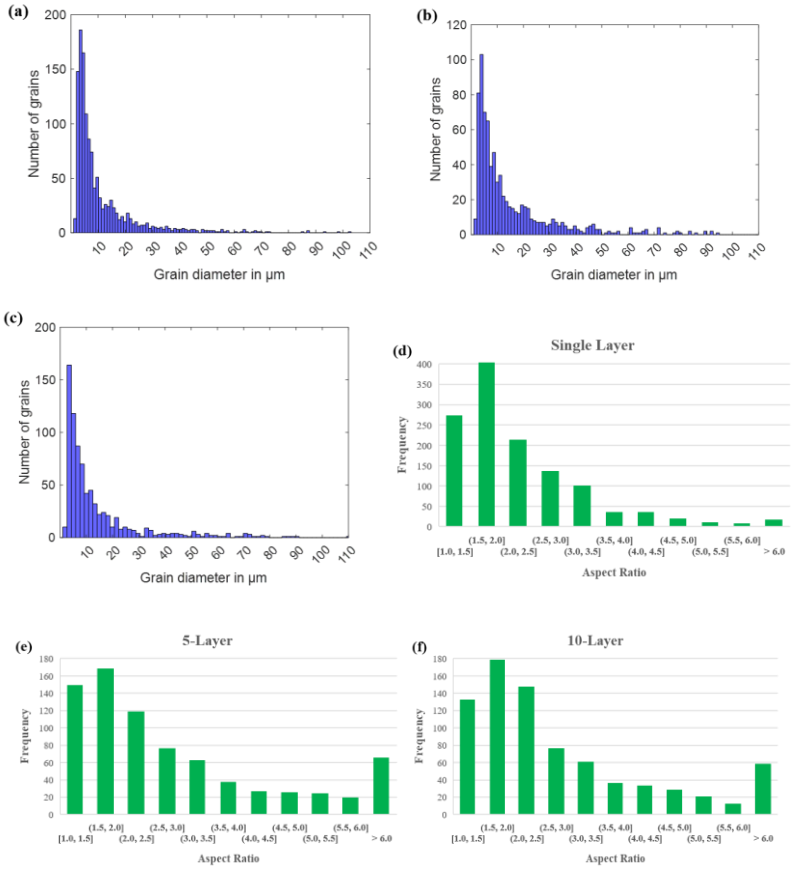

Figure 7.13 Fusion zone grain information for the cross-section investigation (a-c) grain diameter in (a) Single, (b) Five-layer and (c) ten-layer conditions with accompanying aspect ratio for (d) single, (e) five-layer and (f) ten layer conditions.

The pole figures were plotted using the dashed blue box in Figure 7.12 for single (Figure 7.14b, 5-layer (Figure 7.14 c), and 10-layer (Figure 7.14 d), deposition condition. A

transition from <001>//BD weak cube texture to a strong <001>//BD fibre texture was achieved, an example of a standard fibre and rotated cube texture can be found for the (100) pole figure (Figure 7.14 a). This behaviour was previously explained in chapter 5 with the region of equiaxed grains in the top half of the single track being re-melted then re-solidifying with the more favoured FCC direction of <001>//BD aligned. In both the 5-layer and 10-layer deposition conditions, the fusion zone crystallographic texture remains consistent with the strong fibre texture and MUD values double the magnitude of the single deposited track. A slight tilt in the fibre direction into the direction of maximum thermal gradient was achieved in the first layer, as depicted by the black arrows in both (100) and (111) pole figures. In the case of the 5-layer and 10-layer deposition, a marginal tilt in the <001> fibre texture from alignment with almost the same angle (approx. 13.5°) with the BD but what appears to be the direct opposite directions of one another with the 5-layer tilting away from the TD direction and 10-layer tilting towards the TD direction. This could be associated with the ROI extrapolated from the melt pool in the two conditions, whereby the 5-layer ROI appears to be slightly towards the edge of the melt pool more than the 10-layer ROI. Inherently, this could be causing the slight tilt shift of the grains in the opposite direction to the TD. Overall, the PF plotted for both 5-layer and 10-layer conditions appear very similar solidifying the presence of similarity of fusion zone between a 5-layer and 10-layer deposition.

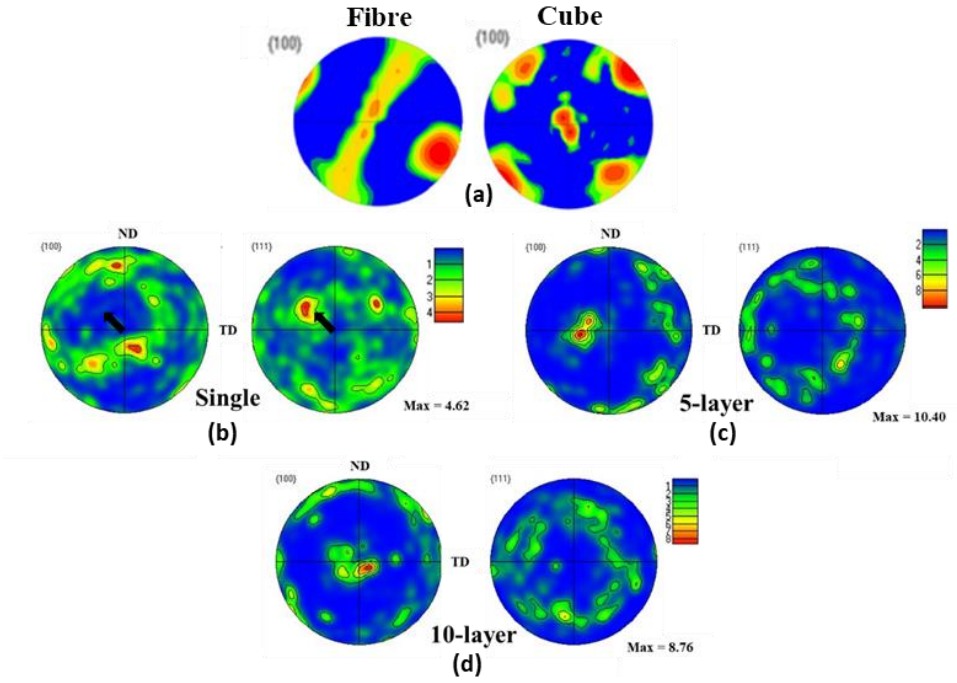

Figure 7.14 Pole figure representation of (a) fibre and cube standard textures from Dinda et al. [429]*, (b) *the fusion zone in the single, (c) 5-layer and (d)10-layer conditions deposited with 750W.

The temperature history for the fusion zone was extrapolated in both the 5-layer & 10-layer thin-walled depositions and can be seen in Figure 7.15. In the case of LMD IN718 the grain growth can be limited during annealing through the Zener pinning effect [430]. The presence of δ hinders the grain growth during δ sub-solvus annealing.

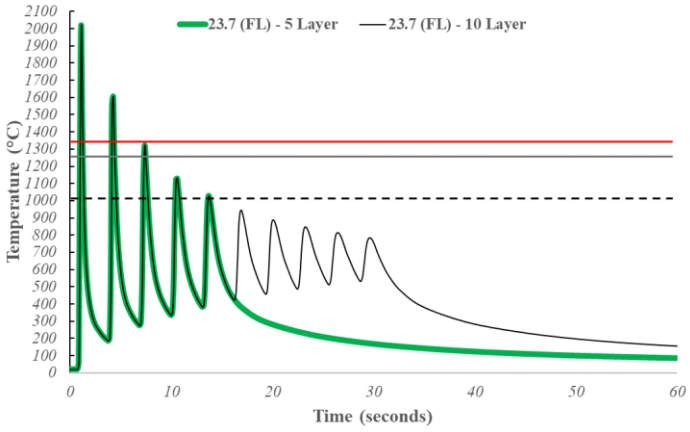

Figure 7.15 Temperature history profile for the ROI in the fusion zone for both 5- and 10-layer deposition (N.b. red, grey and black-dashed line denote the liquidus, solidus and δ-solus temperatures, respectively).

It has been deduced in previous studies that in the absence of deformation stored energy, a microstructure will remain stable during annealing provided that the fraction of δ phase particles is higher than 1%, fully consistent with the classical particle pinning model of Smith-Zener. If strain is applied prior to the annealing, the microstructure becomes unstable and the final microstructure can be governed by the level of applied strain [431]. Given the extent of residual stress measured by the contour method directly in the fusion zone, it can be deduced that the level of residual stress existing in the fusion zone remains low (<200 MPa), meaning that around 1% should be sufficient to pin the microstructure. According to the thermal history, Figure 7.15, the second laser pass is sufficient to remelt the top region of the layer which agrees well with the grain morphology. The region of interest was subjected to continual thermal cycles inside the precipitation window of δ-phase (650°C-900°C), therefore promoting the formation of δ-phase in the interdendritic laves phase regions where the Nb content is richer; TEM would be needed to confirm precipitation. Furthermore, the δ solvus temperature (as denoted by the dashed black line) is not surpassed after layer 5, so any grain growth will be hindered due to the pinning effect remaining. The localised temperature at the fusion zone remains low, <950°C during the deposition of subsequent layers 6 through 10. It can be deduced that the effect of build height and cyclical thermal evolution becomes benign after the 5th layer deposition giving the distance between the local heat source and fusion zone. Hence, the

microstructure at the fusion zone in terms of grain size, aspect ratio and the crystallographic texture remain largely unaltered after the 5th layer compared to the 10th layer due to the solidified grains being pinned by the δ phase present at grain boundaries. Furthermore, the post weld heat treatment performed at sub-solvus temperature should prevent exaggerated grain growth [432].

7.5 Process Parameter Influence on Dendritic Growth Angle

To understand the effect of laser power on grain structure and the microstructure evolution across the interface region, the YZ plane (laser travel direction) was studied for the 550 W, 750 W and 950 W laser powers of unidirectional deposition. By analysing the longitudinal cross-section, conclusive remarks can be made between the microstructural evolvement at the laser front to the trailing edge for the three process conditions. A schematic overview detailing the plane in view and laser travel direction is seen in Figure 7.16.

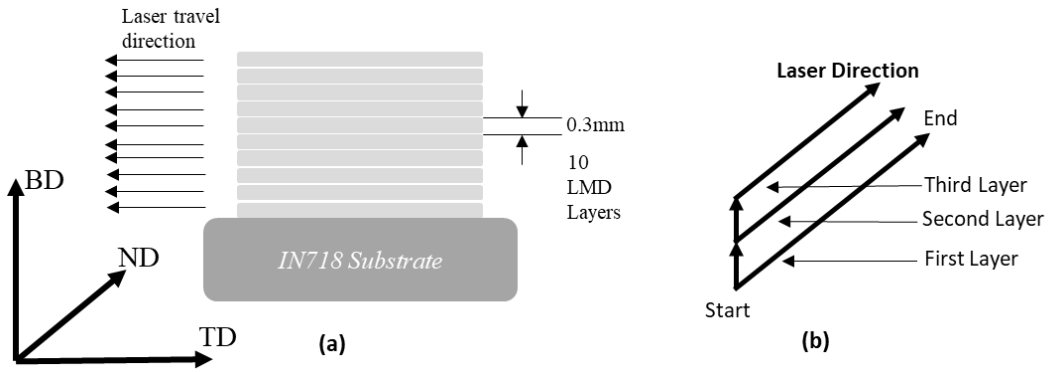

Figure 7.16 Schematic overview of the (a) unidirectional hatch pattern and (b) longitudinal transverse direction of the laser travel.

The growth direction of the dendrites is correlate to the laser scanning direction with the solidification front travelling right to left. It can be noted that the primary dendrites have almost the same orientation throughout the sample, with some dendrites growing across many layers.

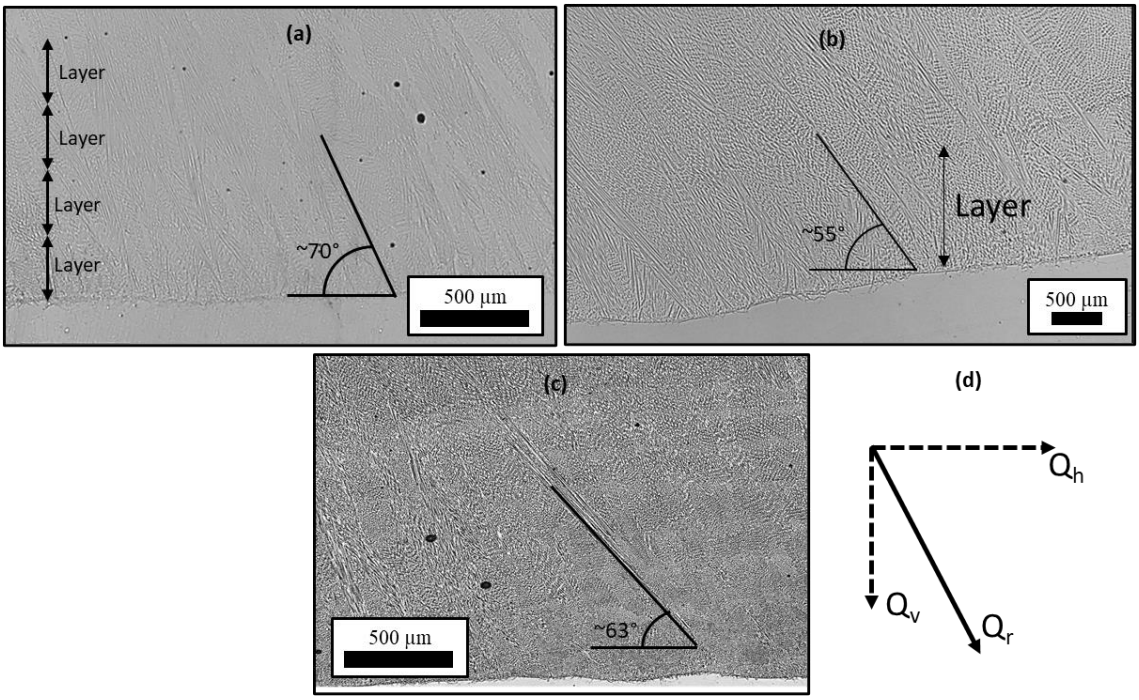

Figure 7.17 Optical microscopy of the cross-sections showing the macro-structural growth for (a) 950W, (b) 750W and (c) 550W laser powers, detailing the resultant growth direction of dendrites and (d) schematically showing the heat flux vector.

Comparing the builds, significant microstructural differences were observed, especially with respect to the dendrite growth morphology. In the 950W laser power sample, the dendrites were unidirectionally orientated at an angle of ~ 68-70° to the substrate across all layers from the interface region as shown in Figure 7.17a. The 750W samples had unidirectional growth at a ~55° angle to the substrate (Figure 7.17b) and the 550W laser power had dendrites oriented at an angle of 61-63°. In all cases, the growth morphology was orientated along the moving heat source. This orientation behaviour is related to the localised retrospective heat flux direction. Research focused on dendritic growth alignment primarily conclude that the laser travel trajectory is the driving force behind directional choice, which is true and can be described as the laser source heat flux (Q_x) [69]. The vector-based describing system of heat flux (Figure 7.17 d) details the direction and magnitude for directional growth during LMD. As the localised temperature subsequently reach below the solidification temperature, the transition from γ-liquidus phase to γ-solidus initiates. Here, most heat is dissipated through the substrate and previously deposited layers. Vector Q_h describes the heat flux through the horizontal previously deposited zone due to laser movement, and vector Q_v represents the heat flux through the vertical previously deposited zone and substate. Additionally, vector Q_y described the heat flux due to heat dissipation through adjacent previously deposited zone, but it can be ignored because it is very small comparative to Q_h and Q_v [68]. From

the optical micrographs, it can be concluded that the resultant heat flux growth (Q_r) is the growth direction vector due to the dendritic growth towards the maximum thermal gradient which is aligned with the build direction and laser scanning direction. The result of an almost vertically aligned dendrite growth in the 950W laser power is a result of the heat sink effect and therefore Q_h being far greater than heat flux through dissipated to adjacently deposited tracks or through natural convection, Q_v. Moreover, in the case of the 950W laser power, the melt pool was sufficiently larger than the comparatively used laser powers meaning an increased solidification time, hence more time to grow towards the maximum thermal gradient and the effect of heat sink, Q_v, working to align the dendrites in the build direction. During the laser deposition, the substrate and previously deposited layers will act as a heat sink, conducting a larger portion of thermal energy comparative to natural convection. This can be described as substrate heat flux (Q_z). The dendrites grow with an alignment to the build direction due to the $Q_{h..}$ As the melt pool solidifies, cooling mostly occurs via the substrate and pre-deposited layers. This leads to the directional growth of the grains counter to the heat flux direction and subsequently the formation of columnar grains. The continuous columnar dendritic growth across multiple layers is caused by epitaxial growth of primary dendrite from partially remelted grains of the previously deposited layer, acting as a pre-nuclei for directional growth of crystal [69]. Literature reports that the dendrite growth direction is mostly perpendicular to the substrate [55], [71] but this investigation found this angle is to be about 55-70° depending on laser power used. The temperature of the deposit at the back of the melt pool is high comparative to the substrate; hence the resultant heat flux direction will be at an angle of more than 45° and less than 90° with the substrate [69]. Comparing the high laser power to low laser power, the Q_r becomes more aligned to the build direction, (90°) to the substrate surface. However, this relationship is challenged by the 750 W laser power which resulted in a shallower angle (approx. 55°) comparative to the 550 W laser power (approx. 63°). This disassociation is related to the uniformity of melt pool geometry seen by the inconsistent melt pool formation in Figure 7.17b, where the melt pool depth represents a non-uniform crescent shape with a definitive power delivery fault. Inconsistent power delivery can be the result of defocussing the laser beam or inconsistencies with the mirroring of the light beam through the Yb-optic [433]. It would be expected that if the beam was stabilized and delivered consistent feed, then the dendritic growth angle would be between 62-69°.

7.6 Process Parameter Influence on γ phase texture

As previously discussed in Chapter 6, the global texture of all specimens deposited in this work varied in either cube or <001>//BD fibre texture. The global texture of the fusion zone after deposition at power levels of 950 W, 750 W, and 550 W is illustrated by the Inverse Pole Figures (IPFs) in Figure 7.18 (a-c), respectively. In Figure 7.18, the 950W specimen shows a cluster of peaks around the centre of the (100) Pole Figure (PF) and a ring of peaks in the (111) PF (*demonstrated by dashed line*), indicating a prevalent <001>//BD fibre texture. Decreasing the laser power to 750W results in a weaker texture of grains. However, the 550W specimen, as depicted in Figure 7.18c, displays a cluster of peaks centralized in the (100) PF and four red circles in the (111) PF. The Multiple of Unity Distribution (MUD) value is notably higher, indicating a strong <001>//BD cube texture (example in Figure 7.14) Figure 7.14in samples processed at 550 W laser power. These results can be associated with the localised thermal conditions. The 550 W specimen can be associated with a high G/R ratio characterized by finer grains. The high G/R indicates a rapid cooling rate relative to the rate of thermal gradient, promoting the formation of smaller grains due to limited grain growth time during solidification. Whereby it has already been demonstrated that a reduction in laser power leads to higher cooling rates, the high thermal gradient in rapid cooling leads to the finer grains growing along the favoured <001>//BD direction during solidification.

By comparing Figure 7.18d vs Figure 7.18e which details the EBSD grain orientation maps which were used to produce the pole figures, it can be highlighted that considerable statistical sampling exists (approx. 300 less grains for the same area analysed) in the lower laser power due to the large γ grain size within the sample. The presence of both textures formation has been noted in AM as-built IN718 components with their rationale behind formation already discussed. However, the reasons for a shift from cube texture to the <001>//BD fibre texture with an increase in laser power remains vague. Possible reasons shall be discussed hereafter.

When analysing the area outlined for the pole figures, the lowest laser power has contributed to an increase in thermal gradient within the melt-pool, facilitating the epitaxial continual growth of γ grains along the favoured crystallographic direction. Figure 7.7 demonstrated that the increase of laser power led to an increased area fraction of heterogeneously nucleated grains at the interface region. This would inherently shift to a more cube texture due to the formation of small or more equiaxed grains with a smaller aspect ratio. Furthermore, this increase of randomly orientated γ grains along the interface

would be given sufficient thermal energy during the multi-layer deposition to facilitate growing mechanisms. Lastly, greater laser power has been previously modelled to produce a greater elongation of the trailing edge of the melt pool. Such geometrical alterations can alter the localised direction of maximum thermal gradient during solidification, therefore influencing texture [434].

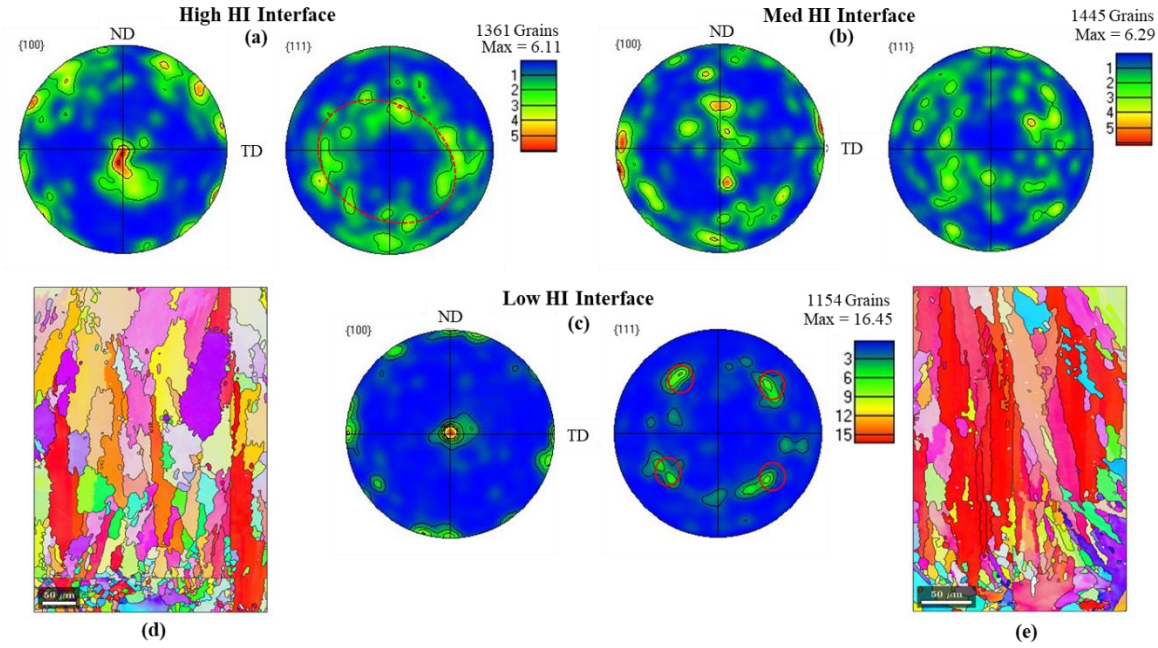

Figure 7.18 IPF pole figures plotted for the fusion zone of the solid block built using laser power (a) 950W, (b)750W and (c)550W. And the EBSD grain orientation maps for the (d) 950W and (e) 550W laser powers.

Parimi's *et al.* research [155] showcased the close resemblance between the texture of the first build layer and that of the substrate, underlining the significant influence of the substrate's grain structure and microtexture on the initial layer. Regarding the 550 W FZ, a greater volume of epitaxial grains emanating from the substrate grains was observed compared to higher laser power settings. This distinction is evident when comparing grain morphology in Figure 7.18d versus Figure 7.18e. The 950 W setting (Figure 7.18d) exhibited larger and more randomly oriented grains due to heightened heat input and faster solidification rates. Conversely, lower laser power facilitated the formation of finer, more aligned columnar grains by enabling slower solidification and finer thermal gradient control [434]. Additionally, the higher thermal gradient associated with lower laser power favored epitaxial growth over nucleation of new grains. Moreover, 950 W led to reduced thermal gradient, enhancing constitutional supercooling and fostering equiaxed grain formation, particularly on incompletely melted powder particles. As the build progressed,

grains with <001> pole alignment parallel to the building direction (BD) became predominant, resulting in the observed global fiber texture.

7.7 Process Parameter Influence on Microhardness

The microhardness vickers distribution maps are shown in Figure 7.19 for the cross-sectioned interface region under each process parameter. Measurements were taken from approximately -2/+1.5 mm along the fusion line, where the fusion line was dictated by the change in microstructure (0 mm). The substrate was characterised by a microhardness around 390±10HV and acts as the unaffected region for comparison with a maximum of 430HV. The HAZ for the 750 W illustrates microhardness fluctuations within these areas. The microhardness indents, measuring approximately 30 x 30 μm, suggest that localized high microhardness might stem from primary carbides distributed throughout the HAZ and substrate (indicated by black arrows in Figure 7.20), or from localized high grain density (highlighted by the red arrow in Figure 7.20). Conversely, lower microhardness readings may indicate areas where the indents were placed intergranularly (marked by the yellow arrow in Figure 7.20). Notably, the areas of concentrated high microhardness varied within both the substrate and the PDZ/HAZ region across all three laser conditions. This justifies the increased redness, denoting higher microhardness in the 950W substrate specimen comparative to the 550 W substrate specimen.

In the as-deposited condition, the microhardness of the LMD deposit was significantly lower than the substrate. Overall, the average microhardness for the deposited layers for all three laser powers was 260±13 HV, 262±6 HV and 257 ±7 HV for the 950 W, 750 W and 550 W, respectively. The initial samples displayed a similar microhardness contour profile after deposition. However, the region deposited with 950W exhibited a notable increase in microhardness compared to the 550W specimen, approximately 8%, indicated by a lighter shade of blue in the 950W sample. This phenomenon could be attributed to an elevated occurrence of transformation and precipitation of γ’’/γ’ and δ phases due to accumulated heat from successive depositions. This warrants further investigation, possibly through Transmission Electron Microscopy (TEM) analysis.

Additionally, a slight rise in microhardness observed in the 950W and 750W specimens compared to the 550W sample may be linked to thermal-induced residual stresses in the deposited area, contributing to a work-hardening effect.

The microhardness transition was relatively smooth in all specimens apart from a transition step seen at the fusion line 0 mm ± 0.25 mm, demonstrating the obvious change

in microstructure and phase constituents from the doubled aged substrate with equiaxed fine grain structure to columnar grains with almost negligible strengthening precipitates.

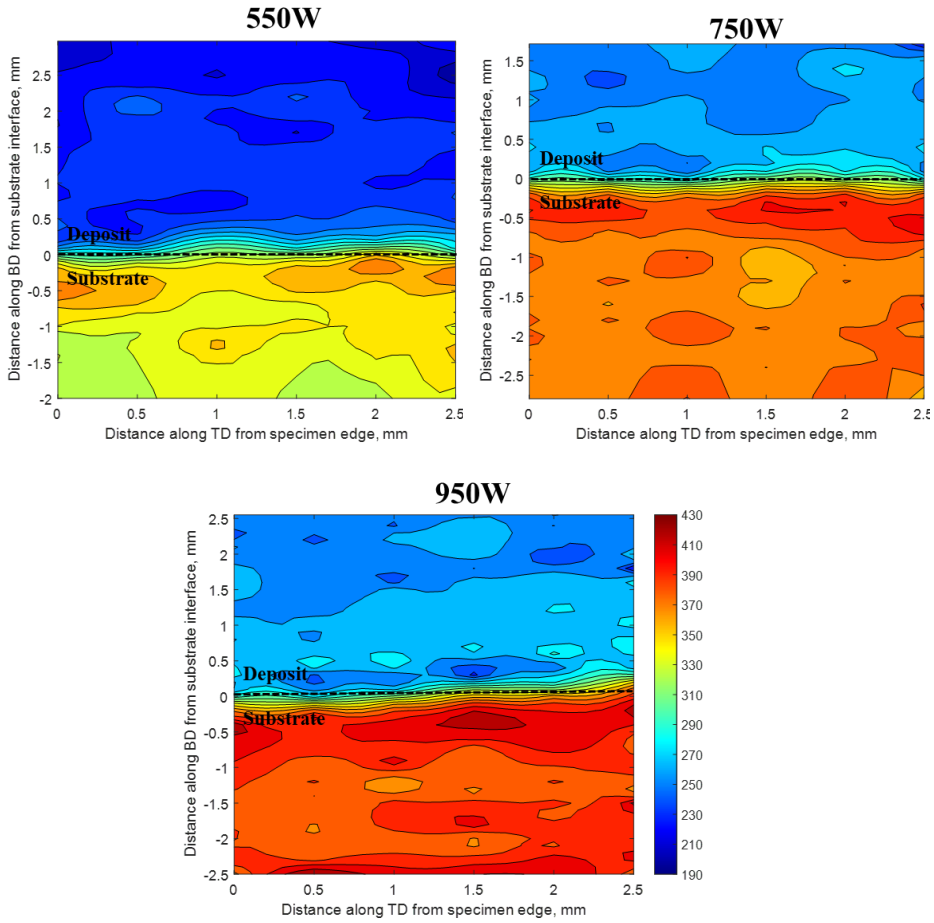

Figure 7.19 Vickers hardness distribution for the interface region in each specimen

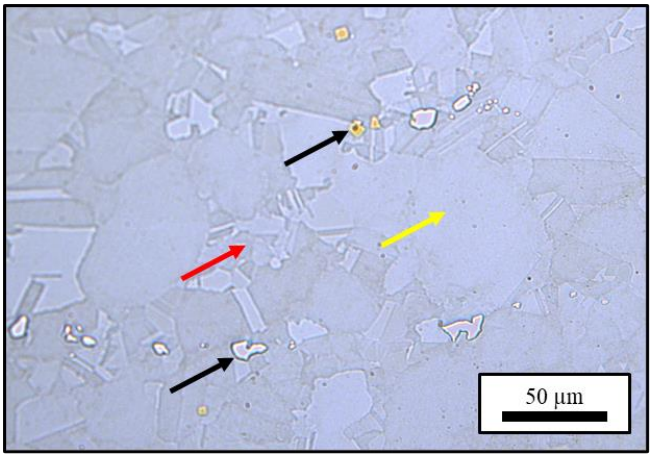

Figure 7.20 Optical micrograph of the HAZ for the 750W specimen detailing microhardness variation

Figure 7.21 shows a more localised microhardness evolution line for the cross-sectional interface region. From -1.3 mm to +1.3 mm this encompasses the substrate, HAZ, PDZ, and FZ to approximately the fifth layer in the build. The reduction in microhardness as it

evolves from the substrate to the HAZ and PDZ could be attributed to dissolution of γ''/γ' phases and δ phase which could lead to marginal grain growth during successive layers. Furthermore, the presence of Laves phase in the PDZ and throughout all the layers as shown in Figure 6.16will continue to deplete Nb sources needed to precipitate the strengthening phases (γ' and γ″).

Following a solution treatment succeeded by double aging, aimed at achieving homogeneity in microhardness across the interface region, the microhardness measurements for all three laser power specimens were determined to be 453±14 HV. In the deposited area, the notable increase in microhardness can be attributed to two main factors. Firstly, the laves phase, which partially dissolves during the solution treatment, Figure 6.19, releases niobium (Nb) alloying elements, thereby promoting the precipitation of the secondary delta (δ) phase at the interdendritic regions. Secondly, the diffusion of the eutectic releases more niobium back into the matrix. Niobium is crucial as it is the primary element in the hard gamma prime (γ'') phase (Ni_3Nb), which precipitates during the subsequent aging treatment and significantly contributes to the increased microhardness.

In the heat-treated specimen's fusion zone ($0 \rightarrow +300\ \mu m$) the microhardness measurements do not reveal a significant difference in values. The reason for this is that the diagonal of the microhardness indents (~30 μm) is large enough to average the microhardness over a larger area which encompasses both well-developed strengthening precipitates and developed precipitates from the dendritic cores. Utilising nano-indentation would have been more appropriate to reveal large differences in nanohardness across the dendritic cores and the γ-phase close to the delta phase [383].

From a macro-structural perspective, a consistent microhardness measurement across the interface region would be attributed to a more even distribution of strengthening precipitates. This even distribution helps to lessen the effect of dissolved particles found in the PDZ of the as-deposited samples. From a micro-structural view, as seen in (demonstrated by Figure 6.20) the depleted dendritic cores caused by Nb segregation (13 wt.% interdendritic vs 5 wt.% dendrite core) could lead to the uneven distribution of the main precipitating phase γ'' during the PWHT. Even with the solution temperature above the γ'' (850 to 950 °C), aiming to evenly distribute the alloying elements, the concentrated Nb surrounding the interdendritic laves phase has been demonstrated to lead to localised plastic deformation [383] . The PWHT employed could have accelerated coarsening of the γ'' strengthening precipitates at the interdendritic region and the γ'' in the dendrite

cores (5 wt.%) are coarsening at a slower rate, leading to an uneven distribution of strain, which could lead to plastic failure if the strain exceeds the elastic limit [383]. A more in-depth analysis on the effect of distribution of strengthening precipitates on mechanical properties is required to validate.

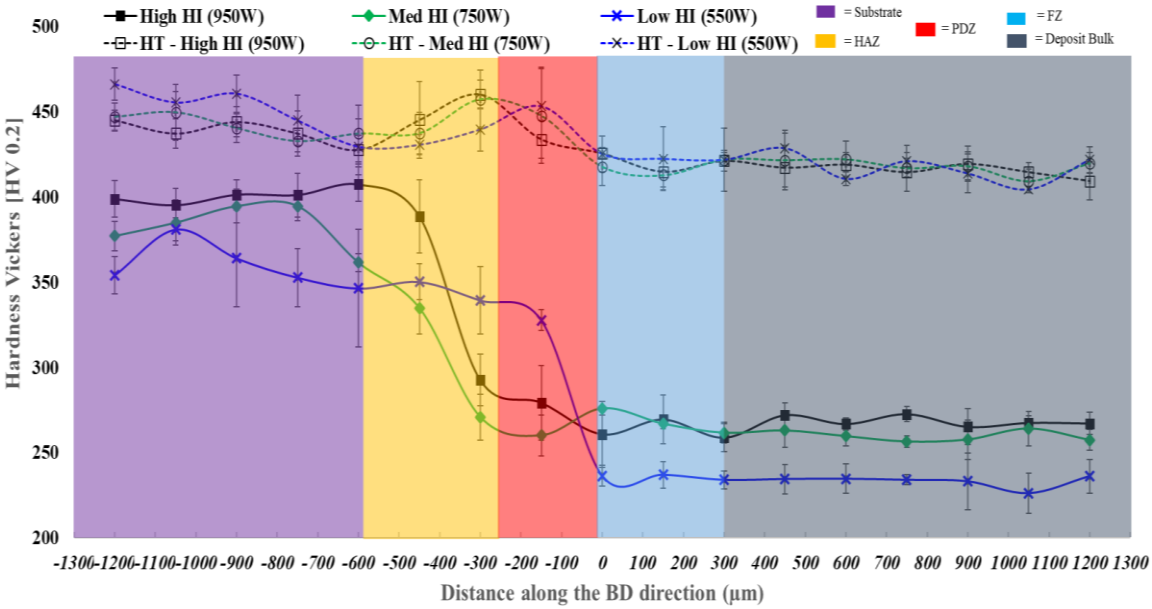

Figure 7.21 Microhardness evolution across the interface region (encompassing the substrate, HAZ,PDZ ,FZ) and deposit bulk for all specimens as deposited and after heat treatment.

Analyzing the hardness gradient in the as-deposited samples from the fusion line to mid-build (Figure 7.22), both the 750 W and 950 W conditions exhibited higher hardness compared to the low laser power build. It might have been expected that the lower laser power would yield the highest microhardness due to experiencing the highest cooling rate, resulting in a finer microstructure and dendrite spacing. However, contrary to this expectation, the low laser power resulted in the lowest microhardness, possibly due to the greater refinement of the hard brittle Laves phase in both volume and morphology. The highest cooling rate limits the time available for micro-segregation, leading to lower microhardness. This decline in microhardness is mainly attributed to the formation of the Laves phase, which often necessitates a post-weld heat treatment for additively manufactured Inconel 718 (homogenization above 1100°C) to eliminate detrimental Laves phase. Additionally, the microhardness measurements reveal no clear gradient from the bottom to mid-build. There is a slight decreasing gradient in the 750 W laser power microhardness with increasing distance from the fusion line. As mentioned in Chapter 6, it could be hypothesized that very fine γ'' precipitates would be found closer to the FZ. These precipitates would start to form in the lower layers due to subsequent

layer addition and coupled with the increase in grain size with increased subsequent layers (due to a cooling rate reduction), resulted in a decreasing microhardness gradient along the build direction. However, high-resolution NanoSEM may have been required to detect the γ'' precipitates (around 10 nm) [435].

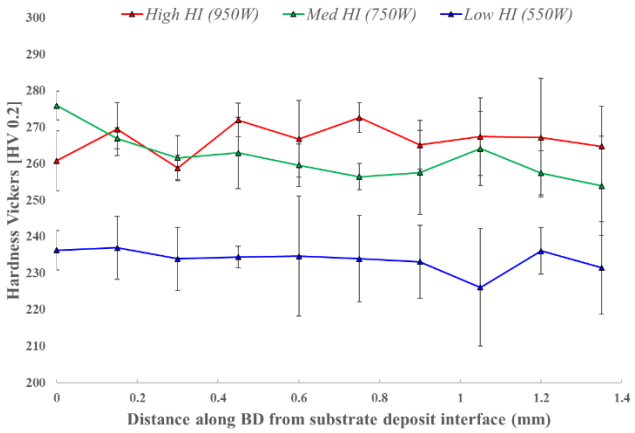

Figure 7.22 Microhardness gradient along the build-up direction up to approx. mid-build.

Finally, Figure 7.23 illustrates a comparison between the SEM microscopy analyses of the volume fraction of δ-phase in the substrate, depicted by red arrows as bright-white phases with needle morphology, under two conditions: (a) as-received and (b) heat-treated. An overview reveals a significantly higher concentration of δ-needles precipitated at the grain boundaries in the heat-treated condition. The average length of the δ-phase needles increased by 639.4%, accompanied by a 489.7% increase in area fraction, indicating a denser distribution of secondary precipitates. This increase in δ-phase, both in average length and volume fraction, contributes to hardness enhancement [387], [436]. Regulating the amount of δ phase is known to enhance material hardness as δ precipitates grow intragranularly in the matrix, thus potentially increasing material ductility by lowering the yield strength. Nonetheless, high levels of intragranular precipitates lead to substantial hardening of the IN718 alloy, consequently lowering ductility [437], [438], [439]. This behaviour significantly raises microhardness, emphasizing the importance of evaluating substrate ductility and strength before and after heat treatment. Unfortunately, these material properties were not tested in the current study but are slated for investigation in future research endeavours.

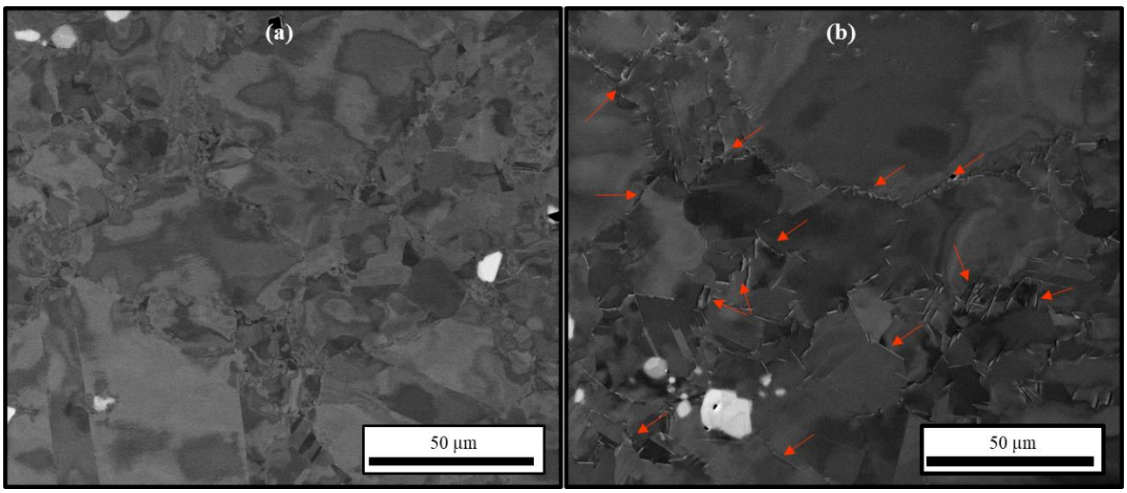

Figure 7.23 Substrate δ-phase precipitate behaviour in the (a) as-received condition vs (b) heat-treated condition.

7.8 Process parameters influence on precipitation– in As Deposited (AD) condition

7.8.1 Microstructural Evolution across Interface

To understand the effect of build height and laser power on the crescent thickness (measured in Figure 7.24) and therefore extent of dissolution, the bright crescent was analysed for the single-track deposition, thin-walled builds, and multi-layered solid blocks (bright band highlighted by the red dashed box in Figure 7.25). Due to the gaussian distribution of the laser behaviour, measurements were taken as the average thickness measurement across the entire crescent. By measuring the crescent thickness, the evolution of key microstructural differences with respect to partially dissolved phases can be deduced from the fusion line into the substrate.

This bright crescent band appears at the bottom of the melt pool in as-deposited IN718 [77], [440], [441] and is subject to extreme temperatures which dissolves the δ-phase (δ solvus temperature, 996-1015°C [440]) which could unpin the microstructure and cause grain morphology change. A common defect reported in literature [442], [443], [444] which is observed in the partially dissolved zone of the build is liquation cracking. Rapid heating below the liquidus temperature of the alloy causes dissolution of certain grain-boundary precipitates such as δ-phase. During the cooling phase, the PMZ is subjected to a tensile force due to solidification shrinkage and thermal contraction of the deposit. Under such force, the liquid films around these grain boundary phases which may act as crack initiation sites.

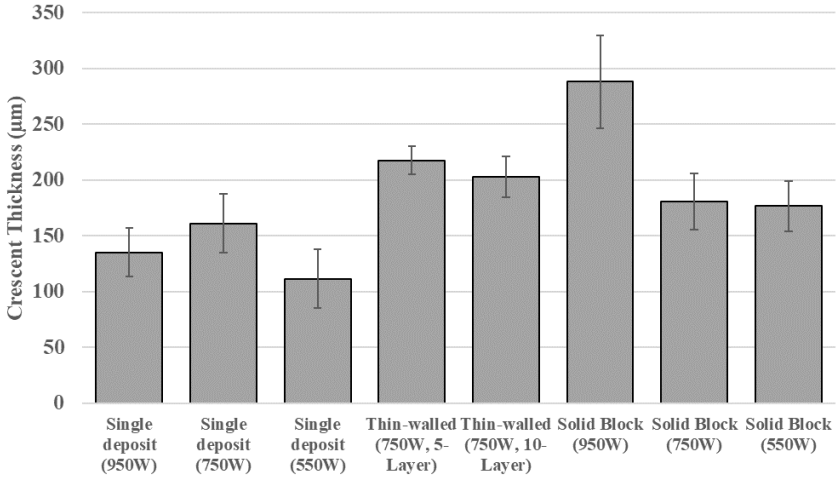

Figure 7.24 Measured crescent thickness at the bottom of the melt pool.

Increasing laser power is consistently associated with a larger heat-affected zone (HAZ) in both single deposits and solid block builds. Comparing 950W and 750W to low laser power, there was a >20% increase in HAZ extent for single deposits. Solid block builds showed a significant 150% increase in crescent thickness when laser power was increased. However, contradictory results were observed, with low and medium laser powers producing consistent crescent thickness in solid blocks, and the 750W laser generating a higher thickness band in single deposits. Nonetheless, it can be inferred that higher laser power leads to a thicker crescent band and an expected linear increase in the dissolution region. This behaviour can be explained by the higher volume of energy provided to the localized region, resulting in greater thermal energy absorption at the bottom of the melt pools.

Microstructural differences and phase dissolution are analysed for each process condition. Figure 7.25 displays the microstructure of the high laser power interface in solid block deposition, revealing the distinct regions. SEM analysis at different depths (P1-P6), compared microstructural features from the PDZ (P1) though to substrate (P6), highlighting changes in Figure 7.26. The phases were correctly determined through EDS analysis. As the distance from the fusion line increased, the localized region's maximum temperature decreased due to thermal energy dissipation through conduction and losses which will be discussed with associated temperature profiles in the following section.

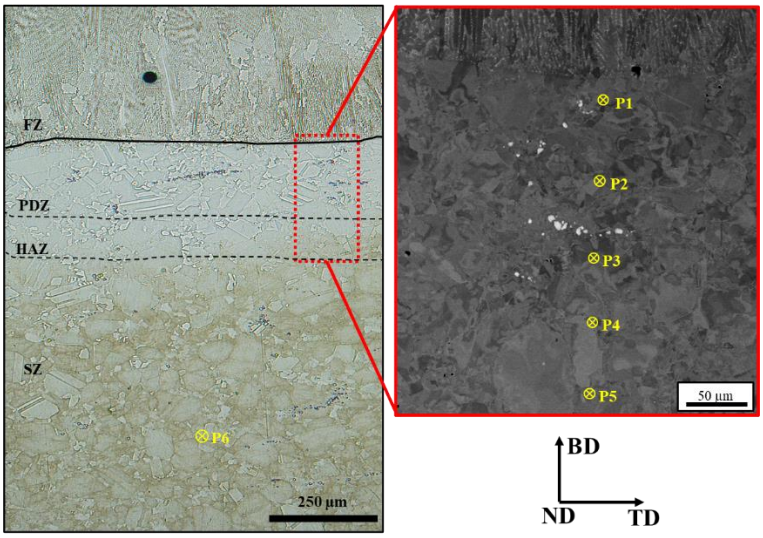

Figure 7.25 (a) OM image illustrating the microstructures in the (FZ), partially dissolved zone (PDZ), heat affected zone (HAZ) and substrate zone (SZ)(P6) of the representative high laser power interface region with (b) SEM image detailing the different regions of inspection P1-P5.

In the partially dissolved zone (PDZ) and heat-affected zone (HAZ), a more complex combination of features was observed compared to the parent material. Close to the fusion line (P1), it was visually challenging to discern distinct grain boundaries, potentially due to beam stabilization interference at high magnification. These grain boundaries appeared amorphous, requiring EBSD analysis for further grain characterization. Precipitated Laves phase (<1 µm) were observed at the grain boundaries in this region and require further discussion in the following section. The temperature simulation indicated that the region exceeded the liquidus temperature (1336°C) for 130 ms, initiating dissolution of the grain boundaries without complete remelting of the grains. The absence of δ-phase, which fully dissolved into the γ matrix, contributed to the grain boundary unpinning. The strengthening phases γ''/γ', which were prominently observed in the substrate as depicted in Figure 6.16 of the previous chapter, were conspicuously absent in this particular region. It is highly probable that these precipitates were dissolved, likely due to the elevated temperature near the melt pool. Previous studies have reported the dissolution of δ and γ'' precipitates at 1150°C, which aligns with the absence of δ-related peaks in the XRD pattern [445]. Additionally, Lass *et al.* [445] showed that the segregated solidification microstructure of PBF IN625 had not fully homogenized, indicating that the time required for δ/γ'' dissolution is shorter than the time needed for complete homogenization at the same temperature. Complete dissolution of secondary precipitates and homogenization at 1150°C typically require 15 min and over 30 min, respectively [446].

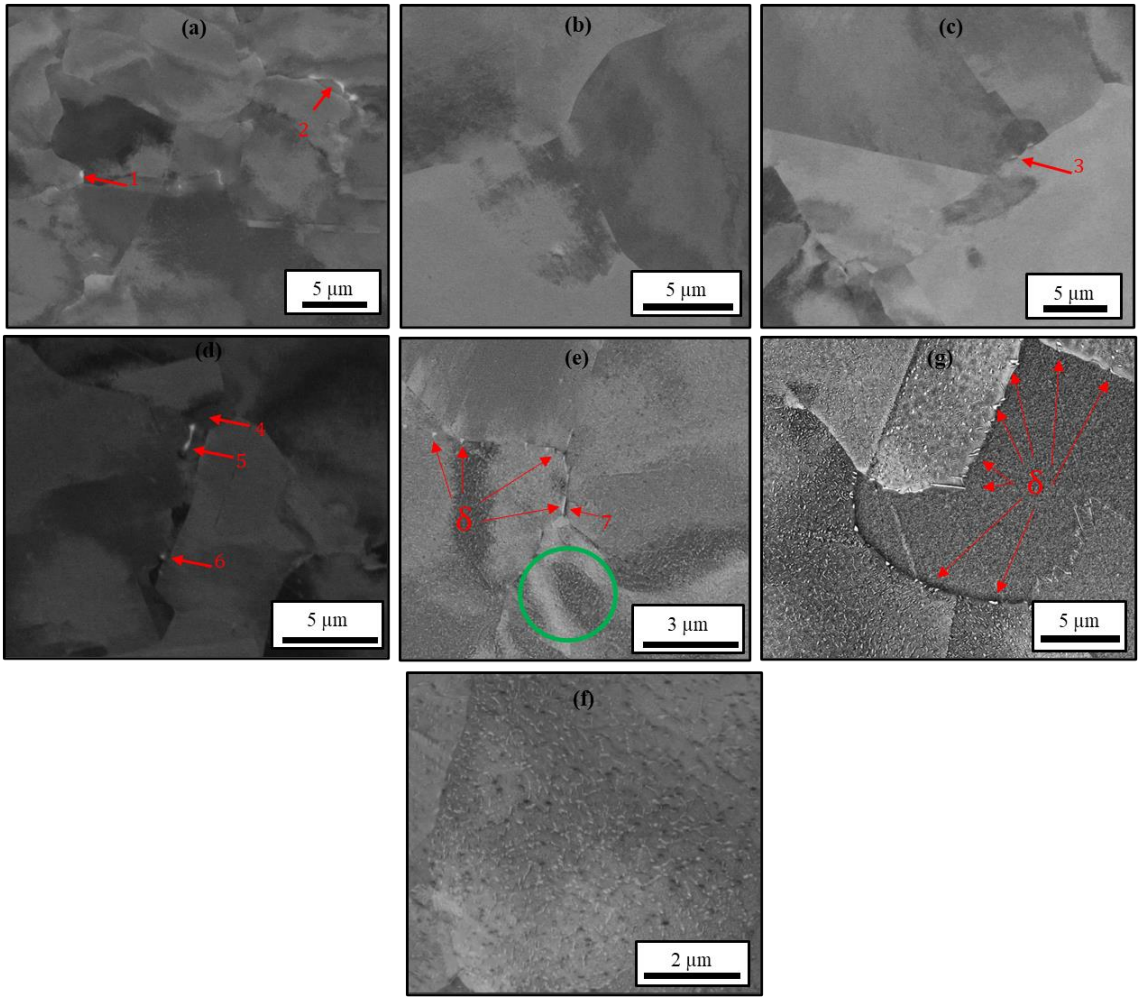

Figure 7.26 SEM Investigation for microstructural features at varied positions with corresponding distance from fusion line (depicted as beginning of dendritic growth) for the 950W specimen; (a) P1 (20µm), (b) P2 (80µm), (c) P3 (150µm), (d)) P4 (190µm), (e) P5 (300µm) with (f) higher magnification SEM and (g) P6 (700µm)(N.b. the red arrows and numbers translate to the EDX information described in Table 7.1)

Table 7.1 Composition of microstructural phases presented in Figure 7.26

Position	Phase Designation	Ni (Wt.%)	Fe (Wt.%)	Cr (Wt.%)	Nb (Wt.%)	Mo (Wt.%)	Ti (Wt.%)	Al (Wt.%)
1	*Laves*	48.5	13.0	13.5	18.7	4.1	1.8	0.4
2	*Region surrounding Laves*	50.2	14.9	16.2	12.9	3.6	1.7	0.5
3	*Nb-rich particulate*	52.6	18.8	18.4	5.6	3.1	1	0.5
4	*Matrix*	53.2	19.3	19.6	3.9	3	0.6	0.4
5	*Delta*	52.1	14.4	14.8	12.8	3.3	2.1	0.5
6	*Nb-rich Particulate*	50.9	18.1	17.9	8.3	3.3	1.1	0.4
7	*Delta*	48.9	13.9	14.7	17.6	3.6	1.1	0.2

The microstructure and its associated features delineated in P1 seamlessly transitioned into P2, with dimensions measuring approximately 80 µm, 80 µm, and 60 µm for the 950W, 750W, and 550W specimens, respectively, as depicted in Figure 7.26b. Nevertheless, the Laves phase, which had precipitated in P1, was conspicuously absent

in this particular region, thereby resulting in an enrichment of the γ matrix with Nb and Mo. Moving away from the fusion line, variations in the microstructure were observed.

At P3 (as depicted in Figure 7.26c), situated roughly 100-150 µm distant from the fusion line across the 550 W, 750 W, and 950 W specimens, the strengthening phases remained undetectable, suggesting a complete dissolution into the γ matrix, consequently augmenting the local area with Nb. However, grain boundaries appeared more defined, and small precipitates (~500 nm) were observed (*Red arrow, number 3*). These precipitates were enriched by ~43.6% with Nb and ~66.6% Ti than the matrix, while being depleted in Fe and Cr. They were identified as Nb-rich "particulates" similar in composition to Ni3Nb-δ and could be hypothesized to form due to the phase transformation of γ'' to Ni3Nb-δ or dissolution of δ precipitates during the subsequent heating stages of laser metal deposition [339]. A high-resolution TEM analysis of the Nb-rich precipitates would be needed to reveal the crystal structure. The δ phase is an equilibrium Ni_3Nb precipitate with an orthorhombic crystal structure which requires about 6-8% Nb and precipitates in the range of 860-995°C [447]. The dissolution of δ-particulates occurred in the PDZ due to high temperatures exceeding the solidus of the δ-phase. This trend continued up to P4, extending another 40-50 µm from P3 shown in Figure 7.26d.

At point P5, delineated in Figure 7.26e, positioned approximately 300 µm beneath the fusion boundary within the Heat Affected Zone and Substrate Zone interface, the microstructural characteristics mirrored those of the SZ. Notably, the structure primarily exhibited globular-shaped δ precipitates situated along the grain boundaries of γ grains. Concurrently, age-hardening γ'' and γ' precipitates, identifiable by bright specks, were uniformly dispersed throughout the matrix. These observations are illustrated by the green encircled region in Figure 7.26e. The needle-like Ni3Nb-δ particles at the grain boundaries measured up to 1.5±0.2µm in length and approx. 131.2±51 nm in width, while globular-δ with very few needle-like δ precipitates measured around 250±210nm. Age-hardening precipitates measured 98.4±30.6 nm. Compared to the SZ (Figure 7.26g), the volume of δ-phase at the grain boundaries was noticeably less.

Figure 7.26g displays the microstructural features of IN718 SZ at P6, located 700 µm below the fusion line. This region appeared largely unaffected by the LMD build, with temperatures suitable for aerospace-grade IN718. Randomly distributed Nb-rich primary carbides and carbonitrides with sizes up to 10 µm were observed at γ matrix grain boundaries and intergranular regions. Globular and needle-like Ni3Nb-δ precipitates,

approximately 1-2 μm in size, were distributed within the grains and at the γ grain boundaries. Minor coarsening or re-precipitation of strengthening phases, γ'' and γ', could occur due to multiple thermal cycles, but further TEM analysis is required for confirmation. To qualitatively analyse the effect of LMD and the influence of power on precipitation behaviour, the dissolution distance of Nb was calculated based on location specific temperature history. The formation and dissolution of the precipitates in question such as γ'', Laves and δ are directly related to the amount of Nb in the microstructure [448].

7.8.2 Diffusivity of Precipitation kinetics in Partially Diffused Zone (PDZ) and Heat Affected Zone (HAZ)

Stress fields from dislocations and vacancies in the Laves phase cause dislocations and solute atoms, including Nb and Mo, to migrate [76]. The non-coherent interface between the Laves phase and the γ-matrix increases vacancy concentration, enhancing solute atom movement and Laves phase dissolution. This also applies to the δ-phase due to its non-coherency. Nb and Mo, highly segregated in IN718, have slow diffusion rates, needing high temperatures or long dwell times for homogenization. High temperatures (>1200°C) at interfaces trigger Nb diffusion into the γ matrix, leading to phase liquation and altering Nb distribution. Nb diffusion in superalloys was assessed using the Arrhenius expression:

Equation 7.2

$$D = D_0 \, x \, exp^{\left(\frac{Q}{RT}\right)}$$

where D_0 is the pre-exponential factor, Q is the activation energy (~234 kJ/mol), R is the gas constant, and T is the absolute temperature. Diffusion studies by Sohrabi *et al.* [449] provided insight into the diffusion of Nb in Ni-based superalloys. The diffusion coefficient (D) for Ni-Nb diffusion couple was determined to be 30 times higher than that of superalloys. The interdiffusion of Nb in highly alloyed Ni-based superalloys is generally slower due to the presence of intermetallic phases and multiple diffusion mechanisms involved:

Equation 7.3

$$D=0.0053\exp{-236600RT} \Leftrightarrow Superalloys$$

Equation 7.4

$$D=0.1618\exp{-234100RT} \Leftrightarrow Ni-Nb$$

Diffusion coefficients for Nb at different temperatures were calculated and are presented in Table 7.2. By applying Fick's second law of diffusion, the diffusion distance (l) of Nb

from Nb-rich phases (δ, γ'', and Laves phases) to the γ-matrix can be determined, considering a numerical constant depending on the dimensionality of diffusion. In this case, three-dimensional diffusion is considered due to the morphology of the precipitate phases.

Table 7.2 Diffusivity values of Nb in superalloy

Temperature (K)	***Temperature (°C)***	***D_{Nb} (cm^2/s)***
1573	*1300*	*$7.71E^{-11}$*
1500	*1227*	*$3.20E^{-11}$*
1473	*1200*	*$2.27E^{-11}$*
1431	*1158*	*$1.29E^{-11}$*
1373	*1100*	*$5.57E^{-12}$*
1323	*1050*	*$2.55E^{-12}$*
1310	*1037*	*$2.06E^{-12}$*
1279	*1006*	*$1.22E^{-12}$*
1272	*999*	*$1.08E^{-12}$*
1236	*963*	*$5.63E^{-13}$*
1223	*950*	*$4.41E^{-13}$*
1173	*900*	*$1.64E^{-13}$*

Knowing the diffusion coefficient at various temperatures and times (in s), the diffusion distance (l) (*mean distance from a start point that a molecule will have diffused in time, t_e*) of Nb from Nb-rich phases in substrate (δ, γ'/ γ'') to the γ-matrix can be determined by Fick's second law of diffusion [450], [451], [452]:

Equation 7.5

$$l = \sqrt{D_e t_e q_i}$$

The diffusion coefficient (D_e) is determined by equivalent time (t_e) and dimensionality (q_i), with values of 1, 2, 4, or 6 for 1D, 2D, or 3D scenarios, respectively. For this study, only 3D diffusion is considered due to the precipitate phase morphology, which is uniformly distributed in three dimensions. Hence, Nb diffusion into the γ-matrix is modelled using Fick's second law with a q_i of 6, ensuring accurate characterization of D_e based on the spatial distribution of the precipitate phases.

Reports indicate that δ diminishes with rising annealing temperatures, suggesting accelerated Nb diffusion into the matrix. Additionally, literature indicates that higher temperatures lead to increased D_{Nb} due to enhanced atomic vibration and higher vacancy concentration [78, 82, 83]. Therefore, the temperature range of 900-1300°C was selected,

based on key temperatures associated in these studies, e.g. δ-solvus temperature (990-1015°C) and solidus temperature (~1260°C). The temperature profiles specific to each position (P1-P5) were extrapolated from the coupled thermomechanical model and are illustrated in Figure 7.27. Based on these temperature profiles, a step-based best fit method (in 100°C increments) was utilized to calculate the diffusion distance. The total diffusion distance based on atomic radius is determined by combining individual diffusion distances calculated from the duration between minimum (900°C) and maximum temperatures (1300°C). It is important to note that Nb diffusivity in superalloys is influenced by several factors such as composition, microstructure, environmental conditions, and the processing history of the alloy[453]. Therefore, more accurate diffusion lengths may require experimental characterization and validation.

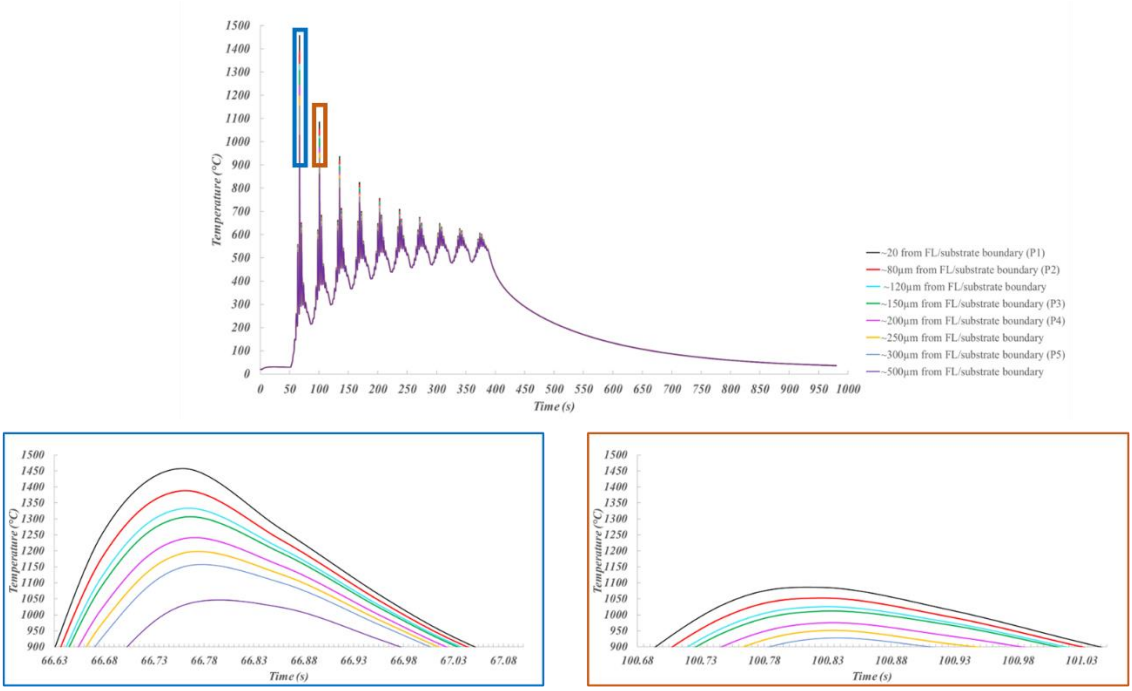

Figure 7.27 Location specific temperature history profile for 950W across the interface region detailing the first- and second-layer pass during the build process.

The key input parameters for diffusion length calculations included the initial size distribution of δ-phase (approximately 422±385 nm or 113±51 nm for shortest length) and γ''-phase (approximately 54.1±18.17 nm) assumed to be plate-like morphology. These measurements were collected from various positions within the substrate. They represent half the maximum length to estimate the position if the Nb was in the middle of the phase, diffusing along the longest measured axis. Additionally, the parameters included the temperature history at specific locations, the diffusivity of the rate-limiting

solute (assumed as Niobium), and the equilibrium of γ-phase [454]. Singh *et al.* [452] showed how the atomic mobility is higher at the grain boundaries than that in grain interiors occurring with lower energy of activation [452]. To estimate the Nb diffusion distance at grain boundaries, the same D_0 value as in the bulk was used. Since no self-diffusion coefficients for Nb at grain boundaries have been reported, an activation energy (Q) half that of the bulk was applied, consistent with FCC metals [455].

The diffusion distances, calculated for both grain boundary and bulk diffusion, are depicted in Figure 7.28. This representation focuses on the area located 20 µm from the fusion line within the 950 W specimen. This specific region experiences the highest temperatures due to its proximity to the fusion line and the maximum laser power applied. A notable exponential rise in the diffusion distance of Nb is observed at grain boundaries as temperature increases, reaching approximately 4.2 µm at 1010°C. This aligns with the observation that diffusion at grain boundaries occurs significantly faster—100 to 1000 times—compared to bulk diffusion rates. Given the order of magnitude greater diffusion distance along grain boundaries compared to bulk, it is anticipated that the δ-phase anchoring these boundaries would experience substantial dissolution during thermal cycling. Studies have shown that when the δ phase dissolves from grain boundaries, grain growth accelerates until precipitation, such as carbides and nitrides, assumes a similar pinning role. However, their impact is generally weaker compared to that of the δ phase [381], [456], [457].

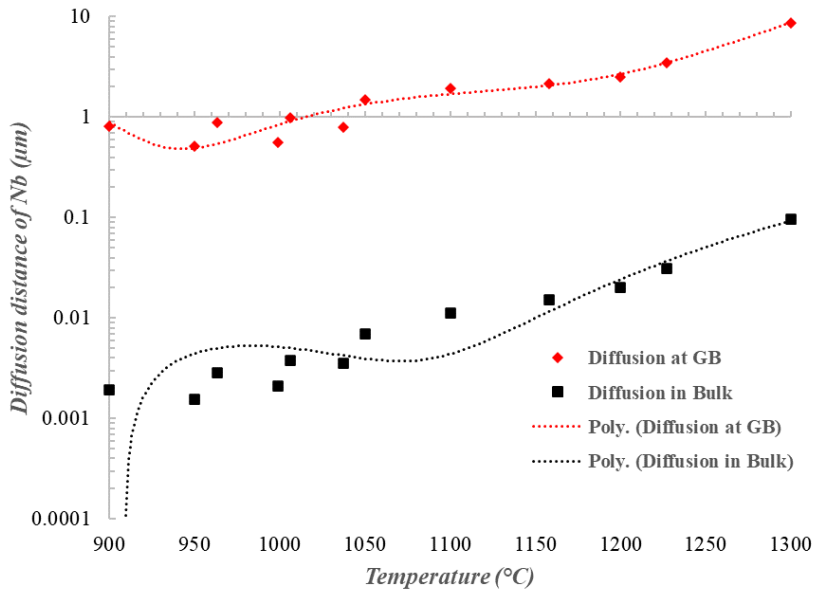

Figure 7.28 Calculated diffusion distances of Nb during layer 1 deposition at a proximity of 20µm from FL with an equivalent time >900°C of 0.4 s

Calculations of diffusion lengths revealed that they were most extensive at elevated temperatures, notably along grain boundaries and with greater distances towards the fusion line. Figure 7.29 depicts the calculated diffusion distances for all three laser power conditions, utilizing localized simulated temperature profiles up to 500 µm from the fusion line (bottom of the melt pool).

Between the fusion line and P2, located roughly 80 µm away, the Nb diffusion length was determined to be 183 nm, 177 nm, and 189 nm for laser powers of 950 W, 750 W, and 550 W, respectively. Furthermore, within a distance of up to 100 µm, the Nb diffusion length was estimated to range from approximately 125 nm to 175 nm for the 550 W, 750 W, and 950 W conditions. This range allows sufficient distance for the complete dissolution of γ'' and δ phases, considering the shortest axis length. At 200 µm from the fusion line in the high laser condition, the Nb diffusion length reduced to around 100 nm, potentially fully dissolving γ'' but only partially dissolving δ-phase, consistent with the microstructural observations of Nb-rich particulates. Beyond 300 µm, although no significant microstructural changes were observed in the δ-phase and γ'' phases, the calculated diffusion distance was approximately 40 nm, suggesting potential dissolution of γ''/γ'. For the 750 W condition, microstructural features appeared unaffected at around 200 µm from the fusion line, while the calculated diffusion length was approximately 65 nm, surpassing the measured γ'' phase, indicating complete dissolution. In the lower laser condition, complete dissolution was observed up to ~100 µm, with Nb-rich particulates observed beyond that distance, although Figure 7.29 indicates complete dissolution of the δ-phase. Features were unaffected around 220 µm, with a calculated diffusion distance of approximately 70 nm at that point.

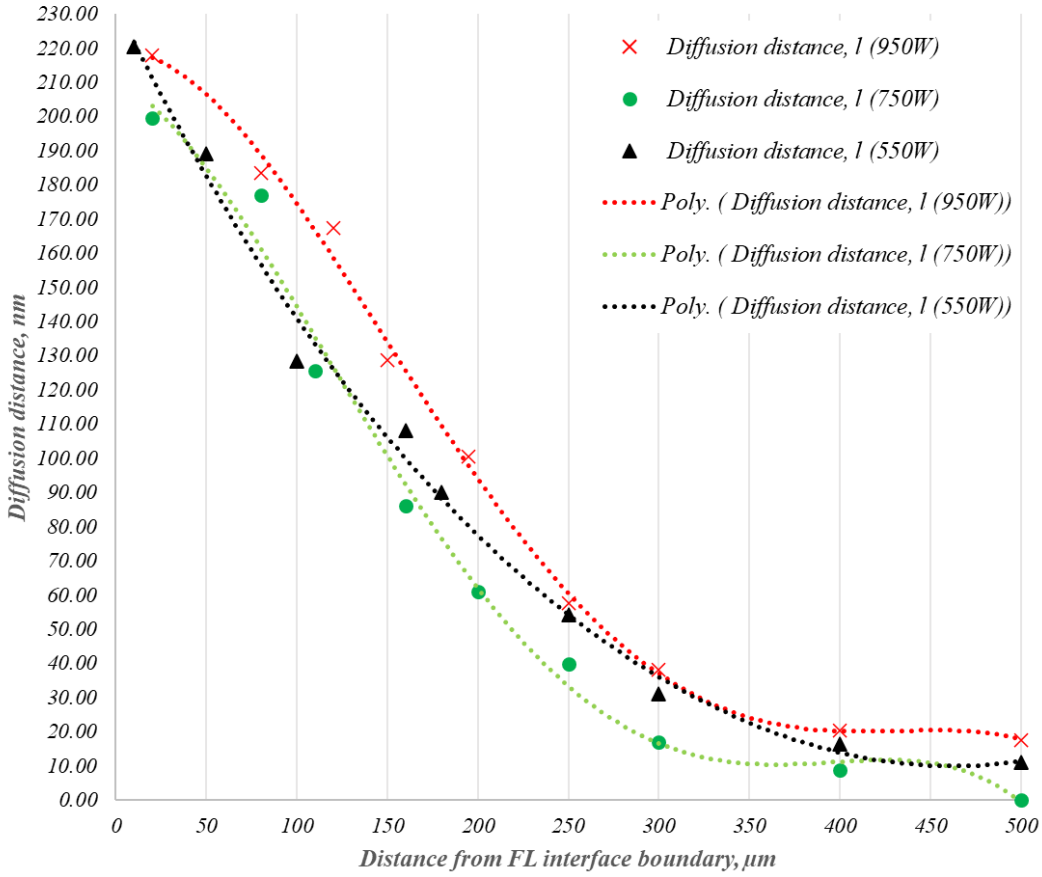

Figure 7.29 Diffusion distance of Nb based on simulated temperature history plots extrapolated from measured distances from fusion line.

Analysis of the calculated diffusion lengths of Nb at the interface region following LMD reveals that both the δ-phase and γ'' precipitates readily dissolve into the γ matrix at elevated temperatures within the immediate vicinity of the melt pool (0→120 µm). This agreed strongly with the experimental investigation of the phases using SEM and the calculated Nb diffusion distance specific to location dependent temperature histories. Experimental and modelling results consistently demonstrate that as laser power and proximity to the fusion line increase, the time for the diffusion-controlled δ+γ"→ γ (enriched) transformation also increases, resulting in higher locally enriched Nb content. It is expected that Nb has the atomic mobility to diffuse back into the matrix, staying in solid solution and participate in local compositional changes of δ and γ'' due to the dissolution time-temperatures experienced. Regarding the 550 W specimen at a distance of 250 µm, the calculated Nb diffusion distance was approximately 54.4 nm. Consequently, it would be anticipated that γ'' would be fully dissolved. However, contrary to this expectation, microstructural examination revealed the presence of γ'' (as indicated by the green arrow in Figure 7.30). Such disagreement between the calculated

diffusion distance and experimental results are in relation to the temperature history extrapolated from the model.

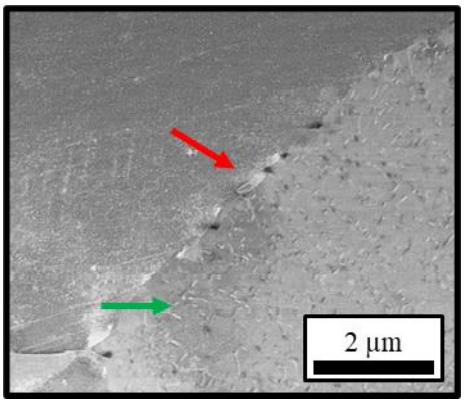

Figure 7.30 A high-magnification SEM image highlighting both the δ-phase (indicated by the red arrow) and γ'' strengthening precipitates (indicated by the green arrow), situated approximately 250µm from the fusion line in the 550 W specimen.

Cross-sectional micrographs reveal the necessity of stabilizing the laser equipment due to inconsistencies observed in melt pool depth. The 750 W laser resulted in a non-uniform melt pool shape (see Figure 7.4), potentially leading to variations in the temperature history profile. Notably, one side of the melt pool appears deeper than the other, suggesting possible irregularities in laser power delivery. Focusing issues and inconsistent power distribution contributed to an uneven melt pool. These limitations warrant further investigation to establish a direct correlation between temperature history and microstructural studies.

The discrepancy between microstructural analysis and calculated Nb diffusion lengths may stem from limitations in the simulated temperature history profile. Future efforts could address this by incorporating computational fluid dynamics (CFD) modelling, which not only accurately depicts laser source geometry studying fluid dynamics but also considers additional factors such buoyancy forces, the Marangoni effect, and recoil pressures. Nevertheless, the calculated diffusion distances provide a valuable qualitative method for enhancing our understanding of the microstructural evolution of precipitates along the PDZ.

7.9 Process parameter influence on microstructural precipitate behaviour – PWHT Condition

Figure 7.31 illustrates the microstructural characteristics within the partially dissolved zone (PDZ), where needle-like Ni3Nb-δ precipitates originating from the Laves phase are evident along the fusion line. A notable abundance of these needle-like δ precipitates is observed in the PDZ near the fusion zone (FZ). These δ precipitates, present in the post-

deposition heat treatment (PDHT) condition, likely result from both liquid particles present in the as-deposited condition and the abundant Nb content derived from dissolved δ-phase and γ''/γ' phases. The solution treatment temperature of 954°C utilized in this study was below the liquidus temperature of δ-precipitates, suggesting that the heat input from LMD was insufficient to fully dissolve all the globular Ni3Nb-δ precipitates in the heat-affected zone (HAZ) and as-deposited material. Consequently, in the PDHT condition, the HAZ exhibits a microstructure resembling that of the as-deposited material, comprising a γ matrix, globular δ-phase, Nb-rich MC-type primary carbides, and γ' and γ'' phases.

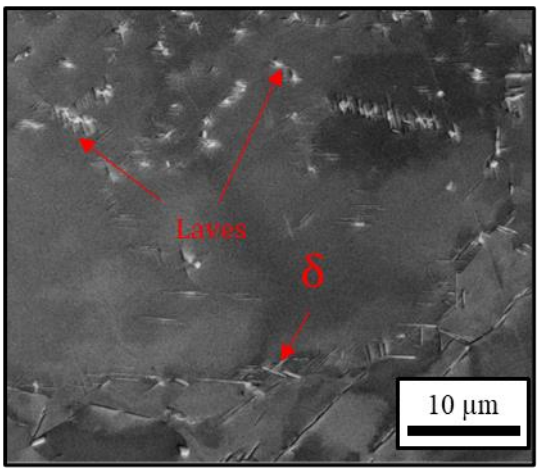

Figure 7.31 SEM micrograph of PDZ in the PDHT condition.

In the partially dissolved zone (PDZ), solid solution carbides of the parent material were observed within approximately <10 µm from the fusion zone. Some of these carbides were found to have intermixed with the deposited region and were present within the fusion zone. The rapid cooling rates in the fusion zone prevented the precipitation of these carbides, and their presence in the fusion zone indicated intermixing from the substrate. Solid solution particles appeared darker in BSE microscopy, resembling TiN, while the brighter particles were NbC carbides due to the presence of heavier elements like Nb. EDS spectra analysis confirmed the composition of these particles, as shown in Table 7.3

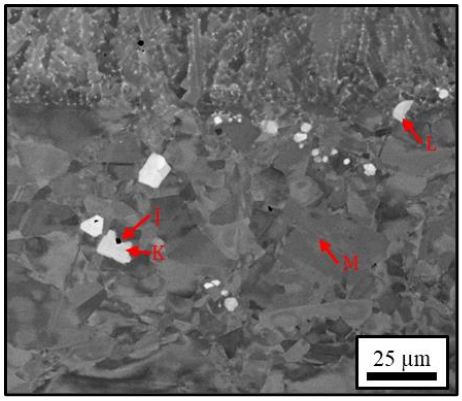

Figure 7.32 BSE image of the PDZ at the 750W interface.

Table 7.3 Chemical composition of elements present at the interface in Figure 7.32

Position	Phase Designation	Ni (Wt.%)	Fe (Wt.%)	Cr (Wt.%)	Nb (Wt.%)	Mo (Wt.%)	Ti (Wt.%)	Al (Wt.%)	C (Wt.%)	N (Wt.%)
J	*Ti-Nitride*	1.2	Na	Na	4.5	Na	63.9	0.4	5.5	14.7
K	*Solid Solution Carbide*	1.5	0.2	0.2	72.6	Na	6.0	0.5	19.0	Na
L	*Solid Solution Carbide*	1.2	0.6	0.5	69.1	1.8	6.1	0.2	20.5	Na
M	*Matrix*	52.6	19.3	18.6	4.9	3.0	0.9	0.5	0.1	Na

The C content of these NbC particles were significantly high, indicating that these particles are compounds of Nb. These carbides were randomly dispersed through the substrate material with irregular morphologies, suggesting the carbides formed during solidification of the substrate. Their presence within the FZ and along the FZ boundary layer is consistent with the fact the carbides have a high melting point (≈3600°C) [440] much higher than that of IN718 (≈1366°C) and measured via thermomechanical model of around 2000°C.

7.10 Process Parameter Influence on Laves Phase Behaviour at the Fusion Line

SEM analysis of the cross-section in the X-Z plane was conducted to examine the behaviour of Laves phase across the fusion line. In Figure 7.33, the dark grey/black phase represents the austenitic matrix, while the brighter interdendritic regions indicate the Laves phase and Nb segregation (mass contrast). The Laves phase and Nb-rich phases formed a network surrounding the dendrite cells, exhibiting channel-like growth parallel to the build direction (Z-direction). The extent of Nb segregation is influenced by the cooling rate and thermal history of the as-deposited build [458]. The bottom region, as expected with dendritic crystal growth, showed the highest concentration of Laves phase forming interdendritic channels. Below the fusion line, small eutectic-Laves islands were observed prior to the transformation into long-chain Nb segregation. The PDZ area,

within 40 µm of the fusion line, experienced very high cooling rates with the substrate acting as a heat sink.

The formation of this Laves phase band during the early stages of solidification, along with the channel-network morphology above it, suggests that it was not a result of heat accumulation from multiple deposition cycles. Furthermore, this band did not undergo complete liquid-phase precipitation, as evidenced by the apparent equiaxed substrate grain boundaries and the absence of full melting of the substrate grains. Laves phase formation typically requires a niobium concentration ranging from 10-30% [459] and is usually enriched with Nb, Mn, and Ti while being depleted in Ni, Fe, and Cr.

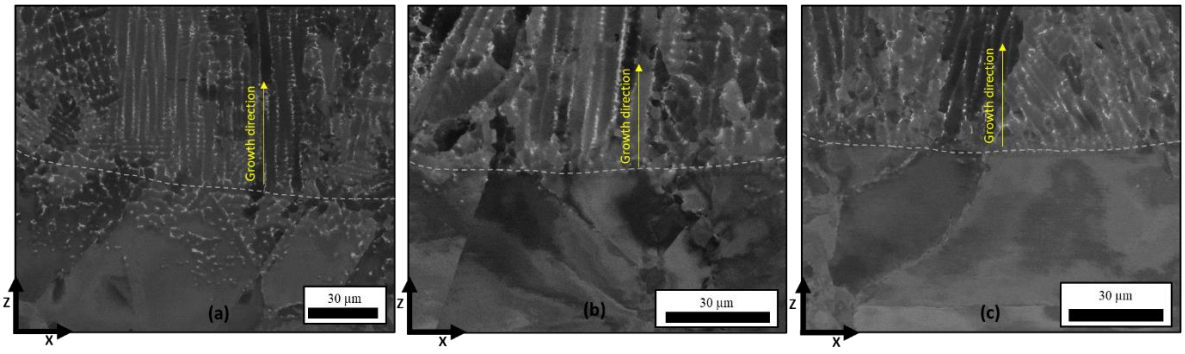

Figure 7.33 As-deposited precipitated laves phase morphology across the fusion line for (a) 950W, (b) 750W and (c) 550W laser power specimen.

Understanding the phase transformations during continuous cooling transformation (CCT) is crucial for microstructure engineering, especially when considering the cyclic heating and cooling complexities of the LMD process. Figure 7.34 displays CCT diagrams for Inconel 718 [460], [461], although they do not account for the multiple thermal cycles typical in LMD. However, they provide an indication of Laves phase formation in the band below the fusion line. The temperatures in this region are expected to surpass the liquidus temperature due to the proximity to the bottom of the melt pool.

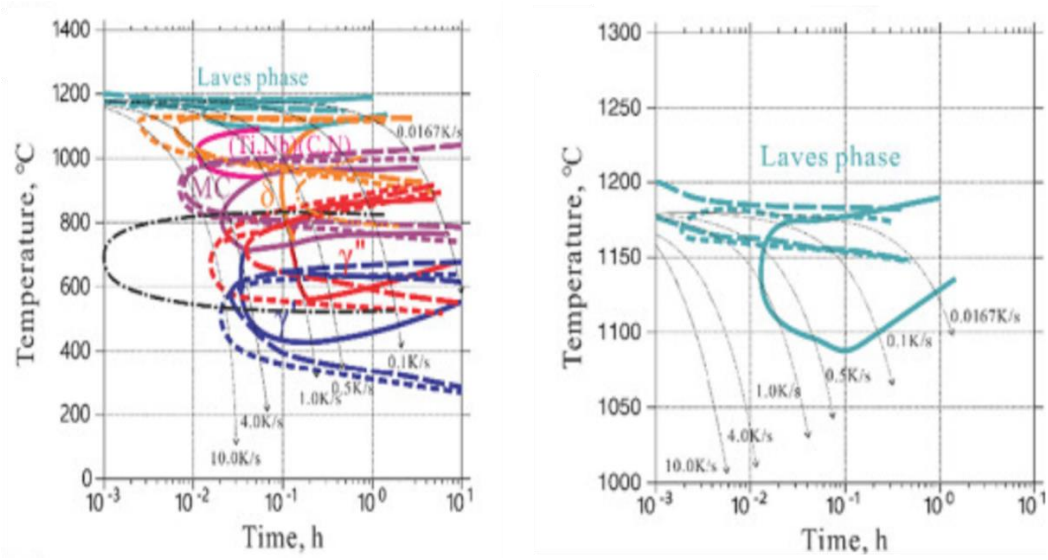

***Figure 7.34 CCT diagram according to Garcia et al.** [460] for (a) phase transformations during the continuous cooling process with (b) separate plot of the CCT diagram related to Laves phase. The different dashed lines represent the CCT curves determined after various homogenization times taken from Zhao et al. [461].*

As concluded in Figure 7.27, the duration spent above the liquidus temperature is minimal (130 ms). The formation of Laves phase occurs during non-equilibrium solidification and follows a microstructural evolution of L→L+γ→L+NbC/γ→L+Laves/γ [462]. No evidence of Laves phase formation during solid-solid phase transformations has been reported to the best of the authors' knowledge. The morphology and size of Laves phase particles are influenced by the cooling rate and the ratio of temperature gradient to columnar dendrite growth rate.

The results obtained from the Schiel model in Thermo-Calc using the TTNi8 database indicate that the γ phase starts to form at 1327°C, followed by the formation of MC carbides at 1164°C. Solidification is concluded with the formation of the eutectic phase (γ+Laves) at 1101°C [463]. The presence of Laves phase, represented as (Ni,Cr,Fe)2(Nb,Mo,Ti), forming near the fusion line (FL) in the partially dissolved zone (PDZ), could be a direct result of laser irradiation dissolving the γ'' phases (Ni3(Nb, Ti, Al)) present in the substrate. This leads to the enrichment of isolated regions with Nb and Ti. When subjected to temperatures between the solidus and liquidus temperatures (>1101°C), these Nb-rich spots undergo eutectic transformation during subsequent solidification. Isolated spots with a high concentration of Nb transform into the eutectic phase (γ+Laves) when undercooling occurs. This suggests that the Laves phase forms at isolated Nb-rich spots [252]. The extent of dissolution increases with higher laser power, resulting in a thicker region with randomized enrichment spots where γ'' has dissolved. The cooling curve in Figure 7.34 shows that Laves phase formation is favoured under high cooling rates of 102-103 °C/s, as reported [463] and confirmed through thermal modelling. Figure 7.33 also displays the presence of substrate grains with locally enriched Nb pockets known to be Laves phase, indicating that the grains in the PDZ have not melted by exceeding the liquidus temperature but have precipitated Laves phase through thermal diffusion across the >20 μm region from the FL. It is believed that the temperature has exceeded the liquidus temperature, but the time spent above the liquidus temperature was insufficient for complete melting of the PDZ grains. However, it was enough to thermally diffuse Laves phase across the FL due to local enrichments of Nb and Ti resulting from the dissolution of γ'/γ'' and δ-phases. Higher laser power results in larger melt pools with reduced cooling rates compared to lower laser powers. By reducing the laser power, the volume of Laves phase is also reduced. A high cooling rate enhances dendritic growth and solute trapping during solidification, causing Nb atoms to be trapped in the γ matrix, resulting in fewer Nb atoms being expelled to form Laves phase [463].

7.11 Chapter Summary

In summary, the single tracks, thin-walled builds and repaired block components deposited under various laser powers have been investigated to determine their influence on deposited geometry, microstructure, crystallographic texture and microhardness through evolution of an LMD IN718 interface. The prominent findings of this chapter are:

1. The bead geometry and measurement of the HAZ, PDZ and FZ increases with larger laser powers. Increased laser power led to a considerably larger bright crescent formation at the bottom of the melt pool.
2. Laser power affected the as-deposited γ grain morphology in the FZ with a combination of columnar to equiaxed grain transition. Increased laser power led to the formation of tertiary and secondary dendrite arm formation, which was absent in the low laser power due to the higher cooling rates experienced.
3. Regardless of power, randomly orientated equiaxed grains were found to nucleate along the fusion line. These grains have been detailed as ‘stray grains’ by the author.
4. The volume of stray grains increases with increasing laser power due to the degree of constitutional supercooled region combined with dendrite fragmentation volume. Additionally, the substrate grain orientation played a considerable role in the volume of stray grains and dense equiaxed grains forming in the FZ. It was determined that with increased laser power, the growth rate remains similar to lower laser power but with reduction in temperature gradient, as a result G/V decreases and the amount of stray grain formation increases.
5. To understand the influence of build height on the interface, 750W-1, 750W-5 and 750W-10 were compared. It was found that although the average grain size didn’t experience noticeable differences, the maximum grain measured increased dramatically from single to ten layers – approx. 161% increase. The grain size and aspect ratio along with crystallographic texture remained largely unaltered when comparing five layers to ten layers due to the solidified microstructure being pinned by δ-phase at the grain boundaries. Localised temperature history remained below the δ-solvus from layer 5 to layer 10 hindering grain growth during subsequent layer addition annealing affect.
6. Dendritic growth angle along the Y-Z plane was found to increase with increased laser power due to the resultant heat flux direction. The results were slightly obscured by the 750W but by drawing comparative remarks on the single-track

analysis, it was determined this was experimental inconsistencies obtained during deposition.

7. The laser power was found to positively affect the global texture in the FZ with the introduction of randomly nucleated grains based on solidification conditions. The lowest laser power had a strong <001>//BD fibre texture with an order of magnitude higher MUD value, leading to anisotropic mechanical properties. The steep thermal cycles generated during the DED are expected to influence grain growth, leading to a degree of texture orientated parallel to the direction of local heat flow. As true with other AM methods, this is normally the building direction. The fastest crystal growth direction for FCC Ni-based superalloys is along <001> directions due to the less densely packed atomic plane.
8. The laser power has influenced the microhardness across the interface region and throughout the LMD deposited build. Higher laser powers lead to a sharper decline in microhardness across the PDZ due to the dissolution of strengthening phases (γ''/γ') with both the 750 W and 950 W measuring comparable results.
9. A microhardness variation was measured from the substrate; it was found to and decrease towards the HAZ, PDZ and reaches a minimum in the deposited build. This reduction in microhardness across the HAZ and PDZ is due to the level of strengthening phases (γ''/γ') dissolving back into the γ matrix, with an increase in power leading to the lowest microhardness in the PDZ.
10. A fairly homogenous microhardness of ≈275 HV was noted in the 950W and 750 W fusion zone, which slightly decreased to ≈225 HV with lower laser power. The areas of higher microhardness have been interrelated with areas containing nano-scale γ'' precipitates formed during subsequent layer addition. A clear decrease in microhardness was attained in all samples as the interface evolved towards the fusion line due to the dissolution of strengthening phases and δ-phase. A PWHT reinstated a homogenous microhardness by precipitating these prior-dissolved phases, establishing a stronger interface region and deminishing the stress concentrated PDZ weak band.
11. Laves phase formed at isolated Nb-rich spots in the PDZ. The extent of γ'' dissolution increases with higher laser power, resulting in a thicker region with randomized enrichment spots where γ'' has dissolved forming randomly isolated islands of Laves phase in the PDZ upon cooling from high temperatures.
12. An extensive investigation of the evolution of microstructural features including SEM and calculation of Nb diffusion distances. It was deduced that both methods

of investigation agree mostly that in the PDZ there was sufficient temperature-time relationship to successfully dissolve the δ/γ'' phases upto an extent of around 100μm in all specimens. However, increased laser power led to a longer range of sufficient diffusion distances of Nb to dissolve the phases in question, this agrees with the SEM investigation and microhardness results detailing a sharp decrease in microhardness in the HAZ for the 950W. It was further concluded that the 750W experienced experimental inconsistency during power delivery, leading to unorthodox results such as single track formation and the extent of dissolved microstrucuture features.

13. It can be concluded that PWHT is deemed essential to homogenize the microstructure and associated mechanical properties across the interface region of an LMD-repaired component. The integrity of the join will infer as a stress concentrated area during in-service opeeration which could lead to mechanical defects or catastrophic failure

Chapter 8: Residual Stress Assessment of Laser Repaired (LRed) Demonstrators

8.1 Introduction

In this chapter, the impact of process parameters on residual stress (RS) in laser-repaired multi-layered aerospace components was analysed. This manufacturing process generates thermal-induced residual stresses at both micro and macro scale [157], affecting the build quality and causing potential issues like distortion, cracking and delamination, when non-uniform and/or excessive plastic deformation has occurred. Heterogenous plastic strains are the source for residual stress induced by mechanical or thermal loads. RS develop distinct nonuniform fields in AM, particularly across the interface for repair applications, which can be detrimental for the mechanical properties and fatigue life of these components. These stresses can adversely affect mechanical properties [464], impacting crack propagation and fatigue life, particularly due to tensile residual stresses [465], [466], [467] .It is crucial to know the expected magnitude, distribution and nature of residual stress components for dimensional accuracy and any subsequent machining. Process parameters affect the generation and evolution of residual stresses [468], [469], necessitating post-deposition heat treatment for stress relaxation in the component. The 950W, 750W and 550W specimens were investigated to understand the direct implications of varying laser power on resultant residual stresses. Residual stress profiles and maps were obtained using X-Ray Diffraction (XRD) and the Contour Method (CM), respectively. For further details on the contour method and data analysis, refer to Chapter 3. Laser repaired applications have the potential to revolutionize the high-cost implications of part replacement when considering specialised engineering manufacturing expenses, meanwhile prolonging the average lifespan of in-service components. However, before LMD repairing or remanufacturing can expand into engineering applications at a larger scale, it is important to investigate and verify their residual stress profiles, especially when considering aerospace applications.

RS primary origination in AM can be explained by the Temperature Gradient Mechanism (TGM), shown in Figure 8.1. The model states that the laser beam heats solid material via irradiation causing thermal expansion. The expansion is partially restrained by the surrounding material, which is cooler, yielding a compressive stress-strain condition in the irradiated area. If the compressive stresses reach the compressive yield strength, the compressive strain will be partially elastic and partially plastic. As the laser beam moves, the melt pool will cool down and shrink. Such shrinkage is partially inhibited due to

plastic deformation created during heating, yielding tensile residual stress in that zone, surrounded by a compressive stress [470]. Heating from the laser source induces local elastoplastic deformations (represented by $\varepsilon_{pl}, \varepsilon_{el}$ and σ_{yield}), tensile stress, and thermal contraction, resulting in the formation of RS in the upper- and lower-layers during cooldown [471]. The TGM model simplifies the complex and transient nature of the LMD process.

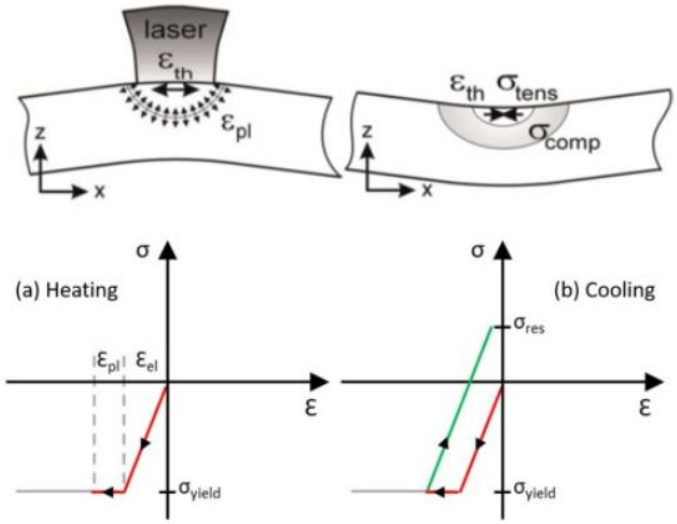

***Figure 8.1 Temperature Gradient Mechanism (TGM). Stresses and deformation during heating (a) and cooling (b) of the melt pool** [468].*

A secondary mechanism which contributes to the generation and evolution of RS is the differential cooling rates across the material. RS further evolve when thermal contraction causes previously solidified material to shrink. The shrinkage is inhibited by the underlying material, creating further tensile stress in the upper layers and compressive stresses in the lower layers [468].

8.2 Measurement of Residual Stresses

Residual Stresses were measured with Contour Method to acquire 2D cross-sectional maps of axial stresses in the bulk and expose the interface at the sectioned part for complementary in-plane measurements of transverse and normal stresses. X-Ray Diffraction measurements of RS were not required in the as-deposited condition, due to the interest on interface stresses which would not be able to directly access with this surface/sub-surface technique. However, CM can overcome this limitation, accessing bulk stresses, and providing valuable information at the interface. Additionally, CM can provide access to XRD for measurement of the remaining two normal stress components with high resolution and accuracy, though this is required to account for the effect of

release and redistribution of the pre-existing stresses through superposition of in-plane stresses from CM and XRD.

8.2.1 Contour Method

Figure 8.2 illustrates the residual stress distribution in the ND axis across the component's cross-section for all three specimens, i.e. scan direction or σ_{yy}. A consistent scale is applied for comparison. Generally, a compressive stress band is observed approximately 5mm below the substrate/deposit interface, though absolute magnitudes were different with peak stresses obtained for 750 W, i.e. the mid laser power scenario. The deposited material exhibits peak tensile stress at the upper layers, while the interface region shows low values of tensile stresses. The compressive stress band serves to balance the tensile region which encompass all the deposited material.

The 750W specimen exhibited both the highest tensile and compressive stresses in the build and substrate, respectively. This stress distribution behaviour was repeated for both the 950W and 550W, but the values were significantly reduced, particularly for the low laser power scenario, i.e. the standard Gaussian type of heat source, though the lack of fusion between tracks should have also influenced results. The high-power scenario displays moderate to low stresses due to the "ring" shape of the melt pool despite the larger heat input into the substrate.

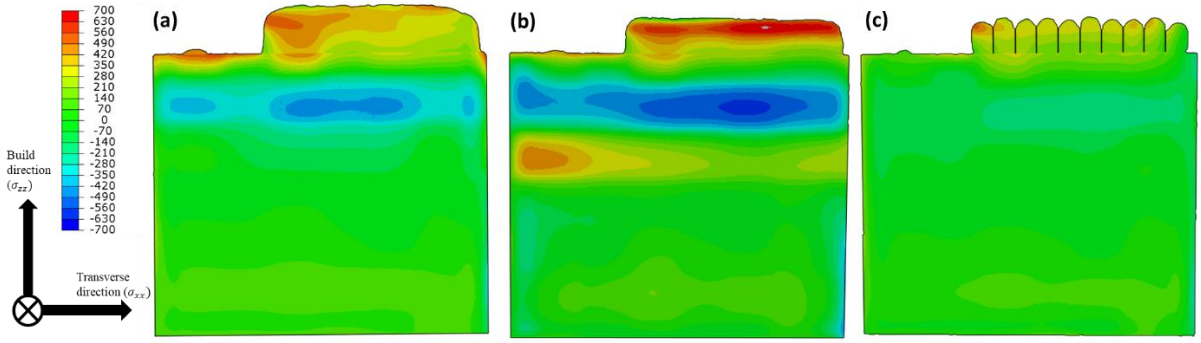

Figure 8.2 Contour maps for residual stress distribution of the specimen cross-section detailing stress contours in the σ_{yy} (ND) direction for (a) 950W, (b) 750W and (c) 550W laser power conditions.

Figure 8.3 illustrates the locations and maximum residual stresses in each laser condition. The highest laser power resulted in a maximum compressive peak stress of ~-473 MPa, located 5 mm below the interface. The 750 W sample exhibited a compressive peak stress of ~-612 MPa at the same location, reduced to ~-220 MPa for the 550 W sample. A consistent compressive band of ~-300 MPa at the right edge of the substrate, is believed to be artifacts from the EDM process observed in all three specimens. Peak tensile stresses

varied, i.e. ~615 MPa at the HAZ of the single deposit in the 950 W case, ~723 MPa and ~524 MPa, respectively for the 750 W and 550 W conditions. Peak tensile stresses were observed at the uppermost region of the deposited material. Similar tensile stress field was observed in the 950W sample but at a lower magnitude. The spike in tensile stress at the HAZ of the substrate for the single deposited track is attributed to the high thermal gradient and peak cooling rates. It is assumed that the maximum tensile stress initially occurs at the interface during the first layer deposition but stresses evolve during subsequent layer addition through the cyclic heating and cooling of the deposited material, which could be captured more accurately over time through a thermomechanical model.

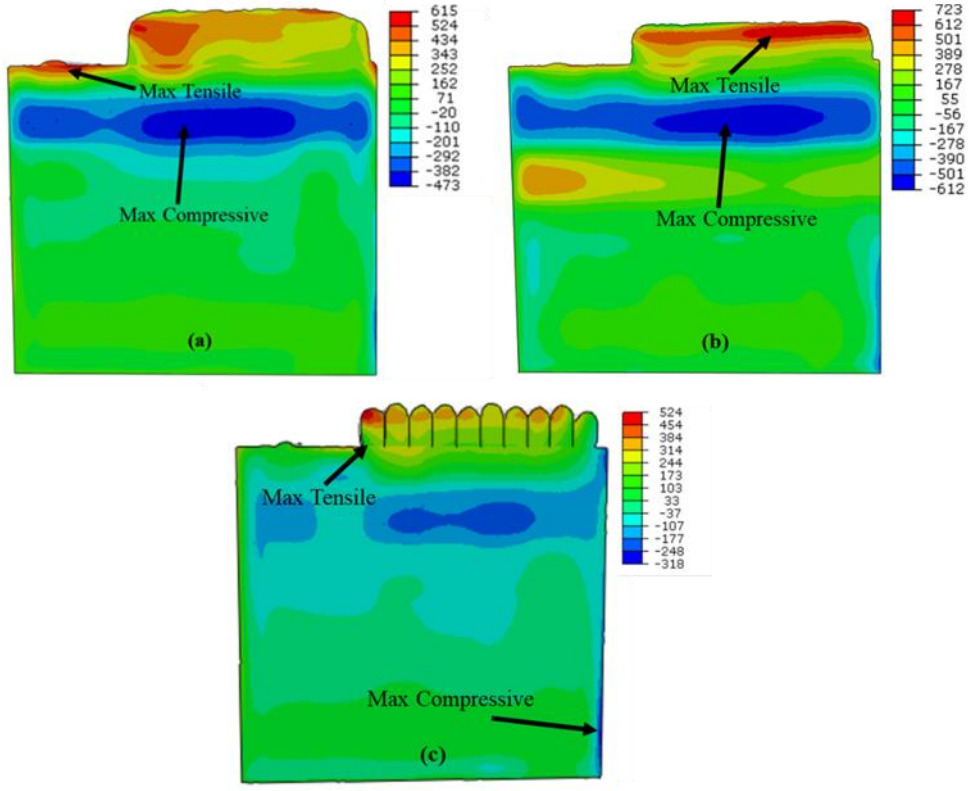

Figure 8.3 Residual stress distribution, scanning direction, i.e. axial stress, for (a) 950 W, (b) 750 W sample and (c) 550 W specimens from contour method.

The compressive stress field at the centre of the top third of the substrate, as depicted in Figure 8.3, has been previously documented in published work [137], [140], [472]. The LMD process generates stress fields akin to cyclic heating and cooling. Bulk residual stresses at the end of the deposition can be understood by considering built-up of stresses track-by-track and layer-by-layer. During cooling from elevated temperatures, localized variations in thermal contraction led to non-uniform stress due to differing rates of cooling in the surface and interior of the as-deposited material. The material at the free surface of

the melt pool, cools quicker and undergoes plastic deformation as it shrinks, resulting in strain mismatch and compressing the hotter inner metal. This deformation occurs at the outer surfaces where the thermal stress exceeds the material's yield strength. Upon further cooling to ambient temperature, the inner material, constrained by the already solidified material, develops tensile residual stress, while the outer portion of the component exhibits residual compressive stress [40]. Consequently, tensile stresses arise in the centre of the as-deposited build, while an equilibrium band of compressive stresses was observed in the region of the substrate below the deposited material which compensates for the tensile region of the deposited material. Notably, the compressive band observed in the top left portion of the substrate for all samples, directly below the single-track deposition, suggest that this compressive band originates from that location and intensifies with subsequent layer addition.

Published work in AM modelling and measurements [473], [474], [475] indicate that an increase in laser power leads to higher residual stresses due to the enlarged melt pool area/volume and larger heat-affected zone. A larger melt pool requires more time to cool and solidify, reducing thermal gradients and cooling rates and mitigating residual stresses. Lower laser powers, yielding a shallower melt pool, generate less strain in the deposited material. However, John *et al.'s* experiments [476] reveal that higher laser power reduces the cooling rate, promoting more uniform shrinkage in and around the melt pool and consequently lower residual stress. This could explain the higher tensile residual stress generated in the 750 W compared to the 950 W. Nevertheless, the cyclic aspect of heating and cooling cannot be underestimated either as the elevated temperatures can have an annealing effect on the stresses which will depend on time under a critical temperature.

The residual stress distribution was captured effectively considering LMD with fluctuating laser power employed for the deposition trial. However, the accurate determination of the magnitude of residual stresses with CM becomes challenging due to multiple challenges with this technique. The contour method introduces uncertainty in the measurement EDM cutting artifacts, while the post-processing of raw data, and its interpretation of results also have an inherent uncertainty. Experimental inconsistencies in laser stabilization, power delivery issues, and obscured melt pool geometries between specimens, as noted in Chapter 4, further complicate the analysis and CM cannot capture differences in the microscale. Drawing conclusive remarks on the impact of laser power on residual stress is challenging because the measurement is carried out at equilibrium conditions after the completion of the manufacturing trial which offers limited

information, and it is only a snapshoot of a specific stress component at a specific location. Consequently, there is a need to analyse the deposition strategy through a thermomechanical model, which will allow for a more controlled and detailed residual stress analysis.

Mukherjee *et al.* [183] integrated fluid flow and thermomechanical models to predict additive manufacturing residual stress fields, which align with the measurements in this study. The non-uniform RS behaviour demonstrated tensile residual stresses at the deposit free edges and mostly compressive residual stresses at the substrate centre. Li *et al.* [477] utilized multiscale modelling and predicted tensile residual stress in the top build layers of an Al alloy cantilever produced via SLM. The model demonstrated results that indicate, during heating, top layer expansion is constrained, inducing compressive stresses. As it cools, top layer contraction, constrained by previously deposited material, leads to tensile residual stress on the build's top layer, making the substrate's top region compressive.

The tensile stress at the substrate of the single deposit's Heat-Affected Zone (HAZ), compared to the ten-layered build HAZ is attributed to the total deposit height. In the 950W specimen, with a larger layer height, the decrease in residual stress with increasing build height is explained by simple physical arguments on melt pool size and cooling rates [476]. In first deposited layer, large thermal gradients develop between the layer and the substrate below. With further addition of subsequent layers, the previously deposited LMD deposit exhibits less intense transient thermal histories while peak and bottom temperatures per cycle are confined within a narrower range, reducing thermal gradients and resulting more uniform shrinkage during cooling between tracks and/or layers, which now also may exhibit an annealing effect. The single deposit remains constrained by the substrate, while larger builds continuously increase in height, which means that the single track has higher stiffness and hence is less susceptible to residual stresses and deformation [476].

The relatively low stresses in the 550 W sample are attributed to the lack of fusion due to inadequate overlap between tracks. The lack of a solid continuum prevents the accumulation of residual stresses, reducing their overall magnitude. This aligns with Simson *et al.'s* findings [478], where lower residual stresses were measured in samples manufactured under low energy densities with a high-volume fraction of pores. It was found in their study that components with high porosity defects and insufficient overlap between tracks, the residual stresses were reduced. In this work, the non-fused or partially fused layers significantly influences residual stress values, and substantial gaps between

inter-tracks lead to a notable reduction in these stresses, as observed in the cross-sectional profile of the deposited region in the case of the 550 W sample.

8.2.2 X-Ray Diffraction

Using XRD, the residual stresses were characterised along the Z-axis from the substrate (-15 mm) to the deposited region (+3 mm) across the interface. Figure 8.4 denotes the global coordinate system used throughout the project, which refers to each stress direction with X, Y and Z being transverse, normal and build direction. These stress tensor directions can also be shortened to σ_{xx}, σ_{yy} and σ_{zz}, respectively.

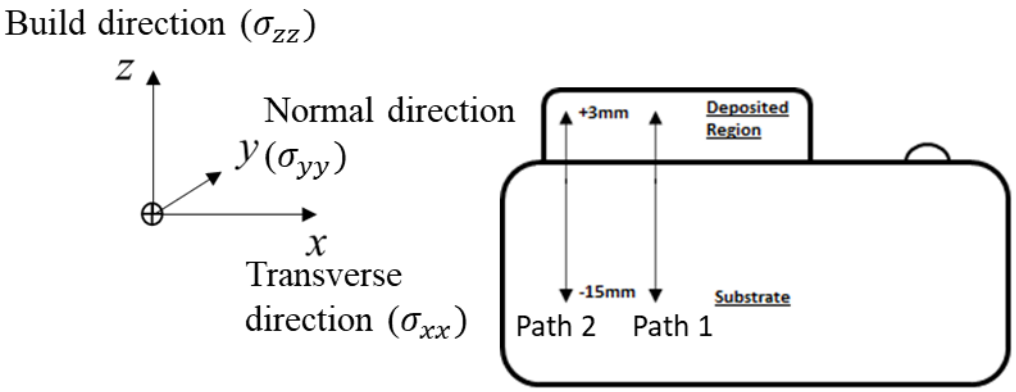

Figure 8.4 Cross-sectional view when sectioned along the XZ plane detailing XRD measurements and stress orientation profile.

8.3 Effect of LMD Laser power on RS in solid blocks

Figure 8.5 shows the raw residual stress development from the substrate (-15 mm) across the interface region to the deposited build (+3 mm) for both σzz (build direction) and σxx (transverse direction) stress directions. By raw measurements, it is emphasised that the measured values correspond to the stresses after the release of the normal stress component followed the EDM sectioning for Contour Method and the redistribution of stresses across the cut face to reach a new equilibrium. The raw measurements can be added to Contour Method result for each in-plane stress component to reconstruct the initial stress state before EDM sectioning. This is called superposition [508], and these results are discussed in Section 8.8.

For all builds, the peak stress value was measured in the σ_{zz} stress component. Both stress components displayed similar behaviours with very low values in the substrate, i.e. up to approximately -5 mm from nominal interface, indicating that there is virtually no stresses in the substrate material. Above that depth level, the σ_{zz} stress component is significantly larger than the σ_{xx}, measuring 1.5 to 5 times greater, meaning that the major component

of residual stress at the specific cut plane for LMD-produced samples is along the build direction, which was also found to be the case in the superposition measurements but to a less magnitude, observed in Figure 8.10. The raw build direction stresses were mostly all tensile up to the substrate/deposit interface (0 mm) and displayed a significant peak at around -2 mm in all laser conditions. A more detailed analysis for the interface can be seen in Figure 8.5a for the residual stress in the build direction. Note that the transverse stress was almost negligible in all three conditions, not exceeding 100 MPa at any location. These results agree strongly with literature, whereby the σ_{zz} stress component supersedes the σxx stress component [155].

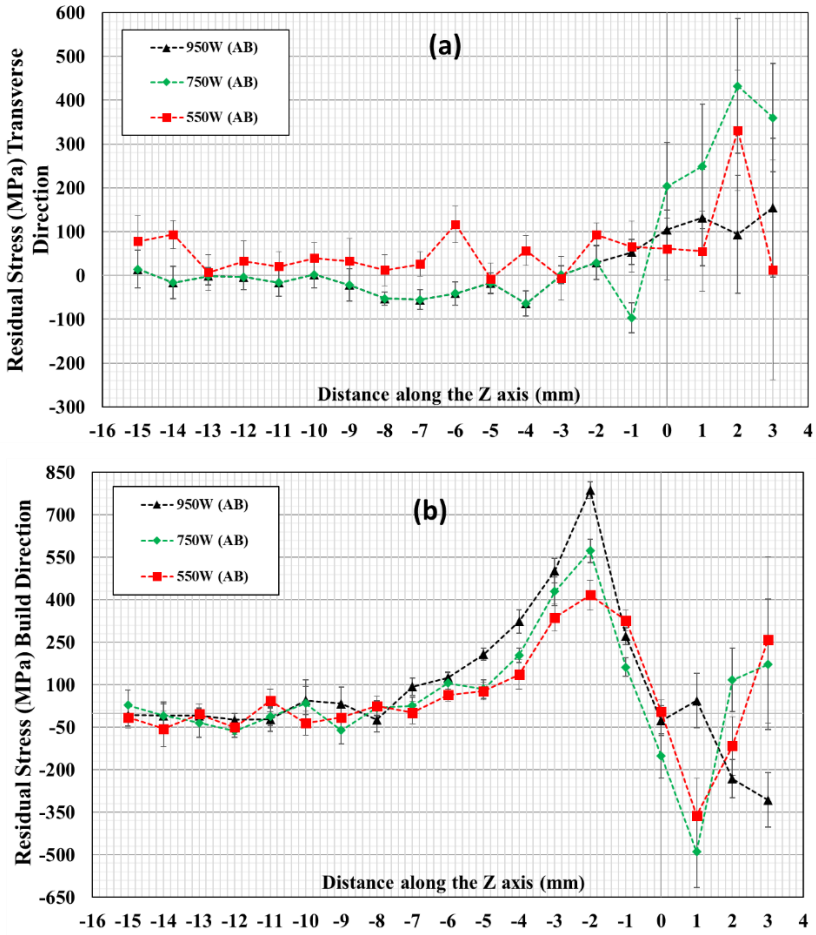

Figure 8.5 Effect of laser power on residual stress distribution across the interface region: a) σxx (TD) stress along the Z axis and (b) σzz (BD) stress along the Z axis

The accumulated errors in XRD measurements of RS in the deposited region were beyond the acceptable levels of uncertainty and in most locations they were of the same magnitude as the actual values, hereby obscuring the measured results in that region (0 → +3 mm). This will be discussed further in Section 8.9. The stresses are measured on the surface but these are actual bulk stresses with respect to the substrate/deposit component.

Specimen 950 W displayed the highest magnitude of tensile stress (i.e. ~787.2 MPa) which decreased proportionally with decreasing laser power (i.e.~572.9 MPa and ~416.6 MPa in 750 W and 550 W, respectively), indicating that higher heat input and slightly larger build height contributed to the observed higher residual stresses. The maximum temperature of the interface region in each specimen was reported in Chapter 5, where it was observed that higher laser power produced higher temperature values. Interestingly, these observations on temperature variations were consistent with those on residual stress distribution as seen in Figure 8.5. In general, when a higher laser power is used, the melt pool becomes larger, and the maximum temperature of the melt pool increases. Heat input and cycling affect peak temperature in the melt pool, thermal gradients and thus microstructure [479], [480], [481]. Additionally, with higher levels of laser power, the tensile residual stress increases in value towards the interface region.

The RS measurement at the interface of the build, directly below the melt pool at the fusion line, are tensile in both directions. However, the magnitude of σ_{zz} is more than 4.5 times greater than the σ_{xx}. During the build process, the substrate experiences heating and cooling cycles which require the material to compensate for thermal expansion and contraction. Towards the interface region, where the effects of thermal cycling are more extreme, the material remains in tension in all principal stress directions. This tensile stress state with higher σ_{zz} stress direction was previously observed at the build substrate interface by Ding [126], Parimi [155], and Zhao *et al*. [146] during multi-layered welding and DLF, respectively.

The maximum tensile stress observed at the build substrate interface in σ_{zz} is due to the location of melt pool interface and moving heat source. As the laser beam passes across the substrate surface establishing a molten pool, significant thermal expansion occurs undergoing tension along the deposition. As the laser path progresses along the ND, a compressive field to compensate this tension. This behaviour has been simulated in the thermomechanical model later in this chapter. Such a compression field in the substrate generated in the vicinity of the interface region in the substrate has been previously observed in welding and DLF [126], [135], [155]. The magnitude of this tensile stress located 2 mm below the substrate surface was ~ 416 to 718 MPa tensile measured in 550W to 950W, respectively, around 40-69% of the tensile yield strength in forged and aged IN718 (~1040 MPa) [140].

A comparison of the profile can be made with Rangaswamy *et al.* [140] whom showed similar stress profiles within LMD 316 stainless steel and IN718, suggesting the similar

trends origin from thermal gradients, independent of the two materials used when the temperatures in the substrate will not induce phase transformations. Generally, softer materials, such as copper, or an Aluminium alloy may exhibit similar trends but at much lower magnitudes due to material properties. A maximum tensile peak around 1-2 mm was also found by Hoye *et al.* [482] whom deposited a single track of Ti64 using a bespoke WAAM process for additive manufacturing. Using neutron diffraction technique, maximum longitudinal stress tensile peaks measuring 70% of the yield strength were measured 1mm below the surface of the baseplate towards the centreline.

8.3.1 Effect of LMD Laser power on RS in solid block interface

Higher resolution XRD measurements were taken across the interface region (-4 mm to +0.5 mm) at 0.1 mm (from -1 mm to +0.5 mm) intervals using a 100 µm aperture on the XRD. This provided a more detailed insight into stress evolution across the interface in the SZ, HAZ, PDZ, and FZ and the results are shown in Figure 8.6.

At the interface in the substrate just below the melt pool crescent, a peak residual stress measurement was captured in the build direction. The tensile residual stress values measured 787.2±29.9 MPa, 572.2±47.9 MPa and 531.4±68.6 MPa for the 950 W, 750 W and 550 W specimens, respectively. Residual tensile stress exceeding the material's yield strength can indeed lead to crack initiation and propagation. When residual tensile stress surpasses the yield strength, it creates conditions favourable for crack formation, especially in materials susceptible to stress corrosion cracking or fatigue [140]. It is important to note that factors such as material properties, loading conditions, environment, and the presence of pre-existing defects all influence crack initiation and propagation. So, while exceeding the yield strength with residual tensile stress increases the risk of cracking, it does not guarantee it in every situation.

According to AMS5662, in double-aged condition the yield strength of IN718 is 1030 MPa and LMD IN718 has shown results ranging 569-729 MPa [252], [483] in as-built condition and for PBF IN718 with post-weld heat treatment was in the range from 620 MPa in solutioned to 1135 MPa in solutioned followed by double aging, and a direct aging (720°C for 24 h) 1245 MPa [484]. Based on the information, it can be summarised that the tensile RS measured close to the interface in the substrate is nearly 75% of the materials yield strength. This region so close to the interface could lead to catastrophic failure during service as a crack initiation and propagation site leading to further complications during post-depositing machining.

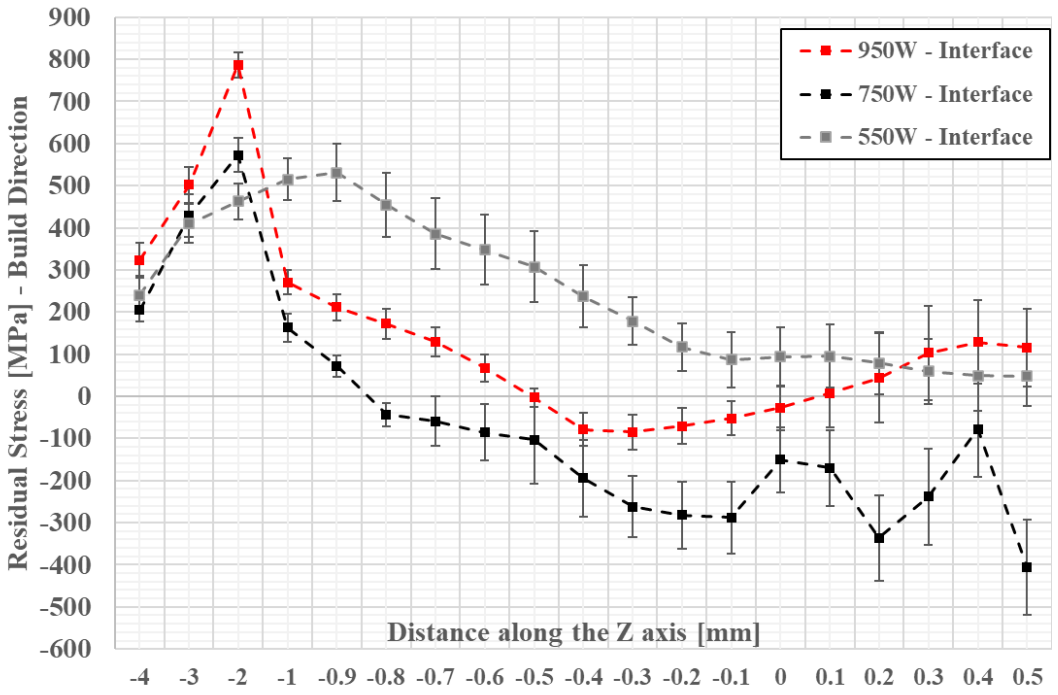

Figure 8.6 Comparative residual stress profile for the build direction σ_z stress profile for all specimens at the interface region

Observed stress profiles result from the transition of material from liquid to solid, generating compensating thermally induced stresses, which increased with laser power. This aligns with findings in literature, such as Yi *et al.* [485], who investigated the linear energy density (LED) effect on IN718 specimens, reporting that higher LED increases deformation and residual stresses. Mukherjee *et al.* [486] demonstrated, through thermal simulations, that increased laser power and layer count elevate residual stress in IN718 parts due to the increasing power [472]. Wang *et al.* [41] observed that laser power affects energy input, and scanning speed affects cooling rates in SLM. It was deduced that increased laser power and increased scanning speeds lead to raised residual stresses. However, the RS measurements were taken from the top of the build and not at the substrate/deposit interface, therefore it gives a general understanding and appreciation to correlate the laser power influence on residual stress behaviour deposited AlSi10Mg. This correlation between beam power and residual stresses was further agreed by modelling conducted by Vastola *et al.* [487] whom showed that 20% laser power increase translated to higher residual stresses in S_{11}, S_{22} and S_{Mises}. It was explained that the higher laser power incurred larger HAZ sizes at the interfaces, and with increased HAZ depth means that the thermal gradients are sufficient to generate yield at a larger depth from the free surface. These findings agree strongly with the measurements and justification found in this work.

To summarise, tensile residual stress rises with higher laser power (550 W to 950 W), as evident in Figure 8.5 and Figure 8.6, showing increased tensile stress 2 mm below the interface. Higher laser power results in larger melt pools, elevated local temperatures, and increased melt pool volumes.

8.4 Effect of location-dependent measurements

The XRD measurements in Figure 8.7 were taken at the edge of the build (aligned with track 9/10) and the middle of the build (track 6) from the substrate/build cross-section in the transverse direction. From Figure 8.7, it can be depicted that at the edge of the build (track 9/10), maximum stresses reached ~780 MPa, 2 mm below the interface at the HAZ edge. At the same depth, the mid-section (track 5/6) had a residual stress of ~620 MPa. Arguably, edge measurements slightly surpassed those from the mid-section, indicating a consistent trend of higher tensile stresses at the edges. Due to differential temperature profiles during deposition, outer surfaces experience higher cooling rates, causing the substrate to deflect upwards upon release from clamping fixtures, giving a concave shape. In the mid-section, the distortion diminishes due to the increased local stiffness at the centre of the plate. However, at the edges, deformation and stresses generated during LMD lead to the centre of the plate distorting and pulling up the edges of the substrate, exacerbated by its comparatively lower stiffness.

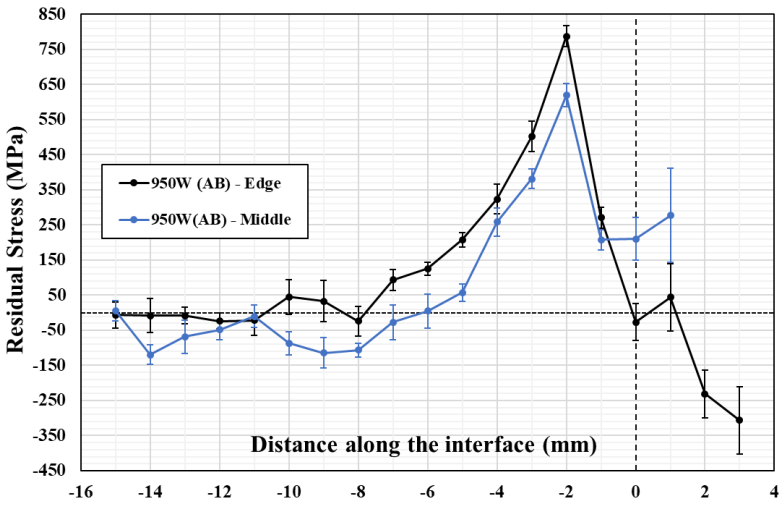

Figure 8.7 Effect of measurement location on residual stress distribution across the interface region for σ_{zz} stress along Z axis.

This behaviour was also observed in the 750 W but some differences were observed for the 550 W. This behaviour and the similarities in residual stress observed along σ_{zz}, can be attributed to the inconsistency of overlap fraction between adjacent tracks. The 550W experienced higher tensile stresses at the mid-point comparative to the edge, whereas the 750W experienced a similar trend and magnitude of residual stresses regardless of

location. The 950W laser power builds achieved substantial overlap and metallurgical bonding between adjacent deposited tracks, whereas the 550 W laser power builds had insufficient overlap, meaning that the residual stress was not influenced as much by adjacent tracks and each track layered along the build would experience similar stress profiles and thought of as thin walled with minimal overlap. When a new layer is deposited and the top of the previous layer is remelted, the previously solidified layer will reach high temperatures, and during cooling will shrink under the new top layer. The shrinkage of the pre-existing layer pulls and stretches the top layer resulting in permanent tensile RS [488]. As for the 750 W laser power, a similar residual stress profile was observed at both the mid and edge region. This could be attributed to the <100 μm insufficient overlap at the interface region.

After removal of clamping fixtures of the additive manufacturing process, the component may deform due to residual stresses [489]. This deformation can resemble a beam in bending, with the substrate acting as the supporting structure. However, since the volume of deposited material relative to the substrate is minimal, the bending moment exerted on the structure is constrained by the size of the substrate. This constraint can result in tensile stresses being introduced in the build direction at the edges of the component compared to the middle and is exasperated at the interface region, near the substrate/deposit interface.

The residual stress measurements recorded at the edges (track 9 /10) of the substrate were substantially higher than the residual stresses measured towards the centre of the substrate in the 950 W specimen. This behaviour can be attributed to several factors:

1. Localised thermal gradients: Near the centre of the substrate aligned with track 6, the thermal gradient would be typically lower as the heat can be evenly distributed to the surrounding volume of substrate and deposit material. Towards the edges, the thermal gradients become steeper leading to larger temperature differences as majority of the thermal energy will be transferred to the environment due to the larger surface area and conducted through previously deposited material and substrate. Thermal conduction coefficient is significantly higher than natural convection coefficient and therefore at the edges, the temperature variation induces thermal stress, contributing to higher residual stresses at the edge.
2. The substrate was clamped during the deposition process. This introduces constraints at the edges at the interface which limit the expansion and contraction of the material as the temperatures vary during deposition and cooling. Such

constraints lead to an accumulation of higher residual stresses at the edges as the material is locked to a greater extent than at the centre.

3. The associated cooling rates will vary across the substrate but as simulated by the FEA model, the edges of the build will cool quicker due to convection, conduction and radiation of free edges which incur higher cooling rates leading to higher tensile stresses accumulated at the edges of the substrate/deposit interface.
4. Cumulative heat input: In the central regions, where heat and temperature accumulate due to successive layering, residual stresses will start to relax. Conversely, at the free edges, where heat loss is higher and material buildup is lower, this behaviour will be less pronounced.

8.5 Effect of heat treatment on Residual Stresses

The specimens underwent a uniform post-weld heat treatment, as detailed in Chapter 3. This treatment comprised of i) an initial step involving a solution treatment in an air furnace at 954 °C for 1 h followed by air cooling, ii) subsequent aging at 760 °C for 5 h with furnace cooling, and iii) finally, a step at 650 °C for 1 h with air cooling. The primary objective of this heat treatment was to dissolve laves phases, bring alloying elements in solid solution, and induce the precipitation of strengthening phases at the interface to reduce mechanical property variations. Furthermore, the post-weld heat treatment effectively mitigated the residual stresses observed in the as-deposited condition. Figure 8.8 illustrates a comparison of residual stress measurements taken from 9 mm below the interface to 1 mm into the build for both as-built (AB) and post-weld heat treatment (PWHT) conditions across all specimens. Above the interface and towards the deposit, the measurements become unreliable due to the challenges discussed in section 8.7 and only the measurements from the build to the substrate should be considered.

It can be observed that the maximum tensile stresses measured are reduced significantly from 787 MPa to 40 MPa, 573 MPa to 65 MPa and 416 MPa to 79 MPa in the 950 W, 750W and 550W specimens, respectively. A reduction of around 95%, 87% and 81% for the 950W, 750W and 550W specimens, respectively. The measurements indicate that there are very low stresses, nearly negligible, present after the thermal stress relief treatment, but complete elimination did not happen due to i) residual stresses being introduced during the heat treatment (air cooling stages), ii) dissimilar material properties between the substrate and deposit which create misfit strains and stresses at the fusion line, iii) high pre-existing stresses and relatively short time under solution temperature.

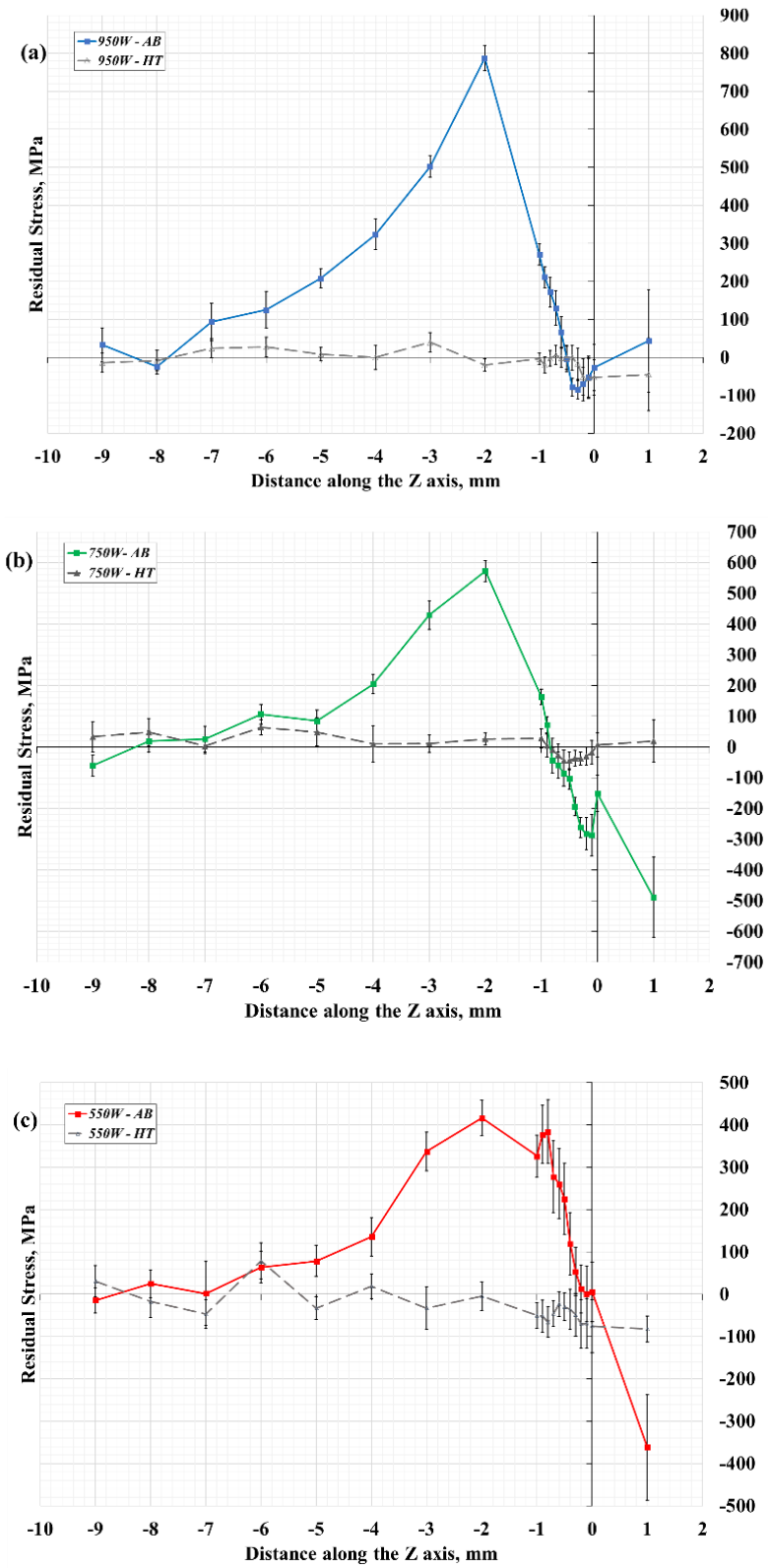

Figure 8.8 Residual stress measured via XRD in as-built (AB) and post-welded heat treated (PWHT) condition: (a) 950W, (b) 750W and (c) 550W specimen.

The PWHT relieved the residual stresses via self-diffusion of atoms in the metallic materials and recovery of dislocation substructure. The solution anneal (SA) temperature of 954°C contributed significantly to the relief of RS. It is possible to hypothesize that partial recrystallization has occurred in the HAZ region of the interface, with a more

predominant necklacing of small equiaxed grain growth being observed in Figure 8.9. Zhang *et al.* [41] reported that RS provide an impetus for grain growth; however, the temperature of the SA treatment employed in this study is not high enough for full recrystallization of wrought or additively manufactured material [99], [490], [491].

All specimens incur a small compressive stress generated near the melt pool (<-0.5mm from top surface) and continues to the substrate/deposit interface. These may exist due to the localized residual stresses generated during the deposition which cannot be eliminated due to the concentrated energy deposition. This concentrated area, in particularly (-0.5<0 mm) experienced intense thermal expansion and uneven contraction during PWHT, resulting in hard-to-remove compressive forces. The rapid heating in LMD, with slow heat conduction, creates steep temperature gradients, inducing elastic compressive strains. When the yield strength is surpassed, the melt pool layer undergoes plastic compression, causing bending upon cooling [492].

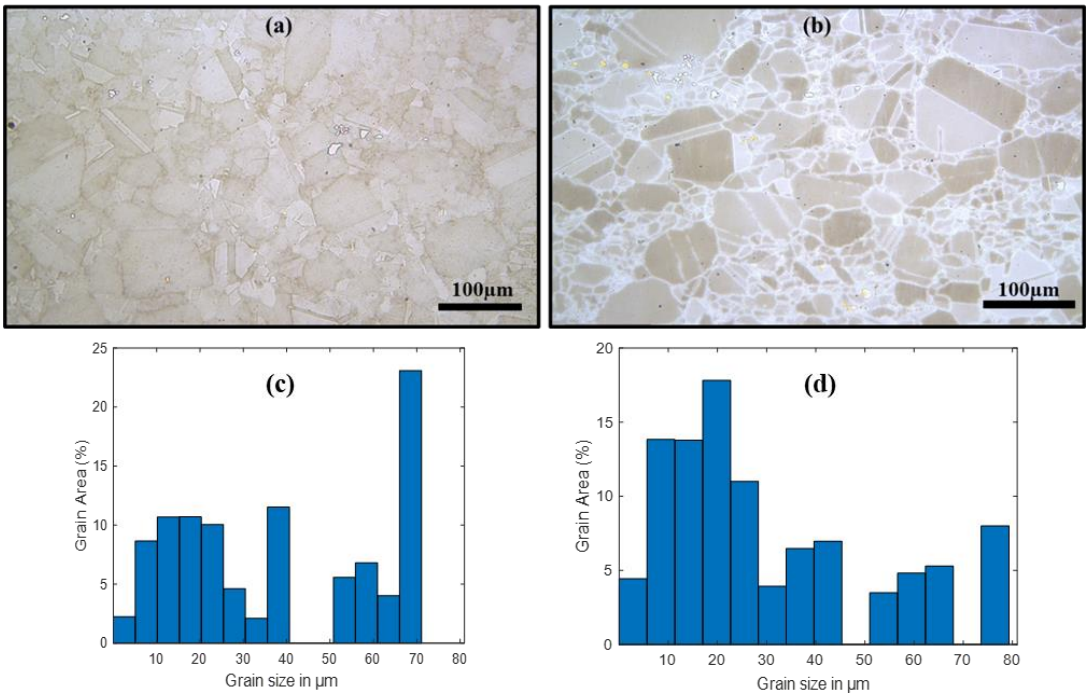

Figure 8.9 Optical micrograph and accompanied grain size analysis of the PDZ in the (a,c) NHT and (b,d) HT condition

8.5.1 Heat Treatment Discussion

Gruber *et al.* [493] studied high temperature stress relieving of IN718 manufactured by PBF. The study found slow stress relief at 1065°C for 1.5 h. The annealing temperature and time resulted in recrystallization and homogenization of the alloy. It was mentioned that a part of non-recrystallized grains with maintained intercellular micro segregation was left indicating that the recovery process preceding recrystallization is slow at 1065°C

due to hindered coalescence of dendritic cells, caused by slow diffusion of Nb, Ti, and Mo in the γ-phase.

Heat-treated (800°C for 1 h) Inconel 625 exhibited gradual relief across the entire build with significant reduction in residual stresses from 598 MPa to -56 MPa in the build direction using XRD [494]. Research conducted on distortion measurements utilizing surface topology [495] demonstrated the significant correlation between stresses induced by LMD and the chosen hatch strategies. These stresses were effectively mitigated by implementing a heat treatment, specifically a solution followed by a two-step ageing process. Nevertheless, it was noted that this heat treatment introduced supplementary stresses, comparatively weaker than those present in the as-deposited state. These stresses were linked to the differences in thermal expansion between the IN718 material and the underlying steel substrate. It was modelled that these stresses would not be introduced if the base-plate was IN718. Barros [496] observed a significant decrease in RS magnitude from as-built to SA condition, up to four times less parallel to the build direction and 8x less in the lateral surface. Solution annealing with aging led to lower compressive stresses near the interface, measuring -170 MPa in the S sample and approximately -50 MPa in the S+DA sample.

The outcomes of this study are in line with existing literature, demonstrating that post-weld heat treatment (PWHT) positively impacts both the evolution of microstructure and the response of residual stresses. Measurements reveal that LMD induces considerable levels of residual stress, approaching the yield limit. While certain thermal stresses may be alleviated through processes like plastic deformation, solidification cracking, and liquation cracking, such relaxation mechanisms were not observed in this investigation. Consequently, the thermally induced stresses within the elastic limit at the interface region, in conjunction with PWHT, may serve as driving forces for recrystallization. Previous research by Son *et al.* [109] noted that temperatures around 1065-1080°C triggered local recrystallization in L-PBF IN718 samples. Figure 8.9 illustrates the partially dissolved zone of the 950W specimen under both as-deposited and PWHT conditions. It can be inferred that approximately 18% of the grain area consists of grains <10 μm after PWHT, compared to only 11% in the as-deposited state. PWHT facilitates the relaxation of microstructural disparities along the interface by homogenizing the microstructure, thereby eliminating or mitigating stress concentrations associated with these irregularities.

8.6 Residual Stresses Using Multiple Methods and Superposition

Is has been shown that superposition of stresses measured post-cutting with results from contour analysis can determine the original (pre-cut) residual stresses. The general superposition theory using Bueckner's principle is developed, as shown by Pagliaro *et al.* show[497]. After a contour method cut to measure the out-of-plane stress component, the remaining in-plane stresses on the cut surface were measured using the XRD method. Superposition of the measured surface stresses with the calculated stress relaxation then determines the original, internal stresses. The transverse (S11) and build (S22) direction residual stress state on the plane of the cut were compared with the thermomechanical model and can be shown in Figure 8.10.

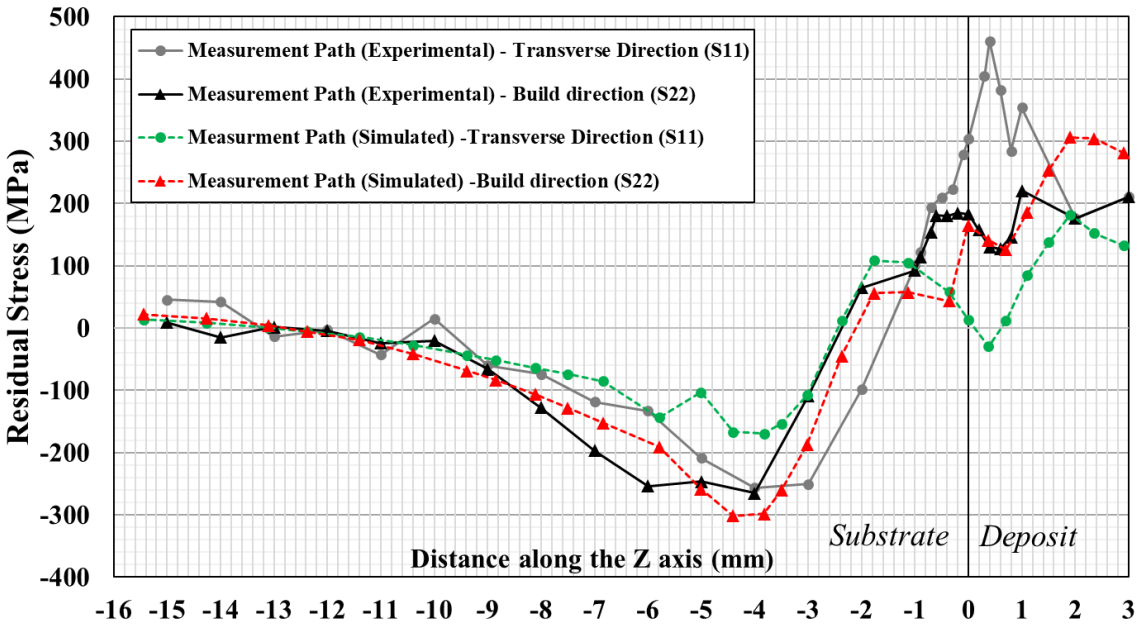

Figure 8.10 Transverse (S11) and Build (S22) direction superposition residual stress measurement for path 1 compared to the simulated measurements from the developed thermomechanical model.

Observations reveal a notable agreement in the profiles of residual stress direction, as depicted by the simulated field. This alignment manifests as a gradual transition to compressive stresses ranging from -15 mm to -4 mm, where a peak compressive stress is consistently measured in both directions and accurately simulated at approximately -4mm. Subsequently, from -4 mm to -0.5 mm, a general decrease in residual stress measurements is evident towards the interface, characterized by relatively low stresses (ranging from 0 to 200 MPa) in both experimental and simulated data.

At the substrate/deposit interface (0 mm), a slight deviation is noted between the simulated and experimentally captured stresses in the transverse direction. While experimental data indicates a sharp peak increase in tensile stresses, the simulation

reflects a decrease in tensile stresses close to ~0 MPa. Furthermore, at approx. +0.5 mm, experimental data reveals peak tensile stresses not replicated in the simulation, posited to be influenced by raw XRD measurements and inherent challenges associated with additive manufacturing grain size issues which is addressed in the following section.

In the build direction (S22), a peak compressive stress is measured at -4 mm, with an approximate value of -285 MPa recorded between -6 mm and -4 mm. This behaviour is faithfully mirrored in the simulation, albeit slightly shifted to the -4 mm to -3 mm range. Additionally, the initial layers of the deposit exhibit progressively increasing tensile residual stresses in the build direction, consistent with both experimental and simulated data.

Conversely, in the transverse direction (S11), stress measurements demonstrate notable similarity with increasing distance, with both experimental and simulated data indicating stress levels of approximately 180 MPa around +2 mm from the substrate/deposit interface.

Moreover, concerning the thermomechanical model, Section 8.11 (Validation of thermomechanical model) will outline several influential factors. These include assigned material properties in both the deposit and substrate, geometric disparities between the model and experimental setup, and variations in the initial state of the material and its processing conditions, all of which impact the flow curves.

Overall, the residual stress profile has been effectively captured through the utilization of the superposition theory to compute the initial stresses prior to contour cutting. This approach demonstrates strong agreement with the thermomechanical model across all two stress components (S11 and S22).

Upon comparing the raw XRD measurements (Figure 8.5) with the original stresses calculated using superposition (Figure 8.10), it elucidates the manner in which these surface stresses are measured post-elastic relaxation. The application of superposition theory enables measurements in regions where internal stresses were previously challenging to ascertain. By amalgamating the strengths of various measurement techniques, it facilitates unparalleled measurements and comprehension.

8.7 Experimental Measurement Challenges

All measurement techniques come with an uncertainty in the form of repreparation, measuring, human and post processing errors. The NPL good practice No.52 is a guide applicable to X-ray stress measurements on crystalline materials. When evaluating the

values, it is important to distinguish between error calculated by XRDWin software and Standard uncertainty calculated according to NPL No.52. The error is the measurement result minus the true value of quantity being measured [240]. The standard uncertainty of residual stress measurement includes a number of mainly contributing factors such as elastic constants used, instrument alignment, number of tilts, peak fitting analysis method and operator competence to name a few. The standard uncertainty values, which include the error values from XRD win data became intrinsically larger as the measurements were taken from the interface to the top region of the build. To ensure compliancy of measurements, low and high stress standards are measured prior to specimen measurement. In accordance with ASTM E837-08 which although calculates residual stress computed by hole drilling method, the same limitations can be applied and therefore a maximum bias of about 10% [498] or maximum uncertainty value of ±60 MPa will be selected when all factors considered.

To be considered qualitative, the reported values in the as-deposited region were ignored as the uncertainties and errors reported supersede 50%, with some values having errors exceeding measurement values. It should be noted that although XRD method is regarded as one of the most mature methods of residual stress measurement, the incurred errors cannot be completely avoided. LMD builds have a very poor response to XRD for RS measurements in the as deposited condition (even after standard sample preparation), due to a combination of large grains and strong texture, which result in weak signals, oscillatory curves and hence large uncertainties [239]. The existence of strong anisotropy in the deposited material also contributes to errors in residual stresses which has been recognized in non-additive manufacturing literature. For example, an extruded aluminium alloy with different crystallographic textures observed in separate locations had developed a strong <100> and <111> texture upon laser peening will generate 25% more compressive residual stress comparative to other locations of the same extruded alloy [499].

Grain size in the irradiated volume have considerable effect on the reading. In the polycrystalline substrate material where grain sizes range from 10-100 µm, measurements with uncertainties were captured well. As for the deposited region, where grains can be seen ranging from 5-500 µm within the irradiated volume, only a small number of grains will contribute to the diffraction peak, obeying Bragg's Law. The combination of large grain size and fewer grains contributing to the diffraction peak results in lower peak intensity and less accurate peak location. Additionally, the presence of

micro/intragranular strains may affect the results in large grain materials [240]. Furthermore, texture development causes discrepancies in residual stress measurement values as it results in peaks of widely differing intensity with ψ tilt. Attempting to overcome this would mean to choose appropriate tilts and oscillations of the sample in ψ to bring more grains into the diffracting condition. These generic instructions were implemented, and appropriate (ψ) psi offsets were selected to catch all diffraction peaks and XRD was tilted from 0° to 30°±3° for all measurements, but the large errors were still persisting leading to the rejection of the measurements above the interface into the deposited material.

8.8 Coupled Thermo-mechanical FEA Modelling Strategy

A thermo-mechanical model assists in the understanding of residual stress developed during manufacturing as the LMD process builds the feature/repairment layer-by-layer. Measurements of Residual Stresses is a technically difficult option due to the experimental set-up and the available techniques and technologies. Predicted residual stresses were evaluated against measurements carried out using contour methods and x-ray diffraction.

8.8.1 Governing Equations

Additive manufacturing induces thermal gradients that lead to both thermal and mechanical strains [237], [500], [501]. The mechanical strains are contingent upon local temperatures-time histories. Strain gradients are also influenced by phase transformation and latent heat, collectively contributing to the total strain and residual stress in the workpiece.

Due to thermal expansion and contraction during laser remanufacturing, the total strain, ε_{ij}^{total}, can be expressed using infinitesimal strain theory [214], [502]:

Equation 8.1 Infinitesimal strain theory

$$\varepsilon_{ij}^{Total} = \varepsilon_{ij}^{e} + \varepsilon_{ij}^{p} + \varepsilon_{ij}^{vp} + \varepsilon_{ij}^{c} + \varepsilon_{ij}^{th} + \varepsilon_{ij}^{tr} + \varepsilon_{ij}^{tp}$$

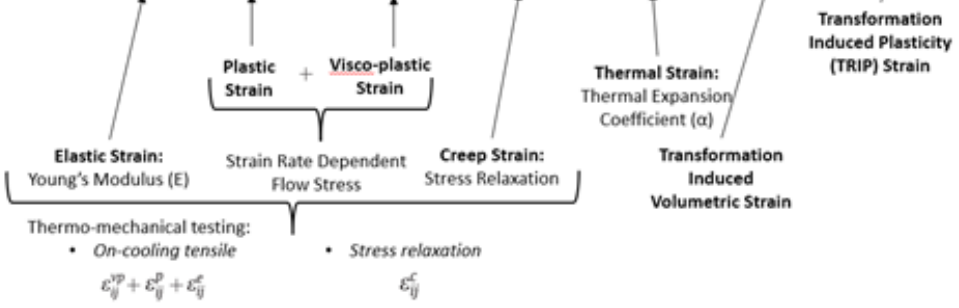

The mechanical induced component of strain (ε_{ij}^{mec}), metallurgically induced component of strain (ε_{ij}^{met}) and thermally induced component of strain (ε_{ij}^{th}) are pertinent to this study. Notably, the creep strain (ε_{ij}^{c}) and viscoplastic strain (ε_{ij}^{vp}) are considered, whereas due to the material behaviour transformation plasticity strain (ε_{ij}^{tp}), can be safely omitted.

An equivalent tensile stress or equivalent von-Mises stress, σv, is used to predict yielding of materials under multiaxial loading conditions using the results from simple uniaxial. The elastic response by linear elasticity relationship can be given as [503]:

Equation 8.2

$$\{\varepsilon_q\} = \sqrt{\frac{3}{2} S_{ij} S_{ij}}$$

Where S_{ij} are components of the stress deviator σ^{dev}:

Equation 8.3

$$\sigma^{dev} = \sigma - \frac{tr(\sigma)}{3} I$$

Where σ is the stress tensor, tr (σ) represents a trace of the stress tensor, the sum of its diagonal elements and I is the identity tensor.

Isotropic yielding occurs when a material yields or undergoes plastic deformation under stress in a manner that is independent of direction. In the context of materials science and solid mechanics, the von Mises yield criterion is commonly used to describe isotropic yielding. The von Mises yield criterion states that yielding occurs when a particular function of the principal stresses reaches a critical value:

Equation 8.4

$$\sqrt{\frac{3}{2}} tr(\sigma^{dev}) \geq \sigma_y$$

When the expression on the left-hand side of the inequality is greater than or equal to the yield stress, σ_y, yielding or plastic deformation occurs. To account for thermal strain in the material, ε_T:

Equation 8.5

$$\varepsilon_T = \alpha(T - T_0)$$

Where α is thermal expansion coefficient of the material, T is temperature experienced while T_0 is the ambient starting temperature.

Rheological models in the FE software define material properties, utilizing curves accounting for viscosity, elasticity, and plasticity at different temperatures, ensuring a comprehensive analysis of material behaviour changes. This approach leads to more precise simulations. Detailed discussion of these rheological curves is in the material property section. The yield stress is a key mechanical property during LMD as it has significant effect on the residual stress formation and behaviour [126]. Hence, accurate temperature-dependent yield curve data was inputted for the thermomechanical model which were taken from solution heat treated IN718 as seen in Figure 8.11. These values were derived using the equation:

Equation 8.6

$$\sigma_y\{T\} = \frac{\sigma_y(RT) - \sigma_y(HT)}{1 + exp\{(T - b)/c\}} + \sigma_y(HT)$$

Where σ_y (RT) is the room temperature yield strength and σ_y (HT) is the yield strength at high temperatures, above the γ'/γ'' solvi. The material constants b and c are determined via fitting of the equation to experimental data. The temperature dependence of the yield curve did not depend on the kinetics of solute precipitation and takes no account of γ'/γ'' coarsening, which is known to have strong effect on the yield strength of nickel-base superalloys [504].

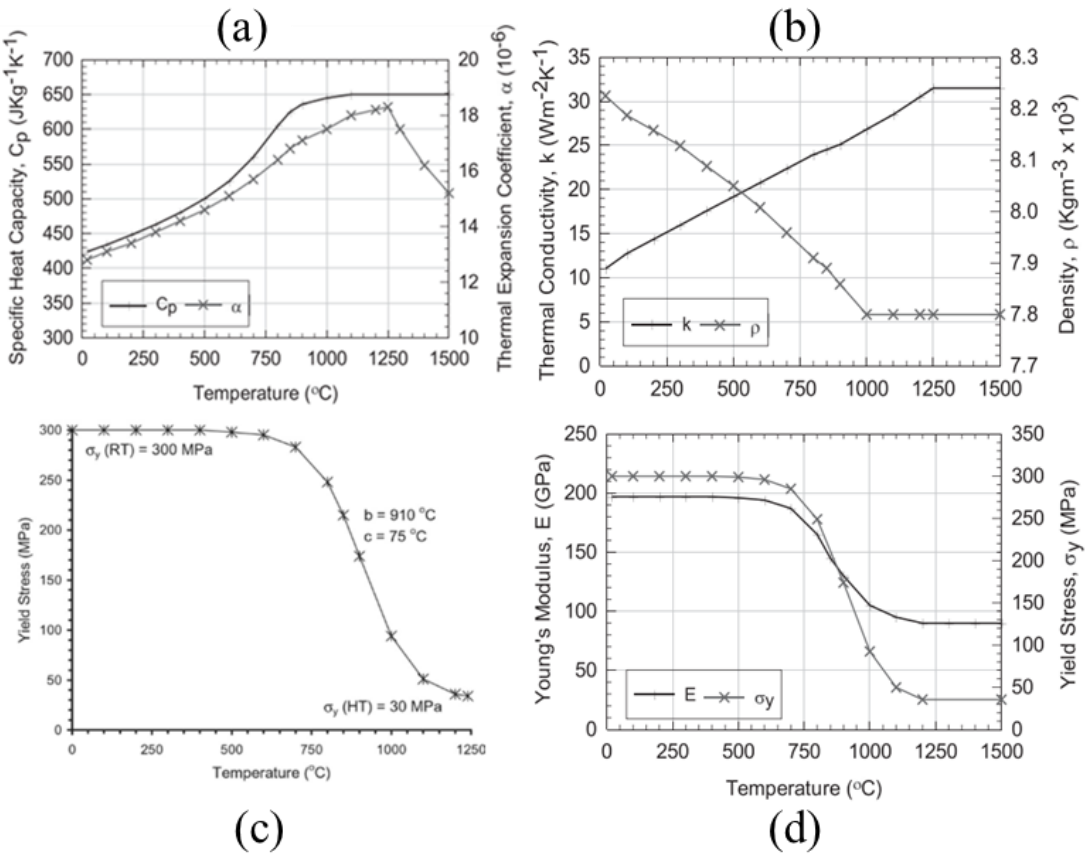

Figure 8.11 Temperature dependant thermomechanical properties of IN718 used for all FE models; (a) Specific heat capacity, Cp , and thermal expansion coefficient, σ; (b) Thermal conductivity, k and density, ρ (c) , Variations in yield stress used for solution treated IN718 (d) Young's modulus, E , and yield stress, σ_y [169], [505], [506].

8.9 Thermomechanical model incorporating creep

In the simulation of LMD-induced residual stresses, it is important to develop advanced material behaviour model that can predict stress fields with higher degree of accuracy. Some factors that can affect the formation and distribution of residual stress and plastic strain in the mechanical analysis are [507]:

1. *Strain hardening:* Researchers have found that combined isotropic-kinematic strain hardening models can give the best predictive welding residual stresses, while isotropic model may overestimate results and kinematic may underestimate [508].
2. *Annealing effect:* The most important consideration for the substrate and interface region due to the raised temperature during subsequent layer addition. The accumulated strain hardening generated during welding thermal cycles is reduced or eliminated at high temperatures due to dynamic recovery and recrystallization of the material. Hence, the modelling of stress relaxation through creep.
3. *Melting effect:* An equally important for the interface region when aiming to simulate the mechanical analysis of the interface region. Materials lose strength

near and above the melting point and restore to the strain-free state during solidification. In mechanical analysis, material properties can be set to small values when approaching or surpassed the melting temperature and the accumulated strain hardening of the material should be removed [509].

Creep is a time-temperature dependent plastic deformation occurring under static loads, and in this case residual stress. Considering stress relief anneal, creep diminishes residual stress by transforming it into additional plastic strain. It was postulated that pervasive cyclic thermal loads introduced during the deposition process resulting in heat accumulation in later stages could induce stress relaxation, creep, effects across the entire build. Studies validating thermomechanical process simulations in additive manufacturing often note an overestimation of simulating distortion and residual stress [510], [511]. This could be attributed to the exclusion of viscoplastic material behaviour, such as creep or stress relaxation, as found in other investigations [512]. In laser metal deposition, subsequent layer addition induces viscoplastic effects due to the combined thermal and mechanical load. Previous research [513], [514], [515] introduced models with stress relaxation implementation to capture these effects in thermomechanical simulation. Most studies concentrate on calibrating and validating residual stress behaviour using experimental thermal and distortion measurements. Although displacement sensors offer insights into part-level residual stress, they provide single-point measurements for the average behaviour of the system under bulk residual stresses, potentially yielding less accurate or scalable/transferable information. Notably, simulation errors are reduced by defining an upper stress relaxation temperature and setting plastic strain to zero above this temperature [516], but this is only valid for certain materials like Ti-6Al-4V and it is unlikely that it is suitable to IN718 where stress relaxation is less pronounced for temperatures within the range of aging treatments. However, there is limited research on stress relaxation behaviour of IN718 simulating creep behaviour to describe the occurring viscoplastic effect during the LMD process [517].

Nonlinear regression curve fitting methods are commonly used to analyse the experimental data obtained from creep tests. By fitting mathematical models or equations to the experimental data, researchers can determine the creep law that best describes the material's behaviour under specific conditions. These creep laws often take the form of empirical equations that relate the creep strain rate to stress, temperature, and time.

In an advanced thermo-mechanical analysis, the fundamental strain theory determines total strain by independently calculating elastic, plastic, and creep strain components and combining them as follows:

Equation 8.7

$$\varepsilon_{total} = \varepsilon_{elastic} + \varepsilon_{plastic} + \varepsilon_{creep}$$

Incorporating the creep law in complex FEA models generally leads to increased deformation, reduced stress, or a combination of both behaviours. When a material undergoes partial deformation due to creep but does not reach the full extent of creep strain, it exhibits a combination of increased total strain and decreased stress. In such cases, FEA modelling of creep can accurately predict both the time-dependent creep deformation and the gradual decrease in stress over time, known as stress relaxation. For this project, the predicted stress relaxation response will be examined with and without creep models to compare against the contour method results with the aim of increasing the efficiency of the thermomechanical model.

8.9.1 Implementing Creep

Incorporating a viscoplastic creep model into thermomechanical simulations using Simufact necessitated delineating creep behaviour in the form of a table with temperature and stress dependencies. It was applied to the substrate to understand the resultant stress relaxation occurred due to subjected cyclic thermal loads. Rahimi *et al*. [518] proposed that the hyperbolic law can be reformulated, allowing the determination of the parameters of the equation from the slope and intersection point of the fitted straight line with the horizontal axis, respectively, fitting a curve to experimental data with a robust fit (95% confidence) on the measured data. Rahimi *et al.* [518] conducted ASTM-compliant annealed IN718 uniaxial creep tests between 620°C and 770°C. The study aimed to predict stress relaxation in highly loaded IN718 superalloy, simulating industrial aging heat treatments. Stress relaxation tests, using the hyperbolic law, yielded numerically adjusted parameters defined by a linear plot of the derivative d_σ/dt against time for each temperature of interest (The results are displayed in Appendix C).

In *Simufact*, the creep behaviour can be described as creep strain rate (1/s) with respect to stress experienced (MPa) for a range of temperatures. Solving plasticity requires applying the hypo-elastoplastic formulation and the strain is decomposed, as Equation 8.8 shows. This formulation of thermomechanical modelling employs an additive approach to plasticity, wherein elastic strain (ε_e), plastic strain (ε_p) and thermal strain (ε_t) are

summed together. In this framework, the total strain, ε, experienced by the material is regarded as the collective result of the individual contributions from elastic, plastic, and thermal strains.

When considering viscoplastic creep behaviour in the simulation, creep strain ε_{cr} is added to the formulation [519]:

Equation 8.8

$$\epsilon = \epsilon_e + \epsilon_p + \epsilon_T + \epsilon_{cr}$$

The material creep properties are calculated by creep strain rate, whereby the appearing creep strain per increment $\Delta\epsilon_{cr}$ is solved by multiplying the creep strain rate $\dot{\epsilon_{cr}}$ with the normal of the stress surface in the applied yield point model with the equivalent stress σ_v and occurring stress σ [520]:

Equation 8.9

$$\Delta\epsilon_{cr} = \underline{\dot{\epsilon_{cr}}} . \frac{\delta \underline{\sigma}}{\delta \sigma_V}$$

During stress relaxation at temperature, the elastic stress relaxes, and the elastic strain is replaced by plastic strain through creep deformation. Hooke's law states:

Equation 8.10

$$\sigma = E\varepsilon_e$$

Or differentiated with respect to time:

Equation 8.11

$$\frac{\partial \sigma}{\partial t} = E \frac{\partial \varepsilon_e}{\partial t}$$

Therefore, the final equation for change in creep strain becomes:

Equation 8.12

$$\frac{\partial \varepsilon_p}{\partial t} = -\frac{1}{E}\frac{\partial \sigma}{\partial t}$$

Where stress, σ, is defined by the stress relaxation equation using the hyperbolic law (Eqn. 8,13) based on data by Rahimi *et al.* [521] . This law was found to be the most appropriate to describe stress as a function of time due to long time tendency of the stress towards an

asymptotic non-zero value. Plotting the derivative dσ(t)/dt against time in the logarithmic scale resulted in a linear plot with slope equal to –(m+1).

Equation 8.13

$$\sigma(t) = \sigma_\infty + b(t+a)^{-m}$$

As mentioned, the hyperbolic creep law can be rearranged to solve the creep strain rate (1/s) as a function of stress (MPa) to implement into the MSc Solver, hence:

$$\sigma(t) = \sigma_\infty + b(t+a)^{-m}$$

$$\sigma(t) - \sigma_\infty = b(t+a)^{-m}$$

$$\frac{\sigma(t) - \sigma_\infty}{b} = (t+a)^{-m}$$

Equation 8.14

$$\left(\frac{\sigma(t) - \sigma_\infty}{b}\right)^{\frac{1}{m}} = t + a$$

Substituting Equation 8.14 into the partial derivative for hyperbolic law with respect to time, to achieve a rate, stress relaxation formula (Equation 8.15), it can be solved for *t* and *a* to achieve creep strain with respect to time for stress behaviour:

Equation 8.15

$$\sigma_\infty + b(t+\alpha)^{-m} \; or \; \frac{\partial\sigma(t)}{\partial t} = -bm(t+\alpha)^{-m-1}$$

$$\frac{\partial\sigma(t)}{\partial t} = -bm(\left(\frac{\sigma(t) - \sigma_\infty}{b}\right)^{-1/m})^{-m-1}$$

Equation 8.16

$$\frac{\partial\sigma(t)}{\partial t} = -bm(\frac{\sigma(t) - \sigma_\infty}{b})^{-\frac{m+1}{m}}$$

After substituting creep stress rate through Equation 8.12, we can solve for creep strain rate in terms of stress and relaxation behaviour:

$$\frac{\partial\sigma(t)}{\partial t} = -bm(\frac{\sigma(t) - \sigma_\infty}{b})^{-\frac{m+1}{m}}$$

Equation 8.17

$$\frac{\Delta\varepsilon_p}{\Delta t} = -\frac{1}{E}\left[-bm\left(\frac{\sigma(t)-\sigma_\infty}{b}\right)^{-\frac{m+1}{m}}\right]$$

Where the Young's modulus, E is taken as 200 GPa for aerospace grade IN178. Since the numerically adjusted values of the parameters of the hyperbolic law were given a range, the 'm' value was altered to fit the Initial stress condition (σ_0), highlighted in Appendix C.

Due to rapid solidification, LMD IN718 differs significantly from wrought or cast material in terms of segregation, grain orientation, and grain size [522]. LMD components exhibit higher strength and lower ductility than wrought material. In Simufact Welding 2021 onwards, the default thermomechanical simulation does not consider creep properties for LMD. However, the simulation program's solver allows defining additional viscoplastic creep material behaviour, typically accounted for in simulations involving heat treatments. To define and implement the material's viscoplastic creep properties, pre-defined creep model parameters were calculated, and flow curves adjusted. Figure 8.12depicts the implemented flow curves in the thermomechanical model for IN718, based on stress relaxation curves obtained using a hyperbolic law function described by Rahimi *et al*. [518]. The creep strain rates at 620°C, 670°C, and 720°C are plotted on the primary y-axis, while the creep strain rate at 770°C is plotted on the secondary y-axis.

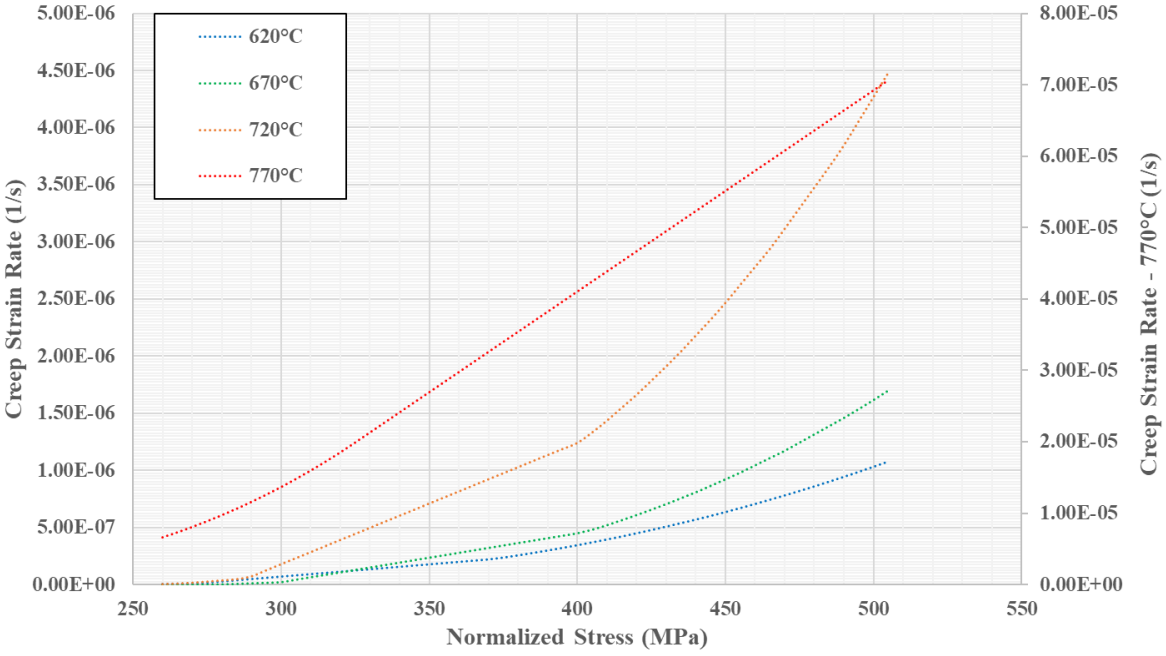

***Figure 8.12 Implemented flow curve generated using hyperbolic creep law and data from* [518].**

8.9.2 Thermo-mechanical bulk stress behaviour

Figure 8.13 shows the σ_{yy} stress behaviour and magnitudes in the entire component upon cooling to ambient temperature.

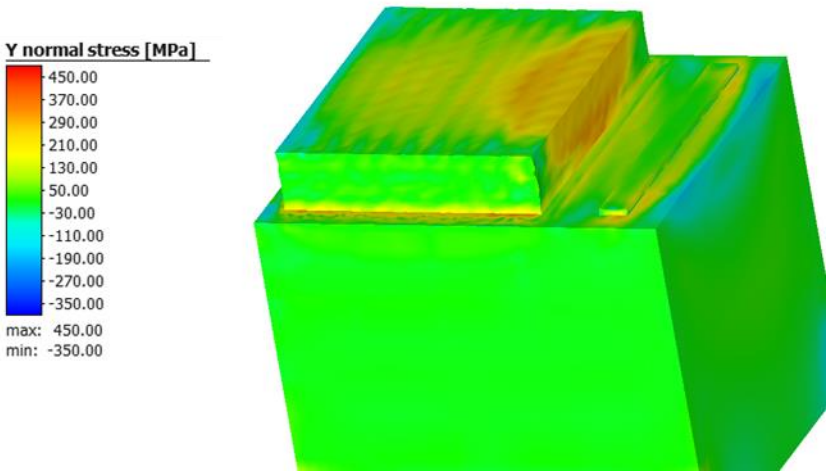

Figure 8.13 FEA model showing σyy stress distribution in the build due to LMD with process parameter of laser power: 950W.

Figure 8.14 presents a cross-section derived from Figure 8.13, elucidating all three stresses (σ_{xx}, σ_{yy}, and σ_{zz}) direction distribution during the cooling process to room temperature for the 950 W specimen. In all three stress components, the stresses pattern reveals a region of low tensile stress (approximately 0→150 MPa) along the interface. The σ_{xx} stress direction, (Figure 8.14a) show a similar band of compressive stresses under the interface (also shown in σ_{yy} direction) which aims to balance the tensile stress generated in the deposited region. At the bottom right corner of the as-deposited build, exists an increased albeit small, region of tensile stresses. It is hypothesised that these stresses have generated due to the contraction of the cooled deposited material and occurs at the corner region acting as a stress concentration area. Results from the thermomechanical model reveal that the σ_{zz} direction (Figure 8.14c) have relatively low stresses throughout the entire component with slight increased tensile stresses at the deposition free edges and a compressive balancing region in the substrate.

A more in-depth analysis of the σ_{yy} stress direction can be compared to the contour method measurements (Figure 8.15). The σ_{yy} stress direction reveal a parabolic shape of maximum compressive stress in the substrate just beneath the interface. The upper half of the substrate exhibits a maximum compressive stress, reaching -344 MPa, slightly off centred towards the left-side free end. The deposition occurred perpendicular to the page, from the left (track 1) to the right side (track 10). Due to the deposition schedule, it can be elucidated that the maximum compression region was slightly concentrated towards

the left-side free edge. Overall, the combination of thermal gradients, material deposition, and microstructural changes during LMD can lead to the accumulation and increase of compressive stresses with each track and layer deposited.

In the deposited region, a comet-shaped distribution of tensile stresses is observed, with the highest tensile stress of 340 MPa situated near the left-side free edge which will increase with each layer and track deposited as this section would be last to cool. The areas near the edges or boundaries of the deposited region tend to experience slower cooling rates compared to the interior regions. As a result, residual stresses, including tensile stresses, can develop in these regions due to thermal gradients and material contraction during cooling. This stress diminishes to 226 MPa towards the tail end, positioned approximately in the centre of the deposit. The maximum tensile stress at the free edge is approximately 0.45 times the yield strength of as-deposited IN178 (~745.07 MPa) and 0.3 times the yield strength of double-aged IN718 (~1100 MPa) [523]. However, careful consideration of stress magnitudes and distribution is required prior to machining to final shape, as the stress magnitude and location may initiate crack formation. Therefore, an appropriate stress-relieving method must be chosen after repair, which can range from thermal (heat-treatment) to mechanical (cold work, vibration) methods.

The tensile stresses in the deposit can be attributed to thermal shrinkage resulting from localized thermal contraction as each layer cools atop the preceding layer. These contractions may induce a bending moment in the sample, and since the volume of the deposit is fused to the thicker substrate, bending is constrained by the substrate, introducing tensile stresses in the build direction towards the edges, counterbalanced by compressive in the top of the substrate [135].

In LMD with multiple passes, the previously deposited layer undergoes partial re-melting, annealing to some extent, thereby alleviating previous deformation, including elastic and plastic strains. This partial re-melting process induces plasticity as the material's yield strength is reduced due to the elevated temperatures associated with the annealing. Each subsequent layer addition and the resultant stresses are the product of the inherently high cooling rates incurred during repeated deposition and heating cycles (heating, cooling, and reheating). Such variations in thermal histories at different locations of the build, result in misfit strains and plastic flow in the material leading to residual stresses. An in-depth analysis into residual stress evolution and the effect of laser power will be discussed

in the following section. The aim of this chapter was to evaluate the capability of and benchmark a thermo-mechanical model against experimental data.

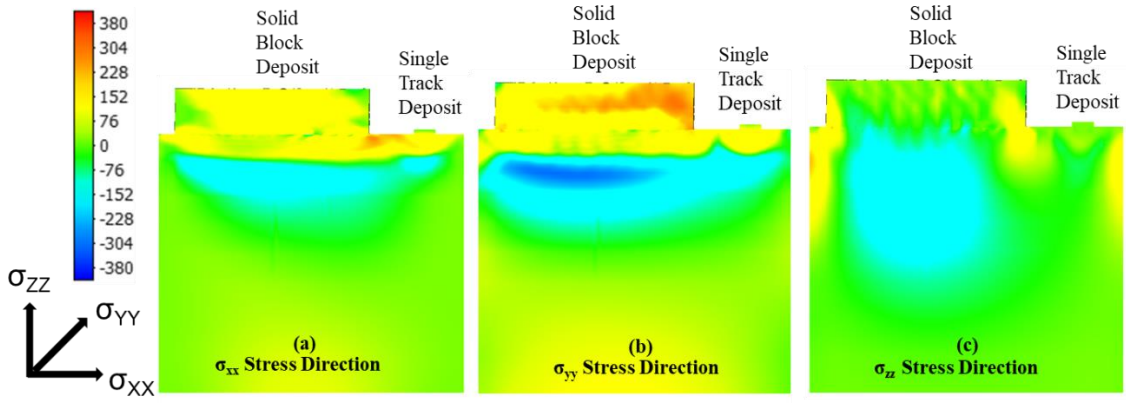

Figure 8.14 FEA model results showing the residual stress in the (a) σ_{xx},(b) σ_{yy} and (c) σ_{zz} direction of the deposit for the 950W specimen.

8.9.3 Model Validation

The findings outlined in Chapter 5 confirm that the thermal loading stages of the thermo-mechanical model have been experimentally calibrated. The subsequent phase entails conducting a comparative examination of the mechanical components. To validate the residual stresses of the model, the simulated σ_{yy} stresses (the S33 direction within ABAQUS) were juxtaposed with experimentally derived measurements obtained through the contour method. Cross-sections of post-deposited blocks were analysed, measuring out-of-plane Y normal stresses to illustrate the macro-stress behaviour under different laser power conditions. Mechanical properties for the deposited material assumed a Young's modulus of 180 GPa and a Poisson's ratio of 0.33. Additionally, residual stress values were assessed at various locations along the length of the dotted line, extending from the substrate bottom to the deposit.

Figure 8.15 displays bulk residual stresses (in the S33 direction, σ_{yy}) obtained through both the contour method and Finite Element Analysis. The simulated stress field closely matches the experimentally captured results from the contour method. There's a progressive development of compressive stress from the substrate bottom to approximately -5 mm, with a maximum compressive band evident around -4 mm in both methods. Stress measurements decrease from this band towards the interface region. Tensile stresses are observed within the deposit, with the maximum tensile stress occurring near the terminus of the cladding (track 10, left-side of deposit) and a minimum near the deposit's interface region, as captured by both methodologies.

In this orientation, stresses assume a compressive nature at the central region of the substrate due to compensatory tensile stresses at the peripheries of the whole component. The clamps situated at the lower extremity of the substrate function as predominant heat sink. The prevailing influence during the cooling phase is attributed to conduction conditions, which results in material shrinkage, as opposed to the comparatively lesser impact of convection and radiation. Following the completion of deposition, the cessation of the beam induces rapid cooling at the peripheries and within the clamped regions, thereby eliciting more substantial shrinkage along the free edges of the deposit where material abundance is lesser than at the central portion. Shrinkage is more pronounced at the centre than at the peripheries, giving rise to tensile stresses towards the free edges and compressive stresses towards the centre.

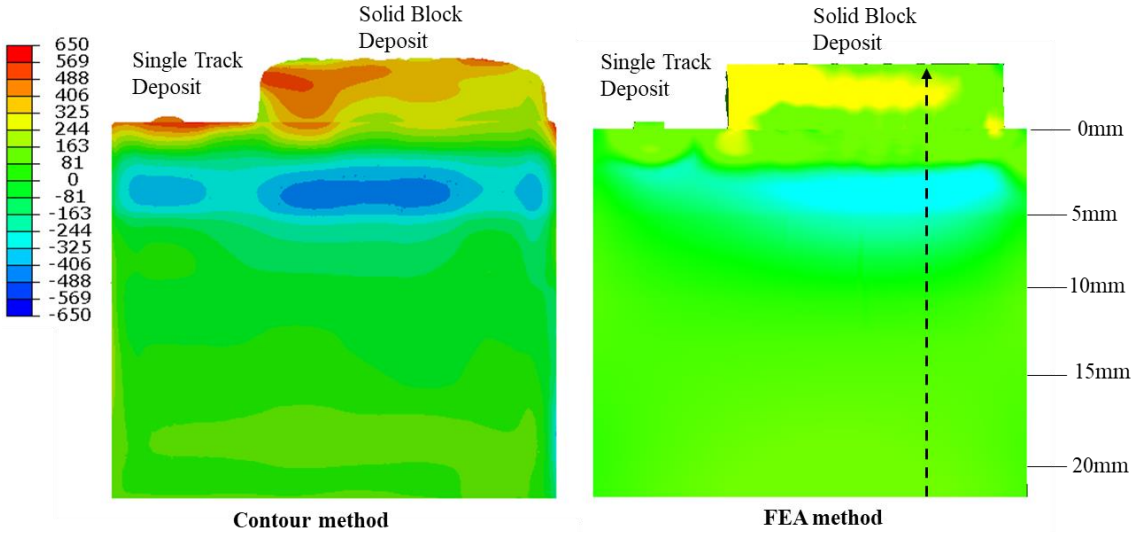

Figure 8.15 Residual stresses simulation results and the comparison with experimental data for the 950W specimen.

Figure 8.16 presents a comparison between FEA predictions and contour measurements derived from the 950 W specimen, indicated by the black dashed line in Figure 8.15. Furthermore, all three stress components have been extrapolated from the model for this dashed line and are presented in Appendix D.

The thermomechanical model is in line with the contour measurements, illustrating low stresses at the substrate bottom transitioning to compressive stresses below the deposit, reaching a peak at approximately -4 mm. Both simulation and experimental methods identify the transition from peak compression to a relatively low tensile region towards the interface (around 0mm), with a subtle stress pivot along the fusion line (0 mm). Within the deposited region, both methodologies show that tensile stresses rise with increasing

build height until a maximum is reached in the model at around +2.8 mm which is not seen in the contour method. Nevertheless, it can be concluded that both the FEA method and Contour method have a good overall agreement which is valuable in understanding the evolution of stresses. However, the magnitude of experimentally measured compressive stresses at the substrate interface are under-predicted by approx. 130 MPa and the maximum tensile stress in the deposited region were underpredicted by approx. 90-100 MPa.

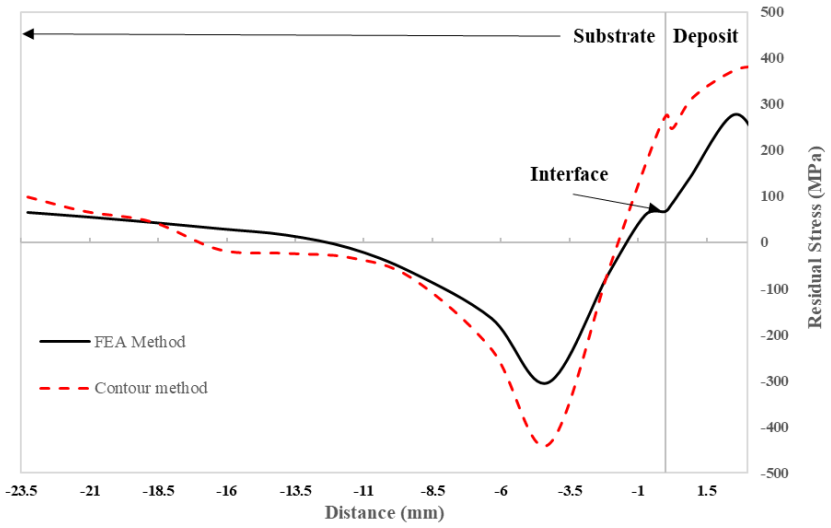

Figure 8.16 Residual stress measurements (σyy) from the substrate to deposit (along black dotted line in Figure 8.15). Comparing measurements from the FEA method and measurements characterised by contour method experiment.

In line with the findings presented in Figure 8.15 and Figure 8.16, it is observed that the simulated stress behaviour is aligned with the experimentally derived stress profile. Nevertheless, obvious differences in stress values exist between the predicted field and the experimental results. Several influential factors contributing to the variance in peak stress values between the predictions and experimental observations include:

1. Homogeneous mechanical properties were assigned in the deposited region. However, it is acknowledged in literature and experimentally shown, that the deposited region encompasses an inhomogeneous microstructure, consequently leading to variations in mechanical properties. Also, the mechanical properties of as-deposited material can change with processing conditions, therefore the mechanical property assigned to the deposited material follow published data closely for solution treated material that have been used for the deposited material.
2. The thermomechanical model does not account for defects seen in the as-deposited sample such as porosity which influences the stress profile.

3. The thermophysical properties assigned to the substrate and deposit are based on literature and were not experimentally verified. Also, the material properties for the substrate for precipitation free regions along the fusion line differ significantly from the rest of the substrate.
4. The creep values used to generate creep flow stress curves have been taken from published data as it was difficult to experimentally collect stress relaxation data.
5. The simulation fails to consider weld pool dynamics and deviations in weld-pool shape, which can result from changes in substrate geometry, roughness, and laser focus during experimental trials. While weld-pool sizes and geometry exhibit good agreement in the same figure, the simulation's simplified representation, stacking featureless blocks, may lead to deviations. The rounded profile observed in experiments is not replicated in the simulated model, potentially influencing the magnitude of residual stress. These simplifications have been acknowledged in literature [524], [525].
6. The experimentally obtained results are derived from contour method, a methodology susceptible to an overall error of 5-10%. This discrepancy arises from inherent uncertainties in the procedure, such as cutting artefacts, which introduce inaccuracies and yield erroneous results.
7. The magnitude of flow stresses is primarily attributed to variations in the initial state of the material and its processing conditions, which affect the flow curves of the materials. As flow curves were not established for the deposited material, Simufact Welding® employs cast material properties with a scaling factor ranging between 2 and 4 to approximate the deposited condition.

Despite the apparent discrepancies in stress values between the predicted field and the experimental results, conducting a thorough review of the transient creep behaviour in the thermomechanical FEA model is beneficial.

8.9.4 Transient creep behaviour

Figure 8.17 depicts the thermomechanical model results for the Y normal stress component in the 950W specimen. Subfigure (a) excludes creep, while subfigure (b) includes creep in the simulation. The hypothesis posited that incorporating flow stresses and activating the creep model would induce an annealing effect in both the substrate and the deposit, given the continuous heat input from subsequent layers. The implementation of a creep model, specifically under bulk diffusion creep, accounts for elevated temperatures during the LMD process, where atoms possess higher kinetic energy,

allowing them to move through the lattice via diffusion. This movement results in the gliding of lattice planes, causing material deformation and subsequently reducing peak residual stress values due to extensive plastic deformation, which was partially captured by the thermomechanical model.

Omitting creep in the simulation led to peak tensile stress regions exhibiting a track-by-track, layer-by-layer pattern, with stress peaks at the centre of each track, as denoted by the arrow in the deposited material. The location of the maximum tensile stresses in the Y normal direction appear near the top layer after the printing of the final layer, which is the same trend as the results in other studies [183], [526]. The introduction of a creep model resulted in a very small stress relaxation effect, diminishing peak stress values, and promoting a more uniform stress distribution. The concentrated tensile stress at the interface region also experienced a reduction in peak value.

However, the incorporation of creep behaviour during LMD did not demonstrate a significant reduction in stresses in both the deposit and substrate, potentially due to the combined influence of temperature and duration under temperature conditions. Furthermore, transient stress values during deposition in the X, Y, and Z directions remained moderate to low. The creep model has an impact but not a significant one potentially due to incorrect creep rate due to the material data not being appropriate to accurately capture the exact RS field. However, analysis of creep and the FEA model it provides useful data into understanding overall generation and evolution of residual stresses.

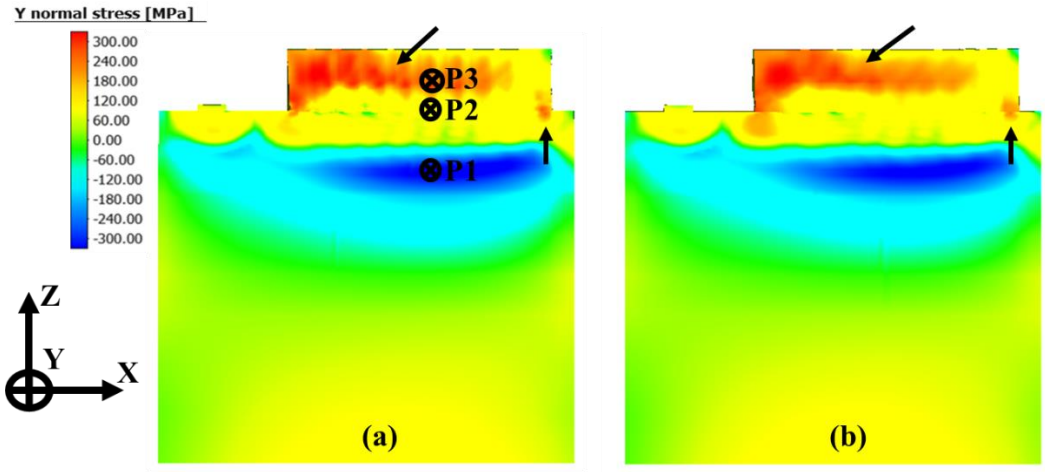

Figure 8.17 Y normal stress (global transverse direction) behaviour of the 950W specimen where (a) creep model is neglected and (b) creep was implemented.

The stress relaxation arising from creep-like mechanism is a transient, temperature-time dependent process occurring over prolonged time. However, in the LMD process,

localized stress fields experience seconds to minutes of creep-like phenomena, which may be insufficient for effective stress relaxation.

To analyse the influence of creep on transient stress fields and strain behaviour during deposition, data was extracted from distinct regions: the compressive area in the substrate (P1), the interface region (melt pool from layer 1) (P2), and the mid-build of the deposited region (P3). Figure 8.18 illustrates the transient stress and strain patterns over time and temperature for the interface region (P2). Detailed graphical transient data for P1 and P3 is provided in Appendix E -Appendix J. The comprehensive transient data spans the entire build process until the interface region reaches room temperature.

The stress behaviour was examined in all three directions—X, Y, and Z—corresponding to transverse, normal, and build directions, respectively. Simultaneously, strain behaviour was extracted to comprehend the elastic, plastic, and creep strain dynamics throughout the transient deposition process.

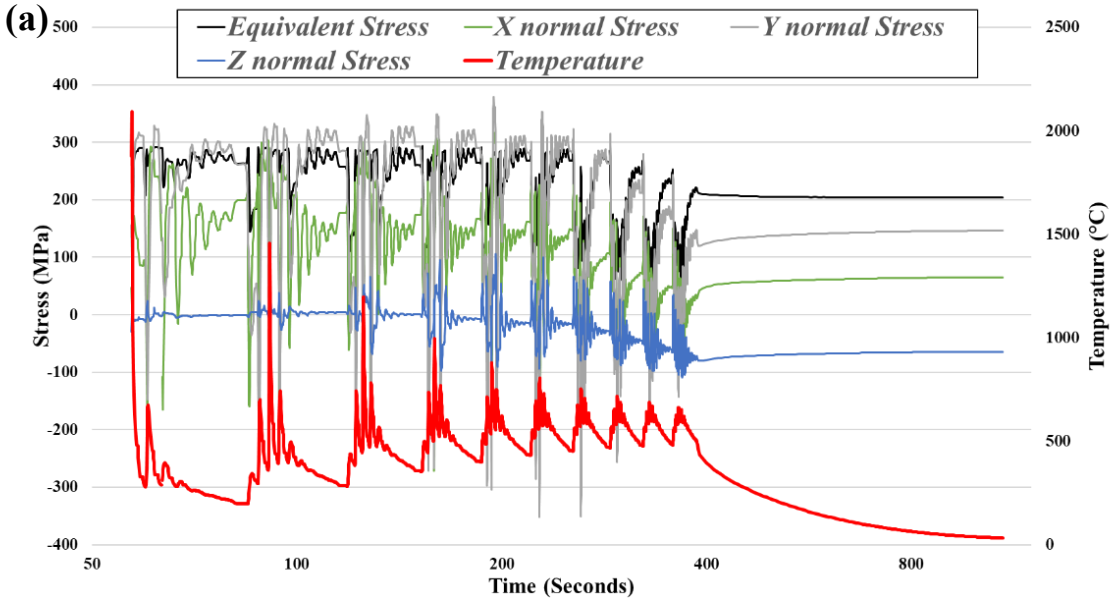

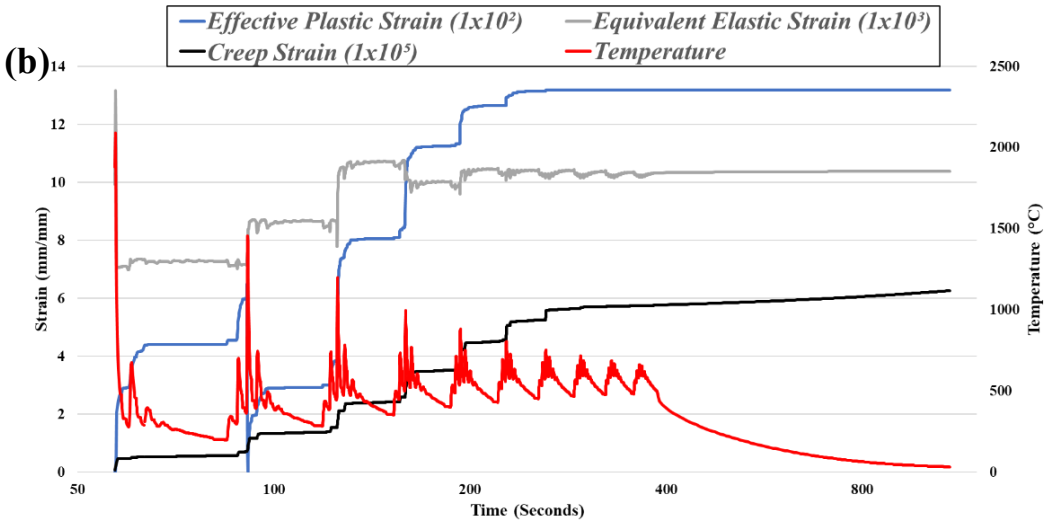

Figure 8.18 Extracted data from the 950W thermomechanical model (creep considered) for the interface region (P2) whereby (a) depicts the stress vs time vs temperature graph and (b) depicts the strain vs time vs temperature graph.

The data indicates that the maximum equivalent stress gradient occurs during layer one within the interface region, attributed to the TGM mechanism. Subsequently, as the melt pool cools below the solidus temperature, a sustained, relatively low elastic strain emerges, leading to a gradual increase in plastic deformation within the interface region.

In the interface region, the evolution of transient stresses can be observed, reaching high values of 300 MPa in tension and -350 MPa as per the deposition schedule. However, as the part cools to room temperature, the stresses stabilize, resulting in moderate to low equilibrium stress values, approximately 200 MPa. Theoretically, with an increased build volume, these stress values would be expected to be larger due to the greater volume of material added and the inherent material constraint. In the final stages of the deposition, a small stress reduction occurs, driven by stress relaxation induced through the increasing creep strain. This relaxation continues as the part cools to room temperature, but it is marginal.

Data extracted from positions P1 and P3, detailed in Appendix E -Appendix H, indicate equivalent stresses of approx. +190 MPa and the Y normal stresses as repeated in the experimental measurements, values of approx. -320 MPa, upon cooling to ambient temperature, respectively. In the mid-build (Appendix G), the Y stresses exhibit a tension band of around 220 MPa, resulting in low stresses across the interface region as the substrate compression band aims to balance the tension band formed during the build. The model illustrates the location of the compressive region, which grows in magnitude with each layer added during the building process. The magnitude of the compressive

substrate band increases to balance the tensile stresses generated in the deposited build material. This process continues until equilibrium is reached in the deposited region.

At approximately 80 s (commencement of layer 2), the plastic strain undergoes a significant drop to zero. This occurs as the localized region is re-melted during layer 2, surpassing a temperature of 1336°C. Concurrently, the elastic strain reaches its peak at 125 s, attributed to a localized temperature surge around 1120°C, below the solidus temperature, causing expansion due to heat. Subsequently, the elastic strains plateau as the region stabilizes at a relatively constant temperature, and the thermal gradient diminishes with subsequent layers indicating the material experiences elastic deformation in response to temperature fluctuations. The prolonged exposure to high temperatures results in a continuous increase in plastic strain and creep strain but having marginal stress relaxation.

The transient deformation behaviour in the top-third region of the substrate (P1) is outlined in Appendix E. The data reveals a notably high Y normal stress, elastic strain, and plastic strain during the initial laser pass, attributed to thermal-induced stresses. This phenomenon is linked to the extreme thermal gradient between the laser-deposited tracks and the cold substrate. Subsequent laser passes reintroduce elastic strain, reaching magnitudes comparable to the first layer.

Around 60 s, (layer 1) and 100 seconds (layer 2), significant plasticity occurs, resulting in a peak plastic strain. The elevated temperature in that region at these specific time increments (>290°C and >380°C) diminishes the yield stress of the material, surpassing the elastic strain field. The combination of thermal-induced equivalent stresses (280-300 MPa) and temperature induces plastic deformation in the top region of the substrate. Approximately at layer 4, the equivalent stress experiences a slight relaxation due to an annealing effect induced by a continual thermal cycle above 460°C. From layer 5 onwards, the substrate stress field average plateaus due to the substrate's relatively low cooling rate, while the plastic strain remains stable.

Following the final layer deposition, creep effect continued to be marginal, and the stresses in the localized region stabilize at around 200 MPa. However, there is a marginal increase in X, Y, and Z normal stresses, accompanied by stress redistribution as the entire part cools down to room temperature and reaches equilibrium.

In summary, two significant spikes in equivalent plastic strain occur due to either encountering maximum equivalent stress values or reaching the maximum elastic strain

possible at the respective temperatures during the deposition of layers 1 and 2. These spikes are likely linked to the pronounced thermal gradients experienced during these early stages of deposition. However, as the deposition progresses, the substrate gradually heats up. Around 100 s onwards (approximately layer 3), the equivalent stress exhibits no notable increase. Several factors contribute to this behaviour: the rising temperature, which reduces the material's yield stress, marginal creep strain, the gradual establishment of thermal equilibrium (indicated by a diminishing temperature gradient with each new layer), and structural accommodation. The latter suggests that after layer 3, the deposited material attains a more stable configuration, resulting in diminished stress concentrations and a more uniform stress distribution.

The incremental addition of layers in the LMD process results in a reduction in thermal mismatch magnitude, coupled with an augmented heat-holding capacity in already solidified layers. This addition induces two concurrent phenomena: firstly, the new layers enlarge the effective surface area for convective heat transfer, thereby intensifying the convective heat transfer rate. Secondly, the thermal resistance for heat conduction rises, facilitating heat accumulation.

Up to a specific deposition build height, the increase in surface area surpasses the rise in conductive resistance, leading to an increase in convective heat transfer rate. Beyond this height, conductive resistance prevails, and conduction becomes the predominant mode of heat transfer. The progressively increased thickness of the build enhances material heat-retaining capacity, diminishing the temperature gradients. This, in turn, results in stress relaxation and consequently reduces residual stress [527]. This elucidates the spatial and temporal variations in temperature gradient concerning equivalent stress, as depicted in Figure 8.18.

8.10 Creep Model Summary

The material properties have a strong influence on the residual stress field prediction in numerical simulations. Although the substrate material and heat-treated condition were experimentally defined in previously published research work, LMD IN718 has more complex material properties as the material is inherently anisotropic. The model does not account for microstructure evolution and the material properties were taken from literature, so their validity for LMD additive manufacturing is questionable.

The incorporation of the creep effect in the thermomechanical analysis has had a negligible impact on the calculated stresses. According to the creep effect outlined in the

Simufact information sheet, the inclusion of creep tends to reduce residual stresses by transforming them into plastic deformation. This holds partially true for plastic deformation, as evident in the final stages of cooling, where the inclusion of creep results in a higher effective plastic strain compared to the model without creep. This phenomenon occurs as stresses equilibrate, and the material actively undergoes yielding under suitable triaxial stress state. The effective plastic strain is computed as follows:

$$effective\ plastic\ strain = total\ true\ stress - true\ strain/E$$

The effective plastic strain is derived as the time integral of the absolute value of the equivalent plastic strain rate, calculated using von Mises strain tensors. The integration involves absolute values to account for instances of plastic deformation that subsequently undergo complete reversal, preventing the effective plastic strain from reaching zero. The observed minimal impact on residual stresses can be attributed to the location-dependent values, which have demonstrated a stress relaxation effect on the cross-sectional faces.

The anticipated reduction in elastic strain with the inclusion of the creep effect has yielded an opposite outcome. This discrepancy is attributable to the distinction between 'effective' and 'equivalent' Strain. The 'equivalent' elastic strain is determined by summing the incremental values of elastic strain and is computed analogously to the equivalent plastic strain. The calculation employs elastic strains instead of plastic strains and follows the same formula outlined [528]:

Equation 8.18

$$Equivalent\ plastic\ strain = \sqrt{\frac{2}{3}\Sigma\Delta\varepsilon_{ij}^{p}\Sigma\Delta\varepsilon_{ij}^{p}}$$

Therefore, by incorporating a ‘creep’ sub-routine into the mechanical analysis has made a marginal but still noticeable impact and should be accounted for during LMD.

Denlinger *et al.* [516], [529] conducted extensive work to model the impact of stress relaxation during LMD of Ti-6Al-4V. Calibration of the mechanical model was achieved through *in situ* distortion measurements using the Laser Doppler System (LDS), and residual stress measurements employed the hole drilling method. The proposed model integrates instantaneous annealing and incorporates creep when a stress-related temperature is reached. Stress relaxation is implemented by resetting stress, elastic strain, thermal strain, plastic strain, and equivalent plastic strain to zero at the previous time increment when the norm temperature at all Gauss points of an element exceeds T_{relax}.

Without stress relaxation, the results were overpredicted by more than 500%, displaying a shift to negative values near the free surfaces, deviating significantly from the measured residual stresses. Incorporating stress relaxation at 690°C (to account for the allotropic transformation from BCC to HCP) results in an underprediction of residual stresses but significantly reduces errors despite still neglecting transformation strains. The instantaneous relaxation of residual stresses contributes to the underprediction, and future work is envisioned to incorporate dynamic stress relaxation occurring over an extended period.

Qiao *et al.* [530] advocated a dynamic reduction of equivalent plastic strain in ABAQUS, based on the duration of material exposure to elevated temperatures. They showed that classical isotropic strain hardening inadequately describes plastic deformation, leading to a 30% overprediction in plastic strain magnitudes compared to experimental measurements. Additionally, the plastic strain distribution in the dynamic strain hardening model closely aligns with the experimentally observed pattern.

8.11 Transient RS behaviour during LMD

Figure 8.19(a-f). illustrates the predicted stress behaviour at various stages of the LMD process. During the deposition phase, as depicted in Figure 8.19a, when subjected to heating, the power source induces localized elastoplastic deformations (depicted by ε_{pl}, ε_{el}, and σ_{yield}) and generates additional tensile stress in the irradiated area. As the molten top layers cool down, thermal contraction prompts shrinkage, resulting in the formation of both tensile and compressive residual stress regions (upper and lower layers, respectively). This phenomenon is explicated through the temperature gradient mechanism (TGM), explained in Figure 8.1.

Following the deposition of the first layer, tensile stresses emerge in the build region towards the centre. To counteract this, a band of compressive stresses evolves directly beneath the interface region. The deposition of the second layer serves to alleviate the tensile stresses induced in the first layer, owing to the heating cycle and re-melting at the top of the initial layer. Subsequent cooling, however, results in the reappearance of these tensile stresses. As the deposition progresses, the initially concentrated tensile stresses in the build disperse across the interface, impacting the compressive region below in a similar fashion as observed in the first layer.

Notably, as the fifth layer is deposited and undergoes cooling, the tensile region in the build ascends higher, moving away from the interface region, while the balancing

compressive stresses at the interface concurrently intensify and expand horizontally. The cumulative maximum compressive stress beneath the interface region increases in magnitude for the first, third, fifth, and seventh layers, measuring -253MPa, -316 MPa, -347 MPa, and -371 MPa, respectively. After the deposition of the seventh layer, minimal variation is discerned in the maximum stress value.

This stress behaviour can be explained through an examination of the temperature history during the build process. In the initial single-track deposition, the substrate is at room temperature and its surface is heated abruptly by the laser and a small volume of molten material is added on top of that creating a small melt pool. As this pool rapidly cools and solidifies, the surrounding solid material undergoes restrained shrinkage, leading to an increased stress state. This phenomenon is replicated in the first layer. However, the stresses remain confined within the solidified material, generating a horizontally oriented compressive balancing stress, due to the adjacent material deposition, with localized maximum compressive forces aligned with the centre of the build.

As the deposition advances, succeeding layers accumulate heat from beneath, facilitating material expansion and slower cooling rates. With a decrease of temperature gradient, the localised tensile stresses diminish in the build region. A compensatory balancing behaviour is observed in the substrate at the interface region. Between the fifth and seventh layers, the influence of the cold substrate diminishes, and the deposit temperature does not fluctuate to the same extend. The variation in maximum tensile stress exhibits is lesser between the fifth and seventh layers, with no discernible changes from the seventh layer onward.

Upon completion of the deposition process, the entire part cools down to room temperature and residual stresses achieve a new equilibrium throughout the entire component. The final stress behaviour becomes apparent upon reaching ambient temperature. The maximum compressive stresses located in the substrate under the interface region reduces from -350 MPa to -334 MPa, with a more pronounced decrease at the interface of the build. Specifically, the maximum tensile stress located at the corner and right-side of the build diminishes from 374 MPa to 254 MPa. The gradual cooling to room temperature facilitates the redistribution of stress.

The compressive stresses at the interface exhibit a parabolic shape, slightly off-centre in the substrate. This configuration serves to offset the parabolic tensile stress profile accumulated in the build due to material constraints. Material expansion toward the build

edges is unrestricted, resulting in lower residual stress values. Conversely, towards the build centre and substrate centre, surrounding material constrains expansion and contraction, leading to increased stress and a parabolic stress distribution in these regions [377]. This stress behaviour aligns with observations made by Moat *et al.* in DLF Waspaloy blocks atop a substrate, where the implemented contour method yielded comparable results [135].

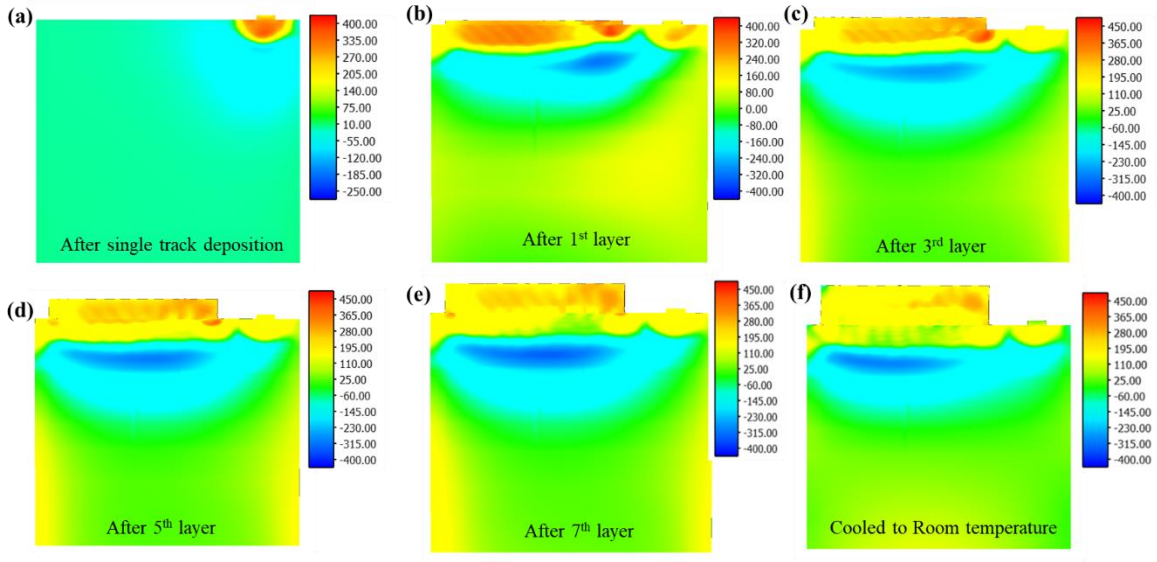

Figure 8.19 Stress in σ_{yy} direction during the deposition of (a) single track (b) 1st layer (c) 3rd layer (d) 5th layer (e) 7th layer and (f) cooled to room temperature.

8.12 Thermo-mechanical Model Summary

The Simufact FEA model significantly enhanced the project by providing more detailed information for complex geometries with multiple tracks and layers at key areas of interest like the interface between substrate and deposited material. A summary of the key findings with respect to the FEA model were:

1. The thermomechanical model's stress distribution behaviour was simulated and verified using the contour method, showing good agreement between experimental and simulated stress behaviours. Discrepancies in maximum values between simulation and experimental measurements may result from various factors outlined.
2. Although creep had minimal effect, incorporating a creep subroutine was crucial for understanding transient behaviour in terms of stresses, strains, and temperature relationships. Recalculating flow stresses with consideration of annealing and creep, as suggested by published literature, is essential since traditional rate-independent strain hardening models may not accurately represent actual behaviour during deposition.

3. Despite efforts to enhance FEA modelling for accurate thermomechanical predictions, limitations persist. Particularly concerning the interface region, simulated effects of powder flow into the melt pool can significantly impact melt-pool shape, deposition shape, and gradients. Cooling effects from gas flow were neglected. Furthermore, as demonstrated in the earlier chapters, there are some inconsistencies in the LMD equipment demonstrated by the melt-pool formations. Such inconsistencies give rise to ambiguity between experimental and simulated stress fields. To enhance thermal model accuracy, especially near the interface, implementing measurement-based forced convection, describing argon jets during laser processes, could improve energy balance in finite models.
4. Recent advancements in LMD computational models necessitate multi-physics packages (e.g., CFD), experimentally validated thermomechanical material properties (like creep curves generated in this study), and *in situ* calibration experiments, such as melt pool thermal measurements.

8.13 Chapter Summary

Employing an experimentally validated FEA model alongside residual stress measurements will assist with capture and understanding of the evolution of residual stress:

1. Additive manufacturing induces intricate residual stress phenomena, primarily stemming from thermal gradients, rapid cooling rates, moving heat sources, and deposit consolidation, with the Thermal Gradient Mechanism providing the most comprehensive explanation.
2. Anisotropic large grain structures in the deposited region posed measurement challenges, despite adhering to best practices, leading to ambiguity in obtained values.
3. Utilizing the Contour Method and XRD facilitated the examination of residual stress distribution and behaviour in the as-deposited normal direction, complemented by post-contour measurements in the build and transverse directions. However, it is important to acknowledge that the XRD method measures the stress profile after sectioning, leading to potential magnitude abnormalities and discrepancies.
4. To assess the as-deposited internal residual stresses prior to the contour cut, the superposition theory was implemented. This method involves segmenting the material using the contour method, followed by the assessment of remaining

stresses through XRD and combining the measurements. Such an approach facilitates stress measurements in regions where internal stresses were previously challenging to ascertain.

5. The S11, S22 and S33 residual stress profiles measured experimentally agreed with the simulated results. From the substrate to the deposited region, encompassing the interface region, the profiles were consistent between the two methods. This alignment manifests as a gradual transition to compressive stresses ranging from -15 mm to -4 mm, where a peak compressive stress is consistently measured in both directions and accurately simulated at approximately -4 mm. However, due to limitations in the FEA modelling method, the magnitudes differed.
6. Increasing the laser power led to increased RS tensile measurements across the interface region as a resultant of melt-pool dynamic fluctuation, volume of liquified material, localised temperature gradients and cooling rates.
7. In all three laser conditions, a maximum tensile stress was measured directly below the melt pool penetration depth (approx. -1.9 mm>- 2 mm) which can be attributed to the localised extreme thermal gradient and cooling rates.
8. A low stress field was captured in the as-build specimens from the bottom of the substrate to around -6 mm. From here, in all three power conditions, a gradual increase in tensile stress magnitude was measured.
9. The tensile residual stress (RS) generation in the build direction exhibited variation across locations. Specifically, it was noted that the edges of the build (Track 1-2) demonstrated a slightly higher magnitude of tensile RS compared to the mid-build region. This phenomenon can be attributed to the constraining nature of the surrounding material and the resultant higher cooling rates at the free edges.
10. An implemented heat treatment to enhance the mechanical properties of the as-deposited successfully diminished the high tensile RS values to a very low (<100 MPa) in all three specimens. This would be crucial to employ prior to service to mitigate any issues with post-manufacturing-machining.
11. The stresses are mainly concentrated at the build substrate interface, due to the very high cooling rates associated with this region, which may lead to localised cracking and catastrophic failure of the repairment.
12. Contour method revealed the RS distribution behaviour in all three specimens where, upon equilibrium, a large compressive band existed in the top-third of the

substrate compensating for the tensile region band across the deposited region. A relatively low σ_{yy} stress component was measured at the interface region which agreed with the simulated profile.

13. The thermal-mechanical coupled FEA was experimentally calibrated with the contour results. The RS distribution across the substrate and deposited region agreed well with the contour results, however discretion in the magnitudes was observed and this was likely due to several influencing factors such as melt-pool dynamics, modelling approach and the mechanical properties of the additively manufactured material.
14. Overall, the residual stress profile has been effectively captured through the utilization of the superposition theory to compute the initial stresses prior to contour cutting. This approach demonstrates strong agreement with the thermomechanical model across all three stress components S11, S22, and S33.
15. The model allowed an in-depth investigation of the *in situ* RS generation and its direct correlation to the local temperature history.
16. A creep sub-routine was implemented into the thermo-mechanical model and appeared to have negligible effect on the stress fields.

Reviewing stress and strain data extracted from the experimentally calibrated model revealed the way multi-directional stresses, elastic and plastic strains were generated and effect of the inclusion of associated creep on the results with respect to time under temperature.

Chapter 9: Summative Discussion, Conclusions, Recommendations and Future Work

9.1 Summative Discussion

In this study, the influence of process variables in Laser Metal Deposition (LMD) of IN718 is critically examined to understand their impact on microstructural characteristics, residual stress distribution, and mechanical properties, particularly in the interface region between the deposited material and the substrate. Both as-deposited and post-weld heat-treated (PWHT) conditions were analysed to assess their suitability for repair applications and feature additions in high-performance components such as hot compression disks.

The process variables, especially laser power, play a pivotal role in defining the microstructure of IN718 during LMD. In the as-deposited state, the microstructure is dominated by large columnar γ-grains that grow in the build direction (BD). The laser power significantly influences the grain size and texture, with higher laser power promoting larger γ-grains and a preferential <001>//BD crystallographic texture. The development of a strong texture and large grains is associated with the thermal gradient during solidification, as higher energy input leads to a slower cooling rate and greater grain growth. Dendritic sub-structures were observed extending across multiple layers, with dendrite cores enriched in nickel, iron, and chromium, while inter-dendritic regions were enriched in niobium and molybdenum. This elemental segregation results from the non-equilibrium solidification associated with the rapid cooling rates typical of LMD. Higher laser power increases the likelihood of this segregation, leading to the formation of Laves phase, a brittle intermetallic compound enriched in niobium. The volume and distribution of Laves phase were found to correlate with the energy input, indicating that controlling the laser power is essential to manage the extent of undesirable phase formation. In the post-weld heat-treated (PWHT) condition, the microstructure undergoes significant transformations, with the precipitation of strengthening γ'' phases. PWHT partially dissolves the Laves phase and promotes the formation of γ'' precipitates, which enhance the mechanical strength of the material. The homogenization of the microstructure post-treatment also contributes to improved ductility and fatigue resistance, which are critical for the longevity of repaired components in service. Thus, a balance between as-deposited and post-weld conditions is crucial to optimize the microstructure for performance.

Residual stresses in LMD are primarily induced by the thermal gradients and rapid heating/cooling cycles during the deposition process. In the as-deposited condition, the Thermal Gradient Mechanism explains the formation of tensile and compressive stresses across different regions of the deposit and substrate. The maximum tensile stress is observed at the peripheries of the deposited region, where extreme thermal gradients exist. Additionally, high tensile stresses near the yield strength were observed very close to the interface in the BD direction. These high tensile stresses are detrimental as they can lead to cracking or warping of the deposited material. The laser power and scanning speed directly affect the magnitude and distribution of residual stresses. Higher laser power leads to greater heat input, which intensifies thermal gradients and the associated stress fields. Conversely, lower power may reduce residual stresses but at the expense of poor bonding or insufficient melting. Thus, controlling the laser power and other process parameters is essential to balance residual stress formation with the quality of the deposited material. In the post-weld heat-treated condition, residual stresses are significantly alleviated. Heat treatment promotes stress relaxation by allowing the material to undergo plastic deformation at elevated temperatures, redistributing the residual stresses that were locked in during the rapid cooling phases of the LMD process. This stress relief enhances the structural integrity of the repaired component, reducing the likelihood of service failure due to fatigue cracking or premature wear. The efficacy of stress relief is strongly dependent on the PWHT parameters, such as temperature and duration, which must be carefully selected to optimize the mechanical properties without degrading the microstructure.

The interface region between the deposited material and the substrate is of particular interest in repair applications, as it is the most critical area in terms of mechanical integrity and bond strength. Process variables such as laser power affect the bonding quality at the interface. Higher laser power enhances material penetration into the substrate, improving the metallurgical bond but also increasing the likelihood of excessive dilution, which can degrade the mechanical properties of the deposited material. Microhardness measurements revealed a distinct variation in hardness across the interface region. In the as-deposited condition, the interface exhibited a lower hardness due to the sufficient melting of strengthening phases and the deposited region displayed the lowest hardness due to insufficient precipitation of these strengthening phases. After PWHT, the hardness across the interface becomes more uniform, owing to the dissolution of Laves phase and the precipitation of γ'' phases, which improve the toughness and fatigue strength of the repaired part.

For repair applications, controlling the process variables is essential to ensure that the repaired component exhibits mechanical properties that are comparable or superior to the original material. Optimizing the laser power is crucial to achieve a balance between sufficient material melting for strong bonding and minimizing residual stress and undesirable phase formation. Fine-tuning the scanning speed and hatch spacing further ensures uniform heat input, reducing the risk of thermal cracking or distortion, which could all be simulated through the FEA experimentally validated model. Although the inclusion of creep appears to have minimal affect on the magnitude of residual stresses, numerical models should consider creep to better understand the stress distribution during the LMD process. The results indicate that post-weld heat treatment plays a vital role in enhancing the mechanical performance of LMD-repaired parts. By promoting precipitation hardening and reducing residual stresses, PWHT ensures that the repaired component can withstand high service loads, making it suitable for high-performance applications such as aerospace or power generation.

9.2 Conclusions

Nickel-based superalloys have firmly established their future use as the material of choice for gas turbine engines, particularly in the compression region, due to their outstanding high-temperature mechanical properties and resistance to fatigue, creep, and oxidation. However, damaged blisk aerofoils often necessitate complete replacement, leading to lengthy lead times and significant costs.

At the core of this research was the interest of Laser Metal Deposition (LMD) being a viable manufacturing technology to repair damaged blisk components. However, limited research has been done on the properties of LMD manufactured IN718 with respect to the interface region between the as-deposited and substrate material. The complexities with steep thermal gradients, super solvus temperatures and associated rapid cooling rates modify the microstructure and mechanical behaviour. A thorough understanding of the thermo-mechanical processing pathway is essential for achieving a tailored microstructure optimized for the intended application.

This exploratory research has been focussed on how process variables in Laser Metal Deposition (LMD) of IN718 influence microstructural characteristics, residual stress distribution, and mechanical properties across the interface region in both as-deposited and post-weld heat-treated conditions for repair applications and feature additions. By

varying the laser power of the LMD process from low, medium to high (550W, 750W and 950W, respectively) conclusive correlations were drawn on the microstructural response to temperature history experienced in each localised region across the interface. The interface region was categorized as fusion zone (FZ) where the temperature exceeds the liquid temperature of the alloy (~1336°C), partially melted zone (PMZ) where the experienced temperature is above the solidus temperature (~1260°C) but below the liquidus temperature, and heat affected zone (HAZ) where the temperature is below the solidus temperature. Single track, thin-walled (5-layer and 10-layer single walls) and solid blocks (10-track, 10-layered builds) were deposited to assess the different temperature fields experienced. Furthermore, this work focusses on the mechanical properties and residual stress behaviour present in the as-deposited and heat-treated components. Alongside experimental work, thermomechanical modelling techniques were developed and employed to complement the experimental findings and enhance the knowledge of residual stress generation during the LMD process.

The significant findings on each chapter are provided hereafter:

Chapter 4: Analytical Modelling of LMD of IN718

A process window was established to achieve excellent metallurgical bonding along the interface and laser power were selected to vary. The analytical thermal model helped to note key differences in melt pool dimensions for the low, intermediate and upper limit of the process window based on laser power and were experimentally compared against single tracks. This chapter established:

1. An extensive review of LMD IN718 literature led to the establishment of a process parameter window optimized to achieve superior as-deposited mechanical properties with the aim of meeting the technical requirements for aerofoil repair applications. For repair applications requiring adequate mechanical performance and strong bonding, energy densities ranging from 25 to 60 J/mm² were identified. Laser powers were selected across this spectrum, specifically at 550 W, 750 W, and 950 W, to represent the lower, intermediate, and upper limits of the process window, respectively.
2. An analytical mathematical model was successfully developed based on the Rosenthal theoretical model to provide a baseline on evolution of the melt pool dimensions evolve with the varied laser powers and provided a prediction for the transient temperature field. Based on the analytical model, the 950 W laser power

created the largest melt pool area (approx. 1 mm^2) with both the greatest width (~2 mm) and depth (~0.7 mm) comparative to the medium and low laser power. The transient temperature behaviour for the substrate/deposit interface was shown to increase with increasing the laser power due to the volume of material above the liquidus temperature.

3. Microstructures in melt-pool cross sections for single-track depositions were compared to simulated dimensions. Good agreement was found at 950 W and 750 W, but significant error occurred at 550 W. Experimental factors not included in the model, like gas parameters and Marangoni forces, impacted accuracy, prompting the need for an experimentally validated model
4. Single-track depositions at all three laser powers met weld quality standards, showing no defects like micro-cracks or porosity. Despite excessive dilution at 550 W and 750 W, a strong metallurgical bond was achieved. Further investigation of microstructure, texture, and residual stresses is discussed in Chapters 6 and 7.

Interface assessment revealed spherical pores at deposition start points, melt pool edges, and the top, caused by poor parameters and gas usage. Despite these defects, no other issues like thermal cracking were found. High laser power (950 W) deposition showed strong bonding, and a 10% overlap reduced waste and energy consumption

Chapter 5: Development of the transient FEA thermal model

A transient finite element analysis (FEA) thermal model was developed in Chapter 5 to simulate the LMD of IN718 process to understand the temperature history at the key locations of FZ, PMZ, HAZ and substrate zone (SZ). To establish the transient temperature evolution:

1. An experimentally validated thermal model was calibrated using data from 12 thermocouples, capturing temperature history during deposition. The double ellipsoidal heat source was validated by comparing simulated and experimental data for each laser power, enhancing accuracy. Temperature-dependent material properties, heat transfer coefficients, and radiation emissivity adjustments improved model precision for IN718
2. A mesh sensitivity analysis was performed to balance accuracy and computational time. Comparing four meshes, Mesh 4 had 15 times more elements but only marginal accuracy improvements (+0.31%), while taking 30 times longer. Mesh

2 provided the best balance, offering reasonable accuracy with efficient computational time based on thermocouple data.

3. Process efficiency, calibrated using thermocouple data, revealed significant energy losses in LMD. Simulations showed 29.5% efficiency for peak temperature, with energy loss from substrate reflection and dispersed powder. Efficiency increased to 36.5% by layer 10, likely due to the workpiece's rising temperature improving powder melt efficiency.
4. Experimentally validated moving heat sources enabled comparison of melt pool temperatures based on process parameters. The 550W laser showed the greatest penetration depth, matching simulations. Simulated temperature data from the interface region provided insights into key microstructural responses, such as IN718 phase dissolution, prompting further investigation of microstructure evolution across the interface.

Chapter 6: Evolution of microstructure and texture across the interface region of an IN718 LMD joint layer

The microstructure and texture evolution across the interface region of a substrate and deposited component was studied in this chapter. The key outcomes were:

1. Metallographic analysis based on chemical etchant response resulted in the identification of a few areas on the macrographs. The interface region included the Fusion Zone (FZ), Partial Melted Zone (PMZ), Heat Affected Zone (HAZ), and Substrate Zone (SZ), each exhibiting distinct microstructural differences. A bright white crescent band delineated the PMZ/HAZ was observed, which fluctuated with change in process parameters. Each zone was investigated further by EBSD and SEM characterization.
2. The microstructure of the LMD IN718 is characterized by large columnar γ grains extending through the BD. The crystallographic texture of the LMD deposited region varied between cube texture and a <001>//BD fibre depending on the process condition. The FCC grains with their {001} plane closely orientated to the direction of maximum thermal gradient will solidify faster and grow to supersede less preferentially orientated grains.
3. The heterogeneously nucleated grains revealed a <001>//BD fibre texture tilted in the laser travel and track succession direction corresponding with the direction of maximum thermal gradient associated with each track.

4. Sub-structure columnar dendrites were observed in the deposited material along the interface which have extended through the BD. Chemical analysis revealed a strong micro-segregation of solutes between the dendrites. The inter-dendritic region was found to be enriched with Niobium, were therefore unavoidably preferable locations for detrimental Laves phase precipitation.
5. Based on the FEA model, the temperature history data extracted from the interface in the 950W specimen, the multiple layer build would impose an aging affect to the as-deposited material at the interface region which would precipitate strengthening phases. However, such presence was inconclusive and would require nano-SEM or TEM analysis.
6. The post-weld heat treatment (PWHT) for repair successfully precipitated γ'' phases in both parent and deposited structures, improving phase distribution and mechanical properties at the interface. This treatment dissolves γ' and γ'' phases while precipitating δ-phase to control grain growth and enhance creep resistance. The Laves phase also dissolved, improving ductility by reducing crack initiation sites.
7. The LMD single track exhibits epitaxial γ grain growth originating from the base of the melt pool, accompanied by a zone of finely equiaxed heterogeneously nucleated grains at the upper and lateral extents of the melt pool. The epitaxial grain development is ascribed to localized conditions characterized by a high thermal gradient and low solidification rate, fostering pronounced directional solidification. The formation of heterogeneously nucleated grains in this region aligns with the interdependence model, wherein partially melted powder particles serve as nucleants for equiaxed grain growth within a supercooled liquid area preceding the solid-liquid interface. Subsequent deposition of multiple tracks and layers, with adequate penetration depth, induces re-melting of this isolated region, leading to the formation of large epitaxially grown γ grains.

Chapter 7: Process Parameter Influence on the Interface region Microstructure

This chapter delved into the key differences in microstructure correlating to the variation in laser power. The salient findings were:

1. Laser power has a strong influence on melt pool geometry. Increase in the laser power results in larger HAZ, PDZ and FZ. Furthermore, the bright crescent band at the bottom of the melt pool increased in thickness with increased laser power.

2. Laser power strongly influenced the γ grain morphology in the FZ with a combination of columnar to equiaxed transition. With increasing the laser power, the sub-structure dendrite formation had lower cooling rates which allowed the formation of secondary and tertiary arm, which was absent in the lower laser powers.
3. Very small equiaxed grains along the fusion line with random orientation and situated at grain boundaries and within larger grains were described as stray grains. The volume of stray grains increased with increasing laser power due to the degree of constitutional supercooled region combined with dendrite fragmentation volume. More stray grains inherently lead to a greater amount of grain boundaries which are locations where failure is more likely to initiate under stress, particularly at high temperatures or in corrosive environments, critical for the compression blisk near the combustion chamber of an aircraft engine.
4. The substrate grain structure and orientation had pivotal effect on the volume and localised density formation of these stray grains forming in the FZ. Increased laser power with a solidification rate similar to the low to medium laser powers lead to a decreased thermal gradient/solidification velocity favouring stray grain formation.
5. Further influence of the built height on the grains in the fusion zone was observed with a noticeable difference in maximum grain measured. Overall, the average grain size in the FZ did not change significantly but the maximum size of the grains found increased substantially from the single to the ten-layered (approx. 161% increase). Grain size, aspect ratio and texture were found mostly unaffected with increasing the layer height from five to ten layers due to the solidification microstructure being pinned by the δ-phase. The temporal history remained below the δ-solvus temperature from layer five to layer ten at the fusion zone.
6. Laser power influence the crystallographic texture of the γ grain formation in the fusion zone based on three fundamental reasons. First, the substrate orientation has the strongest influence on the first layer comparative to the subsequent layers, however in the low laser power, the density of epitaxial grain growth comparative to the high laser power will be higher due to competition boundary conditions. Secondly, the thermal gradient for low laser power is favourable to produce epitaxial fibre grains. Thirdly, higher laser power promoted a higher density of randomly orientation equiaxed grains due to greater constitutional supercooling zone.

7. Increase in the laser power decreased the average γ grain size and resulted in a shift from a cube crystallographic texture to a <001>//BD fibre texture. This exact mechanism for these phenomena remains unclear but the three previously mentioned fundamental reasons were likely to influence such solidification microstructures.
8. The dendritic growth angle along the Y-Z plane was found to increase with increased laser power due to the resultant heat flux.
9. The microhardness of the as-deposited γ phase microstructure is ≅ 250 HV. Increase in the microhardness in the first layer was observed which could be correlated to nano-scale γ'' precipitates formed during aging effect from subsequent layers. The PWHT employed successfully precipitated γ''/γ' in the deposited region as correlated with the microhardness, as the deposited region of the PWHT specimens was characterised by an increase in the microhardness by over 200 HV to near ≅ 450 HV. Interesting to mention, the PWHT substrate microhardness increased by 10% when compared to the as-received due to the increased volume of δ-phase acting as a barrier for dislocation movement.
10. The extensive investigation of microstructural features across the PDZ revealed a sufficient time under temperature to dissolve δ/γ'' based on the Nb diffusion distance. An increased laser power led to a longer range of diffusion which agrees with the SEM investigation and microhardness results.

Chapter 8: Residual Stress Behaviour of Laser Repaired (LRed) Components

Using a combination of the contour method and XRD measurements, the residual stress behaviour was analysed in the bulk of the specimens and across the interface region in as-deposited and the PWHT specimens. The XRD measured stress in both transverse (S11) and build (S22) direction. The accompanied FEA model highlighted the importance of understanding the generation and evolution of residual stress during the LMD process.

1. Utilizing the contour method in combination with XRD allowed the examination of residual stress behaviour in an LMD component in all three directions; normal stress direction (laser travel direction) and post-contour cut, transverse direction (adjacent track deposition direction) and build direction. The maximum stresses were found at the build substrate interface whereby increasing the laser power led to increased tensile RS magnitude because of melt-pool dynamics, volume of liquified material, localised thermal gradient, and cooling rates.

2. In all three laser specimens, the maximum tensile RS (in σzz) was measured directly below the melt pool depth (around -2 mm in the substrate). The 950W specimen displayed the highest magnitude of tensile stress (i.e. ~787.2 MPa) which decreased proportionally with decreasing laser power (i.e. ~572.9 MPa and ~416.6 MPa in 750W and 550W, respectively.), indicating that higher heat input and slightly larger build height contributed to the observed higher residual stresses. These values are of high importance as they identify a specific area analysed to have residual tensile stress around 40-69% of the yield strength in forged and aged IN718. This region so close to the interface could lead to catastrophic failure during service as a crack initiation and propagation site could lead to further complications during the post-depositing machining which requires alignment with dimensional and surface finish accuracy of the aerofoil.
3. In all laser-deposited specimens, the maximum compressive RS profile in the (in σ_{yy}) direction, measured by contour method was observed approximately 5 mm below the substrate/deposit interface, though absolute magnitudes were different. The highest laser power resulted in a maximum compressive peak stress of ~-473MPa, located 5 mm below the interface. The 750W sample exhibited a compressive peak stress of ~-612 MPa at the same location, reduced to ~-220 MPa for the 550W sample. Lower laser power had lowered the overall residual stresses but did not result in their elimination.
4. The residual stresses in the as-deposited condition for the normal direction (in σ_{yy}) generally consisted of a compressive centre in the substrate compensating for tensile stresses of ≈300 MPa adjacent to the free surfaces in the build region. It was important to understand the area and magnitude of these tensile stresses located at the free edges, i.e. the material first in contact with post processing machining.
5. The PWHT aiming to enhance the mechanical properties successfully diminished the high tensile RS found in the build direction to below 100 MPa in all three specimens. This is a crucial stage to employ prior to service to enhance mechanical properties, homogenize the mechanical properties across the entire component and reduce the RS encountered.
6. A thermo-mechanical coupled FEA was experimentally calibrated with the contour results, with the simulated RS behaviour in an equilibrium state agreeing well with the measurements. The RS behaviour and profile across the entire cross-section was well simulated, however discrepancies in magnitude can be improved

by implementing melt-pool dynamic modelling and using the mechanical properties from an additively manufactured IN718 material. The model allowed for an in-depth investigation of *in situ* residual stress generation which directly correlate to the temperature profile (i.e., maximum temperature and cooling rates experienced) which incurred thermal-induced stresses. Furthermore, the FEA model demonstrated evolution of the stress from the first layer to the final layer and generation of the local residual stresses through the temperature gradient mechanism (TGM).

7. A creep sub-routine was implemented to understand the stress relaxation effect from subsequent layer deposition. It was concluded that creep had successfully mitigated tensile stress concentrate regions but the overall effect of stress relaxation on residual stress magnitude was minor, with the values of simulated tensile stress being similar, measuring ~280 MPa and ~277 MPa in the FEA model with creep and without creep implemented, respectively. It was summarised that stress relaxation arising from creep-like mechanism is a transient, temperature-time dependent process occurring over prolonged time. However, in the LMD process, localized stress fields experience seconds to minutes of creep-like phenomena, which may be insufficient for effective stress relaxation. Although, definitive behavioural change in effective plastic strain increase by more than an order of 3 was observed at the interface region when including the creep sub-route.
8. Post processing a range of stress and strain data calculated from experimentally calibrated model revealed the multi-directional stress profiles, elastic and plastic strain fields and an associated creep strain are influenced by time under temperature. The stress vs time vs temperature graphs for each location (substrate zone, substrate/deposit interface and the mid-build of the deposited region) depicted the transient stress behaviour. The graph extracted for the interface region, directly at the substrate/deposit interface revealed the evolution of transient stresses, reaching high values of 300 MPa in tension and -350 MPa as per the deposition schedule. However, as the part cools to room temperature, the stresses stabilize, resulting in moderate to low equilibrium stress values, approximately 200 MPa. In the final stages of the deposition, a small stress reduction occurs, driven by stress relaxation induced through the increasing creep strain. This relaxation continues as the part cools to room temperature.

9. By combining contour method and XRD measurements with stress relaxation calculations, the original internal stresses were determined. Simulation stress data was compared to experimental results, showing excellent agreement. Both methods revealed a transition to compressive stress around -280 MPa, though slight deviations occurred near the interface in the transverse direction for tensile stress predictions
10. Improvements of the numerical FEA thermo-mechanical model will prove vital to future additive manufacturing techniques to understand localised temporal history and stress profiles, as well as bulk residual stresses experienced during and post manufacturing. Such implementation would be pivotal in experimental set-up with respect to process parameters inclusive of laser power, hatch pattern, overlap fraction and geometries in a cost-effective manner prior to experimentation.

In a competitive industrial world and as we move towards a net-zero world of manufacturing, the need for reduced waste, energy consumption and carbon footprints has never been so prevalent. This work offers valuable experimental and simulated information that will be applied to companies such as Rolls-Royce, who are already looking to utilize LMD of IN718 to repair aerofoils on blisk components. By incorporating a FEA analysis, manufacturers can anticipate and mitigate potential issues related to residual stress, leading to improved component quality and reliability. Moreover, understanding the microstructure and microstructural features present along the interface coupled with the predicted stress behaviour facilitates the development of tailored heat treatments and optimised process parameters to enhance material properties for specific applications while reducing manufacturing costs.

9.3 Recommendations

Based on the key findings and developed knowledge through this thesis on LMD IN718, LMD was found to have a potential to be considered as a suitable manufacturing method to repair aircraft components, which could assist with reduction of waste and significant lead times associated with manufacturing in general and machining, in particular. IN718 is especially suitable material to LMD due to its high weldability. However, there are a range of associated challenges with the manufacturing method and the material selection including non-uniform microstructure, unavoidable phases, and residual stresses. The following procedures are recommended for scalability:

Single tracks based on a single set of process parameters must be used to investigate and analyse the melt-pool behaviour, so the machine configurations such as stand-off distance, overlap spacing and stabilization of the laser source can be optimised prior to depositing multi-track, multi-layered builds. The higher laser power selection would be optimal to decrease melt defects, such as porosity, but inherent a higher residual stress towards the build interface. By defocusing the laser beam, *in situ* tailored localised heat treatment could be applied after each track/layer to reduce the thermal gradient, therefore benefiting both microstructural homogeneity and residual stress evolution. A high-speed thermal camera with a feedback control system could experimentally optimise the process parameters and tailored heat-treatment on an *in situ* basis.

IN718 builds give rise to a non-uniform microstructure including unavoidable Laves phase formation due to element micro-segregation. The process parameters, specifically laser power, has shown to influence the grain size, texture development and amount of Laves phase. The interface region becomes increasingly susceptible to localised microstructural inhomogeneity due to the exceeding the liquids temperature, extreme thermal gradient, and high cooling rates. A high laser power in combination with a slower travel speed will reduce the thermal gradient and cooling rates resulting in a more epitaxial growth, suitable for creep applications.

Due to the fine dendritic microstructure with laves phase and dissolution of strengthening phases based in the substrate, it is recommended that a post deposition heat treatment is required to re-precipitate the γ’’/γ’ phases in the interface region without coarsening the base material strengthening phases and reducing the once-achieved mechanical properties. Not only will the post deposition heat treatment enhance the mechanical properties across the interface region, but it will also sufficiently stress relief the residual tensile stresses (approx. 50-70%YS) existing in the as-deposited condition. This is of particular importance to homogenize the mechanical properties across the entire component.

An experimentally validated thermal model is recommended to understand the material response across the interface region and throughout the build. Although it is worthwhile noting that a thermal model needs to be generated for each process parameter change, and simply changing the laser power in the heat source will not suffice as localised melt-pool dynamics completely change thus affecting the temperature history and resultant stress field. Based on the simulation and experimental results, high tensile stress is mainly concentrated at the substrate build interface due to the very high cooling rates associated

in this region and the TGM method. The location of these tensile stresses needs to be mitigated before employing mechanical testing as these will result in catastrophic failure. To avoid this problem, a pre-heated substrate is recommended which can be achieved through an induction heating.

A numerical FEA model associated with the selected additive manufacturing technique will be crucial in future developments of the AM-based components and repairs. Improving the accuracy of these models will require extensive research into fully coupled models including thermo-metallurgical-mechanical models to understand the evolution of microstructure, texture, residual stress behaviour and correlate the resultant mechanical properties. A strong recommendation is to experimentally-validate the model using *in situ* measurements of thermal fields and post-deposition of microstructure examination and RS behaviour with distortion. A thermal, thermo-mechanical, thermo-metallurgical-mechanical models provide invaluable data to correlate phenomenon's by providing *in situ* information which is experimentally difficult and/or impossible to capture. These models will allow researchers, technicians, and engineers to make fundamental process parameter down selections within a short period in a highly cost-effective manner. As the implementation of AM-based manufacturing becomes increasingly popular as a near net-shape manufacturing technique, the advancements in modelling must remain of parallel importance.

9.4 Future Work

Based on the research conducted in this thesis of LMD of IN718, there are several areas that warrant future research, both to understand the material response to LMD but also to advance the prospect of utilizing LMD for a component's repair or features addition in aerospace components applications with IN718. Based on the challenges highlighted with the experimental trials, future work would include the measurement of single-track dimension by simple calliper measurement to ensure a rapid check of process parameters prior to the deposition of the full solid builds. These should have been the preliminary experiments prior to depositing larger builds for further investigations, but due to limited access to the lab and equipment for reasons out with our control, i.e. machine downtime and Covid-19, there was a real need to move through the manufacturing trials. These process parameters were selected alongside and verified by manufacturing engineers and technicians, although the melt pool shape and the overlap were still not sufficiently controlled in larger builds. Regardless, all microstructural work was focussed on the centre of each track and the effect of depositing multiple tracks and layers.

As a result of this work, further experimental optimisation is recommended. Such areas of further investigation include:

1. The thesis predominantly focused on the microstructure, texture, and residual stress response to LMD of IN718. Detailed tensile testing with incorporating Digital Image Correlation with focus on the interface region needs to be executed for various process parameters and microstructure for hybrid manufacturing to be a viable solution.
2. The material response to fluctuating process parameters needs to be fully addressed from a single track to ensure full consolidation of feature addition between adjacent tracks. Even with optimal process parameters selected, the builds were found to contain entrapped pores. A critical assessment of the influence of these pores on the mechanical properties should be undertaken including the influence of HIPing.
3. TEM is recommended in the future to confirm the nature and distribution of precipitates presented in the build and interface region. A modified heat treatment cycle may be required for LMD builds to homogenize the microstructure and precipitation of strengthening phases.
4. The development of novel techniques to optimise the microstructure across the interface region should be investigated. This may include techniques in the LMD process such as a de-focussed laser beam heat treatment pass between each track/layer to increase the microstructural homogeneity and aid the residual stress response. Additionally, an induction heating of the substrate could be investigated to tailor specific heat-treatments to LMD interface/build without detriment to the parent material.
5. Critical to the hot area components of an aircraft engine is the cyclic fatigue life and materials response to creep, therefore future work should include relevant testing. However, these tests are costly to perform due to the volume of material required to extract such test coupons and by orientations and locations to be investigated sufficiently to characterise LMD deposited interface.
6. The thermo-mechanical transient model in this work has predicted the temperature profile very well and the mechanical response adequately, but some ambiguity around the magnitude of stress behaviour remained. Experimentally validated material properties such as tensile/yield strength based on the LMD produced would aid the accuracy.

7. A detailed coupled CFD model and microstructural model needs to be considered to predict the microstructural response, crystallographic texture, and the evolution of residual stress with various process parameters and build geometries.
8. The transient thermo-mechanical model could be optimised to reduce the extensive computational time incurred when simulating larger, more realistic LMD builds utilising approaches such as moving hybrid meshing.
9. To reduce the cost of the final component and make hybrid manufacturing a more cost-efficient process, a more detailed investigation into the powder is required. Moreover, the non-utilised (i.e., waste) powder may be recycled through meshing and could even be made from machining swarf, reflecting on the manufacturing sustainability.

References

[1] K. Yuan *et al.*, “Influence of process parameters and heat treatments on the microstructures and dynamic mechanical behaviors of Inconel 718 superalloy manufactured by laser metal deposition,” *Materials Science and Engineering: A*, vol. 721, pp. 215–225, Apr. 2018, doi: 10.1016/J.MSEA.2018.02.014.

[2] R. B. Bhavsar, A. Collins, and S. Silverman, “USE OF ALLOY 718 AND 725 IN OIL AND GAS INDUSTRY.”

[3] A. Ramakrishnan and G. P. Dinda, “Direct laser metal deposition of Inconel 738,” *Materials Science and Engineering: A*, vol. 740–741, pp. 1–13, Jan. 2019, doi: 10.1016/J.MSEA.2018.10.020.

[4] S. G. K. Manikandan, D. Sivakumar, K. P. Rao, and M. Kamaraj, “Effect of weld cooling rate on Laves phase formation in Inconel 718 fusion zone,” *J Mater Process Technol*, vol. 214, no. 2, pp. 358–364, Feb. 2014, doi: 10.1016/J.JMATPROTEC.2013.09.006.

[5] Renishaw, “In718-0405 powder for additive manufacturing,” vol. 2001, no. Iso 97, pp. 1–3, 2001.

[6] L.-E. Lindgren, A. Lundbäck, M. Fisk, R. Pederson, and J. Andersson, “Simulation of additive manufacturing using coupled constitutive and microstructure models,” *Addit Manuf*, vol. 12, pp. 144–158, Oct. 2016, doi: 10.1016/J.ADDMA.2016.05.005.

[7] R. J. Deffley, “Development of processing strategies for the additive layer manufacture of aerospace components in Inconel 718,” no. January, 2012.

[8] S. Rahimi, M. King, and C. Dumont, “Stress relaxation behaviour in IN718 nickel based superalloy during ageing heat treatments,” *Materials Science and Engineering A*, vol. 708, no. 0, pp. 563–573, 2017, doi: 10.1016/j.msea.2017.09.116.

[9] F. R. Caliari, N. M. Guimarães, A. A. Couto, D. A. P. Reis, K. C. G. Candioto, and C. de Moura Neto, “Study of the Secondary Phases in Inconel 718 Aged Superalloy Using Thermodynamics Modeling,” *Key Eng Mater*,

vol. 553, no. February 2017, pp. 23–28, 2013, doi: 10.4028/www.scientific.net/kem.553.23.

[10] R. C. Reed, *The Superalloys: Fundamentals and Applications*. New York: Cambridge University Press, 2006.

[11] D. Cai, W. Zhang, P. Nie, W. Liu, and M. Yao, "Dissolution kinetics of δ phase and its influence on the notch sensitivity of Inconel 718," *Mater Charact*, vol. 58, no. 3, pp. 220–225, Mar. 2007, doi: 10.1016/J.MATCHAR.2006.04.020.

[12] S. Azadian, "Aspects of Precipitation in the Alloy Inconel 718," *Thesis*, 2004.

[13] D. Deng, "Additively Manufactured Inconel 718 : Microstructures and Mechanical Properties," 2018. doi: 10.3384/lic.diva-144491.

[14] S. Azadian, L.-Y. Wei, and R. Warren, "Delta phase precipitation in Inconel 718," *Mater Charact*, vol. 53, no. 1, pp. 7–16, Sep. 2004, doi: 10.1016/J.MATCHAR.2004.07.004.

[15] P. M. Mignanelli *et al.*, "Gamma-gamma prime-gamma double prime dual-superlattice superalloys," *Scr Mater*, vol. 136, pp. 136–140, Jul. 2017, doi: 10.1016/J.SCRIPTAMAT.2017.04.029.

[16] L. S. B. Ling *et al.*, "Effects of the γ''-Ni3Nb phase on mechanical properties of Inconel 718 superalloys with different heat treatments," *Materials*, vol. 13, no. 1, Jan. 2020, doi: 10.3390/ma13010151.

[17] M. Sundararaman, S. Banerjee, and H. Mori, "The Stability of y" and y' Phases in Alloy 718 Under Electron Irradiation," in *Superalloys 718, 625, 706 and Various Derivatives (2001)*, TMS, 2001, pp. 379–387. doi: 10.7449/2001/Superalloys_2001_379_387.

[18] J. Safari, S. Nategh, and M. Mclean, "Materials Science and Technology Evolution of microstructure of nickel base superalloy at high temperatures Evolution of microstructure of nickel base superalloy at high temperatures," 2013, doi: 10.1179/174328406X91168.

[19] Y. Q. Chen, E. Francis, J. Robson, M. Preuss, and S. J. Haigh, "Compositional variations for small-scale gamma prime (γ′) precipitates

formed at different cooling rates in an advanced Ni-based superalloy," *Acta Mater*, vol. 85, pp. 199–206, Feb. 2015, doi: 10.1016/J.ACTAMAT.2014.11.009.

[20] B. Alabbad, L. Li, and S. Tin, "Controlling the grain boundary morphology and secondary γ′ precipitate size distribution in Ni-base superalloys," *J Alloys Compd*, vol. 775, pp. 931–941, Feb. 2019, doi: 10.1016/J.JALLCOM.2018.10.031.

[21] M. C. Chaturvedi and Y. F. Han, "Strengthening mechanisms in Inconel 718 superalloy," *Metal Science*, vol. 17, no. 3, pp. 145–149, Jan. 1983, doi: 10.1179/030634583790421032.

[22] R. B. Li, M. Yao, W. C. Liu, and X. C. He, "Isolation and determination for d, c 0 and c 00 phases in Inconel 718 alloy." [Online]. Available: www.actamat-journals.com

[23] A. Devaux *et al.*, "Gamma double prime precipitation kinetic in Alloy 718," *Materials Science and Engineering: A*, vol. 486, no. 1–2, pp. 117–122, Jul. 2008, doi: 10.1016/J.MSEA.2007.08.046.

[24] D. Deng, "Additively Manufactured Inconel 718 : Microstructures and Mechanical Properties," 2018. doi: 10.3384/lic.diva-144491.

[25] Y. Huang and T. G. Langdon, "The evolution of delta-phase in a superplastic Inconel 718 alloy," *J Mater Sci*, vol. 42, no. 2, pp. 421–427, 2007, doi: 10.1007/s10853-006-0483-z.

[26] W.-D. C. and R. Kennedy and W.D. Cao and R.L. Kennedy, "Role of Chemistry in 718 Type Alloys–Allvac® 718Plus™ Development," *Superalloys*, vol. 3, pp. 91–99, 2004, doi: DOI: 10.7449/2004/Superalloys_2004_91_99.

[27] M. Anderson, A. L. Thielin, F. Bridier, P. Bocher, and J. Savoie, "δ Phase precipitation in Inconel 718 and associated mechanical properties," *Materials Science and Engineering A*, vol. 679, pp. 48–55, Jan. 2017, doi: 10.1016/j.msea.2016.09.114.

[28] A. Devaux *et al.*, "Gamma double prime precipitation kinetic in Alloy 718," *Materials Science and Engineering: A*, vol. 486, no. 1–2, pp. 117–122, Jul. 2008, doi: 10.1016/J.MSEA.2007.08.046.

[29] J. Hou, F. Yang, Y. Wu, and L. Zhou, "Effect of alloying elements on the precipitation of δ phase in Ni-Nb-Cr-Mo alloys," *J Alloys Compd*, vol. 785, pp. 1038–1046, May 2019, doi: 10.1016/J.JALLCOM.2019.01.250.

[30] J. An, L. Wang, Y. Liu, W. Cai, and X. Song, "The role of δ phase for fatigue crack propagation behavior in a Ni base superalloy at room temperature," *Materials Science and Engineering: A*, vol. 684, pp. 312–317, Jan. 2017, doi: 10.1016/J.MSEA.2016.12.029.

[31] J. Xu, Z. Huang, and L. Jiang, "Effect of heat treatment on low cycle fatigue of IN718 superalloy at the elevated temperatures," *Materials Science and Engineering: A*, vol. 690, pp. 137–145, Apr. 2017, doi: 10.1016/J.MSEA.2017.02.104.

[32] H. Y. Zhang, S. H. Zhang, M. Cheng, and Z. X. Li, "Deformation characteristics of δ phase in the delta-processed Inconel 718 alloy," *Mater Charact*, vol. 61, no. 1, pp. 49–53, Jan. 2010, doi: 10.1016/J.MATCHAR.2009.10.003.

[33] F. J. Xu, Y. H. Lv, B. S. Xu, Y. X. Liu, F. Y. Shu, and P. He, "Effect of deposition strategy on the microstructure and mechanical properties of Inconel 625 superalloy fabricated by pulsed plasma arc deposition," *Mater Des*, vol. 45, pp. 446–455, Mar. 2013, doi: 10.1016/J.MATDES.2012.07.013.

[34] H. Qi, M. Azer, and A. Ritter, "Studies of standard heat treatment effects on microstructure and mechanical properties of laser net shape manufactured INCONEL 718," *Metall Mater Trans A Phys Metall Mater Sci*, vol. 40, no. 10, pp. 2410–2422, 2009, doi: 10.1007/s11661-009-9949-3.

[35] S. Gribbin, S. Ghorbanpour, N. C. Ferreri, J. Bicknell, I. Tsukrov, and M. Knezevic, "Role of grain structure, grain boundaries, crystallographic texture, precipitates, and porosity on fatigue behavior of Inconel 718 at room and elevated temperatures," *Mater Charact*, vol. 149, pp. 184–197, Mar. 2019, doi: 10.1016/J.MATCHAR.2019.01.028.

[36] K.-M. Chang, H.-J. Lai, and J.-Y. Hwang, "Existence of Laves Phase in Nb-Hardened Superalloys," pp. 683–694, 2012, doi: 10.7449/1994/superalloys_1994_683_694.

[37] S. Sui, J. Chen, E. Fan, H. Yang, X. Lin, and W. Huang, "The influence of Laves phases on the high-cycle fatigue behavior of laser additive manufactured Inconel 718," *Materials Science and Engineering: A*, vol. 695, pp. 6–13, May 2017, doi: 10.1016/J.MSEA.2017.03.098.

[38] S. Sui, J. Chen, X. Ming, S. Zhang, X. Lin, and W. Huang, "The failure mechanism of 50% laser additive manufactured Inconel 718 and the deformation behavior of Laves phases during a tensile process," *The International Journal of Advanced Manufacturing Technology*, vol. 91, no. 5–8, pp. 2733–2740, Jul. 2017, doi: 10.1007/s00170-016-9901-9.

[39] K. Sivaprasad and S. G. S. Raman, "Influence of magnetic arc oscillation and current pulsing on fatigue behavior of alloy 718 TIG weldments," *Materials Science and Engineering: A*, vol. 448, no. 1–2, pp. 120–127, Mar. 2007, doi: 10.1016/J.MSEA.2006.10.048.

[40] E. Chlebus, K. Gruber, B. Kuźnicka, J. Kurzac, and T. Kurzynowski, "Effect of heat treatment on the microstructure and mechanical properties of Inconel 718 processed by selective laser melting," *Materials Science and Engineering: A*, vol. 639, pp. 647–655, Jul. 2015, doi: 10.1016/J.MSEA.2015.05.035.

[41] D. Zhang, W. Niu, X. Cao, and Z. Liu, "Effect of standard heat treatment on the microstructure and mechanical properties of selective laser melting manufactured Inconel 718 superalloy," *Materials Science and Engineering: A*, vol. 644, pp. 32–40, Sep. 2015, doi: 10.1016/J.MSEA.2015.06.021.

[42] F. Liu, F. Lyu, F. Liu, X. Lin, and C. Huang, "Laves phase control of inconel 718 superalloy fabricated by laser direct energy deposition via delta aging and solution treatment," *Journal of Materials Research and Technology*, vol. 9, no. 5, pp. 9753–9765, 2020, doi: 10.1016/j.jmrt.2020.06.061.

[43] S. G. K. Manikandan, D. Sivakumar, K. Prasad Rao, and M. Kamaraj, "Laves phase in alloy 718 fusion zone — microscopic and calorimetric

studies," *Mater Charact*, vol. 100, pp. 192–206, Feb. 2015, doi: 10.1016/j.matchar.2014.11.035.

[44] S. G. K. Manikandan, D. Sivakumar, M. Kamaraj, and K. P. Rao, "Laves Phase Control in Inconel 718 Weldments," *Materials Science Forum*, vol. 710, no. December 2014, pp. 614–619, 2012, doi: 10.4028/www.scientific.net/msf.710.614.

[45] H. Xiao, S. Li, X. Han, J. Mazumder, and L. Song, "Laves phase control of Inconel 718 alloy using quasi-continuous-wave laser additive manufacturing," *Mater Des*, vol. 122, pp. 330–339, May 2017, doi: 10.1016/J.MATDES.2017.03.004.

[46] S. Li *et al.*, "Melt-pool motion, temperature variation and dendritic morphology of Inconel 718 during pulsed- and continuous-wave laser additive manufacturing: A comparative study," *Mater Des*, vol. 119, pp. 351–360, Apr. 2017, doi: 10.1016/J.MATDES.2017.01.065.

[47] J. Gordine, "Welding of Inconel 718," *Welding Research - Supplement to Welding Journal*, pp. 531–537, 1970.

[48] P. Schempp *et al.*, "Solidification of GTA aluminum weld metal: Part 1 - Grain morphology dependent upon alloy composition and grain refiner content," *Weld J*, vol. 93, no. 2, pp. 53s–59s, 2014.

[49] P. Liu, Z. Wang, Y. Xiao, M. F. Horstemeyer, X. Cui, and L. Chen, "Insight into the mechanisms of columnar to equiaxed grain transition during metallic additive manufacturing," *Addit Manuf*, vol. 26, pp. 22–29, Mar. 2019, doi: 10.1016/J.ADDMA.2018.12.019.

[50] A. Dass and A. Moridi, "State of the art in directed energy deposition: From additive manufacturing to materials design," *Coatings*, vol. 9, no. 7, pp. 1–26, 2019, doi: 10.3390/COATINGS9070418.

[51] J.-P. Bédécarrats, T. David, and J. Castaing-Lasvignottes, "Ice slurry production using supercooling phenomenon," *International Journal of Refrigeration*, vol. 33, no. 1, pp. 196–204, Jan. 2010, doi: 10.1016/J.IJREFRIG.2009.08.012.

[52] D. A. Porter and K. E. Easterling, *Phase Transformations in Metals and Alloys*. Boston, MA: Springer US, 1992. doi: 10.1007/978-1-4899-3051-4.

[53] M. A. Jaafar, D. R. Rousse, S. Gibout, and J.-P. Bédécarrats, "A review of dendritic growth during solidification: Mathematical modeling and numerical simulations," *Renewable and Sustainable Energy Reviews*, vol. 74, pp. 1064–1079, Jul. 2017, doi: 10.1016/J.RSER.2017.02.050.

[54] W. J. Boettinger and D. K. Banerjee, *Solidification*, vol. 1. 2014. doi: 10.1016/B978-0-444-53770-6.00007-1.

[55] W. Kurz, C. Bezençon, and M. Gäumann, "Columnar to equiaxed transition in solidification processing," *Sci Technol Adv Mater*, vol. 2, no. 1, pp. 185–191, 2001, doi: 10.1016/S1468-6996(01)00047-X.

[56] J. Lipton, M. E. Glicksman, and W. Kurz, "Dendritic growth into undercooled alloy metals," *Materials Science and Engineering*, vol. 65, no. 1, pp. 57–63, 1984, doi: 10.1016/0025-5416(84)90199-X.

[57] M. H. Avazkonandeh-Gharavol, M. Haddad-Sabzevar, and H. Fredriksson, "Effect of partition coefficient on microsegregation during solidification of aluminium alloys," *International Journal of Minerals, Metallurgy and Materials*, vol. 21, no. 10, pp. 980–989, 2014, doi: 10.1007/s12613-014-0999-1.

[58] Y. S. Lee and W. Zhang, "Modeling of heat transfer, fluid flow and solidification microstructure of nickel-base superalloy fabricated by laser powder bed fusion," *Addit Manuf*, vol. 12, pp. 178–188, 2016, doi: 10.1016/j.addma.2016.05.003.

[59] H. L. Wei, J. Mazumder, and T. DebRoy, "Evolution of solidification texture during additive manufacturing," *Sci Rep*, vol. 5, pp. 1–7, 2015, doi: 10.1038/srep16446.

[60] T. Keller *et al.*, "Application of finite element, phase-field, and CALPHAD-based methods to additive manufacturing of Ni-based superalloys," *Acta Mater*, vol. 139, pp. 244–253, 2017, doi: 10.1016/j.actamat.2017.05.003.

[61] W. Kurz and D. J. Fisher, *Fundamentals of Solidification Third Edition*. 1989. doi: AR1RAAAAMAAJ.

[62] R. P. Mooney, J. Lapin, A. Klimová, and S. McFadden, "Conditions for CET in a gamma TiAl alloy," in *IOP Conference Series: Materials Science and Engineering*, Institute of Physics Publishing, Jun. 2015. doi: 10.1088/1757-899X/84/1/012088.

[63] W. Kurz, C. Bezençon, and M. Gäumann, "Columnar to equiaxed transition in solidification processing," *Sci Technol Adv Mater*, vol. 2, no. 1, pp. 185–191, 2001, doi: 10.1016/S1468-6996(01)00047-X.

[64] M. Wu and A. Ludwig, "Using a three-phase deterministic model for the columnar-to-equiaxed transition," in *Metallurgical and Materials Transactions A: Physical Metallurgy and Materials Science*, Jul. 2007, pp. 1465–1475. doi: 10.1007/s11661-007-9175-9.

[65] C. Böhm, C. Hagenlocher, J. Wagner, T. Graf, and S. Weihe, "Analytical Description of the Criterion for the Columnar-To-Equiaxed Transition During Laser Beam Welding of Aluminum Alloys," *Metall Mater Trans A Phys Metall Mater Sci*, vol. 52, no. 7, pp. 2720–2731, Jul. 2021, doi: 10.1007/s11661-021-06238-0.

[66] B. Liu, G. Fang, and L. Lei, "An analytical model for rapid predicting molten pool geometry of selective laser melting (SLM)," *Appl Math Model*, vol. 92, pp. 505–524, 2021, doi: 10.1016/j.apm.2020.11.027.

[67] E. L. Stevens, J. Toman, A. C. To, and M. Chmielus, "Variation of hardness, microstructure, and Laves phase distribution in direct laser deposited alloy 718 cuboids," *Mater Des*, vol. 119, pp. 188–198, Apr. 2017, doi: 10.1016/J.MATDES.2017.01.031.

[68] M. Ma, Z. Wang, and X. Zeng, "Effect of energy input on microstructural evolution of direct laser fabricated IN718 alloy," *Mater Charact*, vol. 106, pp. 420–427, Aug. 2015, doi: 10.1016/J.MATCHAR.2015.06.027.

[69] G. P. Dinda, A. K. Dasgupta, and J. Mazumder, "Laser aided direct metal deposition of Inconel 625 superalloy: Microstructural evolution and thermal stability," *Materials Science and Engineering: A*, vol. 509, no. 1–2, pp. 98–104, May 2009, doi: 10.1016/J.MSEA.2009.01.009.

[70] L. L. Parimi, R. G. A., D. Clark, and M. M. Attallah, "Microstructural and texture development in direct laser fabricated IN718," *Mater Charact*, vol. 89, pp. 102–111, Mar. 2014, doi: 10.1016/J.MATCHAR.2013.12.012.

[71] M. Gäumann, S. Henry, F. Cléton, J.-D. Wagnière, and W. Kurz, "Epitaxial laser metal forming: analysis of microstructure formation," *Materials Science and Engineering: A*, vol. 271, no. 1–2, pp. 232–241, Nov. 1999, doi: 10.1016/S0921-5093(99)00202-6.

[72] X. Shi, S. Duan, W. Yang, H. Guo, and J. Guo, "Solidification and segregation behaviors of superalloy IN718 at a slow cooling ratess," *Materials*, vol. 11, no. 12, pp. 1–15, 2018, doi: 10.3390/ma11122398.

[73] Y. Chen, K. Zhang, J. Huang, S. R. E. Hosseini, and Z. Li, "Characterization of heat affected zone liquation cracking in laser additive manufacturing of Inconel 718," *Mater Des*, vol. 90, pp. 586–594, Jan. 2016, doi: 10.1016/J.MATDES.2015.10.155.

[74] I. Tabernero, A. Lamikiz, S. Martínez, E. Ukar, and J. Figueras, "Evaluation of the mechanical properties of Inconel 718 components built by laser cladding," *Int J Mach Tools Manuf*, vol. 51, no. 6, pp. 465–470, Jun. 2011, doi: 10.1016/J.IJMACHTOOLS.2011.02.003.

[75] S. Sui *et al.*, "The influence of Laves phases on the room temperature tensile properties of Inconel 718 fabricated by powder feeding laser additive manufacturing," *Acta Mater*, vol. 164, pp. 413–427, Feb. 2019, doi: 10.1016/j.actamat.2018.10.032.

[76] A. Segerstark, J. Andersson, L. E. Svensson, and O. Ojo, "Effect of Process Parameters on the Crack Formation in Laser Metal Powder Deposition of Alloy 718," *Metall Mater Trans A Phys Metall Mater Sci*, vol. 49, no. 10, pp. 5042–5050, 2018, doi: 10.1007/s11661-018-4767-0.

[77] S. Sui, J. Chen, R. Zhang, X. Ming, F. Liu, and X. Lin, "The tensile deformation behavior of laser repaired Inconel 718 with a non-uniform microstructure," *Materials Science and Engineering: A*, vol. 688, pp. 480–487, Mar. 2017, doi: 10.1016/J.MSEA.2017.01.110.

[78] W. Kurz and R. Trivedi, "Rapid solidification processing and microstructure formation," *Materials Science and Engineering: A*, vol. 179–180, pp. 46–51, May 1994, doi: 10.1016/0921-5093(94)90162-7.

[79] A. Keshavarzkermani *et al.*, "An investigation into the effect of process parameters on melt pool geometry, cell spacing, and grain refinement during laser powder bed fusion," *Opt Laser Technol*, vol. 116, pp. 83–91, Aug. 2019, doi: 10.1016/J.OPTLASTEC.2019.03.012.

[80] B. Dutta and F. H. Froes, "Additive Manufacturing Technology," *Additive Manufacturing of Titanium Alloys*, pp. 25–40, 2016, doi: 10.1016/B978-0-12-804782-8.00003-3.

[81] R. Udroiu, "Powder Bed Additive Nanufacturing Systems and Its Applications," *Academic Journal of Manufacturing Engineering*, vol. 10, no. 4, pp. 122–129, 2012.

[82] S. Sun, M. Brandt, and M. Easton, "Powder bed fusion processes: An overview," *Laser Additive Manufacturing*, pp. 55–77, Jan. 2017, doi: 10.1016/B978-0-08-100433-3.00002-6.

[83] V. Bhavar, B. Forge, and P. Kattire, "A review on powder bed fusion technology of metal additive manufacturing Business development of Additive Manufacturing View project additive manufacturing View project," no. September, 2014.

[84] C. Seidel and M. F. Zaeh, "Multi-scale Modelling Approach for Contributing to Reduced Distortion in Parts Made by Laser-based Powder Bed Fusion," *Procedia CIRP*, vol. 67, pp. 197–202, 2018, doi: 10.1016/j.procir.2017.12.199.

[85] Trumpf, "Laser metal deposition (LMD) | TRUMPF." Accessed: Feb. 14, 2019. [Online]. Available: https://www.trumpf.com/en_SE/applications/additive-manufacturing/laser-metal-deposition-lmd/

[86] B. Dutta and F. H. Froes, "Additive manufacturing of titanium alloys," *Additive Manufacturing Handbook: Product Development for the Defense Industry*, vol. 72, no. 2, pp. 263–274, 2017, doi: 10.1201/9781315119106.

[87] X. Wu, J. Liang, J. Mei, C. Mitchell, P. S. Goodwin, and W. Voice, "Microstructures of laser-deposited Ti-6Al-4V," *Mater Des*, vol. 25, no. 2, pp. 137–144, 2004, doi: 10.1016/j.matdes.2003.09.009.

[88] O. Yilmaz and A. A. Ugla, "Shaped metal deposition technique in additive manufacturing: A review," *Proc Inst Mech Eng B J Eng Manuf*, vol. 230, no. 10, pp. 1781–1798, 2016, doi: 10.1177/0954405416640181.

[89] B. Graf, A. Gumenyuk, and M. Rethmeier, "Laser Metal Deposition as Repair Technology for Stainless Steel and Titanium Alloys," *Phys Procedia*, vol. 39, pp. 376–381, Jan. 2012, doi: 10.1016/J.PHPRO.2012.10.051.

[90] A. J. Pinkerton, "Laser direct metal deposition: theory and applications in manufacturing and maintenance," *Advances in Laser Materials Processing*, pp. 461–491, Jan. 2010, doi: 10.1533/9781845699819.6.461.

[91] B. Graf, S. Ammer, A. Gumenyuk, and M. Rethmeier, "Design of experiments for laser metal deposition in maintenance, repair and overhaul applications," *Procedia CIRP*, vol. 11, pp. 245–248, 2013, doi: 10.1016/j.procir.2013.07.031.

[92] S. G. Lambrakos, J. G. Michopoulos, A. P. Iliopoulos, A. J. Birnbaum, and J. C. Steuben, "On the multiphysics modeling challenges for metal additive manufacturing processes," *Addit Manuf*, vol. 22, no. June, pp. 784–799, 2018, doi: 10.1016/j.addma.2018.06.019.

[93] S. Maffia, F. Chiappini, G. Maggiani, V. Furlan, M. Guerrini, and B. Previtali, "Enhancing productivity and efficiency in conventional laser metal deposition process for Inconel 718 - part I: the effects of the process parameters," *International Journal of Advanced Manufacturing Technology*, vol. 128, no. 11–12, pp. 5353–5372, Oct. 2023, doi: 10.1007/s00170-023-12196-1.

[94] D. R. Waryoba, J. S. Keist, C. Ranger, and T. A. Palmer, "Microtexture in additively manufactured Ti-6Al-4V fabricated using directed energy deposition," *Materials Science and Engineering: A*, vol. 734, pp. 149–163, Sep. 2018, doi: 10.1016/J.MSEA.2018.07.098.

[95] J. Bai, R. Ma, Y. Zhang, L. Cheng, Y. Wang, and W. Zhou, "Effect of laser power and heat treatment on microstructures and tensile properties of LPBF fabricated Hastelloy X superalloy," *Mater Res Express*, vol. 10, no. 10, Oct. 2023, doi: 10.1088/2053-1591/acff3f.

[96] M. Mueller, K. Franz, M. Riede, E. López, F. Brueckner, and C. Leyens, "Influence of process parameter variation on the microstructure of thin walls made of Inconel 718 deposited via laser-based directed energy deposition with blown powder," *J Mater Sci*, vol. 58, no. 27, pp. 11310–11326, Jul. 2023, doi: 10.1007/s10853-023-08706-x.

[97] S. J. Wolff *et al.*, "Experimentally validated predictions of thermal history and microhardness in laser-deposited Inconel 718 on carbon steel," *Addit Manuf*, 2019, doi: 10.1016/j.addma.2019.03.019.

[98] H. Xiao, S. Li, X. Han, J. Mazumder, and L. Song, "Laves phase control of Inconel 718 alloy using quasi-continuous-wave laser additive manufacturing," *Mater Des*, vol. 122, pp. 330–339, May 2017, doi: 10.1016/J.MATDES.2017.03.004.

[99] D. H. Son, I. S. Kim, B. G. Choi, J. Do, Y. S. Choi, and J. E. Jung, "Effect of Laser Power on the Recrystallization Temperature of an Additively Manufactured IN718," *Metals (Basel)*, vol. 13, no. 8, Aug. 2023, doi: 10.3390/met13081355.

[100] A. Alhuzaim, S. Imbrogno, and M. M. Attallah, "Controlling microstructural and mechanical properties of direct laser deposited Inconel 718 via laser power," *J Alloys Compd*, vol. 872, Aug. 2021, doi: 10.1016/j.jallcom.2021.159588.

[101] L. Zhu, Z. F. Xu, P. Liu, and Y. F. Gu, "Effect of processing parameters on microstructure of laser solid forming Inconel 718 superalloy," *Opt Laser Technol*, vol. 98, pp. 409–415, 2018, doi: 10.1016/j.optlastec.2017.08.027.

[102] R. G. Ding, Z. W. Huang, H. Y. Li, I. Mitchell, G. Baxter, and P. Bowen, "Electron microscopy study of direct laser deposited IN718," *Mater Charact*, vol. 106, pp. 324–337, 2015, doi: 10.1016/j.matchar.2015.06.017.

[103] C. Zhong, A. Gasser, J. Kittel, K. Wissenbach, and R. Poprawe, "Improvement of material performance of Inconel 718 formed by high

deposition-rate laser metal deposition," *Mater Des*, vol. 98, pp. 128–134, 2016, doi: 10.1016/j.matdes.2016.03.006.

[104] R. Wang *et al.*, "Effects of laser scanning speed and building direction on the microstructure and mechanical properties of selective laser melted Inconel 718 superalloy," *Mater Today Commun*, vol. 30, Mar. 2022, doi: 10.1016/j.mtcomm.2021.103095.

[105] Y. Zhang, Z. Li, P. Nie, and Y. Wu, "Effect of cooling rate on the microstructure of laser-remelted INCONEL 718 coating," *Metall Mater Trans A Phys Metall Mater Sci*, vol. 44, no. 12, pp. 5513–5521, 2013, doi: 10.1007/s11661-013-1903-8.

[106] N. U. Rahman *et al.*, "Laser metal deposition of vanadium-rich high speed steel: Microstructural and high temperature wear characterization," *Surf Coat Technol*, vol. 364, no. December 2018, pp. 115–126, 2019, doi: 10.1016/J.SURFCOAT.2019.02.044.

[107] H. Pan, T. Dahmen, M. Bayat, K. Lin, and X. Zhang, "Independent effects of laser power and scanning speed on IN718's precipitation and mechanical properties produced by LBPF plus heat treatment," *Materials Science and Engineering: A*, vol. 849, Aug. 2022, doi: 10.1016/j.msea.2022.143530.

[108] L. L. Parimi, R. G. A., D. Clark, and M. M. Attallah, "Microstructural and texture development in direct laser fabricated IN718," *Mater Charact*, vol. 89, pp. 102–111, Mar. 2014, doi: 10.1016/J.MATCHAR.2013.12.012.

[109] L. L. Parimi, M. M. Attallah, J. C. Gebelin, and R. C. Reed, "Direct Laser Fabrication of Inconel-718: Effects on Distortion and Microstructure," *Superalloys 2012*, pp. 509–519, 2012, doi: 10.1002/9781118516430.ch56.

[110] P. Fino, D. Gallo, S. Biamino, A. Saboori, and M. Lombardi, "An Overview of Additive Manufacturing of Titanium Components by Directed Energy Deposition: Microstructure and Mechanical Properties," *Applied Sciences*, vol. 7, no. 9, p. 883, 2017, doi: 10.3390/app7090883.

[111] G. P. Dinda, A. K. Dasgupta, and J. Mazumder, "Texture control during laser deposition of nickel-based superalloy," *Scr Mater*, vol. 67, no. 5, pp. 503–506, Sep. 2012, doi: 10.1016/J.SCRIPTAMAT.2012.06.014.

[112] H. L. Wei, J. Mazumder, and T. DebRoy, "Evolution of solidification texture during additive manufacturing," *Sci Rep*, vol. 5, pp. 1–7, 2015, doi: 10.1038/srep16446.

[113] F. Liu *et al.*, "The effect of laser scanning path on microstructures and mechanical properties of laser solid formed nickel-base superalloy Inconel 718," *J Alloys Compd*, vol. 509, no. 13, pp. 4505–4509, Mar. 2011, doi: 10.1016/J.JALLCOM.2010.11.176.

[114] H. Helmer, A. Bauereiß, R. F. Singer, and C. Körner, "Grain structure evolution in Inconel 718 during selective electron beam melting," *Materials Science and Engineering: A*, vol. 668, pp. 180–187, Jun. 2016, doi: 10.1016/J.MSEA.2016.05.046.

[115] R. R. Dehoff *et al.*, "Site specific control of crystallographic grain orientation through electron beam additive manufacturing," *Materials Science and Technology (United Kingdom)*, vol. 31, no. 8, pp. 931–938, 2015, doi: 10.1179/1743284714Y.0000000734.

[116] B. Yang, G. Xiong, S. Nie, M. Elchalakani, and Q. Zhu, "Experimental and model investigation on residual stresses in Q460GJ thick-walled I-shaped sections," *J Constr Steel Res*, vol. 145, pp. 489–503, Jun. 2018, doi: 10.1016/j.jcsr.2018.03.008.

[117] P. J. Withers and H. K. D. H. Bhadeshia, "Residual stress Part 1-Measurement techniques."

[118] A. Mishra, M. Hassan, and M. Pal, "A Critical Review on Effects of Residual Stresses on Machining of Titanium alloys by various Non-Conventional Processes," *Int J Res Appl Sci Eng Technol*, vol. 10, no. 3, pp. 63–82, Mar. 2022, doi: 10.22214/ijraset.2022.40583.

[119] L. L. Parimi, "Additive Manufacturing of Nickel Based Superalloys for Aerospace Applications," no. April, pp. 1–12, 2014.

[120] J. W. H. Price, A. Ziara-Paradowska, S. Joshi, T. Finlayson, C. Semetay, and H. Nied, "Comparison of experimental and theoretical residual stresses in welds: The issue of gauge volume," *Int J Mech Sci*, vol. 50, no. 3, pp. 513–521, Mar. 2008, doi: 10.1016/j.ijmecsci.2007.08.008.

[121] P. Mercelis and J. P. Kruth, "Residual stresses in selective laser sintering and selective laser melting," *Rapid Prototyp J*, vol. 12, no. 5, pp. 254–265, 2006, doi: 10.1108/13552540610707013.

[122] I. Yadroitsev, P. Krakhmalev, and I. Yadroitsava, "Selective laser melting of Ti6Al4V alloy for biomedical applications: Temperature monitoring and microstructural evolution," *J Alloys Compd*, vol. 583, pp. 404–409, 2014, doi: 10.1016/j.jallcom.2013.08.183.

[123] J. Yu, M. Rombouts, G. Maes, and F. Motmans, "Material Properties of Ti6Al4 v Parts Produced by Laser Metal Deposition," in *Physics Procedia*, Elsevier B.V., 2012, pp. 416–424. doi: 10.1016/j.phpro.2012.10.056.

[124] H. Zhang, W. Xu, Y. Xu, Z. Lu, and D. Li, "The thermal-mechanical behavior of WTaMoNb high-entropy alloy via selective laser melting (SLM): experiment and simulation," *International Journal of Advanced Manufacturing Technology*, vol. 96, no. 1–4, pp. 461–474, Apr. 2018, doi: 10.1007/s00170-017-1331-9.

[125] L. Van Belle, G. Vansteenkiste, and J. C. Boyer, "Investigation of residual stresses induced during the selective laser melting process," in *Key Engineering Materials*, Trans Tech Publications Ltd, 2013, pp. 1828–1834. doi: 10.4028/www.scientific.net/KEM.554-557.1828.

[126] J. Ding, "Thermo-mechanical Analysis of Wire and Arc Additive Manufacturing Process," Cranfield University.

[127] Z. C. Fang, Z. L. Wu, C. G. Huang, and C. W. Wu, "Review on residual stress in selective laser melting additive manufacturing of alloy parts," Sep. 01, 2020, *Elsevier Ltd*. doi: 10.1016/j.optlastec.2020.106283.

[128] R. J. Moat, A. J. Pinkerton, L. Li, P. J. Withers, and M. Preuss, "Residual stresses in laser direct metal deposited Waspaloy," *Materials Science and Engineering A*, vol. 528, no. 6, pp. 2288–2298, 2011, doi: 10.1016/j.msea.2010.12.010.

[129] E. R. Denlinger, J. C. Heigel, and P. Michaleris, "Residual stress and distortion modeling of electron beam direct manufacturing Ti-6Al-4V," *Proc Inst Mech Eng B J Eng Manuf*, vol. 229, no. 10, pp. 1803–1813, 2015, doi: 10.1177/0954405414539494.

[130] E. R. Denlinger, M. Gouge, J. Irwin, and P. Michaleris, "Thermomechanical model development and in situ experimental validation of the Laser Powder-Bed Fusion process," *Addit Manuf*, vol. 16, pp. 73–80, Aug. 2017, doi: 10.1016/j.addma.2017.05.001.

[131] M. Ghasri-Khouzani *et al.*, "Experimental measurement of residual stress and distortion in additively manufactured stainless steel components with various dimensions," *Materials Science and Engineering A*, vol. 707, no. September, pp. 689–700, 2017, doi: 10.1016/j.msea.2017.09.108.

[132] A. S. Wu, D. W. Brown, M. Kumar, G. F. Gallegos, and W. E. King, "An Experimental Investigation into Additive Manufacturing-Induced Residual Stresses in 316L Stainless Steel," *Metall Mater Trans A Phys Metall Mater Sci*, vol. 45, no. 13, pp. 6260–6270, Oct. 2014, doi: 10.1007/s11661-014-2549-x.

[133] N. C. Levkulich, S. L. Semiatin, J. E. Gockel, J. R. Middendorf, A. T. DeWald, and N. W. Klingbeil, "The effect of process parameters on residual stress evolution and distortion in the laser powder bed fusion of Ti-6Al-4V," *Addit Manuf*, vol. 28, no. January, pp. 475–484, 2019, doi: 10.1016/j.addma.2019.05.015.

[134] N. C. Levkulich, S. L. Semiatin, J. E. Gockel, J. R. Middendorf, A. T. DeWald, and N. W. Klingbeil, "The effect of process parameters on residual stress evolution and distortion in the laser powder bed fusion of Ti-6Al-4V," *Addit Manuf*, vol. 28, pp. 475–484, Aug. 2019, doi: 10.1016/j.addma.2019.05.015.

[135] R. J. Moat, A. J. Pinkerton, L. Li, P. J. Withers, and M. Preuss, "Residual stresses in laser direct metal deposited Waspaloy," *Materials Science and Engineering A*, vol. 528, no. 6, pp. 2288–2298, 2011, doi: 10.1016/j.msea.2010.12.010.

[136] Z. Wang, E. Denlinger, P. Michaleris, A. D. Stoica, D. Ma, and A. M. Beese, "Residual stress mapping in Inconel 625 fabricated through additive manufacturing: Method for neutron diffraction measurements to validate thermomechanical model predictions," *Mater Des*, 2017, doi: 10.1016/j.matdes.2016.10.003.

[137] B. Vrancken, V. Cain, R. Knutsen, and J. Van Humbeeck, "Residual stress via the contour method in compact tension specimens produced via selective laser melting," *Scr Mater*, vol. 87, pp. 29–32, 2014, doi: 10.1016/j.scriptamat.2014.05.016.

[138] P. Pratt, S. D. Felicelli, L. Wang, and C. R. Hubbard, "Residual stress measurement of laser-engineered net shaping AISI 410 thin plates using neutron diffraction," *Metall Mater Trans A Phys Metall Mater Sci*, vol. 39, no. 13, pp. 3155–3163, 2008, doi: 10.1007/s11661-008-9660-9.

[139] B. Ahmad, S. O. van der Veen, M. E. Fitzpatrick, and H. Guo, "Residual stress evaluation in selective-laser-melting additively manufactured titanium (Ti-6Al-4V) and inconel 718 using the contour method and numerical simulation," *Addit Manuf*, vol. 22, pp. 571–582, Aug. 2018, doi: 10.1016/J.ADDMA.2018.06.002.

[140] P. Rangaswamy *et al.*, "Residual stresses in LENS® components using neutron diffraction and contour method," *Materials Science and Engineering A*, vol. 399, no. 1–2, pp. 72–83, 2005, doi: 10.1016/j.msea.2005.02.019.

[141] D. Deng, R. L. Peng, H. Brodin, and J. Moverare, "Microstructure and mechanical properties of Inconel 718 produced by selective laser melting: Sample orientation dependence and effects of post heat treatments," *Materials Science and Engineering: A*, vol. 713, pp. 294–306, Jan. 2018, doi: 10.1016/J.MSEA.2017.12.043.

[142] H. Shipley *et al.*, "Optimisation of process parameters to address fundamental challenges during selective laser melting of Ti-6Al-4V: A review," *Int J Mach Tools Manuf*, vol. 128, no. January, pp. 1–20, 2018, doi: 10.1016/j.ijmachtools.2018.01.003.

[143] Q. Li, B. Gnanasekaran, Y. Fu, and G. R. Liu, "Prediction of Thermal Residual Stress and Microstructure in Direct Laser Metal Deposition via a Coupled Finite Element and Multiphase Field Framework," *Jom*, vol. 72, no. 1, pp. 496–508, 2020, doi: 10.1007/s11837-019-03922-w.

[144] J. Cao, M. A. Gharghouri, and P. Nash, "Finite-element analysis and experimental validation of thermal residual stress and distortion in electron

beam additive manufactured Ti-6Al-4V build plates," *J Mater Process Technol*, 2016, doi: 10.1016/j.jmatprotec.2016.06.032.

[145] T. R. Walker, C. J. Bennett, T. L. Lee, and A. T. Clare, "A validated analytical-numerical modelling strategy to predict residual stresses in single-track laser deposited IN718," *Int J Mech Sci*, 2019, doi: 10.1016/j.ijmecsci.2018.12.004.

[146] H. Zhao, G. Zhang, Z. Yin, and L. Wu, "Three-dimensional finite element analysis of thermal stress in single-pass multi-layer weld-based rapid prototyping," *J Mater Process Technol*, 2012, doi: 10.1016/j.jmatprotec.2011.09.012.

[147] J. Ahn *et al.*, "FEM prediction of welding residual stresses in fibre laser-welded AA 2024-T3 and comparison with experimental measurement," *International Journal of Advanced Manufacturing Technology*, vol. 95, no. 9–12, pp. 4243–4263, 2018, doi: 10.1007/s00170-017-1548-7.

[148] D. Deng and S. Kiyoshima, "Numerical simulation of welding temperature field, residual stress and deformation induced by electro slag welding," *Comput Mater Sci*, vol. 62, pp. 23–34, 2012, doi: 10.1016/j.commatsci.2012.04.037.

[149] Y. C. Lin and K. H. Lee, "Effect of preheating on the residual stress in type 304 stainless steel weldment," *J Mater Process Technol*, vol. 63, no. 1–3, pp. 797–801, 1997, doi: 10.1016/S0924-0136(96)02727-6.

[150] E. Mirkoohi, H. Tran, Y. Lo, Y. Chang, and H. Lin, "Mechanics Modeling of Residual Stress Considering Effect of Preheating in Laser Powder Bed Fusion," no. March, pp. 1–14, 2021.

[151] L. Wang, X. Jiang, Y. Zhu, X. Zhu, J. Sun, and B. Yan, "An approach to predict the residual stress and distortion during the selective laser melting of AlSi10Mg parts," *International Journal of Advanced Manufacturing Technology*, vol. 97, no. 9–12, pp. 3535–3546, Aug. 2018, doi: 10.1007/s00170-018-2207-3.

[152] L. Mugwagwa, D. Dimitrov, S. Matope, and I. Yadroitsev, "Influence of process parameters on residual stress related distortions in selective laser

melting," in *Procedia Manufacturing*, Elsevier B.V., 2018, pp. 92–99. doi: 10.1016/j.promfg.2018.02.099.

[153] Y. Bin Lai, W. J. Liu, J. Bin Zhao, Y. H. Zhao, F. Y. Wang, and W. C. Han, "Experimental study on residual stress in titanium alloy laser additive manufacturing," in *Applied Mechanics and Materials*, 2013, pp. 20–26. doi: 10.4028/www.scientific.net/AMM.431.20.

[154] H. Ali, H. Ghadbeigi, and K. Mumtaz, "Processing Parameter Effects on Residual Stress and Mechanical Properties of Selective Laser Melted Ti6Al4V," *J Mater Eng Perform*, vol. 27, no. 8, pp. 4059–4068, Aug. 2018, doi: 10.1007/s11665-018-3477-5.

[155] L. L. Parimi, "Additive Manufacturing of Nickel Based Superalloys for Aerospace Applications," no. April, pp. 1–12, 2014.

[156] J. Robinson, I. Ashton, P. Fox, E. Jones, and C. Sutcliffe, "Determination of the effect of scan strategy on residual stress in laser powder bed fusion additive manufacturing," *Addit Manuf*, vol. 23, no. June, pp. 13–24, 2018, doi: 10.1016/j.addma.2018.07.001.

[157] S. Goel *et al.*, "Residual stress determination by neutron diffraction in powder bed fusion-built Alloy 718: Influence of process parameters and post-treatment," *Mater Des*, vol. 195, p. 109045, 2020, doi: 10.1016/j.matdes.2020.109045.

[158] L. Mugwagwa, D. Dimitrov, S. Matope, and I. Yadroitsev, "Evaluation of the impact of scanning strategies on residual stresses in selective laser melting," *International Journal of Advanced Manufacturing Technology*, vol. 102, no. 5–8, pp. 2441–2450, 2019, doi: 10.1007/s00170-019-03396-9.

[159] A. N. Jinoop, C. P. Paul, S. K. Mishra, and K. S. Bindra, "Laser Additive Manufacturing using directed energy deposition of Inconel-718 wall structures with tailored characteristics," *Vacuum*, vol. 166, pp. 270–278, Aug. 2019, doi: 10.1016/J.VACUUM.2019.05.027.

[160] V. Luzin and N. P. Hoye, "Stress in Thin Wall Structures Made by Layer Additive Manufacturing," *Residual Stresses 2016*, vol. 2, pp. 497–502, 2017, doi: 10.21741/9781945291173-84.

[161] B. A. Szost *et al.*, "A comparative study of additive manufacturing techniques: Residual stress and microstructural analysis of CLAD and WAAM printed Ti-6Al-4V components," *Mater Des*, vol. 89, pp. 559–567, 2016, doi: 10.1016/j.matdes.2015.09.115.

[162] V. Manvatkar, A. De, and T. Debroy, "Heat transfer and material flow during laser assisted multi-layer additive manufacturing," *J Appl Phys*, vol. 116, no. 12, 2014, doi: 10.1063/1.4896751.

[163] V. Manvatkar, A. De, and T. DebRoy, "Spatial variation of melt pool geometry, peak temperature and solidification parameters during laser assisted additive manufacturing process," *Materials Science and Technology*, vol. 31, no. 8, pp. 924–930, 2014, doi: 10.1179/1743284714y.0000000701.

[164] R. A. Hardin and C. Beckermann, "Simulation of Heat Treatment Distortion," Steel Founders' Society of America, 2005.

[165] P. Foteinopoulos, A. Papacharalampopoulos, and P. Stavropoulos, "On thermal modeling of Additive Manufacturing processes," *CIRP J Manuf Sci Technol*, vol. 20, pp. 66–83, 2018, doi: 10.1016/j.cirpj.2017.09.007.

[166] D. Rosenthal, "The Theory of Moving Sources of Heat and Its Application of Metal Treatments," *Transactions of ASME*, vol. 68, pp. 849–866, 1946.

[167] Y. Chen *et al.*, "Study on the element segregation and Laves phase formation in the laser metal deposited IN718 superalloy by flat top laser and gaussian distribution laser," *Materials Science and Engineering: A*, vol. 754, pp. 339–347, Apr. 2019, doi: 10.1016/J.MSEA.2019.03.096.

[168] A. J. Pinkerton and L. Li, "An analytical model of energy distribution in laser direct metal deposition," *Proc Inst Mech Eng B J Eng Manuf*, vol. 218, no. 4, pp. 363–374, 2004, doi: 10.1243/095440504323055498.

[169] T. R. Walker, C. J. Bennett, T. L. Lee, and A. T. Clare, "A validated analytical-numerical modelling strategy to predict residual stresses in single-track laser deposited IN718," *Int J Mech Sci*, vol. 151, pp. 609–621, Feb. 2019, doi: 10.1016/j.ijmecsci.2018.12.004.

[170] M. Picasso, C. F. Marsden, J. D. Wagniere, A. Frenk, and M. Rappaz, "A simple but realistic model for laser cladding," *Metallurgical and Materials Transactions B*, vol. 25, no. 2, pp. 281–291, 1994, doi: 10.1007/BF02665211.

[171] M. N. Ahsan and A. J. Pinkerton, "An analytical-numerical model of laser direct metal deposition track and microstructure formation," *Model Simul Mat Sci Eng*, vol. 19, no. 5, 2011, doi: 10.1088/0965-0393/19/5/055003.

[172] A. Kumar and S. Roy, "Effect of three-dimensional melt pool convection on process characteristics during laser cladding," 2009, doi: 10.1016/j.commatsci.2009.04.002.

[173] P. Peyre, P. Aubry, R. Fabbro, R. Neveu, and A. Longuet, "Analytical and numerical modelling of the direct metal deposition laser process," *J Phys D Appl Phys*, vol. 41, no. 2, 2008, doi: 10.1088/0022-3727/41/2/025403.

[174] P. Peyre, M. Dal, S. Ebastien Pouzet, O. Castelnau, and S. ebastien Pouzet, "Simplified numerical model for the laser metal deposition additive manufacturing process Simplified numerical model for the laser metal deposition additive manufacturing process Simplified numerical model for the laser metal deposition additive manufacturing process," *J Laser Appl*, vol. 29, no. 2, 2017, doi: 10.2351/1.4983251ï.

[175] A. Anca, V. Fachinotti, G. Palafox-Escobar, and A. Cardona, "Computational modelling of shaped metal deposition," *Int J Numer Methods Eng*, vol. 85, no. February, pp. 84–106, 2011, doi: 10.1002/nme.

[176] M. Söderberg, A. Lundbaĉk, and L. E. Lindgren, "Modeling of metal deposition," in *ASM Proceedings of the International Conference: Trends in Welding Research*, 2013, pp. 853–858. doi: 10.1016/j.finel.2011.05.005.

[177] L. E. Lindgren and A. Lundbäck, "Approaches in computational welding mechanics applied to additive manufacturing: Review and outlook," Nov. 01, 2018, *Elsevier Masson SAS*. doi: 10.1016/j.crme.2018.08.004.

[178] H. Hekmatjou, Z. Zeng, J. Shen, and J. P. Oliveira, "A Comparative Study of Analytical Rosenthal, Finite Element, and Experimental Approaches in Laser Welding of AA5456 Alloy," *Metals (Basel)*, vol. 10(4), no. 436, 2020.

[179] R. Mathews *et al.*, "Temporally continuous thermofluidic–thermomechanical modeling framework for metal additive manufacturing," *Int J Mech Sci*, vol. 254, Sep. 2023, doi: 10.1016/j.ijmecsci.2023.108424.

[180] J. C. Heigel, P. Michaleris, and E. W. Reutzel, "Thermo-mechanical model development and validation of directed energy deposition additive manufacturing of Ti–6Al–4V," *Addit Manuf*, vol. 5, pp. 9–19, Jan. 2015, doi: 10.1016/J.ADDMA.2014.10.003.

[181] P. Michaleris, "Modeling metal deposition in heat transfer analyses of additive manufacturing processes," *Finite Elements in Analysis and Design*, vol. 86, pp. 51–60, Sep. 2014, doi: 10.1016/j.finel.2014.04.003.

[182] Q. Yang, P. Zhang, L. Cheng, Z. Min, and M. Chyu, "Finite element modeling and validation of thermomechanical behavior of Ti-6Al-4V in directed energy deposition additive manufacturing," *Addit Manuf*, vol. 12, pp. 169–177, Oct. 2016, doi: 10.1016/J.ADDMA.2016.06.012.

[183] T. Mukherjee, W. Zhang, and T. DebRoy, "An improved prediction of residual stresses and distortion in additive manufacturing," *Comput Mater Sci*, 2017, doi: 10.1016/j.commatsci.2016.10.003.

[184] L. Wang, S. Felicelli, Y. Gooroochurn, P. T. Wang, and M. F. Horstemeyer, "Optimization of the LENS® process for steady molten pool size," *Materials Science and Engineering A*, vol. 474, no. 1–2, pp. 148–156, Feb. 2008, doi: 10.1016/j.msea.2007.04.119.

[185] M. Biegler, B. Graf, and M. Rethmeier, "In-situ distortions in LMD additive manufacturing walls can be measured with digital image correlation and predicted using numerical simulations," *Addit Manuf*, vol. 20, pp. 101–110, 2018, doi: 10.1016/j.addma.2017.12.007.

[186] Z. Nie *et al.*, "Experimental study and modeling of H13 steel deposition using laser hot-wire additive manufacturing," *J Mater Process Technol*, 2016, doi: 10.1016/j.jmatprotec.2016.04.006.

[187] B. Cheng, S. Shrestha, and K. Chou, "Stress and deformation evaluations of scanning strategy effect in selective laser melting," *Addit Manuf*, 2016, doi: 10.1016/j.addma.2016.05.007.

[188] K. An, L. Yuan, L. Dial, I. Spinelli, A. D. Stoica, and Y. Gao, "Neutron residual stress measurement and numerical modeling in a curved thin-walled structure by laser powder bed fusion additive manufacturing," *Mater Des*, 2017, doi: 10.1016/j.matdes.2017.09.018.

[189] E. R. Denlinger, V. Jagdale, G. V. Srinivasan, T. El-Wardany, and P. Michaleris, "Thermal modeling of Inconel 718 processed with powder bed fusion and experimental validation using in situ measurements," *Addit Manuf*, vol. 11, pp. 7–15, Jul. 2016, doi: 10.1016/j.addma.2016.03.003.

[190] F. Hajializadeh and A. Ince, "Short review on modeling approaches for metal additive manufacturing process," *Material Design and Processing Communications*, vol. 2, no. 2, Apr. 2020, doi: 10.1002/mdp2.56.

[191] Q. Yang, P. Zhang, L. Cheng, Z. Min, and M. Chyu, "Finite element modeling and validation of thermomechanical behavior of Ti-6Al-4V in directed energy deposition additive manufacturing," *Addit Manuf*, vol. 12, pp. 169–177, Oct. 2016, doi: 10.1016/J.ADDMA.2016.06.012.

[192] S. Ruiz de Galarreta, J. R. T. Jeffers, and S. Ghouse, "A validated finite element analysis procedure for porous structures," *Mater Des*, vol. 189, Apr. 2020, doi: 10.1016/j.matdes.2020.108546.

[193] W. Chen, X. Zheng, and S. Liu, "Finite-element-mesh based method for modeling and optimization of lattice structures for additive manufacturing," *Materials*, vol. 11, no. 11, Oct. 2018, doi: 10.3390/ma11112073.

[194] Z. Luo and Y. Zhao, "A survey of finite element analysis of temperature and thermal stress fields in powder bed fusion Additive Manufacturing," *Addit Manuf*, vol. 21, pp. 318–332, May 2018, doi: 10.1016/J.ADDMA.2018.03.022.

[195] J. Baiges, M. Chiumenti, C. A. Moreira, M. Cervera, and R. Codina, "An Adaptive Finite Element strategy for the numerical simulation of Additive Manufacturing processes," 2020.

[196] R. F. V. Sampaio, J. P. M. Pragana, I. M. F. Bragança, C. M. A. Silva, C. V. Nielsen, and P. A. F. Martins, "Modelling of wire-arc additive manufacturing – A review," May 01, 2023, *Elsevier B.V.* doi: 10.1016/j.aime.2023.100121.

[197] M. P. Mughal, H. Fawad, and R. A. Mufti, "Three-dimensional finite-element modelling of deformation in weld-based rapid prototyping," *Proc Inst Mech Eng C J Mech Eng Sci*, vol. 220, no. 6, pp. 875–885, Jun. 2006, doi: 10.1243/09544062JMES164.

[198] A. Bandyopadhyay and K. D. Traxel, "Invited review article: Metal-additive manufacturing—Modeling strategies for application-optimized designs," *Addit Manuf*, vol. 22, no. June, pp. 758–774, 2018, doi: 10.1016/j.addma.2018.06.024.

[199] A. A. Deshpande, D. W. J. Tanner, W. Sun, T. H. Hyde, and G. McCartney, "Combined butt joint welding and post weld heat treatment simulation using SYSWELD and ABAQUS," *Proceedings of the Institution of Mechanical Engineers, Part L: Journal of Materials: Design and Applications*, vol. 225, no. 1, pp. 1–10, 2011, doi: 10.1177/14644207JMDA349.

[200] T. R. Walker, C. J. Bennett, T. L. Lee, and A. T. Clare, "A validated analytical-numerical modelling strategy to predict residual stresses in single-track laser deposited IN718," *Int J Mech Sci*, 2019, doi: 10.1016/j.ijmecsci.2018.12.004.

[201] M. Biegler, B. Graf, and M. Rethmeier, "In-situ distortions in LMD additive manufacturing walls can be measured with digital image correlation and predicted using numerical simulations," *Addit Manuf*, 2018, doi: 10.1016/j.addma.2017.12.007.

[202] A. J. Pinkerton and L. Li, "The development of temperature fields and powder flow during laser direct metal deposition wall growth," *Proc Inst Mech Eng C J Mech Eng Sci*, vol. 218, no. 5, pp. 531–542, 2004, doi: 10.1243/095440604323052319.

[203] S. M. Kelly and S. L. Kampe, "Microstructural evolution in laser-deposited multilayer Ti-6Al-4V builds: Part II. Thermal Modeling," *Metall Mater Trans A Phys Metall Mater Sci*, vol. 35 A, no. 6, pp. 1869–1879, 2004, doi: 10.1007/s11661-004-0095-7.

[204] X. He, G. Yu, and J. Mazumder, "Temperature and composition profile during double-track laser cladding of H13 tool steel," *J Phys D Appl Phys*, vol. 43, no. 1, 2010, doi: 10.1088/0022-3727/43/1/015502.

[205] R. Jendrzejewski, I. Kreja, and G. Śliwiński, "Temperature distribution in laser-clad multi-layers," *Materials Science and Engineering: A*, vol. 379, no. 1–2, pp. 313–320, Aug. 2004, doi: 10.1016/J.MSEA.2004.02.053.

[206] K. Dortkasli, M. Isik, and E. Demir, "A thermal finite element model with efficient computation of surface heat fluxes for directed-energy deposition process and application to laser metal deposition of IN718."

[207] J. Xiong, R. Li, Y. Lei, and H. Chen, "Heat propagation of circular thin-walled parts fabricated in additive manufacturing using gas metal arc welding," *J Mater Process Technol*, 2018, doi: 10.1016/j.jmatprotec.2017.08.007.

[208] E. R. Denlinger, V. Jagdale, G. V. Srinivasan, T. El-Wardany, and P. Michaleris, "Thermal modeling of Inconel 718 processed with powder bed fusion and experimental validation using in situ measurements," *Addit Manuf*, vol. 11, pp. 7–15, 2016, doi: 10.1016/j.addma.2016.03.003.

[209] E. R. Denlinger, J. Irwin, and P. Michaleris, "Thermomechanical Modeling of Additive Manufacturing Large Parts," *J Manuf Sci Eng*, vol. 136, no. 6, p. 061007, 2014, doi: 10.1115/1.4028669.

[210] J. Ding *et al.*, "Thermo-mechanical analysis of Wire and Arc Additive Layer Manufacturing process on large multi-layer parts," *Comput Mater Sci*, vol. 50, no. 12, pp. 3315–3322, 2011.

[211] L. E. Lindgren, H. Runnemalm, and M. O. Näsström, "Simulation of multipass welding of a thick plate," *Int J Numer Methods Eng*, vol. 44, no. 9, pp. 1301–1316, 1999, doi: 10.1002/(SICI)1097-0207(19990330)44:9<1301::AID-NME479>3.0.CO;2-K.

[212] M. Söderberg, A. Lundbačk, and L. E. Lindgren, "Modeling of metal deposition," *Finite Elements in Analysis and Design*, vol. 47, pp. 1169–1177, 2011, doi: 10.1016/j.finel.2011.05.005.

[213] A. Segerstark, J. Andersson, and L. E. Svensson, "Evaluation of a temperature measurement method developed for laser metal deposition," *Science and Technology of Welding and Joining*, vol. 22, no. 1, pp. 1–6, 2017, doi: 10.1080/13621718.2016.1169363.

[214] J. Ahn, E. He, L. Chen, R. C. Wimpory, J. P. Dear, and C. M. Davies, "Prediction and measurement of residual stresses and distortions in fibre laser welded Ti-6Al-4V considering phase transformation," *Mater Des*, vol. 115, pp. 441–457, 2017, doi: 10.1016/j.matdes.2016.11.078.

[215] B. Li, J. Zhang, J. Yin, E. Gao, G. Yang, and Y. E. Cn, "Distortion prediction method for large-scale additive metal components based on feature partitioning and temperature function method," *The International Journal of Advanced Manufacturing Technology*, 2023, doi: 10.21203/rs.3.rs-3061817/v1.

[216] E. R. Denlinger, J. C. Heigel, P. Michaleris, and T. A. Palmer, "Effect of inter-layer dwell time on distortion and residual stress in additive manufacturing of titanium and nickel alloys," *J Mater Process Technol*, vol. 215, pp. 123–131, 2015, doi: 10.1016/j.jmatprotec.2014.07.030.

[217] X. Lu *et al.*, "Residual stress and distortion of rectangular and S-shaped Ti-6Al-4V parts by Directed Energy Deposition: Modelling and experimental calibration," *Addit Manuf*, vol. 26, no. February, pp. 166–179, 2019, doi: 10.1016/j.addma.2019.02.001.

[218] J. M. Lee, M. Cheepu, and H. Chung, "Experiment-based distortion prediction model for wire-based additive manufactured parts," *Journal of Mechanical Science and Technology*, vol. 36, no. 12, pp. 6227–6237, Dec. 2022, doi: 10.1007/s12206-022-1136-0.

[219] M. Biegler, B. Graf, and M. Rethmeier, "In-situ distortions in LMD additive manufacturing walls can be measured with digital image correlation and predicted using numerical simulations," *Addit Manuf*, 2018, doi: 10.1016/j.addma.2017.12.007.

[220] X. Lu *et al.*, "Finite Element Analysis and Experimental Validation of Thermomechanical Behavior in Laser Solid Forming of Ti-6Al-4V."

[221] T. R. Walker, C. J. Bennett, T. L. Lee, and A. T. Clare, "A validated analytical-numerical modelling strategy to predict residual stresses in single-track laser deposited IN718," *Int J Mech Sci*, 2019, doi: 10.1016/j.ijmecsci.2018.12.004.

[222] N. Ahmed, I. Barsoum, and R. K. Abu Al-Rub, "Numerical investigation of residual stresses in thin-walled additively manufactured structures from selective laser melting," *Heliyon*, vol. 9, no. 9, Sep. 2023, doi: 10.1016/j.heliyon.2023.e19385.

[223] Q. Li, B. Gnanasekaran, Y. Fu, and G. R. Liu, "Prediction of Thermal Residual Stress and Microstructure in Direct Laser Metal Deposition via a Coupled Finite Element and Multiphase Field Framework," *Jom*, vol. 72, no. 1, pp. 496–508, 2020, doi: 10.1007/s11837-019-03922-w.

[224] M. E. Stenderl, L. L. Beghinil, J. D. Sugar%, C. R. D'elia2, M. R. Hi112, and C. W. San Marchil, "Simulations and Experimental Validation of Residual Stresses in Additively-Manufactured Components."

[225] B. Vrancken, V. Cain, R. Knutsen, and J. Van Humbeeck, "Residual stress via the contour method in compact tension specimens produced via selective laser melting," *Scr Mater*, vol. 87, pp. 29–32, 2014, doi: 10.1016/j.scriptamat.2014.05.016.

[226] J. F. Radavich, "The Physical Metallurgy of Cast and Wrought Alloy 718," in *Superalloys 718 Metallurgy and Applications*, Vol. 1989., TMS, 1989, pp. 229–240. doi: 10.7449/1989/superalloys_1989_229_240.

[227] A. Mitchell, "Primary Carbides in Alloy 718," *Superalloy 718 and Derivatives*, pp. 161–167, 2012, doi: 10.1002/9781118495223.ch11.

[228] A.S.T.M., "ASTM B637-06: Standard Specification for Precipitation-Hardening Nickel Alloy Bars , Forgings , and Forging Stock for High-Temperature Service," *Book of Standards*, 2006, doi: 10.1520/B0637-06E01.2.

[229] C. Zhong, A. Gasser, J. Kittel, K. Wissenbach, and R. Poprawe, "Improvement of material performance of Inconel 718 formed by high deposition-rate laser metal deposition," *Mater Des*, vol. 98, pp. 128–134, 2016, doi: 10.1016/j.matdes.2016.03.006.

[230] K. Gruber, I. Smolina, M. Kasprowicz, and T. Kurzynowski, "Evaluation of inconel 718 metallic powder to optimize the reuse of powder and to improve the performance and sustainability of the laser powder bed fusion (Lpbf) process," *Materials*, vol. 14, no. 6, 2021, doi: 10.3390/ma14061538.

[231] C. Zhong, J. Chen, S. Linnenbrink, A. Gasser, S. Sui, and R. Poprawe, "A comparative study of Inconel 718 formed by High Deposition Rate Laser Metal Deposition with GA powder and PREP powder," *Mater Des*, vol. 107, pp. 386–392, 2016, doi: 10.1016/j.matdes.2016.06.037.

[232] B. Vrancken, "Study of Residual Stresses in Selective Laser Melting," KU Leuven Arenberg Doctoral School, 2016.

[233] W. Cheng, I. Finnie, M. Gremaud, and M. B. Prime, "Measurement of near surface residual stresses using electric discharge wire machining," *Journal of Engineering Materials and Technology, Transactions of the ASME*, vol. 116, no. 1, pp. 1–7, 1994, doi: 10.1115/1.2904251.

[234] L. Zhou, A. Mehta, B. McWilliams, K. Cho, and Y. Sohn, "Microstructure, precipitates and mechanical properties of powder bed fused inconel 718 before and after heat treatment," *J Mater Sci Technol*, vol. 35, no. 6, pp. 1153–1164, Jun. 2019, doi: 10.1016/J.JMST.2018.12.006.

[235] T. Keya, "MICROSTRUCTURE AND MECHANICAL PROPERTIES OF ADDITIVELY MANUFACTURED PARTS WITH STAIRCASE FEATURE."

[236] MatWeb, "Special Metals INCONEL® 718SPF™ Nickel Superalloy, Annealed + Aged." Accessed: Sep. 08, 2020. [Online]. Available: http://www.matweb.com/search/datasheet.aspx?matguid=8eabfa5d91954540b3f18c2d34c5dc21

[237] W. Rae, Z. Lomas, M. Jackson, and S. Rahimi, "Measurements of residual stress and microstructural evolution in electron beam welded Ti-6Al-4V using multiple techniques," *Mater Charact*, vol. 132, no. July, pp. 10–19, 2017, doi: 10.1016/j.matchar.2017.07.042.

[238] M. B. Prime and A. T. DeWald, "The Contour Method," *Practical Residual Stress Measurement Methods*, pp. 109–138, 2013, doi: 10.1002/9781118402832.ch5.

[239] M. E. Fitzpatrick, A. Fry, P. Holdway, F. a Kandil, J. Shackleton, and L. Suominen, "Measurement Good Practice Guide No. 52. Determination of Residual Stresses by X-ray Diffraction," *Measurement Good Practice Guide*, no. 2, p. 74, 2005.

[240] M. E. Fitzpatrick, A. Fry, P. Holdway, F. a Kandil, J. Shackleton, and L. Suominen, "Measurement Good Practice Guide No. 52. Determination of Residual Stresses by X-ray Diffraction," *Measurement Good Practice Guide*, no. 2, p. 74, 2005.

[241] O. Anderoglu, "Residual Stress Measurement Using X-Ray Diffraction," Texas A&M, 2004.

[242] L. J. Kumar and C. G. K. Nair, "Laser metal deposition repair applications for Inconel 718 alloy," in *Materials Today: Proceedings*, 2017, pp. 11068–11077. doi: 10.1016/j.matpr.2017.08.068.

[243] F. Calignano, D. Manfredi, E. P. Ambrosio, L. Iuliano, and P. Fino, "Influence of process parameters on surface roughness of aluminum parts produced by DMLS," *International Journal of Advanced Manufacturing Technology*, vol. 67, no. 9–12, pp. 2743–2751, 2013, doi: 10.1007/s00170-012-4688-9.

[244] J. Sun, Y. Yang, and D. Wang, "Parametric optimization of selective laser melting for forming Ti6Al4V samples by Taguchi method," *Opt Laser Technol*, vol. 49, pp. 118–124, Jul. 2013, doi: 10.1016/J.OPTLASTEC.2012.12.002.

[245] R. M. Mahamood and E. T. Akinlabi, "Processing Parameters Optimization for Material Deposition Efficiency in Laser Metal Deposited Titanium Alloy," *Lasers in Manufacturing and Materials Processing*, vol. 3, no. 1, pp. 9–21, 2016, doi: 10.1007/s40516-015-0020-5.

[246] Z. Liu, H. Kim, W. Liu, W. Cong, Q. Jiang, and H. Zhang, "Influence of energy density on macro/micro structures and mechanical properties of as-deposited Inconel 718 parts fabricated by laser engineered net shaping," *J Manuf Process*, vol. 42, pp. 96–105, Jun. 2019, doi: 10.1016/J.JMAPRO.2019.04.020.

[247] J. H. Yu, Y. S. Choi, D. S. Shim, and S. H. Park, "Repairing casting part using laser assisted additive metal-layer deposition and its mechanical properties," *Opt Laser Technol*, vol. 106, pp. 87–93, 2018, doi: 10.1016/j.optlastec.2018.04.007.

[248] M. Praniewicz, T. Kurfess, and C. Saldana, "Adaptive geometry transformation and repair for hybrid manufacturing," *Procedia Manuf*, vol. 26, pp. 228–236, 2018, doi: 10.1016/j.promfg.2018.07.031.

[249] D. Liu, J. C. Lippold, J. Li, S. R. Rohklin, J. Vollbrecht, and R. Grylls, "Laser engineered net shape (LENS) technology for the repair of Ni-base superalloy turbine components," *Metall Mater Trans A Phys Metall Mater Sci*, vol. 45, no. 10, pp. 4454–4469, 2014, doi: 10.1007/s11661-014-2397-8.

[250] X. Zhao, J. Chen, X. Lin, and W. Huang, "Study on microstructure and mechanical properties of laser rapid forming Inconel 718," *Materials Science and Engineering: A*, vol. 478, no. 1–2, pp. 119–124, Apr. 2008, doi: 10.1016/J.MSEA.2007.05.079.

[251] J. L. Bennett *et al.*, "Cooling rate effect on tensile strength of laser deposited Inconel 718," in *Procedia Manufacturing*, Elsevier B.V., 2018, pp. 912–919. doi: 10.1016/j.promfg.2018.07.118.

[252] L. Zhu, Z. F. Xu, P. Liu, and Y. F. Gu, "Effect of processing parameters on microstructure of laser solid forming Inconel 718 superalloy," *Opt Laser Technol*, vol. 98, pp. 409–415, 2018, doi: 10.1016/j.optlastec.2017.08.027.

[253] C. D. Jamieson, M. C. Brennan, T. J. Spurgeon, S. W. Brown, J. S. Keist, and E. W. Reutzel, "Tailoring alloy 718 laser directed energy deposition process strategies for repair applications," *J Laser Appl*, vol. 34, no. 1, pp. 12–18, Feb. 2022, doi: 10.2351/7.0000534.

[254] F. Soffel, D. Eisenbarth, E. Hosseini, and K. Wegener, "Interface strength and mechanical properties of Inconel 718 processed sequentially by casting, milling, and direct metal deposition," *J Mater Process Technol*, vol. 291, p. 117021, 2021, doi: 10.1016/j.jmatprotec.2020.117021.

[255] Y. Tian *et al.*, "Rationalization of microstructure heterogeneity in INCONEL 718 builds made by the direct laser additive manufacturing process," *Metall Mater Trans A Phys Metall Mater Sci*, vol. 45, no. 10, pp. 4470–4483, 2014, doi: 10.1007/s11661-014-2370-6.

[256] L. J. Kumar and C. G. K. Nair, "Laser metal deposition repair applications for Inconel 718 alloy," *Mater Today Proc*, vol. 4, no. 10, pp. 11068–11077, Jan. 2017, doi: 10.1016/J.MATPR.2017.08.068.

[257] Q. Zhang, J. Yao, and J. Mazumder, "Laser Direct Metal Deposition Technology and Microstructure and Composition Segregation of Inconel 718 Superalloy," *Journal of Iron and Steel Research International*, vol. 18, no. 4, pp. 73–78, Apr. 2011, doi: 10.1016/S1006-706X(11)60054-X.

[258] E. L. Stevens, J. Toman, A. C. To, and M. Chmielus, "Variation of hardness, microstructure, and Laves phase distribution in direct laser deposited alloy 718 cuboids," *Mater Des*, 2017, doi: 10.1016/j.matdes.2017.01.031.

[259] C. Zhong, J. Kittel, A. Gasser, and J. H. Schleifenbaum, "Study of nickel-based super-alloys Inconel 718 and Inconel 625 in high-deposition-rate laser metal deposition," *Opt Laser Technol*, vol. 109, no. August 2018, pp. 352–360, 2019, doi: 10.1016/j.optlastec.2018.08.003.

[260] M. Moradi *et al.*, "Direct Laser Metal Deposition (DLMD) Additive Manufacturing (AM)of Inconel 718 Superalloy: Elemental, Microstructural and Physical Properties Evaluation," *International Journal of Advanced Manufacturing Technology*, no. Dlmd, 2021, doi: 10.21203/rs.3.rs-455976/v1.

[261] A. N. Jinoop, C. P. Paul, S. K. Mishra, and K. S. Bindra, "Laser Additive Manufacturing using directed energy deposition of Inconel-718 wall structures with tailored characteristics," *Vacuum*, vol. 166, no. May, pp. 270–278, 2019, doi: 10.1016/j.vacuum.2019.05.027.

[262] L. Zhu, Z. Xu, and Y. Gu, "Effect of laser power on the microstructure and mechanical properties of heat treated Inconel 718 superalloy by laser solid forming," *J Alloys Compd*, vol. 746, pp. 159–167, 2018, doi: 10.1016/j.jallcom.2018.02.268.

[263] Y. Zhai, D. A. Lados, E. J. Brown, and G. N. Vigilante, "Understanding the microstructure and mechanical properties of Ti-6Al-4V and Inconel 718 alloys manufactured by Laser Engineered Net Shaping," *Addit Manuf*, vol. 27, no. February, pp. 334–344, 2019, doi: 10.1016/j.addma.2019.02.017.

[264] S. of A. Engineers, “AMS5597H - Nickel Alloy, Corrosion And Heat Resistant, Sheet, Strip, And Plate 52.5Ni - 19Cr - 3.0Mo - 5.1Cb (Nb) - 0.90Ti - 0.50Al - 18Fe Consumable Electrode Or Vacuum Induction Melted 1950 °F (1066 °C) Solution Heat Treated,” 2022.

[265] A. INTERNATIONAL, “Standard Specification for Precipitation-Hardening Nickel Alloy (UNS N07718) Plate, Sheet, and Strip for High-Temperature Service,” *Book of Standards*, vol. 02.04, 2018, doi: 10.1520/B0670-07R18.

[266] Z. Liu, X. Wang, H. Kim, Y. Zhou, W. Cong, and H. Zhang, “Investigations of Energy Density Effects on Forming Accuracy and Mechanical Properties of Inconel 718 Fabricated by LENS Process,” in *Procedia Manufacturing*, 2018. doi: 10.1016/j.promfg.2018.07.083.

[267] J. Cao, F. Liu, X. Lin, C. Huang, J. Chen, and W. Huang, “Effect of overlap rate on recrystallization behaviors of Laser Solid Formed Inconel 718 superalloy,” *Opt Laser Technol*, vol. 45, no. 1, pp. 228–235, 2013, doi: 10.1016/j.optlastec.2012.06.043.

[268] F. Liu *et al.*, “Microstructural changes in a laser solid forming Inconel 718 superalloy thin wall in the deposition direction,” *Opt Laser Technol*, vol. 45, pp. 330–335, Feb. 2013, doi: 10.1016/J.OPTLASTEC.2012.06.028.

[269] T. Wang, Y. Y. Zhu, S. Q. Zhang, H. B. Tang, and H. M. Wang, “Grain morphology evolution behavior of titanium alloy components during laser melting deposition additive manufacturing,” *J Alloys Compd*, vol. 632, pp. 505–513, May 2015, doi: 10.1016/J.JALLCOM.2015.01.256.

[270] Y. Zhang, L. Yang, W. Lu, D. Wei, T. Meng, and S. Gao, “Microstructure and elevated temperature mechanical properties of IN718 alloy fabricated by laser metal deposition,” *Materials Science and Engineering: A*, vol. 771, no. October 2019, p. 138580, Jan. 2020, doi: 10.1016/j.msea.2019.138580.

[271] D. Rosenthal, “The Theory of Moving Sources of Heat and Its Application of Metal Treatments,” *Transactions of ASME*, vol. 68, pp. 849–866, 1946.

[272] C. SAINTE-CATHERINE, M. JEANDIN, D. KECHEMAIR, J.-P. RICAUD, and L. SABATIER, “ STUDY OF DYNAMIC ABSORPTIVITY AT 10.6 µm (CO 2) AND 1.06 µm (Nd-YAG) WAVELENGTHS AS A

FUNCTION OF TEMPERATURE ," *Le Journal de Physique IV*, vol. 01, no. C7, pp. C7-151-C7-157, 1991, doi: 10.1051/jp4:1991741.

[273] C. Montgomery, J. Beuth, L. Sheridan, and N. Klingbeil, "Process mapping of Inconel 625 in laser powder bed additive manufacturing," *Proceedings - 26th Annual International Solid Freeform Fabrication Symposium - An Additive Manufacturing Conference, SFF 2015*, pp. 1195–1204, 2020.

[274] Y. S. Lee and W. Zhang, "Modeling of heat transfer, fluid flow and solidification microstructure of nickel-base superalloy fabricated by laser powder bed fusion," *Addit Manuf*, vol. 12, pp. 178–188, 2016, doi: 10.1016/j.addma.2016.05.003.

[275] V. Coen, L. Goossens, and B. Van Hooreweder, "Methodology and experimental validation of analytical melt pool models for laser powder bed fusion," *J Mater Process Technol*, vol. 304, no. August 2021, p. 117547, 2022, doi: 10.1016/j.jmatprotec.2022.117547.

[276] J. Weirather *et al.*, "A Smoothed Particle Hydrodynamics Model for Laser Beam Melting of Ni-based Alloy 718," *Computers and Mathematics with Applications*, vol. 78, no. 7, pp. 2377–2394, 2019, doi: 10.1016/j.camwa.2018.10.020.

[277] H. Yang, Z. Li, and S. Wang, "The analytical prediction of thermal distribution and defect generation of inconel 718 by selective laser melting," *Applied Sciences (Switzerland)*, vol. 10, no. 20, pp. 1–19, 2020, doi: 10.3390/app10207300.

[278] T. Huynh, "Parametric Investigation and Optimization for Inconel 718 Nickel-Based Superalloy in Laser Powder Bed Fusion," University of Central Florida, 2019.

[279] J. C. Steuben, A. J. Birnbaum, J. G. Michopoulos, and A. P. Iliopoulos, "Enriched analytical solutions for additive manufacturing modeling and simulation," *Addit Manuf*, vol. 25, no. January 2021, pp. 437–447, 2019, doi: 10.1016/j.addma.2018.10.017.

[280] M. Bayat *et al.*, "Keyhole-induced porosities in Laser-based Powder Bed Fusion (L-PBF) of Ti6Al4V: High-fidelity modelling and experimental

validation," *Addit Manuf*, vol. 30, no. April, p. 100835, 2019, doi: 10.1016/j.addma.2019.100835.

[281] W. E. King *et al.*, "Observation of keyhole-mode laser melting in laser powder-bed fusion additive manufacturing," *Journal of Materials Processing Tech.*, vol. 214, no. 12, pp. 2915–2925, 2014, doi: 10.1016/j.jmatprotec.2014.06.005.

[282] L. Wang, Y. Zhang, H. Y. Chia, and W. Yan, "Mechanism of keyhole pore formation in metal additive manufacturing," 2021, doi: 10.1038/s41524-022-00699-6.

[283] A. Aversa *et al.*, "Single scan track analyses on aluminium based powders," *J Mater Process Technol*, vol. 255, pp. 17–25, May 2018, doi: 10.1016/J.JMATPROTEC.2017.11.055.

[284] F. Wirth, D. Eisenbarth, and K. Wegener, "Absorptivity measurements and heat source modeling to simulate laser cladding," *Phys Procedia*, vol. 83, pp. 1424–1434, 2016, doi: 10.1016/j.phpro.2016.08.148.

[285] B. Liu, G. Fang, and L. Lei, "An analytical model for rapid predicting molten pool geometry of selective laser melting (SLM)," *Appl Math Model*, vol. 92, pp. 505–524, 2021, doi: 10.1016/j.apm.2020.11.027.

[286] A. R. A. Dezfoli, W. S. Hwang, W. C. Huang, and T. W. Tsai, "Determination and controlling of grain structure of metals after laser incidence: Theoretical approach," *Sci Rep*, vol. 7, no. 1, pp. 1–11, 2017, doi: 10.1038/srep41527.

[287] K. Guo, Y. Ji, Y. Li, X. Kang, H. Bai, and H. Ren, "Numerical Simulation of Temperature Field and Melt Pool Characteristics of CP-Ti Manufactured by Laser Powder Bed Fusion," *Metals (Basel)*, vol. 13, no. 1, Jan. 2023, doi: 10.3390/met13010011.

[288] A. Keshavarzkermani *et al.*, "An investigation into the effect of process parameters on melt pool geometry, cell spacing, and grain refinement during laser powder bed fusion," *Opt Laser Technol*, vol. 116, no. March, pp. 83–91, 2019, doi: 10.1016/j.optlastec.2019.03.012.

[289] X. Xiao, C. Lu, Y. Fu, X. Ye, and L. Song, "Progress on Experimental Study of Melt Pool Flow Dynamics in Laser Material Processing," in *Liquid Metals*, J. Chelladurai, S. Gnanasekaran, and S. Mayilswamy, Eds., London: InTech, 2021, p. 16.

[290] A. A. Martin *et al.*, "Ultrafast dynamics of laser-metal interactions in additive manufacturing alloys captured by in situ X-ray imaging," *Mater Today Adv*, vol. 1, p. 100002, 2019, doi: 10.1016/j.mtadv.2019.01.001.

[291] F. Bayle and M. Doubenskaia, "Selective laser melting process monitoring with high speed infra-red camera and pyrometer," SPIE, Jan. 2008, pp. 698505-698505–8. doi: 10.1117/12.786940.

[292] R. McCann *et al.*, "In-situ sensing, process monitoring and machine control in Laser Powder Bed Fusion: A review," Sep. 01, 2021, *Elsevier B.V.* doi: 10.1016/j.addma.2021.102058.

[293] S. M. Kelly, "Thermal and Microstructure Modeling of Metal Deposition Processes with Application to Ti-6Al-4V," Virginia Polytechnic Institute and State University, 2004.

[294] P. Ferro, "The Use of Matlab in Advanced Design of Bonded and Welded Joints," in *Applications of MATLAB in Science and Engineering*, Prof. Tadeusz Michalowsk, Ed., intech, 2011, ch. 19, pp. 387–408.

[295] J. T. Hofman, D. F. de Lange, B. Pathiraj, and J. Meijer, "FEM modeling and experimental verification for dilution control in laser cladding," *J Mater Process Technol*, vol. 211, no. 2, pp. 187–196, Feb. 2011, doi: 10.1016/J.JMATPROTEC.2010.09.007.

[296] American National Standards Institute., American Welding Society. D17 Committee on Welding in the Aircraft and Aerospace Industries., and American Welding Society. Technical Activities Committee., "Specification for fusion welding for aerospace applications," p. 86, 2001.

[297] International Organization for Standardization, "ISO 13919-1:2019 Electron and laser-beam welded joints — Requirements and recommendations on quality levels for imperfections," *International Standard*, 2019.

[298] I. T. Committee, “ISO 12932: Laser-arc hybrid welding of steels, nickel and nickel alloys,” vol. 2013, 2013.

[299] I. T. Committee, “BS EN ISO 6520-1:2007 Welding and allied processes — Classification of geometric imperfections in metallic materials — Part 1 Fusion welding.,” 2007.

[300] J. Ahn, “Experimental characterisation and numerical simulation of fibre laser welding of AA 2024-T3 and Ti-6Al-4V,” no. October, pp. 188–250, 2016, doi: 10.13140/RG.2.2.26191.07848.

[301] A. Mitchell, “Primary Carbides in Alloy 718,” *Superalloy 718 and Derivatives*, pp. 161–167, 2012, doi: 10.1002/9781118495223.ch11.

[302] L. Costa, R. Vilar, T. Reti, and A. M. Deus, “Rapid tooling by laser powder deposition: Process simulation using finite element analysis,” *Acta Mater*, vol. 53, no. 14, pp. 3987–3999, Aug. 2005, doi: 10.1016/J.ACTAMAT.2005.05.003.

[303] X. Lu *et al.*, “In situ measurements and thermo-mechanical simulation of Ti–6Al–4V laser solid forming processes,” *Int J Mech Sci*, vol. 153–154, no. January, pp. 119–130, 2019, doi: 10.1016/j.ijmecsci.2019.01.043.

[304] J. L. Bennett, S. J. Wolff, G. Hyatt, K. Ehmann, and J. Cao, “Thermal effect on clad dimension for laser deposited Inconel 718,” *J Manuf Process*, vol. 28, pp. 550–557, Aug. 2017, doi: 10.1016/j.jmapro.2017.04.024.

[305] V. A. Popovich, E. V. Borisov, A. A. Popovich, V. S. Sufiiarov, D. V. Masaylo, and L. Alzina, “Impact of heat treatment on mechanical behaviour of Inconel 718 processed with tailored microstructure by selective laser melting,” *Mater Des*, vol. 131, no. January, pp. 12–22, 2017, doi: 10.1016/j.matdes.2017.05.065.

[306] C. Zhong, A. Gasser, J. Kittel, K. Wissenbach, and R. Poprawe, “Improvement of material performance of Inconel 718 formed by high deposition-rate laser metal deposition,” *Mater Des*, vol. 98, pp. 128–134, 2016, doi: 10.1016/j.matdes.2016.03.006.

[307] J. Cao, F. Liu, X. Lin, C. Huang, J. Chen, and W. Huang, “Effect of overlap rate on recrystallization behaviors of Laser Solid Formed Inconel 718

superalloy," *Opt Laser Technol*, vol. 45, no. 1, pp. 228–235, 2013, doi: 10.1016/j.optlastec.2012.06.043.

[308] Y. Chen *et al.*, "Study on the element segregation and Laves phase formation in the laser metal deposited IN718 superalloy by flat top laser and gaussian distribution laser," *Materials Science and Engineering: A*, vol. 754, pp. 339–347, Apr. 2019, doi: 10.1016/J.MSEA.2019.03.096.

[309] F. Mazzucato, A. Aversa, R. Doglione, S. Biamino, A. Valente, and M. Lombardi, "Influence of process parameters and deposition strategy on laser metal deposition of 316L powder," *Metals (Basel)*, vol. 9, no. 11, pp. 11–14, 2019, doi: 10.3390/met9111160.

[310] F. Montevecchi, G. Venturini, A. Scippa, and G. Campatelli, "Finite Element Modelling of Wire-arc-additive-manufacturing Process," *Procedia CIRP*, vol. 55, pp. 109–114, 2016, doi: 10.1016/j.procir.2016.08.024.

[311] G. Fu, M. I. Lourenço, M. Duan, and S. F. Estefen, "Influence of the welding sequence on residual stress and distortion of fillet welded structures," *Marine Structures*, vol. 46, pp. 30–55, 2016, doi: 10.1016/j.marstruc.2015.12.001.

[312] B. Huang, J. Liu, S. Zhang, Q. Chen, and L. Chen, "Effect of post-weld heat treatment on the residual stress and deformation of 20/0Cr18Ni9 dissimilar metal welded joint by experiments and simulations," *Journal of Materials Research and Technology*, vol. 9, no. 3, pp. 6186–6200, 2020, doi: 10.1016/j.jmrt.2020.04.022.

[313] Trumpf, "Laser Metal Deposition (LMD)," Additive Manufacturing. Accessed: Apr. 28, 2021. [Online]. Available: https://www.trumpf.com/en_US/solutions/applications/additive-manufacturing/laser-metal-deposition-lmd/

[314] S. MSC Software, "Infosheet Meshing," 2020.

[315] S. MSC Software, "Infosheet Welding parameters," pp. 1–6, 2020.

[316] J. Ding, "Thermo-mechanical Analysis of Wire and Arc Additive Manufacturing Process," Cranfield University, 2012.

[317] G. Machina, I. Simonovski, and O. Martin, “Influence of Different Factors on Finite Element Simulation of Transient Heat Transfer Problem in Welding,” in *21st International Conference Nuclear Energy for New Europe*, Ljubljana, 2012, pp. 1–8.

[318] D. Dye, B. A. Roder, S. Tin, M. A. Rist, J. A. James, and M. R. Daymond, “Modeling and measurement of residual stresses in a forged IN718 superalloy disc,” *Proceedings of the International Symposium on Superalloys*, pp. 315–322, 2004, doi: 10.7449/2004/superalloys_2004_315_322.

[319] E. R. Denlinger and P. Michaleris, “Effect of stress relaxation on distortion in additive manufacturing process modeling,” *Addit Manuf*, vol. 12, pp. 51–59, 2016, doi: 10.1016/j.addma.2016.06.011.

[320] J. Ning, D. E. Sievers, H. Garmestani, and S. Y. Liang, “Analytical Modeling of In-Process Temperature in Powder Bed Additive Manufacturing Considering Laser Power Absorption, Latent Heat, Scanning Strategy, and Powder Packing,” *Materials*, vol. 12, no. 808, 2019, doi: 10.3390/ma12050808.

[321] H. L. Wei, G. L. Knapp, T. Mukherjee, and T. DebRoy, “Three-dimensional grain growth during multi-layer printing of a nickel-based alloy Inconel 718,” *Addit Manuf*, vol. 25, pp. 448–459, Jan. 2019, doi: 10.1016/J.ADDMA.2018.11.028.

[322] M. Biegler, B. Graf, and M. Rethmeier, “In-situ distortions in LMD additive manufacturing walls can be measured with digital image correlation and predicted using numerical simulations,” *Addit Manuf*, vol. 20, pp. 101–110, 2018, doi: 10.1016/j.addma.2017.12.007.

[323] T. R. Walker, C. J. Bennett, T. L. Lee, and A. T. Clare, “A validated analytical-numerical modelling strategy to predict residual stresses in single-track laser deposited IN718,” *Int J Mech Sci*, 2019, doi: 10.1016/j.ijmecsci.2018.12.004.

[324] T. Mukherjee, W. Zhang, and T. DebRoy, “An improved prediction of residual stresses and distortion in additive manufacturing,” *Comput Mater Sci*, vol. 126, pp. 360–372, 2017, doi: 10.1016/j.commatsci.2016.10.003.

[325] E. R. Denlinger, J. Irwin, and P. Michaleris, "Thermomechanical Modeling of Additive Manufacturing Large Parts," *J Manuf Sci Eng*, vol. 136, no. 6, p. 061007, 2014, doi: 10.1115/1.4028669.

[326] E. R. Denlinger, J. C. Heigel, P. Michaleris, and T. A. Palmer, "Effect of inter-layer dwell time on distortion and residual stress in additive manufacturing of titanium and nickel alloys," *J Mater Process Technol*, vol. 215, pp. 123–131, 2015, doi: 10.1016/j.jmatprotec.2014.07.030.

[327] H. Lee, C. H. J. Lim, M. J. Low, N. Tham, V. M. Murukeshan, and Y. J. Kim, "Lasers in additive manufacturing: A review," *International Journal of Precision Engineering and Manufacturing - Green Technology*, vol. 4, no. 3, pp. 307–322, 2017, doi: 10.1007/s40684-017-0037-7.

[328] S. M. Kelly, "Thermal and Microstructure Modeling of Metal Deposition Processes with Application to Ti-6Al-4V," Virginia Polytechnic Institute and State University, 2004. [Online]. Available: http://scholar.lib.vt.edu/theses/available/etd-11242004-211009/

[329] P. Pratt, S. D. Felicelli, L. Wang, and C. R. Hubbard, "Residual stress measurement of laser-engineered net shaping AISI 410 thin plates using neutron diffraction," *Metall Mater Trans A Phys Metall Mater Sci*, vol. 39, no. 13, pp. 3155–3163, 2008, doi: 10.1007/s11661-008-9660-9.

[330] X. He, G. Yu, and J. Mazumder, "Temperature and composition profile during double-track laser cladding of H13 tool steel," *J Phys D Appl Phys*, vol. 43, no. 1, 2010, doi: 10.1088/0022-3727/43/1/015502.

[331] P. Foteinopoulos, A. Papacharalampopoulos, and P. Stavropoulos, "On thermal modeling of Additive Manufacturing processes," *CIRP J Manuf Sci Technol*, vol. 20, pp. 66–83, 2018, doi: 10.1016/j.cirpj.2017.09.007.

[332] M. Söderberg, A. Lundbačk, and L. E. Lindgren, "Modeling of metal deposition," *Finite Elements in Analysis and Design*, vol. 47, pp. 1169–1177, 2011, doi: 10.1016/j.finel.2011.05.005.

[333] M. F. Gouge, J. C. Heigel, P. Michaleris, and T. A. Palmer, "Modeling forced convection in the thermal simulation of laser cladding processes," *International Journal of Advanced Manufacturing Technology*, vol. 79, no. 1–4, pp. 307–320, 2015, doi: 10.1007/s00170-015-6831-x.

[334] C. Hicks, "Laser Metal Deposition of the Ti-5553 Alloy on Forged Substrate for Aerospace Applications," University of Strathclyde, 2021.

[335] J. L. Bennett, S. J. Wolff, G. Hyatt, K. Ehmann, and J. Cao, "Thermal effect on clad dimension for laser deposited Inconel 718," *J Manuf Process*, 2017, doi: 10.1016/j.jmapro.2017.04.024.

[336] F. Mazzucato, A. Aversa, R. Doglione, S. Biamino, A. Valente, and M. Lombardi, "Influence of process parameters and deposition strategy on laser metal deposition of 316L powder," *Metals (Basel)*, vol. 9, no. 11, pp. 11–14, 2019, doi: 10.3390/met9111160.

[337] F. Mazzucato, D. Forni, A. Valente, and E. Cadoni, "Laser metal deposition of inconel 718 alloy and as-built mechanical properties compared to casting," *Materials*, vol. 14, no. 2, pp. 1–21, 2021, doi: 10.3390/ma14020437.

[338] G. L. Knapp, N. Raghavan, A. Plotkowski, and T. DebRoy, "Experiments and simulations on solidification microstructure for Inconel 718 in powder bed fusion electron beam additive manufacturing," *Addit Manuf*, vol. 25, pp. 511–521, Jan. 2019, doi: 10.1016/J.ADDMA.2018.12.001.

[339] Y. N. Zhang, X. Cao, and P. Wanjara, "Microstructure and hardness of fiber laser deposited Inconel 718 using filler wire," *International Journal of Advanced Manufacturing Technology*, vol. 69, no. 9–12, pp. 2569–2581, 2013, doi: 10.1007/s00170-013-5171-y.

[340] L. N. Carter *et al.*, "Process optimisation of selective laser melting using energy density model for nickel based superalloys," *Materials Science and Technology (United Kingdom)*, vol. 32, no. 7, pp. 657–661, 2016, doi: 10.1179/1743284715Y.0000000108.

[341] Y. N. Zhang, X. Cao, P. Wanjara, and M. Medraj, "Fiber laser deposition of INCONEL 718 using powders," *Materials Science and Technology Conference and Exhibition 2013, MS and T 2013*, vol. 1, no. December 2015, pp. 37–49, 2013.

[342] L. J. Kumar and C. G. K. Nair, "Laser metal deposition repair applications for Inconel 718 alloy," *Mater Today Proc*, vol. 4, no. 10, pp. 11068–11077, Jan. 2017, doi: 10.1016/J.MATPR.2017.08.068.

[343] B. Xin, J. Ren, X. Wang, L. Zhu, and Y. Gong, "Effect of Laser Remelting on Cladding Layer of Inconel 718 Superalloy Formed by Laser Metal Deposition.," *Materials (Basel)*, vol. 13, no. 21, Nov. 2020, doi: 10.3390/ma13214927.

[344] M. Moradi, A. Hasani, Z. Pourmand, and J. Lawrence, "Direct laser metal deposition additive manufacturing of Inconel 718 superalloy: Statistical modelling and optimization by design of experiments," *Opt Laser Technol*, vol. 144, Dec. 2021, doi: 10.1016/j.optlastec.2021.107380.

[345] L. Zhu, Z. F. Xu, and Y. F. Gu, "Microstructural evolution of laser solid forming Inconel 718 superalloy under different laser power," *Mater Lett*, vol. 217, pp. 159–162, 2018, doi: 10.1016/j.matlet.2018.01.099.

[346] O. Andreau *et al.*, "Texture control of 316L parts by modulation of the melt pool morphology in selective laser melting," *J Mater Process Technol*, vol. 264, no. August 2018, pp. 21–31, 2019, doi: 10.1016/j.jmatprotec.2018.08.049.

[347] C. Wang, T. G. Liu, P. Zhu, Y. H. Lu, and T. Shoji, "Study on microstructure and tensile properties of 316L stainless steel fabricated by CMT wire and arc additive manufacturing," *Materials Science and Engineering A*, vol. 796, no. July, 2020, doi: 10.1016/j.msea.2020.140006.

[348] M. Ni, S. Liu, C. Chen, R. Li, X. Zhang, and K. Zhou, "Effect of heat treatment on the microstructural evolution of a precipitation-hardened superalloy produced by selective laser melting," *Materials Science and Engineering A*, vol. 748, no. January, pp. 275–285, 2019, doi: 10.1016/j.msea.2019.01.109.

[349] C. E. Seow, H. E. Coules, G. Wu, R. H. U. Khan, X. Xu, and S. Williams, "Wire + Arc Additively Manufactured Inconel 718: Effect of post-deposition heat treatments on microstructure and tensile properties," *Mater Des*, vol. 183, p. 108157, 2019, doi: 10.1016/j.matdes.2019.108157.

[350] W. S. James, S. Ganguly, and G. Pardal, "Microstructure and Mechanical Properties of Inconel 718 and Inconel 625 Produced Through the Wire + Arc Additive Manufacturing Process," *AVT-356 Physics of Failure for Military Platform Critical Subsystems*, pp. 1–16, 2021.

[351] M. H. Farshidianfar, “Control of Microstructure in Laser Additive Manufacturing,” 2014.

[352] H. M. Singer, “Measurements of the three-dimensional shape of ice crystals in supercooled water,” *Phys Rev E Stat Nonlin Soft Matter Phys*, vol. 73, no. 5, pp. 5–8, 2006, doi: 10.1103/PhysRevE.73.051606.

[353] L.-E. Lindgren, A. Lundbäck, M. Fisk, R. Pederson, and J. Andersson, “Simulation of additive manufacturing using coupled constitutive and microstructure models,” *Addit Manuf*, vol. 12, pp. 144–158, Oct. 2016, doi: 10.1016/J.ADDMA.2016.05.005.

[354] F. Yan, W. Xiong, and E. J. Faierson, “Grain structure control of additively manufactured metallic materials,” *Materials*, vol. 10, no. 11, p. 1260, 2017, doi: 10.3390/ma10111260.

[355] M. Okugawa, Y. Ohigashi, Y. Furishiro, Y. Koizumi, and T. Nakano, “Equiaxed grain formation by intrinsic heterogeneous nucleation via rapid heating and cooling in additive manufacturing of aluminum-silicon hypoeutectic alloy,” *J Alloys Compd*, vol. 919, Oct. 2022, doi: 10.1016/j.jallcom.2022.165812.

[356] Y. Y. Zhu, H. B. Tang, Z. Li, C. Xu, and B. He, “Solidification behavior and grain morphology of laser additive manufacturing titanium alloys,” *J Alloys Compd*, vol. 777, pp. 712–716, 2019, doi: 10.1016/j.jallcom.2018.11.055.

[357] C. Hicks, T. Konkova, and P. Blackwell, “Influence of laser power and powder feed rate on the microstructure evolution of laser metal deposited Ti-5553 on forged substrates,” *Mater Charact*, vol. 170, no. February, p. 110675, 2020, doi: 10.1016/j.matchar.2020.110675.

[358] M. Gäumann, R. Trivedi, and W. Kurz, “Nucleation ahead of the advancing interface in directional solidification,” *Materials Science and Engineering A*, vol. 226–228, pp. 763–769, 1997, doi: 10.1016/s0921-5093(97)80081-0.

[359] S. Suwas, R. K. Ray, and R. K. R. Satyam Suwas, *Crystallographic Texture of Materials*. 2014. doi: 10.1007/978-1-4471-6314-5.

[360] S. M. Copley, A. F. Giamei, S. M. Johnson, and M. F. Hornbecker, "The Origin of Freckles in Unidirectionally Solidified Castings," *Metallurgical Transactions 1*, vol. 1, no. 3455, pp. 2193–2204, 1970.

[361] A. A. Antonysamy, J. Meyer, and P. B. Prangnell, "Effect of build geometry on the β-grain structure and texture in additive manufacture of Ti6Al4V by selective electron beam melting," *Mater Charact*, vol. 84, pp. 153–168, 2013, doi: 10.1016/j.matchar.2013.07.012.

[362] L. Zhan, M. Wu, and X. Qin, "Research on homogeneous nucleation and microstructure evolution of aluminium alloy melt," *R Soc Open Sci*, vol. 8, no. 8, Aug. 2021, doi: 10.1098/rsos.210501.

[363] R. J. Moat, A. J. Pinkerton, L. Li, P. J. Withers, and M. Preuss, "Crystallographic texture and microstructure of pulsed diode laser-deposited Waspaloy," *Acta Mater*, vol. 57, no. 4, pp. 1220–1229, 2009, doi: 10.1016/j.actamat.2008.11.004.

[364] J. Dutkiewicz *et al.*, "Microstructure and properties of inconel 625 fabricated using two types of laser metal deposition methods," *Materials*, vol. 13, no. 21, pp. 1–17, 2020, doi: 10.3390/ma13215050.

[365] C. M. Liu, X. J. Tian, H. B. Tang, and H. M. Wang, "Microstructural characterization of laser melting deposited Ti-5Al-5Mo-5V-1Cr-1Fe near β titanium alloy," *J Alloys Compd*, vol. 572, pp. 17–24, 2013, doi: 10.1016/j.jallcom.2013.03.243.

[366] J. Xu, Y. Ding, Y. Gao, H. Wang, Y. Hu, and D. Zhang, "Grain refinement and crack inhibition of hard-to-weld Inconel 738 alloy by altering the scanning strategy during selective laser melting," *Mater Des*, vol. 209, p. 109940, 2021, doi: 10.1016/j.matdes.2021.109940.

[367] T. Gundgire, S. Goel, U. Klement, and S. Joshi, "Response of different electron beam melting produced Alloy 718 microstructures to thermal post-treatments," *Mater Charact*, vol. 167, no. July, p. 110498, 2020, doi: 10.1016/j.matchar.2020.110498.

[368] J. Jones, M. Whittaker, R. Buckingham, R. Johnston, M. Bache, and D. Clark, "Microstructural characterisation of a nickel alloy processed via

blown powder direct laser deposition (DLD)," *Mater Des*, vol. 117, pp. 47–57, 2017, doi: 10.1016/j.matdes.2016.12.062.

[369] J. Xu, *Alloy Design and Characterization of γ' Strengthened Nickel-based Superalloys for Additive Manufacturing*. 2021. doi: 10.3384/lic.diva-173042.

[370] T. Antonsson and H. Fredriksson, "The effect of cooling rate on the solidification of INCONEL 718," *Metallurgical and Materials Transactions B*, vol. 36, no. 1, pp. 85–96, Feb. 2005, doi: 10.1007/s11663-005-0009-0.

[371] F. Liu, F. Lyu, F. Liu, X. Lin, and C. Huang, "Laves phase control of inconel 718 superalloy fabricated by laser direct energy deposition via ı aging and solution treatment," *Journal of Materials Research and Technology*, vol. 9, no. 5, pp. 9753–9765, 2020, doi: 10.1016/j.jmrt.2020.06.061.

[372] S. Sui, J. Chen, R. Zhang, X. Ming, F. Liu, and X. Lin, "The tensile deformation behavior of laser repaired Inconel 718 with a non-uniform microstructure," *Materials Science and Engineering: A*, vol. 688, pp. 480–487, Mar. 2017, doi: 10.1016/J.MSEA.2017.01.110.

[373] S. Sui, J. Chen, X. Ming, S. Zhang, X. Lin, and W. Huang, "The failure mechanism of 50% laser additive manufactured Inconel 718 and the deformation behavior of Laves phases during a tensile process," *The International Journal of Advanced Manufacturing Technology*, vol. 91, no. 5–8, pp. 2733–2740, Jul. 2017, doi: 10.1007/s00170-016-9901-9.

[374] Y. Liu, S. Zhang, C. Guo, T. Long, and J. Li, "Comparative study on CCTIG welding and PCTIG welding of GH4169 under the same heat input," *Materials Science and Technology (United Kingdom)*, vol. 38, no. 17, pp. 1451–1458, 2022, doi: 10.1080/02670836.2022.2081775.

[375] I. Tabernero, A. Lamikiz, S. Martínez, E. Ukar, and J. Figueras, "Evaluation of the mechanical properties of Inconel 718 components built by laser cladding," *Int J Mach Tools Manuf*, vol. 51, no. 6, pp. 465–470, Jun. 2011, doi: 10.1016/J.IJMACHTOOLS.2011.02.003.

[376] X. Shi, S. C. Duan, W. S. Yang, H. J. Guo, and J. Guo, "Effect of Cooling Rate on Microsegregation During Solidification of Superalloy INCONEL

718 Under Slow-Cooled Conditions," *Metallurgical and Materials Transactions B: Process Metallurgy and Materials Processing Science*, vol. 49, no. 4, pp. 1883–1897, 2018, doi: 10.1007/s11663-018-1169-z.

[377] L. L. Parimi, M. M. Attallah, J. C. Gebelin, and R. C. Reed, "Direct Laser Fabrication of Inconel-718: Effects on Distortion and Microstructure," *Superalloys 2012*, pp. 509–519, 2012, doi: 10.1002/9781118516430.ch56.

[378] A. Segerstark, J. Andersson, L.-E. Svensson, and O. Ojo, "Microstructural characterization of laser metal powder deposited Alloy 718," *Mater Charact*, vol. 142, pp. 550–559, Aug. 2018, doi: 10.1016/J.MATCHAR.2018.06.020.

[379] S. Katayama and A. Matsunawa, "Solidification Microstructure of Laser Welded Stainless Steels.," *LIA (Laser Institute of America)*, vol. 43–48, no. 1984, pp. 60–67, 1985, doi: 10.2351/1.5057623.

[380] R. G. Ding, Z. W. Huang, H. Y. Li, I. Mitchell, G. Baxter, and P. Bowen, "Electron microscopy study of direct laser deposited IN718," *Mater Charact*, vol. 106, pp. 324–337, 2015, doi: 10.1016/j.matchar.2015.06.017.

[381] Y. Gao *et al.*, "Effect of δ phase on high temperature mechanical performances of Inconel 718 fabricated with SLM process," *Materials Science and Engineering: A*, vol. 767, Nov. 2019, doi: 10.1016/j.msea.2019.138327.

[382] Y. Idell *et al.*, "Unexpected δ-Phase Formation in Additive-Manufactured Ni-Based Superalloy," *JOM*, vol. 68, no. 3, pp. 950–959, Mar. 2016, doi: 10.1007/s11837-015-1772-2.

[383] A. Segerstark, J. Andersson, L.-E. Svensson, and O. Ojo, "Microstructural characterization of laser metal powder deposited Alloy 718," *Mater Charact*, vol. 142, pp. 550–559, Aug. 2018, doi: 10.1016/J.MATCHAR.2018.06.020.

[384] J. Jang, D. Van, and S. H. Lee, "Precipitation kinetics of secondary phases induced by heat accumulation in the deposit of Inconel 718," *Addit Manuf*, vol. 55, Jul. 2022, doi: 10.1016/j.addma.2022.102831.

[385] Y. L. Kuo, S. Horikawa, and K. Kakehi, "The effect of interdendritic δ phase on the mechanical properties of Alloy 718 built up by additive manufacturing," *Mater Des*, vol. 116, pp. 411–418, Feb. 2017, doi: 10.1016/j.matdes.2016.12.026.

[386] Michael. L. Barron, "Crack Growth-Based Predictive Methodology for the Maintenance of the Structural Integrity of Repaired and Nonrepaired Aging Engine Stationary Components," Washington D.C., 1999.

[387] F. Lyu, F. Liu, X. Hu, X. Yang, C. Huang, and D. Shi, "The δ phase precipitation of an Inconel 718 superalloy fabricated by electromagnetic stirring assisted laser solid forming," *Materials*, vol. 12, no. 16, Aug. 2019, doi: 10.3390/ma12162604.

[388] H. Y. Zhang, S. H. Zhang, M. Cheng, and Z. Zhao, "Microstructure evolution of IN718 alloy during the delta process," *Procedia Eng*, vol. 207, pp. 1099–1104, Jan. 2017, doi: 10.1016/J.PROENG.2017.10.1137.

[389] X. Li *et al.*, "Effect of heat treatment on microstructure evolution of Inconel 718 alloy fabricated by selective laser melting," *J Alloys Compd*, vol. 764, pp. 639–649, 2018, doi: 10.1016/j.jallcom.2018.06.112.

[390] E. M. Fayed, D. Shahriari, M. Saadati, V. Brailovski, M. Jahazi, and M. Medraj, "Influence of homogenization and solution treatments time on the microstructure and hardness of Inconel 718 fabricated by laser powder bed fusion process," *Materials*, vol. 13, no. 11, Jun. 2020, doi: 10.3390/ma13112574.

[391] P. Li, J. Zhou, Y. Gong, X. Meng, and J. Lu, "Effect of post-heat treatment on the microstructure and mechanical properties of laser metal deposition Inconel 718," *Journal of Mechanical Science and Technology*, vol. 35, no. 7, pp. 2871–2878, Jul. 2021, doi: 10.1007/s12206-021-0610-4.

[392] W. Huang, J. Yang, H. Yang, G. Jing, Z. Wang, and X. Zeng, "Heat treatment of Inconel 718 produced by selective laser melting: Microstructure and mechanical properties," *Materials Science and Engineering A*, vol. 750, no. November 2018, pp. 98–107, 2019, doi: 10.1016/j.msea.2019.02.046.

[393] F. Liu, F. Lyu, F. Liu, X. Lin, and C. Huang, "Laves phase control of inconel 718 superalloy fabricated by laser direct energy deposition via delta aging and solution treatment," *Journal of Materials Research and Technology*, vol. 9, no. 5, pp. 9753–9765, 2020, doi: 10.1016/j.jmrt.2020.06.061.

[394] C. Kumara *et al.*, "Microstructure modelling of laser metal powder directed energy deposition of alloy 718," *Addit Manuf*, vol. 25, pp. 357–364, Jan. 2019, doi: 10.1016/J.ADDMA.2018.11.024.

[395] Y. Idell *et al.*, "Unexpected δ-Phase Formation in Additive-Manufactured Ni-Based Superalloy," *Jom*, vol. 68, no. 3, pp. 950–959, 2016, doi: 10.1007/s11837-015-1772-2.

[396] X. Li *et al.*, "Effect of heat treatment on microstructure evolution of Inconel 718 alloy fabricated by selective laser melting," *J Alloys Compd*, vol. 764, pp. 639–649, 2018, doi: 10.1016/j.jallcom.2018.06.112.

[397] X. ping Wei, W. jie Zheng, Z. gang Song, T. Lei, Q. long Yong, and Q. cheng Xie, "Strain-induced precipitation behavior of δ phase in inconel 718 alloy," *Journal of Iron and Steel Research International*, vol. 21, no. 3, pp. 375–381, 2014, doi: 10.1016/S1006-706X(14)60058-3.

[398] Y. L. Kuo, S. Horikawa, and K. Kakehi, "Effects of build direction and heat treatment on creep properties of Ni-base superalloy built up by additive manufacturing," *Scr Mater*, vol. 129, pp. 74–78, 2017, doi: 10.1016/j.scriptamat.2016.10.035.

[399] A. Chamanfar, L. Sarrat, M. Jahazi, M. Asadi, A. Weck, and A. K. Koul, "Microstructural characteristics of forged and heat treated Inconel-718 disks," *Mater Des*, vol. 52, pp. 791–800, 2013, doi: 10.1016/j.matdes.2013.06.004.

[400] Y. Desvallees, M. Bouzidi, F. Bois, and N. Beaude, "Delta Phase in INCONEL 718: Mechanical Properties and Forging Process Requirements," pp. 281–291, 2012, doi: 10.7449/1994/superalloys_1994_281_291.

[401] R. G. Thompson, J. R. Dobbs, and D. E. Mayo, "Effect of Heat Treatment on Microfissuring in Alloy 718.," *Welding Journal (Miami, Fla)*, vol. 65, no. 11, 1986.

[402] P. Tao, H. Li, B. Huang, Q. Hu, S. Gong, and Q. Xu, "The crystal growth, intercellular spacing and microsegregation of selective laser melted Inconel 718 superalloy," *Vacuum*, vol. 159, no. September 2018, pp. 382–390, 2019, doi: 10.1016/j.vacuum.2018.10.074.

[403] A. Rai, H. Helmer, and C. Körner, "Simulation of grain structure evolution during powder bed based additive manufacturing," *Addit Manuf*, vol. 13, pp. 124–134, Jan. 2017, doi: 10.1016/J.ADDMA.2016.10.007.

[404] S. Kou, *Welding Metallurgy*. Hoboken, NJ, USA: John Wiley & Sons, Inc., 2002. doi: 10.1002/0471434027.

[405] Y. J. Liang and H. M. Wang, "Origin of stray-grain formation and epitaxy loss at substrate during laser surface remelting of single-crystal nickel-base superalloys," *Mater Des*, vol. 102, pp. 297–302, 2016, doi: 10.1016/j.matdes.2016.04.051.

[406] L. Wang and N. Wang, "Effect of substrate orientation on the formation of equiaxed stray grains in laser surface remelted single crystal superalloys: Experimental investigation," *Acta Mater*, vol. 104, pp. 250–258, 2016, doi: 10.1016/j.actamat.2015.11.018.

[407] T. D. Anderson, J. N. DuPont, and T. DebRoy, "Origin of stray grain formation in single-crystal superalloy weld pools from heat transfer and fluid flow modeling," *Acta Mater*, vol. 58, no. 4, pp. 1441–1454, 2010, doi: 10.1016/j.actamat.2009.10.051.

[408] J. N. DuPont and T. D. Anderson, "Stray Grain Formation and Solidification Cracking Susceptibility of Single Crystal Ni-Base Superalloy CMSX-4," in *Hot Cracking Phenomena in Welds III*, Berlin, Heidelberg: Springer Berlin Heidelberg, 2011, pp. 429–439. doi: 10.1007/978-3-642-16864-2_22.

[409] T. D. Anderson, J. N. Dupont, and T. Debroy, "Stray grain formation in welds of single-crystal Ni-base superalloy CMSX-4," *Metall Mater Trans A Phys Metall Mater Sci*, vol. 41, no. 1, pp. 181–193, 2010, doi: 10.1007/s11661-009-0078-9.

[410] Z. J. Lou *et al.*, "Stray grain formation associated with constitutional supercooling during plasma re-melting of Ni-based single crystal superalloy based on temperature field simulation and actual substrate orientation," *J*

Alloys Compd, vol. 890, p. 161865, 2022, doi: 10.1016/j.jallcom.2021.161865.

[411] J. M. Drezet and S. Mokadem, "Marangoni Convection and Fragmentation in LASER Treatment," *Materials Science Forum*, vol. 508, pp. 257–262, Mar. 2006, doi: 10.4028/www.scientific.net/MSF.508.257.

[412] A. Gutierrez and J. C. Lippold, "A proposed mechanism for equiaxed grain formation along the fusion boundary in aluminum-copper-lithium alloys," *Welding Journal (Miami, Fla)*, vol. 77, no. 6, pp. 123-s, 1998.

[413] A. M. Rausch, J. Pistor, C. Breuning, M. Markl, and C. Körner, "New grain formation mechanisms during powder bed fusion," *Materials*, vol. 14, no. 12, pp. 12–17, 2021, doi: 10.3390/ma14123324.

[414] J. N. DuPont and T. D. Anderson, "Stray Grain Formation and Solidification Cracking Susceptibility of Single Crystal Ni-Base Superalloy CMSX-4," in *Hot Cracking Phenomena in Welds III*, Berlin, Heidelberg: Springer Berlin Heidelberg, 2011, pp. 429–439. doi: 10.1007/978-3-642-16864-2_22.

[415] L. Wang and N. Wang, "Effect of substrate orientation on the formation of equiaxed stray grains in laser surface remelted single crystal superalloys: Experimental investigation," *Acta Mater*, vol. 104, pp. 250–258, 2016, doi: 10.1016/j.actamat.2015.11.018.

[416] Y. J. Liang and H. M. Wang, "Origin of stray-grain formation and epitaxy loss at substrate during laser surface remelting of single-crystal nickel-base superalloys," *Mater Des*, vol. 102, pp. 297–302, 2016, doi: 10.1016/j.matdes.2016.04.051.

[417] J. D. Hunt, "Steady state columnar and equiaxed growth of dendrites and eutectic," *Materials Science and Engineering*, vol. 65, no. 1, pp. 75–83, 1984, doi: 10.1016/0025-5416(84)90201-5.

[418] Z. J. Lou *et al.*, "Stray grain formation associated with constitutional supercooling during plasma re-melting of Ni-based single crystal superalloy based on temperature field simulation and actual substrate orientation," *J Alloys Compd*, vol. 890, p. 161865, 2022, doi: 10.1016/j.jallcom.2021.161865.

[419] T. D. Anderson, J. N. DuPont, and T. DebRoy, "Origin of stray grain formation in single-crystal superalloy weld pools from heat transfer and fluid flow modeling," *Acta Mater*, vol. 58, no. 4, pp. 1441–1454, 2010, doi: 10.1016/j.actamat.2009.10.051.

[420] S. Mokadem, C. Bezençon, A. Hauert, A. Jacot, and W. Kurz, "Laser repair of superalloy single crystals with varying substrate orientations," *Metall Mater Trans A Phys Metall Mater Sci*, vol. 38 A, no. 7, pp. 1500–1510, 2007, doi: 10.1007/s11661-007-9172-z.

[421] M. Gäumann, S. Henry, F. Cléton, J.-D. Wagnière, and W. Kurz, "Epitaxial laser metal forming: analysis of microstructure formation," *Materials Science and Engineering: A*, vol. 271, no. 1–2, pp. 232–241, Nov. 1999, doi: 10.1016/S0921-5093(99)00202-6.

[422] Z. Lei, N. Lu, and X. Yu, "Epitaxy and new stray grain formation mechanism during epitaxial laser melting deposition of Inconel 718 on directionally solidified nickel-based superalloys," *J Manuf Process*, vol. 42, no. April, pp. 11–19, 2019, doi: 10.1016/j.jmapro.2019.04.016.

[423] R. H. Mathiesen, L. Arnberg, P. Bleuet, and A. Somogyi, "Crystal fragmentation and columnar-to-equiaxed transitions in Al-Cu studied by synchrotron X-ray video microscopy," *Metallurgical and Materials Transactions A*, vol. 37, no. 8, pp. 2515–2524, Aug. 2006, doi: 10.1007/BF02586224.

[424] B. Babu, *Mechanism-Based Flow Stress Model for Ti-6Al-4V Applicable for Simulation of Additive Manufacturing and Machinin g Material Mechanics*, no. January. 2019. doi: 10.13140/RG.2.2.12160.69128.

[425] W. Ou, G. L. Knapp, T. Mukherjee, Y. Wei, and T. DebRoy, "An improved heat transfer and fluid flow model of wire-arc additive manufacturing," *Int J Heat Mass Transf*, vol. 167, Mar. 2021, doi: 10.1016/j.ijheatmasstransfer.2020.120835.

[426] H. Yasuda *et al.*, "Direct observation of stray crystal formation in unidirectional solidification of Sn-Bi alloy by X-ray imaging," *J Cryst Growth*, vol. 262, no. 1–4, pp. 645–652, 2004, doi: 10.1016/j.jcrysgro.2003.09.052.

[427] S. Liu, S. Z. Lu, and A. Hellawell, "Dendritic array growth in the systems NH4Cl-H2O and [CH2 CN]2-H2O: The detachment of dendrite side arms induced by deceleration," *J Cryst Growth*, vol. 234, no. 4, pp. 740–750, 2002, doi: 10.1016/S0022-0248(01)01680-3.

[428] D. Ruvalcaba, R. H. Mathiesen, D. G. Eskin, L. Arnberg, and L. Katgerman, "In situ observations of dendritic fragmentation due to local solute-enrichment during directional solidification of an aluminum alloy," *Acta Mater*, vol. 55, no. 13, pp. 4287–4292, 2007, doi: 10.1016/j.actamat.2007.03.030.

[429] G. P. Dinda, A. K. Dasgupta, and J. Mazumder, "Texture control during laser deposition of nickel-based superalloy," *Scr Mater*, vol. 67, no. 5, pp. 503–506, Sep. 2012, doi: 10.1016/J.SCRIPTAMAT.2012.06.014.

[430] A. Agnoli *et al.*, "UNDERSTANDING AND MODELING OF GRAIN BOUNDARY PINNING IN INCONEL 718," 2012. [Online]. Available: https://minesparis-psl.hal.science/hal-00742033

[431] A. Agnoli, M. Bernacki, R. Logé, J. M. Franchet, J. Laigo, and N. Bozzolo, "Selective Growth of Low Stored Energy Grains During δ Sub-solvus Annealing in the Inconel 718 Nickel-Based Superalloy," *Metall Mater Trans A Phys Metall Mater Sci*, vol. 46, no. 9, pp. 4405–4421, 2015, doi: 10.1007/s11661-015-3035-9.

[432] A. Agnoli, N. Bozzolo, R. Logé, J. M. Franchet, J. Laigo, and M. Bernacki, "Development of a level set methodology to simulate grain growth in the presence of real secondary phase particles and stored energy - Application to a nickel-base superalloy," *Comput Mater Sci*, vol. 89, pp. 233–241, 2014, doi: 10.1016/j.commatsci.2014.03.054.

[433] R. R. Unocic and J. N. DuPont, "Process Efficiency Measurements in the Laser Engineered Net Shaping Process," *Metallurgical and Materials Transactions B: Process Metallurgy and Materials Processing Science*, vol. 35, no. 1, pp. 143–152, 2004, doi: 10.1007/s11663-004-0104-7.

[434] J. Xu *et al.*, "Microstructure and mechanical properties of laser-assisted epitaxial growth of nickel-based single crystal superalloys," *Journal of*

Materials Research and Technology, vol. 24, pp. 1910–1921, May 2023, doi: 10.1016/j.jmrt.2023.03.115.

[435] A. Segerstark, *Laser Metal Deposition using Alloy 718 Powder Influence of Process*, vol. 63, no. January. 2017.

[436] M. Jambor, O. Bok, F. Nový, L. Trško, and J. Belan, "Phase Transformations in Nickel base Superalloy Inconel 718 during Cyclic Loading at High Temperature," *Production Engineering Archives*, vol. 15, pp. 2013–2016, 2017.

[437] M. Anderson, A. L. Thielin, F. Bridier, P. Bocher, and J. Savoie, "δ Phase precipitation in Inconel 718 and associated mechanical properties," *Materials Science and Engineering: A*, vol. 679, pp. 48–55, Jan. 2017, doi: 10.1016/j.msea.2016.09.114.

[438] S. Mahadevan, S. Nalawade, J. B. Singh, A. Verma, B. Paul, and K. Ramaswamy, "Evolution of Delta Phase Microstructure in Alloy 718," in *7th International Symposium on Superalloy 718 and Derivatives*, 2010. Accessed: Apr. 10, 2019. [Online]. Available: https://www.tms.org/Superalloys/10.7449/2010/Superalloys_2010_737_750.pdf

[439] H. M. Lalvani, M. A. Rist, and J. W. Brooks, "Effect of delta phase on the hot deformation behaviour and microstructural evolution of inconel 718," *Adv Mat Res*, vol. 89–91, no. May 2018, pp. 313–318, 2010, doi: 10.4028/www.scientific.net/AMR.89-91.313.

[440] R. G. Ding, Z. W. Huang, H. Y. Li, I. Mitchell, G. Baxter, and P. Bowen, "Electron microscopy study of direct laser deposited IN718," *Mater Charact*, vol. 106, pp. 324–337, 2015, doi: 10.1016/j.matchar.2015.06.017.

[441] Y. Ono, T. Yuri, N. Nagashima, H. Sumiyoshi, T. Ogata, and N. Nagao, "High-cycle fatigue properties of Alloy718 base metal and electron beam welded joint," *Phys Procedia*, vol. 67, pp. 1028–1035, 2015, doi: 10.1016/j.phpro.2015.06.196.

[442] Y. Chen, K. Zhang, J. Huang, S. R. E. Hosseini, and Z. Li, "Characterization of heat affected zone liquation cracking in laser additive manufacturing of

Inconel 718," *Mater Des*, vol. 90, pp. 586–594, 2016, doi: 10.1016/j.matdes.2015.10.155.

[443] M. Qian and J. C. Lippold, "The effect of annealing twin-generated special grain boundaries on HAZ liquation cracking of nickel-base superalloys," *Acta Mater*, vol. 51, no. 12, pp. 3351–3361, 2003, doi: 10.1016/S1359-6454(03)00090-9.

[444] T. Raza, K. Hurtig, G. Asala, J. Andersson, L. E. Svensson, and O. A. Ojo, "Influence of heat treatments on heat affected zone cracking of gas tungsten arc welded additive manufactured alloy 718," *Metals (Basel)*, vol. 9, no. 8, 2019, doi: 10.3390/met9080881.

[445] E. A. Lass, M. R. Stoudt, M. B. Katz, and M. E. Williams, "Precipitation and dissolution of δ and γ″ during heat treatment of a laser powder-bed fusion produced Ni-based superalloy," *Scr Mater*, vol. 154, pp. 83–86, 2018, doi: 10.1016/j.scriptamat.2018.05.025.

[446] F. Zhang *et al.*, "Homogenization kinetics of a nickel-based superalloy produced by powder bed fusion laser sintering," *Scr Mater*, vol. 131, pp. 98–102, 2017, doi: 10.1016/j.scriptamat.2016.12.037.

[447] G. D. Janaki Ram, A. Reddy, K. Prasad Rao, G. M. Reddy, and J. K. Sarin Sundar, "Microstructure and tensile properties of Inconel 718 pulsed Nd-YAG laser welds," *J Mater Process Technol*, vol. 167, no. 1, pp. 73–82, 2005, doi: 10.1016/j.jmatprotec.2004.09.081.

[448] M. Rafiei, H. Mirzadeh, M. Malekan, and M. J. Sohrabi, "Homogenization kinetics of a typical nickel-based superalloy," *J Alloys Compd*, vol. 793, pp. 277–282, 2019, doi: 10.1016/j.jallcom.2019.04.147.

[449] M. J. Sohrabi and H. Mirzadeh, "Revisiting the Diffusion of Niobium in an As-Cast Nickel-Based Superalloy During Annealing at Elevated Temperatures," *Metals and Materials International*, vol. 26, no. 3, pp. 326–332, 2020, doi: 10.1007/s12540-019-00342-y.

[450] S. Singh, F. Hanning, and J. Andersson, "Influence of homogenisation treatments on the hot ductility of cast ATI® 718Plus®: Effect of niobium and minor elements on liquation characteristics," *Materials Science and*

Engineering A, vol. 799, no. June 2020, p. 140151, 2021, doi: 10.1016/j.msea.2020.140151.

[451] J. Spiechowicz, I. G. Marchenko, P. Hänggi, and J. Łuczka, "Diffusion Coefficient of a Brownian Particle in Equilibrium and Nonequilibrium: Einstein Model and Beyond," *Entropy*, vol. 25, no. 1, pp. 1–25, 2023, doi: 10.3390/e25010042.

[452] S. Singh, F. Hanning, and J. Andersson, "Influence of Hot Isostatic Pressing on the Hot Ductility of Cast Alloy 718: The Effect of Niobium and Minor Elements on the Liquation Mechanism," *Metall Mater Trans A Phys Metall Mater Sci*, vol. 51, no. 12, pp. 6248–6257, 2020, doi: 10.1007/s11661-020-06004-8.

[453] M. J. Sohrabi and H. Mirzadeh, "Revisiting the Diffusion of Niobium in an As-Cast Nickel-Based Superalloy During Annealing at Elevated Temperatures," *Metals and Materials International*, vol. 26, no. 3, pp. 326–332, 2020, doi: 10.1007/s12540-019-00342-y.

[454] M. Kulakov, S. Rahimi, and S. L. Semiatin, "Effect of Deformation Heating on Microstructure Evolution During Hot Forging of Ti-6Al-4V," *Metall Mater Trans A Phys Metall Mater Sci*, vol. 53, no. 2, pp. 407–419, 2022, doi: 10.1007/s11661-021-06493-1.

[455] D. A. Porter, K. E. Easterling, and K. E. Easterling, *Phase Transformations in Metals and Alloys (Revised Reprint)*. CRC Press, 2009. doi: 10.1201/9781439883570.

[456] H. Y. Zhang, S. H. Zhang, M. Cheng, and Z. Zhao, "Microstructure evolution of IN718 alloy during the delta process," in *Procedia Engineering*, Elsevier Ltd, 2017, pp. 1099–1104. doi: 10.1016/j.proeng.2017.10.1137.

[457] S. Azadian, L.-Y. Wei, and R. Warren, "Delta phase precipitation in Inconel 718," *Mater Charact*, vol. 53, no. 1, pp. 7–16, Sep. 2004, doi: 10.1016/J.MATCHAR.2004.07.004.

[458] A. Alhuzaim, S. Imbrogno, and M. M. Attallah, "Controlling microstructural and mechanical properties of direct laser deposited Inconel

718 via laser power," *J Alloys Compd*, vol. 872, p. 159588, 2021, doi: 10.1016/j.jallcom.2021.159588.

[459] C. Radhakrishna and K. Prasad Rao, "The formation and control of Laves phase in superalloy 718 welds," *J Mater Sci*, vol. 32, no. 8, pp. 1977–1984, 1997, doi: 10.1023/A:1018541915113.

[460] C. I. Garcia, A. K. Lis, E. A. Loria, and A. J. DeArdo, "Thermomechanical Processing and Continuous Cooling Transformation Behavior of IN-718," pp. 527–536, 1992, doi: 10.7449/1992/superalloys_1992_527_536.

[461] Y. Zhao, L. Hao, Q. Zhang, and W. Xiong, "Phase transformations during continuous cooling in Inconel 718 alloys manufactured by laser powder bed fusion and suction casting," *Mater Charact*, vol. 185, no. January, p. 111764, 2022, doi: 10.1016/j.matchar.2022.111764.

[462] B. Xin, J. Ren, X. Wang, L. Zhu, and Y. Gong, "Effect of Laser Remelting on Cladding Layer of Inconel 718 Superalloy Formed by Laser Metal Deposition.," *Materials (Basel)*, vol. 13, no. 21, Nov. 2020, doi: 10.3390/ma13214927.

[463] S. Zhang, L. Wang, X. Lin, H. Yang, and W. Huang, "The formation and dissolution mechanisms of Laves phase in Inconel 718 fabricated by selective laser melting compared to directed energy deposition and cast," *Compos B Eng*, vol. 239, no. May, p. 109994, 2022, doi: 10.1016/j.compositesb.2022.109994.

[464] W. Zhang *et al.*, "Additive manufacturing of metallic components – Process, structure and properties," *Prog Mater Sci*, vol. 92, pp. 112–224, 2017, doi: 10.1016/j.pmatsci.2017.10.001.

[465] J. Zhang, X. Wang, S. Paddea, and X. Zhang, "Fatigue crack propagation behaviour in wire+arc additive manufactured Ti-6Al-4V: Effects of microstructure and residual stress," *Mater Des*, vol. 90, pp. 551–561, 2016, doi: 10.1016/j.matdes.2015.10.141.

[466] E. El Shrief, A. El-Megharbel, A. El Domiaty, and H. Abd El-Hafez, "Residual stress effects on fatigue crack propagation in Butt-Welded joints for 304 stainless steel sheets," *Manuf Rev (Les Ulis)*, vol. 8, 2021, doi: 10.1051/mfreview/2021017.

[467] S. Chen, M. Guo, Y. Li, X. Dong, and J. He, "Effects of Residual Stresses on Fatigue Crack Propagation of T-Joint Using Extended Finite Element Method (XFEM)," *Metals (Basel)*, vol. 12, no. 8, 2022, doi: 10.3390/met12081368.

[468] J.-P. Kruth, J. Deckers, E. Yasa, and R. Wauthlé, "Assessing and comparing influencing factors of residual stresses in selective laser melting using a novel analysis method," *Proc Inst Mech Eng B J Eng Manuf*, vol. 226, no. 6, pp. 980–991, Jun. 2012, doi: 10.1177/0954405412437085.

[469] H. Ali, H. Ghadbeigi, and K. Mumtaz, "Effect of scanning strategies on residual stress and mechanical properties of Selective Laser Melted Ti6Al4V," *Materials Science and Engineering: A*, vol. 712, no. December 2017, pp. 175–187, 2018, doi: 10.1016/j.msea.2017.11.103.

[470] R. B. O. Acevedo, K. Kantarowska, E. C. Santos, and M. C. Fredel, "Residual stress measurement techniques for Ti6Al4V parts fabricated using selective laser melting: state of the art review," *Rapid Prototyp J*, vol. 29, no. 8, pp. 1549–1564, 2023, doi: 10.1108/RPJ-04-2019-0097.

[471] R. Acevedo, P. Sedlak, R. Kolman, and M. Fredel, "Residual stress analysis of additive manufacturing of metallic parts using ultrasonic waves: State of the art review," *Journal of Materials Research and Technology*, vol. 9, no. 4, pp. 9457–9477, 2020, doi: 10.1016/j.jmrt.2020.05.092.

[472] M. Balichakra, S. Bontha, P. Krishna, and V. K. Balla, "Prediction and validation of residual stresses generated during laser metal deposition of γ titanium aluminide thin wall structures," *Mater Res Express*, vol. 6, no. 10, 2019, doi: 10.1088/2053-1591/ab38ee.

[473] G. Vastola, G. Zhang, Q. X. Pei, and Y. W. Zhang, "Controlling of residual stress in additive manufacturing of Ti6Al4V by finite element modeling," *Addit Manuf*, vol. 12, pp. 231–239, 2016, doi: 10.1016/j.addma.2016.05.010.

[474] P. Bian, J. Shi, Y. Liu, and Y. Xie, "Influence of laser power and scanning strategy on residual stress distribution in additively manufactured 316L steel," *Opt Laser Technol*, vol. 132, no. July, p. 106477, 2020, doi: 10.1016/j.optlastec.2020.106477.

[475] L. Parry, I. Ashcroft, D. Bracket, and R. D. Wildman, “Investigation of residual stresses in selective laser melting,” *Key Eng Mater*, vol. 627, pp. 129–132, 2015, doi: 10.4028/www.scientific.net/KEM.627.129.

[476] N. C. Levkulich, S. L. Semiatin, J. E. Gockel, J. R. Middendorf, A. T. DeWald, and N. W. Klingbeil, “The effect of process parameters on residual stress evolution and distortion in the laser powder bed fusion of Ti-6Al-4V,” *Addit Manuf*, vol. 28, no. January, pp. 475–484, 2019, doi: 10.1016/j.addma.2019.05.015.

[477] C. Li, J. F. Liu, X. Y. Fang, and Y. B. Guo, “Efficient predictive model of part distortion and residual stress in selective laser melting,” *Addit Manuf*, vol. 17, pp. 157–168, 2017, doi: 10.1016/j.addma.2017.08.014.

[478] T. Simson, A. Emmel, A. Dwars, and J. Böhm, “Residual stress measurements on AISI 316L samples manufactured by selective laser melting,” *Addit Manuf*, vol. 17, pp. 183–189, 2017, doi: 10.1016/j.addma.2017.07.007.

[479] P. Bian, J. Shi, Y. Liu, and Y. Xie, “Influence of laser power and scanning strategy on residual stress distribution in additively manufactured 316L steel,” *Opt Laser Technol*, vol. 132, no. May, p. 106477, 2020, doi: 10.1016/j.optlastec.2020.106477.

[480] A. Hussein, L. Hao, C. Yan, and R. Everson, “Finite element simulation of the temperature and stress fields in single layers built without-support in selective laser melting,” *Mater Des*, vol. 52, pp. 638–647, 2013, doi: 10.1016/j.matdes.2013.05.070.

[481] I. A. Roberts, C. J. Wang, R. Esterlein, M. Stanford, and D. J. Mynors, “A three-dimensional finite element analysis of the temperature field during laser melting of metal powders in additive layer manufacturing,” *Int J Mach Tools Manuf*, vol. 49, no. 12–13, pp. 916–923, 2009, doi: 10.1016/j.ijmachtools.2009.07.004.

[482] N. Hoye, H. J. Li, D. Cuiuri, and A. M. Paradowska, “Measurement of Residual Stresses in Titanium Aerospace Components Formed via Additive Manufacturing,” *Materials Science Forum*, vol. 777, pp. 124–129, Feb. 2014, doi: 10.4028/www.scientific.net/MSF.777.124.

[483] F. Mazzucato, D. Forni, A. Valente, and E. Cadoni, "Laser metal deposition of inconel 718 alloy and as-built mechanical properties compared to casting," *Materials*, vol. 14, no. 2, pp. 1–21, 2021, doi: 10.3390/ma14020437.

[484] T. G. Gallmeyer, S. Moorthy, B. B. Kappes, M. J. Mills, B. Amin-Ahmadi, and A. P. Stebner, "Knowledge of process-structure-property relationships to engineer better heat treatments for laser powder bed fusion additive manufactured Inconel 718," *Addit Manuf*, vol. 31, no. August 2019, p. 100977, 2020, doi: 10.1016/j.addma.2019.100977.

[485] J. H. Yi *et al.*, "Effect of laser energy density on the microstructure, mechanical properties, and deformation of Inconel 718 samples fabricated by selective laser melting," *J Alloys Compd*, vol. 786, pp. 481–488, 2019, doi: 10.1016/j.jallcom.2019.01.377.

[486] T. Mukherjee, V. Manvatkar, A. De, and T. DebRoy, "Mitigation of thermal distortion during additive manufacturing," *Scr Mater*, vol. 127, pp. 79–83, 2017, doi: 10.1016/j.scriptamat.2016.09.001.

[487] G. Vastola, G. Zhang, Q. X. Pei, and Y. W. Zhang, "Controlling of residual stress in additive manufacturing of Ti6Al4V by finite element modeling," *Addit Manuf*, vol. 12, pp. 231–239, Oct. 2016, doi: 10.1016/j.addma.2016.05.010.

[488] A. V. Gusarov, M. Pavlov, and I. Smurov, "Residual stresses at laser surface remelting and additive manufacturing," *Phys Procedia*, vol. 12, no. PART 1, pp. 248–254, 2011, doi: 10.1016/j.phpro.2011.03.032.

[489] N. Hoye, H. J. Li, D. Cuiuri, and A. M. Paradowska, "Measurement of Residual Stresses in Titanium Aerospace Components Formed via Additive Manufacturing," *Materials Science Forum*, vol. 777, pp. 124–129, Feb. 2014, doi: 10.4028/www.scientific.net/MSF.777.124.

[490] N. Kouraytem *et al.*, "A recrystallization heat-treatment to reduce deformation anisotropy of additively manufactured Inconel 718," *Mater Des*, vol. 198, 2021, doi: 10.1016/j.matdes.2020.109228.

[491] Y. Zhao, K. Li, M. Gargani, and W. Xiong, "A comparative analysis of Inconel 718 made by additive manufacturing and suction casting:

Microstructure evolution in homogenization," *Addit Manuf*, vol. 36, Dec. 2020, doi: 10.1016/j.addma.2020.101404.

[492] P. Sandmann *et al.*, "Influence of laser shock peening on the residual stresses in additively manufactured 316L by Laser Powder Bed Fusion: A combined experimental–numerical study," *Addit Manuf*, vol. 60, no. PA, p. 103204, 2022, doi: 10.1016/j.addma.2022.103204.

[493] K. Gruber, R. Dziedzic, B. Kuźnicka, B. Madejski, and M. Malicki, "Impact of high temperature stress relieving on final properties of Inconel 718 processed by laser powder bed fusion," *Materials Science and Engineering: A*, vol. 813, no. January, 2021, doi: 10.1016/j.msea.2021.141111.

[494] D. Shrestha, F. Azarmi, and X. W. Tangpong, "Effect of Heat Treatment on Residual Stress of Cold Sprayed Nickel-based Superalloys," *Journal of Thermal Spray Technology*, vol. 31, no. 1–2, pp. 197–205, 2022, doi: 10.1007/s11666-021-01284-x.

[495] E. Uhlmann, J. Düchting, T. Petrat, E. Krohmer, B. Graf, and M. Rethmeier, "Effects on the distortion of Inconel 718 components along a hybrid laser-based additive manufacturing process chain using laser powder bed fusion and laser metal deposition," *Progress in Additive Manufacturing*, vol. 6, no. 3, pp. 385–394, 2021, doi: 10.1007/s40964-021-00171-9.

[496] R. Barros *et al.*, "Laser powder bed fusion of inconel 718: Residual stress analysis before and after heat treatment," *Metals (Basel)*, vol. 9, no. 12, 2019, doi: 10.3390/met9121290.

[497] P. Pagliaro *et al.*, "Measuring Inaccessible Residual Stresses Using Multiple Methods and Superposition," *Exp Mech*, vol. 51, no. 7, pp. 1123–1134, Sep. 2011, doi: 10.1007/s11340-010-9424-5.

[498] M. Scafidi, E. Valentini, and B. Zuccarello, "Error and uncertainty analysis of the residual stresses computed by using the hole drilling method," *Strain*, vol. 47, no. 4, pp. 301–312, 2011, doi: 10.1111/j.1475-1305.2009.00688.x.

[499] S. Zabeen, K. Langer, and M. E. Fitzpatrick, "Effect of texture on the residual stress response from laser peening of an aluminium-lithium alloy," *J Mater Process Technol*, vol. 251, no. April 2017, pp. 317–329, 2018, doi: 10.1016/j.jmatprotec.2017.07.032.

[500] J. Rohde and A. Jeppsson, "Literature review of heat treatment simulations with respect to phase transformation, residual stresses and distortion," *Scandinavian Journal of Metallurgy*, vol. 29, no. 2, pp. 47–62, 2000, doi: 10.1034/j.1600-0692.2000.d01-6.x.

[501] B. A. Behrens, A. Bouguecha, C. Bonk, and A. Chugreev, "Numerical and experimental investigations of the anisotropic transformation strains during martensitic transformation in a low alloy Cr-Mo steel 42CrMo4," *Procedia Eng*, vol. 207, pp. 1815–1820, 2017, doi: 10.1016/j.proeng.2017.10.944.

[502] J. Ahn, E. He, L. Chen, R. C. Wimpory, J. P. Dear, and C. M. Davies, "Prediction and measurement of residual stresses and distortions in fibre laser welded Ti-6Al-4V considering phase transformation," *Mater Des*, vol. 115, pp. 441–457, 2017, doi: 10.1016/j.matdes.2016.11.078.

[503] S. Yniesta and S. J. Brandenberg, "A Constitutive Model Controlling Damping for 2D and 3D Site Response," American Society of Civil Engineers (ASCE), Jun. 2018, pp. 17–24. doi: 10.1061/9780784481479.002.

[504] M. P. Jackson and R. C. Reed, "Heat treatment of UDIMET 720Li: The effect of microstructure on properties," *Materials Science and Engineering A*, vol. 259, no. 1, pp. 85–97, 1999, doi: 10.1016/S0921-5093(98)00867-3.

[505] D. Dye, B. A. Roder, S. Tin, M. A. Rist, J. A. James, and M. R. Daymond, "Modeling and measurement of residual stresses in a forged IN718 superalloy disc," *Proceedings of the International Symposium on Superalloys*, pp. 315–322, 2004, doi: 10.7449/2004/superalloys_2004_315_322.

[506] D. Dye, O. Hunziker, S. M. Roberts, and R. C. Reed, "Modeling of the mechanical effects induced by the tungsten inert-gas welding of the IN718 superalloy," *Metall Mater Trans A Phys Metall Mater Sci*, vol. 32, no. 7, pp. 1713–1725, 2001, doi: 10.1007/s11661-001-0149-z.

[507] S. Li, J. Li, G. Sun, and D. Deng, "Modeling of welding residual stress in a dissimilar metal butt-welded joint between P92 ferritic steel and SUS304 austenitic stainless steel," *Journal of Materials Research and Technology*, vol. 23, pp. 4938–4954, 2023, doi: 10.1016/j.jmrt.2023.02.123.

[508] O. Muránsky, C. J. Hamelin, M. C. Smith, P. J. Bendeich, and L. Edwards, "The effect of plasticity theory on predicted residual stress fields in numerical weld analyses," *Comput Mater Sci*, vol. 54, no. 1, pp. 125–134, 2012, doi: 10.1016/j.commatsci.2011.10.026.

[509] L. E. Lindgren, "Finite element modeling and simulation of welding. part 2: Improved material modeling," *Journal of Thermal Stresses*, vol. 24, no. 3, pp. 195–231, 2001, doi: 10.1080/014957301300006380.

[510] M. Biegler, A. Marko, B. Graf, and M. Rethmeier, "Finite element analysis of in-situ distortion and bulging for an arbitrarily curved additive manufacturing directed energy deposition geometry," *Addit Manuf*, vol. 24, no. August, pp. 264–272, 2018, doi: 10.1016/j.addma.2018.10.006.

[511] X. Song *et al.*, "Advances in additive manufacturing process simulation: Residual stresses and distortion predictions in complex metallic components," *Mater Des*, vol. 193, p. 108779, 2020, doi: 10.1016/j.matdes.2020.108779.

[512] M. Megahed, H. W. Mindt, N. N'Dri, H. Duan, and O. Desmaison, *Metal additive-manufacturing process and residual stress modeling*, vol. 5, no. 1. Integrating Materials and Manufacturing Innovation, 2016. doi: 10.1186/s40192-016-0047-2.

[513] X. Lu *et al.*, "Finite element analysis and experimental validation of the thermomechanical behavior in laser solid forming of Ti-6Al-4V," *Addit Manuf*, vol. 21, no. February, pp. 30–40, 2018, doi: 10.1016/j.addma.2018.02.003.

[514] E. R. Denlinger, J. C. Heigel, and P. Michaleris, "Residual stress and distortion modeling of electron beam direct manufacturing Ti-6Al-4V," *Proc Inst Mech Eng B J Eng Manuf*, vol. 229, no. 10, pp. 1803–1813, 2015, doi: 10.1177/0954405414539494.

[515] E. R. Denlinger, J. C. Heigel, P. Michaleris, and T. A. Palmer, "Effect of inter-layer dwell time on distortion and residual stress in additive manufacturing of titanium and nickel alloys," *J Mater Process Technol*, vol. 215, pp. 123–131, 2015, doi: 10.1016/j.jmatprotec.2014.07.030.

[516] E. R. Denlinger and P. Michaleris, "Effect of stress relaxation on distortion in additive manufacturing process modeling," *Addit Manuf*, vol. 12, pp. 51–59, 2016, doi: 10.1016/j.addma.2016.06.011.

[517] S. Springer *et al.*, "Implementation of a viscoplastic substrate creep model in the thermomechanical simulation of the WAAM process," *Welding in the World*, vol. 66, no. 3, pp. 441–453, 2022, doi: 10.1007/s40194-021-01232-x.

[518] S. Rahimi, M. King, and C. Dumont, "Stress relaxation behaviour in IN718 nickel based superalloy during ageing heat treatments," *Materials Science and Engineering A*, vol. 708, no. September, pp. 563–573, 2017, doi: 10.1016/j.msea.2017.09.116.

[519] L.-E. Lindgren, *Computational welding mechanics: thermomechanical and microstructructural simulations*. Woodhead Publishing in materials, 2007.

[520] MSC.Software Corporation, "Marc Volume C: Program Input," 2022.

[521] S. Rahimi, M. King, and C. Dumont, "Stress relaxation behaviour in IN718 nickel based superalloy during ageing heat treatments," *Materials Science and Engineering A*, vol. 708, no. 0, pp. 563–573, 2017, doi: 10.1016/j.msea.2017.09.116.

[522] N. Nadammal *et al.*, "Effect of hatch length on the development of microstructure, texture and residual stresses in selective laser melted superalloy Inconel 718," *Mater Des*, vol. 134, pp. 139–150, 2017, doi: 10.1016/j.matdes.2017.08.049.

[523] Z. Li, J. Chen, S. Sui, C. Zhong, X. Lu, and X. Lin, "The microstructure evolution and tensile properties of Inconel 718 fabricated by high-deposition-rate laser directed energy deposition," *Addit Manuf*, vol. 31, Jan. 2020, doi: 10.1016/j.addma.2019.100941.

[524] E. R. Denlinger, J. C. Heigel, and P. Michaleris, "Residual stress and distortion modeling of electron beam direct manufacturing Ti-6Al-4V," *Proc Inst Mech Eng B J Eng Manuf*, vol. 229, no. 10, pp. 1803–1813, 2015, doi: 10.1177/0954405414539494.

[525] J. C. Heigel, M. F. Gouge, P. Michaleris, and T. A. Palmer, “Selection of powder or wire feedstock material for the laser cladding of Inconel® 625,” *J Mater Process Technol*, vol. 231, pp. 357–365, 2016, doi: 10.1016/j.jmatprotec.2016.01.004.

[526] X. Li, M. Zhang, J. Qi, Z. Yang, and Z. Jiao, “A Simulation Study on the Effect of Residual Stress on the Multi-Layer Selective Laser Melting Processes Considering Solid-State Phase Transformation,” *Materials*, vol. 15, no. 20, 2022, doi: 10.3390/ma15207175.

[527] U. P. Singh, S. Swaminathan, and G. Phanikumar, “Thermo-mechanical approach to study the residual stress evolution in part-scale component during laser additive manufacturing of alloy 718,” *Mater Des*, vol. 222, p. 111048, 2022, doi: 10.1016/j.matdes.2022.111048.

[528] MSC.Software Corporation, “Marc Volume C: Program Input,” 2022.

[529] E. R. Denlinger, “Thermo-mechanical model development and experimental validation for metallic parts in additive manufacturing,” *The Pennsylvania State University*, p. 231, 2015.

[530] D. Qiao and Y. Wang, “Modeling of Weld Residual Plastic Strain and Stress in,” in *Pressure Vessels and Piping Conference*, 2016, pp. 1–8.

Appendices

Appendix A Welding quality acceptance criteria from Ahn, AWS D17.1:2001 and BS EN ISO13919-1-2019 (t=thickness, l=length of imperfection, s=weld penetration, d=maximum size of imperfection) [296], [297], [300]

	AWS D17.1:2001			BS EN ISO 13919-1:2019		
Imperfection	Class A	Class B	Class C	Level D	Level C	Level B
Cracks	Reject	Reject	Reject	Reject	Reject	Reject
Incomplete Fusion	Reject	Reject	Reject	L ≤0.25 s or 1mm, whichever is smaller	Reject	Reject
Incomplete Penetration	Reject	Reject	Reject	Short imperfections: l≤0.25s or 1mm, whichever is smaller	Reject	Reject
Porosity	0.33t or 1.5mm, whichever smaller	0.5t or 2.3mm, whichever smaller	N/A	D ≤0.3s, but max 3mm	D≤0.2s, but max 2mm*[12932]	Reject
Porosity Spacing	4x larger adjacent pore	2 x larger adjacent pore	N/A	N/A	N/A	N/A
Undercut	0.5mm	0.015t or 0.005mm, whichever smaller	0.025t or 0.05mm, whichever smaller	h≤0.15t, max 1mm	h≤0.1t, max 0.5mm	h≤0.05t, max 0.5mm
Underfill, Concavity or Shrinkage Groove	0.13mm	0.015t or 0.13mm, whichever greater	0.025t or 0.13mm, whichever greater	h≤0.3t, max 1mm	h≤0.2t, max 0.5mm	h≤0.1t, max 0.5mm
Excess Weld Metal or Penetration	0.033t or 0.76mm, whichever greatest	N/A	N/A	h≤0.02mm + 0.3t or 5mm, whichever smallest	h≤0.02mm + 0.2t or 5mm, whichever smallest	h≤0.02mm + 0.15t or 5mm, whichever smallest

Appendix B Mesh Description for mesh sensitivity study

	Mesh 1	***Mesh 2***	***Mesh 3***	***Mesh 4***
X direction	8 constant sized elements for Zone 1 and Single Deposit 13 Constant sized elements for Zone 2 4 Elements for Zone 3	10 constant sized elements for Zone 1 and Single Deposit 20 Constant sized elements for Zone 2 4 Elements in Zone 3	12 constant sized elements for Zone 1 and Single Deposit 24 Constant sized elements for Zone 2 4 Elements in Zone 3	14 constant sized elements for Zone 1 and Single Deposit 30 Constant sized elements for Zone 2 4 Elements in Zone 3
Y direction	30 constant sized elements for Zone 1 and Single Deposit 25 elements in Zones 2 and 3	60 constant sized elements for Zone 1 and Single Deposit 25 elements in Zones 2 and 3	120 constant sized elements for Zone 1 and Single Deposit 25 elements in Zones 2 and 3	180 constant sized elements for Zone 1 and Single Deposit 25 elements in Zones 2 and 3
Z direction	3 constant sized elements for Single Deposit 11 Constant sized elements for Zone 2 6 Elements for Zone 3	4 constant sized elements for Single Deposit 14 Constant sized elements for Zone 2 6 Elements for Zone 3	5 constant sized elements for Single Deposit 20 Constant sized elements for Zone 2 6 Elements for Zone 3	6 constant sized elements for Single Deposit 28 Constant sized elements for Zone 2 6 Elements for Zone 3
Total Element Number	720 elements in Single Deposition 13718 elements in substrate	2400 elements in Single Deposition 42840 elements in substrate	7200 elements in Single Deposition 112575 elements in substrate	15120 elements in Single Deposition 197914 elements in substrate
DOF for linear elements (Node Count)	16452	49786	128596	225400

Appendix C Experimental data and numerically adjusted values for the hyperbolic law parameters for stress relaxation *[518]*

Temperature (°C)	Initial Strain (%)	Initial stress (σ_0) (10^6 Pa)	Asymptotic Stress (σ_∞) (10^6 Pa)	Numerically Adjusted Parameters		
				m	a (s)	b (10^9 S.I. unit)
620	0.5	459	202	0.79±0.2	440±26	2.34
	1.1	491	215	0.71±0.3	135±23	2.15
	2.1	506	229	0.72±0.2	347±24	1.95
670	0.5	553	203	0.64±0.1	200±10	1.27
	1.1	582	223	0.65±0.1	121±5	1.02
	2.1	598	258	0.66±0.1	210±3	1.43
720	0.5	542	169	0.63±0.1	80±5	0.74
	1.1	702	244	0.64±0.1	121±4	1.11
	2.1	714	243	0.64±0.1	115±3	1.1
770	0.5	476	109	0.62±0.2	160±15	1.28
	1.1	672	115	0.59±0.2	200±12	1.2
	2.1	696	120	0.6±0.1	178±10	0.9

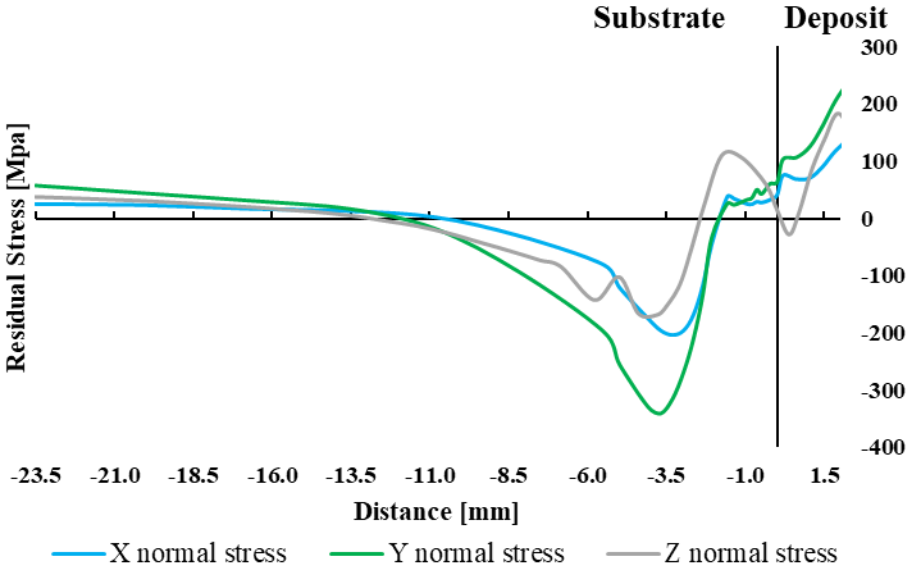

Appendix D Extrapolated stress data for X,Y and Z normal directions for the dashed line in Figure 8.15

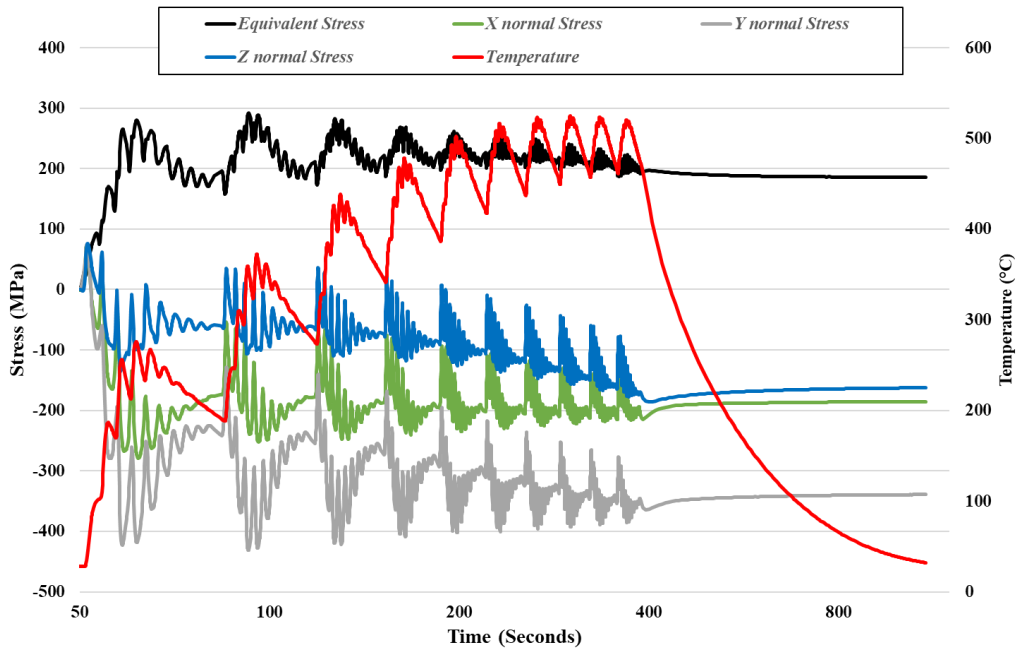

Appendix E Extracted data from the 950W thermomechanical model (creep considered) for the top third of substrate region (P1) depicting the stress vs time vs temperature graph.

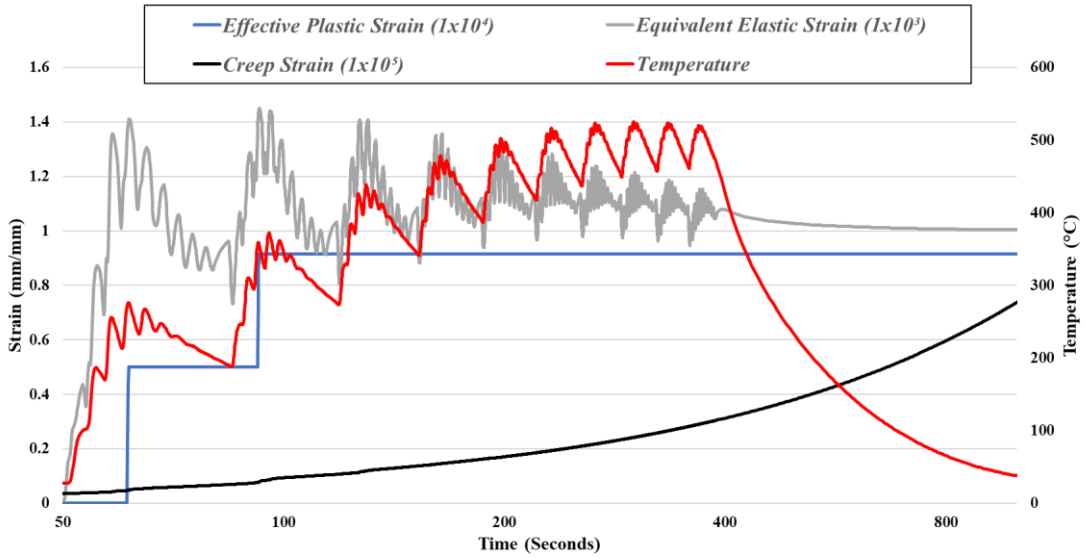

Appendix F Extracted data from the 950W thermomechanical model (creep considered) for the top third of substrate region (P1) depicting the effective plastic strain, equivalent elastic strain and creep strain vs time vs temperature.

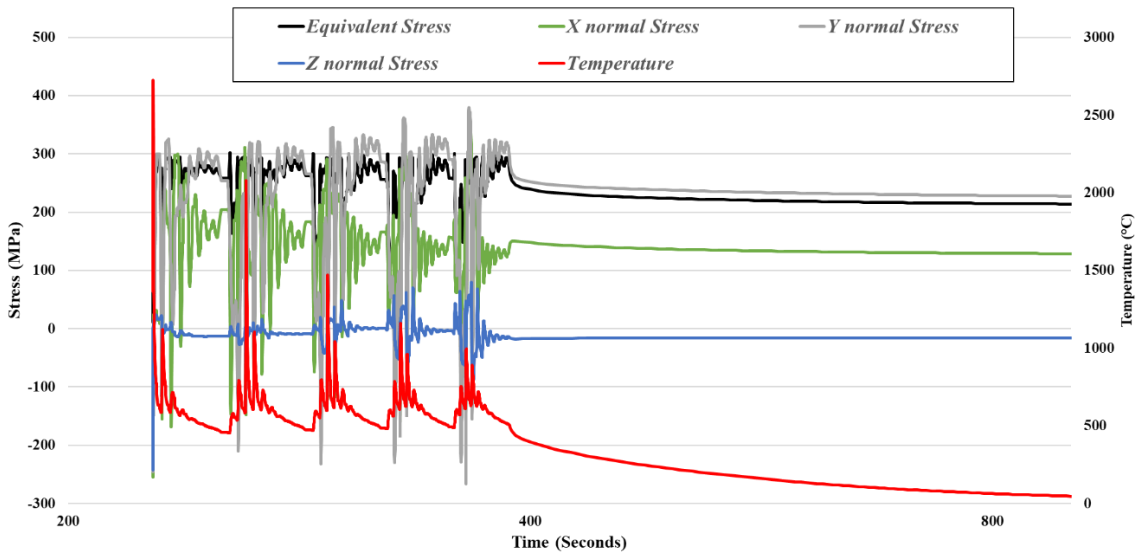

Appendix G Extracted data from the 950W thermomechanical model (creep considered) for the deposited mid-build substrate region (P3) depicting the stress vs time vs temperature graph.

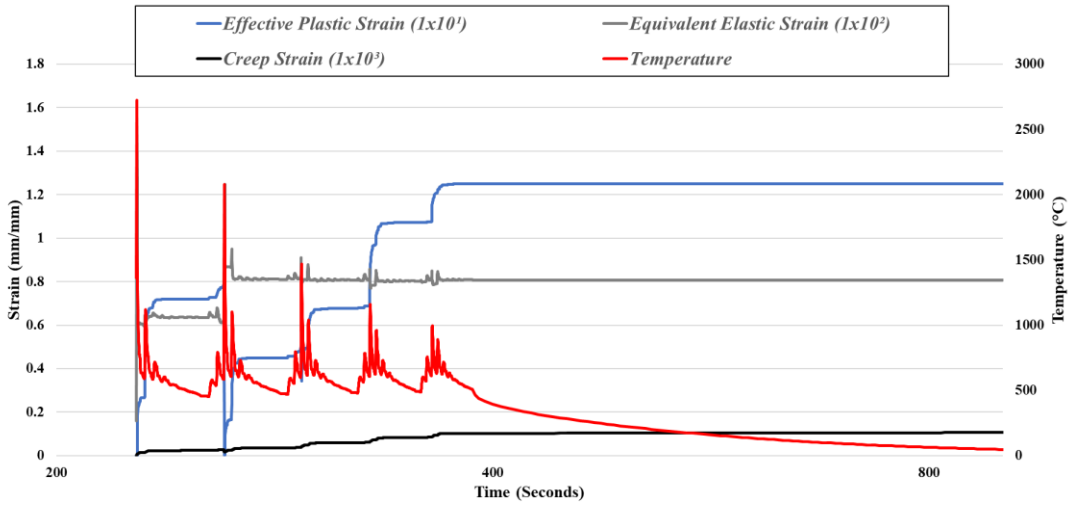

Appendix H Extracted data from the 950W thermomechanical model (creep considered) for the deposited mid-build substrate region (P3) depicting the effective plastic strain, equivalent elastic strain and creep strain vs time vs temperature.

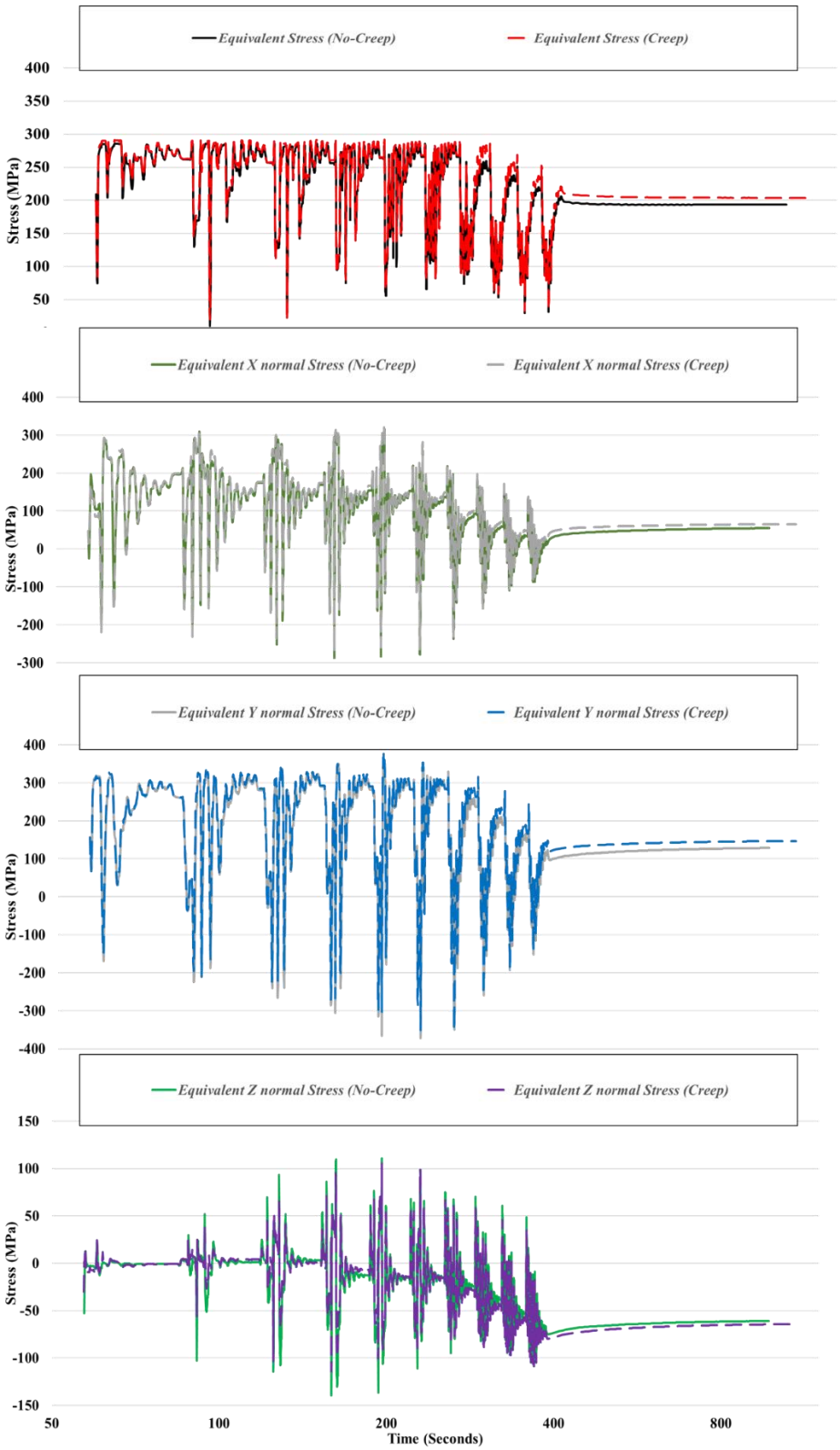

Appendix I Extracted data from the 950W thermomechanical model comparing creep vs non-creep for the interface region (P2) depicting the stress vs time vs temperature graph.

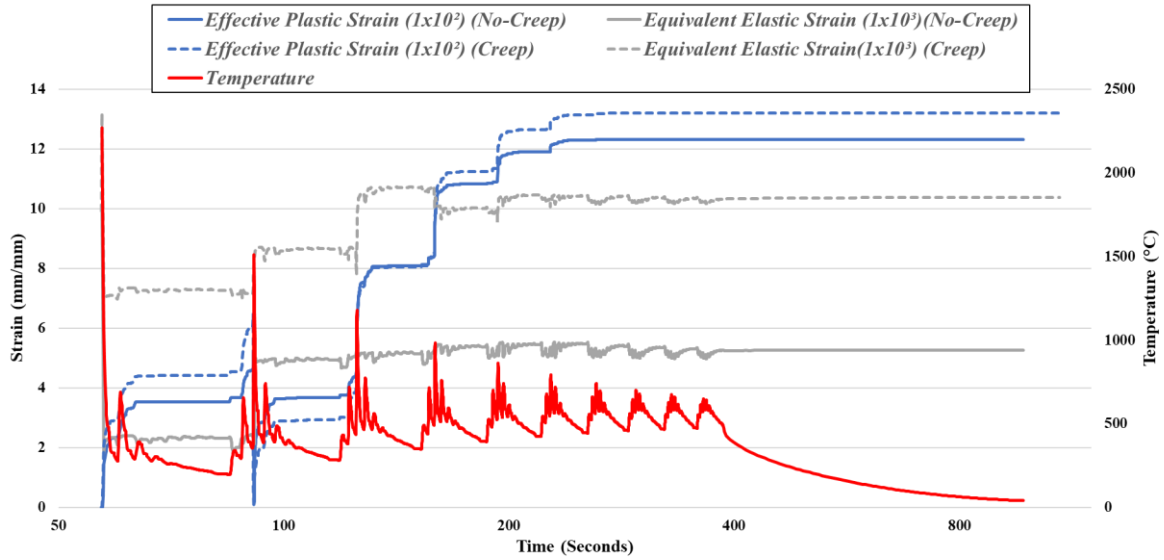

Appendix J Extracted data from the 950W thermomechanical model comparing creep vs non-creep for the interface region (P2) depicting the effective plastic strain, equivalent elastic strain and creep strain vs time vs temperature.